Karel Pacak
David Taïeb   *Editors*

Diagnostic and Therapeutic Nuclear Medicine for Neuroendocrine Tumors

Humana Press

Contemporary Endocrinology

Series Editor
Leonid Poretsky
Division of Endocrinology
Lenox Hill Hospital
New York, New York, USA

More information about this series at http://www.springer.com/series/7680

Karel Pacak • David Taïeb
Editors

Diagnostic and Therapeutic Nuclear Medicine for Neuroendocrine Tumors

Humana Press

Editors
Karel Pacak
Section on Medical Neuroendocrinology
Eunice Kennedy Shriver NICHD, NIH
Bethesda, Maryland, USA

David Taïeb
Department of Nuclear Medicine
Aix-Marseille University
Marseille, France

Series Editor Foreword

Neuroendocrine tumors often present challenging diagnostic and therapeutic dilemmas. I am therefore delighted to introduce our readers to this sorely needed volume. I am certain that it will be extremely useful to endocrinologists, both in training and in practice, as well as to the students and practitioners of nuclear medicine. Drs. Pacak and Taïeb assembled a superb international "crew" of authors, each of whom is an expert in the field. The topics covered in the book go well beyond the imaging and therapy issues, as the classification, genetics, and metabolism of endocrine tumors are addressed in detail.

The interdisciplinary nature of the book is of particular value as endocrinologists, nuclear medicine physicians, and other specialists, who commonly work together taking care of patients with neuroendocrine tumors, share their knowledge and experience on its pages. Undoubtedly, the physicians in all relevant specialties will enjoy reading *Diagnostic and Therapeutic Nuclear Medicine for Neuroendocrine Tumors* and will keep referring to this text as they are presented with new cases. The ultimate beneficiaries of this volume will be our patients.

New York, NY, USA   Leonid Poretsky, MD

Preface

The glory of medicine is that it is constantly moving forward, that there is always more to learn.
Dr. William Mayo (1928)

Diagnostic and Therapeutic Nuclear Medicine for Neuroendocrine Tumors provides readers with the most updated approaches regarding endocrine tumor-specific functional imaging, which is tightly linked to therapy in the evolving era of precision medicine.

Two years ago, we thought about what was missing from the field of neuroendocrine tumors. We soon realized that precision medicine-related diagnostic imaging was becoming fundamental for neuroendocrine tumor management, radiotherapy, and follow-up, but it had not been well-summarized or presented to clinicians or other healthcare professionals of various subspecialties. In writing this book, we were further supported by novel pathogenesis-related genetic discoveries and the introduction of new radiopharmaceuticals that further secured and bolstered the unique and irreplaceable position of precision imaging and therapies of these tumors. Due to their unique cellular characteristics, it would even appear that neuroendocrine tumors were born to be imaged. These tumors take up hormone precursors; synthesize, store, and release hormones in specific ways; express tumor-specific transporters and receptors; and, finally, contain specific gene mutations – all of which can be used to design personalized imaging and therapies. Thus, it is not surprising that each of the above characteristics demonstrates how radionuclide imaging of these tumors can provide a window into their cellular metabolism, uptake and storage of hormones, expression of receptors and transporters, gene expression and their signaling pathways, gene delivery and vector kinetics, tissue perfusion, and oxygenation and respiration, as well as DNA and protein synthesis. *In vivo* histology and molecular imaging nicely reflect the power of radionuclide imaging, both currently and in the near future.

This book covers important, well-connected components of neuroendocrine tumors, including their classification of neuroendocrine tumors; molecular genetics of gastroenteropancreatic and multiple endocrine neoplasia type 1 and

type 2 neuroendocrine tumors, pheochromocytoma, and neuroblastoma; principles of SPECT/CT, PET/CT, and PET/MR and dosimetry principles and application to neuroendocrine tumors; molecular imaging of neuroendocrine tumors in the era of personalized medicine; metabolomics of pheochromocytoma and paraganglioma; radionuclide imaging of pheochromocytoma and paraganglioma, gastrointestinal, pancreatic, pulmonary and thymic neuroendocrine tumors, and medullary thyroid carcinoma; radiotherapies of neuroendocrine tumors using ^{131}I-metaiodobenzylguanidine, somatostatin receptors therapies, alpha radionuclide therapy, and nanoparticles for radionuclide imaging and therapy.

The value of this book is further enhanced by the participation of well-recognized contributors in the field of neuroendocrine tumors and their radiotherapies. Their long-term expertise, dedication to clinical and basic research, and excellence in patient care serves as a guarantee that this book will satisfy the most demanding experts and readers in the field of clinical medicine. All of the authors in this book have worked extremely diligently to provide our readers with not only their personal views of how to approach these tumors but also with the views of their respected colleagues who represent neuroendocrine tumors and have contributed to moving this field ahead. We are very thankful to them for their extraordinary work and contributions.

We are extremely thankful for the support we received from Springer, especially from Mr. Kristopher Spring and Mr. Karthik Periyasamy, who not only assisted us initially, but continued their guidance throughout the entire process by always being available for questions and offering their valuable comments and suggestions. Additionally, we would like to thank Katherine Wolf for her assistance with preparation and book assembly.

Finally, we would like to thank our wives, Michaela and Palma, for their love, support, and understanding that while writing this book, we were often kept very busy and away from them.

On behalf of all the authors, we hope you enjoy this book, and find it practical and well-informed on the current diagnostic and therapeutic approaches to neuroendocrine tumors. First and foremost, we hope you will be able to use this to aid those who suffer most – our patients.

Bethesda, MD, USA   Karel Pacak
Marseille, France   David Taïeb

Contents

Contributors

Sunita K. Agarwal, PhD National Institutes of Health, NIDDK, Metabolic Diseases Branch, Bethesda, MD, USA

Valentina Ambrosini, MD, PhD Nuclear Medicine, DIMES, Alma Mater Studiorum University of Bologna, S. Orsola-Malpighi Hospital, Bologna, Italy

Ananda Appavoo Research Engineer, Université de Bordeaux, Bordeaux, France
INSERM U1212, UMR CNRS 5320, Bordeaux, France

Samuel Backman, MB Experimental Surgery, Department of Surgical Sciences, Uppsala University, Uppsala University Hospital, Uppsala, Sweden

Philippe Barthélémy, PhD Université de Bordeaux, Bordeaux, France
INSERM U1212, UMR CNRS 5320, Bordeaux, France

Peyman Björklund, MD, PhD Experimental Surgery, Department of Surgical Sciences, Uppsala University, Uppsala University Hospital, Uppsala, Sweden

Jorge A. Carrasquillo, MD Molecular Imaging and Therapy Service, Department of Radiology, Memorial Sloan Kettering Cancer Center, New York, NY, USA

Alberto Cascón, PhD Hereditary Endocrine Cancer Group, Spanish National Cancer Research Centre (CNIO), Madrid, Spain

Maria Currás-Freixes, MD Hereditary Endocrine Cancer Group, Spanish National Cancer Research Centre (CNIO), Madrid, Spain

Christophe M. Deroose, MD, PhD Nuclear Medicine, University Hospitals Leuven, and Department of Imaging & Pathology, KU Leuven, Leuven, Belgium

Uta Eberlein, Dr. rer. nat Klinik und Poliklinik für Nuklearmedizin, Universitätsklinikum Würzburg, Würzburg, Germany

Graeme Eisenhofer, PhD Institute of Clinical Chemistry and Laboratory Medicine, University Hospital Carl Gustav Carus, Medical Faculty Carl Gustav Carus, Technische Universität Dresden, Dresden, Germany

Melpomeni Fani, PhD Division of Radiopharmaceutical Chemistry, Clinic of Radiology and Nuclear Medicine, University Hospital of Basel, Basel, Switzerland

Stefano Fanti, MD Nuclear Medicine, DIMES, Alma Mater Studiorum University of Bologna, S. Orsola-Malpighi Hospital, Bologna, Italy

Karin Frank-Raue, MD Endocrine Practice, Molecular Laboratory, Heidelberg, Germany

Luca Giovanella, MD, PhD Department of Nuclear Medicine, PET/CT and Thyroid Centre, Oncology Institute of Southern Switzerland, Bellinzona, Switzerland

Bernard Goichot, MD, PhD Internal Medicine Department, Hautepierre Hospital, University Hospitals of Strasbourg, Strasbourg, France

Michel Hesse, PhD Laboratory of Molecular Imaging and Experimental Radiotherapy, Catholic University of Louvain, Brussels, Belgium

Elif Hindié, MD, PhD Nuclear Medicine Department, Haut-Lévêque Hospital, CHU Bordeaux, University of Bordeaux, Pessac, France

LabEx TRAIL, University of Bordeaux, Bordeaux, France

Michael S. Hofman, MBBS, FRACP, FAANMS Centre for Molecular Imaging, Peter MacCallum Cancer Centre, Melbourne, Australia

Sir Peter MacCallum Department of Oncology, The University of Melbourne, Melbourne, Australia

Ioannis Ilias, MD, PhD Endocrine Unit, Elena Venizelou Hospital, Athens, Greece

Alessio Imperiale, MD, PhD Biophysics and Nuclear Medicine Department, Hautepierre Hospital, University Hospitals of Strasbourg, Strasbourg, France

ICube, University of Strasbourg, Strasbourg, France

Frediano Inzani, MD, PhD Institute of Pathology, Università Cattolica – Fondazione Policlinico Universitario Agostino Gemelli, Rome, Italy

Francois Jamar, MD, PhD Laboratory of Molecular Imaging and Experimental Radiotherapy, Catholic University of Louvain, Brussels, Belgium

Ingo Janssen, MD Section on Medical Neuroendocrinology, Eunice Kennedy Shriver National Institute of Child Health and Human Development (NICHD), National Institutes of Health (NIH), Bethesda, MD, USA

Sellam Karunanithi, MD, FANMB Department of Nuclear Medicine, Aster MIMS Hospital, Malabar Institute of Medical Sciences Ltd, Calicut, Kerala, India

Sybille Kennel, PhD Université de Bordeaux, Bordeaux, France

CNRS, INCIA, UMR 5287, Talence, France

Ganesh Kumar, MD Division of Diagnostic Nuclear Medicine, Department of Nuclear Medicine, All India Institute of Medical Sciences, AIIMS Campus, New Delhi, India

Rakesh Kumar, MD, PhD Division of Diagnostic Nuclear Medicine, Department of Nuclear Medicine, All India Institute of Medical Sciences, New Delhi, India

Michael Lassmann, Dr. rer. nat Klinik und Poliklinik für Nuklearmedizin, Universitätsklinikum Würzburg, Würzburg, Germany

Zhihui Liu, PhD National Cancer Institute, Bethesda, MD, USA

Yusuf Menda, MD Department of Radiology, University of Iowa Carver College of Medicine, Iowa City, IA, USA

Georgios Meristoudis, MD Department of Nuclear Medicine, Hippokration Hospital, Thessaloniki, Greece

M. Sue O'Dorisio, MD, PhD Department of Pediatrics, University of Iowa Carver College of Medicine, Iowa City, IA, USA

Thomas O'Dorisio, MD Department of Internal Medicine, University of Iowa Carver College of Medicine, Iowa City, IA, USA

Karel Pacak, MD, PhD, DSc, FACE Section on Medical Neuroendocrinology, Developmental Endocrine Oncology and Genetics Affinity Group, Eunice Kennedy Shriver National Institute of Child Health and Human Development, National Institutes of Health, Bethesda, MD, USA

Arnoldo Piccardo, MD Department of Nuclear Medicine, Galliera Hospital, Genoa, Italy

Janet Pollard, MD Department of Radiology, University of Iowa Carver College of Medicine, Iowa City, IA, USA

Friedhelm Raue, MD Endocrine Practice, Molecular Laboratory, Heidelberg, Germany

Endokrinologisch, Nuklearmedizinische Praxis, Heidelberg, Germany

Susan Richter, PhD Institute of Clinical Chemistry and Laboratory Medicine, University Hospital Carl Gustav Carus, Medical Faculty Carl Gustav Carus, Technische Universität Dresden, Dresden, Germany

Guido Rindi, MD, PhD Institute of Pathology, Università Cattolica – Fondazione Policlinico Universitario Agostino Gemelli, Rome, Italy

Mercedes Robledo, PhD Hereditary Endocrine Cancer Group, Spanish National Cancer Research Centre (CNIO), Madrid, Spain

Jürgen Schulz Research Engineer, Université de Bordeaux, Bordeaux, France

CNRS, INCIA, UMR 5287, Talence, France

David Taïeb, MD, PhD Department of Nuclear Medicine, La Timone University Hospital, CERIMED, European Center for Research in Medical Imaging, Aix-Marseille University, Marseille, France

Carol J. Thiele, PhD National Cancer Institute, Bethesda, MD, USA

Henri J. L. M. Timmers, MD, PhD Department of Internal Medicine, Section of Endocrinology (471), Radboud University Medical Centre, Nijmegen, The Netherlands

Giorgio Treglia, MD, MSc (HTA) Department of Nuclear Medicine, PET/CT and Thyroid Centre, Oncology Institute of Southern Switzerland, Bellinzona, Switzerland

Arthur Varoquaux, MD, PhD Department of Medical Imaging, Conception Hospital, Aix-Marseille University, Marseille, France

Stephen Walrand, PhD Laboratory of Molecular Imaging and Experimental Radiotherapy, Catholic University of Louvain, Brussels, Belgium

Chapter 1
Classification of Neuroendocrine Neoplasms

Frediano Inzani and Guido Rindi

1.1   Generalities

Neuroendocrine neoplasms (NENs) are classified variably according to their site of origin. Clinically relevant NENs are found in the pituitary, the sympathetic and parasympathetic ganglia, the skin, the thyroid, the parathyroid, the adrenals and all visceral organs including the respiratory tract, the thymus, the gastroenteropancreatic tract, the biliary tree, the kidney, the bladder, the prostate, the uterus, and the gonads. No wonder that a common classification scheme was not developed and presently does not exist. The current and different classifications can be found organized according to anatomical site in the blue books collection that the World Health Organization (WHO) dedicates to this topic, now in its fourth edition for most sites [1–8]. So the first adjective that well describes such tumor disease is "complex," given the diverse site-related nature of the NENs.

The second connoting attribute is "rare." NENs are indeed uncommon cancers and generally stand in the single-digit cancer incidence zone. All cancers that do not exceed the age-adjusted incidence of 15/100,000 new cases per year in the USA are considered as rare, while in EU the threshold is at <6/100,000 new cases per year [9, 10]. Indeed as an example, the lung and gastroenteropancreatic (GEP) NENs account for about six new age-adjusted cases per 100,000 persons per year in western countries [11–13], a value well below the threshold for rare cancers in the

F. Inzani • G. Rindi (✉)
Institute of Pathology, Università Cattolica – Fondazione Policlinico Universitario Agostino Gemelli, Largo A. Gemelli, 8, 00168 Rome, Italy
e-mail: guido.rindi@unicatt.it

USA and at the upper limit for the EU. The rarity of NENs made difficult the collection of significant case cohorts so that evidence-based data on most aspects on NENs are overall lacking or feeble. Nonetheless the incremental incidence trend demonstrated in recent years in most countries [13] called increased attention on NENs [11, 12].

The third denoting adjective is "diverse." NENs are invariably and in fact different under a multiplicity of aspects including risk factors, incidence, hormone/mediator production, clinical significance, and aggressiveness. All such aspects are strictly site dependent, the anatomical site of insurgence probably being per se the most important determinant of all such features. In brief it is expected that NENs also follow the general rules of regular cancer at specific anatomical sites. And this applies for complex systems like the digestive apparatus where all single portions of the gut and associated glands display significantly different neuroendocrine cancer behavior. Following are just few examples of site-specific rules:

(i) In the brain, the general concept dictating that a small brain lesion results in big effects/deficits on the whole body applies to intracranial NENs as well when, for instance, a small functioning hyperplastic/neoplastic lesion of the anterior pituitary produces unregulated levels of ACTH resulting in a potentially devastating Cushing syndrome.
(ii) In the lung, cigarette smoking is the most important risk factor for cancer, and this is true for both the regular cancer and the high-grade NEN small cell carcinoma.
(iii) In the digestive tract and pancreas, NEN hormone production is highly segregated at specific sites, and this is reflected in NEN cell components and hyperfunction when present, though with rare possible exceptions [14].

Altogether, the connoting aspects of complexity, rarity, and diversity make NENs difficult to tackle for diagnosis, therapy, and basic and clinical investigation.

1.2 Definition and Common Classification Features

NENs may be defined as neoplasms made by transformed cells producing hormone/mediators and characterized by the shared expression of some neural-specific antigens. This broad definition necessarily embraces neoplasms arising in nerve structures (e.g., ganglia and paraganglia), in pure endocrine organs (e.g., pituitary, thyroid, parathyroid, adrenal), and in the so-called diffuse (neuro)endocrine system at different organs (Fig. 1.1).

It is well understood that NENs largely retain the specific and peculiar antigen asset of the organ or structure where they originate. Briefly, this means that a paraganglioma arising in the lung or the digestive tract usually does not express
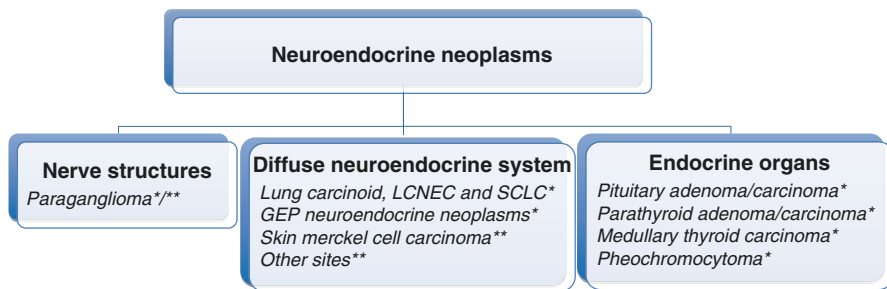
Fig. 1.1 Types of neuroendocrine neoplasms according to structure, system or organ of insurgence. *LCNEC* large cell neuroendocrine carcinoma, *SCLC* small cell lung carcinoma, *GEP* gastroenteropancreatic tract. World Health Organization classification of tumors – blue book series; *: digestive system (2010) [4]; lung, pleura, thymus, and heart (2015) [7]; endocrine organs (2004) [1]; **: head and neck (2005) [2]; female reproductive organs (2014) [6]; breast (2012) [5]; urinary system and male genital organs (WHO 2016) [8]; skin (2006) [3]

epithelial markers of differentiation (e.g., cytokeratin) while retaining vimentin expression, a broad marker of mesenchymal signature. Vice versa, cytokeratin expression is usually retained in NENs arising in the anterior pituitary, the lung, the gut, the pancreas, and the endocrine organs. As expected for cancer, exceptions do exist and may confuse this relatively simple rule though are relatively well described in the mentioned WHO pathology reference blue books.

The shared neural antigen expression refers to the so-called general markers of neuroendocrine differentiation which include the membrane-associated neural adhesion molecule (N-CAM, CD56), the cytosol-associated markers neuron-specific enolase (NSE) and PGP 9.5, the large dense core vesicle (LDCV)-associated chromogranins (including the most popular chromogranin A), and the small synaptic-like vesicle (SSV)-associated synaptophysin [14]. All these antigens are known to have variable degrees of specificity and sensitivity in NENs that should be taken into due account for diagnostic purposes. In addition, the so-called specific markers of neuroendocrine differentiation are also found in NENs, though with a tissue-specific distribution that reflects the distribution of the normal cell counterpart [14]. As exemplification the expression of insulin identifies the beta cell of the islets of the pancreas and is almost invariably expressed only in NEN arising in the pancreas, mostly functioning and thus defined as insulinomas. Again rare exceptions of non-pancreatic insulinomas do exist [15].

NENs have a typical morphology, no matter their site of origin and their name (Fig. 1.2). The structure is "organoid" with either trabecular, acinar, glandular components that may be variably represented and admixed. The tumor cells are usually monomorphic with variably represented either polygonal epithelial-like or fusiform mesenchymal-like types, low or almost undetectable mitotic activity and low proliferation fraction as measured by Ki-67 index. These morphological aspects are consistent with a well-differentiated morphology, usually also defining a low-grade
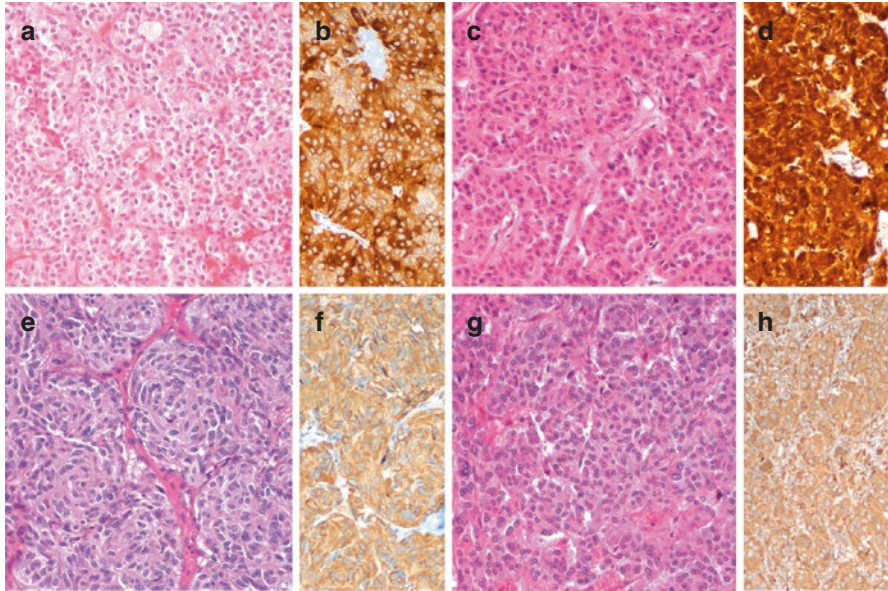
Fig. 1.2 Morphology of low-grade, well-differentiated NEN in pituitary (**a**, prolactin-producing adenoma, **b** prolactin immunoreactivity), thyroid (**c**, calcitonin-producing medullary thyroid carcinoma, **d** calcitonin immunoreactivity), lung (**e**, typical carcinoid, **f** chromogranin **A** immunoreactivity), and adrenal (**g**, pheochromocytoma, **h** chromogranin A immunoreactivity). **a**, **c**, **e**, **g** hematoxylin and eosin; **b**, **d**, **f** and **h** immunoperoxidase

NEN. In some specific anatomical location and, namely, in the adrenal and other paraganglia, NEN cells may display abnormal features that are unequivocally identified as severe atypia, though always with low mitotic and Ki-67 indexes. Such aspects are considered as regressive features and are known possible exception to the usual, typical morphology. The bland features and low proliferation activity of the majority of NENs are the morphological counterpart of their bland clinical behavior which makes NENs slow-pace malignant neoplasms with fairly long/ excellent prognosis.

A consistent fraction of NENs are still characterized by organoid structure though with more solid aspects, moderate cell atypia with detectable mitotic activity or proliferation fraction by Ki-67 (Fig. 1.3) and possible necrosis though in focal spots. These aspects connote what has been variably defined as atypical NENs. The atypical morphology of NENs may often be accompanied by other standard aggressive feature including invasion of vessels and perineural spaces as well as of surrounding structures, suggesting a potentially different (more aggressive) clinical behavior. This morphology, though largely overlapping the well-differentiated morphology of the typical NEN, probably identifies a condition of well to moderate differentiation and usually defines NENs of intermediate grade. Indeed it is now well understood
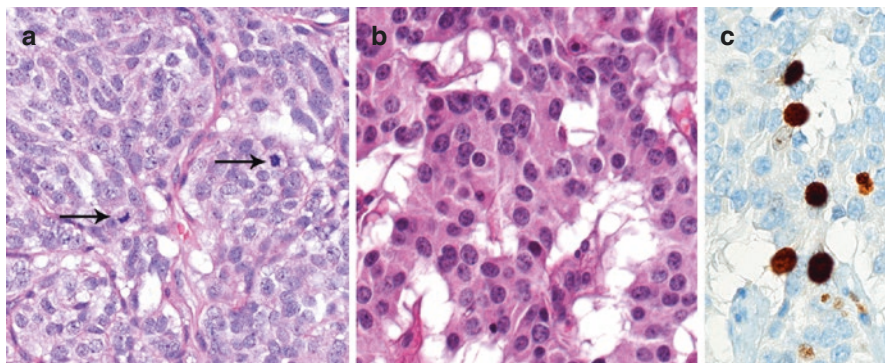
Fig. 1.3 Morphology of low-/intermediate-grade, well-intermediately differentiated NEN in lung (**a**, atypical carcinoid; note the mitoses [*arrows*]) and pancreas (**b**, neuroendocrine tumor; Ki-67 16 % corresponding to a NET G2). **a**, **b** hematoxylin and eosin; **c** immunoperoxidase

that for some anatomical site (e.g., the respiratory system and the digestive tract and pancreas), increased proliferation activity either measured by mitotic count or Ki-67 proliferation index with or without overt atypical morphology associates with still relatively slow-pace but surely more aggressive clinical behavior [16, 17].

Finally a fraction of NENs, usually small at most sites but quite frequent in the lung, display very aggressive morphological features, characterized by sort of organoid but prevalently solid structure with large areas of necrosis, often defined as geographical chart necrosis, and severe cell atypia with brisk mitotic activity, atypical mitoses, and elevated proliferation fraction by Ki-67 (Fig. 1.4). Cell types are either of small type with little cytoplasm and fine nuclear chromatin or large type with abundant cytoplasm, spotted chromatin, and prominent nucleoli. These morphological features are quite different from the typical and, at large extent also, the atypical NEN morphology, are consistent with poor tumor cell differentiation, and are usually defined high-grade NENs. Their clinical behavior is invariably highly malignant and the prognosis is very poor.

Overall such morphological features would describe three steps of NEN cancer aggressiveness better defined as grades and as such identified in the lung and the digestive tract and pancreas. This is a common theme for NENs overall, although the presence and incidence of each of such three types is quite variable and different at different anatomical location (Table 1.1). In addition, when solely considering morphology, it appears that two NEN cancer types are probably represented, one including the NENs with typical and atypical morphology that are both rather close each other and a second one with poorly differentiated morphology, rather different versus typical and atypical NENs. Clinical and morphological features connecting morphologically typical and atypical NENs are certainly evident, easily observed, and relatively frequent. By converse clinical and morphological features blending morphologically atypical and poorly differentiated NENs are rare.
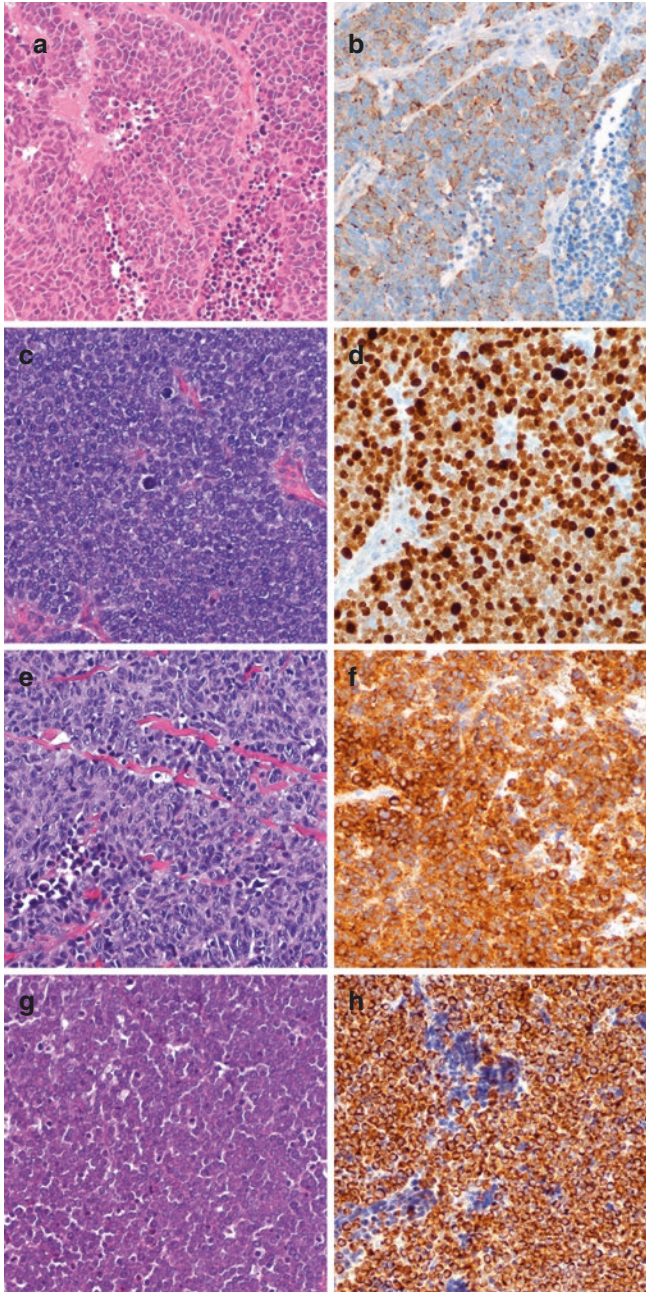
Fig. 1.4 Morphology of high-grade poorly differentiated NEN in lung (**a**, small cell carcinoma, **b** chromogranin A immunoreactivity), stomach (**c**, small cell carcinoma, **d** Ki-67 nuclear immunoreactivity), bladder (**e**, small cell carcinoma, SmCC **f** synaptophysin immunoreactivity), skin (**g**, small cell carcinoma, **h** cytokeratin 20 immunoreactivity). **a**, **c**, **e**, **g** hematoxylin and eosin; **b**, **d**, **f**, **h** immunoperoxidase

Table 1.1 Neuroendocrine neoplasm definitions according to the current WHO classifications

Anatomical site	Classification definitions			Classification reference
	Low grade		High grade	
	Well differentiated	*Moderately differentiated*[a]	Poorly differentiated	
Pituitary	*Typical adenoma* (monomorph, rare mitoses, low Ki-67)	*Atypical adenoma* (invasive growth, high mitoses and Ki-67; no metastases) *Pituitary carcinoma* (atypical features; metastasis)	nd	WHO classification of Tumors of Endocrine Organs 2004
Thyroid	*Medullary thyroid carcinoma*		nd	WHO classification of Tumors of Endocrine Organs 2004
Parathyroid	*Adenoma* (encapsulated neoplasm, usually single gland) *carcinoma* (invasion of vessels, perineural space, capsule, adjacent tissues and/or metastases)		nd	WHO classification of Tumors of Endocrine Organs 2004
Lung and thymus	*Typical carcinoid* (carcinoid morphology and <2 mitoses/2 mm²; no necrosis)	*Atypical carcinoid* (carcinoid morphology and 2–10 mitoses/2 mm² and/or necrosis)	*Small cell lung carcinoma* (*SCLC*) *Large cell NE carcinoma* (*LCNEC*) (small or large cells; >10 mitoses/2 mm² and necrosis)	WHO classification of Tumors of Lung, Pleura, Thymus, and Heart 2015
Digestive tract and pancreas	*NE tumor – NET G1* (mitotic count < 2/10HPF and Ki-67 ≦2 %)	*NE Tumor – NET G2* (mitotic count 2–20/10HPF and/or Ki-67 3–20%)	*NE carcinoma – NEC G3* (*Small or Large cell*) (mitotic count >20/10HPF and/or Ki-67 >20%)	WHO classification of Tumors of the Digestive System 2010
Head and neck	*Typical carcinoid*	*Atypical carcinoid*	*Small cell carcinoma NE type* (*SCCNET*)	WHO classification of Tumors of Head and Neck 2005
Adrenal and extra-adrenal paraganglia	*Benign pheochromocytoma* and *extra-adrenal paraganglioma* *Malignant pheochromocytoma* and *paraganglioma* (metastatic)		nd	WHO classification of Tumors of Endocrine Organs 2004

(continued)

Table 1.1 (continued)

Anatomical site	Classification definitions			Classification reference
Skin	nd		*Merkel cell carcinoma*	WHO classification of Tumors of Skin 2006
Female genital organs	*Low-grade NE tumor G1*	*Low-grade NE tumor G2*	*High-grade NE carcinoma G3* (small and large cell type)	WHO classification of Female Reproductive Organs tumors 2015
Breast	*NE tumor*		*NE carcinoma* (small cell carcinoma)	WHO classification of Tumors of Breast tumors 2012
Urinary system and male genital organs	*Typical carcinoid*	*Atypical carcinoid*	*NE carcinoma* (large and small cell carcinoma [SmCC])	WHO classification of Tumors of Urinary System and Male Genital Tract Tumors 2016

nd not described, *WHO* World Health Organization, *NE* neuroendocrine
[a]Questioned

1.3 The Current Classifications of NENs at Different Anatomical Sites

Below are reported in brief the current classifications for selected anatomical sites. For a complete description of NEN cancer types, the reader should refer to the quoted WHO blue books.

1.3.1 Pituitary

The current classification of pituitary NENs identifies adenomas, typical and atypical, and pituitary carcinoma with proven metastases [1]. Proliferation assessment especially with Ki-67 has been proposed and is used in clinical practice though has not gained a formal definition in an official classification. No high-grade, poorly differentiated NEN has been described. Rare, embryonic-type pituitary blastomas of the infancy are a very aggressive neuroendocrine-type cancer that may assimilate high-grade NENs at other anatomical sites [18].

1.3.2   Head and Neck (Nasal Cavity, Hypopharynx, Larynx, and Trachea)

The current classification of NENs in nasal cavity, hypopharynx, larynx, and trachea is similar to that applied for the lung and thymus [2]. Typical carcinoid (TC), atypical carcinoid (AC), and small cell carcinoma of neuroendocrine type (SCCNET) are identified and correspond to three formal grades. Mitotic count is indicated to separate TC versus AC similar to the lung NEN though higher values are allowed for AC as compared to the lung. Rare non-chromaffin paragangliomas are also included.

1.3.3   Parathyroid

The current classification of parathyroid NENs identifies parathyroid adenoma and carcinoma with proven invasive behavior and metastases [1]. As for other anatomical sites, mitotic count as well Ki-67 index proved of some utility though did not reach consensus and clinical utility to be formalized in a grading classification. No high-grade NEN is described.

1.3.4   Thyroid

The current classification of thyroid NENs identifies the medullary thyroid carcinoma (MTC) and rare paragangliomas [1]. At least 12 variants of MTC are described including the encapsulated variant equalized to C-cell adenoma and the small cell variant, suggesting that low- and high-grade MTC may indeed exist [19, 20]. A formal definition of histological grade in MTC is lacking.

1.3.5   Lung and Thymus

The current classification of NENs identifies typical carcinoid, atypical carcinoid, large cell neuroendocrine carcinoma (LCNEC), and small cell lung carcinomas (SCLC) [7]. The classification is based on morphology, presence of necrosis and proliferation assessed by mitotic count. The four morphological categories translate into three grades of clinical aggressiveness, with higher grade being poorly differentiated carcinomas either with small (for SCLC) or large cell type features (for LCNEC) [17]. The highest incidence is observed for the SCLC, while LCNEC, carcinoid (either typical or atypical), is definitely less frequent. Rare other NENs may occur also including pulmonary paragangliomas.

1.3.6 Digestive Tract and Pancreas

The current classification of NENs identifies neuroendocrine tumors (NET) of low to intermediate grade (G1 and G2) and neuroendocrine carcinoma (NEC) by definition of high grade (G3) [4]. The classification is based on morphology and proliferation assessed by mitotic count and Ki-67 index [21]. The three morphological categories display three grades of clinical aggressiveness, G3 equalizing to poorly differentiated carcinomas either with small or large cell types [22, 23]. Recently also neoplasms with NET morphology and high-grade (G3) proliferation index have been described and defined as NET G3 [24–28]. NET G3 displays an intermediate clinical aggressiveness more similar to NET G2 than to NEC. Data on large series are needed to confirm these observations. In pancreas and gut, high-grade NECs are a minor NEN fraction, at specific sites (namely, small intestine and appendix) being extremely rare [24–28]. Rare paragangliomas are found in the digestive tract and pancreas too, in the duodenum with relatively higher incidence and defined as gangliocytic paraganglioma [4].

1.3.7 Adrenals and Extra-Adrenal Paraganglia

The current classification identifies chromaffin adrenal neoplasms as NENs and includes the benign and malignant pheochromocytoma [1]. Scoring systems are applied and require the assessment of multiple parameters including proliferation index by Ki-67 and mitotic count that define different risk grades. Nonetheless no consensus today exists and a formal grade classification is lacking. No high-grade NEN is described.

1.3.8 Urinary System and Male Genital Organs

NENs are described in the kidney, the urinary system, prostate, and testis, the latter one within teratoma of prepuberal type [8]. Low-grade well-differentiated neuroendocrine tumors (defined as carcinoid, typical, and atypical) and high-grade poorly differentiated neuroendocrine carcinoma (defined as large cell neuroendocrine carcinoma and small cell carcinoma [SmCC]) are included. The use of mitotic count or Ki-67 proliferation for risk assessment in not formalized as recently proposed [29]. Rare pheochromocytomas (chromaffin paragangliomas) are also included.

1.3.9 Female Genital Organs

NENs of the ovary (arising from a dermoid cyst), the uterine corpus, cervix, and vulva adopt overall the same terminology and three tier system devised for the digestive tract and pancreas [6]. There is however no formal use of Ki-67 index or

mitotic count for risk assessment. In the ovary the term carcinoid is preferential. Rare paragangliomas are also described in the ovary and the vagina.

1.3.10 Breast

NENs are defined as "carcinomas with neuroendocrine differentiation" and include both well-differentiated neuroendocrine tumors of low- and intermediate-grade and high-grade poorly differentiated/small cell carcinoma [5]. No formal grading is defined.

1.3.11 Skin

Classified in the neural tumors section, the only NEN neoplasm described is the Merkel cell carcinoma [3]. This is a rare cancer equalizing the high-grade, poorly differentiated, small cell type neuroendocrine carcinoma described at most other anatomical sites. No low-grade NEN counterparts are described in the skin.

1.4 Concluding Remarks

NENs are found at any site of the body and are characterized by shared morphological and behavioral aspects. Common themes can be perceived through the differences invariably characterizing NENs at different anatomical locations. The current classifications are historical, derive from the progression of knowledge for each site-specific NEN, and, in many instances, lack a clear definition of risk for the different NEN types identified. A common classification system is however emerging at many sites at least with shared terminology. In the near future, efforts should be put in place to agree on definitions and to generate data at different anatomical sites for grading risk assessment.

References

1. DeLellis RA, Lloyd RV, Heitz PU, Eng C. Pathology and genetics of tumours of endocrine organs. 3rd ed. World Health Organization classification of tumours. Lyon: IARC Press; 2004.
2. Barnes L, Eveson JW, Reichart P, Sidransky D. Pathology and genetics of tumours of head and neck. 3rd ed. World Health Organization classification of tumours. Lyon: IARC Press; 2005.

3. LeBoit PE, Burg G, Weedon D, Sarasain A. Pathology and genetics of skin tumours. 3rd ed. World Health Organization classification of tumours. Lyon: IARC Press; 2006.

4. Bosman F, Carneiro F, Hruban RH, Theise ND. Pathology and genetics of tumours of the digestive system. 4th ed. World Health Organization classification of tumours. Lyon: IARC Press; 2010.

5. Lakhani SR, Ellis IO, Schnitt SJ, Tan PH, van de Vijver MJ. Pathology and genetics of tumours of the breast. 4th ed. World Health Organization Classification of tumours. Lyon: IARC Press; 2012.

6. Kurman RJ, Carcangiu ML, Herrington CS, Young RH. Pathology and genetics of tumours of female reproductive organs. 4th ed. World Health Organization classification of tumours. Lyon: IARC Press; 2014.

7. Travis WD, Brambilla E, Burke AP, Marx A, Nicholson AG. Pathology and genetics of tumours of the lung, pleura, thymus and heart. 4th ed. World Health Organization classification of tumours. Lyon: IARC Press; 2015.

8. Moch H, Humphrey PA, Ulbright TM, Reuter VE. Pathology and genetics of tumours of the urinary system and male genital organs. 4th ed. World Health Organization classification of tumours. Lyon: IARC Press; 2016.

9. RareCancersEurope. http://www.rarecancerseurope.org/About-Rare-Cancers.

10. Howard J. Rare Cancers. 2014. http://www.cdc.gov/wtc/pdfs/WTCHP_PP_RareCancers05052014.pdf.

11. Modlin IM, Oberg K, Chung DC, Jensen RT, de Herder WW, Thakker RV, et al. Gastroenteropancreatic neuroendocrine tumours. Lancet Oncol. 2008;9(1):61–72. doi:10.1016/S1470-2045(07)70410-2.

12. Modlin IM, Moss SF, Chung DC, Jensen RT, Snyderwine E. Priorities for improving the management of gastroenteropancreatic neuroendocrine tumours. J Natl Cancer Inst. 2008;100(18):1282–9. doi:10.1093/jnci/djn275.

13. Hallet J, Law CH, Cukier M, Saskin R, Liu N, Singh S. Exploring the rising incidence of neuroendocrine tumours: a population-based analysis of epidemiology, metastatic presentation, and outcomes. Cancer. 2015;121(4):589–97. doi:10.1002/cncr.29099.

14. Rindi G, Wiedenmann B. Neuroendocrine neoplasms of the gut and pancreas: new insights. Nat Rev Endocrinol. 2012;8(1):54–64. doi:10.1038/nrendo.2011.120.

15. La Rosa S, Pariani D, Calandra C, Marando A, Sessa F, Cortese F, et al. Ectopic duodenal insulinoma: a very rare and challenging tumour type. Description of a case and review of the literature. Endocr Pathol. 2013;24(4):213–9. doi:10.1007/s12022-013-9262-y.

16. Rindi G, Falconi M, Klersy C, Albarello L, Boninsegna L, Buchler MW, et al. TNM staging of neoplasms of the endocrine pancreas: results from a large international cohort study. J Natl Cancer Inst. 2012;104(10):764–77. doi:10.1093/jnci/djs208.

17. Rindi G, Klersy C, Inzani F, Fellegara G, Ampollini L, Ardizzoni A, et al. Grading the neuroendocrine tumours of the lung: an evidence-based proposal. Endocr Relat Cancer. 2014;21(1):1–16. doi:10.1530/ERC-13-0246.

18. Scheithauer BW, Horvath E, Abel TW, Robital Y, Park SH, Osamura RY, et al. Pituitary blastoma: a unique embryonal tumour. Pituitary. 2012;15(3):365–73. doi:10.1007/s11102-011-0328-x.

19. Kodama T, Okamoto T, Fujimoto Y, Obara T, Ito Y, Aiba M, et al. C cell adenoma of the thyroid: a rare but distinct clinical entity. Surgery. 1988;104(6):997–1003.

20. Eusebi V, Damiani S, Riva C, Lloyd RV, Capella C. Calcitonin free oat-cell carcinoma of the thyroid gland. Virchows Arch A Pathol Anat Histopathol. 1990;417(3):267–71.

21. Rindi G, Arnold R, Capella C, Klimstra DS, Klöppel G, Komminoth P, et al. Nomenclature and classification of digestive neuroendocrine tumours. In: Bosman F, Carneiro F, editors. World Health Organization classification of tumours, pathology and genetics of tumours of the digestive system. Lyon: IARC Press; 2010. p. 10–2.

22. Rindi G, Kloppel G, Alhman H, Caplin M, Couvelard A, de Herder WW, et al. TNM staging of foregut (neuro)endocrine tumours: a consensus proposal including a grading system. Virchows Arch. 2006;449(4):395–401. doi:10.1007/s00428-006-0250-1.
23. Rindi G, Kloppel G, Couvelard A, Komminoth P, Korner M, Lopes JM, et al. TNM staging of midgut and hindgut (neuro) endocrine tumours: a consensus proposal including a grading system. Virchows Arch. 2007;451(4):757–62. doi:10.1007/s00428-007-0452-1.
24. Velayoudom-Cephise FL, Duvillard P, Foucan L, Hadoux J, Chougnet CN, Leboulleux S, et al. Are G3 ENETS neuroendocrine neoplasms heterogeneous? Endocr Relat Cancer. 2013;20(5):649–57. doi:10.1530/ERC-13-0027.
25. Sorbye H, Welin S, Langer SW, Vestermark LW, Holt N, Osterlund P, et al. Predictive and prognostic factors for treatment and survival in 305 patients with advanced gastrointestinal neuroendocrine carcinoma (WHO G3): The NORDIC NEC study. Ann Oncol Off J Eur Soc Med Oncol/ESMO. 2013;24:152–60. doi:10.1093/annonc/mds276.
26. Hijioka S, Hosoda W, Mizuno N, Hara K, Imaoka H, Bhatia V, et al. Does the WHO 2010 classification of pancreatic neuroendocrine neoplasms accurately characterize pancreatic neuroendocrine carcinomas? J Gastroenterol. 2015;50(5):564–72. doi:10.1007/s00535-014-0987-2.
27. Basturk O, Yang Z, Tang LH, Hruban RH, Adsay V, McCall CM, et al. The high-grade (WHO G3) pancreatic neuroendocrine tumour category is morphologically and biologically heterogenous and includes both well differentiated and poorly differentiated neoplasms. Am J Surg Pathol. 2015;39(5):683–90. doi:10.1097/PAS.0000000000000408.
28. Heetfeld M, Chougnet CN, Olsen IH, Rinke A, Borbath I, Crespo G, et al. Characteristics and treatment of patients with G3 gastroenteropancreatic neuroendocrine neoplasms. Endocr Relat Cancer. 2015;22(4):657–64. doi:10.1530/ERC-15-0119.
29. Epstein JI, Amin MB, Beltran H, Lotan TL, Mosquera JM, Reuter VE, et al. Proposed morphologic classification of prostate cancer with neuroendocrine differentiation. Am J Surg Pathol. 2014;38(6):756–67. doi:10.1097/PAS.0000000000000208.

Chapter 2
Molecular Genetics of Pheochromocytoma and Paraganglioma

Mercedes Robledo, Maria Currás-Freixes, and Alberto Cascón

2.1 Inherited Pheochromocytomas and Paragangliomas

Pheochromocytomas (PCCs) and paragangliomas (PGLs), together abbreviated as PPGL, are neural crest-derived catecholamine-secreting tumors arising from the adrenal medulla and sympathetic/parasympathetic paraganglia, respectively. These tumors can develop in an apparently sporadic manner or as part of one of several tumoral syndromes associated with alterations in distinct genes. Particularly in the latter case, PPGLs can present with other pathologies within a family and even in the same individual. This variable clinical phenotype is reflection of the genetic complexity that underlies the development of this disease (Fig. 2.1).

While initially it was thought that only 10 % of cases were caused by germline mutations, the discovery of mutations in several additional susceptibility genes during the last 15 years has brought the percentage of hereditary cases up to approximately 40 %. Genes such as *VHL*, *RET*, *NF1*, *SDHA*, *SDHB*, *SDHC*, *SDHD*, *SDHAF2*, *MEN1*, *KIF1Bβ*, *EGLN1*, *EGLN2*, *TMEM127*, *MAX*, *EPAS1* (*HIF2A*), *FH*, and *MDH2* are involved in PPGL susceptibility [1–3]. Recent findings have uncovered new candidate genes involved in chromatin remodeling [4], and the contribution of this genetic pathway to disease etiology requires further exploration.

Approximately 40 % of hereditary PPGLs develop primarily in the context of three familial tumor syndromes: von Hippel–Lindau disease (VHL), multiple endocrine neoplasia type 2 (MEN2), and familial PPGL. Patients diagnosed with multiple endocrine neoplasia type 1 (MEN1) and those with neurofibromatosis type 1 (NF1) can also develop PCC, but do so less frequently. PGLs present almost

M. Robledo (✉) • M. Currás-Freixes • A. Cascón
Hereditary Endocrine Cancer Group, Spanish National Cancer Research Centre (CNIO),
Melchor Fernández Almagro 3, 28029 Madrid, Spain
e-mail: mrobledo@cnio.es; mcurras@cnio.es; acascon@cnio.es
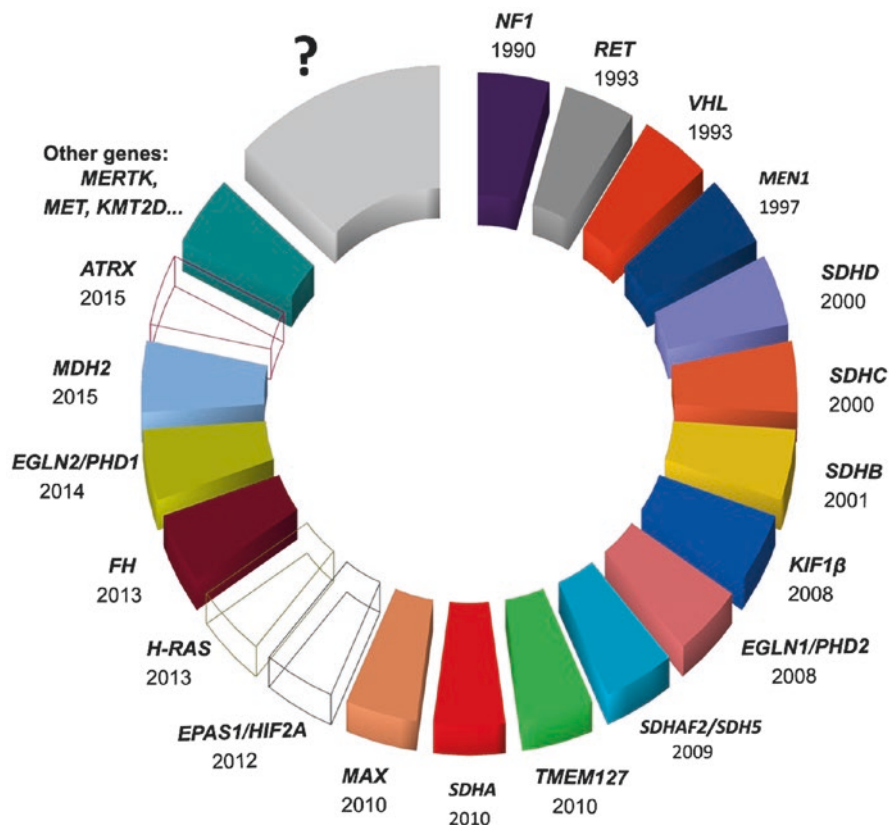
Fig. 2.1 Representation of all reported pheochromocytoma/paraganglioma susceptibility genes, specifying the year of publication, with special attention to the genes involved in the hereditary predisposition to the disease (*opaque colored boxes*). Genes recently reported or lacking further demonstration of their involvement are grouped in "other genes." *Question mark* indicates that other unknown genes are pending to be uncovered

exclusively as part of familial PPGL, although there are very rare tumor syndromes in which these tumors are part of the clinical features (Table 2.1).

Between 10 and 20 % of patients with PPGL are diagnosed during childhood or adolescence [5–7], and PCC is the most frequently diagnosed endocrine tumor in children [8]. The proportion of pediatric patients with a germline mutation in one of the known susceptibility PPGL genes is higher than that found in adults. Recent studies have reported that up to 70–80 % of children with PCC are mutation carriers, regardless of their family history [5, 6, 9]. In addition, a proportion of patients with clinical characteristics indicative of hereditary disease (bilateral PCC, multiple PGLs, family history, and/or early-onset disease) do not carry mutations in any of the known genes, suggesting that other loci remain to be discovered (Fig. 2.1). The

Table 2.1 Genetic and clinical characteristics of syndromes associated with the development of PCC/PGL

Syndrome	Gene	Inheritance	Biochemical phenotype	Associated pathology
MEN2	*RET*	Autosomal dominant	E	MTC, PCC, infrequently PGL Type 2A: PHPT, cutaneous lichen amyloidosis Type 2B: Marfanoid body habitus, mucocutaneous neuromas, intestinal ganglioneuromatosis
VHL	*VHL*	Autosomal dominant	NE, D	HB (CNS and retina), ccRCC, neuroendocrine pancreatic tumors, cysts and cystadenoma of the pancreas, kidney epididymis, or broad ligament, renal cysts, endolymphatic sac tumors, PCC, PGL, etc.
PGL1	*SDHD*	Autosomal dominant (paternal transmission)	NS or NE	PGL (head and neck, thoracic and abdominal), PCC, infrequently GIST, pituitary adenoma, infrequently ccRCC
PGL3	*SDHC*	Autosomal dominant	NS or NE	PGL (head and neck), infrequently PCC or GIST, infrequently pituitary adenoma
PGL4	*SDHB*	Autosomal dominant	NE, D	PGL, PCC, infrequently ccRCC, GIST, pituitary adenoma or PTC
NF1	*NF1*	Autosomal dominant	E	Neurofibromas, cafe au lait spots, axillary freckling, optic gliomas, pigmented hamartomas of the iri*s*, PCC
MEN1	*MEN1*	Autosomal dominant	E	PHPT, pituitary adenoma, neuroendocrine gastroenteropancreatic tumors, PCC
PGL2	*SDHAF2*	Autosomal dominant (paternal transmission)	NS	PGL (head and neck)
PGL5/FPCC1	*TMEM127*	Autosomal dominant	E, NE	PCC, infrequently PGL (head and neck); ccRCC
PGL6	*SDHA*	Autosomal dominant	NE	PGL (head and neck, thoracic and abdominal), PCC; GIST, infrequently ccRCC and pituitary adenoma

Table 2.1 (continued)

Syndrome	Gene	Inheritance	Biochemical phenotype	Associated pathology
PGL7/FPCC2	*MAX*	Autosomal dominant (paternal transmission)	NE, E	PCC (single, bilateral, multiple); up to 20 % of patients also develop PGL (thoracic and abdominal)
PGL8	*FH*	Autosomal dominant	NE	PGL (head and neck, thoracic and abdominal), PCC; cutaneous and uterine leiomyoma, type 2 papillary renal carcinoma
KIF1B	*KIF1B*	Autosomal dominant	NE	PCC (bilateral); neuroblastoma
PHD1/2	*PHD1/2*	Autosomal dominant	NE	PGL (multiple), PCC (bilateral); polycythemia
MDH2	*MDH2*	Autosomal dominant	NE	PGL, PCC; no other associated tumors
Pacak–Zhuang	*EPAS1*	Somatic mosaicism	NE	Polycythemia, somatostatinoma, CNS HB, PGL (multiple), PCC (single)

MTC medullary thyroid carcinoma, *PCC* pheochromocytoma, *PGL* paraganglioma, *PHPT* primary hyperparathyroidism, *HB* hemangioblastomas, *CNS* central nervous system, *ccRCC* clear cell renal cell carcinoma, *GIST* gastrointestinal stromal tumor, *PTC* papillary thyroid carcinoma, *FPCC* familial PCC, *E* epinephrine, *NE* norepinephrine, *D* dopamine, *NS* non-secreting

task of identifying new susceptibility genes is complicated by the fact that this disease can follow an autosomal dominant model, with or without preferential paternal transmission [10–14], and that post-zygotic somatic events have also been observed [4, 15]. It is probable that other models of inheritance, such as recessive, occur in some families with the disease. While uncovering this unexplained heritability of PPGL remains a substantial challenge, new approaches based on next-generation sequencing have begun to shed new light on the comprehensive biology of this tumor. It is paramount to correctly genetically classify each patient in order to be able to offer them the most appropriate clinical follow-up.

2.1.1 Syndromic PCC

Some patients develop PCC or PGL as part of a hereditary tumor syndrome; they present with other clinical signs that can help identify the gene most likely to be involved and therefore be used to prioritize genetic testing. Such patients have often developed other neoplasms or have a family history indicative of a strong genetic etiology, as is the case for PCC associated with multiple endocrine neoplasia type 2 (MEN2), von Hippel–Lindau (VHL), or neurofibromatosis type 1 (NF1) and to a lesser extent other syndromes such as Carney triad, Carney–Stratakis syndrome, and neoplasia endocrine multiple type 1 (MEN1). Patients with a germline mutation

in *RET* have more often been previously diagnosed with medullary thyroid carcinoma (MTC), while those from MEN1 families tend to have had primary hyperparathyroidism (PHPT) and those from NF1 families cafe au lait spots. As described in detail below, one exception to this tendency to have particular comorbidities are patients with specific germline mutations in *VHL*, who tend to develop PCC as the sole manifestation of their disease.

2.1.1.1 MEN2-Associated PCC

MEN2 (OMIM 171400) has an estimated annual incidence of 5 per 10,000,000 persons and a prevalence of 1 in 30,000. MEN2 follows an autosomal dominant mode of inheritance. MEN2 patients can develop MTC (medullary thyroid carcinoma), PCC, and/or PHPT (primary hyperparathyroidism), the latter resulting from hyperplasia or from parathyroid adenomas. The syndrome is classified into three subtypes, MEN2A, MEN2B, and familial MTC (FMTC), each defined according to the combination of pathologies developed by the individuals affected (Table 2.1). MEN2A patients may develop all three pathologies. They are also more likely to develop "cutaneous lichen amyloidosis," a pruritic skin lesion in the upper area of the back caused by the uncontrolled deposition of amyloid protein between the dermis and epidermis. In addition, these patients may occasionally develop Hirschsprung disease (HSCR). Patients are classified as MEN2B if they develop, in the absence of parathyroid disease, MTC; PCC; multiple mucocutaneous neuromas involving the lips, tongue, and eyelids; corneal nerve myelination; intestinal ganglioneuromas (hyperganglionic megacolon); or *marfanoid habitus*, including skeletal deformities and hypermobility of joints. Finally, families in which affected members have developed only MTC or C-cell hyperplasia (CCH) are considered to have the third subtype, FMTC, but only if more than ten members have MTC. A less conservative definition has been proposed by [16], based on the presence in at least four family members of MTC without other manifestations of MEN2A. Defining and distinguishing FMTC from MEN2A is challenging, and an exhaustive clinical follow-up of these families is required to rule out the presence of other tumors characteristic of MEN2, especially in older family members.

In the early 1990s, activating mutations in the rearranged during transfection (*RET*) proto-oncogene were identified as the genetic basis for MEN2A, MEN2B, and FMTC [17–20]. Since then, germline *RET* mutations have been identified in 98 % of patients with MEN2A, 95 % of patients with MEN2B, and 88 % of patients with FMTC [21].

RET is located on chromosomal band 10q11.2 and encodes a tyrosine kinase receptor that is mainly expressed in cells derived from the neural crest (C cells, parafollicular thyroid cells, and adrenal medulla cells, among others) and in urogenital system precursor cells [22]. The genetic testing of *RET* is relatively simple, since the mutations associated with the development of MEN2 are mainly located on exons 10, 11 and 13–16. Additional, less frequent mutations on exon 5 and 8 have been also reported in MEN2 patients. Sequencing of the entire coding region

of *RET* is recommended only for those who meet clinical criteria for MEN2 but in whom initial sequencing of selected exons gives negative results [23] or if there is a discrepancy between the MEN2 phenotype and the expected genotype [24]. If a *RET* variant is detected at a noncanonical position, it is important to consult different databases for evidences that the variant may be a polymorphism with no clinical significance [25]. A sequence change in *RET* is considered to be a causative MEN2 mutation if it segregates with the clinical expression of disease within a family including at least two affected individuals having the MEN2 phenotype.

The established genotype–phenotype relationships for MEN2 syndrome are based on the classification of individual mutations according to their transforming ability, and therefore the expected aggressiveness with which the disease they cause will develop [24]. The impact of *RET* mutation testing on the management of MEN2 patients is without doubt one of the most robust examples of the utility of genetic diagnosis in personalizing clinical follow-up [24].

Approximately 50 % of MEN2 patients develop PCC in their lifetime, and the mean age at diagnosis is 35 years. A PCC is the first manifestation of MEN2 in only 12–15 % of cases, and so *RET* explains relatively few cases of non-syndromic disease (around 5 %), compared to other syndromes [26, 27]. *RET* mutations are very rarely found in patients diagnosed with PCC before age 20 [5–7]. Thus, *RET* is not a priority in the genetic testing of pediatric patients, although it should still be included in genetic diagnosis algorithms [5]. PCCs developed by *RET* mutation carriers are bilateral in 50–80 % of patients, they tend to be epinephrine-secreting tumors, and very few (no more than 5 %) are malignant.

It is recommended that screening for PCC begins between ages 5 and 16 for carriers of highest-, high-, and moderate-risk mutations [24, 27].

2.1.1.2   VHL

VHL (OMIM 193300), with an incidence of 1 in 36,000 live births, is a dominantly inherited familial cancer syndrome caused by germline mutations in the *VHL* tumor suppressor gene [28, 29]. This gene encodes three gene products: a protein comprising 213 amino acids and two shorter isoforms, one produced by alternative splicing (excluding exon 2) and the other by alternative initiation. While the protein (pVHL) is involved in multiple processes, its best characterized role is the regulation of the proteasomal degradation of hypoxia-inducible factors (HIFs) [30]. Under normal oxygen tension, the α subunits of HIF (HIF-1α, HIF-2α, and HIF-3α) are hydroxylated by the dioxygenases PHD (PHD1, PHD2, and PHD3). The hydroxylated HIF-α are then targeted by pVHL for proteasomal degradation [31, 32]. Under hypoxia conditions, HIF-α is stabilized and binds to the HIF-β subunit to form an active transcription factor that regulates expression of a large repertory of genes involved in angiogenesis, cell survival, erythropoiesis, and tumor progression [30]. This explains the highly vascularized nature of the tumors associated with VHL syndrome [33].

Table 2.2 Clinical classification of VHL patients

Clinical features	Subtype				
	VHL-1A	VHL-1B	VHL-2A	VHL-2B	VHL-2C
HB (CNS, retina)					
ccRCC			Low risk	High risk	
Cysts and cystadenoma of the pancreas					
PCC					

HB hemangioblastoma, *CNS* central nervous system, *ccRCC* clear cell renal cell carcinoma, *PCC* pheochromocytoma

The penetrance of causal mutations is age dependent, and the disease demonstrates marked phenotypic variability. Patients with VHL are at a higher risk of developing hemangioblastomas (HBs) of the retina and central nervous system (CNS), PCC and/or PGL, clear cell renal cell carcinoma (ccRCC), renal and pancreatic cysts (serous cystadenoma), neuroendocrine pancreas tumors, endolymphatic sac tumors, pancreatic serous cystadenomas, and papillary cystadenomas of the epididymis in men and of the broad ligament in women (Table 2.1) [27, 33, 34]. After identifying *VHL* in 1993, the phenotype associated with *VHL* gene mutations was expanded to include VHL disease, dominantly inherited familial PCC, and, in cases with particular mutations, autosomal recessive congenital polycythemia (also known as familial erythrocytosis-2; MIM# 263400) [35, 36]. It has been suggested that VHL accounts for approximately a third of patients with a CNS HBs, >50 % of patients with a retinal angioma, 1 % of patients with RCC, 50 % of patients with apparently isolated familial PCC, and 11 % of patients with an apparently sporadic PCC [37].

The disease is classified into four subtypes (1, 2A–2C) based on the clinical phenotype. VHL type 1 families have a relatively low risk of developing PCC, but may present with any of the other tumors associated with the disease. VHL type 2 is subdivided into three categories corresponding to a low (2A) or high risk (2B) of developing ccRCC or to a higher risk of PCC and PGLs as the only clinical sign of the disease (2C) (Table 2.2).

Systematic characterization of germline *VHL* mutations has led to the identification of genotype–phenotype correlations such that germline mutations causing amino acid changes on the surface of pVHL are associated with a higher risk of PCC [34]. *VHL* germline deletions, mutations predicted to cause a truncated protein, and missense mutations that disrupt the structural integrity of the VHL protein are associated with a lower risk of PCC (and therefore associated with type 1 VHL syndrome). However, phenotypes related to *VHL* gene deletions appear to be influenced by the retention of some genes surrounding *VHL*. In particular, *VHL* deletions associated with the loss of the actin regulator *HSPC300* gene (also known as *BRICK1*) are associated with protection against ccRCC [38–40]. These clinical findings led McNeill et al. (2009) to suggest that the subclassification of VHL syndrome should take into account not only clinical phenotype but also *VHL* mutation data [40] (Table 2.2).

PCCs/PGLs Associated with VHL

Approximately 20 % of patients with VHL develop PCC or PGL (sympathetic and parasympathetic), although the latter is much less frequent. Tumors are exclusively norepinephrine-secreting, related to a low, or no, expression of phenylethanolamine N-methyltransferase (PNMT), multifocal or bilateral in 43–45 % of cases and malignant in less than 5 % [41–43]. The median age at diagnosis of PCC/PGL is 29 years, which is lower than for other syndromes and particularly relevant for genetic testing since between 12 and 32 % of patients with PCC diagnosed during childhood are found to carry a germline mutation in *VHL* [44]. Also of note is that PCC (principally) or PGL (occasionally) is the first manifestation for 30–50 % of patients with VHL [41]. For these reasons, *VHL* mutation screening is essential in patients diagnosed before age 18. Furthermore, *VHL* has a high mutation rate (20–21 %) [45, 46], and so germline mutation testing of this gene is recommended specifically for patients with single tumors and non-syndromic cases. As we will review in this chapter, the role of *VHL* is also relevant in sporadic presentation, as a notable proportion of tumors develop as consequence of somatic *VHL* mutations [47].

The development of VHL-related tumors has been linked to the alteration of interactions between pVHL and other proteins with which it forms complexes, specifically pVHL-ElonginC-ElonginB complexes (CBC^VHL). The most accepted hypothesis in this regard is that the development of PCC in the context of VHL is associated with a partial retention in the function of pVHL to assemble at least to some extent into CBC^VHL [48, 49], which protects them from rapid intracellular degradation [50–52]. A hot spot in *VHL* that is associated with the development of PCC affects residue 167, located in the alpha domain. This domain has the role of interacting with other proteins, so that mutations giving rise to amino acid changes in this region do not result in loss of function of pVHL. The finding that 23 % (7/30) of patients with PCC who carry deleterious germline variants in *VHL*, but have no signs of either VHL or MEN2, have a mutation that affects this residue is consistent with this hypothesis [53]. On the basis of the above findings, it has been proposed that the measurement of change in pVHL stability could be used as an additional tool to understand the clinical features developed by a VHL patient [52]. Indeed, the use of this tool led to the identification of an association between ccRCC and missense mutations that significantly alter pVHL stability. A subsequent study classified these mutations as "surface" or "deep," depending on the location of the affected residue in the protein structure, and found a clear difference between them in the associated risk of PCC [34].

Based on the earliest described age at PCC diagnosis, it is recommended that screening be initiated at age 5 years [27, 44].

2.1.1.3 Neurofibromatosis Type 1

Neurofibromatosis type 1 (NF1), formerly known as von Recklinghausen disease, is a common hereditary disease with an incidence of 1 per 2,500–3,300 newborns that primarily involves the skin and nervous system. The condition is usually diagnosed in

early childhood, when cutaneous manifestations are apparent. It is characterized by the appearance of multiple neurofibromas, cafe au lait spots, freckling in the armpits and groin, iris hamartomas (Lisch nodules), bone lesions such as scoliosis, sphenoid dysplasia or pseudoarthrosis, macrocephaly, learning disorders, cognitive deficits, predisposition to optic and CNS glioma, and leukemia [27, 54]. Other malignancies occur less frequently in patients with NF1, including PCC, rhabdomyosarcoma, leukemia, and brain tumors other than optic gliomas [55]. Some features of neurofibromatosis 1 are present at birth, and others are age-related manifestations, which means that periodic monitoring is required to address ongoing health and developmental problems and to minimize the risk of serious medical complications [56].

The gene responsible for NF1, *NF1* (17q11.2), encodes the protein neurofibromin, which is expressed primarily in the nervous system and has the role of suppressing cell proliferation by inactivating RAS proteins. Loss-of-function mutations in *NF1* lead to the activation of RAS and the PI3K/AKT/mTOR pathway, which depends on RAS [54].

The detection of mutations in *NF1* by DNA analysis has proven to be challenging because of the gene's large size (it has 58 exons), the lack of mutation hot spots, and the existence of pseudogenes. *NF1* mutations are predominantly truncating and often accompanied by loss of the wild-type allele in the tumor. Although molecular technology is now available to detect most mutations in *NF1* [57], it is typically not required because in 95% of cases a diagnosis of NF1 can be made by age 11 years on the basis of clinical findings alone. *NF1* has one of the highest rates of spontaneous mutation of any gene in the human genome. This in part explains why between 30 and 50% of patients have de novo mutations, which if they occur post-zygotically, can give rise to mosaic phenotypes [58]. Events of germline mosaicism are very rare in this condition [59].

PCCs Associated with NF1 Disease

An estimated 0.1–5.7% of NF1 patients develop PCC, although this figure is 3.3–13% based on autopsy studies. Therefore, NF1 is not a common diagnosis in PPGL patients [60]. These tumors are more prevalent among NF1 patients with hypertension (20–50%) [61]. NF1-associated PCCs tend to develop at a later age (mean 41 years), can be unilateral or bilateral, and are rarely extra-adrenal and slightly more often malignant (up to 12%) than those in VHL and MEN2 cases [62]. The earliest recorded age at diagnosis of PCC is 7 years, but given the low penetrance of *NF1* mutations for this tumor development, screening of the gene is only recommended in cases of hypertension or symptoms suggestive of disease [27].

2.2 Non-syndromic PCC/PGL

In addition to the syndromic forms, many genes have been described over the last few years related to susceptibility to develop PCC or PGL as the only disease manifestation. Associations with other tumors have been reported, but only in a limited

number of patients. We will outline the functions of the SDH genes, as well as *FH*, *MDH2*, *TMEM127* and *MAX*, and detail the clinical manifestations associated with mutations in each of these. Other genes will be also reviewed.

2.2.1 Non-syndromic PCC/PGL Associated with Mutations in the SDH Genes, FH, and MDH2

2.2.1.1 SDH Gene Function

The connection between the SDH genes and the development of neuroendocrine tumors was established in 2000 when germline mutations in *SDHD* were first described in patients with familial PGL [14]. The SDH genes encode complex II of the mitochondrial respiratory chain, also known as succinate dehydrogenase (SDH), which plays a key role in both the electron transport chain and the oxidation of succinate to fumarate at the tricarboxylic acid (TCA) cycle. SDH is a heterotetramer composed of four proteins: two catalytic (SDHA and SDHB) and two structural (SDHC and SDHD). The latter are responsible for attaching the SDH complex to the inner mitochondrial wall (reviewed on [63]).

An associated protein, SDHAF2, is a highly conserved cofactor of flavin adenine dinucleotide (FAD) which is implicated in the flavination of SDHA and is essential for SDH function. *SDHAF2* mutations have been reported to be associated with the development of PPGLs, confirming the importance of this complex for the disease [12, 13].

Heterozygous mutations in the *SDHA*, *SDHB*, *SDHC*, and *SDHD* genes cause complex II destabilization affecting the ability of cells to detect oxygen. SDH dysfunction results in the accumulation of succinate [64], its TCA cycle substrate, which acts as a competitive inhibitor of the 2-oxoglutarate (2-OG)-dependent HIF prolyl hydroxylases [65, 66]. This stabilizes HIF-alpha and, mediated by pVHL, activates genes that facilitate angiogenesis and anaerobic metabolism [66]. This link between mutations in the SDH genes and the HIF-1α pathway is also corroborated by results from tumor expression profiling studies of PPGLs [67]. Mutations in the SDH genes, both catalytic and structural, cause defects in the enzymatic activity of the complex, which lead to accumulation of succinate [68], along with the absence of SDHB [69]. Thus, negative SDHB immunostaining indicates the likely involvement of these genes in disease etiology; these findings represent robust tools that can be used to select patients for genetic testing, if paraffin-embedded tumor material is available.

Global DNA hypermethylation has been described as a hallmark of tumors with TCA cycle abnormalities resulting from SDH genes and *FH* and *MDH2* mutations [1, 70, 71]. This CpG island methylator phenotype (CIMP) has revealed that succinate acts as an oncometabolite, inhibiting 2-oxoglutarate-dependent dioxygenases, such as hypoxia-inducible factor prolyl hydroxylases and histone and DNA demethylases.

Prognosis associated with high CIMP is cell-type dependent. For instance, in glioblastoma high CIMP is associated with a more favorable prognosis, whereas poor prognosis has been reported for neuroblastoma and PPGL [70, 72]. SDH gene-related, and particularly *SDHB*-related, PPGLs have a higher risk of progressing to metastatic disease [73]. It has been found that although all SDH gene-mutated tumors displayed CIMP, the level of hypermethylation is significantly higher, and the expression of target genes significantly lower, in *SDHB*-mutated tumors. As target genes include genes implicated in neuroendocrine differentiation and epithelial-to-mesenchymal transition (EMT), this could explain the particular metastasis-prone nature of *SDHB*-mutated tumors [70].

Loss-of-function mutations in the four SDH complex subunits and SDHAF2 have been demonstrated to cause PPGL, though the frequency of mutations and associated tumor types vary by genes. In addition to PPGL, *SDHB* and *SDHD* mutations have been associated with ccRCC [74, 75] and thyroid carcinoma [76, 77]. In addition, mutations in *SDHB*, *SDHC*, and *SDHD* can give rise to Carney–Stratakis syndrome [78], characterized by the dyad of PGL and gastrointestinal stromal tumors (GISTs). These findings revealed a novel molecular mechanism underlying the development of GISTs, which are usually related to gain-of-function mutations in *KIT* or *PDGFRA* [79, 80]. It has more recently been recognized that SDH gene mutations are associated with the development of pituitary adenomas (PA) ([81–83] and reviewed in [84]).

2.2.1.2 Mutations in the SDH/FH/MDH2 Genes: Genotype–Phenotype Relationship

Clinical Presentation Associated with Mutations in SDHD

The hereditary syndrome PGL1 (OMIM ID: 168000) is caused by mutations in the *SDHD* gene. The estimated penetrance of germline mutations in *SDHD* (11q23.1) is 86 % to age 50 years, and carriers normally present with multiple PGLs at a mean age of 35 years. *SDHD* carriers primarily develop head and neck PGL (84 % of cases), although up to 22 % also develop thoracic and abdominal PGL and 12–24 % PCC, the latter rarely being bilateral [76, 85, 86] (Table 2.1). Although PCCs and extra-adrenal PGLs are relatively rare in patients with *SDHD* germline mutations, it has been described that the type of mutation influences the phenotype. *SDHD* mutations predicted to result in an absent or unstable SDHD protein were associated with an increased risk of PCCs and PGLs, compared to missense mutations or in-frame deletions, which were not predicted to impair protein stability [76].

SDHD-related disease follows an autosomal dominant mode of inheritance, with preferential paternal transmission [87]. That is, a mutation carrier will only develop the disease if their mutation came from their father; if it came from their mother, they will not be affected, although they will still be able to pass on the mutation to their children. While this pattern of inheritance suggests the existence of maternal genomic imprinting of this gene, the observed bi-allelic expression of *SDHD* in

different normal tissues and in neural crest-derived tumors does not support this hypothesis [88–90]. In order to explain this *SDHD*-linked parental effect, it has been proposed that the loss of the entire maternal copy of chromosome 11, a hallmark of *SDHD*-linked tumors, leads to the simultaneous deletion of the *SDHD* gene and an exclusively maternally expressed gene [91, 92].

Regardless of the mechanism underlying this preferential paternal transmission, the hereditary nature of disease is masked in families in which by chance the mutation has been transmitted from generation to generation only from mother to child. The disease skips generations and these can only be identified in genetic counseling centers that collect information from second- and third-degree relatives.

A key issue in clinical follow-up is the fact that 3–10 % of carriers of a germline mutation in *SDHD* develop metastasis [76, 77, 93–95]. In the case of pediatric patients, despite the possible lack of family history, it has been suggested that a diagnosis of at least one head and neck PGL is sufficient to justify genetic testing; in fact, 8–16 % of patients under age 20 years carry a germline alteration in *SDHD* [5, 6].

In relation to the development of other tumors, it should be noted that there has been some controversy around two variants in *SDHD*, p.H50R, and p.G12S. Both were initially reported to be associated with the development of Merkel cell carcinoma and familial CCH and even Cowden-like syndrome. However, they were subsequently classified as polymorphisms, present in several healthy populations (http://www.lovd.nl/3.0/home), and their associations with the proposed diseases have therefore been ruled out [96].

Even though the earliest reported age at diagnosis is 5 years, screening is recommended from the age of 10 years [27].

Clinical Presentation Associated with Mutations in SDHB

The PGL4 syndrome (OMIM ID: 115310) is due to mutations in the *SDHB* gene (1p36.13). Overall, the *SDHB* gene is the most commonly mutated of all the SDH-related genes [97]. An estimated 67 % of patients carrying mutations in *SDHB* develop primarily thoracic and abdominal PGL, 27 % develop head and neck PGL, and 17–29 % develop adrenal PCC, which is rarely bilateral [69, 85, 86].

Although, to date, a clear genotype–phenotype relationship does not exist for *SDHB* mutations, an association between *SDHB* missense mutations and an increased risk of head and neck PGL have been described, compared to truncating mutations [76]. Large deletions seem to lead to similar phenotypes and penetrance to those patients with point mutations. Several large germline founder deletions in *SDHB* have been reported in multiple unrelated subjects from the Netherlands [98] and Spain [86, 99]. In these populations, the proportion of carriers of these founder mutations could be sufficiently high for the testing of large deletion in *SDHB* to be the first step in genetic screening.

At least 40 % of *SDHB* mutation carriers develop metastatic disease [97]. Thus, it is widely accepted that the identification of a mutation in *SDHB* is a marker of poor prognosis and more close clinically monitoring of the patient is required.

Of all the known susceptibility genes for hereditary PCC/PGL, *SDHB* constitutes a paradigm of heterogeneity in and of itself. Mutations in this gene are usually associated with the presence at diagnosis of a single retroperitoneal tumor [100]. In fact, only 25–40 % of all carriers will ever develop a tumor [101, 102]. This explains why most patients have no family history of disease at the time of their diagnosis. This fact, along with the frequent appearance of a single tumor in affected individuals, makes it very difficult to identify potentially hereditary cases. Although the underlying cause of reduced penetrance is unknown, possible genetic explanations include inhibition of cell proliferation due to secondary loss of vital genetic material in the proximity of the remaining normal allele or that additional loss of chromosome 11 is required (Hensen model) [63]. For all these reasons, and principally because of the high risk of developing metastases, all the algorithms currently used to guide genetic diagnoses include the testing of *SDHB* in patients with PPGL.

Although the earliest reported age at diagnosis is 6 years, screening is recommended from age 5 years [27].

Clinical Presentation Associated with Mutations in SDHC

Mutations in the *SDHC* gene (1q23.3) cause the PGL3 syndrome (OMIM #605373) [103]. Since relatively few mutations in *SDHC* have been described worldwide, the associated clinical manifestations have not been clearly defined; nevertheless, it is known that mutation carriers tend to develop PGL (93 % parasympathetic and 7 % sympathetic) and infrequently PCC or GIST. Up to 23 % of affected individuals have multiple PGLs and 25 % have a family history, suggesting that mutations have incomplete penetrance [85, 86, 104]. Thus, the clinical features of *SDHC*-associated cases are similar to those found in patients with sporadic head and neck PGLs. Mutation carriers typically present with solitary head and neck PGLs and a very low tendency to be malignant [105]. The mediastinum is the second most common location for *SDHC*-related PGL (10 % of all tumors), occurring in up to 13 % of patients [106]. The mean age at diagnosis is 38 years [62], and very little is known about the involvement of this gene in pediatric disease.

Epigenetic inactivation of *SDHC* is a recently discovered phenomenon in GISTs and PPGLs from patients with Carney triad syndrome [107, 108]. This event has been reported as the genetic cause of a patient that presented with two abdominal PGLs and an adrenocortical adenoma, providing evidence that *SDHC* promoter methylation can cause PGLs due to *SDHC* inactivation [109].

Clinical Presentation Associated with Mutations in SDHA

Mutations in the *SDHA* gene (5p15.33) cause the rare familial PGL5 syndrome (OMIM #614165) [110]. Based on currently available information, *SDHA* (5p15.33) appears to contribute little to PCC/PGL. Korpershoek and colleagues reported that 3 % of their series of 198 patients with apparently sporadic PCC or PGL were found to carry mutations in *SDHA* [69]. These carriers developed PCC, head and neck PGL, or thoracic and abdominal PGL (Table 2.1), but rarely metastatic disease. Although it has been established through biochemical analysis that nonsense *SDHA* mutations are associated with disease, these same mutations have been found in unaffected population controls, suggesting that these mutations have very low penetrance; these findings add additional complexity to the genetic counseling offered to carriers, most of which will not develop clinical symptoms [63].

Nevertheless, *SDHA* should be considered in genetic testing for patients presenting with clinical evidence of familial PPGL who test negative for the other known susceptibility genes. As previously mentioned, mutations in any of the SDH genes have the effect of suppressing the enzymatic activity of complex II and a key indicator that this has occurred is negative immunostaining for SDHB. Furthermore, it is now known that mutations in *SDHA* also give rise to negative immunostaining for SDHA [69]. This relatively easily implemented clinical screening tool should be incorporated into molecular diagnostic protocols to ensure that appropriate mutation testing is carried out in the most efficient and cost-effective manner.

Clinical Presentation Associated with Mutations in SDHAF2

SDHAF2, also known as *SDH5*, was identified as the susceptibility gene for the PGL2 syndrome (OMIM ID: 601650) [13]. *SDHAF2* (11q12.2) is similar to *SDHD* in that it has an autosomal dominant mode of inheritance, with a preferential paternal transmission. To date only head and neck PGLs have been reported in *SDHAF2* mutation carriers, most diagnosed at an early age and all with a family history of the disease ([12] and references contain therein). Few distinct *SDHAF2* mutations have been described [12, 111, 112]. While available data suggest that mutations in *SDHAF2* do not explain a substantial portion of cases (<1 %), further studies in different populations are required to determine their relevance. Nevertheless, genetic testing of *SDHAF2* should be offered to patients with head and neck PGLs with negative tumor staining for SDHB and who test negative for mutations in *SDHD*, *SDHC*, and *SDHB*. While currently too few data are available to draw clear conclusions, no affected mutation carriers developed PGL before age 20 years, suggesting that mutations are not relevant to the development of pediatric tumors.

FH: Clinical Presentation Associated with Mutations in FH

FH is the TCA cycle enzyme involved in the reversible hydration/dehydration of fumarate to malate. It is known that germline mutations in *FH* (1q43) predispose to leiomyomas and papillary RCC in an autosomal dominant hereditary syndrome

named hereditary leiomyomatosis and renal cell cancer (HLRCC) [113]. Inactivation of FH leads to accumulation of its substrate, fumarate, and inhibits α-ketoglutarate-dependent HIF prolyl hydroxylases, leading to HIF activation [64, 66]. Other dioxygenases, including histone demethylases and the TET (ten–eleven translocation) family of 5-methylcytosine (5 mC) hydroxylases, are also inhibited by succinate and fumarate accumulation [114]. Very recently, Letouze et al. [70] identified a germline mutation in *FH* by whole-exome sequencing applied to blood and tumor DNA obtained from a 63-year-old female presenting with one PCC. The patient was selected to be sequenced because the tumor showed a methylome- and transcriptome-based profile very similar to that found in tumors carrying mutations in the SDH genes. The subsequent screening of almost 600 patients with PPGL but no mutations in the major susceptibility genes revealed that five carried pathogenic germline *FH* mutations, providing further evidence of the involvement of this gene in the development of PPGL [115]. Clinically, a metastatic phenotype and multiple tumors were significantly more frequent in patients with *FH* mutations than those without such mutations. Recently, as previously mentioned for succinate, fumarate has been reported as an epigenetic modifier that elicits epithelial-to-mesenchymal transition [164]. *FH* should thus be added to the list of PPGL susceptibility genes and should be considered in mutation screening, to assess the risk of metastatic disease.

MDH2: Clinical Presentation Associated with Mutations in MDH2

MDH2, which encodes another TCA cycle enzyme implicated in the reversible conversion of malate to oxaloacetate with the concurrent reduction of NAD to NADH, has been recently described as a new PPGL susceptibility gene [1]. The causal mutation was identified by whole-exome sequencing, which revealed a germline mutation in the mitochondrial malate dehydrogenase gene (*MDH2*) in a patient with multiple malignant PGLs.

As explained above, the accumulation of succinate and fumarate leads to the enzymatic inhibition of multiple alpha-KG-dependent dioxygenases. This inhibition causes impaired histone demethylation and 5-mC hydroxylation (5-hmC) and, consequently, a characteristic CIMP [70]. Expression profiling analysis focused on hypermethylated and downregulated genes in SDH gene-mutated and non-SDH gene-mutated tumors revealed that the *MDH2*-mutated tumor clustered with SDH gene-mutated tumors, suggesting a similar CIMP (CIMP-like) profile. Findings from additional immunohistochemical studies evaluating 5-hmC and trimethylation of histone H3 lysine 27 (H3K27me3) were also consistent with the *MDH2*-mutated tumor exhibiting a CIMP-like profile [1]. Apart from this study, no other PPGL patient has been reported to carry a *MDH2* mutation. An international consortium has undertaken an initiative to establish the prevalence of *MDH2* mutations among PPGL patients with no mutations in known susceptibility genes. Nevertheless, the contribution of *MDH2* mutations to disease seems to be low (<0.5 %; unpublished data), and the associated clinical features associated and penetrance are yet to be established.

Nevertheless, these findings once again link the disruption of the TCA cycle to PPGL development and indicate that other alterations of this major metabolic pathway may explain additional cases of this disease.

2.2.2 Non-syndromic PPGL Associated with Mutations in TMEM127

2.2.2.1 The TMEM127 Gene

TMEM127 (2q11) was identified as a new PCC susceptibility gene in 2010, via an integrated analysis of results from studies using several genomic platforms, including linkage analysis, gene expression profiling, and mapping of chromosomal gains and losses [116]. Loss of heterozygosity (LOH) of the wild-type allele was observed in all available tumors from carriers of *TMEM127* mutations, suggesting that the gene acts as a classic tumor suppressor.

TMEM127 encodes a transmembrane protein with no known functional domains. Functional studies suggest that the protein (TMEM127) localizes to the plasmatic membrane and cytoplasm and is associated with a subpopulation of vesicular organelles, including the Golgi and lysosomes. TMEM127 is dynamically distributed at the subcellular level in response to nutrient signals [116]. It has also been demonstrated that TMEM127 modulates mTOR complex 1 (mTORC1). The mTOR kinase is a common component of two complexes, mTORC1 and mTORC2, which control some relevant aspects of cell metabolism, growth, proliferation, survival, and differentiation [117, 118]. *TMEM127* downregulation leads to hyperphosphorylation of mTORC1 targets 4EBP1 (eukaryotic translation initiation factor 4E-binding protein 1) and S6K (ribosomal protein S6 kinase), as well as to the increase of cell size and proliferation [116], indicating that TMEM127 is associated with mTORC1 downregulation.

Subsequent analysis of the global expression profile of *TMEM127* tumors grouped them with those associated with *RET* and *NF1* mutations [47, 119].

2.2.2.2 Clinical Presentation Associated with Mutations in TMEM127

Few studies have been published to date based on patient series genetically tested for mutations in *TMEM127*. The most relevant of these reported the genetic findings in 990 patients with PPGL who tested negative for mutations in *RET*, *VHL*, and *SDHB/C/D* [120]; 2% carried germline *TMEM127* mutations and presented with disease at a mean age of 43 years. Subsequent reports have described two mutation carriers with PGL, one thoracic and abdominal and the other with multiple head and neck tumors [121]. Globally, more than 30 mutations have been identified in *TMEM127*. Most (60%) result in a truncated protein or predominantly target one of the transmembrane regions of the protein (reviewed in [2]). Although all variants are germline in nature, less than 20% of patients carrying a *TMEM127* mutation report a family history of PPGL [120]. In addition, germline *TMEM127* mutations have also been detected in rare cases of ccRCC patients without PPGL [122].

As for other susceptibility genes, the findings published to date suggest that mutations in *TMEM127* have incomplete penetrance, which would tend to mask the underlying hereditary disease and in many cases mean that patients may not meet the selection criteria for genetic testing. Given the mean age at disease onset for mutation carriers studied to date, genetic testing of *TMEM127* is not recommended in pediatric patients with PPGL.

2.2.3   Non-syndromic PPGL Associated with Mutations in MAX

2.2.3.1   The MAX Gene and Its Protein

MAX (14q23.3) encodes a transcription factor that plays an important role in the regulation of cell proliferation, cell differentiation, and apoptosis, as part of the MYC/MAX/MXD1 axis. These proteins form dimers to bind to DNA; in fact, MYC forms a heterodimer with MAX to bind to specific DNA sequences called "E-boxes," which are located in MYC target genes, and this entire complex acts as a transcription activator. Both the lethal character demonstrated in *Max* knockout mice and the fact that *MAX* is constitutively expressed in many cell types make it difficult to understand how MYC can carry out its function without the presence of MAX. However, the PC12 cell-line, derived from PCC in rat, carries a homozygous *Max* mutation [123], which points to the existence of an additional unknown factor that is able to regulate the function of MYC ([124] and reviewed in [10]).

The identification of *MAX* as a PCC susceptibility gene was the result of a study of the entire exomes of three unrelated patients with PCC and a family history of the disease [10]. These patients had been selected because their tumors had a common transcription profile that differentiated them from tumors related to other known susceptibility genes [67]. LOH in the tumors of germline *MAX* mutation carriers, along with the absence of MAX protein shown by an immunohistochemical analysis, suggested that *MAX* acts as a tumor suppressor gene.

2.2.3.2   Clinical Presentation Associated with Mutations in MAX

Following the identification of pathogenic mutations in *MAX* in the three initial families, the genetic study was extended to 59 patients that had tested negative for the key known susceptibility genes. These 59 patients were chosen because they were diagnosed with PCC before age 30 years, had bilateral disease, or had a family history of the disease. *MAX* mutations were found in 8.5 % of them; 67 % of mutation carriers had bilateral disease and 25 % had developed metastases. The malignant behavior of tumors with mutations in *MAX* seemed to be consistent with what was known about neuroblastoma, the other tumor derived from neural crest and developed mainly from the adrenal medulla. Up to 22 % of neuroblastomas show MYC amplification; they are strongly associated with advanced disease stages and rapid tumor progression [125], which would support the idea that MAX loss of function was related to metastatic potential, since MAX is the main regulator of MYC. An additional striking finding was that the mutated allele had to have been inherited paternally in order for the carrier to develop the disease, as is the case for *SDHD* and *SDHAF2*, although the mechanism behind this remains unknown.

A subsequent study screening for mutations in *MAX* in a series of 1,694 patients and 245 tumors was undertaken in order to establish the prevalence of *MAX* mutations and the associated clinical presentation. This study was made possible through the collaboration of 17 reference centers from around the world [11]. The interpretation

of findings took into account only the pathogenic germline mutations identified, excluding all those classified as variants of unknown significance. The study reported pathogenic mutations in 1.3 % of patients; 21 % of them had developed thoracic and abdominal PGL in addition to PCC, although none of the patients diagnosed only with PGL carried a *MAX* mutation. Thirty-seven percent had a family history of the disease and 10 % had metastases. Thus, the association with metastatic disease described in the first study was not confirmed. The mean age at diagnosis for mutation carriers was 32 years and 21 % were diagnosed at or before age 18. These findings suggest that *MAX* should be included along with *VHL* and *SDHB* in genetic testing protocols for pediatric cases [5].

It was also established that the frequency of somatic mutations was 1.65 % and that the associated biochemical-secretor profile was characterized by elevated levels of normetanephrine and associated with normal or slightly increased levels of metanephrine [11]. It should be noted that, though the overall prevalence of *MAX* mutations in the entire series only slightly exceeded 1 %, this increased to 12 % in patients with isolated tumors and to 66 % in cases with bilateral PCC, when considering only cases with PCC and family history [11]. Thus, this second study elucidated the importance of *MAX* mutations in PPGL susceptibility, pointing to the need for the inclusion of this gene in the genetic workup of affected patients, particularly those with PCC (bilateral or multifocal), and/or with family history. These conclusions have been confirmed in more recent studies, which have also identified additional *MAX* germline mutations [126].

2.2.4   Rare PPGL Susceptibility Genes

In addition to the twelve PPGL susceptibility genes already discussed, there are others such as *MEN1*, *KIF1B*, *PDH1* (also called *EGLN2*, egl nine homolog 2), *PDH2* (also called *EGLN1*, egl nine homolog1), *MERTK*, and *MET* [4, 127] that have recently been added to the list of genes related to PPGL susceptibility.

It is known that mutations in the *MEN1* gene (11q13) are responsible for multiple endocrine neoplasia type 1 development. This syndrome is characterized by tumors of the pancreatic islet cells, anterior pituitary, and parathyroid gland [128]. Some patients may also develop adrenal cortical tumors, carcinoid tumors, facial angiofibromas, collagenomas, and lipomas. PCC is observed in less than 1 % of MEN1 germline mutation carriers [129].

A germline mutation in *EGLN1* (1q42.1) was reported in a patient with PGL and congenital erythrocytosis [130]. Germline mutations in *EGLN1* had previously been reported in patients with erythrocytosis, but not in association with tumors [131]. The detected mutation affected EGLN1 function and stabilized HIF-1α and HIF-2α in HEK-293 cells. LOH was detected in the tumors, suggesting that *EGLN1* may act as a tumor suppressor gene. The first germline mutation in *EGLN2* (19q13.2) was also found in one patient suffering from multiple PGLs and congenital polycythemia [3]. A novel germline *EGLN1* was described in a second patient. Both mutant

tumors exhibited reduced protein stability with substantial quantitative protein loss and thus compromised catalytic activities [3].

KIF1B is a large gene located at 1p36.22 that is frequently deleted in neural crest-derived tumors. The gene has two splice variants, *KIF1Bα* and *KIF1Bβ*. The beta isoform functions as a tumor suppressor that is necessary for neuronal apoptosis [132]. *KIF1Bβ* has been found mutated in one sporadic PCC, and in the germline of one apparently sporadic patient and a single family affected by PCC and neuroblastoma [132–134]. No metastases were reported in these studies. Other tumors such as ganglioneuroma, leiomyosarcoma, and lung adenocarcinoma have also been reported in a family with *KIF1Bβ* mutations [133]. It is likely that this gene has a more relevant role in PPGL development than expected, but the large size of its coding sequence makes screening for additional deleterious mutations a difficult task. The use of next-generation sequencing in routine genetic screening will likely help to determine the role of *KIF1Bβ* in the disease.

2.3 Sporadic PPGL

Only few years ago, it was accepted that the proportion of PPGLs explained by somatic events was very low, these mainly affecting *VHL*, *RET*, *SDHB*, and *SDHD* [135–137]. The scenario changed completely after it was reported that 14 % of PPGLs were explained by somatic *RET* and *VHL* mutations [47] and the *NF1* somatic events were found in 21–24 % of PPGLs [138, 139]. It is now clear that somatic mutations play a role in PPGLs as they have been described in up to 40 % of tumors [9, 47, 138–141]. These mutations involve not only the genes involved in heritable susceptibility but also others that have emerged as new predisposition genes, thereby giving insights into the mechanisms and pathways implicated in the disease (Fig. 2.2). Furthermore, these findings highlight the importance of working with germline and tumor DNA from the same patients in order to provide a comprehensive genetic diagnosis [9].

Other genes not previously mentioned in this chapter will be reviewed in the following sections.

2.3.1 PPGLs with Mutations in EPAS1

The HIF family of transcription factors (HIF-1α, HIF-2α [EPAS1], and HIF-3α) plays a key role in the regulation of response to hypoxia to counteract the lack of oxygen in normal homeostasis. It has been suggested that HIF-1α preferentially drives genes implicated in apoptosis and glycolysis and HIF-2α is involved in cell proliferation and angiogenesis [142, 143]. Recently, a new and direct link has been found between HIF proteins and PPGL development [15]; post-zygotic somatic mutations in *EPAS1* (located at 2p21) were found in two unrelated patients with
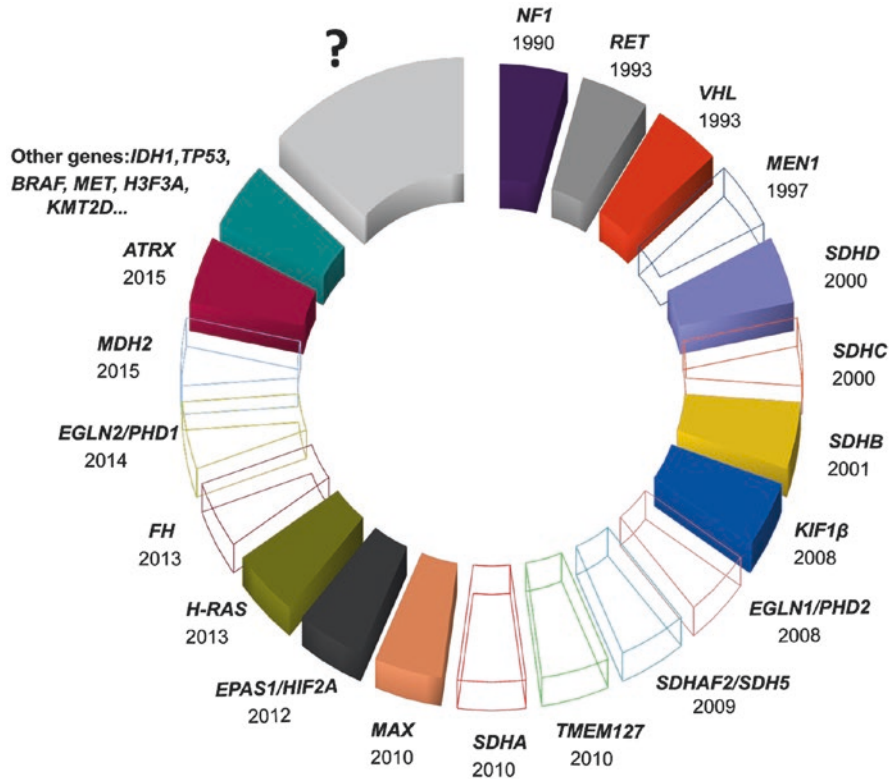
Fig. 2.2 Representation of all reported pheochromocytoma/paraganglioma susceptibility genes, specifying the year of publication, with special attention to the genes involved in the sporadic presentation of the disease (*opaque colored boxes*). Genes recently reported or mutated in only one sporadic tumor are grouped in "other genes." *Question mark* indicates that other unknown genes are pending to be uncovered

multiple PGLs, somatostatinomas, and polycythemia. The mutations were found in the residues located close to the prolyl hydroxylation site of the protein (proline 531) which was shown to disrupt the recognition of EPAS1 by members of the PHD family, as well as its hydroxylation and the consequent degradation by VHL [144, 145]. Thus, mutations affecting the *EPAS1* gene stabilize the protein, causing the aforementioned pseudohypoxia, indicating that *EPAS1* behaves as an oncogene. Later, somatic mutations in *EPAS1* were found in sporadic PPGL cases, demonstrating that the mutations in *EPAS1* are involved in a considerable proportion (~6 %) [9] of the sporadic presentation of the disease [146]. A germline alteration affecting *EPAS1* was also found in a patient with multiple PGLs and polycythemia. Although it was demonstrated that this latter variant stabilized the protein, its location outside the prolyl hydroxylation sites, and the absence of segregation with the disease in the family of the variant carrier, made this result somewhat controversial [147].

Moreover, the clinical implications of mutations affecting residues located in other prolyl hydroxylation sites remain unclear [148].

2.3.2   *PPGLs with Mutations in* **HRAS**

The members of the RAS family of oncoproteins (e.g., *HRAS*, *NRAS*, and *KRAS*) are small GTP-binding proteins that affect multiple downstream pathways related to cell growth and homeostasis. They were first linked to cancer in 1982 (reviewed in [149]), and it is now known that together they represent around 30 % of all oncogene-activating mutations found in many different cancers [149, 150]. Somatic mutations in the *Harvey rat sarcoma viral oncogene homolog* (*HRAS*) gene (11p15.5) was first described in one PCC by Yoshimoto *et al*. [151]. Crona et al. [141] applied whole-exome sequencing to 58 PCCs and found that four harbored somatic mutations in *HRAS*. The subsequent study of a larger series of tumors determined that 10–15 % of sporadic PCCs have mutations in *HRAS* and ruled out the involvement of *NRAS* and *KRAS* in the disease [9, 152]. The presence of mutations in one of the isoforms of RAS was not a new discovery in the development of endocrine tumors since they were known to be present in around 10–20 % of follicular cell-derived thyroid cancers and in 18 % of *RET*-negative sporadic MTCs [153–155]. A very recent gene expression analysis including seven *HRAS*-mutated tumors grouped all mutated tumors within the so-called transcriptional cluster 2 and confirmed that *HRAS* mutations and alterations in the known PPGL susceptibility genes are mutually exclusive [119].

2.3.3   *PPGLs with Mutations in* **ATRX**

Recently *ATRX* has been reported to be recurrently mutated in PPGL tumors [156]. The authors reported that 12.6 % of PPGLs analyzed had somatic *ATRX* mutations, one-third truncating mutations, and two-thirds missense mutations affecting a known functional domain and classified as deleterious by three in silico prediction algorithm. Considering only the tumors that had been genetically characterized, it seemed that *ATRX* mutations coexisted with other known PPGL driver mutations, mainly in the SDH genes "although ATRX has been recently described as a driver gene in PCC" [156, 164].

   ATRX is a large gene located on the X chromosome (Xq21.1) that encodes a member of the SWI/SNF family of chromatin remodeling proteins. Mutations in this gene are associated with an X-linked mental retardation syndrome most often accompanied by alpha-thalassemia (ATR-X syndrome) [157]. *ATRX* plays a role in telomere maintenance, chromosomal segregation in mitosis, and transcriptional regulation [158, 159]. It is frequently lost in tumor cells that use ALT (alternative
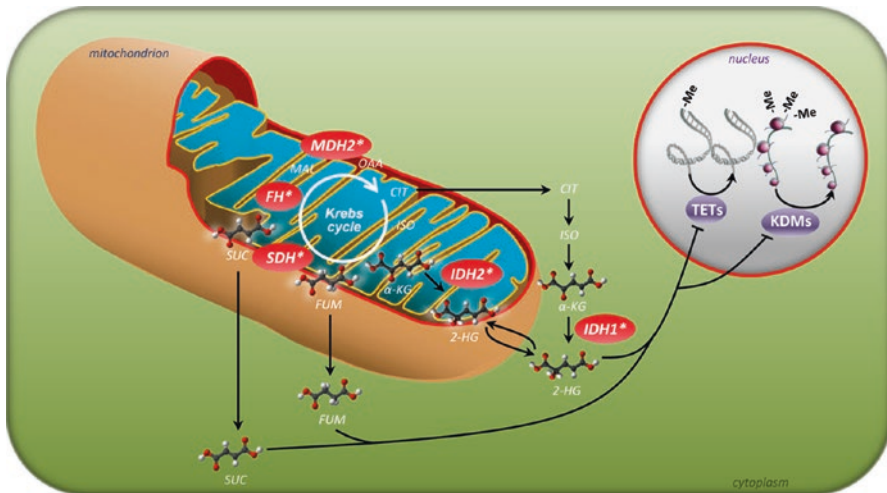
Fig. 2.3 Mutations (*) in genes belonging to the Krebs cycle (*IDH1/2*, SDH genes, *FH*, and now *MDH2*) lead to the accumulation of metabolites (2-hidroxyglutarate [2-*HG*], succinate [*SUC*], and fumarate [*FUM*], respectively) structurally similar to α-ketoglutarate (α-*KG*), a co-substrate pivotal for several dioxygenases. These "oncometabolites" act as competitive inhibitors of demethylases of DNA (*TETs*) and histone lysines (*KDMs*), causing important alterations in gene expression

lengthening of telomeres) for telomere maintenance [160, 161], which is associated with poor prognosis [160, 162].

2.3.4 Other Somatically Mutated PPGL-Related Genes

The knowledge of the genetic landscape of PPGL has dramatically increased since the application of new technologies to interrogate genetic alterations across the exome. Some of the previously mentioned susceptibility genes were in fact discovered using these platforms, and other genes have been reported, although their relative contribution to disease incidence is not yet well established. Among this latter group are somatic mutations in *TP53*, *BRAF*, *IDH1*, *FGFR1*, *H3F3A*, *MET*, *KMT2D*, *SETD2*, *JMJD1C*, *KMT2B*, or *EZH2* [4] (Fig. 2.2). It is particularly interesting that part of these genes is involved in chromatin-mediated gene regulation, suggesting it is likely other members of this and related pathways also contribute to PPGL pathogenesis.

Epigenetic changes leading to enhanced DNA and histone methylation have been linked to loss of function of TCA cycle-related genes. These mutations lead to elevated levels of intermediates that act as oncometabolites. The accumulation of these metabolites is postulated to cause hypermethylation by inhibiting 2-oxoglutarate-dependent histone and DNA demethylase enzymes [1, 70, 163] (Fig. 2.3). New findings described by Toledo *et al*. point to mutations of chromatin

remodeling genes that could represent another mechanism underlying chromatin architecture defects, something which is a feature of a considerable proportion of PPGLs [4].

2.4 Conclusions

Faced with the complex genetic etiology of PPGL described in this chapter, it is essential to collect comprehensive clinical information as well as germline and tumor DNA from patients in order to perform efficient genetic testing and to offer appropriate genetic counseling. The detection of a germline mutation in one of the genes related to the development of these tumors has clear implications for the clinical follow-up of the patient. The identification of a somatic mutation avoids additional germline genetic screening as new susceptibility genes are discovered and represents a valuable source of knowledge for future therapeutic opportunities.

New insights are emerging with the use of next-generation sequencing-based approaches, and it is probable that findings reviewed herein are only the tip of the iceberg in terms of the genetic landscape underlying PPGL.

References

1. Cascon A, Comino-Mendez I, Curras-Freixes M, de Cubas AA, Contreras L, Richter S, et al. Whole-exome sequencing identifies MDH2 as a new familial paraganglioma gene. J Natl Cancer Inst. 2015;107(5).
2. Dahia PL. Pheochromocytoma and paraganglioma pathogenesis: learning from genetic heterogeneity. Nat Rev Cancer. 2014;14(2):108–19.
3. Yang C, Zhuang Z, Fliedner SM, Shankavaram U, Sun MG, Bullova P, et al. Germ-line PHD1 and PHD2 mutations detected in patients with pheochromocytoma/paraganglioma-polycythemia. J Mol Med (Berl). 2015;93(1):93–104.
4. Toledo RA, Qin Y, Cheng ZM, Gao Q, Iwata S, Silva G, et al. Recurrent mutations of chromatin remodeling genes and kinase receptors in pheochromocytomas and paragangliomas. Clin Cancer Res. 2016;22:2301–10.
5. Cascon A, Inglada-Perez L, Comino-Mendez I, de Cubas AA, Leton R, Mora J, et al. Genetics of pheochromocytoma and paraganglioma in Spanish pediatric patients. Endocr Relat Cancer. 2013;20:L1–6.
6. King KS, Prodanov T, Kantorovich V, Fojo T, Hewitt JK, Zacharin M, et al. Metastatic pheochromocytoma/paraganglioma related to primary tumour development in childhood or adolescence: significant link to SDHB mutations. J Clin Oncol. 2011;29(31):4137–42.
7. Barontini M, Levin G, Sanso G. Characteristics of pheochromocytoma in a 4- to 20-year-old population. Ann N Y Acad Sci. 2006;1073:30–7.
8. Pacak K, Lenders JWM, Eisenhofer G. Pheochromocytoma: diagnosis, localization, and treatment. Malden: Blackwell Pub.; 2007.
9. Curras-Freixes M, Inglada-Perez L, Mancikova V, Montero-Conde C, Leton R, Comino-Mendez I, et al. Recommendations for somatic and germline genetic testing of single pheochromocytoma and paraganglioma based on findings from a series of 329 patients. J Med Genet. 2015;52:647–56.

10. Comino-Mendez I, Gracia-Aznarez FJ, Schiavi F, Landa I, Leandro-Garcia LJ, Leton R, et al. Exome sequencing identifies MAX mutations as a cause of hereditary pheochromocytoma. Nat Genet. 2011;43(7):663–7.

11. Burnichon N, Cascon A, Schiavi F, Morales NP, Comino-Mendez I, Abermil N, et al. MAX mutations cause hereditary and sporadic pheochromocytoma and paraganglioma. Clin Cancer Res. 2012;18(10):2828–37.

12. Bayley JP, Kunst HP, Cascon A, Sampietro ML, Gaal J, Korpershoek E, et al. SDHAF2 mutations in familial and sporadic paraganglioma and phaeochromocytoma. Lancet Oncol. 2010;11(4):366–72.

13. Hao HX, Khalimonchuk O, Schraders M, Dephoure N, Bayley JP, Kunst H, et al. SDH5, a gene required for flavination of succinate dehydrogenase, is mutated in paraganglioma. Science. 2009;325(5944):1139–42.

14. Baysal BE, Ferrell RE, Willett-Brozick JE, Lawrence EC, Myssiorek D, Bosch A, et al. Mutations in SDHD, a mitochondrial complex II gene, in hereditary paraganglioma. Science. 2000;287(5454):848–51.

15. Zhuang Z, Yang C, Lorenzo F, Merino M, Fojo T, Kebebew E, et al. Somatic HIF2A gain-of-function mutations in paraganglioma with polycythemia. N Engl J Med. 2012;367(10):922–30.

16. Eng C, Clayton D, Schuffenecker I, Lenoir G, Cote G, Gagel RF, et al. The relationship between specific RET proto-oncogene mutations and disease phenotype in multiple endocrine neoplasia type 2. International RET mutation consortium analysis. JAMA. 1996;276(19):1575–9.

17. Donis-Keller H, Dou S, Chi D, Carlson KM, Toshima K, Lairmore TC, et al. Mutations in the RET proto-oncogene are associated with MEN 2A and FMTC. Hum Mol Genet. 1993;2(7):851–6.

18. Eng C, Smith DP, Mulligan LM, Nagai MA, Healey CS, Ponder MA, et al. Point mutation within the tyrosine kinase domain of the RET proto-oncogene in multiple endocrine neoplasia type 2B and related sporadic tumours. Hum Mol Genet. 1994;3(2):237–41.

19. Hofstra RM, Landsvater RM, Ceccherini I, Stulp RP, Stelwagen T, Luo Y, et al. A mutation in the RET proto-oncogene associated with multiple endocrine neoplasia type 2B and sporadic medullary thyroid carcinoma. Nature. 1994;367(6461):375–6.

20. Mulligan LM, Kwok JB, Healey CS, Elsdon MJ, Eng C, Gardner E, et al. Germ-line mutations of the RET proto-oncogene in multiple endocrine neoplasia type 2A. Nature. 1993;363(6428):458–60.

21. Figlioli G, Landi S, Romei C, Elisei R, Gemignani F. Medullary thyroid carcinoma (MTC) and RET proto-oncogene: mutation spectrum in the familial cases and a meta-analysis of studies on the sporadic form. Mutat Res. 2013;752(1):36–44.

22. de Groot JW, Links TP, Plukker JT, Lips CJ, Hofstra RM. RET as a diagnostic and therapeutic target in sporadic and hereditary endocrine tumours. Endocr Rev. 2006;27(5):535–60.

23. Kloos RT, Eng C, Evans DB, Francis GL, Gagel RF, Gharib H, et al. Medullary thyroid cancer: management guidelines of the American Thyroid Association. Thyroid. 2009;19(6):565–612.

24. Wells Jr SA, Asa SL, Dralle H, Elisei R, Evans DB, Gagel RF, et al. Revised American Thyroid Association guidelines for the management of medullary thyroid carcinoma. Thyroid. 2015;25(6):567–610.

25. Chernock RD, Hagemann IS. Molecular pathology of hereditary and sporadic medullary thyroid carcinomas. Am J Clin Pathol. 2015;143(6):768–77.

26. Milos IN, Frank-Raue K, Wohllk N, Maia AL, Pusiol E, Patocs A, et al. Age-related neoplastic risk profiles and penetrance estimations in multiple endocrine neoplasia type 2A caused by germ line RET Cys634Trp (TGC > TGG) mutation. Endocr Relat Cancer. 2008;15(4):1035–41.

27. Waguespack SG, Rich T, Grubbs E, Ying AK, Perrier ND, Ayala-Ramirez M, et al. A current review of the etiology, diagnosis, and treatment of pediatric pheochromocytoma and paraganglioma. J Clin Endocrinol Metab. 2010;95(5):2023–37.

28. Latif F, Tory K, Gnarra J, Yao M, Duh FM, Orcutt ML, et al. Identification of the von Hippel-Lindau disease tumour suppressor gene. Science. 1993;260(5112):1317–20.
29. Gnarra JR, Tory K, Weng Y, Schmidt L, Wei MH, Li H, et al. Mutations of the VHL tumour suppressor gene in renal carcinoma. Nat Genet. 1994;7(1):85–90.
30. Kaelin Jr WG. The von Hippel-Lindau tumour suppressor protein: O2 sensing and cancer. Nat Rev Cancer. 2008;8(11):865–73.
31. Maxwell PH, Wiesener MS, Chang GW, Clifford SC, Vaux EC, Cockman ME, et al. The tumour suppressor protein VHL targets hypoxia-inducible factors for oxygen-dependent proteolysis. Nature. 1999;399(6733):271–5.
32. Stebbins CE, Kaelin Jr WG, Pavletich NP. Structure of the VHL-ElonginC-ElonginB complex: implications for VHL tumour suppressor function. Science. 1999;284(5413):455–61.
33. Lonser RR, Glenn GM, Walther M, Chew EY, Libutti SK, Linehan WM, et al. Von Hippel-Lindau disease. Lancet. 2003;361(9374):2059–67.
34. Ong KR, Woodward ER, Killick P, Lim C, Macdonald F, Maher ER. Genotype-phenotype correlations in von Hippel-Lindau disease. Hum Mutat. 2007;28(2):143–9.
35. Ang SO, Chen H, Hirota K, Gordeuk VR, Jelinek J, Guan Y, et al. Disruption of oxygen homeostasis underlies congenital Chuvash polycythemia. Nat Genet. 2002;32(4):614–21.
36. Pastore YD, Jelinek J, Ang S, Guan Y, Liu E, Jedlickova K, et al. Mutations in the VHL gene in sporadic apparently congenital polycythemia. Blood. 2003;101(4):1591–5.
37. Maher ER, Neumann HP, Richard S. Von Hippel-Lindau disease: a clinical and scientific review. Eur J Hum Genet. 2011;19(6):617–23.
38. Maranchie JK, Afonso A, Albert PS, Kalyandrug S, Phillips JL, Zhou S, et al. Solid renal tumour severity in von Hippel Lindau disease is related to germline deletion length and location. Hum Mutat. 2004;23(1):40–6.
39. Cascon A, Escobar B, Montero-Conde C, Rodriguez-Antona C, Ruiz-Llorente S, Osorio A, et al. Loss of the actin regulator HSPC300 results in clear cell renal cell carcinoma protection in Von Hippel-Lindau patients. Hum Mutat. 2007;28(6):613–21.
40. McNeill A, Rattenberry E, Barber R, Killick P, MacDonald F, Maher ER. Genotype-phenotype correlations in VHL exon deletions. Am J Med Genet A. 2009;149A(10):2147–51.
41. Gimm O, Koch CA, Januszewicz A, Opocher G, Neumann HP. The genetic basis of pheochromocytoma. Front Horm Res. 2004;31:45–60.
42. Eisenhofer G, Huynh TT, Pacak K, Brouwers FM, Walther MM, Linehan WM, et al. Distinct gene expression profiles in norepinephrine- and epinephrine-producing hereditary and sporadic pheochromocytomas: activation of hypoxia-driven angiogenic pathways in von Hippel-Lindau syndrome. Endocr Relat Cancer. 2004;11(4):897–911.
43. Eisenhofer G, Lenders JW, Timmers H, Mannelli M, Grebe SK, Hofbauer LC, et al. Measurements of plasma methoxytyramine, normetanephrine, and metanephrine as discriminators of different hereditary forms of pheochromocytoma. Clin Chem. 2011;57(3):411–20.
44. Aufforth RD, Ramakant P, Sadowski SM, Mehta A, Trebska-McGowan K, Nilubol N, et al. Pheochromocytoma screening initiation and frequency in von Hippel-Lindau syndrome. J Clin Endocrinol Metab. 2015;100(12):4498–504.
45. Sgambati MT, Stolle C, Choyke PL, Walther MM, Zbar B, Linehan WM, et al. Mosaicism in von Hippel-Lindau disease: lessons from kindreds with germline mutations identified in offspring with mosaic parents. Am J Hum Genet. 2000;66(1):84–91.
46. Evans DG, Howard E, Giblin C, Clancy T, Spencer H, Huson SM, et al. Birth incidence and prevalence of tumour-prone syndromes: estimates from a UK family genetic register service. Am J Med Genet A. 2010;152A(2):327–32.
47. Burnichon N, Vescovo L, Amar L, Libe R, de Reynies A, Venisse A, et al. Integrative genomic analysis reveals somatic mutations in pheochromocytoma and paraganglioma. Hum Mol Genet. 2011;20(20):3974–85.
48. Knauth K, Bex C, Jemth P, Buchberger A. Renal cell carcinoma risk in type 2 von Hippel-Lindau disease correlates with defects in pVHL stability and HIF-1alpha interactions. Oncogene. 2006;25(3):370–7.

49. Knauth K, Cartwright E, Freund S, Bycroft M, Buchberger A. VHL mutations linked to type 2C von Hippel-Lindau disease cause extensive structural perturbations in pVHL. J Biol Chem. 2009;284(16):10514–22.

50. Schoenfeld AR, Davidowitz EJ, Burk RD. Elongin BC complex prevents degradation of von Hippel-Lindau tumour suppressor gene products. Proc Natl Acad Sci U S A. 2000; 97(15):8507–12.

51. Kamura T, Brower CS, Conaway RC, Conaway JW. A molecular basis for stabilization of the von Hippel-Lindau (VHL) tumour suppressor protein by components of the VHL ubiquitin ligase. J Biol Chem. 2002;277(33):30388–93.

52. Ruiz-Llorente S, Bravo J, Cebrian A, Cascon A, Pollan M, Telleria D, et al. Genetic characterization and structural analysis of VHL Spanish families to define genotype-phenotype correlations. Hum Mutat. 2004;23(2):160–9.

53. Neumann HP, Bausch B, McWhinney SR, Bender BU, Gimm O, Franke G, et al. Germ-line mutations in nonsyndromic pheochromocytoma. N Engl J Med. 2002;346(19):1459–66.

54. Boyd KP, Korf BR, Theos A. Neurofibromatosis type 1. J Am Acad Dermatol. 2009;61(1):1– 14; quiz 5–6.

55. Cassidy SB, Allanson JE. Management of genetic syndromes. 2nd ed. Hoboken: Wiley-Liss; 2005.

56. Hersh JH. Health supervision for children with neurofibromatosis. Pediatrics. 2008; 121(3):633–42.

57. Pasmant E, Parfait B, Luscan A, Goussard P, Briand-Suleau A, Laurendeau I, et al. Neurofibromatosis type 1 molecular diagnosis: what can NGS do for you when you have a large gene with loss of function mutations? Eur J Hum Genet. 2015;23(5):596–601.

58. Kehrer-Sawatzki H, Cooper DN. Mosaicism in sporadic neurofibromatosis type 1: variations on a theme common to other hereditary cancer syndromes? J Med Genet. 2008;45(10):622–31.

59. Trevisson E, Forzan M, Salviati L, Clementi M. Neurofibromatosis type 1 in two siblings due to maternal germline mosaicism. Clin Genet. 2014;85(4):386–9.

60. Bausch B, Koschker AC, Fassnacht M, Stoevesandt J, Hoffmann MM, Eng C, et al. Comprehensive mutation scanning of NF1 in apparently sporadic cases of pheochromocytoma. J Clin Endocrinol Metab. 2006;91(9):3478–81.

61. Jimenez C, Cote G, Arnold A, Gagel RF. Review: should patients with apparently sporadic pheochromocytomas or paragangliomas be screened for hereditary syndromes? J Clin Endocrinol Metab. 2006;91(8):2851–8.

62. Fishbein L, Nathanson KL. Pheochromocytoma and paraganglioma: understanding the complexities of the genetic background. Cancer Genet. 2012;205(1–2):1–11.

63. Hoekstra AS, Bayley JP. The role of complex II in disease. Biochim Biophys Acta. 2013;1827(5):543–51.

64. Pollard PJ, Briere JJ, Alam NA, Barwell J, Barclay E, Wortham NC, et al. Accumulation of Krebs cycle intermediates and over-expression of HIF1alpha in tumours which result from germline FH and SDH mutations. Hum Mol Genet. 2005;14(15):2231–9.

65. Briere JJ, Favier J, Benit P, El Ghouzzi V, Lorenzato A, Rabier D, et al. Mitochondrial succinate is instrumental for HIF1alpha nuclear translocation in SDHA-mutant fibroblasts under normoxic conditions. Hum Mol Genet. 2005;14(21):3263–9.

66. Selak MA, Armour SM, MacKenzie ED, Boulahbel H, Watson DG, Mansfield KD, et al. Succinate links TCA cycle dysfunction to oncogenesis by inhibiting HIF-alpha prolyl hydroxylase. Cancer Cell. 2005;7(1):77–85.

67. Lopez-Jimenez E, Gomez-Lopez G, Leandro-Garcia LJ, Munoz I, Schiavi F, Montero-Conde C, et al. Research resource: transcriptional profiling reveals different pseudohypoxic signatures in SDHB and VHL-related pheochromocytomas. Mol Endocrinol. 2010;24(12): 2382–91.

68. King A, Selak MA, Gottlieb E. Succinate dehydrogenase and fumarate hydratase: linking mitochondrial dysfunction and cancer. Oncogene. 2006;25(34):4675–82.

69. Korpershoek E, Favier J, Gaal J, Burnichon N, van Gessel B, Oudijk L, et al. SDHA immunohistochemistry detects germline SDHA gene mutations in apparently sporadic paragangliomas and pheochromocytomas. J Clin Endocrinol Metab. 2011;96(9):E1472–6.

70. Letouze E, Martinelli C, Loriot C, Burnichon N, Abermil N, Ottolenghi C, et al. SDH mutations establish a hypermethylator phenotype in paraganglioma. Cancer Cell. 2013;23(6):739–52.

71. de Cubas AA, Korpershoek E, Inglada-Perez L, Letouze E, Curras-Freixes M, Fernandez AF, et al. DNA methylation profiling in pheochromocytoma and paraganglioma reveals diagnostic and prognostic markers. Clin Cancer Res. 2015;21(13):3020–30.

72. Abe M, Ohira M, Kaneda A, Yagi Y, Yamamoto S, Kitano Y, et al. CpG island methylator phenotype is a strong determinant of poor prognosis in neuroblastomas. Cancer Res. 2005;65(3):828–34.

73. Amar L, Baudin E, Burnichon N, Peyrard S, Silvera S, Bertherat J, et al. Succinate dehydrogenase B gene mutations predict survival in patients with malignant pheochromocytomas or paragangliomas. J Clin Endocrinol Metab. 2007;92(10):3822–8.

74. Vanharanta S, Buchta M, McWhinney SR, Virta SK, Peczkowska M, Morrison CD, et al. Early-onset renal cell carcinoma as a novel extraparaganglial component of SDHB-associated heritable paraganglioma. Am J Hum Genet. 2004;74(1):153–9.

75. Ricketts C, Woodward ER, Killick P, Morris MR, Astuti D, Latif F, et al. Germline SDHB mutations and familial renal cell carcinoma. J Natl Cancer Inst. 2008;100(17):1260–2.

76. Ricketts CJ, Forman JR, Rattenberry E, Bradshaw N, Lalloo F, Izatt L, et al. Tumour risks and genotype-phenotype-proteotype analysis in 358 patients with germline mutations in SDHB and SDHD. Hum Mutat. 2010;31(1):41–51.

77. Neumann HP, Pawlu C, Peczkowska M, Bausch B, McWhinney SR, Muresan M, et al. Distinct clinical features of paraganglioma syndromes associated with SDHB and SDHD gene mutations. JAMA. 2004;292(8):943–51.

78. Stratakis CA, Carney JA. The triad of paragangliomas, gastric stromal tumours and pulmonary chondromas (Carney triad), and the dyad of paragangliomas and gastric stromal sarcomas (Carney-Stratakis syndrome): molecular genetics and clinical implications. J Intern Med. 2009;266(1):43–52.

79. Hirota S, Isozaki K, Moriyama Y, Hashimoto K, Nishida T, Ishiguro S, et al. Gain-of-function mutations of c-kit in human gastrointestinal stromal tumours. Science. 1998;279(5350):577–80.

80. Hirota S, Ohashi A, Nishida T, Isozaki K, Kinoshita K, Shinomura Y, et al. Gain-of-function mutations of platelet-derived growth factor receptor alpha gene in gastrointestinal stromal tumours. Gastroenterology. 2003;125(3):660–7.

81. Xekouki P, Szarek E, Bullova P, Giubellino A, Quezado M, Mastroyannis SA, et al. Pituitary adenoma with paraganglioma/pheochromocytoma (3PAs) and succinate dehydrogenase defects in humans and mice. J Clin Endocrinol Metab. 2015;100(5):E710–9.

82. Papathomas TG, Gaal J, Corssmit EP, Oudijk L, Korpershoek E, Heimdal K, et al. Non-pheochromocytoma (PCC)/paraganglioma (PGL) tumours in patients with succinate dehydrogenase-related PCC-PGL syndromes: a clinicopathological and molecular analysis. Eur J Endocrinol. 2014;170(1):1–12.

83. Denes J, Swords F, Rattenberry E, Stals K, Owens M, Cranston T, et al. Heterogeneous genetic background of the association of pheochromocytoma/paraganglioma and pituitary adenoma: results from a large patient cohort. J Clin Endocrinol Metab. 2015;100(3):E531–41.

84. O'Toole SM, Denes J, Robledo M, Stratakis CA, Korbonits M. 15 YEARS OF PARAGANGLIOMA: the association of pituitary adenomas and phaeochromocytomas or paragangliomas. Endocr Relat Cancer. 2015;22(4):T105–22.

85. Mannelli M, Castellano M, Schiavi F, Filetti S, Giacche M, Mori L, et al. Clinically guided genetic screening in a large cohort of italian patients with pheochromocytomas and/or functional or nonfunctional paragangliomas. J Clin Endocrinol Metab. 2009;94(5):1541–7.

86. Cascon A, Pita G, Burnichon N, Landa I, Lopez-Jimenez E, Montero-Conde C, et al. Genetics of pheochromocytoma and paraganglioma in Spanish patients. J Clin Endocrinol Metab. 2009;94(5):1701–5.

87. Baysal BE, Willett-Brozick JE, Lawrence EC, Drovdlic CM, Savul SA, McLeod DR, et al. Prevalence of SDHB, SDHC, and SDHD germline mutations in clinic patients with head and neck paragangliomas. J Med Genet. 2002;39(3):178–83.

88. Cascon A, Ruiz-Llorente S, Fraga MF, Leton R, Telleria D, Sastre J, et al. Genetic and epigenetic profile of sporadic pheochromocytomas. J Med Genet. 2004;41(3):e30.

89. Yamashita R, Usui T, Hashimoto S, Suzuki H, Takahashi M, Honkura K, et al. Predominant expression of mutated allele of the succunate dehydrogenase D (SDHD) gene in the SDHD-related paragangliomas. Endocr J. 2009;56(9):1129–35.

90. Baysal BE, McKay SE, Kim YJ, Zhang Z, Alila L, Willett-Brozick JE, et al. Genomic imprinting at a boundary element flanking the SDHD locus. Hum Mol Genet. 2011;20(22):4452–61.

91. Hensen EF, Jordanova ES, van Minderhout IJ, Hogendoorn PC, Taschner PE, van der Mey AG, et al. Somatic loss of maternal chromosome 11 causes parent-of-origin-dependent inheritance in SDHD-linked paraganglioma and phaeochromocytoma families. Oncogene. 2004;23(23):4076–83.

92. Pigny P, Vincent A, Cardot Bauters C, Bertrand M, de Montpreville VT, Crepin M, et al. Paraganglioma after maternal transmission of a succinate dehydrogenase gene mutation. J Clin Endocrinol Metab. 2008;93(5):1609–15.

93. Burnichon N, Rohmer V, Amar L, Herman P, Leboulleux S, Darrouzet V, et al. The succinate dehydrogenase genetic testing in a large prospective series of patients with paragangliomas. J Clin Endocrinol Metab. 2009;94(8):2817–27.

94. Havekes B, Corssmit EP, Jansen JC, van der Mey AG, Vriends AH, Romijn JA. Malignant paragangliomas associated with mutations in the succinate dehydrogenase D gene. J Clin Endocrinol Metab. 2007;92(4):1245–8.

95. Amar L, Bertherat J, Baudin E, Ajzenberg C, Bressac-de Paillerets B, Chabre O, et al. Genetic testing in pheochromocytoma or functional paraganglioma. J Clin Oncol. 2005;23(34):8812–8.

96. Cascon A, Ruiz-Llorente S, Cebrian A, Leton R, Telleria D, Benitez J, et al. G12S and H50R variations are polymorphisms in the SDHD gene. Genes Chromosomes Cancer. 2003;37(2):220–1.

97. Lenders JW, Duh QY, Eisenhofer G, Gimenez-Roqueplo AP, Grebe SK, Murad MH, et al. Pheochromocytoma and paraganglioma: an endocrine society clinical practice guideline. J Clin Endocrinol Metab. 2014;99(6):1915–42.

98. Bayley JP, Grimbergen AE, van Bunderen PA, van der Wielen M, Kunst HP, Lenders JW, et al. The first Dutch SDHB founder deletion in paraganglioma-pheochromocytoma patients. BMC Med Genet. 2009;10:34.

99. Cascon A, Landa I, Lopez-Jimenez E, Diez-Hernandez A, Buchta M, Montero-Conde C, et al. Molecular characterisation of a common SDHB deletion in paraganglioma patients. J Med Genet. 2008;45(4):233–8.

100. Cascon A, Lopez-Jimenez E, Landa I, Leskela S, Leandro-Garcia LJ, Maliszewska A, et al. Rationalization of genetic testing in patients with apparently sporadic pheochromocytoma/paraganglioma. Horm Metab Res. 2009;41(9):672–5.

101. Hes FJ, Weiss MM, Woortman SA, de Miranda NF, van Bunderen PA, Bonsing BA, et al. Low penetrance of a SDHB mutation in a large Dutch paraganglioma family. BMC Med Genet. 2010;11:92.

102. Schiavi F, Milne RL, Anda E, Blay P, Castellano M, Opocher G, et al. Are we overestimating the penetrance of mutations in SDHB? Hum Mutat. 2010;31(6):761–2.

103. Niemann S, Muller U. Mutations in SDHC cause autosomal dominant paraganglioma, type 3. Nat Genet. 2000;26(3):268–70.

104. Welander J, Soderkvist P, Gimm O. Genetics and clinical characteristics of hereditary pheochromocytomas and paragangliomas. Endocr Relat Cancer. 2011;18(6):R253–76.

105. Schiavi F, Boedeker CC, Bausch B, Peczkowska M, Gomez CF, Strassburg T, et al. Predictors and prevalence of paraganglioma syndrome associated with mutations of the SDHC gene. JAMA. 2005;294(16):2057–63.
106. Else T, Marvin ML, Everett JN, Gruber SB, Arts HA, Stoffel EM, et al. The clinical phenotype of SDHC-associated hereditary paraganglioma syndrome (PGL3). J Clin Endocrinol Metab. 2014;99(8):E1482–6.
107. Haller F, Moskalev EA, Faucz FR, Barthelmess S, Wiemann S, Bieg M, et al. Aberrant DNA hypermethylation of SDHC: a novel mechanism of tumour development in Carney triad. Endocr Relat Cancer. 2014;21(4):567–77.
108. Killian JK, Miettinen M, Walker RL, Wang Y, Zhu YJ, Waterfall JJ, et al. Recurrent epimutation of SDHC in gastrointestinal stromal tumours. Sci Transl Med. 2014;6(268):268ra177.
109. Richter S, Klink B, Nacke B, deCubas AA, Mangelis A, Rapizzi E, et al. Epigenetic mutation of the succinate dehydrogenase C promoter in a patient with two paragangliomas. J Clin Endocrinol Metab. 2015;101:359–63
110. Burnichon N, Briere JJ, Libe R, Vescovo L, Riviere J, Tissier F, et al. SDHA is a tumour suppressor gene causing paraganglioma. Hum Mol Genet. 2010;19(15):3011–20.
111. Piccini V, Rapizzi E, Bacca A, Di Trapani G, Pulli R, Giache V, et al. Head and neck paragangliomas: genetic spectrum and clinical variability in 79 consecutive patients. Endocr Relat Cancer. 2012;19(2):149–55.
112. Kunst HP, Rutten MH, de Monnink JP, Hoefsloot LH, Timmers HJ, Marres HA, et al. SDHAF2 (PGL2-SDH5) and hereditary head and neck paraganglioma. Clin Cancer Res. 2011;17(2):247–54.
113. Schmidt LS, Linehan WM. Hereditary leiomyomatosis and renal cell carcinoma. Int J Nephrol Renov Dis. 2014;7:253–60.
114. Xiao M, Yang H, Xu W, Ma S, Lin H, Zhu H, et al. Inhibition of alpha-KG-dependent histone and DNA demethylases by fumarate and succinate that are accumulated in mutations of FH and SDH tumour suppressors. Genes Dev. 2012;26(12):1326–38.
115. Castro-Vega LJ, Buffet A, De Cubas AA, Cascon A, Menara M, Khalifa E, et al. Germline mutations in FH confer predisposition to malignant pheochromocytomas and paragangliomas. Hum Mol Genet. 2014;23(9):2440–6.
116. Qin Y, Yao L, King EE, Buddavarapu K, Lenci RE, Chocron ES, et al. Germline mutations in TMEM127 confer susceptibility to pheochromocytoma. Nat Genet. 2010;42(3):229–33.
117. Bhaskar PT, Hay N. The two TORCs and Akt. Dev Cell. 2007;12(4):487–502.
118. Guertin DA, Sabatini DM. Defining the role of mTOR in cancer. Cancer Cell. 2007;12(1):9–22.
119. Stenman A, Welander J, Gustavsson I, Brunaud L, Backdahl M, Soderkvist P, et al. HRAS mutation prevalence and associated expression patterns in pheochromocytoma. Genes Chromosomes Cancer. 2016;55:452–9.
120. Yao L, Schiavi F, Cascon A, Qin Y, Inglada-Perez L, King EE, et al. Spectrum and prevalence of FP/TMEM127 gene mutations in pheochromocytomas and paragangliomas. JAMA. 2010;304(23):2611–9.
121. Neumann HP, Sullivan M, Winter A, Malinoc A, Hoffmann MM, Boedeker CC, et al. Germline mutations of the TMEM127 gene in patients with paraganglioma of head and neck and extraadrenal abdominal sites. J Clin Endocrinol Metab. 2011;96(8):E1279–82.
122. Qin Y, Deng Y, Ricketts CJ, Srikantan S, Wang E, Maher ER, et al. The tumour susceptibility gene TMEM127 is mutated in renal cell carcinomas and modulates endolysosomal function. Hum Mol Genet. 2014;23:2428–39.
123. Hopewell R, Ziff EB. The nerve growth factor-responsive PC12 cell line does not express the Myc dimerization partner Max. Mol Cell Biol. 1995;15(7):3470–8.
124. Ribon V, Leff T, Saltiel AR. c-Myc does not require max for transcriptional activity in PC-12 cells. Mol Cell Neurosci. 1994;5(3):277–82.
125. Seeger RC, Brodeur GM, Sather H, Dalton A, Siegel SE, Wong KY, et al. Association of multiple copies of the N-myc oncogene with rapid progression of neuroblastomas. N Engl J Med. 1985;313(18):1111–6.

126. Peczkowska M, Kowalska A, Sygut J, Waligorski D, Malinoc A, Janaszek-Sitkowska H, et al. Testing new susceptibility genes in the cohort of apparently sporadic phaeochromocytoma/paraganglioma patients with clinical characteristics of hereditary syndromes. Clin Endocrinol (Oxf). 2013;79(6):817–23.
127. Castro-Vega LJ, Letouze E, Burnichon N, Buffet A, Disderot PH, Khalifa E, et al. Multi-omics analysis defines core genomic alterations in pheochromocytomas and paragangliomas. Nat Commun. 2015;6:6044.
128. Raue F, Zink A. Clinical features of multiple endocrine neoplasia type 1 and type 2. Horm Res. 1992;38 Suppl 2:31–5.
129. Brandi ML, Gagel RF, Angeli A, Bilezikian JP, Beck-Peccoz P, Bordi C, et al. Guidelines for diagnosis and therapy of MEN type 1 and type 2. J Clin Endocrinol Metab. 2001; 86(12):5658–71.
130. Ladroue C, Carcenac R, Leporrier M, Gad S, Le Hello C, Galateau-Salle F, et al. PHD2 mutation and congenital erythrocytosis with paraganglioma. N Engl J Med. 2008;359(25): 2685–92.
131. Percy MJ, Zhao Q, Flores A, Harrison C, Lappin TR, Maxwell PH, et al. A family with erythrocytosis establishes a role for prolyl hydroxylase domain protein 2 in oxygen homeostasis. Proc Natl Acad Sci U S A. 2006;103(3):654–9.
132. Schlisio S, Kenchappa RS, Vredeveld LC, George RE, Stewart R, Greulich H, et al. The kinesin KIF1Bbeta acts downstream from EglN3 to induce apoptosis and is a potential 1p36 tumour suppressor. Genes Dev. 2008;22(7):884–93.
133. Yeh IT, Lenci RE, Qin Y, Buddavarapu K, Ligon AH, Leteurtre E, et al. A germline mutation of the KIF1B beta gene on 1p36 in a family with neural and nonneural tumours. Hum Genet. 2008;124(3):279–85.
134. Welander J, Andreasson A, Juhlin CC, Wiseman RW, Backdahl M, Hoog A, et al. Rare germline mutations identified by targeted next-generation sequencing of susceptibility genes in pheochromocytoma and paraganglioma. J Clin Endocrinol Metab. 2014;99(7): E1352–60.
135. Dannenberg H, De Krijger RR, van der Harst E, Abbou M, IJzendoorn Y, Komminoth P, et al. Von Hippel-Lindau gene alterations in sporadic benign and malignant pheochromocytomas. Int J Cancer. 2003;105(2):190–5.
136. Gimm O, Armanios M, Dziema H, Neumann HP, Eng C. Somatic and occult germ-line mutations in SDHD, a mitochondrial complex II gene, in nonfamilial pheochromocytoma. Cancer Res. 2000;60(24):6822–5.
137. van Nederveen FH, Korpershoek E, Lenders JW, de Krijger RR, Dinjens WN. Somatic SDHB mutation in an extraadrenal pheochromocytoma. N Engl J Med. 2007;357(3):306–8.
138. Burnichon N, Buffet A, Parfait B, Letouze E, Laurendeau I, Loriot C, et al. Somatic NF1 inactivation is a frequent event in sporadic pheochromocytoma. Hum Mol Genet. 2012;21(26):5397–405.
139. Welander J, Larsson C, Backdahl M, Hareni N, Sivler T, Brauckhoff M, et al. Integrative genomics reveals frequent somatic NF1 mutations in sporadic pheochromocytomas. Hum Mol Genet. 2012;21(26):5406–16.
140. Luchetti A, Walsh D, Rodger F, Clark G, Martin T, Irving R, et al. Profiling of somatic mutations in phaeochromocytoma and paraganglioma by targeted next generation sequencing analysis. Int J Endocrinol. 2015;2015:138573.
141. Crona J, Delgado Verdugo A, Maharjan R, Stalberg P, Granberg D, Hellman P, et al. Somatic mutations in H-RAS in sporadic pheochromocytoma and paraganglioma identified by exome sequencing. J Clin Endocrinol Metab. 2013;98(7):E1266–71.
142. Semenza GL. HIF-1, O(2), and the 3 PHDs: how animal cells signal hypoxia to the nucleus. Cell. 2001;107(1):1–3.
143. Gruber M, Simon MC. Hypoxia-inducible factors, hypoxia, and tumour angiogenesis. Curr Opin Hematol. 2006;13(3):169–74.
144. McDonough MA, Li V, Flashman E, Chowdhury R, Mohr C, Lienard BM, et al. Cellular oxygen sensing: crystal structure of hypoxia-inducible factor prolyl hydroxylase (PHD2). Proc Natl Acad Sci U S A. 2006;103(26):9814–9.

145. Min JH, Yang H, Ivan M, Gertler F, Kaelin Jr WG, Pavletich NP. Structure of an HIF-1alpha -pVHL complex: hydroxyproline recognition in signaling. Science. 2002;296(5574):1886–9.
146. Comino-Mendez I, de Cubas AA, Bernal C, Alvarez-Escola C, Sanchez-Malo C, Ramirez-Tortosa CL, et al. Tumoural EPAS1 (HIF2A) mutations explain sporadic pheochromocytoma and paraganglioma in the absence of erythrocytosis. Hum Mol Genet. 2013;22(11):2169–76.
147. Lorenzo FR, Yang C, Ng Tang Fui M, Vankayalapati H, Zhuang Z, Huynh T, et al. A novel EPAS1/HIF2A germline mutation in a congenital polycythemia with paraganglioma. J Mol Med (Berl). 2013;91(4):507–12.
148. Welander J, Andreasson A, Brauckhoff M, Backdahl M, Larsson C, Gimm O, et al. Frequent EPAS1/HIF2alpha exons 9 and 12 mutations in non-familial pheochromocytoma. Endocr Relat Cancer. 2014;21(3):495–504.
149. Cox AD, Der CJ. Ras history: the saga continues. Small GTPases. 2010;1(1):2–27.
150. Karnoub AE, Weinberg RA. Ras oncogenes: split personalities. Nat Rev Mol Cell Biol. 2008;9(7):517–31.
151. Yoshimoto K, Iwahana H, Fukuda A, Sano T, Katsuragi K, Kinoshita M, et al. ras mutations in endocrine tumours: mutation detection by polymerase chain reaction-single strand conformation polymorphism. Jpn J Cancer Res. 1992;83(10):1057–62.
152. Oudijk L, de Krijger RR, Rapa I, Beuschlein F, de Cubas AA, Dei Tos AP, et al. H-RAS mutations are restricted to sporadic pheochromocytomas lacking specific clinical or pathological features: data from a multi-institutional series. J Clin Endocrinol Metab. 2014;99(7):E1376–80.
153. Nikiforov YE, Nikiforova MN. Molecular genetics and diagnosis of thyroid cancer. Nat Rev Endocrinol. 2011;7(10):569–80.
154. Agrawal N, Jiao Y, Sausen M, Leary R, Bettegowda C, Roberts NJ, et al. Exomic sequencing of medullary thyroid cancer reveals dominant and mutually exclusive oncogenic mutations in RET and RAS. J Clin Endocrinol Metab. 2013;98(2):E364–9.
155. Ciampi R, Mian C, Fugazzola L, Cosci B, Romei C, Barollo S, et al. Evidence of a low prevalence of RAS mutations in a large medullary thyroid cancer series. Thyroid. 2013;23(1):50–7.
156. Fishbein L, Khare S, Wubbenhorst B, DeSloover D, D'Andrea K, Merrill S, et al. Whole-exome sequencing identifies somatic ATRX mutations in pheochromocytomas and paragangliomas. Nat Commun. 2015;6:6140.
157. Gibbons RJ, Picketts DJ, Villard L, Higgs DR. Mutations in a putative global transcriptional regulator cause X-linked mental retardation with alpha-thalassemia (ATR-X syndrome). Cell. 1995;80(6):837–45.
158. Eid R, Demattei MV, Episkopou H, Auge-Gouillou C, Decottignies A, Grandin N, et al. Genetic inactivation of ATRX leads to a decrease in the amount of telomeric cohesin and level of telomere transcription in human glioma cells. Mol Cell Biol. 2015;35(16):2818–30.
159. Ratnakumar K, Bernstein E. ATRX: the case of a peculiar chromatin remodeler. Epigenetics. 2013;8(1):3–9.
160. Liau JY, Tsai JH, Yang CY, Lee JC, Liang CW, Hsu HH, et al. Alternative lengthening of telomeres phenotype in malignant vascular tumours is highly associated with loss of ATRX expression and is frequently observed in hepatic angiosarcomas. Hum Pathol. 2015;46(9):1360–6.
161. Kurihara S, Hiyama E, Onitake Y, Yamaoka E, Hiyama K. Clinical features of ATRX or DAXX mutated neuroblastoma. J Pediatr Surg. 2014;49(12):1835–8.
162. Marinoni I, Kurrer AS, Vassella E, Dettmer M, Rudolph T, Banz V, et al. Loss of DAXX and ATRX are associated with chromosome instability and reduced survival of patients with pancreatic neuroendocrine tumours. Gastroenterology. 2014;146(2):453–60. e5.
163. Yang M, Pollard PJ. Succinate: a new epigenetic hacker. Cancer Cell. 2013;23(6):709–11.
164. Sciacovelli M, et al. Fumarate is an epigenetic modifier that elicits epithelial-to-mesenchymal transition. "https://www.ncbi.nlm.nih.gov/pubmed/27580029" \o "Nature." Nature. 2016;537(7621):544–7. doi:10.1038/nature19353. [Epub ahead of print].
165. Comino-Méndez I, et al. ATRX driver mutation in a composite malignant pheochromocytoma. https://www.ncbi.nlm.nih.gov/pubmed/?term=cascon+ATRX \o "Cancer genetics." Cancer Genet. 2016;209(6):272–7. doi:10.1016/j.cancergen.2016.04.058.

Chapter 3
Molecular Genetics of MEN1-Related Neuroendocrine Tumors

Sunita K. Agarwal

3.1 Multiple Endocrine Neoplasia Type 1 (MEN1)

The multiple endocrine neoplasia type 1 (MEN1) syndrome is characterized by the presence of neoplasia in two or more endocrine organs that include the parathyroids, duodenopancreatic neuroendocrine tissues, and the anterior pituitary [1–5]. Familial MEN1 is defined as a clinical MEN1 case with at least one first-degree relative with a tumor in one of these three principal endocrine organs [2, 3, 5]. The incidence of MEN1 is reported to be 1 in 30,000 and in 0.25 % of autopsies [3, 5]. MEN1 is inherited as an autosomal dominant disorder with a high degree of penetrance; more than 98 % of MEN1 patients show clinical and biochemical manifestations by age 50 years [3, 5]. Parathyroid tumors and primary hyperparathyroidism occur in 90–100 % of MEN1 patients [3, 5]. Pancreatic neuroendocrine tumors (PNETs/PanNETs) occur in 30–70 % of MEN1 patients manifesting as duodenal gastrinomas (40 %), insulinomas (10 %), pancreatic polypeptide-secreting tumors (20 %), and nonfunctioning PNETs (20 %); also observed are glucagonomas, vasoactive intestinal polypeptide (VIP)omas, and somatostatinomas in less than 1–2 % of MEN1 patients [3, 5]. Anterior pituitary tumors occur in 30–40 % of patients manifesting as prolactinomas (20 %), somatotropinomas (10 %), corticotropinomas (less than 5 %), and nonfunctioning adenomas (5 %) [3, 5]. Other endocrine tumors observed in MEN1 patients include nonfunctioning adrenal tumors (25–40 %) and the nonfunctioning foregut carcinoids: gastric NET (10 %), thymic NET (2–4 %), and bronchopulmonary NET (2 %) [3, 5]. MEN1 patients can also present with nonendocrine features such as skin lesions – lipomas (30 %), facial angiofibromas (85 %), and collagenomas (70 %) [3, 5–7]. Other nonendocrine manifestations of

S.K. Agarwal
National Institutes of Health, NIDDK, Metabolic Diseases Branch,
Bldg 10, Room 8C-101, Bethesda, MD 20892, USA
e-mail: SunitaA@mail.nih.gov

MEN1 are the central nervous system tumors, meningioma and ependymoma (1-8%); smooth muscle tumors, esophageal leiomyoma (5%); and uterine leiomyoma (30% in females) [3, 5]. With a potential to present a large variety of tumors, MEN1 is an excellent model to investigate and understand the pathophysiology of tumors in endocrine and other tissues.

3.2   MEN1-Related Neuroendocrine Tumors

Gastrin-secreting neuroendocrine tumors (gastrinomas), PNETs, and carcinoids are the frequently observed NETs in MEN1 patients [3, 5]. Gastrinomas are the most common functional neuroendocrine tumor in MEN1 [3, 5, 8]. MEN1-related gastrinomas are rarely found in the pancreas; they are usually found in the first portion of the duodenum [9]. Fifty percent of patients with MEN1 present with gastrinomas, and these tumors are accompanied by marked gastric acid production and recurrent peptic ulceration, a condition referred to as the Zollinger–Ellison syndrome (ZES) [8]. MEN1-related PNETs of the pancreatic islet cells present as functioning tumors with distinct clinical syndromes due to excessive hormone secretion (insulin and rarely glucagon, VIP, gastrin, or somatostatin), while most are nonfunctioning with no clinical symptoms [3, 5]. MEN1-related carcinoids present in the foregut and are nonfunctioning – gastric enterochromaffin-cell NET, thymic NET, and bronchopulmonary NET [3, 5, 10–12]. Although MEN1 shows no gender bias, bronchial carcinoids have a female bias (male/female ratio, 1:4), and thymic carcinoids in European MEN1 patients are observed predominantly in men (male/female ratio, 20:1); however, Japanese MEN1 patients do not show a gender bias for thymic carcinoids [5, 13–15]. Most of the MEN1-related tumors are benign. However, approximately 25% of MEN1 patients die from cancer due to malignancy associated with gastrinomas, nonfunctioning PNETs, or carcinoid NETs [5, 16–18]. MEN1-related thymic NETs are highly aggressive and have been reported to be the cause of death in 70% of patients [19]. MEN1-related NETs are frequently multiple and with an earlier age of onset in contrast to NETs in patients without MEN1 and with a potential for malignancy [9, 20, 21]. Therefore, suitable screening and treatment options specific for MEN1-related NETs will be beneficial for the patients [22–25].

3.3   *MEN1* Gene, Mutations, and Genetic Testing

3.3.1   *MEN1* Gene

The gene causative for the MEN1 syndrome is located on chromosome 11q13 as determined by linkage analysis and loss of heterozygosity (LOH) mapping [26–28]. Cloning of the *MEN1* gene in 1997 has shown that this 9-kb gene consists of 10

exons, transcribed into a 2.8-kb mRNA, that is translated into a 610 amino acid protein that has been named menin (GenBank Accession No.: U93236.1) (Fig. 3.1a) [29, 30]. The NCBI reference sequence "human menin transcript variant-2" (NM_130799.2) has 610 amino acids. The other reference sequence "human menin transcript variant-1" (NM_000244.3) has 615 amino acids; the extra five amino acids are located at the end of exon 2 due to an alternative splice site that extends exon 2 by 15 nucleotides. This 615 amino acid variant of human menin has not been validated as normal menin cDNA in various cell lines and tissues.

3.3.2 MEN1 Germline Mutations

Germline heterozygous inactivating mutations in *MEN1* are observed in 70–90 % of familial MEN1 patients that predisposes to tumor development [29–32]. The frequency of detecting a germline *MEN1* mutation is much lower in cases without a family history of MEN1 and in similar sporadic MEN1 cases who present with hyperparathyroidism and pituitary tumor but no PNETs [33, 34]. MEN1-related tumors show LOH at chromosome 11q13 from loss of the region corresponding to the normal non-mutated *MEN1* allele [29, 30]. Thus *MEN1* acts as a tumor suppressor gene, and its biallelic loss/inactivation leads to tumorigenesis. More than 1000 mutations have been reported in the *MEN1* gene [35]. Two studies have reviewed the published germline *MEN1* mutations from 1997 to 2007 and 2007 to 2015, and they found a total of 576 unique mutations [35, 36]. A vast majority (65–70 %) of the mutations predict C-terminal truncation of menin or deletion of internal exons encoding menin (nonsense, frameshift, and splicing). Other mutations observed are missense (25 %), in-frame deletion/insertion (5 %), and gross deletions (2 %) [35–37]. The expression of some menin missense mutant proteins has been shown to be unstable and degraded by the proteasome [38]. There is a need to develop assays to study the adverse physiological effect of rare *MEN1* mutations, especially for mutations that do not delete a large region of menin, such as missense and single amino acid in-frame del/ins. Such assays may help to determine whether mutations are pathologic or benign.

3.3.3 Genetic Screening of MEN1 Patients

Genetic testing for germline *MEN1* mutations helps to confirm the clinical diagnosis, to identify at-risk individuals in a family, and to exclude noncarriers [3, 5]. Tumors and biochemical features of MEN1 are typically established at age 40–50 years; however, a few children before the age of 10 years have been reported with MEN1-related tumors [39–41]. This observation justifies the recommendation of genetic testing at the earliest opportunity [3, 5]. Patients with features of MEN1 but
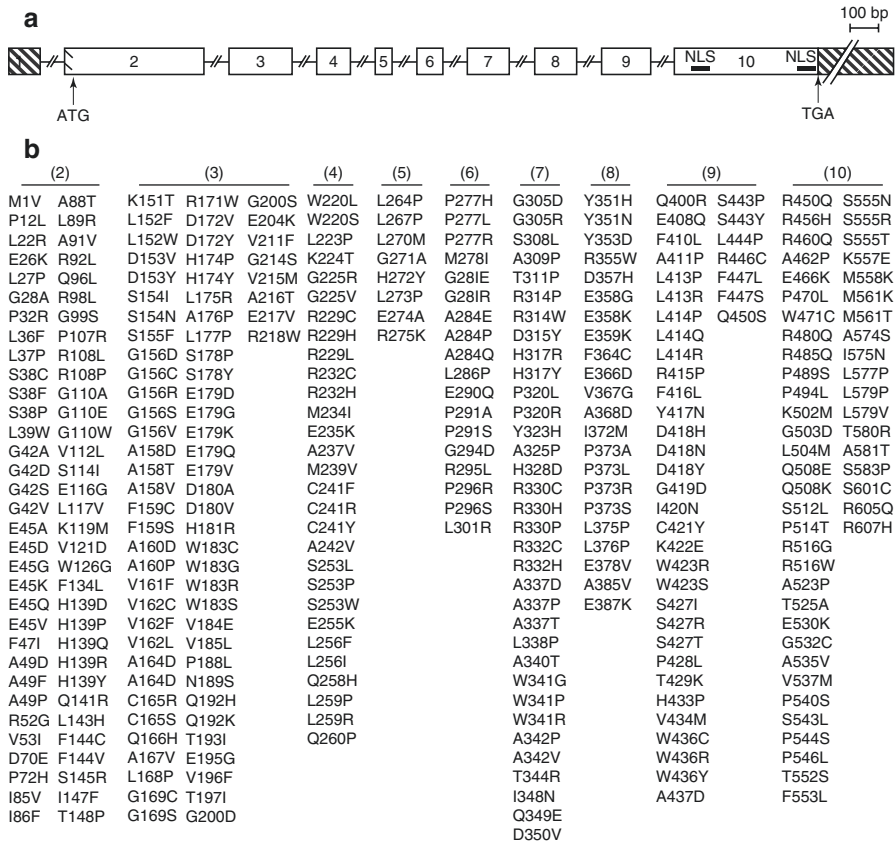
a

100 bp

Exon diagram (boxes sized to 100-bp scale, introns as broken lines, striped untranslated regions): 2 | 3 | 4 | 5 | 6 | 7 | 8 | 9 | NLS — 10 — NLS

ATG (start codon, exon 2) ... TGA (stop codon, exon 10)

b

(2)		(3)			(4)	(5)	(6)	(7)	(8)		(9)		(10)	
M1V	A88T	K151T	R171W	G200S	W220L	L264P	P277H	G305D	Y351H	A385V	Q400R	S443P	R450Q	S555N
P12L	L89R	L152F	D172V	E204K	W220S	L267P	P277L	G305R	Y351N	E387K	E408Q	S443Y	R456H	S555R
L22R	A91V	L152W	D172Y	V211F	L223P	L270M	P277R	S308L	Y353D		F410L	L444P	R460Q	S555T
E26K	R92L	D153V	H174R	V215M	K224T	G271A	M278I	A309P	R355W		A411P	R446C	A462P	K557E
L27P	Q96L	D153Y	H174Y	A216T	G225R	H272Y	G281E	T311P	D357H		L413P	F447L	E466K	M558K
G28A	R98L	S154I	L175R	E217V	G225V	L273P	G281R	R314P	E358G		L413R	F447S	P470L	M561K
P32R	G99S	S154N	A176P	R218W	R229C	E274A	A284E	R314W	E358K		L414P	Q450S	W471C	M561T
L36F	P107R	S155F	L177M		R229H	R275K	A284P	D315Y	E359K		L414Q		R480Q	A574S
L37P	R108L	G156D	S178P		R229L		A284Q	H317R	F364C		L414R		R485Q	I575N
S38C	R108P	G156C	S178Y		R232C		L286P	H317Y	E366D		R415P		P489S	L577P
S38F	G110A	G156R	E179D		R232H		E290Q	P320L	V367G		F416L		P494L	L579P
S38P	G110E	G156S	E179G		M234I		P291A	P320R	A368D		Y417N		K502M	L579V
L39W	G110W	G156V	E179K		E235K		P291S	Y323H	I372M		D418H		G503D	T580R
G42A	V112L	A158D	E179Q		A237V		G294D	A325P	P373A		D418N		L504M	A581T
G42D	S114I	A158T	E179V		M239V		R295L	H328D	P373L		D418Y		Q508E	S583P
G42S	E116G	A158V	D180A		C241F		P296R	R330C	P373R		I420N		Q508K	S601C
G42V	L117V	F159S	D180V		C241R		P296S	R330H	P373S		C421Y		S512L	R605Q
E45A	K119M	F159N	H181R		C241Y		L301R	R330P	L375P		K422E		P514T	R607H
E45D	V121D	A160D	W183C		A242V			R332C	L376P		W423R		R516G	
E45G	W126G	A160P	W183G		S253L			R332H	E378V		W423S		R516W	
E45K	F134L	V161F	W183R		S253P			A337D			S427I		A523P	
E45Q	H139D	V162C	W183S		S253W			A337P			S427R		T525A	
E45V	H139P	V162F	V184E		E255K			A337T			S427T		E530K	
F47I	H139Q	V162L	V185L		L256F			L338P			P428L		G532C	
A49D	H139R	A164D	P188L		L256I			A340T			T429K		A535V	
A49F	H139Y	A164D	N189S		Q258H			W341G			H433P		V537M	
A49P	Q141F	C165R	Q192H		L259P			W341P			V434M		P540S	
R52G	L143H	C165S	Q192K		L259R			W341R			W436C		P544S	
V53I	F144C	Q166H	T193I		Q260P			A342P			W436R		P546L	
D70E	F144V	A167D	E195G					A342V			W436Y		T552S	
P72H	S145R	L168P	V196F					T344R			A437D		F553L	
I85V	I147F	G169C	T197I					I348N						
I86F	T148P	G169S	G200D					Q349E						
								D350V						

Fig. 3.1 *MEN1* gene and missense mutations. (**a**) Genomic structure of the *MEN1* gene. The 10 exons of the gene are shown as boxes that are sized with the indicated 100-bp scale. The broken lines in-between the boxes are introns, not drawn to scale. Striped parts indicate untranslated regions that are not present in the menin coding region, marked with the start codon ATG in exon 2 and stop codon TGA in exon 10. The two nuclear localization signals (NLS) at amino acids 479–497 and 588–608 are marked in exon 10. (**b**) Germline and somatic missense mutations in the *MEN1* gene. The menin coding region consists of 610 amino acids (aa) that starts in exon 2 and ends in exon 10. The extent of the coding region in each exon is as follows: ex2(aa1-148), ex3(aa149-218), ex4(aa219-261), ex5(aa262-275), ex6(aa276-304), ex7(aa305-350), ex8(aa351-395), ex9(aa396-450), and ex10(aa451-610). Missense mutations in each exon are shown. The germline and somatic missense mutations have been assembled from References 35 and 36 and from the COSMIC database. There are 340 different missense mutations affecting 239 amino acids. The amino acids are numbered as per menin transcript variant-2 that has 610 amino acids. Note that menin transcript variant-1 has 615 amino acids. Readers should be careful about the interpretation of *MEN1* mutation nomenclature whether the nucleotides and amino acids are numbered as per transcript variant-1 or variant-2, particularly for mutations located after exon 2 (see explanation in the text). (**c**) Location of germline and somatic missense mutations in menin. Menin missense mutations at each amino acid (from Fig. 3.1b) are plotted to show the number of unique mutations in each amino acid. Exons are marked below the mutation plot. Missense mutations are distributed over the entire 610 amino acid coding region indicating that all parts of menin are essential. There are six amino acids affected by more than three different mutations (amino acids G42, E45, H139, G156, E179, and P373)
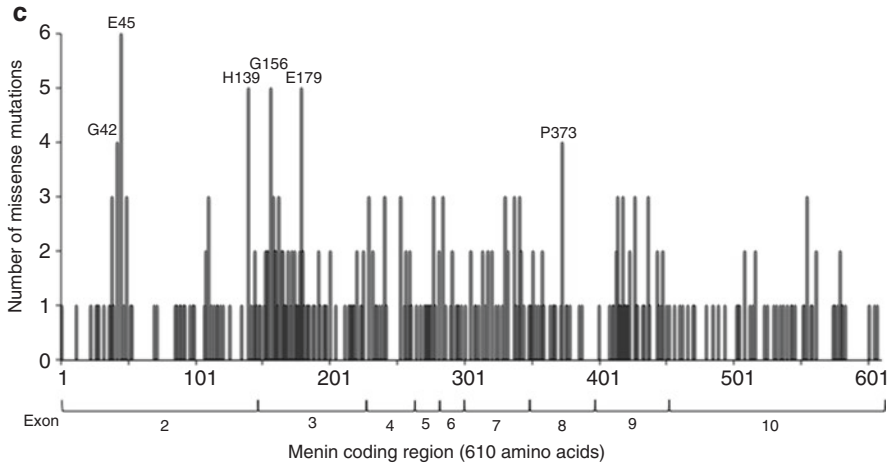
Fig. 3.1 (continued)

who do not test positive for germline *MEN1* mutations by the standard genetic testing methods (that screen the menin coding region and gross deletions) may show germline heterozygous mutations in the *CDKN1B/p27* gene or probably in similar cyclin-dependent kinase inhibitor (CDKI) genes *p15*, *p18*, or *p21* [42–44]. The MEN1-like syndrome with *p27* mutations has been named MEN4 [37, 45]. Approximately 1–2 % of MEN1-like cases have been reported to possess germline heterozygous *p27* mutations, and less than 1 % with probable *p15*, *p18*, or *p21* mutations [5, 46]. The CDKI genes of the INK4 family (*p15*, *p16*, *p18*, and *p19*) and the Cip/Kip family (*p21*, *p27*, and *p57*) are cell cycle inhibitors for specific cyclin-CDK complexes [47]. No genotype–phenotype correlation has been observed for *p27* mutation with MEN1 or MEN1-like features.

3.3.4 Somatic Mutations in Sporadic Tumors

MEN1-related tumors can also occur sporadically. Some of these non-inherited tumors show somatic inactivating mutations in *MEN1* with or without 11q13 LOH. The prevalence of *MEN1* mutations in sporadic tumors is glucagonoma (60 %), VIPoma (57 %), nonfunctioning pancreatic tumor (44 %), gastrinoma (38 %), bronchial carcinoid (35 %), parathyroid adenoma (35 %), lipoma (28 %) insulinoma (2–19 %), angiofibroma (10 %), anterior pituitary tumor (3.5 %), and adrenocortical tumor (2 %) [37, 48–54]. Exome sequencing of sporadic PNETs has shown that 43 % of nonfunctioning PNETs have mutations in chromatin remodeling factors *DAXX* and *ATRX* [50], and 13–33 % of functioning PNETs (insulinomas) have a recurrent somatic heterozygous missense mutation T372R in the transcription factor *YY1* [54–56].

3.3.5 *MEN1 Mutation Analysis*

Mutations in the *MEN1* gene (germline or somatic) are dispersed over the entire coding region and with no obvious genotype–phenotype correlation with an individual sporadic or MEN1-related tumor, or MEN1-related tumor spectrum, or with specific clinical/biochemical features [4, 35, 36]. To date 340 unique missense mutations have been reported that affect 239 amino acids of menin ([35, 36] + additional somatic from the COSMIC database [57]). The location of all the missense mutations (Fig. 3.1b) illustrates how the mutations hit just about every region of menin (Fig. 3.1c) implying that all regions of menin are essential.

3.4 Structure and Function of Menin

3.4.1 *Menin Subcellular Localization and Structure*

Menin is a ubiquitously expressed 67-kDa protein that is predominantly localized in the nucleus due to the presence of two nuclear localization signals (NLS), NLS1 (amino acid residues 479–497) and NLS2 (amino acid residues 588–608) [58]; a third accessory NLS, NLSa (amino acid residues 546–572), has also been reported [59]. Menin is highly conserved in animal species but with no known homologs in yeast and nematodes. The crystal structure of *Nematostella* menin (the starlet sea anemone) and human menin has been deciphered, and they are very similar [60, 61]. The structure resembles a curved left hand, with a deep pocket formed by the thumb and the palm [60, 61]. Menin is an α-helical protein with 4 domains: a long β-hairpin N-terminal domain, a transglutaminase-like domain that forms the thumb, a helical palm domain that contains three tetratricopeptide motifs, followed by a C-terminal fingers domain [60, 61]. The deep cavity in the palm may act as a binding site for interacting proteins [60, 61]. Both structures lack some parts of menin that have been predicted as disordered regions – in *Nematostella* menin, an unstructured loop (amino acid residues 426–442) and the C-terminus (amino acid residues 487–539), and in human menin, an internal unstructured loop (amino acid residues 460–519) [60, 61]. Therefore, the crystal structure of the entire menin protein in its free form or together with an interacting partner remains to be determined.

3.4.2 *Menin-Interacting Proteins*

Menin does not show homology to any known proteins and it does not possess any enzymatic activity. Therefore to elucidate the function of menin, interacting proteins have been sought, and approximately 40 different proteins have been shown to partner with menin – transcription factors, chromatin modification factors,

Transcription factors/DNA-binding

DNMT1 (Hedgehog pathway)

HLXB9/MNX1

JUND*

c-MYB

NFkB - p50, p52, p65

Nuclear receptors

  (AR, Erα, LXRα, PPARY, RAR, VDR)

PEM

RUNX2 (BMP2 signaling)

SMADs (TGFβ signaling

  (SMAD1, SMAD3, SMAD5)

SIRT1

TCF3, TCF4, β-Catenin (Wnt signaling)

Transcription/Chromatin modification

FBP1

HDACs, mSIN3A

LEDGF*

MLL*-complex (H3K4me3)

  (ASH2L, hDPY30, MLL1 or MLL2,

  RBBP5, RPB2, HCF-2, WDR5)

PRMT5 (H4R3me2)

SuV39H1 (H3K9me3)

Transcription initiation or elongation

RNAPII isoforms (pSer5 and pSer2)

SKIP/c-MYC (HIV-1 Tat:P-TEFb transcription)

Cytoskeleton/cell division/ adhesion/motility

GFAP

IQGAP1

NMMHC-IIA

VIMENTIN

DNA-repair

ASK

CHES1

FANCD2

RPA2

Protein degradation

CHIP (interacts with

  menin missense

  mutants)

mRNA biogenesis

ARS2

Signaling mediators in the cytoplasm

AKT1

FOXO1

NM23β

Fig. 3.2 Menin interacting proteins. More than 40 different protein partners of menin are shown. The proteins are divided into functional categories. Majority of the interactions are observed in the nucleus with proteins involved in transcriptional regulation. Menin binding regions of three proteins have been shown in co-crystal structures with menin (proteins marked in bold with an asterisk). Similar analysis of the other menin interacting proteins has not been performed

transcription initiation and elongation factors, cytoskeletal proteins associated with cell division/adhesion/motility, DNA repair proteins, an mRNA biogenesis factor, and signaling mediators in the cytoplasm (Fig. 3.2) [37, 62–64]. These interactions predict that menin may participate in a variety of functions in different cell types. A majority of the interactions are with proteins involved in transcriptional regulation; however, menin by itself does not possess a DNA-binding domain to directly

regulate transcription [60, 61]. Protein and DNA interaction studies have revealed some menin target genes (cell cycle inhibitors *p18* and *p27*, the long noncoding RNA *MEG3*, *IGFBP2*, and the *HOX* genes) that are regulated by menin from interactions with the mixed lineage leukemia (MLL) protein in a protein complex that is responsible for a specific chromatin mark of gene activation, histone H3 lysine 4 trimethylation (H3K4me3) [65–73]. Loss of menin results in loss of H3K4me3 at specific genes and, at the same genes, gain of H3K27me3 that is an epigenetic mark of gene repression [71]. Phosphorylation at six different amino acid residues of menin has been reported – Ser394, Thr397, Thr399, Ser487, Ser543, and Ser583 – constitutively (Ser543) or in response to DNA damage (Ser394 and Ser487) or upon loss of phosphorylation at Ser394 (Thr397 and Thr399) [74]. Menin is reported to undergo another posttranslational modification, SUMOylation at Lys591 [75]. The impact of phosphorylation or SUMOylation on the crystal structure of menin or in protein–protein interactions is not known. Most of the protein interaction studies have been conducted in cell lines unrelated to NETs or other tumors of MEN1 [76]. In order to confirm the MEN1-related relevance of the functions of menin through its interacting proteins, there is a need to develop cell lines from tissues (normal and tumor) affected in MEN1. Such studies may help to define the biological functions of menin that are critical to prevent the development of MEN1-related tumors.

3.5 Molecular Genetics of MEN1-Related NETs in Mouse Models

3.5.1 Germline Men1 Knockout Mice

Germline homozygous loss of the *Men1* gene (*Men1*−/−) in mice results in death in utero between embryonic days 10.5 and 14.5, but germline heterozygous loss of the *Men1* gene (*Men1*+/−) does not cause embryonic lethality [77–81]. After 9–16 months, *Men1*(+/−) mice develop MEN1-related endocrine tumors: parathyroid tumors, pancreatic islet tumors (mainly insulinoma), and anterior pituitary tumors (mainly prolactinoma in female) [77, 79–81]. Gastrinomas are seen in only one of the four different mouse models of MEN1 [79]. Foregut carcinoids are not seen in the mouse models of MEN1. Other tumors observed in the *Men1*(+/−) mouse model of MEN1 are adrenal cortical tumors, gonadal tumors (Leydig cells in male or ovarian stroma in female), and bilateral pheochromocytoma [82, 83]. Similar to MEN1-related human tumors, the tumors in *Men1*(+/−) mice develop after loss of the wild-type *Men1* allele (LOH). Given that menin may regulate the expression of cell cycle genes, mouse models with loss of tumor suppressor genes known to regulate the cell cycle (*Rb* or *p53*) or cell cycle regulator genes (*Cdk2*, *Cdk4*, *p18*, or *p27*) have been generated in the *Men1*(+/−) background to study the impact on the development of MEN1-related NETs, PNETs in particular (Table 3.1). Combined loss of *Men1*(+/−) with *Rb* or *p53* did not show any significant effect [84–86]. Combined loss of *Men1*(+/−) with *p18* but not *p27* accelerated the rate of insulinoma

Table 3.1 PNETs (insulinoma) in mouse models of *Men1* loss upon combined genetic manipulation with candidate genes

Genotype	Phenotype	Ref.
Men1(+/−)	Parathyroid hyperplasia, anterior pituitary tumor, and pancreatic islets tumors (insulinoma) at ages 12–18 months Tumors with *Men1* LOH	[77, 79–81]
p18(−/−)	Islet tumor phenotype similar to *Men1*(+/−)	[87]
p18(−/−); *Men1*(+/−)	Develop islet tumors at an accelerated rate and with an increased incidence Tumors without *Men1* LOH	[87]
p27(−/−)	Do not develop islet hyperplasia	[87]
p27(−/−); *Men1*(+/−)	Islet tumorigenesis comparable to *Men1*(+/−)	[87]
Cdk2(−/−)	No developmental or functional defects in neuroendocrine tissues	[88]
Cdk2(−/−); Men1(+/−)	Islet tumorigenesis comparable to *Men1*(+/−) Tumors with *Men1* LOH	[88]
Cdk4(−/−)	Hypoplasia of the anterior pituitary and pancreatic islets during postnatal periods	[88]
Cdk4(−/−); *Men1*(+/−)	Do not develop any tumors; islets and pituitaries remained hypoplastic No LOH for *Men1*	[88]
Rb(+/−)	Hyperplasia of pancreatic islets	[84, 85]
Rb(+/−); *Men1*(+/−)	Islet tumorigenesis comparable to *Men1*(+/−) Tumors with *Men1* LOH	[84, 85]
p53(+/−)	Do not develop islet tumors	[86]
p53(+/−); *Men1*(+/−)	Islet tumorigenesis comparable to *Men1*(+/−)	[86]
Men1(f/f); RIP-Cre	Pancreatic islet tumors (insulinoma) at ages 6–8 months and anterior pituitary tumors	[91–93]
K-RAS(G12D)	K-RAS(G12D) inhibited β-cell proliferation (P5 neonates)	[101]
K-RAS(G12D); *Men1*(+/f); RIP-Cre	K-RAS(G12D) enhanced, rather than inhibited β-cell proliferation (P5 neonates)	[101]
Ctnnb1(f/f); RIP-Cre	No significant effect of β-catenin loss on mature islets	[102]
Ctnnb1(f/f); *Men1*(f/f); RIP-Cre	Loss of β-catenin suppressed islet growth and tumorigenesis	[102]
Rbp2(f/f); RIP-Cre	Rbp2 loss did not grossly affect islet histology or function	[103]
Rbp2(f/f); *Men1*(f/f); RIP-Cre	Decreased islet tumor formation and prolonged survival	[103]
Inhβ(−/−)	No significant effect of ActivinB loss on mature islets	[108]
Inhβ(−/−); *Men1*(f/f); RIP-Cre	Prolonged survival after 10 months of age	[104]
Men1(f/f); PDX1-Cre	Selective development of a single islet tumor (insulinoma)	[90]
Arc(−/−)	No basal phenotype from Arc loss	[109]
Arc(−/−); *Men1*(f/f); PDX1-Cre	Did not significantly alter tumor load	[109]

formation and with an increased tumor incidence [87]. Mice with combined loss of *Men1*(+/−) with *Cdk4* but not *Cdk2* did not develop insulinoma [88]. These mouse models show that *p18* inactivation and Cdk4 activation may be critical for PNET formation upon menin loss.

3.5.2   Tissue-Specific Men1 Knockout Mice

Mice with tissue-specific homozygous loss of *Men1* in the parathyroids, pancreas, or pancreatic islet β-cells are viable and develop tumors in the specific tissue at an earlier age than in the *Men1*(+/−) mice [89–93]. The exception is a mouse model with liver-specific homozygous *Men1* knockout that lacks tumors in the liver, a tissue not associated with tumors in MEN1 patients, underscoring tissue-specific actions of menin in MEN1-related target tissues [94]. The tissue-specific action of menin as a tumor suppressor in the pancreatic β-cells is highlighted by the observation that homozygous loss of *Men1* in β-cells (*Men1*(f/f); RIP-Cre) or in the whole pancreas (*Men1*(f/f); PDX1-Cre), both show only β-cell tumors (insulinomas) [90–93]. Another interesting observation in mouse models is that mice with pancreatic α-cell-specific loss of *Men1* develop insulinomas rather than the expected glucagonomas due to possible transdifferentiation of α-cells into β-cells, or perhaps paracrine signals that induce β-cell proliferation [95, 96]. The molecular mechanisms underlying β-cell-specific tumorigenesis from menin loss remain to be determined. Perhaps menin has tissue-specific interactions or regulates tissue-specific factors as indicated in a few studies that have implicated β-cell-specific differentiation factors MafA or Hlxb9/Mnx1 [97–100]. Effect of menin loss together with target genes associated with β-cell proliferation and function has been studied in mouse models (Table 3.1). Combined genetic manipulation of candidate genes in mice with β-cell-specific *Men1* knockout (*Men1*(f/f); RIP-Cre) shows that expression of activated K-RAS(G12D) enhances rather than inhibits β-cell proliferation, β-catenin loss can suppress islet growth and tumorigenesis, histone demethylase Rbp2 loss decreases islet tumor formation and prolongs survival, and ActivinB loss prolongs survival after 10 months of age [101–104]. Further studies of these mouse models may help to understand β-cell-specific disease-associated pathways and to develop potential therapies for MEN1-related PNETs.

3.5.3   Men1 Knockout Mice for Preclinical Studies

Mouse models of *Men1* loss have served as preclinical models to study the potential of various treatment options in PNETs (insulinoma) and pituitary tumors (prolactinoma) – an angiogenesis inhibitor (anti-VEGF-A monoclonal antibody, mAb G6-31), a small molecular tyrosine kinase inhibitor of all VEGF receptors (sunitinib), a somatostatin analog (pasireotide/SOM230), and menin replacement

therapy [105–107]. Similar preclinical investigations may be possible from the results described above about studies in mouse models with combined loss of *Men1* and genetic manipulation of candidate genes such as inhibitors of CDK, β-catenin, ActivinB, or histone demethylation.

3.6 Conclusions

Patients with the MEN1 syndrome can undergo germline genetic testing for the *MEN1* gene that can help to confirm the clinical diagnosis, to identify at-risk individuals within families for early monitoring of tumors, and to exclude individuals who will not develop tumors. However, 10–30 % of cases with clinical MEN1 features lack germline *MEN1* mutations. To identify the causative gene/s in these *MEN1* mutation-negative cases, studies can be conducted by using whole genome/exome sequencing approaches to analyze germline DNA of patients and family members with different combinations of MEN1-related tumors. Molecular genetic studies in cell lines and mouse models have revealed candidate genetic interactions, many protein partners, and menin-dependent target genes. There is a need for integrated analysis of data from these studies that will help to define the exact role/s of menin in normal physiology and the molecular events after menin loss that lead to tumor formation in specific tissues. Such a comprehensive understanding of the process of tumorigenesis in MEN1-related NETs in man and mouse can provide considerable support to translational efforts for developing antitumor therapeutic options in human patients. In contrast to NETs in patients without MEN1, MEN1-related NETs are frequently multiple and with an earlier age of onset and with a potential for malignancy; therefore, screening and treatment options specific for MEN1-related NETs have to account for these differences.

References

1. Wermer P. Genetic aspects of adenomatosis of endocrine glands. Am J Med. 1954;16:363–71.
2. Marx S, Spiegel AM, Skarulis MC, Doppman JL, Collins FS, Liotta LA. Multiple endocrine neoplasia type 1: clinical and genetic topics. Ann Intern Med. 1998;129:484–94.
3. Brandi ML, Gagel RF, Angeli A, Bilezikian JP, Beck-Peccoz P, Bordi C, et al. Guidelines for diagnosis and therapy of MEN type 1 and type 2. J Clin Endocrinol Metab. 2001;86:5658–71.
4. Thakker RV. Multiple endocrine neoplasia type 1 (MEN1). Best Pract Res Clin Endocrinol Metab. 2010;24:355–70. doi:10.1016/j.beem.2010.07.003.

5. Thakker RV, Newey PJ, Walls GV, Bilezikian J, Dralle H, Ebeling PR, et al. Clinical practice guidelines for multiple endocrine neoplasia type 1 (MEN1). J Clin Endocrinol Metab. 2012;97:2990–3011. doi:10.1210/jc.2012-1230.

6. Darling TN, Skarulis MC, Steinberg SM, Marx SJ, Spiegel AM, Turner M. Multiple facial angiofibromas and collagenomas in patients with multiple endocrine neoplasia type 1. Arch Dermatol. 1997;133:853–7.

7. Asgharian B, Turner ML, Gibril F, Entsuah LK, Serrano J, Jensen RT. Cutaneous tumors in patients with multiple endocrine neoplasm type 1 (MEN1) and gastrinomas: prospective study of frequency and development of criteria with high sensitivity and specificity for MEN1. J Clin Endocrinol Metab. 2004;89:5328–36. doi:10.1210/jc.2004-0218.

8. Gibril F, Schumann M, Pace A, Jensen RT. Multiple endocrine neoplasia type 1 and Zollinger-Ellison syndrome: a prospective study of 107 cases and comparison with 1009 cases from the literature. Medicine. 2004;83:43–83. doi:10.1097/01.md.0000112297.72510.32.

9. Norton JA, Krampitz G, Jensen RT. Multiple endocrine neoplasia: genetics and clinical management. Surg Oncol Clin N Am. 2015;24:795–832. doi:10.1016/j.soc.2015.06.008.

10. Berna MJ, Annibale B, Marignani M, Luong TV, Corleto V, Pace A, et al. A prospective study of gastric carcinoids and enterochromaffin-like cell changes in multiple endocrine neoplasia type 1 and Zollinger-Ellison syndrome: identification of risk factors. J Clin Endocrinol Metab. 2008;93:1582–91. doi:10.1210/jc.2007-2279.

11. Gibril F, Chen YJ, Schrump DS, Vortmeyer A, Zhuang Z, Lubensky IA, et al. Prospective study of thymic carcinoids in patients with multiple endocrine neoplasia type 1. J Clin Endocrinol Metab. 2003;88:1066–81. doi:10.1210/jc.2002-021314.

12. Sachithanandan N, Harle RA, Burgess JR. Bronchopulmonary carcinoid in multiple endocrine neoplasia type 1. Cancer. 2005;103:509–15. doi:10.1002/cncr.20825.

13. Goudet P, Bonithon-Kopp C, Murat A, Ruszniewski P, Niccoli P, Menegaux F, et al. Gender-related differences in MEN1 lesion occurrence and diagnosis: a cohort study of 734 cases from the Groupe d'etude des Tumeurs Endocrines. Eur J Endocrinol/Eur Federation Endocrine Soc. 2011;165:97–105. doi:10.1530/EJE-10-0950.

14. Ito T, Igarashi H, Uehara H, Berna MJ, Jensen RT. Causes of death and prognostic factors in multiple endocrine neoplasia type 1: a prospective study: comparison of 106 MEN1/Zollinger-Ellison syndrome patients with 1613 literature MEN1 patients with or without pancreatic endocrine tumors. Medicine. 2013;92:135–81. doi:10.1097/MD.0b013e3182954af1.

15. Sakurai A, Suzuki S, Kosugi S, Okamoto T, Uchino S, Miya A, et al. Multiple endocrine neoplasia type 1 in Japan: establishment and analysis of a multicentre database. Clin Endocrinol (Oxf). 2012;76:533–9. doi:10.1111/j.1365-2265.2011.04227.x.

16. Goudet P, Murat A, Binquet C, Cardot-Bauters C, Costa A, Ruszniewski P, et al. Risk factors and causes of death in MEN1 disease. A GTE (Groupe d'Etude des Tumeurs Endocrines) cohort study among 758 patients. World J Surg. 2010;34:249–55. doi:10.1007/s00268-009-0290-1.

17. Dean PG, van Heerden JA, Farley DR, Thompson GB, Grant CS, Harmsen WS, et al. Are patients with multiple endocrine neoplasia type I prone to premature death? World J Surg. 2000;24:1437–41.

18. Doherty GM, Olson JA, Frisella MM, Lairmore TC, Wells Jr SA, Norton JA. Lethality of multiple endocrine neoplasia type I. World J Surg. 1998;22:581–6; discussion 6–7.

19. Goudet P, Murat A, Cardot-Bauters C, Emy P, Baudin E, du Boullay CH, et al. Thymic neuroendocrine tumors in multiple endocrine neoplasia type 1: a comparative study on 21 cases among a series of 761 MEN1 from the GTE (Groupe des Tumeurs Endocrines). World J Surg. 2009;33:1197–207. doi:10.1007/s00268-009-9980-y.

20. Machens A, Schaaf L, Karges W, Frank-Raue K, Bartsch DK, Rothmund M, et al. Age-related penetrance of endocrine tumours in multiple endocrine neoplasia type 1 (MEN1): a multicentre study of 258 gene carriers. Clin Endocrinol (Oxf). 2007;67:613–22. doi:10.1111/j.1365-2265.2007.02934.x.

21. Tonelli F, Fratini G, Falchetti A, Nesi G, Brandi ML. Surgery for gastroenteropancreatic tumours in multiple endocrine neoplasia type 1: review and personal experience. J Intern Med. 2005;257:38–49. doi:10.1111/j.1365-2796.2004.01424.x.

22. Raymond E, Dahan L, Raoul JL, Bang YJ, Borbath I, Lombard-Bohas C, et al. Sunitinib malate for the treatment of pancreatic neuroendocrine tumors. N Engl J Med. 2011;364:501–13. doi:10.1056/NEJMoa1003825.

23. Yao JC, Shah MH, Ito T, Bohas CL, Wolin EM, Van Cutsem E, et al. Everolimus for advanced pancreatic neuroendocrine tumors. N Engl J Med. 2011;364:514–23. doi:10.1056/NEJMoa1009290.

24. Spiegel AM, Libutti SK. Targeted therapies: good news for advanced-stage pancreatic neuro-endocrine tumors. Nat Rev Clin Oncol. 2011;8:258–9. doi:10.1038/nrclinonc.2011.50.

25. Sadowski SM, Millo C, Cottle-Delisle C, Merkel R, Yang LA, Herscovitch P, et al. Results of (68)Gallium-DOTATATE PET/CT Scanning in Patients with Multiple Endocrine Neoplasia Type 1. J Am Coll Surg. 2015;221:509–17. doi:10.1016/j.jamcollsurg.2015.04.005.

26. Larsson C, Skogseid B, Oberg K, Nakamura Y, Nordenskjold M. Multiple endocrine neoplasia type 1 gene maps to chromosome 11 and is lost in insulinoma. Nature. 1988;332:85–7. doi:10.1038/332085a0.

27. Bystrom C, Larsson C, Blomberg C, Sandelin K, Falkmer U, Skogseid B, et al. Localization of the MEN1 gene to a small region within chromosome 11q13 by deletion mapping in tumors. Proc Natl Acad Sci U S A. 1990;87:1968–72.

28. Lubensky IA, Debelenko LV, Zhuang Z, Emmert-Buck MR, Dong Q, Chandrasekharappa S, et al. Allelic deletions on chromosome 11q13 in multiple tumors from individual MEN1 patients. Cancer Res. 1996;56:5272–8.

29. Chandrasekharappa SC, Guru SC, Manickam P, Olufemi SE, Collins FS, EmmertBuck MR, et al. Positional cloning of the gene for multiple endocrine neoplasia-type 1. Science. 1997;276:404–7. doi:10.1126/science.276.5311.404.

30. Lemmens I, Van de Ven WJ, Kas K, Zhang CX, Giraud S, Wautot V, et al. Identification of the multiple endocrine neoplasia type 1 (MEN1) gene. The European Consortium on MEN1. Hum Mol Genet. 1997;6:1177–83.

31. Agarwal SK, Kester MB, Debelenko LV, Heppner C, Emmert-Buck MR, Skarulis MC, et al. Germline mutations of the MEN1 gene in familial multiple endocrine neoplasia type 1 and related states. Hum Mol Genet. 1997;6:1169–75.

32. Giraud S, Zhang CX, Serova-Sinilnikova O, Wautot V, Salandre J, Buisson N, et al. Germline mutation analysis in patients with multiple endocrine neoplasia type 1 and related disorders. Am J Hum Genet. 1998;63:455–67. doi:10.1086/301953.

33. Hai N, Aoki N, Shimatsu A, Mori T, Kosugi S. Clinical features of multiple endocrine neoplasia type 1 (MEN1) phenocopy without germline MEN1 gene mutations: analysis of 20 Japanese sporadic cases with MEN1. Clin Endocrinol (Oxf). 2000;52(4):509–18.

34. Odou MF, Cardot-Bauters C, Vantyghem MC, Carnaille B, Leteurtre E, Pigny P, et al. Contribution of genetic analysis in screening for MEN1 among patients with sporadic disease and one or more typical manifestation. Ann Endocrinol (Paris). 2006;67(6):581–7.

35. Lemos MC, Thakker RV. Multiple endocrine neoplasia type 1 (MEN1): analysis of 1336 mutations reported in the first decade following identification of the gene. Hum Mutat. 2008;29:22–32. doi:10.1002/humu.20605.

36. Concolino P, Costella A, Capoluongo E. Multiple endocrine neoplasia type 1 (MEN1): An update of 208 new germline variants reported in the last nine years. Cancer Genet. 2015. doi:10.1016/j.cancergen.2015.12.002.

37. Thakker RV. Multiple endocrine neoplasia type 1 (MEN1) and type 4 (MEN4). Mol Cell Endocrinol. 2014;386:2–15. doi:10.1016/j.mce.2013.08.002.

38. Canaff L, Vanbellinghen JF, Kanazawa I, Kwak H, Garfield N, Vautour L, et al. Menin missense mutants encoded by the MEN1 gene that are targeted to the proteasome: restoration of expression and activity by CHIP siRNA. J Clin Endocrinol Metab. 2012;97(2):E282–91. doi:10.1210/jc.2011-0241.

39. Stratakis CA, Schussheim DH, Freedman SM, Keil MF, Pack SD, Agarwal SK, et al. Pituitary macroadenoma in a 5-year-old: an early expression of multiple endocrine neoplasia type 1. J Clin Endocrinol Metab. 2000;85:4776–80. doi:10.1210/jcem.85.12.7064.

40. Fabbri HC, Mello MP, Soardi FC, Esquiaveto-Aun AM, Oliveira DM, Denardi FC, et al. Long-term follow-up of an 8-year-old boy with insulinoma as the first manifestation of a familial form of multiple endocrine neoplasia type 1. Arq Bras Endocrinol Metabol. 2010;54:754–60.

41. Newey PJ, Jeyabalan J, Walls GV, Christie PT, Gleeson FV, Gould S, et al. Asymptomatic children with multiple endocrine neoplasia type 1 mutations may harbor nonfunctioning pancreatic neuroendocrine tumors. J Clin Endocrinol Metab. 2009;94:3640–6. doi:10.1210/jc.2009-0564.

42. Pellegata NS, Quintanilla-Martinez L, Siggelkow H, Samson E, Bink K, Hofler H, et al. Germ-line mutations in p27Kip1 cause a multiple endocrine neoplasia syndrome in rats and humans. Proc Natl Acad Sci U S A. 2006;103:15558–63. doi:10.1073/pnas.0603877103.

43. Georgitsi M, Raitila A, Karhu A, van der Luijt RB, Aalfs CM, Sane T, et al. Germline CDKN1B/p27Kip1 mutation in multiple endocrine neoplasia. J Clin Endocrinol Metab. 2007;92:3321–5. doi:10.1210/jc.2006-2843.

44. Agarwal SK, Mateo CM, Marx SJ. Rare germline mutations in cyclin-dependent kinase inhibitor genes in multiple endocrine neoplasia type 1 and related states. J Clin Endocrinol Metab. 2009;94:1826–34. doi:10.1210/jc.2008-2083.

45. Lee M, Pellegata NS. Multiple endocrine neoplasia type 4. Front Horm Res. 2013;41:63–78. doi:10.1159/000345670.

46. Lee M, Pellegata NS. Multiple endocrine neoplasia syndromes associated with mutation of p27. J Endocrinol Invest. 2013;36:781–7. doi:10.3275/9021.

47. Santamaria D, Ortega S. Cyclins and CDKS in development and cancer: lessons from genetically modified mice. Front Biosci. 2006;11:1164–88.

48. Cromer MK, Starker LF, Choi M, Udelsman R, Nelson-Williams C, Lifton RP, et al. Identification of somatic mutations in parathyroid tumors using whole-exome sequencing. J Clin Endocrinol Metab. 2012;97:E1774–81. doi:10.1210/jc.2012-1743.

49. Newey PJ, Nesbit MA, Rimmer AJ, Attar M, Head RT, Christie PT, et al. Whole-exome sequencing studies of nonhereditary (sporadic) parathyroid adenomas. J Clin Endocrinol Metab. 2012;97:E1995–2005. doi:10.1210/jc.2012-2303.

50. Jiao Y, Shi C, Edil BH, de Wilde RF, Klimstra DS, Maitra A, et al. DAXX/ATRX, MEN1, and mTOR pathway genes are frequently altered in pancreatic neuroendocrine tumors. Science. 2011;331:1199–203. doi:10.1126/science.1200609.

51. Zhuang Z, Vortmeyer AO, Pack S, Huang S, Pham TA, Wang C, et al. Somatic mutations of the MEN1 tumor suppressor gene in sporadic gastrinomas and insulinomas. Cancer Res. 1997;57:4682–6.

52. Gortz B, Roth J, Krahenmann A, de Krijger RR, Muletta-Feurer S, Rutimann K, et al. Mutations and allelic deletions of the MEN1 gene are associated with a subset of sporadic endocrine pancreatic and neuroendocrine tumors and not restricted to foregut neoplasms. Am J Pathol. 1999;154:429–36. doi:10.1016/S0002-9440(10)65289-3.

53. Corbo V, Dalai I, Scardoni M, Barbi S, Beghelli S, Bersani S, et al. MEN1 in pancreatic endocrine tumors: analysis of gene and protein status in 169 sporadic neoplasms reveals alterations in the vast majority of cases. Endocr Relat Cancer. 2010;17:771–83. doi:10.1677/ERC-10-0028.

54. Cao Y, Gao Z, Li L, Jiang X, Shan A, Cai J, et al. Whole exome sequencing of insulinoma reveals recurrent T372R mutations in YY1. Nat Commun. 2013;4:2810. doi:10.1038/ncomms3810.

55. Cromer MK, Choi M, Nelson-Williams C, Fonseca AL, Kunstman JW, Korah RM, et al. Neomorphic effects of recurrent somatic mutations in Yin Yang 1 in insulin-producing adenomas. Proc Natl Acad Sci U S A. 2015;112:4062–7. doi:10.1073/pnas.1503696112.

56. Lichtenauer UD, Di Dalmazi G, Slater EP, Wieland T, Kuebart A, Schmittfull A, et al. Frequency and clinical correlates of somatic Ying Yang 1 mutations in sporadic insulinomas. J Clin Endocrinol Metab. 2015;100:E776–82. doi:10.1210/jc.2015-1100.

57. Forbes SA, Beare D, Gunasekaran P, Leung K, Bindal N, Boutselakis H, et al. COSMIC: exploring the world's knowledge of somatic mutations in human cancer. Nucleic Acids Res. 2015;43:D805–11. doi:10.1093/nar/gku1075.

58. Guru SC, Goldsmith PK, Burns AL, Marx SJ, Spiegel AM, Collins FS, et al. Menin, the product of the MEN1 gene, is a nuclear protein. Proc Natl Acad Sci U S A. 1998;95:1630–4.

59. La P, Desmond A, Hou Z, Silva AC, Schnepp RW, Hua X. Tumor suppressor menin: the essential role of nuclear localization signal domains in coordinating gene expression. Oncogene. 2006;25:3537–46. doi:10.1038/sj.onc.1209400.

60. Murai MJ, Chruszcz M, Reddy G, Grembecka J, Cierpicki T. Crystal structure of menin reveals binding site for Mixed Lineage Leukemia (MLL) protein. J Biol Chem. 2011;286:31742–8. doi:10.1074/jbc.M111.258186.

61. Huang J, Gurung B, Wan B, Matkar S, Veniaminova NA, Wan K, et al. The same pocket in menin binds both MLL and JUND but has opposite effects on transcription. Nature. 2012;482:542–6. doi:10.1038/nature10806.

62. Hendy GN, Kaji H, Canaff L. Cellular functions of menin. Adv Exp Med Biol. 2009;668:37–50.

63. Matkar S, Thiel A, Hua X. Menin: a scaffold protein that controls gene expression and cell signaling. Trends Biochem Sci. 2013;38:394–402. doi:10.1016/j.tibs.2013.05.005.

64. Agarwal SK. *MEN1*. Frontiers in hormone research. 2013:1–15.

65. Hughes CM, Rozenblatt-Rosen O, Milne TA, Copeland TD, Levine SS, Lee JC, et al. Menin associates with a trithorax family histone methyltransferase complex and with the hoxc8 locus. Mol Cell. 2004;13:587–97.

66. Yokoyama A, Somervaille TC, Smith KS, Rozenblatt-Rosen O, Meyerson M, Cleary ML. The menin tumor suppressor protein is an essential oncogenic cofactor for MLL-associated leukemogenesis. Cell. 2005;123:207–18. doi:10.1016/j.cell.2005.09.025.

67. Milne TA, Hughes CM, Lloyd R, Yang Z, Rozenblatt-Rosen O, Dou Y, et al. Menin and MLL cooperatively regulate expression of cyclin-dependent kinase inhibitors. Proc Natl Acad Sci U S A. 2005;102:749–54. doi:10.1073/pnas.0408836102.

68. Karnik SK, Hughes CM, Gu X, Rozenblatt-Rosen O, McLean GW, Xiong Y, et al. Menin regulates pancreatic islet growth by promoting histone methylation and expression of genes encoding p27Kip1 and p18INK4c. Proc Natl Acad Sci U S A. 2005;102:14659–64. doi:10.1073/pnas.0503484102.

69. Agarwal SK, Jothi R. Genome-wide characterization of menin-dependent H3K4me3 reveals a specific role for menin in the regulation of genes implicated in MEN1-like tumors. PLoS One. 2012;7, e37952. doi:10.1371/journal.pone.0037952.

70. Modali SD, Parekh VI, Kebebew E, Agarwal SK. Epigenetic regulation of the lncRNA MEG3 and its target c-MET in pancreatic neuroendocrine tumors. Mol Endocrinol. 2015;29:224–37. doi:10.1210/me.2014-1304.

71. Lin W, Watanabe H, Peng S, Francis JM, Kaplan N, Pedamallu CS, et al. Dynamic epigenetic regulation by menin during pancreatic islet tumor formation. Mol Cancer Res. 2015;13:689–98. doi:10.1158/1541-7786.MCR-14-0457.

72. Scacheri PC, Davis S, Odom DT, Crawford GE, Perkins S, Halawi MJ, et al. Genome-wide analysis of menin binding provides insights into MEN1 tumorigenesis. PLoS Genet. 2006;2, e51. doi:10.1371/journal.pgen.0020051.

73. Wang P, Lin C, Smith ER, Guo H, Sanderson BW, Wu M, et al. Global analysis of H3K4 methylation defines MLL family member targets and points to a role for MLL1-mediated H3K4 methylation in the regulation of transcriptional initiation by RNA polymerase II. Mol Cell Biol. 2009;29(22):6074–85. doi:10.1128/MCB.00924-09.

74. Francis J, Lin W, Rozenblatt-Rosen O, Meyerson M. The menin tumor suppressor protein is phosphorylated in response to DNA damage. PLoS One. 2011;6, e16119. doi:10.1371/journal.pone.0016119.

75. Feng ZJ, Gurung B, Jin GH, Yang XL, Hua XX. SUMO modification of menin. Am J Cancer Res. 2013;3:96–106.

76. Pieterman CR, Conemans EB, Dreijerink KM, de Laat JM, Timmers HT, Vriens MR, et al. Thoracic and duodenopancreatic neuroendocrine tumors in multiple endocrine neoplasia type 1: natural history and function of menin in tumorigenesis. Endocr Relat Cancer. 2014;21:R121–42. doi:10.1530/ERC-13-0482.

77. Crabtree JS, Scacheri PC, Ward JM, Garrett-Beal L, Emmert-Buck MR, Edgemon KA, et al. A mouse model of multiple endocrine neoplasia, type 1, develops multiple endocrine tumors. Proc Natl Acad Sci U S A. 2001;98:1118–23. doi:10.1073/pnas.98.3.1118.

78. Bertolino P, Radovanovic I, Casse H, Aguzzi A, Wang ZQ, Zhang CX. Genetic ablation of the tumor suppressor menin causes lethality at mid-gestation with defects in multiple organs. Mech Dev. 2003;120:549–60.

79. Bertolino P, Tong WM, Galendo D, Wang ZQ, Zhang CX. Heterozygous Men1 mutant mice develop a range of endocrine tumors mimicking multiple endocrine neoplasia type 1. Mol Endocrinol. 2003;17:1880–92. doi:10.1210/me.2003-0154.

80. Loffler KA, Biondi CA, Gartside M, Waring P, Stark M, Serewko-Auret MM, et al. Broad tumor spectrum in a mouse model of multiple endocrine neoplasia type 1. Int J Cancer. 2007;120:259–67. doi:10.1002/ijc.22288.

81. Harding B, Lemos MC, Reed AA, Walls GV, Jeyabalan J, Bowl MR, et al. Multiple endocrine neoplasia type 1 knockout mice develop parathyroid, pancreatic, pituitary and adrenal tumours with hypercalcaemia, hypophosphataemia and hypercorticosteronaemia. Endocr Relat Cancer. 2009;16:1313–27. doi:10.1677/ERC-09-0082.

82. Piret SE, Thakker RV. Mouse models for inherited endocrine and metabolic disorders. J Endocrinol. 2011;211:211–30. doi:10.1530/JOE-11-0193.

83. Agarwal SK. Exploring the tumors of multiple endocrine neoplasia type 1 in mouse models for basic and preclinical studies. Int J Endocr Oncol. 2014;1:153–61. doi:10.2217/ije.14.16.

84. Loffler KA, Biondi CA, Gartside MG, Serewko-Auret MM, Duncan R, Tonks ID, et al. Lack of augmentation of tumor spectrum or severity in dual heterozygous Men1 and Rb1 knockout mice. Oncogene. 2007;26:4009–17. doi:10.1038/sj.onc.1210163.

85. Matoso A, Zhou Z, Hayama R, Flesken-Nikitin A, Nikitin AY. Cell lineage-specific interactions between Men1 and Rb in neuroendocrine neoplasia. Carcinogenesis. 2008;29:620–8. doi:10.1093/carcin/bgm207.

86. Loffler KA, Mould AW, Waring PM, Hayward NK, Kay GF. Menin and p53 have non-synergistic effects on tumorigenesis in mice. BMC Cancer. 2012;12:252. doi:10.1186/1471-2407-12-252.

87. Bai F, Pei XH, Nishikawa T, Smith MD, Xiong Y. p18Ink4c, but not p27Kip1, collaborates with Men1 to suppress neuroendocrine organ tumors. Mol Cell Biol. 2007;27:1495–504. doi:10.1128/MCB.01764-06.

88. Gillam MP, Nimbalkar D, Sun L, Christov K, Ray D, Kaldis P, et al. MEN1 tumorigenesis in the pituitary and pancreatic islet requires Cdk4 but not Cdk2. Oncogene. 2015;34:932–8. doi:10.1038/onc.2014.3.

89. Libutti SK, Crabtree JS, Lorang D, Burns AL, Mazzanti C, Hewitt SM, et al. Parathyroid gland-specific deletion of the mouse Men1 gene results in parathyroid neoplasia and hypercalcemic hyperparathyroidism. Cancer Res. 2003;63:8022–8.

90. Shen HC, He M, Powell A, Adem A, Lorang D, Heller C, et al. Recapitulation of pancreatic neuroendocrine tumors in human multiple endocrine neoplasia type I syndrome via Pdx1-directed inactivation of Men1. Cancer Res. 2009;69:1858–66. doi:10.1158/0008-5472.CAN-08-3662.

91. Crabtree JS, Scacheri PC, Ward JM, McNally SR, Swain GP, Montagna C, et al. Of mice and MEN1: Insulinomas in a conditional mouse knockout. Mol Cell Biol. 2003;23:6075–85.

92. Bertolino P, Tong WM, Herrera PL, Casse H, Zhang CX, Wang ZQ. Pancreatic beta-cell-specific ablation of the multiple endocrine neoplasia type 1 (MEN1) gene causes full penetrance of insulinoma development in mice. Cancer Res. 2003;63:4836–41.

93. Biondi CA, Gartside MG, Waring P, Loffler KA, Stark MS, Magnuson MA, et al. Conditional inactivation of the MEN1 gene leads to pancreatic and pituitary tumorigenesis but does not affect normal development of these tissues. Mol Cell Biol. 2004;24:3125–31.

94. Scacheri PC, Crabtree JS, Kennedy AL, Swain GP, Ward JM, Marx SJ, et al. Homozygous loss of menin is well tolerated in liver, a tissue not affected in MEN1. Mamm Genome Off J Int Mamm Genome Soc. 2004;15:872–7.

95. Shen HC, Ylaya K, Pechhold K, Wilson A, Adem A, Hewitt SM, et al. Multiple endocrine neoplasia type 1 deletion in pancreatic alpha-cells leads to development of insulinomas in mice. Endocrinology. 2010;151:4024–30. doi:10.1210/en.2009-1251.

96. Lu J, Herrera PL, Carreira C, Bonnavion R, Seigne C, Calender A, et al. Alpha cell-specific Men1 ablation triggers the transdifferentiation of glucagon-expressing cells and insulinoma development. Gastroenterology. 2010;138:1954–65. doi:10.1053/j.gastro.2010.01.046.

97. Hamze Z, Vercherat C, Bernigaud-Lacheretz A, Bazzi W, Bonnavion R, Lu J, et al. Altered MENIN expression disrupts the MAFA differentiation pathway in insulinoma. Endocr Relat Cancer. 2013;20:833–48. doi:10.1530/ERC-13-0164.

98. Shi K, Parekh VI, Roy S, Desai SS, Agarwal SK. The embryonic transcription factor Hlxb9 is a menin interacting partner that controls pancreatic beta-cell proliferation and the expression of insulin regulators. Endocr Relat Cancer. 2013;20:111–22. doi:10.1530/ERC-12-0077.

99. Desai SS, Modali SD, Parekh VI, Kebebew E, Agarwal SK. GSK-3beta protein phosphorylates and stabilizes HLXB9 protein in insulinoma cells to form a targetable mechanism of controlling insulinoma cell proliferation. J Biol Chem. 2014;289:5386–98. doi:10.1074/jbc.M113.533612.

100. Desai SS, Kharade SS, Parekh VI, Iyer S, Agarwal SK. Pro-oncogenic Roles of HLXB9 Protein in Insulinoma Cells through Interaction with Nono Protein and Down-regulation of the c-Met Inhibitor Cblb (Casitas B-lineage Lymphoma b). J Biol Chem. 2015;290:25595–608. doi:10.1074/jbc.M115.661413.

101. Chamberlain CE, Scheel DW, McGlynn K, Kim H, Miyatsuka T, Wang J, et al. Menin determines K-RAS proliferative outputs in endocrine cells. J Clin Invest. 2014;124:4093–101. doi:10.1172/JCI69004.

102. Jiang X, Cao Y, Li F, Su Y, Li Y, Peng Y, et al. Targeting beta-catenin signaling for therapeutic intervention in MEN1-deficient pancreatic neuroendocrine tumours. Nat Commun. 2014;5:5809. doi:10.1038/ncomms6809.

103. Lin W, Cao J, Liu J, Beshiri ML, Fujiwara Y, Francis J, et al. Loss of the retinoblastoma binding protein 2 (RBP2) histone demethylase suppresses tumorigenesis in mice lacking Rb1 or Men1. Proc Natl Acad Sci U S A. 2011;108:13379–86. doi:10.1073/pnas.1110104108.

104. Ripoche D, Charbord J, Hennino A, Teinturier R, Bonnavion R, Jaafar R, et al. ActivinB is induced in Insulinoma to promote tumor plasticity through a beta-cell induced dedifferentiation. Mol Cell Biol. 2015. doi:10.1128/MCB.00930-15.

105. Korsisaari N, Ross J, Wu X, Kowanetz M, Pal N, Hall L, et al. Blocking vascular endothelial growth factor-a inhibits the growth of pituitary adenomas and lowers serum prolactin level in a mouse model of multiple endocrine neoplasia type 1. Clin Cancer Res Off J Am Assoc Cancer Res. 2008;14:249–58. doi:10.1158/1078-0432.CCR-07-1552.

106. Quinn TJ, Yuan Z, Adem A, Geha R, Vrikshajanani C, Koba W, et al. Pasireotide (SOM230) is effective for the treatment of pancreatic neuroendocrine tumors (PNETs) in a multiple

endocrine neoplasia type 1 (MEN1) conditional knockout mouse model. Surgery. 2012;152:1068–77. doi:10.1016/j.surg.2012.08.021.

107. Walls GV, Lemos MC, Javid M, Bazan-Peregrino M, Jeyabalan J, Reed AA, et al. MEN1 gene replacement therapy reduces proliferation rates in a mouse model of pituitary adenomas. Cancer Res. 2012;72:5060–8. doi:10.1158/0008-5472.CAN-12-1821.

108. Vassalli A, Matzuk MM, Gardner HA, Lee KF, Jaenisch R. Activin/inhibin beta B subunit gene disruption leads to defects in eyelid development and female reproduction. Genes Dev. 1994;8:414–27.

109. McKimpson WM, Yuan Z, Zheng M, Crabtree JS, Libutti SK, Kitsis RN. The cell death inhibitor ARC is induced in a tissue-specific manner by deletion of the tumor suppressor gene Men1, but not required for tumor development and growth. PLoS One. 2015;10, e0145792. doi:10.1371/journal.pone.0145792.

Chapter 4
Molecular Genetics of MEN2-Related Neuroendocrine Tumours

Friedhelm Raue and Karin Frank-Raue

Abbreviations

MTC   medullary thyroid carcinoma
MEN   multiple endocrine neoplasia
RET gene rearranged during transfection gene
TKI   Tyrosine kinase inhibitor

4.1   Introduction

Multiple endocrine neoplasia type 2 (MEN2) is an autosomal dominant hereditary cancer syndrome caused by missense mutations in the *RET* proto-oncogene that result in gain of function. Offspring of a carrier have a 50 % risk of inheriting the disease [1]. Two distinct clinical subtypes of MEN2 have been characterized (Table 4.1): MEN2A, by the presence of medullary thyroid carcinoma (MTC), variable incidence of bilateral pheochromocytoma and primary hyperparathyroidism within a single patient or family, and MEN2B, by the association between MTC, pheochromocytoma and mucosal neuroma and other clinical features (Table 4.1) [2]. This syndrome is characterized by strong genotype–phenotype correlations,

F. Raue (✉)
Endocrine Practice, Molecular Laboratory, Heidelberg, Germany

Endokrinologisch, Nuklearmedizinische Praxis, Brückenstr.21, 69120 Heidelberg, Germany
e-mail: friedhelm.raue@raue-endokrinologie.de

K. Frank-Raue
Endocrine Practice, Molecular Laboratory, Heidelberg, Germany

Table 4.1 Clinical classification of multiple endocrine neoplasia type 2 (MEN2) and occurrence of medullary thyroid carcinoma (MTC), associated tumors and other diseases

Subtype	% of total cases	MTC (%)	Pheo (%)	HPT (%)	Associated diseases
MEN2A	91	98			
Classical	46	100	50	25	
Hirschsprung's disease	5	100	20		Hirschsprung's disease
Cutaneous lichen amyloidosis	5	100	50		Cutaneous lichen amyloidosis
FMTC	35	95	0	0	
MEN2B	9	100	50	0	Ganglioneuromatosis, marfanoid habitus

Pheo pheochromocytoma, *HPT* hyperparathyroidism, *FMTC* familial MTC

and a specific *RET* mutation may suggest a predilection toward a particular phenotype and clinical course.

Based on a model that utilizes these genotype–phenotype correlations, *RET* mutations have been stratified into three risk levels (moderate, high, highest) concerning the aggressiveness of MTC [2]. This stratification system was reclassified recently [2]; the former four-level categories were now subdivided into three risk groups [3]. Genetic testing detects nearly 100 % of mutation carriers and is considered the standard of care for all first-degree relatives of patients with newly diagnosed MTC. Recommendations on the timing of prophylactic/early thyroidectomy and extent of surgery are based on classification of *RET* mutations into these three risk levels (Table 4.2). The main factors influencing survival are stage of disease at diagnosis, the different RET mutations, but also the postoperative calcitonin level.

4.2 Phenotype: Clinical Syndromes of MEN2

MEN2 (OMIM 171400) is an autosomal dominant tumor syndrome with an estimated prevalence of 1 per 30,000 in the general population. MEN2 syndrome occurs in two clinically distinct varieties with MTC as a common manifestation. Affected individuals initially develop primary C-cell hyperplasia (CCH) that progresses to invasive MTC. Only familial primary CCH is a preneoplastic lesion. Secondary CCH, which has been associated with chronic lymphocytic thyroiditis, hypergastrinemia, near other follicular cell-derived thyroid tumors, and even ageing, has a much lower, if any, potential for malignancy [4]. The two subtypes of MEN2 differ with respect to incidence, genetics, age of onset, association with other diseases, aggressiveness of MTC and prognosis [2, 3, 5] (Table 4.1).

Table 4.2 Risk groups of *RET* mutations based on age at manifestation, the aggressiveness of MTC and penetrance of pheochromocytoma or primary hyperparathyroidism

ATA risk level[a]	Moderate	High	Highest
RET mutation (common codon)	533, 609, 611, 618, 620, 630, 631, 768, 790, 804, 891, 912	634, 883	918
MEN2 subtype	MEN2A/FMTC	MEN2A/ MEN2B	MEN2B
MTC aggressiveness	Moderate	Higher	Highest
Recommended age for genetic testing	5 years	3 years	As soon as possible (first year of life)
MTC age of onset	5 years to young adults	Before the age of 5 years	First year of life
Timing of early thyroidectomy	Age 5 or 10 years or when calcitonin rises	Before the age of 5 years	As soon as possible, first months of life
Screening for Pheo	Start at 16 years, periodically	Start at 11 years, annually	Start at 11 years, annually
Screening for HPT	Start at 16 years, periodically	Start at 11 years, annually	–

MTC medullary thyroid carcinoma, *FMTC* familial MTC, *HPT* primary hyperparathyroidism, *Pheo* pheochromocytoma, *ATA* American Thyroid Association
[a]Risk for aggressive MTC [2]

4.2.1 MEN2A Syndrome

MEN2A syndrome is characterized by MTC in combination with pheochromocytoma and/or multiple tumors of the parathyroid glands in a single patient or the presence of two or more tumor types in multiple members of a single family. It is the most common form of all MEN2 syndromes, representing 55% of cases [6]. The frequency of MTC is over 95% among patients with MEN2A, while the frequencies of pheochromocytoma and multiple parathyroid gland hyperplasia are 40–50% and 10–20%, respectively [7, 8]. MTC is generally the first manifestation of MEN2A and presents when patients are between 5 and 25 years of age. MEN2 is further subdivided into four groups [2]: (i) classical MEN2A, which includes MTC with pheochromocytoma or hyperparathyroidism or both; (ii) MEN2A with Hirschsprung's disease; (iii) MEN2A with cutaneous lichen amyloidosis; and (iv) familial MTC (FMTC). FMTC, formerly considered a distinct variant of MEN2A, affects families as well as individuals who have *RET* germline mutations and who mainly show MTC (and rarely pheochromocytoma). Nowadays, FMTC is viewed as a phenotypic continuum of MEN2A rather than a distinct disease with decreased penetrance of pheochromocytoma and primary hyperparathyroidism. In general, the clinical course of MTC in FMTC is more benign than that of MEN2A or MEN2B, and some FMTC subtypes have late onset or no clinically manifest disease. Usually FMTC carries a good prognosis [2, 9, 10].

4.2.2 MEN2B Syndrome

MEN2B syndrome is the most rare and aggressive form of MEN2 and accounts for 5–10 % of MEN2 cases. It is characterized by MTC, pheochromocytoma, the absence of hyperparathyroidism, visible physical stigmata such as raised bumps on the lips and tongue (due to cutaneous neuromas), ganglioneuromas of the intestine and marfanoid habitus with skeletal deformations and joint laxity. Patients with MEN2B typically have disease onset during the first year of life and have a more aggressive form of MTC with higher morbidity and mortality rates than do patients with MEN2A. Multivariate analysis suggests that the higher mortality rate of MEN2B reflects a more advanced tumor stage at presentation rather than a more aggressive tumor behaviour once established [3]. Patients with MEN2B often do not have a family history of the disease; in more than 50 % of cases, the syndrome is due to de novo germline *RET* mutation primarily paternal in origin, which reflects the role of *RET* in spermatogonial stem cell renewal [11].

4.2.3 Diagnostic Procedure

A family history is often inadequate for diagnosing familial disease; more thorough genetic and biochemical screening often reveals a family history of MTC in patients originally thought to have the sporadic form of the disease. About 1–7 % of apparently sporadic cases have identifiable germline *RET* mutations, including about 2–9 % with de novo germline mutations [3, 12]. Strong genotype–phenotype correlations are recognized between specific mutations and MEN2 disease phenotypes, and these correlations have proved to be valuable in predicting disease onset and prognosis, as well as in guiding therapeutic intervention and patient management [8]. Earlier identification of patients with MTC by *RET* mutation analysis has changed the presentation from clinical tumors to preclinical disease, resulting in a high cure rate for affected patients and a much better prognosis.

4.3 Genotype: *RET* Proto-Oncogene Structure, Function and Abnormalities

4.3.1 RET Receptor Structure and Function

The *RET* proto-oncogene is localized in the pericentromeric region on chromosome 10q11.2, has 21 exons and encodes a receptor tyrosine kinase that appears to transduce growth and differentiation signals in several developing tissues, including those derived from the neural crest [13, 14] (Fig. 4.1). The protein consists of a large extracellular segment with a cadherin (Ca^{2+}-dependent cell adhesion)-like domain,
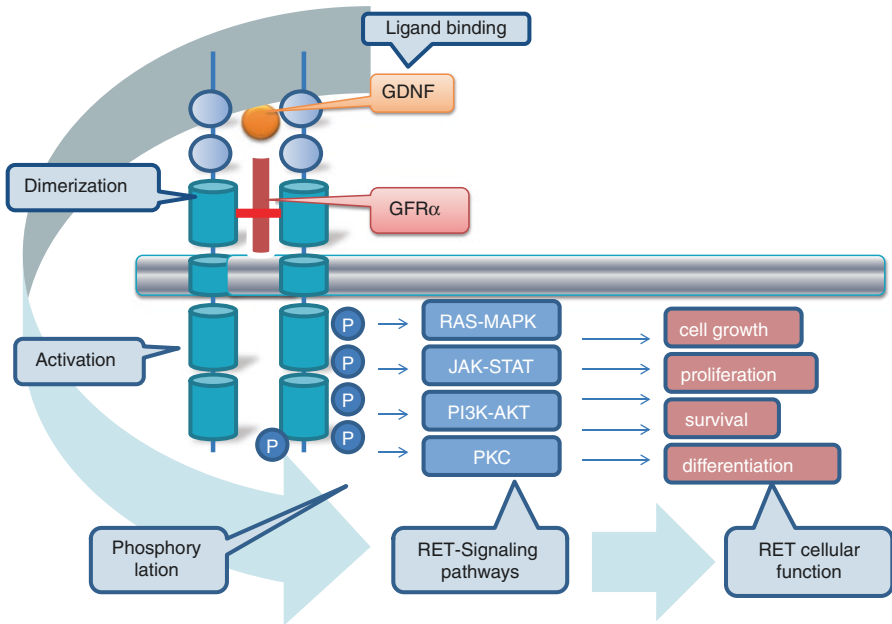
Fig. 4.1 RET receptor interaction and signal transduction network

which is important for stabilizing RET dimers and a cysteine-rich domain that is positioned near the cell membrane, which is crucial for protein conformation and ligand binding. RET protein has a single transmembrane domain and an intracellular segment with two tyrosine kinase subdomains, TK1 and TK2. It is activated by ligand-induced dimerization [14–17]. RET binds ligands of the glial-derived neurotrophic factor (GDNF) family in conjunction with a co-receptor, designated GDNF family receptor α (GFRα). Upon binding of the ligand–co-receptor complex, RET dimerization and autophosphorylation on intracellular tyrosine residues recruit adaptor and signalling proteins to stimulate multiple downstream pathways like the RAS–MAPK and PI3K–AKT pathways [15, 18]. These signals are important for many of the RET-mediated functions, including kidney and nervous system development, neuronal survival and differentiation, and maintenance of spermatogonial stem cells [19, 20]. In addition, phospholipase Cγ (PLCγ) binding to RET and the activation of protein kinase C (PKC) signalling are crucial for kidney morphogenesis and the migration of neuro-progenitors in the developing brain [21, 22]. The RET receptor is expressed at its highest levels in early embryogenesis and decreases to relatively low levels in normal adult tissues [23, 24]. RET is expressed in several neural and neuroendocrine cell lineages [25]. It is found in neuroendocrine-derived cell types in many organs, such as the thyroid C cells, the precursors of MTC, and adrenal chromaffin cells, precursors of pheochromocytomas. RET signalling also maintains the enteric nervous system, and loss of RET function in these neurons leads to Hirschsprung's disease [26], in which neuroblasts fail to migrate to the

developing gut and neurons and ganglia of the enteric nervous system fail to mature owing to a lack of RET signals [27] resulting in a aganglionosis of the colon. RET loss-of-function mutations have also been recognized in patients with congenital abnormalities of the kidney and urinary tract.

RET oncogene mechanism implicates either through gain-of-function mutations that lead to constitutive activation or through aberrant expression or activation of wild-type receptors. Oncogenic *RET* mutations can be either activating point mutations within the full-length RET protein or genomic rearrangements that produce chimeric RET oncoproteins that are generally localized in the cytosol. While *RET* mutation has been primarily associated with thyroid cancer, somatic structural *RET* alterations or changes of its expression have been described in lung, breast and pancreatic cancers [28–30].

4.3.2   *RET Mutations in MEN2*

Hereditary MTC is caused by autosomal dominant gain-of-function mutations in the *RET* proto-oncogene. The MEN2 gene was localized by genetic linkage analysis in 1987 [31, 32]. Subsequently, point mutations of the *RET* proto-oncogene were identified in MEN2A and MEN2B in eight exons 5, 8, 10, 11, and 13–16 (Fig. 4.2). Analysis of *RET* in families with MEN2A revealed that nearly all of these families have germline mutations and that only those family members with the germline missense mutations have the disease. More than 80 different *RET* mutations have been associated with hereditary MTC [33].

Mutations present in the *extracellular* domain (exons 8, 10, 11) are known to target highly conserved cysteine residues. Because these residues are normally involved in intramolecular disulphide bond formation, mutation generates an unpaired cysteine residue with free sulphydryl group. Mutant RET receptors in close proximity will then form intermolecular disulphide bonds, which function to stabilize dimerization even in the absence of the ligand and enhanced phosphorylation of intracellular substrates [34]. The most common mutations are substitutions of RET C634 which occur in patients with the classical MEN2A subtype and are associated with greater risks of pheochromocytoma and parathyroid hyperplasia. These classical MEN2A disease phenotypes are relatively rare in patients with other mutations of the extracellular domain (exons 10, 8, 5). In rare cases, a subgroup of these *RET* cysteine variants (affecting C609, C611, C618 and C620), termed 'Janus mutations', can confer both *RET* gain-of-function and loss-of-function phenotypes [35]. Although these mutations lead to constitutive RET activation and are associated with MEN2A phenotypes, the mutant proteins are poorly matured and are expressed at lower levels on the cell surface [36]. As a result, in tissues such as the enteric nervous system that require GDNF-mediated RET activation for appropriate formation [37], the reduced mature protein expression mimics loss-of-function *RET* mutations that occur in HSCR, and both MEN2 and HSCR phenotypes can co-occur in some families [8, 38].
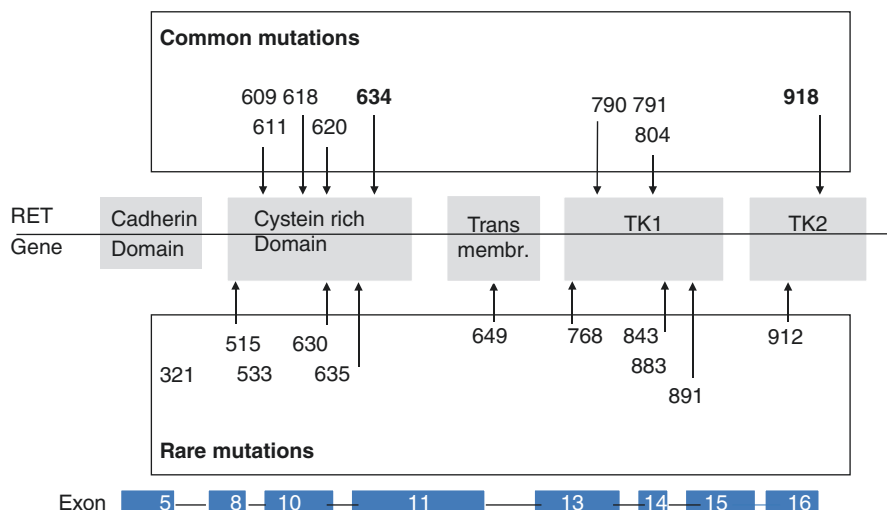
Fig. 4.2 Germline mutations in the *RET* proto-oncogene associated with multiple endocrine neo-plasia type 2 and familial medullary thyroid carcinoma. Numbers indicate mutated codons of the *RET* gene

Mutations of the *intracellular* tyrosine kinase domain of RET (codons 13–16) are known to target regions associated with the ATP-binding pocket, activation loop and substrate-binding pocket. Depending on their specific location, they induce structural changes and alter RET substrate specificity. This results in phosphoryla-tion of alternative intracellular proteins [17]. Therefore, the mutated receptor no longer needs dimerization to become active.

The two specific amino acid substitutions in the RET kinase domain, M918T and A883F, are found exclusively in patients with the MEN2B phenotype. These residues flank the activation loop of the RET kinase and are associated with more complex functional outcomes, including protein conformational changes that decrease autoinhibition, increase kinase activity and ATP binding by tenfold, and might modify substrate recognition. Although M918T proteins are the most trans-forming *RET* mutants *in vitro* and are associated with the most severe disease phenotypes, the natural history of A883F mutants might be somewhat more indo-lent [10, 39].

Other mutations that affect the *RET* intracellular domain (residues E768, L790, Y791, V804 and S891) are predominantly associated with more indolent MEN2A phenotypes, later onset or a reduced penetrance of MTC and rarely pheochromocy-toma [40], although there can be considerable interfamilial and intrafamilial varia-tion associated with a single mutant. Mutations of Y791, which were originally detected in patients with FMTC and MEN2A, have also been identified in HSCR-only families and have been described in about 1 % of control populations, which is suggestive of a polymorphism rather than a pathological variant [41–43]. However, molecular studies have confirmed that the Y791F RET mutant proteins

are constitutively activated and autophosphorylated as protein monomers and can induce downstream signalling and transformed phenotypes [44–47]. The tandem occurrence of Y791F with other *RET* substitutions (such as L790F or C634Y) seems to increase the aggressiveness and/or penetrance of MEN2 phenotypes [42, 48]. Although the molecular mechanisms that underlie this remain to be elucidated, the data are consistent with Y791F functioning on the one hand as a low-penetrance modifier or enhancer of other oncogenic mutations and, on the other hand, producing a receptor that is unable to respond to ligand activation or, therefore, to chemotactic signals, and this confers a risk of HSCR phenotypes. Other intracellular mutations have varying functional effects; for example, substitutions of V804 affect RET–ATP-binding [49], co-occurrence of the V804M mutation in cis with other kinase domain variants (Q781R, E805K, Y806C, or S904C) can result in additional conformational changes.

4.3.3   Rare and New RET Mutations: Polymorphisms

In newly detected germline RET sequence changes, it is mandatory to clarify if this 'mutation' is causative of MEN2 and segregates with the MEN2 disease symptoms within a family. The web-based ARUP online Scientific Resource RET database (http://www.arup.utah.edu/database/MEN2/MEN2_welcome.php) [33] uses the following classification definition: mutation, polymorphism and variant of unknown significance (VUS).

Mutation is defined as causative for the disease and segregates with the disease in (i) at least two affected family members in which at least one has MTC and the other one has a clinical feature of MEN2 or (ii) if at least three unrelated individuals with MTC have the same germline *RET* sequence variant [33].

Polymorphisms are benign germline RET sequence changes that are not causative for MEN2 like G691S, L679L, S836S, S904S and intron 14 c.2608-24G > A. These *RET* polymorphic sequence variants might have some implications as either low-penetrance risk alleles for *RET*-associated cancers or as genetic modifiers of oncogenic risk. A G691S substitution in the *RET* intracellular juxtamembrane region is overrepresented in sporadic MTC, pancreatic cancer and cutaneous and desmoplastic malignant melanomas [50–52]. This polymorphisms might also modify the age at which tumors develop in patients with MEN2A in association with other *RET* mutations [53, 54]. This is not confirmed by others: in a study with 150 patients with sporadic MTC carriers and noncarriers of the *RET* variants G691S, L767L, S836S and S904S appeared clinically and pathologically indistinguishable [55]. The functional mechanisms that underlie these phenotypic effects are not yet clear.

Variants of unknown significance (VUS) or uncertain are *RET* sequence changes in which there is not enough clinical evidence to indicate a causative role and further clinical studies are necessary to clarify if this sequence change is a mutation or a polymorphism. Prediction of disease association for novel mutations and

uncertain gene variants may be performed using in silico and *in vitro* analysis. There is a positive correlation between the in silico risk score and *in vitro* focus formation units [45].

4.3.4 Somatic Mutations in MTC

Approximately 23–60 % of sporadic MTCs have an acquired somatic *RET* M918T mutation in tumor tissue. This mutation is identical to the germline mutation found in MEN2B [56, 57]. The prevalence of somatic M918T *RET* mutations varies depending on tumor size: small tumors (<1 cm) rarely have the mutation (11.3 %), while M918T is found in 58.8 % of patients with tumors >3 cm [58]. Patients with sporadic MTC with M918T have more aggressive tumor growth and a poor prognosis [56, 59, 60]. It is important to recognize that somatic mutations are heterogeneous. For instance, in the context of metastatic sporadic MTC, some metastatic foci have a codon 918 mutation, while the primary tumor or another focus can be devoid of this mutation [56]. RET does not seem to be the early initiator of tumor growth in sporadic MTC; rather, RET is activated later in oncogenesis as a driver of tumor growth, and other genes must play a significant role in MTC onset. It was recently discovered that 18–80 % of sporadic MTCs lacking somatic RET mutations have somatic mutations in *KRAS*, *HRAS* or, rarely, in *NRAS* [61]. No other common genetic mutation has been detected in subsequent exome sequencing studies of MTCs [62].

4.4 Genotype–Phenotype Correlation in MEN2

Clear associations have been documented between specific *RET* mutations (MEN2 genotype) and the age of onset and aggressiveness of MTC and the presence or absence of other endocrine neoplasms (MEN2 phenotype), such as pheochromocytoma or hyperparathyroidism. Approximately 98 % of index patients with MEN2 have an identifiable *RET* mutation [63]. Some overlap exists between *RET* mutations and the resulting clinical subtype of MEN2. This genotype–phenotype correlation between specific mutations and MEN2 disease phenotype has been proved to be valuable in predicting disease onset and prognosis, as well as in guiding therapeutic intervention and patient management [2, 38].

Initially, the frequency of *RET* codon 634 mutations in patients with 'classical' MEN2A reached 85 %; mutations in codons 609, 611, 618 and 620 accounted for an additional 10–15 % of cases [8] (Fig. 4.2). In recent years, there has been a change in the spectrum of *RET* mutations detected in patients with hereditary MTC. Specifically, there has been a shift from the 'classical' mutation at codon 634 in exon 11 to more cases with mutations in exons 13–15 and less aggressive
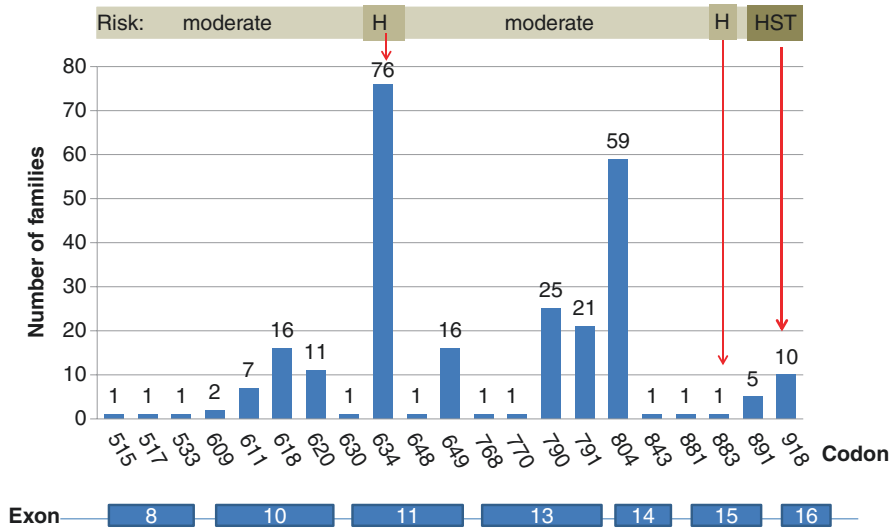
Fig. 4.3 Frequency of different *RET* mutations in 258 MEN2 families diagnosed between 2000 and 2015 (authors' experience) (*H* high, *HST* highest)

disease [6]. Our recent analysis of the *RET* proto-oncogene in patients with hereditary MTC provides evidence for this change in the spectrum of detected mutations. Exon 13–15 mutations, so-called rare mutations, were diagnosed in 39 % of families, exon 10 and 11 mutations in 54 % and exon 16 mutations in 6 % (Fig. 4.3). This change in the frequency of diagnosed mutations in MEN2A families from high-risk mutations to the so-called mild mutations in codons 13, 14 and 15 with late manifested and slowly growing MTC and rarely developing pheochromocytoma and hyperparathyroidism has changed the clinical presentation with a better prognosis of hereditary MTC. The reasons underlying this change in mutation spectrum detected may include the routine *RET* diagnostics in all patients diagnosed with MTC, the discovery of hereditary cases in apparently sporadic (4–7 %) cases [12], and the extension of the analyses to include mutations other than the known "hot spots" [42]. In addition, there is a distinct distribution of *RET* mutations in different parts of the world that depend on the genetic background of the local population, which may also affect the detection rates of specific *RET* mutations.

Pheochromocytoma is associated with exon 634 and 918 mutations in approximately 50 % of patients, with exon 10 mutations (codons 609, 611, 618 and 620) in up to 20 % patients and rarely with mutations in exons 13–15 [38, 64–66]. The pheochromocytomas are almost always benign and are usually multicentric and bilateral and confined to the adrenal gland. Patients with MEN2A and a unilateral pheochromocytoma usually develop a contralateral pheochromocytoma within 10 years.

Hyperparathyroidism in MEN2A is most commonly associated with codon 634 mutations, with C634R in particular [67, 68] with a moderate penetrance, up to 30 %. *RET* mutations in codons 609, 611, 618, and 620 are associated with a

penetrance between 2 and 5 % [38]. The primary hyperparathyroidism in patients with classical MEN2A is usually mild and associated with few if any symptoms. From one to four parathyroid glands may be enlarged. For practical reasons, screening for hyperparathyroidism should be done concurrently with screening for pheochromocytoma [2].

All cases of MEN2A with Hirschsprung's diseases are associated with mutations in exon 10 (codons 609, 611, 618, 620) [69]. MEN2A with cutaneous lichen amyloidosis, a dermatological lesions that are particularly evident in the scapular region of the back corresponding to dermatomes T2–T6, is associated with mutations in codon 634 [70–72].

Patients with MEN2B have a unique physical appearance characterized by typical facies, ophthalmologic abnormalities, skeletal malformations and a generalized ganglioneuromatosis throughout the aerodigestive tract and develop in 50 % of patients pheochromocytomas. They have mutations in exon 16 (M918T), less often in exon 15 (A883F) and rarely double mutations with V804M and either codon Y806C, S904C or E805K [73, 74].

Numerous reports in the literature show a correlation between the specific germline *RET* mutation, the age of onset and aggressiveness of MTC development, and the presence of nodal metastases [75]. Patients with codon M918T mutation and MEN2B have a high risk of aggressive MTC occurring at a young age [76]. In contrast, patients with codon 790 and 791 mutations have a low risk of aggressive disease and develop slow-growing tumors as a late manifestation [77]. According to recent data, although limited in numbers, membrane proximity of the mutation seems to be an important determinant of tumor development in carriers of *RET* mutations in exon 10 [38, 78]. These genotype–phenotype correlations between mutation, age of onset and tumor aggressiveness are the bases for clinical decision making when managing patients with MEN2. This is particularly true in presymptomatic *RET* mutation carriers because early thyroidectomy must be performed as long as the tumor is confined to the thyroid gland. This strategy for preventing familial MTC should be tailored according to the specific mutation carried by each patient. Recommendations for the timing of early thyroidectomy and the extent of surgical resection are based on a model that utilizes these genotype–phenotype correlations to stratify mutations into three risk levels [2] (Table 4.2).

4.5   Clinical Implications

The association between disease phenotype, aggressiveness of MTC and *RET* genotype has important implications for the clinical management of MEN2 patients and their families. Recommendations for the timing of early thyroidectomy in MEN2 patients are based on a model that utilizes genotype–phenotype correlations to stratify mutations into three risk levels, namely, moderate, high and highest risk (Table 4.2).

Patients with mutations in codon 918 (MEN2B) have the highest risk of advanced-stage disease at presentation [79] and should be operated as early as possible, preferably within the first year after birth. Mutations in RET codons 634 and 883 are characterized by an early age of MTC onset, and there is good evidence that there is significant age-related progression from CCH to MTC. A larger series demonstrated that MTC associated with any mutation at codon 634 commonly appears before 10 years of age but is rarely associated with lymph node metastases in patients younger than 14 years [75]. In the cases of these higher risk mutations, thyroidectomy is recommended before the age of 5 years.

In patients with moderate-risk *RET* mutations, the lifetime MTC risk is high, but typically shows later onset, and is less aggressive compared with the high-risk and highest-risk groups. The earliest ages at which MTC was reported in patients with exon 10 mutations (identified by family screening) were between 5 and 15 years, respectively, while lymph node metastases were reported at the ages between 10 and 39, respectively [38, 80]. Patients with moderate-risk mutations should have a thyroidectomy in childhood or young adulthood, or surgery may be postponed until an abnormal calcitonin level is observed.

There is general agreement that tumor stage and surgical management favourably influence the clinical course of the disease. Early detection and surgical treatment of MTC are likely to be curative: more than 95 % of patients whose disease was detected at an early stage remain disease-free (normal or undetectable calcitonin values) [75, 81, 82]. The excellent prognosis associated with identification of hereditary MTC at its earliest stage underscores the importance of early diagnosis by *RET* mutation analysis for patients at risk for familial MTC and systematic *RET* analysis in apparently sporadic MTC.

4.6 Targeted Therapy with Tyrosine Kinase Inhibitors

Germline *RET* mutations are present in virtually all patients with MEN2. Approximately half of the patients with sporadic MTC have somatic RET mutations, and 18–80 % of patients without somatic *RET* mutations have somatic RAS mutations. Also, vascular endothelial growth factor receptors are often overexpressed in MTC, both in tumor cells and in the supporting vascular endothelium [83]. The role of *RET* in thyroid cancer development make it an important target for therapeutic intervention in MTC. Many agents that target vascular endothelial growth factor receptors kinase also target RET kinase. In recent years several TKIs have been evaluated in clinical trials of patients with advanced MTC. Vandetanib and cabozantinib were approved for the treatment of patients with advanced progressive MTC, demonstrating significant improvement of progression-free survival compared with placebo [84, 85]. Patients with somatic *RET* 918 mutation seem to respond better to the treatment with an improvement of overall survival in the cabozantinib group. Inhibiting oncogenic RET activity using targeted tyrosine kinase inhibitors could be an effective strategy for treating aggressive MTC. Notably,

however, specific *RET* mutation V804 (V804M and V804L) alter the key 'gate-keeper' residue of the RET–ATP-binding site and have been shown to block vandetanib binding and subsequent RET inhibition [49], thereby making this TKI ineffective in patients with these sequence variants. Other, new and hopefully more potential agents with known activity against RET, RAS or other known genes to be mutated in MTC or other potential targets such as mTOR, ATF4 or other factors that interact with RET-mediated signalling pathways are being tested. It is possible that genetic testing of tumor tissue to predict response to a particular targeted agent, as is currently done for other cancer types such as the colon and lung, may come into practice in the future in MTC.

References

1. Raue F, Frank-Raue K. Update multiple endocrine neoplasia type 2. Fam Cancer. 2010;9(3): 449–57.
2. Wells Jr SA, Asa SL, Dralle H, Elisei R, Evans DB, Gagel RF, et al. Revised American Thyroid Association guidelines for the management of medullary thyroid carcinoma. Thyroid Off J Am Thyroid Assoc. 2015;25(6):567–610.
3. American Thyroid Association Guidelines Task F, Kloos RT, Eng C, Evans DB, Francis GL, Gagel RF, et al. Medullary thyroid cancer: management guidelines of the American Thyroid Association. Thyroid Off J Am Thyroid Assoc. 2009;19(6):565–612.
4. Albores-Saavedra JA, Krueger JE. C-cell hyperplasia and medullary thyroid microcarcinoma. Endocr Pathol. 2001;12(4):365–77.
5. Brandi ML, Gagel RF, Angeli A, Bilezikian JP, Beck-Peccoz P, Bordi C, et al. Guidelines for diagnosis and therapy of MEN type 1 and type 2. J Clin Endocrinol Metab. 2001;86(12): 5658–71.
6. Frank-Raue K, Rondot S, Schulze E, Raue F. Change in the spectrum of RET mutations diagnosed between 1994 and 2006. Clin Lab. 2007;53(5–6):273–82.
7. Milos IN, Frank-Raue K, Wohllk N, Maia AL, Pusiol E, Patocs A, et al. Age-related neoplastic risk profiles and penetrance estimations in multiple endocrine neoplasia type 2A caused by germ line RET Cys634Trp (TGC>TGG) mutation. Endocr Relat Cancer. 2008;15(4): 1035–41.
8. Eng C, Clayton D, Schuffenecker I, Lenoir G, Cote G, Gagel RF, et al. The relationship between specific RET proto-oncogene mutations and disease phenotype in multiple endocrine neoplasia type 2. International RET mutation consortium analysis. JAMA. 1996;276(19): 1575–9.
9. Frank-Raue K, Rondot S, Raue F. Molecular genetics and phenomics of RET mutations: impact on prognosis of MTC. Mol Cell Endocrinol. 2010;322(1–2):2–7.
10. Wells Jr SA, Pacini F, Robinson BG, Santoro M. Multiple endocrine neoplasia type 2 and familial medullary thyroid carcinoma: an update. J Clin Endocrinol Metab. 2013;98(8): 3149–64.
11. Choi SK, Yoon SR, Calabrese P, Arnheim N. Positive selection for new disease mutations in the human germline: evidence from the heritable cancer syndrome multiple endocrine neoplasia type 2B. PLoS Genet. 2012;8(2), e1002420.
12. Elisei R, Romei C, Cosci B, Agate L, Bottici V, Molinaro E, et al. RET genetic screening in patients with medullary thyroid cancer and their relatives: experience with 807 individuals at one center. J Clin Endocrinol Metab. 2007;92(12):4725–9.
13. Ishizaka Y, Itoh F, Tahira T, Ikeda I, Sugimura T, Tucker J, et al. Human ret proto-oncogene mapped to chromosome 10q11.2. Oncogene. 1989;4(12):1519–21.

14. Mulligan LM. RET revisited: expanding the oncogenic portfolio. Nat Rev Cancer. 2014;14(3): 173–86.
15. Liu X, Vega QC, Decker RA, Pandey A, Worby CA, Dixon JE. Oncogenic RET receptors display different autophosphorylation sites and substrate binding specificities. J Biol Chem. 1996;271(10):5309–12.
16. Takahashi M, Buma Y, Iwamoto T, Inaguma Y, Ikeda H, Hiai H. Cloning and expression of the ret proto-oncogene encoding a tyrosine kinase with two potential transmembrane domains. Oncogene. 1988;3(5):571–8.
17. Santoro M, Carlomagno F, Romano A, Bottaro DP, Dathan NA, Grieco M, et al. Activation of RET as a dominant transforming gene by germline mutations of MEN2A and MEN2B. Science. 1995;267(5196):381–3.
18. Kawamoto Y, Takeda K, Okuno Y, Yamakawa Y, Ito Y, Taguchi R, et al. Identification of RET autophosphorylation sites by mass spectrometry. J Biol Chem. 2004;279(14):14213–24.
19. Coulpier M, Anders J, Ibanez CF. Coordinated activation of autophosphorylation sites in the RET receptor tyrosine kinase: importance of tyrosine 1062 for GDNF mediated neuronal differentiation and survival. J Biol Chem. 2002;277(3):1991–9.
20. Jijiwa M, Kawai K, Fukihara J, Nakamura A, Hasegawa M, Suzuki C, et al. GDNF-mediated signaling via RET tyrosine 1062 is essential for maintenance of spermatogonial stem cells. Genes Cells. 2008;13(4):365–74.
21. Jain S, Encinas M, Johnson Jr EM, Milbrandt J. Critical and distinct roles for key RET tyrosine docking sites in renal development. Genes Dev. 2006;20(3):321–33.
22. Lundgren TK, Nakahata K, Fritz N, Rebellato P, Zhang S, Uhlen P. RET PLCgamma phosphotyrosine binding domain regulates Ca2+ signaling and neocortical neuronal migration. PLoS One. 2012;7(2), e31258.
23. Pachnis V, Mankoo B, Costantini F. Expression of the c-ret proto-oncogene during mouse embryogenesis. Development. 1993;119(4):1005–17.
24. Tsuzuki T, Takahashi M, Asai N, Iwashita T, Matsuyama M, Asai J. Spatial and temporal expression of the ret proto-oncogene product in embryonic, infant and adult rat tissues. Oncogene. 1995;10(1):191–8.
25. Airaksinen MS, Holm L, Hatinen T. Evolution of the GDNF family ligands and receptors. Brain Behav Evol. 2006;68(3):181–90.
26. Luesma MJ, Cantarero I, Alvarez-Dotu JM, Santander S, Junquera C. New insights into c-Ret signalling pathway in the enteric nervous system and its relationship with ALS. Biomed Res Int. 2014;2014:328348.
27. Amiel J, Sproat-Emison E, Garcia-Barcelo M, Lantieri F, Burzynski G, Borrego S, et al. Hirschsprung disease, associated syndromes and genetics: a review. J Med Genet. 2008;45(1): 1–14.
28. Gainor JF, Shaw AT. Novel targets in non-small cell lung cancer: ROS1 and RET fusions. Oncologist. 2013;18(7):865–75.
29. Morandi A, Martin LA, Gao Q, Pancholi S, Mackay A, Robertson D, et al. GDNF-RET signaling in ER-positive breast cancers is a key determinant of response and resistance to aromatase inhibitors. Cancer Res. 2013;73(12):3783–95.
30. Sawai H, Okada Y, Kazanjian K, Kim J, Hasan S, Hines OJ, et al. The G691S RET polymorphism increases glial cell line-derived neurotrophic factor-induced pancreatic cancer cell invasion by amplifying mitogen-activated protein kinase signaling. Cancer Res. 2005;65(24): 11536–44.
31. Mulligan LM, Kwok JB, Healey CS, Elsdon MJ, Eng C, Gardner E, et al. Germ-line mutations of the RET proto-oncogene in multiple endocrine neoplasia type 2A. Nature. 1993;363(6428): 458–60.
32. Donis-Keller H, Dou S, Chi D, Carlson KM, Toshima K, Lairmore TC, et al. Mutations in the RET proto-oncogene are associated with MEN 2A and FMTC. Hum Mol Genet. 1993;2(7): 851–6.

33. Margraf RL, Crockett DK, Krautscheid PM, Seamons R, Calderon FR, Wittwer CT, et al. Multiple endocrine neoplasia type 2 RET protooncogene database: repository of MEN2-associated RET sequence variation and reference for genotype/phenotype correlations. Hum Mutat. 2009;30(4):548–56.
34. Asai N, Iwashita T, Matsuyama M, Takahashi M. Mechanism of activation of the ret proto-oncogene by multiple endocrine neoplasia 2A mutations. Mol Cell Biol. 1995;15(3):1613–9.
35. Arighi E, Popsueva A, Degl'Innocenti D, Borrello MG, Carniti C, Perala NM, et al. Biological effects of the dual phenotypic Janus mutation of ret cosegregating with both multiple endocrine neoplasia type 2 and Hirschsprung's disease. Mol Endocrinol. 2004;18(4):1004–17.
36. Takahashi M, Iwashita T, Santoro M, Lyonnet S, Lenoir GM, Billaud M. Co-segregation of MEN2 and Hirschsprung's disease: the same mutation of RET with both gain and loss-of-function? Hum Mutat. 1999;13(4):331–6.
37. Lake JI, Heuckeroth RO. Enteric nervous system development: migration, differentiation, and disease. Am J Physiol Gastrointest Liver Physiol. 2013;305(1):G1–24.
38. Frank-Raue K, Rybicki LA, Erlic Z, Schweizer H, Winter A, Milos I, et al. Risk profiles and penetrance estimations in multiple endocrine neoplasia type 2A caused by germline RET mutations located in exon 10. Hum Mutat. 2011;32(1):51–8.
39. Jasim S, Ying AK, Waguespack SG, Rich TA, Grubbs EG, Jimenez C, et al. Multiple endocrine neoplasia type 2B with a RET proto-oncogene A883F mutation displays a more indolent form of medullary thyroid carcinoma compared with a RET M918T mutation. Thyroid Off J Am Thyroid Assoc. 2011;21(2):189–92.
40. Machens A, Dralle H. Familial prevalence and age of RET germline mutations: implications for screening. Clin Endocrinol (Oxf). 2008;69(1):81–7.
41. Erlic Z, Hoffmann MM, Sullivan M, Franke G, Peczkowska M, Harsch I, et al. Pathogenicity of DNA variants and double mutations in multiple endocrine neoplasia type 2 and von Hippel-Lindau syndrome. J Clin Endocrinol Metab. 2010;95(1):308–13.
42. Berndt I, Reuter M, Saller B, Frank-Raue K, Groth P, Grussendorf M, et al. A new hot spot for mutations in the ret protooncogene causing familial medullary thyroid carcinoma and multiple endocrine neoplasia type 2A. J Clin Endocrinol Metab. 1998;83(3):770–4.
43. Seri M, Yin L, Barone V, Bolino A, Celli I, Bocciardi R, et al. Frequency of RET mutations in long- and short-segment Hirschsprung disease. Hum Mutat. 1997;9(3):243–9.
44. Plaza Menacho I, Koster R, van der Sloot AM, Quax WJ, Osinga J, van der Sluis T, et al. RET-familial medullary thyroid carcinoma mutants Y791F and S891A activate a Src/JAK/STAT3 pathway, independent of glial cell line-derived neurotrophic factor. Cancer Res. 2005;65(5):1729–37.
45. Cosci B, Vivaldi A, Romei C, Gemignani F, Landi S, Ciampi R, et al. In silico and in vitro analysis of rare germline allelic variants of RET oncogene associated with medullary thyroid cancer. Endocr Relat Cancer. 2011;18(5):603–12.
46. Hyndman BD, Gujral TS, Krieger JR, Cockburn JG, Mulligan LM. Multiple functional effects of RET kinase domain sequence variants in Hirschsprung disease. Hum Mutat. 2013;34(1):132–42.
47. Mise N, Drosten M, Racek T, Tannapfel A, Putzer BM. Evaluation of potential mechanisms underlying genotype-phenotype correlations in multiple endocrine neoplasia type 2. Oncogene. 2006;25(50):6637–47.
48. Valente FO, da Silva MR D, Camacho CP, Kunii IS, Bastos AU, da Fonseca CC, et al. Comprehensive analysis of RET gene should be performed in patients with multiple endocrine neoplasia type 2 (MEN 2) syndrome and no apparent genotype-phenotype correlation: an appraisal of p.Y791F and p.C634Y RET mutations in five unrelated Brazilian families. J Endocrinol Invest. 2013;36(11):975–81.
49. Carlomagno F, Guida T, Anaganti S, Vecchio G, Fusco A, Ryan AJ, et al. Disease associated mutations at valine 804 in the RET receptor tyrosine kinase confer resistance to selective kinase inhibitors. Oncogene. 2004;23(36):6056–63.

50. Lantieri F, Caroli F, Ceccherini I, Griseri P. The involvement of the RET variant G691S in medullary thyroid carcinoma enlightened by a meta-analysis study. Int J Cancer J international du cancer. 2013;132(12):2808–19.
51. Narita N, Tanemura A, Murali R, Scolyer RA, Huang S, Arigami T, et al. Functional RET G691S polymorphism in cutaneous malignant melanoma. Oncogene. 2009;28(34):3058–68.
52. Barr J, Amato CM, Robinson SE, Kounalakis N, Robinson WA. The RET G691S polymorphism is a germline variant in desmoplastic malignant melanoma. Melanoma Res. 2012;22(1):92–5.
53. Robledo M, Gil L, Pollan M, Cebrian A, Ruiz S, Azanedo M, et al. Polymorphisms G691S/S904S of RET as genetic modifiers of MEN 2A. Cancer Res. 2003;63(8):1814–7.
54. Borrello MG, Aiello A, Peissel B, Rizzetti MG, Mondellini P, Degl'Innocenti D, et al. Functional characterization of the MTC-associated germline RET-K666E mutation: evidence of oncogenic potential enhanced by the G691S polymorphism. Endocr Relat Cancer. 2011;18(4):519–27.
55. Machens A, Frank-Raue K, Lorenz K, Rondot S, Raue F, Dralle H. Clinical relevance of RET variants G691S, L769L, S836S and S904S to sporadic medullary thyroid cancer. Clin Endocrinol (Oxf). 2012;76(5):691–7.
56. Schilling T, Burck J, Sinn HP, Clemens A, Otto HF, Hoppner W, et al. Prognostic value of codon 918 (ATG → ACG) RET proto-oncogene mutations in sporadic medullary thyroid carcinoma. Int J Cancer J international du cancer. 2001;95(1):62–6.
57. Marsh DJ, Learoyd DL, Andrew SD, Krishnan L, Pojer R, Richardson AL, et al. Somatic mutations in the RET proto-oncogene in sporadic medullary thyroid carcinoma. Clin Endocrinol (Oxf). 1996;44(3):249–57.
58. Romei C, Ugolini C, Cosci B, Torregrossa L, Vivaldi A, Ciampi R, et al. Low prevalence of the somatic M918T RET mutation in micro-medullary thyroid cancer. Thyroid Off J Am Thyroid Assoc. 2012;22(5):476–81.
59. Elisei R, Cosci B, Romei C, Bottici V, Renzini G, Molinaro E, et al. Prognostic significance of somatic RET oncogene mutations in sporadic medullary thyroid cancer: a 10-year follow-up study. J Clin Endocrinol Metab. 2008;93(3):682–7.
60. Moura MM, Cavaco BM, Pinto AE, Domingues R, Santos JR, Cid MO, et al. Correlation of RET somatic mutations with clinicopathological features in sporadic medullary thyroid carcinomas. Br J Cancer. 2009;100(11):1777–83.
61. Ciampi R, Mian C, Fugazzola L, Cosci B, Romei C, Barollo S, et al. Evidence of a low prevalence of RAS mutations in a large medullary thyroid cancer series. Thyroid Off J Am Thyroid Assoc. 2013;23(1):50–7.
62. Agrawal N, Jiao Y, Sausen M, Leary R, Bettegowda C, Roberts NJ, et al. Exomic sequencing of medullary thyroid cancer reveals dominant and mutually exclusive oncogenic mutations in RET and RAS. J Clin Endocrinol Metab. 2013;98(2):E364–9.
63. Niccoli-Sire P, Murat A, Rohmer V, Franc S, Chabrier G, Baldet L, et al. Familial medullary thyroid carcinoma with noncysteine ret mutations: phenotype-genotype relationship in a large series of patients. J Clin Endocrinol Metab. 2001;86(8):3746–53.
64. Imai T, Uchino S, Okamoto T, Suzuki S, Kosugi S, Kikumori T, et al. High penetrance of pheochromocytoma in multiple endocrine neoplasia 2 caused by germ line RET codon 634 mutation in Japanese patients. Eur J Endocrinol/Eur Federation Endocrine Soc. 2013;168(5):683–7.
65. Machens A, Brauckhoff M, Holzhausen HJ, Thanh PN, Lehnert H, Dralle H. Codon-specific development of pheochromocytoma in multiple endocrine neoplasia type 2. J Clin Endocrinol Metab. 2005;90(7):3999–4003.
66. Quayle FJ, Fialkowski EA, Benveniste R, Moley JF. Pheochromocytoma penetrance varies by RET mutation in MEN 2A. Surgery. 2007;142(6):800–5; discussion 5 e1.
67. Schuffenecker I, Virally-Monod M, Brohet R, Goldgar D, Conte-Devolx B, Leclerc L, et al. Risk and penetrance of primary hyperparathyroidism in multiple endocrine neoplasia type 2A families with mutations at codon 634 of the RET proto-oncogene. Groupe D'etude des Tumeurs a Calcitonine. J Clin Endocrinol Metab. 1998;83(2):487–91.

68. Raue F, Kraimps JL, Dralle H, Cougard P, Proye C, Frilling A, et al. Primary hyperparathy-roidism in multiple endocrine neoplasia type 2A. J Intern Med. 1995;238(4):369–73.
69. Mulligan LM, Ponder BA. Genetic basis of endocrine disease: multiple endocrine neoplasia type 2. J Clin Endocrinol Metab. 1995;80(7):1989–95.
70. Kouvaraki MA, Shapiro SE, Perrier ND, Cote GJ, Gagel RF, Hoff AO, et al. RET proto-oncogene: a review and update of genotype-phenotype correlations in hereditary medullary thyroid cancer and associated endocrine tumors. Thyroid Off J Am Thyroid Assoc. 2005;15(6):531–44.
71. Gagel RF, Levy ML, Donovan DT, Alford BR, Wheeler T, Tschen JA. Multiple endocrine neoplasia type 2a associated with cutaneous lichen amyloidosis. Ann Intern Med. 1989; 111(10):802–6.
72. Verga U, Fugazzola L, Cambiaghi S, Pritelli C, Alessi E, Cortelazzi D, et al. Frequent associa-tion between MEN 2A and cutaneous lichen amyloidosis. Clin Endocrinol (Oxf). 2003; 59(2):156–61.
73. Menko FH, van der Luijt RB, de Valk IA, Toorians AW, Sepers JM, van Diest PJ, et al. Atypical MEN type 2B associated with two germline RET mutations on the same allele not involving codon 918. J Clin Endocrinol Metab. 2002;87(1):393–7.
74. Cranston AN, Carniti C, Oakhill K, Radzio-Andzelm E, Stone EA, McCallion AS, et al. RET is constitutively activated by novel tandem mutations that alter the active site resulting in mul-tiple endocrine neoplasia type 2B. Cancer Res. 2006;66(20):10179–87.
75. Machens A, Niccoli-Sire P, Hoegel J, Frank-Raue K, van Vroonhoven TJ, Roeher HD, et al. Early malignant progression of hereditary medullary thyroid cancer. N Engl J Med. 2003;349(16):1517–25.
76. Zenaty D, Aigrain Y, Peuchmaur M, Philippe-Chomette P, Baumann C, Cornelis F, et al. Medullary thyroid carcinoma identified within the first year of life in children with hereditary multiple endocrine neoplasia type 2A (codon 634) and 2B. Eur J Endocrinol/Eur Federation Endocrine Soc. 2009;160(5):807–13.
77. Frank-Raue K, Machens A, Scheuba C, Niederle B, Dralle H, Raue F, et al. Difference in development of medullary thyroid carcinoma among carriers of RET mutations in codons 790 and 791. Clin Endocrinol (Oxf). 2008;69(2):259–63.
78. Machens A, Hauptmann S, Dralle H. Modification of multiple endocrine neoplasia 2A pheno-type by cell membrane proximity of RET mutations in exon 10. Endocr Relat Cancer. 2009;16(1):171–7.
79. Yip L, Cote GJ, Shapiro SE, Ayers GD, Herzog CE, Sellin RV, et al. Multiple endocrine neo-plasia type 2: evaluation of the genotype-phenotype relationship. Arch Surg. 2003;138(4):409–16; discussion 16.
80. Rich TA, Feng L, Busaidy N, Cote GJ, Gagel RF, Hu M, et al. Prevalence by age and predictors of medullary thyroid cancer in patients with lower risk germline RET proto-oncogene muta-tions. Thyroid Off J Am Thyroid Assoc. 2014;24(7):1096–106.
81. Skinner MA, Moley JA, Dilley WG, Owzar K, Debenedetti MK, Wells Jr SA. Prophylactic thy-roidectomy in multiple endocrine neoplasia type 2A. N Engl J Med. 2005;353(11):1105–13.
82. Frank-Raue K, Buhr H, Dralle H, Klar E, Senninger N, Weber T, et al. Long-term outcome in 46 gene carriers of hereditary medullary thyroid carcinoma after prophylactic thyroidectomy: impact of individual RET genotype. Eur J Endocrinol/Eur Federation Endocrine Soc. 2006; 155(2):229–36.
83. Capp C, Wajner SM, Siqueira DR, Brasil BA, Meurer L, Maia AL. Increased expression of vascular endothelial growth factor and its receptors, VEGFR-1 and VEGFR-2, in medullary thyroid carcinoma. Thyroid Off J Am Thyroid Assoc. 2010;20(8):863–71.
84. Wells Jr SA, Robinson BG, Gagel RF, Dralle H, Fagin JA, Santoro M, et al. Vandetanib in patients with locally advanced or metastatic medullary thyroid cancer: a randomized, double-blind phase III trial. J Clin Oncol Off J Am Soc Clin Oncol. 2012;30(2):134–41.
85. Elisei R, Schlumberger MJ, Muller SP, Schoffski P, Brose MS, Shah MH, et al. Cabozantinib in progressive medullary thyroid cancer. J Clin Oncol Off J Am Soc Clin Oncol. 2013; 31(29):3639–46.

Chapter 5
Molecular Genetics of Neuroblastoma

Zhihui Liu and Carol J. Thiele

Abbreviations

^{131}I-MIBG	^{131}I-metaiodobenzylguanidine
AKT	V-Akt murine thymoma viral oncogene homolog
ALCL	Anaplastic large cell lymphomas
ALK	Anaplastic lymphoma kinase
ALT	Alternative lengthening of telomeres
ARID1A	AT-rich interactive domain 1A (SWI-like)
ARID1B	AT-rich interactive domain 1B (SWI-like)
ATM	Ataxia telangiectasia mutated
ATRA	All-trans retinoic acid
ATRX	Alpha thalassemia/mental retardation syndrome X-linked
BARD1	BRCA1-associated RING domain 1
BARD1ß	BRCA1-associated RING domain 1, beta isoform
BCL2	B-cell CLL/lymphoma 2
BDNF	Brain-derived neurotrophic factor
BIM	BCL2-like 11
BMI1	B lymphoma Mo-MLV insertion region 1 homolog
BRAF	B-Raf proto-oncogene, serine/threonine kinase
CADM1	Cell adhesion molecule 1
CAMTA1	Calmodulin-binding transcription activator 1
CASC15	Cancer susceptibility candidate 15
CASC15-S	CASC15 short isoform

Z. Liu (✉) • C.J. Thiele (✉)
National Cancer Institute, 10 Center Dr. MSC-1105, Building 10, CRC, Room 1W-3940, Bethesda, MD 20892, USA
e-mail: liuzhihu@mail.nih.gov; thielec@mail.nih.gov

CASP8 Caspase 8	Apoptosis-related cysteine peptidase
CASZ1	Castor zinc finger 1
CCHS	Congenital central hypoventilation syndrome
CCND1	Cyclin D1
CDK	Cyclin-dependent kinase
CDK4	Cyclin-dependent kinase 4
CDK6	Cyclin-dependent kinase 6
CDKN1A	Cyclin-dependent kinase inhibitor 1A (P21, Cip1)
CDKN2A	Cyclin-dependent kinase inhibitor 2A
CHD5	Chromodomain helicase DNA-binding protein 5
CHK1	Checkpoint kinase 1
CLU	Clusterin
CRKL	V-Crk avian sarcoma virus CT10 oncogene homolog-like
CSC	Cancer stem cell
CSF3R	Colony-stimulating factor 3 receptor (granulocyte)
DKK1	Dickkopf WNT signaling pathway inhibitor 1
DOCK8	Dedicator of cytokinesis 8
E2F3	E2F transcription factor 3
EFS	Event-free survival
EZH2	Enhancer of zeste 2 polycomb repressive complex 2 subunit
FACT	Facilitates chromatin transcription
FAN1	FANCD2/FANCI-associated nuclease 1 2 3 4
FANCM	Fanconi anemia, complementation group M
FGFR1	Fibroblast growth factor receptor 1
G-CSF	Colony-stimulating factor
GATA	GATA-binding protein
GATA3	GATA-binding protein 3
GD2	Surface glycolipid molecule disialoganglioside
GWAS	Genome-wide association study
HDACs	Histone deacetylases
HRAS	Harvey rat sarcoma viral oncogene homolog
HSCR	Hirschsprung disease
INRGSS	International Neuroblastoma Risk Group Staging System
INSS	International Neuroblastoma Staging System
JAK	Janus kinase
KIF1B-beta	Kinesin family member 1B, beta isoform
KRAS	Kirsten RAS viral oncogene homolog
LIN28B	Lin-28 homolog B
LMO1	LIM domain only 1
lncRNA	Long noncoding RNA

LSD1	Lysine-specific demethylase
MAPK	Mitogen-activated protein kinase
MAX	MYC Associated factor X
miRNA	microRNA
MIZ1	Zinc finger and BTB domain containing 17
mTOR	Mechanistic target of rapamycin (serine/threonine kinase)
MYCN	V-Myc avian myelocytomatosis viral oncogene neuroblastoma derived homolog
NBAT-1	Neuroblastoma-associated transcript 1
NET	Norepinephrine transporter
NF1	Neurofibromin 1
NGFR	Nerve growth factor receptor
NPM1	Nucleophosmin
NRAS	Neuroblastoma RAS viral (V-Ras) oncogene homolog
NuRD	Nuclear remodeling and histone deacetylase
ODC1	Ornithine decarboxylase 1
OS	Overall survival
PCC/PGL	Pheochromocytomas and paragangliomas
PHOX2B	Paired-like homeobox 2B
PI3K	Phosphatidylinositol-4,5-bisphosphate 3-kinase
pRb	Retinoblastoma 1
PRC1	Polycomb repressive complex 1
PRC2	Polycomb repressive complex 2
PTPN11	Protein tyrosine phosphatase, non-receptor type 11
PTPN14	Protein tyrosine phosphatase, non-receptor type 14
PTPRD	Protein tyrosine phosphatase, receptor type D
RAP1	Ras-related Protein 1
RASSF1A	Ras association (RalGDS/AF-6) domain family member 1
ROS1	ROS proto-oncogene 1, receptor tyrosine kinase
SDHB	Succinate dehydrogenase complex, subunit B
SHH	Sonic hedgehog
SNP	Single nucleotide polymorphism
SP1	Specificity protein 1
STAT	Signal transducer and activator of transcription
STAT3	Signal transducer and activator of transcription 3
SWI/SNF	SWItch/Sucrose Non-fermentable, a nucleosome-remodeling complex
T-UCRs	Transcribed ultra-conserved regions
TERT	Telomerase reverse transcriptase
TGF-beta	Transforming growth factor, beta 1

TIAM1   T-cell lymphoma invasion and metastasis 1
TP53   Tumor protein P53
TSLC1   Tumor suppressor in lung cancer 1
WGS   Whole-genome sequencing
XLMR   X-linked mental retardation

5.1   Introduction

Neuroblastoma is a neural crest-derived tumor that occurs with an incidence of ten cases per million children, comprises more than 7 % of malignancies in patients younger than 15 years and accounts for 15 % of cancer-related deaths in childhood [1–5]. Neuroblastoma typically arises in the adrenal medullary tissue or paraspinal sympathetic ganglia and presents in the abdomen, chest, pelvis, or neck [1–3]. The high-risk clinical prognostic factors of age >18 months and advanced stage are associated with MYCN amplification, loss of heterozygosity of chromosome 1p and 11q, and unfavorable histopathology [1, 3]. Survival rates have significantly improved during the past three decades for neuroblastoma patients with low-stage disease. However, long-term survival rates of neuroblastoma patients with high-risk disease remain below 50 % [1, 2, 6, 7]. Familial neuroblastoma occurs at a very low frequency of 1–2 % of patients [1, 8]. Most patients have sporadic neuroblastoma, which suggests that these tumors arise from *de novo* somatic mutations and are not inherited. Next-generation sequencing and genome-wide association studies of primary tumor samples from neuroblastoma patients have led to the discovery of novel germline mutations, multiple somatically acquired genetic alterations, and single nucleotide polymorphisms in the past decade [4, 9–16]. Figure 5.1 shows the landscape of the genetic variations of a representative cohort of 240 high-risk neuroblastoma patients and includes the commonly observed chromosomal and genetic alterations based on the whole-exome, genome, and transcriptome sequencing [9]. In this chapter, we will review these genetic alterations in neuroblastoma and highlight potential targeted therapeutic opportunities.

5.2   Chromosomal Abnormalities

Low-stage neuroblastoma is marked by numeric changes of chromosomal copy number, whereas high-stage neuroblastoma is marked by segmental chromosomal aberrations (gains or losses of chromosomal fragments) that result in hemizygous deletion of the chromosome arms 1p and 11q and gain of chromosome 17q. These tumor-associated segmental chromosome aberrations, *MYCN* amplification and DNA diploidy, are associated with poor prognosis for these neuroblastoma patients [1, 3, 17, 18]. Moreover, recent next-generation sequencing of
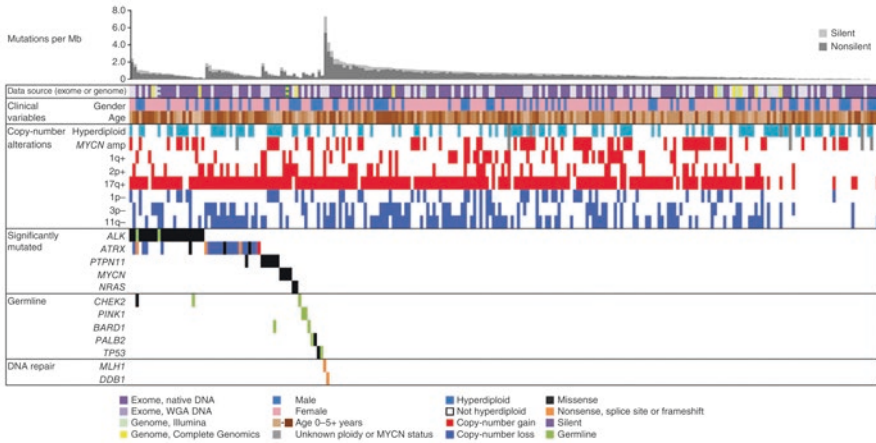
Fig. 5.1 Landscape of genetic variation in high-risk neuroblastoma (Nature Genetics 2013). *MYCN* amplification, deletion of chromosomes 1p, 3p, and 11q, gain of chromosomes 1q, 2p, and 17q, as well as genetic alterations of *ALK*, *ATRX*, and other genes are depicted in the landscape [9] This figure is from a paper written by Trevor J Pugh et al. entitled "The genetic landscape of high-risk neuroblastoma," which was published in Nature Genetics in 2013

neuroblastoma has identified a new chromosome alteration phenomenon termed chromothripsis [12].

5.2.1 **MYCN** *Amplification*

MYCN oncogene amplification on chromosome 2p24 is associated with advanced stage disease and poor outcome and occurs in approximately 20 % of primary neuroblastoma tumors and approximately 40 % of high-risk neuroblastomas [3, 17, 19–21]. *MYCN* amplification has been used for treatment stratification of neuroblastoma patients since the late 1980s [1]. In addition to the chromosome 2p locus, *MYCN* amplification also maps to the cytogenetic manifestations of gene amplification: the double-minute chromatin bodies (DMs) or homogenously staining region (HSRs). DMs may accumulate by uneven segregation during mitosis, and HSR may arise by integration of the amplified DNA into different chromosomal loci [22, 23]. Neuroblastoma tumors with *MYCN* amplification usually express *MYCN* at higher levels than tumors without amplification. It has been reported that *MYCN* expression is inversely correlated with survival probability [24], but this correlation may only be limited to stage 2, 3, and 4 neuroblastomas, the latter which contains the high-risk group of patients [25, 26]. *MYCN* genomic amplification with overexpression serves as prognostic markers for survival. Stage 4 patients with *MYCN* amplification but without overexpression had no increased likelihood of death, whereas cases with *MYCN* overexpression but no genomic amplification showed low survival [27]. Recent transcriptome analyses have identified a *MYC/MYCN* gene signature that identifies patients with a poorer prognosis even in the absence of *MYCN*

amplification [28]. *MYCN* was first identified as a *bona fide* oncogene with the development of the tyrosine hydroxylase-*MYCN* (*TH-MYCN*) transgenic mouse model in which mice transgenic for tyrosine hydroxylase promoter-driven MYCN expression develop tumors similar to human neuroblastomas [29]. This was supported by studies in which knockdown of *MYCN* in neuroblastoma cell lines suppressed cell proliferation [30, 31]. The *MYCN* gene encodes N-Myc, a helix-loop-helix/leucine zipper transcription factor that regulates genes involved in cell cycle progression, apoptosis, and stemness. Genes regulated by *MYCN* include the self-renewal protein *BMI1*, anaplastic lymphoma kinase (*ALK*), tumor suppressor p53, antiproliferative protein Dickkopf-1, histone chaperone *FACT* (facilitates chromatin transcription), and myriad polyamine enzyme *ODC1* [32–37]. N-Myc dimerizes with MAX to activate gene transcription and forms a repression complex with transcription factor SP1 and MIZ1 to repress gene transcription [38, 39]. N-Myc has also been reported to associate with EZH2, a subunit of polycomb repressor complex 2 to repress tumor suppressor gene clusterin, suggesting a role for N-Myc in epigenetic regulation [40, 41]. Moreover, although not formally proven, it is possible that *MYCN*, like *MYC*, may function as a universal amplifier of gene transcription [42, 43]. Knockdown of *MYCN* decreases cell proliferation, and overexpression of *MYCN* suppresses neuroblastoma cell differentiation and promotes proliferation and cell cycle progression presumably via regulation of its target genes. However, the critical molecular mechanisms and signaling pathways by which *MYCN* stimulates tumorigenesis remain to be critically investigated.

5.2.2 TERT *Rearrangement*

Whole-genome sequencing (WGS) of 56 neuroblastomas identified recurrent genomic rearrangements proximal to the telomerase reverse transcriptase gene (*TERT*) locus (chromosome 5p15.33). These events occurred predominantly in high-risk neuroblastoma (12 of 39 high-risk neuroblastomas) in a mutually exclusive fashion with *MYCN* amplifications and *ATRX* mutations [44]. *TERT* rearrangements were validated in 217 additional cases, and *TERT* rearrangements define a subgroup of high-risk neuroblastomas with poor outcome [44]. In a similar whole-genome sequencing study, structural rearrangements of *TERT* were identified in 17 of 75 high-stage neuroblastomas (23 %). Consistent with previous studies, *TERT* rearrangements, *ATRX* deletions, and *MYCN* amplifications were detected in high-risk neuroblastomas, and they were mutually exclusive and associated with poor prognosis [45]. From these studies, *TERT* rearrangements were identified to be the second most frequent genetic alteration after *MYCN* amplification [44, 45]. Induced transcriptional upregulation of *TERT* is caused by the acquisition of a super enhancer or strong enhancer by diverse structural genomic rearrangements [44, 45]. In normal cells, telomeres shorten with every cell cycle to restrict lifespan. However, in cancer cells, the telomeres can be preserved through alternative lengthening of telomeres (ALT) or activation of *TERT. TERT* can be activated by mutations of the

promoter region or upstream rearrangements [46, 47]. In neuroblastoma, no mutations have been identified in the *TERT* promoter region (10). Instead, structural rearrangements at the *TERT* locus lead to activation of its transcription [44, 45]. Furthermore, in *MYCN* amplified neuroblastomas without *TERT* rearrangements, *MYCN* functions as a transcription activator of *TERT* leading to elevated levels of *TERT* mRNA although not to the extent seen in tumors with *TERT* rearrangements [44, 48]. Importantly, the majority of the high-risk neuroblastomas are affected by either *MYCN* amplification, *TERT* activation, or *ATRX* mutations, all of which lead to telomere lengthening and contribute to the immortality of this subtype of neuroblastomas [44, 45].

5.2.3 Alterations of Chromosome

Even though *MYCN* status is a prognostic biomarker in neuroblastoma, segmental chromosomal aberrations (gains or losses of chromosomal fragments) can also be used to assess neuroblastoma aggressiveness. Loss of chromosomes 1p, 3p, 4p, 14q, 16p, and 19q or gain of chromosomes 1q, 2p, 7q, 9p, 11p, 12q, and 17q are observed in neuroblastoma [3, 49, 50]. Among them, deletion of chromosomes 1p and 11q and gain of 17q are the most frequently occurring chromosomal alterations in high-stage disease [1, 17, 18, 51, 52]. A study from the international neuroblastoma risk group (INRG) analyzing a cohort of 8,800 children diagnosed with neuroblastoma shows that deletions of 1p or 11q and gain of 17q are significantly associated with poor outcome of patients [17].

5.2.3.1 Alterations of Chromosome 1p

Loss of heterozygosity (LOH) at chromosome 1p occurs in 30–35 % of primary neuroblastomas. In addition, 1p LOH is frequently found in unfavorable neuroblastoma and is associated with *MYCN* amplification [3, 17, 53, 54]. LOH at chromosome band 1p36 is the smallest region of overlap, and 1p36 LOH is independently associated with a poor outcome in patients with neuroblastoma [55]. The frequent LOH on chromosome 1p raises the possibility that this region contains tumor suppressor genes and the loss of such tumor suppressor genes contributes to tumorigenesis. Consistent with this hypothesis, reintroduction of chromosome 1p into neuroblastoma induces differentiation and cell death [56]. Recent studies have shown that multiple genes on chromosome 1p suppress neuroblastoma cell growth; these candidate neuroblastoma tumor suppressor genes include *CHD5*, *CASZ1*, *CAMTA1*, *KIF1Bβ*, and microRNA-34a [57]. *CHD5* is the commonly deleted tumor suppressor genes in neuroblastoma. It is a member of the chromodomain superfamily, which is a key component of nucleosome-remodeling complexes (NuRD) [58]. Expression of *CHD5* is silenced through both 1pLOH and promoter methylation [59]. High *CHD5* expression is strongly

associated with favorable event-free and overall survival even after correction for *MYCN* amplification and 1p deletion [60]. Forced expression of *CHD5* in neuroblastoma cells with low endogenous *CHD5* suppresses neuroblastoma growth in mouse xenografts [60]. *CASZ1* encodes a zinc finger transcriptional factor, and low expression of *CASZ1* is associated with poor prognosis of neuroblastoma [61, 62]. Biallelic inactivation of *CASZ1* by both 1pLOH and EZH2-mediated epigenetic silencing leads to its decreased expression in neuroblastomas of poor outcome [63]. CASZ1 transcriptional activity is mediated by recruitment of NuRD complexes, and the recent identification of binding between CASZ1 and CHD5 indicates a potential interaction between these two neuroblastoma tumor suppressors [64]. Restoration of *CASZ1* in neuroblastoma cells induces cell differentiation, inhibits cell proliferation and migration, and suppresses neuroblastoma xenograft growth [61]. The expression of *CAMTA1* (calmodulin-binding transcription activator 1) is an independent predictor of poor outcome of neuroblastoma and inhibits neuroblastoma cell growth and activates differentiation program [65]. *KIF1Bβ* is a member of the kinesin superfamily proteins, and hemizygous deletion of *KIF1Bβ* in primary neuroblastoma is correlated with advanced stages and *MYCN* amplification [66]. Forced expression of *KIF1Bβ* in neuroblastoma cells results in apoptosis [66, 67]. Micro RNA *miR-34a* is underexpressed in unfavorable neuroblastomas and reintroduction of miR-34a in neuroblastoma cell lines with low endogenous *miR-34a* suppressed cell proliferation [68, 69]. Until now, no recurrent nonsynonymous mutations have been identified in these candidate 1p36 tumor suppressor genes. Moreover, the link between the loss of any of these candidate 1p tumor suppressors and the development of neuroblastoma tumors in mice has not been reported. It is possible that the haploinsufficiency of multiple genes at the 1p locus is required for neuroblastoma tumorigenesis.

5.2.3.2 Alterations of Chromosome 11q

Allelic loss of chromosome 11q occurs in approximately 33–43 % of neuroblastomas patients and is associated with poor prognosis. Importantly, deletion of 11q is inversely associated with 1p deletion and *MYCN* amplification (Fig. 5.1), which makes it a potential biomarker for the aggressive tumors in patients without *MYCN* amplification [4, 55, 70, 71]. Within the chromosome bands 11q22-q23, the region that is most frequently lost in neuroblastoma [70–72], there are several candidate tumor suppressor genes including *ATM*, *TSLC1*, and *CADM1*. *ATM* is the gene mutated in ataxia telangiectasia (AT), and knockdown of *ATM* in neuroblastoma cell lines with intact 11q promotes neuroblastoma progression in soft agar assays and in subcutaneous xenografts in nude mice [73]; *TSLC1*, a tumor suppressor in lung cancer 1, suppresses neuroblastoma cell proliferation [74]; *CADM1*, cell adhesion molecule 1, when overexpressed in neuroblastoma cells, results in a significant reduction in colony formation on soft agar [75, 76]. *ATM* is involved in the DNA repair pathway, and alteration in its activity is consistent with the finding that

high-risk neuroblastoma tumors with the 11q loss display a chromosome instability phenotype [73]. Like 1p deletion, no recurrent inactivating mutations have been found in these genes at 11q; thus, whether these genes are *bona fide* tumor suppressor genes need to be further investigated.

5.2.3.3   Alterations of Chromosome 17q

Gain of distal chromosome arm 17q (17q21-qter) is the most common aberration found in neuroblastomas and occurs in 50–70 % of tumors. Gain of 17q is frequently associated with 1p LOH, 11q LOH, *MYCN* amplification, older age, and advanced stage [77–79]. Interestingly, in the neuroblastoma tumors that developed from *MYCN* transgenic mice, the murine equivalent of chromosome 17 is the most commonly gained chromosome [29]. Consistently, overexpression of MYCN in neuroblastoma cell lines with a single copy of *MYCN* and intact 17q leads to an unbalanced gain of 17q [29, 80]. These results suggest a functional relationship between *MYCN* overexpression and the gain of 17q in neuroblastoma. Although the mechanism by which 17q gain results in a more aggressive malignancy is not clear, the gain of 17q does lead to increased expression of the 17q resident anti-apoptotic protein BIRC5/ survivin [81, 82], which might contribute to neuroblastoma progression.

5.2.4   Chromothripsis

At the level of genome structure, a local shredding of chromosomes with subsequent random reassembly of the fragments (localized massive genome rearrangements) has been found in some types of cancers. This phenomenon has been termed chromothripsis [83, 84]. Whole-genome sequencing (WGS) in 87 untreated primary neuroblastoma tumors of all stages identified a number of genetic alterations, and an analysis of the frequency of the structural variations per chromosome showed that chromothripsis occurred in ten tumors [12]. Chromothripsis was not found in low-stage tumors but in 18 % of the stage 3 and 4 neuroblastoma, although the prognostic impact of chromothripsis was not independent of age and stage in a multivariate analysis. Chromothripsis was associated with *MYCN* amplification, 1p LOH, and a poor prognosis. In one tumor from this study, chromothripsis resulted in *MYC* (*c-Myc*) amplification and high expression [12]. In another WGS study, chromothripsis occurred at the *TERT* locus in 5 of 75 high-stage neuroblastomas, leading to structural rearrangements and high expression of *TERT* gene [45]. Chromothripsis-induced structural aberrations frequently affected oncogene expression, which might contribute to neuroblastoma tumorigenesis. The finding that an inactivating deletion in *FANCM* occurred in one chromothripsis tumor and missense mutation in *FAN1* in another tumor suggests that inactivating events in the fanconi anemia signal transduction and DNA repair pathway in neuroblastoma may be associated with chromothripsis [12].

5.3   Genetic Mutations

Cancer is a genetic disease, and cancer develops when genetic mutations occur in genes that affect cell proliferation and differentiation. Familial neuroblastoma, in which mutations in neuroblastoma-associated genes are inherited, is observed in 1–2 % of patients [85]. In contrast, sporadic neuroblastoma occurs in most patients and is typified by nonheritable somatic mutations. Recent studies using next-generation sequencing techniques discovered germline mutations and recurrent somatic mutations in primary neuroblastoma, but these cases are rare. Almost 90 % of familial neuroblastomas contain *ALK* mutations with the remaining predominantly having mutations in *PHOX2B*. In sporadic neuroblastomas, *ALK*, *ATRX*, *PTPN11*, *MYCN*, *NRAS*, *ARID1A*, and *ARID1B* are the major genes in which somatic mutations occur, but their frequency is low, from 1.7 to 11 % [9–12]. Other rare cases having recurrent somatic mutations in primary neuroblastoma include protein tyrosine phosphatase, receptor type D (*PTPRD*), odd Oz/ten-m homolog 3 (*ODZ3*) and T-cell lymphoma invasion and metastasis 1 (*TIAM1*) [9, 10, 12]. This is consistent with the observation that pediatric malignancies have a lower frequency of somatic mutation than most adult cancers [86].

5.3.1   Germline Mutations

5.3.1.1   *ALK*

Next-generation sequencing of primary neuroblastoma samples elucidated activating mutations in anaplastic lymphoma kinase (*ALK*) in most hereditary and 7–8 % of sporadic neuroblastomas [87–91]. The *ALK* gene maps chromosome 2p23 and encodes a receptor tyrosine kinase (RTK). *ALK* is expressed in the central and peripheral nervous system, and in drosophila, *ALK* plays a critical role during the nervous system development [92–94]. The oncogenic activity of *ALK* was identified when it was found to be fused to nucleophosmin (NPM1) through a 2;5 chromosome translocation in most anaplastic large cell lymphomas (ALCL). Thus far, over 20 different genes have been described as being translocated with *ALK*, and *ALK* fusions have been found in diffuse large B-cell lymphomas, inflammatory myofibroblastic tumors, esophageal squamous cell carcinomas, and non-small-cell lung carcinomas [93, 95, 96]. *ALK* and *ALK* fusion proteins regulate cell survival, proliferation, and differentiation through the activation of *JAK-STAT*, *PI3K-AKT*, *mTOR*, sonic hedgehog (*SHH*), or *CRKL-C3G-RAP1 GTPase* pathways in different cell types [96, 97]. Unlike other cancers, no *ALK* fusions were observed in neuroblastoma; instead, point mutations and amplifications leading to aberrant *ALK* overexpression and activation were found in neuroblastoma [98]. Germline mutations discovered in neuroblastoma include R1275Q, R1192P, G1128A, T1151M, T1087I [87–90], and, in rare cases, the more potent F1245V and F1174V *ALK* mutations

[99]. The R1275Q, R1245V, R1192P, F1174V, and T1151M mutations fall within the kinase activation domain. The G1128A mutation occurs at the third glycine of the glycine loop, and identical mutations of this glycine residue to alanine in BRAF have been shown to increase kinase activity [87, 89, 99]. Mutant *ALK* R1275Q occurs in many neuroblastoma cell lines, and cells that express mutant ALK R1275Q but not wild-type ALK exhibit strong kinase activity indicating constitutive activation [88]. Consistently, knockdown of *ALK* in neuroblastoma cells that express mutant *ALK* R1275Q resulted in a significant decrease in cell proliferation and colony formation on plastic [88], supporting an oncogenic role of ALK mutants in neuroblastoma. The incidence of *ALK* mutations is about 8 % in neuroblastoma, and they occur in all stages although the frequency of *ALK* alterations is higher in high-risk neuroblastoma, with 10 % containing point mutations and 4 % containing *ALK* amplification [87–91]. Somatic mutations of *ALK* will be described later in this review.

5.3.1.2 *PHOX2B*

A majority of patients with congenital malformation of neural crest-derived cells such as Hirschsprung disease (HSCR) and congenital central hypoventilation syndrome (CCHS) harbor paired-like homeobox 2b (*PHOX2B*) mutations, and neuroblastoma occurs in a subset of these patients [100, 101], suggesting *PHOX2B* may be associated with neuroblastoma tumorigenesis. DNA sequence analysis showed that *PHOX2B* germline mutations occur in families with neuroblastoma; thus, *PHOX2B* can be considered a *bona fide* neuroblastoma predisposition gene when mutated in the germline [102, 103]. The *PHOX2B* gene maps to chromosome 4p12 and encodes a homeobox transcription factor. *PHOX2B* directly regulates ALK transcription in neuroblastoma, which provides a link between these two mutated pathways in familial neuroblastoma [104]. *PHOX2B* is the master regulatory gene for both central and peripheral automatic nervous system development in mice [105]. In zebrafish, loss of *PHOX2B* impairs sympathetic neuronal differentiation [106] and suggests that perturbations in *PHOX2B*-regulated differentiation may contribute to neuroblastoma tumorigenesis. Heterozygous germline mutations that have been described in neuroblastoma include R100L, R141G, and frameshift mutations. *PHOX2B* R100 amino acid has been shown to bind DNA of target genes, and *PHOX2B* R100L may lose DNA-binding ability but retain the ability to dimerize with the wild-type *PHOX2B* or other cofactors. Thus, *PHOX2B* mutations may result in loss of function or dominant-negative activities [102, 103]. Consistently, forced overexpression of wild-type *PHOX2B* but not mutant *PHOX2B* suppresses neuroblastoma cell proliferation and synergizes with all-trans retinoic acid to promote differentiation [107]. Introduction of a patient-derived *PHOX2B* mutation into the mouse phox2b locus recapitulates the clinical features of CCHS but did not give rise to neuroblastoma [108], suggesting that *PHOX2B* alone might not be sufficient to drive neuroblastoma tumorigenesis. Unlike *ALK* mutations, *PHOX2B* mutations only account for approximately 6.4 % of familial neuroblastoma [107]. Some other

genes (TP53, *EZH2*, *SDHB*, *PTPN11*, *HRAS*, and *NF1*) may be considered candidate neuroblastoma predisposition genes [4], but these cases are very rare. Until now, the cause of the remaining familial neuroblastomas that do not harbor *ALK* or *PHOX2B* mutations remains unresolved.

5.3.2 Recurrent Somatic Mutations

5.3.2.1 ALK

As described above, activating mutations in *ALK* occurred in 7–8 % of sporadic neuroblastomas [87–91]. Comprehensive analyses of *ALK* mutations across 1,596 diagnostic neuroblastoma samples showed that over 10 different residues are mutated in *ALK* and most mutations occurred within the kinase domain, and the most commonly mutated residues accounted for 85 % of mutations are F1174 (30 %), R1245 (12 %), and R1275 (43 %) [91]. Across the whole cohort, the presence of *ALK* mutation correlated with reduced event-free survival (EFS) and overall survival (OS) [91]. Oncogenic transformation occurred when NIH3T3 cells were transfected with certain *ALK* mutation constructs. In some neuroblastoma cell lines with certain *ALK* mutations, the kinase was constitutively activated, and knockdown of *ALK* mutants or treatment with *ALK* inhibitor crizotinib suppressed cell proliferation [87–91], which indicates that *ALK* is an oncogenic driver in neuroblastoma. More convincingly, the targeted expression of the most aggressive *ALK* mutant F1174L alone induces neuroblastoma in transgenic mice [109]. Moreover, coexpression of *ALK* mutant F1174L and *MYCN* accelerated tumor onset and increased tumor penetrance compared with *MYCN* alone suggests a cooperative effect between these two oncogenes [109–112]. Interestingly, *MYCN* directly regulates *ALK* transcription, and *ALK* stimulates the kinase ERK5 to promote the expression of MYCN in neuroblastoma [34, 113], which provides a connection between these two oncogenes in neuroblastoma. Although F1174L is the most frequent and aggressive mutation in sporadic neuroblastoma, it has been rarely observed in familial neuroblastoma suggesting that this mutation may not be tolerated in the germline.

5.3.2.2 ATRX

A WGS study of 40 neuroblastoma tumors and subsequent validation sequencing of 60 neuroblastoma tumors showed that mutations in alpha thalassemia/mental retardation syndrome X-linked gene (*ATRX*) occurred in about 10 % of neuroblastoma and are enriched in older patients [9, 11, 12]. Based on age, *ATRX* mutations were found in 44 % of tumors from patients in the adolescent and young adult group (≥12 years), in 17 % of tumors from children (18 months-<12 years), and 0 % of tumors from infants (0−<18 months) [11]. *ATRX* maps to the X chromosome and encodes a *SWI/SNF* chromatin-remodeling helicase, which plays a role in

chromatin remodeling, nucleosome assembly, and telomere maintenance [11, 114]. *ATRX* mutations are associated with X-linked mental retardation (XLMR) and alpha thalassemia. *ATRX* mutations have also been identified in pheochromocytomas and paragangliomas (PCC/PGL) and pancreatic neuroendocrine tumors [115, 116]. *ATRX* mutations include missense, nonsense, frameshift, or in-frame deletion, and they are mutually exclusive of *MYCN* amplification [11]. Neuroblastoma samples with *ATRX* mutations had complete or mosaic loss of the nuclear *ATRX* protein and show longer telomeres [11]. Most of the neuroblastomas with *ATRX* mutations had evidence of alternative lengthening of telomere (ALT) pathway activation, and this was consistent with findings that loss of *ATRX/DAXX* is associated with ALT in different cell lines [11, 117]. *ATRX* mutations were associated with age at diagnosis in children and young adults with stage 4 neuroblastoma. A larger study is required to determine the prognostic impact of *ATRX* mutations on survival [11]. How *ATRX* mutations lead to neuroblastoma progression remains unclear.

5.3.2.3 *ARID1A* and *ARID1B*

Next-generation sequencing, genome-wide rearrangement analyses, and targeted analysis of specific genomic loci of 71 neuroblastoma patients identified mutations in chromatin-remodeling genes AT-rich interaction domain 1A (*ARID1A*) and AT-rich interaction domain 1B (*ARID1B*) in eight cases (11 %). The mutations include missense, nonsense, frameshift, or in-frame deletion, and the *ARID1A* and *ARID1B* mutations were associated with decreased survival of neuroblastoma patients [10]. Both *ARID1A* and *ARID1B* are subunits of the *SWI/SNF* transcriptional complex [118, 119]. Mutations of *ARID1A* and *ARID1B* have also been identified in other types of cancer such as ovarian, endometrial, hepatocellular, breast, and microsatellite unstable colorectal cancers [120–125]. *ARID1A* and *ARID1B* have emerged as tumor suppressor genes [119, 124, 126]; thus, mutations of these genes may drive neuroblastoma tumorigenesis. Little is known as to how *ARID1A* and *ARID1B* mutations affect neuroblastoma tumorigenesis.

5.3.2.4 *RAS*

In primary neuroblastomas, mutations in neuroblastoma *RAS* viral oncogene homolog (*NRAS*) or Harvey *RAS* viral oncogene homolog (*HRAS*) are rare [9, 10], although mutations in the *RAS-MAPK* pathway occur more frequently in relapsed neuroblastoma [127]. WGS studies identified clonally enriched somatic mutations predicted to activate the *RAS-MAPK* pathway in 78 % relapsed neuroblastoma tumors (18 out of 23 patients). Activating mutations in the *RAS-MAPK* pathway were also identified in 60 % of tested neuroblastoma cell lines of which the majority have been established from relapsed neuroblastoma patients [127]. Mutated genes associated with the RAS-MAPK pathway include *ALK*, *NRAS*, *HRAS*, Kirsten *RAS* viral oncogene homolog (*KRAS*), *B-Raf* proto-oncogene, serine/threonine kinase

(*BRAF*), protein tyrosine phosphatase non-receptor type 11 (*PTPN11*), fibroblast growth factor receptor 1 (*FGFR1*), and neurofibromin 1 (*NF1*) [127]. Another study also discovered new recurrent mutations in *HRAS* and *KRAS*, as well as *CHD5*, *DOCK8*, and *PTPN14* in relapsed neuroblastomas [128]. Consistently, the constitutive activation of *RAS-MAPK* pathway was observed in neuroblastoma cell lines with *MAPK* pathway mutations.

5.4 Single Nucleotide Polymorphisms

The paucity of recurrent somatic mutations in neuroblastoma suggests that a complex genetic phenotype might contribute to the penetrance of neuroblastoma in the population. Genome-wide association study (GWAS) of DNA samples from neuroblastoma patients using high-density single nucleotide polymorphism (SNP)-based microarray has identified SNPs associated with different clinical features of neuroblastoma; the identified genes with SNPs include *BARD1*, *CASC15*, *DDX4*, *DUSP12*, *HACE1*, *HSD17B12*, *IL31RA*, *LIN28B*, *LMO1*, *NBPF23*, and *NEFL* [16, 129–138]. Among these genes, the SNPs of *DDX4*, *DUSP12*, *HSD17B12*, and *IL31RA* are associated with low-risk neuroblastoma, whereas the SNPs of *BARD1*, *CASC15*, *HACE1*, *LIN28B*, and *LMO1* are associated with aggressive, high-risk disease [4, 15, 16, 137]. Moreover, *BARD1*, *LIN28B*, and *LMO1* have been shown to be important predisposition genes and oncogenic drivers in neuroblastoma [16, 129, 130, 132–134].

5.4.1 **BARD1**

GWAS of 397 high-risk European-American neuroblastoma cases and 2,043 controls identified significant association of six SNPs at 2q35 within the *BRCA1*-associated RING domain 1 (*BARD1*) locus, which were further confirmed in a second series of 189 high-risk neuroblastoma cases and 1,178 controls [16]. Common *BARD1* SNPs affect risk of neuroblastoma in African Americans based on the GWAS studies focused on 390 African-American neuroblastoma patients compared with 2,500 ethnically matched controls [139]. Similar association of *BARD1* SNPs was observed in an Italian population (370 cases and 809 controls) [137]. *BARD1* is an important regulator and interactor of the tumor suppressor *BRCA1*, yet it can also function by itself as a tumor suppressor [140]. In neuroblastoma, the disease-associated variations correlate with increased expression of the *BARD1β*, which is an oncogenically activated isoform of *BARD1*. Overexpression of *BARD1β* in NIH3T3 fibroblasts induces neoplastic transformation, and *BARD1β* is required for neuroblastoma cell survival *in vitro* through interacting and stabilizing Aurora kinase B [134]. These results indicate SNPs of *BARD1* are a major genetic contributor to neuroblastoma risk, and *BARD1β* is an oncogenic driver of high-risk neuroblastoma.

5.4.2 **LIN28b**

GWAS of 2,817 neuroblastoma cases and 7,473 controls identified a significant association of SNP (rs17065417) within protein lin-28 homolog B (*LIN28B*) locus [129]. *LIN28B* is an RNA-binding protein that represses the *let-7* family of microRNAs, and it is highly expressed and functions as an oncogene in many types of cancers [141–143]. *LIN28B* expression is higher, and *let-7* microRNA expression is lower in neuroblastoma cell lines homozygous for the rs17085417 risk allele compared to heterozygous cell lines [129]. High *LIN28B* expression is associated with worse overall survival in primary neuroblastoma tumors and is an independent risk factor for adverse outcome in neuroblastoma [129, 131]. Knockdown of *LIN28B* in neuroblastoma cells leads to growth inhibition [129]. Importantly, in a mouse model expression of *LIN28B* in the sympathoadrenal lineage results in the development of neuroblastoma [131]. Suppression of *let-7* microRNAs by *LIN28B* resulted in elevated *MYCN* expression in neuroblastoma cell lines, and similarly in the neuroblastoma developed from the *LIN2B* transgenic mouse, *let-7* microRNA level is low and *MYCN* level is high [131]. Vice versa, *MYCN* upregulates *LIN28B* expression either directly through binding *LIN28B* promoter or indirectly through *miR-26a-5p* and *miR-26b-5p* [144]. The cross-regulation between *LIN28B* and *MYCN* provides a connection between these two oncogenes in neuroblastoma. *LIN28B* regulates expression of the oncogene *RAN* and cooperates with *RAN* to activate Aurora kinase A to drive neuroblastoma oncogenesis [130], identifying another pathway by which high levels of *LIN28B* expression drive neuroblastoma tumorigenesis.

5.4.3 **LMO1**

GWAS on 2,251 neuroblastoma patients and 6,097 control subjects of European-Americans identified a significant association within LIM domain only 1 (*LMO1*) at 11p15.4 (rs110419), and the signal was enriched in the subset of most aggressive neuroblastoma patients [133]. Similarly, a significant association within *LMO1* (rs204926) was identified in a Chinese population [145]. Moreover, genome-wide DNA copy number alterations in 701 primary tumors identified 12.4 % with aberrations at the *LMO1* locus, and this event was associated with more advanced disease [133]. *LMO1* encodes a cysteine-rich transcriptional regulator, which has been implicated in cancer [146–148]. *LMO1* expression levels are higher in primary tumors and neuroblastoma cell lines with SNP risk alleles and somatic copy number gains. Knockdown of *LMO1* in neuroblastoma cells with high endogenous *LMO1* levels inhibited cell proliferation, whereas overexpression of *LMO1* in neuroblastoma with low *LMO1* levels increased proliferation. A recent study identified another highly associated SNP (rs2168101 G>T) within the first intron of *LMO1* gene locus that occurs in a super enhancer [132]. The ancestral G allele that is associated with tumor formation resides in a conserved *GATA* transcription

factor-binding motif, while the more recently evolved protective TATA allele is associated with decreased total *LMO1* expression and does not bind *GATA3* [132].

5.5   MicroRNA

MiRNAs (microRNAs) are short RNAs (9–22 nucleotides in length) that regulate more than 60 % of human gene expression by causing mRNA degradation or inhibiting protein translation [149]. MiRNA profiling studies in neuroblastoma identified miRNAs that are differentially expressed in favorable and unfavorable, *MYCN* non-amplified and *MYCN* amplified, low-risk and high-risk neuroblastomas [150–154]. A miRNA profiling study using over 500 neuroblastoma samples identified a 25-miRNA gene signature that can significantly discriminate patients with respect to progression-free and overall survival, and this 25 miRNA gene signature can be used for risk stratification in both archived and fresh neuroblastoma tumor samples [155]. In the past decades, many miRNAs have been linked to tumor suppressor or oncogenic roles [156]. Recently miRNAs with tumor suppressor roles include *miR-337-3p* and *miR-584-5p* that target matrix metalloproteinase 14 [157, 158], *miR-362-5p* which targets phosphatidylinositol 3-kinase-C2beta [159], *miR-449a* targeting *CDK6*, *miR-542-3p* targeting survivin [160], and *miR-375* targeting *MYCN* [161]. Oncogenic miRNAs include *miR-558* that targets heparanase [162] and *miR-421* that targets the tumor suppressor menin [163]. Interestingly, unlike the traditional miRNAs that decrease target gene mRNA or protein levels, *miR-558* stimulates heparanase transcription via activation of epigenetic histone active marks and increases in RNA polymerase II on the heparanase promoter in neuroblastoma cells [162]. Among those miRNAs studied in neuroblastoma, *miR-34a* and *miR-17-92* are the most commonly reported and best-characterized miRNAs. *MiR-34a* localizes to chromosome 1p36 and is frequently included in 1pLOH. MiR-34a is under-expressed in unfavorable neuroblastomas, and its reintroduction suppresses cell proliferation likely through targeting oncogenes *E2F3* and *MYCN* and anti-apoptotic gene *BCL2* [68, 69, 164]. The *miR-17-92* cluster is directly activated by *MYCN* and plays an oncogenic role by targeting an apoptosis facilitator *BIM*, cell cycle inhibitor *CDKN1A*, as well as genes with tumor suppressor activity including *TGF-beta* and *DKK1*. Inhibition of *miR-17-92* upregulates *BIM* and *CDKN1A* and suppresses tumor growth [165–167].

5.6   Long Noncoding RNA (lncRNA)

LncRNAs are ubiquitously expressed RNA molecules longer than 200 bp in length that lack protein-coding features and account for approximately 68 % of the human transcriptome of expressed genes [168]. LncRNAs have been recognized as integral

components of the eukaryotic regulatory gene network [168, 169]. LncRNAs can act as a scaffold for the recruitment of epigenetic regulators such as polycomb repressive complex 2 (*PRC2*) and chromatin remodeling complex *SWI/SNF* to regulate gene transcription or serve as sponges to sequester miRNAs or proteins [168–172]. Almost 500 lncRNAs show 100 % conservation between human, rat, and mouse genomes, and these lncRNAs are defined as transcribed ultra-conserved regions (T-UCRs). The precise roles of these T-UCRs are unknown [173]. Real-time PCR analysis of the 481 T-UCRs in 34 high-risk, stage 4 neuroblastoma patients defined a 15 T-UCRs signature can be used to discriminate short- from long-term survivors in this group of patients [174]. The expression of a significant number of T-UCRs is altered after neuroblastoma cells are treated with all-trans retinoic acid (ATRA) [175]. *T-UC.300A* is downregulated by ATRA, and knockdown *T-UC.300A* in neuroblastoma decreased viability and invasiveness of ATRA-responsive cell lines [175], which suggests that some of the T-UCRs may play an oncogenic role in neuroblastoma. Very few recurrent mutations in protein-coding genes were identified in neuroblastoma [9–11]; thus, it highlights the importance of investigating nonprotein-coding RNA since approximately 70 % of the transcribed genome is transcribed into different types of RNAs other than protein-coding mRNAs [176, 177]. In fact, GWAS has shown that high-risk-associated SNPs are present in the introns of lncRNAs such as *NBAT1* and *CASC15* [129, 135]. Further studies showed that low-level expression of a short *CASC15* isoform (*CASC15-S*) is associated with advanced neuroblastoma and poor patient survival, and *CASC15-S* regulates neuroblastoma cell proliferation and migration and functions as a tumor suppressor [178]. Similarly, the risk-associated lncRNA *NBAT-1* controls neuroblastoma progression by regulating cell proliferation, migration, and neuronal differentiation and functions as a tumor suppressor [179]. *LncUSMycN* is a recently discovered lncRNA in neuroblastoma that is coamplified with MYCN in 88 of 341 human neuroblastoma tissues and is associated with poor patient prognoses [180]. Further study showed that *lncUSMycN* interacts with RNA-binding protein NonO, leading to N-Myc RNA upregulation and neuroblastoma proliferation. Furthermore, antisense oligonucleotides targeting *lncUSMycN* treatment suppressed neuroblastoma tumor growth in murine xenograft model [180]. In addition, many other lncRNAs were identified to play a role in neuroblastoma [181]. These findings suggest that lncRNAs may be implicated in neuroblastoma tumorigenesis.

5.7 Epigenetics

Cancer is driven by progressive genetic and epigenetic alterations [182]. Unlike adult cancer, fewer recurrent mutations have been identified in pediatric cancers including neuroblastoma [183]; thus, epigenetic alterations may be associated with certain subtypes of neuroblastomas. In fact, as described above, in the few recurrent genetic mutations present in neuroblastoma, *ATRX*, *ARID1A*, and

ARID1B are chromatin regulators and key mediators of epigenetic regulation [10, 11]. Epigenetic regulation of gene expression is controlled by DNA methylation, modification of histones, and changes in nucleosome constitution, conformation, and structure.

Hypermethylation of CpG-island in gene promoters is a way to inactivate tumor-associated genes. Methyl-CpG-binding domain sequencing and methylation-specific PCR determined a 58-marker methylation signature that can be used to predict overall and event-free survival [184]. This is consistent with the other reports that the hypermethylation of some genes are associated with various clinical risk groups in neuroblastomas [185, 186]. In neuroblastoma, the most commonly reported genes that are silenced through promoter hypermethylation are *RASSF1A*, a tumor suppressor gene that interferes with RAS signaling [187], and *CASP8*, *a* tumor suppressor important in the death receptor-mediated apoptosis pathway [188]. Other methylated genes in neuroblastoma include *CHD5*, *p14ARF*, *p16INK4a*, *CCND2*, *RARbeta2*, *TP73*, *RB1*, *DAPK1*, *HOXA9*, *TMS1*, *THBS1*, *MGMT*, and *TIMP-3* [59, 185, 189]. Importantly, many of these genes are involved in apoptotic signaling pathways; thus, DNA methylation-mediated silencing of these genes may contribute to the resistance or relapse of neuroblastoma tumors to cytotoxic chemotherapy.

Histone modifications such as acetylation, methylation, ubiquitination, and phosphorylation alter chromatin structure and affect the accessibility of transcription factors to DNA. In neuroblastoma, the majority of histone deacetylase (*HDAC*) family members are detectable, and some of them are aberrantly overexpressed [190]. Among these *HDACs*, high *HDAC8* expression correlates with poor event-free and overall survival of neuroblastoma patients [191]. Knockdown of some of the individual *HDAC* family members in neuroblastoma cells leads to cell differentiation or apoptosis, and targeting *HDACs* with *HDAC* inhibitors suppresses tumor growth [191–193]. *HDAC* family members are candidate drug targets for neuroblastoma therapy.

The aberrant expression of other epigenetic modifiers that affect histone methylation and chromatin remodeling has also been observed in neuroblastoma: the lysine-specific demethylase, *LSD1* (also named Lysine (K)-Specific Demethylase 1A, *KDM1A*), and the polycomb repressive complex1 (PRC1) subunit *BMI-1* are overexpressed in poorly differentiated tumors, and silencing of *LSD1* or *BMI-1* induces differentiation [194, 195]. The 1p36 tumor suppressor gene *CHD5* is a chromodomain protein that normally functions in nucleosome-remodeling complexes, and it is lost both through DNA methylation at the promoter region and 1p LOH. Restoration of *CHD5* suppresses tumor growth [60]. As in other types of cancer, elevated levels of *EZH2* are also found in undifferentiated neuroblastoma, and its methylation of H3K27 leads to the silencing of a number of genes in neuroblastoma with tumor suppressor activity such as *CASZ1*, *NGFR*, and *CLU* [63].

These studies indicate that there are alterations in the epigenome in neuroblastoma. Since enzymes that are potentially druggable regulate the epigenome, it provides a number of novel therapeutic options for neuroblastoma patients.

5.8 Therapy

Neuroblastoma patients younger than 6 months with small adrenal masses have an excellent event-free survival and overall survival rate (>95%) without surgical intervention [196]. Low-risk patients with International Neuroblastoma Staging System (INSS) 1 and 2 and International Neuroblastoma Risk Group Staging System (INRGSS) L1 whose tumors have no unfavorable features, the outcome is excellent with surgery alone, and immediate use of chemotherapy may be restricted to a minority of patients with low-risk patients [197, 198]. Intermediate-risk neuroblastoma patients with tumors that are unresectable at diagnosis (INRGSS L2 or INSS 3 tumors), who received dose-intensive chemotherapy, have an excellent overall survival rate (>80%) [199, 200]. Further studies demonstrated that duration of chemotherapy and doses of chemotherapeutic agents could be reduced to prevent side effects [200, 201]. High-risk neuroblastoma patients mainly include stage 4, > 18 months of age, and stage 3 with *MYCN* amplification or stage 3 > 18 months with unfavorable histology. Additionally, for children with metastatic disease or unresectable tumors with *MYCN* amplification, the outcome remains poor despite improvements in survival after primary tumor resection, multiagent chemotherapy, irradiation, anti-GD2 immunotherapy, and/or 13-cis-retinoic acid treatment [6, 202–204]. Despite these advances, the overall survival rate of high-risk neuroblastoma patients is still <50%, and 5-year overall survival of patients with relapse disease is only 8% [202, 205]. Thus, research into novel, rationally designed therapies that target high-risk neuroblastoma patients is urgently required. Figure 5.2 displays an overview of the therapeutic targets in neuroblastoma based on recent genetic and epigenetic studies.

5.8.1 Anti-GD2 Immunotherapy

Surface glycolipid molecule disialoganglioside (*GD2*) is overexpressed in pediatric and adult solid tumor such as neuroblastoma, glioma, retinoblastoma, sarcomas, and melanoma [206]. However, *GD2* expression level is low in normal tissues and restricted to neurons, melanocytes, some nerve fibers, and basal layer of the skin [206–208], which makes *GD2* a suitable target for cancer immunotherapy. *GD2* is associated with cancer cell proliferation, migration, and invasion, presumably via activation of the receptor tyrosine kinase (RTK) pathway or other tyrosine kinases [209–213]. The first developed anti-GD2 monoclonal antibodies (mAb) were murine anti-GD2 mAbs including 3F8, 14G2a, and ME36.1 [214–216]. Phase II studies showed antitumor effects of the anti-GD2 mAbs in high-risk neuroblastoma patients [217]. To reduce the human anti-mouse antibody levels in the serum, chimeric (murine x human) and humanized anti-GD2 mAbs were developed. Chimeric 14.18 (ch14.18) is one such antibody. In a phase III study, a total 226 eligible patients were randomly assigned to a treatment group. One hundred thirteen patients
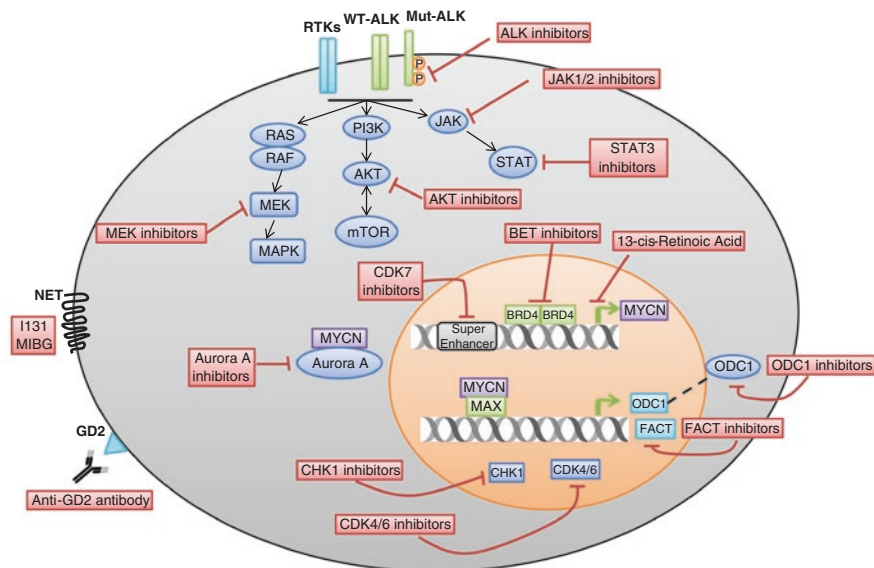
Fig. 5.2 Therapeutic targets in neuroblastoma. (i) Receptor tyrosine kinases (*RTKs*), wild-type *ALK* (*WT-ALK*) or mutant *ALK* (*Mut-ALK*), as well as downstream *RAS-MAPK*, *PI3K/AKT/mTOR*, and *JAK/STAT* pathways are aberrantly activated in neuroblastoma; thus, they are therapeutic targets in neuroblastoma. (ii) *MYCN* is an oncogenic driver in neuroblastoma, and compounds that can inhibit *MYCN* transcription, destabilize N-Myc protein, or inhibit its downstream mediators are potential drugs for neuroblastoma therapy. (iii) Cyclin-dependent kinases *CDK4/6* and checkpoint proteins *CHK1* in neuroblastoma are aberrantly activated; thus, they are therapeutic targets for neuroblastoma. (iv) *GD2* is overexpressed in almost all of the neuroblastomas yet shows restricted normal tissue expression making it a good target for immunotherapy of neuroblastoma. (v) Norepinephrine transporter (*NET*) is expressed in 90 % of neuroblastoma tumors, and *NET* is able to uptake radiopharmaceutical ^{131}I-metaiodobenzylguanidine (^{131}I-MIBG); thus, ^{131}I-MIBG is used for irradiation targeted therapy of neuroblastoma

received standard therapy (isotretinoin), and a similar cohort received immunotherapy (isotretinoin combined with GD2 antibody ch14.18, GM-CSF, and IL-2). The results showed that the immunotherapy group had significantly higher event-free survival ($66 \pm 5\%$ vs. $46 \pm 5\%$ at 2 years, $P = 0.01$) and overall survival compared to control group ($86 \pm 4\%$ vs. $75 \pm 5\%$ at 2 years, $P = 0.02$ without adjustment for interim analyses). This indicates that the cohort receiving immunotherapy had improved outcomes compared with standard therapy in high-risk neuroblastoma patients [218]. However, the role of anti-GD2 immunotherapy in the relapse setting and patients with bulky disease needs to be further investigated. In addition to anti-GD2 IgG mAbs, other studies that target GD2 are ongoing, which include the generation of chimeric antigen receptor (CAR)-modified T cells, radiolabeled antibodies, drug conjugates, and nanoparticles [206].

5.8.2 ^{131}I-metaiodobenzylguanidine Therapy

Norepinephrine transporter (*NET*) is expressed in 90 % of neuroblastoma tumors, and *NET* is able to uptake radiopharmaceutical ^{131}I-metaiodobenzylguanidine (^{131}I-MIBG), which is used to image disease burden in neuroblastoma patients and is currently being evaluated for its therapeutic potential [219, 220]. Clinical trials in relapsed neuroblastoma showed positive responses albeit with severe side effects due to myelosuppression, which could be abrogated by hematopoietic stem cell transplant [221–223]. While the majority of neuroblastomas are avid for ^{131}I-MIBG on imaging, only 30–40 % of patients have partial or complete responses [220, 221], suggesting combination treatment may be required to improve the efficacy of ^{131}I-MIBG therapies. In fact, a clinical trial using ^{131}I-MIBG in combination with chemotherapy showed promising results: in a phase II study, combination of ^{131}I-MIBG with the chemo-drug topotecan in newly diagnosed high-risk neuroblastoma patients leads to an overall objective response rate of 57 %, and a response of 94 % in the primary tumor indicates that it is an effective treatment option for these patients [224].

5.8.3 Targeting ALK

In neuroblastoma, ALK is the most commonly mutated gene (8 %), with an additional 3 % harboring *ALK* amplification [87–91]. Crizotinib is an ATP-competitive dual-specific inhibitor of *ALK*/*c-Met* that has been approved for treatment of *ALK*-rearranged non-small-cell lung cancer [225]. The treatment of neuroblastoma cells with crizotinib inhibits proliferation of neuroblastoma cell lines expressing either R1275Q-mutated *ALK* or amplified wild-type *ALK*, but is not effective for cell lines harboring the F1174L-mutated *ALK*. The crizotinib resistance of *ALK* 1174 L tumors is due to a failure of crizotinib to bind to the ALK ATP-binding pocket [91, 226, 227]. In a phase I study of crizotinib in 34 neuroblastoma patients (11 with known *ALK* status), only one patient had a complete response, while two had stable disease [228]. Recently, several new and more potent *ALK* inhibitors such as ceritinib (LDK378), alectinib (CH5424802), AP26113, RXDX-101, and PF-06463922 have emerged and are in preclinical studies [229]. The next-generation *ALK*/*ROS1* inhibitor PF-06463922 showed excellent activity in *ALK* F1174L neuroblastoma models that were resistant to crizotinib [230]. In addition to small molecules, an antibody targeting *ALK* has been found to inhibit neuroblastoma cells growth with either wild-type or mutated *ALK*, suggesting that ALK-targeted immunotherapy is a promising therapeutic strategy for neuroblastoma [231].

5.8.4   *Targeting* **MYCN**

MYCN oncogene amplification is associated with aggressive neuroblastoma and occurs in approximately 20 % of primary neuroblastoma tumors and approximately 40 % of high-risk neuroblastomas. Although it is an oncogenic driver in neuroblastoma, it appears that the elevated levels of MYCN may give tumors with this genetic alteration an "Achilles heel" making them more sensitive to a variety of therapeutic approaches. Thus targeting *MYCN* has great potential for high-risk neuroblastoma therapy. One of the early attempts to target *MYCN* evolved from the finding that retinoids inhibited *MYCN* transcription resulting in tumor cell growth arrest and differentiation [232]. Later retinoids were integrated into the consolidation phase of high-risk patient therapy and resulting in an increase in overall survival [233]. Blockade of MYC-MAX dimerization is a proposed mechanism to inhibit MYC transcriptional activity [234]. Recent studies showed that a characterized c-*MYC/MAX* inhibitor 10058-F4 also targets MYCN/Max interaction, which leads to suppression of *MYCN* amplified neuroblastoma cell proliferation and an increase in *MYCN* transgenic mice survival [235]. Recent preclinical studies suggest that bromodomain and extraterminal domain (*BET*) inhibitors inhibit *MYCN* transcription and induce cell death [236, 237]. Like some other critical oncogenes, it has been shown that the transcription of *MYCN* is driven by a super enhancer [238, 239] and a covalent inhibitor of cyclin-dependent kinase 7 (*CDK7*) disrupts the transcription of *MYCN* as well as other super-enhancer-associated genes, leading to the tumor regression in a mouse model of high-risk neuroblastoma [238]. Activation of the phosphatidylinositol 3'-kinase (*PI3K*) signal transduction pathway and Aurora A kinase act at various levels to block the N-Myc protein degradation pathway and contribute to high N-Myc protein levels in tumor cells [240–242]. PI3K and Aurora A kinase inhibitors destabilize N-Myc protein and inhibit neuroblastoma tumor growth [240–242]. Identifying the requisite biopathways downstream of *MYCN* can also provide therapeutic opportunities. *ODC1*, the rate-limiting enzyme in polyamine biosynthesis, and histone chaperone *FACT* (facilitates chromatin transcription) are found to be crucial mediators of the *MYCN* signal. *ODC1* or *FACT* inhibitor treatment suppresses tumor growth in a mouse model of high-risk neuroblastoma (*MYCN* transgenic mouse model) [36, 37]. These findings indicate small molecules that target *MYCN* transcription, destabilize N-Myc protein stability, or inhibit *MYCN* downstream mediators may have great potential for the treatment of high-risk neuroblastoma patients.

5.8.5   *Targeting* **RAS-MAPK**

WGS identified clonally enriched somatic mutations that are predicted to activate the *RAS-MAPK* pathway in 78 % of relapsed neuroblastoma tumors [127], making the *RAS-MAPK* a good target for treating relapsed high-risk neuroblastoma therapy.

Neuroblastoma cell lines with mutations in *RAS-MAPK* pathway but not wild-type *RAS-MAPK* are sensitive to *MEK* inhibitors in preclinical xenograft mouse models suggesting a role for these agents in the relapsed disease [127]. Loss of the tumor suppressor *NF1* activates *RAS-MEK* signaling in neuroblastoma cells and makes the cells resistant to retinoic acid-induced cell differentiation, which can be overcome by addition of *MEK* inhibitors [243]. These data indicate that the combination of *MEK* inhibitor and retinoic acid treatment may be beneficial to patients with high-risk neuroblastoma.

5.8.6   *Targeting Receptor Tyrosine Kinases and* PI3K-AKT

Neuroblastoma patients with high brain-derived neurotrophic factor (*BDNF*) and its receptor tyrosine kinase *TrkB* have an unfavorable prognosis, and activation of *TrkB* protects neuroblastoma cells from chemotherapy-induced apoptosis through *PI3K/AKT* pathway [244–247]. Immunohistochemical staining of neuroblastoma samples showed that phosphorylation of *Akt* occurred in the majority of the samples and is associated with reduced event-free and overall survival [248]. The aberrant activation of *PI3K/AKT/mTOR* pathway was also found in high-risk neuroblastoma patients by others [249]. The *PI3K/AKT/mTOR* pathway drives the malignant process in neuroblastoma partially due to MYCN stabilization [242, 250, 251]. Many preclinical studies have been performed using compounds against *PI3K*, *AKT*, and *mTOR*. *PI3K* inhibitor such as NVP-BKM120 alone or in combination with chemotherapeutics has been show to inhibit neuroblastoma cell growth [252, 253]. In preclinical studies, *AKT* inhibitors such as perifosine alone or in combination with chemotherapeutics suppress neuroblastoma growth [254–256]. *MTOR* inhibitors such as rapamycin or temsirolimus have been shown to inhibit neuroblastoma growth *in vitro* and *in vivo* in preclinical studies [257–259], but clinical studies showed little activity in the Phase II setting [260]. Recent preclinical studies have shown that *MYCN* amplified tumors may be sensitive to the combination of the allosteric *AKT* inhibitor MK2206 and rapamycin by preventing the feedback activation of *AKT* or *mTOR* when either agent is used alone [256]. Taken together, inhibition of the *PI3K/AKT/mTOR* pathway alone or in combination with standard therapy is a promising approach for high-risk neuroblastoma.

5.8.7   *Targeting* JAK-STAT3

The *JAK/STAT* pathway is implicated in the pathogenesis of many human cancers. AZD1480 is a pharmacological *JAK1/2* inhibitor. AZD1480 treatment blocks endogenous and IL-6-induced *STAT3* activity and suppresses neuroblastoma cell growth *in vitro* and in neuroblastoma xenografts [261]. Moreover, in neuroblastoma, a highly tumorigenic subpopulation termed cancer stem cell (CSC) has been

shown to express *CSF3R*, a receptor for granulocyte-colony-stimulating factor (*G-CSF*), and the receptor ligand *G-CSF* activates *STAT3* in neuroblastoma CSC subpopulations [262]. Blockade of this *G-CSF-STAT3* signaling loop with either anti-*G-CSF* antibody or *STAT3* inhibitor depleted the CSC subpopulation within tumors, resulting in tumor growth inhibition, decreased metastasis, and increased chemosensitivity [263]. Thus, inhibition of *JAK/STAT* signal transduction could be a promising therapeutic target for primary neuroblastoma as well as relapsed neuroblastoma enriched with CSCs.

5.8.8   Targeting Cell Cycle Genes

In the primary neuroblastomas, about 30 % of the tumors contain genomic aberrations of G1 cell cycle regulating genes such as gain and amplification of cyclin D1 (*CCND1*) and cyclin-dependent kinase 4 (*CDK4*) and deletion of *CDK* inhibitor *CDKN2A* [264, 265]. The deregulation of *Cyclin D1-CDK4/6-pRb* pathway correlates with *MYCN* amplification [264, 265]. Knockdown of *Cyclin D1* and *CDK4* restores *pRb* activity and reduces cell proliferation, resulting in a G1 cell cycle arrest [265, 266]. *CDK4/6* inhibitor treatment reduced growth of a large subset of neuroblastoma cell lines that contain genomic amplification of *MYCN in vitro* and *in vivo* [267]. In addition to G1 cell cycle genes, the cell cycle checkpoint kinase 1 (*CHK1/CHEK1*) is highly expressed in *MYCN* amplified and high-risk neuroblastomas; moreover, *CHK1* is constitutively phosphorylated in a majority of high-risk primary tumors but not low-risk primary tumors [268]. Treatment of *CHK1* inhibitors shows marked antitumor activity in neuroblastoma [268, 269]. These findings suggest that cell cycle genes such as *CDK4/6* and *CHK1* are potential therapeutic targets in neuroblastoma patients.

5.8.9   Targeting Epigenetic Enzymes

Some epigenetic enzymes are aberrantly overexpressed in neuroblastoma. Eleven classical *HDAC* family members are expressed in neuroblastoma, and high expression of *HDAC8* is associated with poor survival [190] [191]. *HDAC* inhibitor alone or in combination with other agents suppresses neuroblastoma cell growth in preclinical studies, and some clinical trials are underway [192, 270–273]. In neuroblastoma, many tumor suppressor genes such as *CASP8* and *RASSF1A* are inactivated through promoter hypermethylation, which lead to resistance to apoptosis induced by therapeutic drugs [188, 274]. Neuroblastoma cells treated with demethylating agent 5-aza-2'-deoxycytidine significantly increased the levels of apoptosis induced by chemotherapeutic drugs compared to chemotherapeutic drugs alone [275]. Currently, demethylating agents such as decitabine in combination with other agents are currently in Phase I study [276, 277]. *LSD1* is strongly expressed in poorly

differentiated neuroblastoma, and *LSD1* inhibitor monoamine oxidase treatment suppresses neuroblastoma growth *in vitro* and in the xenograft models [194]. Elevated level of PRC2 complex subunit *EZH2* is found in poorly differentiated neuroblastoma, and *EZH2* inhibitor DZNep treatment suppresses neuroblastoma tumor growth in mouse xenograft model [63]. Epigenetic enzymes are druggable, so they are promising targets in neuroblastoma, and currently new *EZH2* specific inhibitors have emerged, which need to be further evaluated in preclinical neuroblastoma models.

5.9 Conclusion

Outcomes for neuroblastoma patients with lower-stage disease have significantly improved in the past three decades. However, long-term survival rates of neuroblastoma patients with high-risk disease remain below 50 %. The recent advances in understanding the molecular genetics of neuroblastoma provide opportunities to establish therapeutic strategies specifically targeting genetic, epigenetic, and signal pathway alterations in high-risk neuroblastoma tumors. Targeted therapies focusing on recurrent mutations such as *ALK* mutations or *RAS-MAPK* mutations should be carefully investigated in preclinical models. Next-generation sequencing should be used to identify somatic mutations in neuroblastoma patients, which could provide knowledge on the treatment of patients with the combinations of molecularly targeted therapies, broad-spectrum chemotherapy, and immunotherapy for high-risk patients but reduce therapy for low-risk patients.

References

1. Maris JM. Recent advances in neuroblastoma. N Engl J Med. 2010;362(23):2202–11.
2. Maris JM, Hogarty MD, Bagatell R, Cohn SL. Neuroblastoma. Lancet. 2007;369(9579):2106–20.
3. Brodeur GM. Neuroblastoma: biological insights into a clinical enigma. Nat Rev Cancer. 2003;3(3):203–16.
4. Bosse KR, Maris JM. Advances in the translational genomics of neuroblastoma: from improving risk stratification and revealing novel biology to identifying actionable genomic alterations. Cancer. 2015;122:20–33.
5. Schulte JH, Eggert A. Neuroblastoma. Crit Rev Oncog. 2015;20(3–4):245–70.
6. Matthay KK, Reynolds CP, Seeger RC, Shimada H, Adkins ES, Haas-Kogan D, Gerbing RB, London WB, Villablanca JG. Long-term results for children with high-risk neuroblastoma treated on a randomized trial of myeloablative therapy followed by 13-cis-retinoic acid: a children's oncology group study. J Clin Oncol. 2009;27(7):1007–13.
7. Canete A, Gerrard M, Rubie H, Castel V, Di Cataldo A, Munzer C, Ladenstein R, Brichard B, Bermudez JD, Couturier J, de Bernardi B, Pearson AJ, Michon J. Poor survival for infants with MYCN-amplified metastatic neuroblastoma despite intensified treatment: the International Society of Paediatric Oncology European Neuroblastoma Experience. J Clin Oncol. 2009;27(7):1014–9.

8. Tonini GP, Longo L, Coco S, Perri P. Familial neuroblastoma: a complex heritable disease. Cancer Lett. 2003;197(1-2):41–5.

9. Pugh TJ, Morozova O, Attiyeh EF, Asgharzadeh S, Wei JS, Auclair D, Carter SL, Cibulskis K, Hanna M, Kiezun A, Kim J, Lawrence MS, Lichenstein L, McKenna A, Pedamallu CS, Ramos AH, et al. The genetic landscape of high-risk neuroblastoma. Nat Genet. 2013;45(3):279–84.

10. Sausen M, Leary RJ, Jones S, Wu J, Reynolds CP, Liu X, Blackford A, Parmigiani G, Diaz Jr LA, Papadopoulos N, Vogelstein B, Kinzler KW, Velculescu VE, Hogarty MD. Integrated genomic analyses identify ARID1A and ARID1B alterations in the childhood cancer neuroblastoma. Nat Genet. 2013;45(1):12–7.

11. Cheung NK, Zhang J, Lu C, Parker M, Bahrami A, Tickoo SK, Heguy A, Pappo AS, Federico S, Dalton J, Cheung IY, Ding L, Fulton R, Wang J, Chen X, Becksfort J, et al. Association of age at diagnosis and genetic mutations in patients with neuroblastoma. JAMA. 2012;307(10):1062–71.

12. Molenaar JJ, Koster J, Zwijnenburg DA, van Sluis P, Valentijn LJ, van der Ploeg I, Hamdi M, van Nes J, Westerman BA, van Arkel J, Ebus ME, Haneveld F, Lakeman A, Schild L, Molenaar P, Stroeken P, et al. Sequencing of neuroblastoma identifies chromothripsis and defects in neuritogenesis genes. Nature. 2012;483(7391):589–93.

13. Lee YH, Kim JH, Song GG. Genome-wide pathway analysis in neuroblastoma. Tumour Biol. 2014;35(4):3471–85.

14. Capasso M, Diskin SJ. Genetics and genomics of neuroblastoma. Cancer Treat Res. 2010;155:65–84.

15. le Nguyen B, Diskin SJ, Capasso M, Wang K, Diamond MA, Glessner J, Kim C, Attiyeh EF, Mosse YP, Cole K, Iolascon A, Devoto M, Hakonarson H, Li HK, Maris JM. Phenotype restricted genome-wide association study using a gene-centric approach identifies three low-risk neuroblastoma susceptibility Loci. PLoS Genet. 2011;7(3):e1002026.

16. Capasso M, Devoto M, Hou C, Asgharzadeh S, Glessner JT, Attiyeh EF, Mosse YP, Kim C, Diskin SJ, Cole KA, Bosse K, Diamond M, Laudenslager M, Winter C, Bradfield JP, Scott RH, et al. Common variations in BARD1 influence susceptibility to high-risk neuroblastoma. Nat Genet. 2009;41(6):718–23.

17. Cohn SL, Pearson AD, London WB, Monclair T, Ambros PF, Brodeur GM, Faldum A, Hero B, Iehara T, Machin D, Mosseri V, Simon T, Garaventa A, Castel V, Matthay KK, Force IT. The International Neuroblastoma Risk Group (INRG) classification system: an INRG Task Force report. J Clin Oncol. 2009;27(2):289–97.

18. Janoueix-Lerosey I, Schleiermacher G, Michels E, Mosseri V, Ribeiro A, Lequin D, Vermeulen J, Couturier J, Peuchmaur M, Valent A, Plantaz D, Rubie H, Valteau-Couanet D, Thomas C, Combaret V, Rousseau R, et al. Overall genomic pattern is a predictor of outcome in neuroblastoma. J Clin Oncol. 2009;27(7):1026–33.

19. Brodeur GM, Seeger RC, Schwab M, Varmus HE, Bishop JM. Amplification of N-myc in untreated human neuroblastomas correlates with advanced disease stage. Science. 1984;224(4653):1121–4.

20. Seeger RC, Brodeur GM, Sather H, Dalton A, Siegel SE, Wong KY, Hammond D. Association of multiple copies of the N-myc oncogene with rapid progression of neuroblastomas. N Engl J Med. 1985;313(18):1111–6.

21. Kreissman SG, Seeger RC, Matthay KK, London WB, Sposto R, Grupp SA, Haas-Kogan DA, Laquaglia MP, Yu AL, Diller L, Buxton A, Park JR, Cohn SL, Maris JM, Reynolds CP, Villablanca JG. Purged versus non-purged peripheral blood stem-cell transplantation for high-risk neuroblastoma (COG A3973): a randomised phase 3 trial. Lancet Oncol. 2013;14(10):999–1008.

22. Schneider SS, Hiemstra JL, Zehnbauer BA, Taillon-Miller P, Le Paslier DL, Vogelstein B, Brodeur GM. Isolation and structural analysis of a 1.2-megabase N-myc amplicon from a human neuroblastoma. Mol Cell Biol. 1992;12(12):5563–70.

23. Reiter JL, Brodeur GM. High-resolution mapping of a 130-kb core region of the MYCN amplicon in neuroblastomas. Genomics. 1996;32(1):97–103.
24. Chan HS, Gallie BL, DeBoer G, Haddad G, Ikegaki N, Dimitroulakos J, Yeger H, Ling V. MYCN protein expression as a predictor of neuroblastoma prognosis. Clin Cancer Res. 1997;3(10):1699–706.
25. Bordow SB, Norris MD, Haber PS, Marshall GM, Haber M. Prognostic significance of MYCN oncogene expression in childhood neuroblastoma. J Clin Oncol. 1998;16(10):3286–94.
26. Cohn SL, London WB, Huang D, Katzenstein HM, Salwen HR, Reinhart T, Madafiglio J, Marshall GM, Norris MD, Haber M. MYCN expression is not prognostic of adverse outcome in advanced-stage neuroblastoma with nonamplified MYCN. J Clin Oncol. 2000;18(21):3604–13.
27. Alaminos M, Gerald WL, Cheung NK. Prognostic value of MYCN and ID2 overexpression in neuroblastoma. Pediatr Blood Cancer. 2005;45(7):909–15.
28. Valentijn LJ, Koster J, Haneveld F, Aissa RA, van Sluis P, Broekmans ME, Molenaar JJ, van Nes J, Versteeg R. Functional MYCN signature predicts outcome of neuroblastoma irrespective of MYCN amplification. Proc Natl Acad Sci U S A. 2012;109(47):19190–5.
29. Weiss WA, Aldape K, Mohapatra G, Feuerstein BG, Bishop JM. Targeted expression of MYCN causes neuroblastoma in transgenic mice. EMBO J. 1997;16(11):2985–95.
30. Nara K, Kusafuka T, Yoneda A, Oue T, Sangkhathat S, Fukuzawa M. Silencing of MYCN by RNA interference induces growth inhibition, apoptotic activity and cell differentiation in a neuroblastoma cell line with MYCN amplification. Int J Oncol. 2007;30(5):1189–96.
31. Woo CW, Tan F, Cassano H, Lee J, Lee KC, Thiele CJ. Use of RNA interference to elucidate the effect of MYCN on cell cycle in neuroblastoma. Pediatr Blood Cancer. 2008;50(2):208–12.
32. Ochiai H, Takenobu H, Nakagawa A, Yamaguchi Y, Kimura M, Ohira M, Okimoto Y, Fujimura Y, Koseki H, Kohno Y, Nakagawara A, Kamijo T. Bmi1 is a MYCN target gene that regulates tumorigenesis through repression of KIF1Bbeta and TSLC1 in neuroblastoma. Oncogene. 2010;29(18):2681–90.
33. Huang R, Cheung NK, Vider J, Cheung IY, Gerald WL, Tickoo SK, Holland EC, Blasberg RG. MYCN and MYC regulate tumor proliferation and tumorigenesis directly through BMI1 in human neuroblastomas. FASEB J. 2011;25(12):4138–49.
34. Hasan MK, Nafady A, Takatori A, Kishida S, Ohira M, Suenaga Y, Hossain S, Akter J, Ogura A, Nakamura Y, Kadomatsu K, Nakagawara A. ALK is a MYCN target gene and regulates cell migration and invasion in neuroblastoma. Sci Rep. 2013;3:3450.
35. Chen L, Iraci N, Gherardi S, Gamble LD, Wood KM, Perini G, Lunec J, Tweddle DA. p53 is a direct transcriptional target of MYCN in neuroblastoma. Cancer Res. 2010;70(4):1377–88.
36. Carter DR, Murray J, Cheung BB, Gamble L, Koach J, Tsang J, Sutton S, Kalla H, Syed S, Gifford AJ, Issaeva N, Biktasova A, Atmadibrata B, Sun Y, Sokolowski N, Ling D. Therapeutic targeting of the MYC signal by inhibition of histone chaperone FACT in neuroblastoma. Sci Transl Med. 2015;7(312):312ra176.
37. Hogarty MD, Norris MD, Davis K, Liu X, Evageliou NF, Hayes CS, Pawel B, Guo R, Zhao H, Sekyere E, Keating J, Thomas W, Cheng NC, Murray J, Smith J, Sutton R, et al. ODC1 is a critical determinant of MYCN oncogenesis and a therapeutic target in neuroblastoma. Cancer Res. 2008;68(23):9735–45.
38. Iraci N, Diolaiti D, Papa A, Porro A, Valli E, Gherardi S, Herold S, Eilers M, Bernardoni R, Della Valle G, Perini G. A SP1/MIZ1/MYCN repression complex recruits HDAC1 at the TRKA and p75NTR promoters and affects neuroblastoma malignancy by inhibiting the cell response to NGF. Cancer Res. 2011;71(2):404–12.
39. Wenzel A, Schwab M. The mycN/max protein complex in neuroblastoma. Short review. Eur J Cancer. 1995;31A(4):516–9.

40. Corvetta D, Chayka O, Gherardi S, D'Acunto CW, Cantilena S, Valli E, Piotrowska I, Perini G, Sala A. Physical interaction between MYCN oncogene and polycomb repressive complex 2 (PRC2) in neuroblastoma: functional and therapeutic implications. J Biol Chem. 2013;288(12):8332–41.

41. He S, Liu Z, Oh DY, Thiele CJ. MYCN and the epigenome. Front Oncol. 2013;3:1.

42. Nie Z, Hu G, Wei G, Cui K, Yamane A, Resch W, Wang R, Green DR, Tessarollo L, Casellas R, Zhao K, Levens D. c-Myc is a universal amplifier of expressed genes in lymphocytes and embryonic stem cells. Cell. 2012;151(1):68–79.

43. Lin CY, Loven J, Rahl PB, Paranal RM, Burge CB, Bradner JE, Lee TI, Young RA. Transcriptional amplification in tumor cells with elevated c-Myc. Cell. 2012;151(1):56–67.

44. Peifer M, Hertwig F, Roels F, Dreidax D, Gartlgruber M, Menon R, Kramer A, Roncaioli JL, Sand F, Heuckmann JM, Ikram F, Schmidt R, Ackermann S, Engesser A, Kahlert Y, Vogel W, et al. Telomerase activation by genomic rearrangements in high-risk neuroblastoma. Nature. 2015;526(7575):700–4.

45. Valentijn LJ, Koster J, Zwijnenburg DA, Hasselt NE, van Sluis P, Volckmann R, van Noesel MM, George RE, Tytgat GA, Molenaar JJ, Versteeg R. TERT rearrangements are frequent in neuroblastoma and identify aggressive tumors. Nat Genet. 2015;47(12):1411–4.

46. Huang FW, Hodis E, Xu MJ, Kryukov GV, Chin L, Garraway LA. Highly recurrent TERT promoter mutations in human melanoma. Science. 2013;339(6122):957–9.

47. Davis CF, Ricketts CJ, Wang M, Yang L, Cherniack AD, Shen H, Buhay C, Kang H, Kim SC, Fahey CC, Hacker KE, Bhanot G, Gordenin DA, Chu A, Gunaratne PH, Biehl M, et al. The somatic genomic landscape of chromophobe renal cell carcinoma. Cancer Cell. 2014;26(3):319–30.

48. Mac SM, D'Cunha CA, Farnham PJ. Direct recruitment of N-myc to target gene promoters. Mol Carcinog. 2000;29(2):76–86.

49. Mosse YP, Greshock J, Weber BL, Maris JM. Measurement and relevance of neuroblastoma DNA copy number changes in the post-genome era. Cancer Lett. 2005;228(1-2):83–90.

50. Mosse YP, Diskin SJ, Wasserman N, Rinaldi K, Attiyeh EF, Cole K, Jagannathan J, Bhambhani K, Winter C, Maris JM. Neuroblastomas have distinct genomic DNA profiles that predict clinical phenotype and regional gene expression. Genes Chromosomes Cancer. 2007;46(10):936–49.

51. Chen QR, Bilke S, Wei JS, Whiteford CC, Cenacchi N, Krasnoselsky AL, Greer BT, Son CG, Westermann F, Berthold F, Schwab M, Catchpoole D, Khan J. cDNA array-CGH profiling identifies genomic alterations specific to stage and MYCN-amplification in neuroblastoma. BMC Genomics. 2004;5:70.

52. Vandesompele J, Speleman F, Van Roy N, Laureys G, Brinskchmidt C, Christiansen H, Lampert F, Lastowska M, Bown N, Pearson A, Nicholson JC, Ross F, Combaret V, Delattre O, Feuerstein BG, Plantaz D. Multicentre analysis of patterns of DNA gains and losses in 204 neuroblastoma tumors: how many genetic subgroups are there? Med Pediatr Oncol. 2001;36(1):5–10.

53. Caren H, Erichsen J, Olsson L, Enerback C, Sjoberg RM, Abrahamsson J, Kogner P, Martinsson T. High-resolution array copy number analyses for detection of deletion, gain, amplification and copy-neutral LOH in primary neuroblastoma tumors: four cases of homozygous deletions of the CDKN2A gene. BMC Genomics. 2008;9:353.

54. van Noesel MM, Versteeg R. Pediatric neuroblastomas: genetic and epigenetic 'danse macabre'. Gene. 2004;325:1–15.

55. Attiyeh EF, London WB, Mosse YP, Wang Q, Winter C, Khazi D, McGrady PW, Seeger RC, Look AT, Shimada H, Brodeur GM, Cohn SL, Matthay KK, Maris JM, Children's OG. Chromosome 1p and 11q deletions and outcome in neuroblastoma. N Engl J Med. 2005;353(21):2243–53.

56. Bader SA, Fasching C, Brodeur GM, Stanbridge EJ. Dissociation of suppression of tumorigenicity and differentiation in vitro effected by transfer of single human chromosomes into human neuroblastoma cells. Cell Growth Differ. 1991;2(5):245–55.

57. Henrich KO, Schwab M, Westermann F. 1p36 tumor suppression--a matter of dosage? Cancer Res. 2012;72(23):6079–88.

58. Kolla V, Naraparaju K, Zhuang T, Higashi M, Kolla S, Blobel GA, Brodeur GM. The tumour suppressor CHD5 forms a NuRD-type chromatin remodelling complex. Biochem J. 2015;468(2):345–52.

59. Koyama H, Zhuang T, Light JE, Kolla V, Higashi M, McGrady PW, London WB, Brodeur GM. Mechanisms of CHD5 Inactivation in neuroblastomas. Clin Cancer Res. 2012;18(6):1588–97.

60. Fujita T, Igarashi J, Okawa ER, Gotoh T, Manne J, Kolla V, Kim J, Zhao H, Pawel BR, London WB, Maris JM, White PS, Brodeur GM. CHD5, a tumor suppressor gene deleted from 1p36.31 in neuroblastomas. J Natl Cancer Inst. 2008;100(13):940–9.

61. Liu Z, Yang X, Li Z, McMahon C, Sizer C, Barenboim-Stapleton L, Bliskovsky V, Mock B, Ried T, London WB, Maris J, Khan J, Thiele CJ. CASZ1, a candidate tumor-suppressor gene, suppresses neuroblastoma tumor growth through reprogramming gene expression. Cell Death Differ. 2011;18(7):1174–83.

62. Liu Z, Naranjo A, Thiele CJ. CASZ1b, the short isoform of CASZ1 gene, coexpresses with CASZ1a during neurogenesis and suppresses neuroblastoma cell growth. PLoS One. 2011;6(4):e18557.

63. Wang C, Liu Z, Woo CW, Li Z, Wang L, Wei JS, Marquez VE, Bates SE, Jin Q, Khan J, Ge K, Thiele CJ. EZH2 Mediates epigenetic silencing of neuroblastoma suppressor genes CASZ1, CLU, RUNX3, and NGFR. Cancer Res. 2012;72(1):315–24.

64. Liu Z, Lam N, Thiele CJ. Zinc finger transcription factor CASZ1 interacts with histones, DNA repair proteins and recruits NuRD complex to regulate gene transcription. Oncotarget. 2015;6(29):27628–40.

65. Henrich KO, Bauer T, Schulte J, Ehemann V, Deubzer H, Gogolin S, Muth D, Fischer M, Benner A, Konig R, Schwab M, Westermann F. CAMTA1, a 1p36 tumor suppressor candidate, inhibits growth and activates differentiation programs in neuroblastoma cells. Cancer Res. 2011;71(8):3142–51.

66. Munirajan AK, Ando K, Mukai A, Takahashi M, Suenaga Y, Ohira M, Koda T, Hirota T, Ozaki T, Nakagawara A. KIF1Bbeta functions as a haploinsufficient tumor suppressor gene mapped to chromosome 1p36.2 by inducing apoptotic cell death. J Biol Chem. 2008;283(36):24426–34.

67. Schlisio S, Kenchappa RS, Vredeveld LC, George RE, Stewart R, Greulich H, Shahriari K, Nguyen NV, Pigny P, Dahia PL, Pomeroy SL, Maris JM, Look AT, Meyerson M, Peeper DS, Carter BD, et al. The kinesin KIF1Bbeta acts downstream from EglN3 to induce apoptosis and is a potential 1p36 tumor suppressor. Genes Dev. 2008;22(7):884–93.

68. Wei JS, Song YK, Durinck S, Chen QR, Cheuk AT, Tsang P, Zhang Q, Thiele CJ, Slack A, Shohet J, Khan J. The MYCN oncogene is a direct target of miR-34a. Oncogene. 2008;27(39):5204–13.

69. Welch C, Chen Y, Stallings RL. MicroRNA-34a functions as a potential tumor suppressor by inducing apoptosis in neuroblastoma cells. Oncogene. 2007;26(34):5017–22.

70. Guo C, White PS, Weiss MJ, Hogarty MD, Thompson PM, Stram DO, Gerbing R, Matthay KK, Seeger RC, Brodeur GM, Maris JM. Allelic deletion at 11q23 is common in MYCN single copy neuroblastomas. Oncogene. 1999;18(35):4948–57.

71. Caren H, Kryh H, Nethander M, Sjoberg RM, Trager C, Nilsson S, Abrahamsson J, Kogner P, Martinsson T. High-risk neuroblastoma tumors with 11q-deletion display a poor prognostic, chromosome instability phenotype with later onset. Proc Natl Acad Sci U S A. 2010;107(9):4323–8.

72. Maris JM, Guo C, White PS, Hogarty MD, Thompson PM, Stram DO, Gerbing R, Matthay KK, Seeger RC, Brodeur GM. Allelic deletion at chromosome bands 11q14-23 is common in neuroblastoma. Med Pediatr Oncol. 2001;36(1):24–7.
73. Mandriota SJ, Valentijn LJ, Lesne L, Betts DR, Marino D, Boudal-Khoshbeen M, London WB, Rougemont AL, Attiyeh EF, Maris JM, Hogarty MD, Koster J, Molenaar JJ, Versteeg R, Ansari M, Gumy-Pause F. Ataxia-telangiectasia mutated (ATM) silencing promotes neuroblastoma progression through a MYCN independent mechanism. Oncotarget. 2015;6(21):18558–76.
74. Ando K, Ohira M, Ozaki T, Nakagawa A, Akazawa K, Suenaga Y, Nakamura Y, Koda T, Kamijo T, Murakami Y, Nakagawara A. Expression of TSLC1, a candidate tumor suppressor gene mapped to chromosome 11q23, is downregulated in unfavorable neuroblastoma without promoter hypermethylation. Int J Cancer. 2008;123(9):2087–94.
75. Nowacki S, Skowron M, Oberthuer A, Fagin A, Voth H, Brors B, Westermann F, Eggert A, Hero B, Berthold F, Fischer M. Expression of the tumour suppressor gene CADM1 is associated with favourable outcome and inhibits cell survival in neuroblastoma. Oncogene. 2008;27(23):3329–38.
76. Michels E, Hoebeeck J, De Preter K, Schramm A, Brichard B, De Paepe A, Eggert A, Laureys G, Vandesompele J, Speleman F. CADM1 is a strong neuroblastoma candidate gene that maps within a 3.72 Mb critical region of loss on 11q23. BMC Cancer. 2008;8:173.
77. Bown N, Cotterill S, Lastowska M, O'Neill S, Pearson AD, Plantaz D, Meddeb M, Danglot G, Brinkschmidt C, Christiansen H, Laureys G, Speleman F, Nicholson J, Bernheim A, Betts DR, Vandesompele J, et al. Gain of chromosome arm 17q and adverse outcome in patients with neuroblastoma. N Engl J Med. 1999;340(25):1954–61.
78. Meddeb M, Danglot G, Chudoba I, Venuat AM, Benard J, Avet-Loiseau H, Vasseur B, Le Paslier D, Terrier-Lacombe MJ, Hartmann O, Bernheim A. Additional copies of a 25 Mb chromosomal region originating from 17q23.1-17qter are present in 90% of high-grade neuroblastomas. Genes Chromosomes Cancer. 1996;17(3):156–65.
79. Bown N, Lastowska M, Cotterill S, O'Neill S, Ellershaw C, Roberts P, Lewis I, Pearson AD, Group UKCC and the UKCsCSG. 17q gain in neuroblastoma predicts adverse clinical outcome. U.K. Cancer Cytogenetics Group and the U.K. Children's Cancer Study Group. Med Pediatr Oncol. 2001;36(1):14–9.
80. Kuzyk A, Booth S, Righolt C, Mathur S, Gartner J, Mai S. MYCN overexpression is associated with unbalanced copy number gain, altered nuclear location, and overexpression of chromosome arm 17q genes in neuroblastoma tumors and cell lines. Genes Chromosomes Cancer. 2015;54(10):616–28.
81. Hagenbuchner J, Kiechl-Kohlendorfer U, Obexer P, Ausserlechner MJ. BIRC5/Survivin as a target for glycolysis inhibition in high-stage neuroblastoma. Oncogene. 2015;35:2052–61.
82. Islam A, Kageyama H, Takada N, Kawamoto T, Takayasu H, Isogai E, Ohira M, Hashizume K, Kobayashi H, Kaneko Y, Nakagawara A. High expression of Survivin, mapped to 17q25, is significantly associated with poor prognostic factors and promotes cell survival in human neuroblastoma. Oncogene. 2000;19(5):617–23.
83. Stephens PJ, Greenman CD, Fu B, Yang F, Bignell GR, Mudie LJ, Pleasance ED, Lau KW, Beare D, Stebbings LA, McLaren S, Lin ML, McBride DJ, Varela I, Nik-Zainal S, Leroy C, et al. Massive genomic rearrangement acquired in a single catastrophic event during cancer development. Cell. 2011;144(1):27–40.
84. Kloosterman WP, Koster J, Molenaar JJ. Prevalence and clinical implications of chromothripsis in cancer genomes. Curr Opin Oncol. 2014;26(1):64–72.
85. Shojaei-Brosseau T, Chompret A, Abel A, de Vathaire F, Raquin MA, Brugieres L, Feunteun J, Hartmann O, Bonaiti-Pellie C. Genetic epidemiology of neuroblastoma: a study of 426 cases at the Institut Gustave-Roussy in France. Pediatr Blood Cancer. 2004;42(1):99–105.
86. Vogelstein B, Papadopoulos N, Velculescu VE, Zhou S, Diaz Jr LA, Kinzler KW. Cancer genome landscapes. Science. 2013;339(6127):1546–58.

87. Mosse YP, Laudenslager M, Longo L, Cole KA, Wood A, Attiyeh EF, Laquaglia MJ, Sennett R, Lynch JE, Perri P, Laureys G, Speleman F, Kim C, Hou C, Hakonarson H, Torkamani A, et al. Identification of ALK as a major familial neuroblastoma predisposition gene. Nature. 2008;455(7215):930–5.

88. Janoueix-Lerosey I, Lequin D, Brugieres L, Ribeiro A, de Pontual L, Combaret V, Raynal V, Puisieux A, Schleiermacher G, Pierron G, Valteau-Couanet D, Frebourg T, Michon J, Lyonnet S, Amiel J, Delattre O. Somatic and germline activating mutations of the ALK kinase receptor in neuroblastoma. Nature. 2008;455(7215):967–70.

89. George RE, Sanda T, Hanna M, Frohling S, Luther 2nd W, Zhang J, Ahn Y, Zhou W, London WB, McGrady P, Xue L, Zozulya S, Gregor VE, Webb TR, Gray NS, Gilliland DG, et al. Activating mutations in ALK provide a therapeutic target in neuroblastoma. Nature. 2008;455(7215):975–8.

90. Chen Y, Takita J, Choi YL, Kato M, Ohira M, Sanada M, Wang L, Soda M, Kikuchi A, Igarashi T, Nakagawara A, Hayashi Y, Mano H, Ogawa S. Oncogenic mutations of ALK kinase in neuroblastoma. Nature. 2008;455(7215):971–4.

91. Bresler SC, Weiser DA, Huwe PJ, Park JH, Krytska K, Ryles H, Laudenslager M, Rappaport EF, Wood AC, McGrady PW, Hogarty MD, London WB, Radhakrishnan R, Lemmon MA, Mosse YP. ALK mutations confer differential oncogenic activation and sensitivity to ALK inhibition therapy in neuroblastoma. Cancer Cell. 2014;26(5):682–94.

92. Iwahara T, Fujimoto J, Wen D, Cupples R, Bucay N, Arakawa T, Mori S, Ratzkin B, Yamamoto T. Molecular characterization of ALK, a receptor tyrosine kinase expressed specifically in the nervous system. Oncogene. 1997;14(4):439–49.

93. Webb TR, Slavish J, George RE, Look AT, Xue L, Jiang Q, Cui X, Rentrop WB, Morris SW. Anaplastic lymphoma kinase: role in cancer pathogenesis and small-molecule inhibitor development for therapy. Expert Rev Anticancer Ther. 2009;9(3):331–56.

94. Bazigou E, Apitz H, Johansson J, Loren CE, Hirst EM, Chen PL, Palmer RH, Salecker I. Anterograde Jelly belly and Alk receptor tyrosine kinase signaling mediates retinal axon targeting in Drosophila. Cell. 2007;128(5):961–75.

95. Chiarle R, Voena C, Ambrogio C, Piva R, Inghirami G. The anaplastic lymphoma kinase in the pathogenesis of cancer. Nat Rev Cancer. 2008;8(1):11–23.

96. Hallberg B, Palmer RH. Mechanistic insight into ALK receptor tyrosine kinase in human cancer biology. Nat Rev Cancer. 2013;13(10):685–700.

97. Souttou B, Carvalho NB, Raulais D, Vigny M. Activation of anaplastic lymphoma kinase receptor tyrosine kinase induces neuronal differentiation through the mitogen-activated protein kinase pathway. J Biol Chem. 2001;276(12):9526–31.

98. Azarova AM, Gautam G, George RE. Emerging importance of ALK in neuroblastoma. Semin Cancer Biol. 2011;21(4):267–75.

99. de Pontual L, Kettaneh D, Gordon CT, Oufadem M, Boddaert N, Lees M, Balu L, Lachassinne E, Petros A, Mollet J, Wilson LC, Munnich A, Brugiere L, Delattre O, Vekemans M, Etchevers H, et al. Germline gain-of-function mutations of ALK disrupt central nervous system development. Hum Mutat. 2011;32(3):272–6.

100. Amiel J, Laudier B, Attie-Bitach T, Trang H, de Pontual L, Gener B, Trochet D, Etchevers H, Ray P, Simonneau M, Vekemans M, Munnich A, Gaultier C, Lyonnet S. Polyalanine expansion and frameshift mutations of the paired-like homeobox gene PHOX2B in congenital central hypoventilation syndrome. Nat Genet. 2003;33(4):459–61.

101. Weese-Mayer DE, Berry-Kravis EM, Zhou L, Maher BS, Silvestri JM, Curran ME, Marazita ML. Idiopathic congenital central hypoventilation syndrome: analysis of genes pertinent to early autonomic nervous system embryologic development and identification of mutations in PHOX2b. Am J Med Genet A. 2003;123A(3):267–78.

102. Mosse YP, Laudenslager M, Khazi D, Carlisle AJ, Winter CL, Rappaport E, Maris JM. Germline PHOX2B mutation in hereditary neuroblastoma. Am J Hum Genet. 2004;75(4):727–30.

103. Trochet D, Bourdeaut F, Janoueix-Lerosey I, Deville A, de Pontual L, Schleiermacher G, Coze C, Philip N, Frebourg T, Munnich A, Lyonnet S, Delattre O, Amiel J. Germline mutations of the paired-like homeobox 2B (PHOX2B) gene in neuroblastoma. Am J Hum Genet. 2004;74(4):761–4.

104. Bachetti T, Di Paolo D, Di Lascio S, Mirisola V, Brignole C, Bellotti M, Caffa I, Ferraris C, Fiore M, Fornasari D, Chiarle R, Borghini S, Pfeffer U, Ponzoni M, Ceccherini I, Perri P. PHOX2B-mediated regulation of ALK expression: in vitro identification of a functional relationship between two genes involved in neuroblastoma. PLoS One. 2010;5(10):e13108:1–15

105. Pattyn A, Goridis C, Brunet JF. Specification of the central noradrenergic phenotype by the homeobox gene Phox2b. Mol Cell Neurosci. 2000;15(3):235–43.

106. Pei D, Luther W, Wang W, Paw BH, Stewart RA, George RE. Distinct neuroblastoma-associated alterations of PHOX2B impair sympathetic neuronal differentiation in zebrafish models. PLoS Genet. 2013;9(6):e1003533.

107. Raabe EH, Laudenslager M, Winter C, Wasserman N, Cole K, LaQuaglia M, Maris DJ, Mosse YP, Maris JM. Prevalence and functional consequence of PHOX2B mutations in neuroblastoma. Oncogene. 2008;27(4):469–76.

108. Nagashimada M, Ohta H, Li C, Nakao K, Uesaka T, Brunet JF, Amiel J, Trochet D, Wakayama T, Enomoto H. Autonomic neurocristopathy-associated mutations in PHOX2B dysregulate Sox10 expression. J Clin Invest. 2012;122(9):3145–58.

109. Heukamp LC, Thor T, Schramm A, De Preter K, Kumps C, De Wilde B, Odersky A, Peifer M, Lindner S, Spruessel A, Pattyn F, Mestdagh P, Menten B, Kuhfittig-Kulle S, Kunkele A, Konig K, et al. Targeted expression of mutated ALK induces neuroblastoma in transgenic mice. Sci Transl Med. 2012;4(141):141ra191.

110. Berry T, Luther W, Bhatnagar N, Jamin Y, Poon E, Sanda T, Pei D, Sharma B, Vetharoy WR, Hallsworth A, Ahmad Z, Barker K, Moreau L, Webber H, Wang W, Liu Q, et al. The ALK(F1174L) mutation potentiates the oncogenic activity of MYCN in neuroblastoma. Cancer Cell. 2012;22(1):117–30.

111. Zhu S, Lee JS, Guo F, Shin J, Perez-Atayde AR, Kutok JL, Rodig SJ, Neuberg DS, Helman D, Feng H, Stewart RA, Wang W, George RE, Kanki JP, Look AT. Activated ALK collaborates with MYCN in neuroblastoma pathogenesis. Cancer Cell. 2012;21(3):362–73.

112. Liu Z, Thiele CJ. ALK and MYCN: when two oncogenes are better than one. Cancer Cell. 2012;21(3):325–6.

113. Umapathy G, El Wakil A, Witek B, Chesler L, Danielson L, Deng X, Gray NS, Johansson M, Kvarnbrink S, Ruuth K, Schonherr C, Palmer RH, Hallberg B. The kinase ALK stimulates the kinase ERK5 to promote the expression of the oncogene MYCN in neuroblastoma. Sci Signal. 2014;7(349):ra102.

114. Cheung NK, Dyer MA. Neuroblastoma: developmental biology, cancer genomics and immunotherapy. Nat Rev Cancer. 2013;13(6):397–411.

115. Fishbein L, Khare S, Wubbenhorst B, DeSloover D, D'Andrea K, Merrill S, Cho NW, Greenberg RA, Else T, Montone K, LiVolsi V, Fraker D, Daber R, Cohen DL, Nathanson KL. Whole-exome sequencing identifies somatic ATRX mutations in pheochromocytomas and paragangliomas. Nat Commun. 2015;6:6140.

116. Jiao Y, Shi C, Edil BH, de Wilde RF, Klimstra DS, Maitra A, Schulick RD, Tang LH, Wolfgang CL, Choti MA, Velculescu VE, Diaz Jr LA, Vogelstein B, Kinzler KW, Hruban RH, Papadopoulos N. DAXX/ATRX, MEN1, and mTOR pathway genes are frequently altered in pancreatic neuroendocrine tumors. Science. 2011;331(6021):1199–203.

117. Lovejoy CA, Li W, Reisenweber S, Thongthip S, Bruno J, de Lange T, De S, Petrini JH, Sung PA, Jasin M, Rosenbluh J, Zwang Y, Weir BA, Hatton C, Ivanova E, Macconaill L, et al. Loss of ATRX, genome instability, and an altered DNA damage response are hallmarks of the alternative lengthening of telomeres pathway. PLoS Genet. 2012;8(7):e1002772.

118. Wang X, Nagl NG, Wilsker D, Van Scoy M, Pacchione S, Yaciuk P, Dallas PB, Moran E. Two related ARID family proteins are alternative subunits of human SWI/SNF complexes. Biochem J. 2004;383(Pt 2):319–25.

119. Wu RC, Wang TL, Shih IM. The emerging roles of ARID1A in tumor suppression. Cancer Biol Ther. 2014;15(6):655–64.

120. Takeda T, Banno K, Okawa R, Yanokura M, Iijima M, Irie-Kunitomi H, Nakamura K, Iida M, Adachi M, Umene K, Nogami Y, Masuda K, Kobayashi Y, Tominaga E, Aoki D. ARID1A gene mutation in ovarian and endometrial cancers (Review). Oncol Rep. 2015;35:607–13.

121. Park JH, Park EJ, Lee HS, Kim SJ, Hur SK, Imbalzano AN, Kwon J. Mammalian SWI/SNF complexes facilitate DNA double-strand break repair by promoting gamma-H2AX induction. EMBO J. 2006;25(17):3986–97.

122. Hara R, Sancar A. The SWI/SNF chromatin-remodeling factor stimulates repair by human excision nuclease in the mononucleosome core particle. Mol Cell Biol. 2002;22(19):6779–87.

123. Jones S, Wang TL, Shih Ie M, Mao TL, Nakayama K, Roden R, Glas R, Slamon D, Diaz Jr LA, Vogelstein B, Kinzler KW, Velculescu VE, Papadopoulos N. Frequent mutations of chromatin remodeling gene ARID1A in ovarian clear cell carcinoma. Science. 2010;330(6001):228–31.

124. Wu JN, Roberts CW. ARID1A mutations in cancer: another epigenetic tumor suppressor? Cancer Discov. 2013;3(1):35–43.

125. Cajuso T, Hanninen UA, Kondelin J, Gylfe AE, Tanskanen T, Katainen R, Pitkanen E, Ristolainen H, Kaasinen E, Taipale M, Taipale J, Bohm J, Renkonen-Sinisalo L, Mecklin JP, Jarvinen H, Tuupanen S, et al. Exome sequencing reveals frequent inactivating mutations in ARID1A, ARID1B, ARID2 and ARID4A in microsatellite unstable colorectal cancer. Int J Cancer. 2014;135(3):611–23.

126. Khursheed M, Kolla JN, Kotapalli V, Gupta N, Gowrishankar S, Uppin SG, Sastry RA, Koganti S, Sundaram C, Pollack JR, Bashyam MD. ARID1B, a member of the human SWI/SNF chromatin remodeling complex, exhibits tumour-suppressor activities in pancreatic cancer cell lines. Br J Cancer. 2013;108(10):2056–62.

127. Eleveld TF, Oldridge DA, Bernard V, Koster J, Daage LC, Diskin SJ, Schild L, Bentahar NB, Bellini A, Chicard M, Lapouble E, Combaret V, Legoix-Ne P, Michon J, Pugh TJ, Hart LS, et al. Relapsed neuroblastomas show frequent RAS-MAPK pathway mutations. Nat Genet. 2015;47(8):864–71.

128. Schramm A, Koster J, Assenov Y, Althoff K, Peifer M, Mahlow E, Odersky A, Beisser D, Ernst C, Henssen AG, Stephan H, Schroder C, Heukamp L, Engesser A, Kahlert Y, Theissen J, et al. Mutational dynamics between primary and relapse neuroblastomas. Nat Genet. 2015;47(8):872–7.

129. Diskin SJ, Capasso M, Schnepp RW, Cole KA, Attiyeh EF, Hou C, Diamond M, Carpenter EL, Winter C, Lee H, Jagannathan J, Latorre V, Iolascon A, Hakonarson H, Devoto M, Maris JM. Common variation at 6q16 within HACE1 and LIN28B influences susceptibility to neuroblastoma. Nat Genet. 2012;44(10):1126–30.

130. Schnepp RW, Khurana P, Attiyeh EF, Raman P, Chodosh SE, Oldridge DA, Gagliardi ME, Conkrite KL, Asgharzadeh S, Seeger RC, Madison BB, Rustgi AK, Maris JM, Diskin SJ. A LIN28B-RAN-AURKA signaling network promotes neuroblastoma tumorigenesis. Cancer Cell. 2015;28(5):599–609.

131. Molenaar JJ, Domingo-Fernandez R, Ebus ME, Lindner S, Koster J, Drabek K, Mestdagh P, van Sluis P, Valentijn LJ, van Nes J, Broekmans M, Haneveld F, Volckmann R, Bray I, Heukamp L, Sprussel A, et al. LIN28B induces neuroblastoma and enhances MYCN levels via let-7 suppression. Nat Genet. 2012;44(11):1199–206.

132. Oldridge DA, Wood AC, Weichert-Leahey N, Crimmins I, Sussman R, Winter C, McDaniel LD, Diamond M, Hart LS, Zhu S, Durbin AD, Abraham BJ, Anders L, Tian L, Zhang S, Wei JS, et al. Genetic predisposition to neuroblastoma mediated by a LMO1 super-enhancer polymorphism. Nature. 2015;528:418–21.

133. Wang K, Diskin SJ, Zhang H, Attiyeh EF, Winter C, Hou C, Schnepp RW, Diamond M, Bosse K, Mayes PA, Glessner J, Kim C, Frackelton E, Garris M, Wang Q, Glaberson W, et al.

Integrative genomics identifies LMO1 as a neuroblastoma oncogene. Nature. 2011;469(7329):216–20.

134. Bosse KR, Diskin SJ, Cole KA, Wood AC, Schnepp RW, Norris G, le Nguyen B, Jagannathan J, Laquaglia M, Winter C, Diamond M, Hou C, Attiyeh EF, Mosse YP, Pineros V, Dizin E, et al. Common variation at BARD1 results in the expression of an oncogenic isoform that influences neuroblastoma susceptibility and oncogenicity. Cancer Res. 2012;72(8):2068–78.

135. Maris JM, Mosse YP, Bradfield JP, Hou C, Monni S, Scott RH, Asgharzadeh S, Attiyeh EF, Diskin SJ, Laudenslager M, Winter C, Cole KA, Glessner JT, Kim C, Frackelton EC, Casalunovo T, et al. Chromosome 6p22 locus associated with clinically aggressive neuroblastoma. N Engl J Med. 2008;358(24):2585–93.

136. Capasso M, Diskin S, Cimmino F, Acierno G, Totaro F, Petrosino G, Pezone L, Diamond M, McDaniel L, Hakonarson H, Iolascon A, Devoto M, Maris JM. Common genetic variants in NEFL influence gene expression and neuroblastoma risk. Cancer Res. 2014;74(23):6913–24.

137. Capasso M, Diskin SJ, Totaro F, Longo L, De Mariano M, Russo R, Cimmino F, Hakonarson H, Tonini GP, Devoto M, Maris JM, Iolascon A. Replication of GWAS-identified neuroblastoma risk loci strengthens the role of BARD1 and affirms the cumulative effect of genetic variations on disease susceptibility. Carcinogenesis. 2013;34(3):605–11.

138. Diskin SJ, Hou C, Glessner JT, Attiyeh EF, Laudenslager M, Bosse K, Cole K, Mosse YP, Wood A, Lynch JE, Pecor K, Diamond M, Winter C, Wang K, Kim C, Geiger EA, et al. Copy number variation at 1q21.1 associated with neuroblastoma. Nature. 2009;459(7249):987–91.

139. Latorre V, Diskin SJ, Diamond MA, Zhang H, Hakonarson H, Maris JM, Devoto M. Replication of neuroblastoma SNP association at the BARD1 locus in African-Americans. Cancer Epidemiol Biomarkers Prev. 2012;21(4):658–63.

140. Irminger-Finger I, Jefford CE. Is there more to BARD1 than BRCA1? Nat Rev Cancer. 2006;6(5):382–91.

141. Zhou J, Ng SB, Chng WJ. LIN28/LIN28B: an emerging oncogenic driver in cancer stem cells. Int J Biochem Cell Biol. 2013;45(5):973–8.

142. Iliopoulos D, Hirsch HA, Struhl K. An epigenetic switch involving NF-kappaB, Lin28, Let-7 MicroRNA, and IL6 links inflammation to cell transformation. Cell. 2009;139(4):693–706.

143. West JA, Viswanathan SR, Yabuuchi A, Cunniff K, Takeuchi A, Park IH, Sero JE, Zhu H, Perez-Atayde A, Frazier AL, Surani MA, Daley GQ. A role for Lin28 in primordial germ-cell development and germ-cell malignancy. Nature. 2009;460(7257):909–13.

144. Beckers A, Van Peer G, Carter DR, Gartlgruber M, Herrmann C, Agarwal S, Helsmoortel HH, Althoff K, Molenaar JJ, Cheung BB, Schulte JH, Benoit Y, Shohet JM, Westermann F, Marshall GM, Vandesompele J, et al. MYCN-driven regulatory mechanisms controlling LIN28B in neuroblastoma. Cancer Lett. 2015;366(1):123–32.

145. Lu J, Chu P, Wang H, Jin Y, Han S, Han W, Tai J, Guo Y, Ni X. Candidate gene association analysis of neuroblastoma in Chinese children strengthens the role of LMO1. PLoS One. 2015;10(6):e0127856.

146. Lin YW, Deveney R, Barbara M, Iscove NN, Nimer SD, Slape C, Aplan PD. OLIG2 (BHLHB1), a bHLH transcription factor, contributes to leukemogenesis in concert with LMO1. Cancer Res. 2005;65(16):7151–8.

147. Chervinsky DS, Lam DH, Melman MP, Gross KW, Aplan PD. scid Thymocytes with TCRbeta gene rearrangements are targets for the oncogenic effect of SCL and LMO1 transgenes. Cancer Res. 2001;61(17):6382–7.

148. Chervinsky DS, Zhao XF, Lam DH, Ellsworth M, Gross KW, Aplan PD. Disordered T-cell development and T-cell malignancies in SCL LMO1 double-transgenic mice: parallels with E2A-deficient mice. Mol Cell Biol. 1999;19(7):5025–35.

149. Esteller M. Non-coding RNAs in human disease. Nat Rev Genet. 2011;12(12):861–74.

150. Chen Y, Stallings RL. Differential patterns of microRNA expression in neuroblastoma are correlated with prognosis, differentiation, and apoptosis. Cancer Res. 2007;67(3):976–83.

151. Schulte JH, Horn S, Otto T, Samans B, Heukamp LC, Eilers UC, Krause M, Astrahantseff K, Klein-Hitpass L, Buettner R, Schramm A, Christiansen H, Eilers M, Eggert A, Berwanger B. MYCN regulates oncogenic MicroRNAs in neuroblastoma. Int J Cancer. 2008;122(3):699–704.

152. Bray I, Bryan K, Prenter S, Buckley PG, Foley NH, Murphy DM, Alcock L, Mestdagh P, Vandesompele J, Speleman F, London WB, McGrady PW, Higgins DG, O'Meara A, O'Sullivan M, Stallings RL. Widespread dysregulation of MiRNAs by MYCN amplification and chromosomal imbalances in neuroblastoma: association of miRNA expression with survival. PLoS One. 2009;4(11):e7850.

153. Mestdagh P, Fredlund E, Pattyn F, Schulte JH, Muth D, Vermeulen J, Kumps C, Schlierf S, De Preter K, Van Roy N, Noguera R, Laureys G, Schramm A, Eggert A, Westermann F, Speleman F, et al. MYCN/c-MYC-induced microRNAs repress coding gene networks associated with poor outcome in MYCN/c-MYC-activated tumors. Oncogene. 2010;29(9):1394–404.

154. Lin RJ, Lin YC, Chen J, Kuo HH, Chen YY, Diccianni MB, London WB, Chang CH, Yu AL. microRNA signature and expression of Dicer and Drosha can predict prognosis and delineate risk groups in neuroblastoma. Cancer Res. 2010;70(20):7841–50.

155. De Preter K, Mestdagh P, Vermeulen J, Zeka F, Naranjo A, Bray I, Castel V, Chen C, Drozynska E, Eggert A, Hogarty MD, Izycka-Swieszewska E, London WB, Noguera R, Piqueras M, Bryan K, et al. miRNA expression profiling enables risk stratification in archived and fresh neuroblastoma tumor samples. Clin Cancer Res. 2011;17(24):7684–92.

156. Zhi F, Wang R, Wang Q, Xue L, Deng D, Wang S, Yang Y. MicroRNAs in neuroblastoma: small-sized players with a large impact. Neurochem Res. 2014;39(4):613–23.

157. Xiang X, Mei H, Zhao X, Pu J, Li D, Qu H, Jiao W, Zhao J, Huang K, Zheng L, Tong Q. miRNA-337-3p suppresses neuroblastoma progression by repressing the transcription of matrix metalloproteinase 14. Oncotarget. 2015;6(26):22452–66.

158. Xiang X, Mei H, Qu H, Zhao X, Li D, Song H, Jiao W, Pu J, Huang K, Zheng L, Tong Q. miRNA-584-5p exerts tumor suppressive functions in human neuroblastoma through repressing transcription of matrix metalloproteinase 14. Biochim Biophys Acta. 2015;1852(9):1743–54.

159. Wu K, Yang L, Chen J, Zhao H, Wang J, Xu S, Huang Z. miR-362-5p inhibits proliferation and migration of neuroblastoma cells by targeting phosphatidylinositol 3-kinase-C2beta. FEBS Lett. 2015;589(15):1911–9.

160. Althoff K, Lindner S, Odersky A, Mestdagh P, Beckers A, Karczewski S, Molenaar JJ, Bohrer A, Knauer S, Speleman F, Epple M, Kozlova D, Yoon S, Baek K, Vandesompele J, Eggert A, et al. miR-542-3p exerts tumor suppressive functions in neuroblastoma by downregulating Survivin. Int J Cancer. 2015;136(6):1308–20.

161. Zhang H, Liu T, Yi S, Gu L, Zhou M. Targeting MYCN IRES in MYCN-amplified neuroblastoma with miR-375 inhibits tumor growth and sensitizes tumor cells to radiation. Mol Oncol. 2015;9(7):1301–11.

162. Qu H, Zheng L, Pu J, Mei H, Xiang X, Zhao X, Li D, Li S, Mao L, Huang K, Tong Q. miRNA-558 promotes tumorigenesis and aggressiveness of neuroblastoma cells through activating the transcription of heparanase. Hum Mol Genet. 2015;24(9):2539–51.

163. Li Y, Li W, Zhang JG, Li HY, Li YM. Downregulation of tumor suppressor menin by miR-421 promotes proliferation and migration of neuroblastoma. Tumour Biol. 2014;35(10):10011–7.

164. Cole KA, Attiyeh EF, Mosse YP, Laquaglia MJ, Diskin SJ, Brodeur GM, Maris JM. A functional screen identifies miR-34a as a candidate neuroblastoma tumor suppressor gene. Mol Cancer Res. 2008;6(5):735–42.

165. Fontana L, Fiori ME, Albini S, Cifaldi L, Giovinazzi S, Forloni M, Boldrini R, Donfrancesco A, Federici V, Giacomini P, Peschle C, Fruci D. Antagomir-17-5p abolishes the growth of therapy-resistant neuroblastoma through p21 and BIM. PLoS One. 2008;3(5):e2236.

166. Mestdagh P, Bostrom AK, Impens F, Fredlund E, Van Peer G, De Antonellis P, von Stedingk K, Ghesquiere B, Schulte S, Dews M, Thomas-Tikhonenko A, Schulte JH, Zollo M, Schramm

A, Gevaert K, Axelson H, et al. The miR-17-92 microRNA cluster regulates multiple components of the TGF-beta pathway in neuroblastoma. Mol Cell. 2010;40(5):762–73.

167. De Brouwer S, Mestdagh P, Lambertz I, Pattyn F, De Paepe A, Westermann F, Schroeder C, Schulte JH, Schramm A, De Preter K, Vandesompele J, Speleman F. Dickkopf-3 is regulated by the MYCN-induced miR-17-92 cluster in neuroblastoma. Int J Cancer. 2012;130(11):2591–8.

168. Iyer MK, Niknafs YS, Malik R, Singhal U, Sahu A, Hosono Y, Barrette TR, Prensner JR, Evans JR, Zhao S, Poliakov A, Cao X, Dhanasekaran SM, Wu YM, Robinson DR, Beer DG, et al. The landscape of long noncoding RNAs in the human transcriptome. Nat Genet. 2015;47(3):199–208.

169. Mercer TR, Dinger ME, Mattick JS. Long non-coding RNAs: insights into functions. Nat Rev Genet. 2009;10(3):155–9.

170. Gupta RA, Shah N, Wang KC, Kim J, Horlings HM, Wong DJ, Tsai MC, Hung T, Argani P, Rinn JL, Wang Y, Brzoska P, Kong B, Li R, West RB, van de Vijver MJ, et al. Long non-coding RNA HOTAIR reprograms chromatin state to promote cancer metastasis. Nature. 2010;464(7291):1071–6.

171. Pandey RR, Mondal T, Mohammad F, Enroth S, Redrup L, Komorowski J, Nagano T, Mancini-Dinardo D, Kanduri C. Kcnq1ot1 antisense noncoding RNA mediates lineage-specific transcriptional silencing through chromatin-level regulation. Mol Cell. 2008;32(2):232–46.

172. Gibb EA, Brown CJ, Lam WL. The functional role of long non-coding RNA in human carcinomas. Mol Cancer. 2011;10:38.

173. Bejerano G, Pheasant M, Makunin I, Stephen S, Kent WJ, Mattick JS, Haussler D. Ultraconserved elements in the human genome. Science. 2004;304(5675):1321–5.

174. Scaruffi P, Stigliani S, Moretti S, Coco S, De Vecchi C, Valdora F, Garaventa A, Bonassi S, Tonini GP. Transcribed-Ultra Conserved Region expression is associated with outcome in high-risk neuroblastoma. BMC Cancer. 2009;9:441.

175. Watters KM, Bryan K, Foley NH, Meehan M, Stallings RL. Expressional alterations in functional ultra-conserved non-coding RNAs in response to all-trans retinoic acid--induced differentiation in neuroblastoma cells. BMC Cancer. 2013;13:184.

176. Manolio TA, Collins FS, Cox NJ, Goldstein DB, Hindorff LA, Hunter DJ, McCarthy MI, Ramos EM, Cardon LR, Chakravarti A, Cho JH, Guttmacher AE, Kong A, Kruglyak L, Mardis E, Rotimi CN, et al. Finding the missing heritability of complex diseases. Nature. 2009;461(7265):747–53.

177. Bertone P, Stolc V, Royce TE, Rozowsky JS, Urban AE, Zhu X, Rinn JL, Tongprasit W, Samanta M, Weissman S, Gerstein M, Snyder M. Global identification of human transcribed sequences with genome tiling arrays. Science. 2004;306(5705):2242–6.

178. Russell MR, Penikis A, Oldridge DA, Alvarez-Dominguez JR, McDaniel L, Diamond M, Padovan O, Raman P, Li Y, Wei JS, Zhang S, Gnanchandran J, Seeger R, Asgharzadeh S, Khan J, Diskin SJ, et al. CASC15-S is a tumor suppressor lncRNA at the 6p22 neuroblastoma susceptibility locus. Cancer Res. 2015;75(15):3155–66.

179. Pandey GK, Mitra S, Subhash S, Hertwig F, Kanduri M, Mishra K, Fransson S, Ganeshram A, Mondal T, Bandaru S, Ostensson M, Akyurek LM, Abrahamsson J, Pfeifer S, Larsson E, Shi L, et al. The risk-associated long noncoding RNA NBAT-1 controls neuroblastoma progression by regulating cell proliferation and neuronal differentiation. Cancer Cell. 2014;26(5):722–37.

180. Liu PY, Erriquez D, Marshall GM, Tee AE, Polly P, Wong M, Liu B, Bell JL, Zhang XD, Milazzo G, Cheung BB, Fox A, Swarbrick A, Huttelmaier S, Kavallaris M, Perini G. Effects of a novel long noncoding RNA, lncUSMycN, on N-Myc expression and neuroblastoma progression. J Natl Cancer Inst. 2014;106(7):dju113.

181. Pandey GK, Kanduri C. Long noncoding RNAs and neuroblastoma. Oncotarget. 2015;6(21):18265–75.

182. Boumber Y, Issa JP. Epigenetics in cancer: what's the future? Oncology (Williston Park). 2011;25(3):220–6, 228.

183. Lawrence MS, Stojanov P, Polak P, Kryukov GV, Cibulskis K, Sivachenko A, Carter SL, Stewart C, Mermel CH, Roberts SA, Kiezun A, Hammerman PS, McKenna A, Drier Y, Zou L, Ramos AH, et al. Mutational heterogeneity in cancer and the search for new cancer-associated genes. Nature. 2013;499(7457):214–8.

184. Decock A, Ongenaert M, Cannoodt R, Verniers K, De Wilde B, Laureys G, Van Roy N, Berbegall AP, Bienertova-Vasku J, Bown N, Clement N, Combaret V, Haber M, Hoyoux C, Murray J, Noguera R, et al. Methyl-CpG-binding domain sequencing reveals a prognostic methylation signature in neuroblastoma. Oncotarget. 2015;7(2):1960–72.

185. Alaminos M, Davalos V, Cheung NK, Gerald WL, Esteller M. Clustering of gene hypermethylation associated with clinical risk groups in neuroblastoma. J Natl Cancer Inst. 2004;96(16):1208–19.

186. Asada K, Abe M, Ushijima T. Clinical application of the CpG island methylator phenotype to prognostic diagnosis in neuroblastomas. J Hum Genet. 2013;58(7):428–33.

187. Astuti D, Agathanggelou A, Honorio S, Dallol A, Martinsson T, Kogner P, Cummins C, Neumann HP, Voutilainen R, Dahia P, Eng C, Maher ER, Latif F. RASSF1A promoter region CpG island hypermethylation in phaeochromocytomas and neuroblastoma tumours. Oncogene. 2001;20(51):7573–7.

188. Teitz T, Wei T, Valentine MB, Vanin EF, Grenet J, Valentine VA, Behm FG, Look AT, Lahti JM, Kidd VJ. Caspase 8 is deleted or silenced preferentially in childhood neuroblastomas with amplification of MYCN. Nat Med. 2000;6(5):529–35.

189. Gonzalez-Gomez P, Bello MJ, Lomas J, Arjona D, Alonso ME, Aminoso C, Lopez-Marin I, Anselmo NP, Sarasa JL, Gutierrez M, Casartelli C, Rey JA. Aberrant methylation of multiple genes in neuroblastic tumours. relationship with MYCN amplification and allelic status at 1p. Eur J Cancer. 2003;39(10):1478–85.

190. Witt O, Deubzer HE, Lodrini M, Milde T, Oehme I. Targeting histone deacetylases in neuroblastoma. Curr Pharm Des. 2009;15(4):436–47.

191. Oehme I, Deubzer HE, Wegener D, Pickert D, Linke JP, Hero B, Kopp-Schneider A, Westermann F, Ulrich SM, von Deimling A, Fischer M, Witt O. Histone deacetylase 8 in neuroblastoma tumorigenesis. Clin Cancer Res. 2009;15(1):91–9.

192. Panicker J, Li Z, McMahon C, Sizer C, Steadman K, Piekarz R, Bates SE, Thiele CJ. Romidepsin (FK228/depsipeptide) controls growth and induces apoptosis in neuroblastoma tumor cells. Cell Cycle. 2010;9(9):1830–8.

193. Delcuve GP, Khan DH, Davie JR. Targeting class I histone deacetylases in cancer therapy. Expert Opin Ther Targets. 2013;17(1):29–41.

194. Schulte JH, Lim S, Schramm A, Friedrichs N, Koster J, Versteeg R, Ora I, Pajtler K, Klein-Hitpass L, Kuhfittig-Kulle S, Metzger E, Schule R, Eggert A, Buettner R, Kirfel J. Lysine-specific demethylase 1 is strongly expressed in poorly differentiated neuroblastoma: implications for therapy. Cancer Res. 2009;69(5):2065–71.

195. Cui H, Ma J, Ding J, Li T, Alam G, Ding HF. Bmi-1 regulates the differentiation and clonogenic self-renewal of I-type neuroblastoma cells in a concentration-dependent manner. J Biol Chem. 2006;281(45):34696–704.

196. Nuchtern JG, London WB, Barnewolt CE, Naranjo A, McGrady PW, Geiger JD, Diller L, Schmidt ML, Maris JM, Cohn SL, Shamberger RC. A prospective study of expectant observation as primary therapy for neuroblastoma in young infants: a Children's Oncology Group study. Ann Surg. 2012;256(4):573–80.

197. Strother DR, London WB, Schmidt ML, Brodeur GM, Shimada H, Thorner P, Collins MH, Tagge E, Adkins S, Reynolds CP, Murray K, Lavey RS, Matthay KK, Castleberry R, Maris JM, Cohn SL. Outcome after surgery alone or with restricted use of chemotherapy for patients with low-risk neuroblastoma: results of Children's Oncology Group study P9641. J Clin Oncol. 2012;30(15):1842–8.

198. Perez CA, Matthay KK, Atkinson JB, Seeger RC, Shimada H, Haase GM, Stram DO, Gerbing RB, Lukens JN. Biologic variables in the outcome of stages I and II neuroblastoma treated with surgery as primary therapy: a children's cancer group study. J Clin Oncol. 2000;18(1):18–26.
199. Matthay KK, Perez C, Seeger RC, Brodeur GM, Shimada H, Atkinson JB, Black CT, Gerbing R, Haase GM, Stram DO, Swift P, Lukens JN. Successful treatment of stage III neuroblastoma based on prospective biologic staging: a Children's Cancer Group study. J Clin Oncol. 1998;16(4):1256–64.
200. Bagatell R, Rumcheva P, London WB, Cohn SL, Look AT, Brodeur GM, Frantz C, Joshi V, Thorner P, Rao PV, Castleberry R, Bowman LC. Outcomes of children with intermediate-risk neuroblastoma after treatment stratified by MYCN status and tumor cell ploidy. J Clin Oncol. 2005;23(34):8819–27.
201. Baker DL, Schmidt ML, Cohn SL, Maris JM, London WB, Buxton A, Stram D, Castleberry RP, Shimada H, Sandler A, Shamberger RC, Look AT, Reynolds CP, Seeger RC, Matthay KK, Children's Oncology G. Outcome after reduced chemotherapy for intermediate-risk neuroblastoma. N Engl J Med. 2010;363(14):1313–23.
202. Pinto NR, Applebaum MA, Volchenboum SL, Matthay KK, London WB, Ambros PF, Nakagawara A, Berthold F, Schleiermacher G, Park JR, Valteau-Couanet D, Pearson AD, Cohn SL. Advances in risk classification and treatment strategies for neuroblastoma. J Clin Oncol. 2015;33(27):3008–17.
203. Pearson AD, Pinkerton CR, Lewis IJ, Imeson J, Ellershaw C, Machin D, European Neuroblastoma Study G, Children's C and Leukaemia G. High-dose rapid and standard induction chemotherapy for patients aged over 1 year with stage 4 neuroblastoma: a randomised trial. Lancet Oncol. 2008;9(3):247–56.
204. Matthay KK, Villablanca JG, Seeger RC, Stram DO, Harris RE, Ramsay NK, Swift P, Shimada H, Black CT, Brodeur GM, Gerbing RB, Reynolds CP. Treatment of high-risk neuroblastoma with intensive chemotherapy, radiotherapy, autologous bone marrow transplantation, and 13-cis-retinoic acid. Children's Cancer Group. N Engl J Med. 1999;341(16):1165–73.
205. London WB, Castel V, Monclair T, Ambros PF, Pearson AD, Cohn SL, Berthold F, Nakagawara A, Ladenstein RL, Iehara T, Matthay KK. Clinical and biologic features predictive of survival after relapse of neuroblastoma: a report from the International Neuroblastoma Risk Group project. J Clin Oncol. 2011;29(24):3286–92.
206. Suzuki M, Cheung NK. Disialoganglioside GD2 as a therapeutic target for human diseases. Expert Opin Ther Targets. 2015;19(3):349–62.
207. Svennerholm L, Bostrom K, Fredman P, Jungbjer B, Lekman A, Mansson JE, Rynmark BM. Gangliosides and allied glycosphingolipids in human peripheral nerve and spinal cord. Biochim Biophys Acta. 1994;1214(2):115–23.
208. Lammie G, Cheung N, Gerald W, Rosenblum M, Cordoncardo C. Ganglioside gd(2) expression in the human nervous-system and in neuroblastomas - an immunohistochemical study. Int J Oncol. 1993;3(5):909–15.
209. Battula VL, Shi Y, Evans KW, Wang RY, Spaeth EL, Jacamo RO, Guerra R, Sahin AA, Marini FC, Hortobagyi G, Mani SA, Andreeff M. Ganglioside GD2 identifies breast cancer stem cells and promotes tumorigenesis. J Clin Invest. 2012;122(6):2066–78.
210. Furukawa K, Hamamura K, Ohkawa Y, Ohmi Y, Furukawa K. Disialyl gangliosides enhance tumor phenotypes with differential modalities. Glycoconj J. 2012;29(8-9):579–84.
211. Julien S, Bobowski M, Steenackers A, Le Bourhis X, Delannoy P. How Do gangliosides regulate RTKs signaling? Cells. 2013;2(4):751–67.
212. Shibuya H, Hamamura K, Hotta H, Matsumoto Y, Nishida Y, Hattori H, Furukawa K, Ueda M, Furukawa K. Enhancement of malignant properties of human osteosarcoma cells with disialyl gangliosides GD2/GD3. Cancer Sci. 2012;103(9):1656–64.
213. Probstmeier R, Pesheva P. Tenascin-C inhibits beta1 integrin-dependent cell adhesion and neurite outgrowth on fibronectin by a disialoganglioside-mediated signaling mechanism. Glycobiology. 1999;9(2):101–14.

214. Cheung NK, Saarinen UM, Neely JE, Landmeier B, Donovan D, Coccia PF. Monoclonal antibodies to a glycolipid antigen on human neuroblastoma cells. Cancer Res. 1985;45(6):2642–9.
215. Thurin J, Thurin M, Kimoto Y, Herlyn M, Lubeck MD, Elder DE, Smereczynska M, Karlsson KA, Clark Jr WM, Steplewski Z, et al. Monoclonal antibody-defined correlations in melanoma between levels of GD2 and GD3 antigens and antibody-mediated cytotoxicity. Cancer Res. 1987;47(5):1229–33.
216. Mujoo K, Cheresh DA, Yang HM, Reisfeld RA. Disialoganglioside GD2 on human neuroblastoma cells: target antigen for monoclonal antibody-mediated cytolysis and suppression of tumor growth. Cancer Res. 1987;47(4):1098–104.
217. Cheung NK, Cheung IY, Kushner BH, Ostrovnaya I, Chamberlain E, Kramer K, Modak S. Murine anti-GD2 monoclonal antibody 3F8 combined with granulocyte-macrophage colony-stimulating factor and 13-cis-retinoic acid in high-risk patients with stage 4 neuroblastoma in first remission. J Clin Oncol. 2012;30(26):3264–70.
218. Yu AL, Gilman AL, Ozkaynak MF, London WB, Kreissman SG, Chen HX, Smith M, Anderson B, Villablanca JG, Matthay KK, Shimada H, Grupp SA, Seeger R, Reynolds CP, Buxton A, Reisfeld RA, et al. Anti-GD2 antibody with GM-CSF, interleukin-2, and isotretinoin for neuroblastoma. N Engl J Med. 2010;363(14):1324–34.
219. Streby KA, Shah N, Ranalli MA, Kunkler A, Cripe TP. Nothing but NET: a review of norepinephrine transporter expression and efficacy of 131I-mIBG therapy. Pediatr Blood Cancer. 2015;62(1):5–11.
220. DuBois SG, Matthay KK. Radiolabeled metaiodobenzylguanidine for the treatment of neuroblastoma. Nucl Med Biol. 2008;35 Suppl 1:S35–48.
221. Matthay KK, Yanik G, Messina J, Quach A, Huberty J, Cheng SC, Veatch J, Goldsby R, Brophy P, Kersun LS, Hawkins RA, Maris JM. Phase II study on the effect of disease sites, age, and prior therapy on response to iodine-131-metaiodobenzylguanidine therapy in refractory neuroblastoma. J Clin Oncol. 2007;25(9):1054–60.
222. Polishchuk AL, Dubois SG, Haas-Kogan D, Hawkins R, Matthay KK. Response, survival, and toxicity after iodine-131-metaiodobenzylguanidine therapy for neuroblastoma in preadolescents, adolescents, and adults. Cancer. 2011;117(18):4286–93.
223. Matthay KK, DeSantes K, Hasegawa B, Huberty J, Hattner RS, Ablin A, Reynolds CP, Seeger RC, Weinberg VK, Price D. Phase I dose escalation of 131I-metaiodobenzylguanidine with autologous bone marrow support in refractory neuroblastoma. J Clin Oncol. 1998;16(1):229–36.
224. Kraal KC, Tytgat GA, van Eck-Smit BL, Kam B, Caron HN, van Noesel M. Upfront treatment of high-risk neuroblastoma with a combination of 131I-MIBG and topotecan. Pediatr Blood Cancer. 2015;62(11):1886–91.
225. Ou SH, Bartlett CH, Mino-Kenudson M, Cui J, Iafrate AJ. Crizotinib for the treatment of ALK-rearranged non-small cell lung cancer: a success story to usher in the second decade of molecular targeted therapy in oncology. Oncologist. 2012;17(11):1351–75.
226. Bresler SC, Wood AC, Haglund EA, Courtright J, Belcastro LT, Plegaria JS, Cole K, Toporovskaya Y, Zhao H, Carpenter EL, Christensen JG, Maris JM, Lemmon MA, Mosse YP. Differential inhibitor sensitivity of anaplastic lymphoma kinase variants found in neuroblastoma. Sci Transl Med. 2011;3(108):108ra114.
227. Doebele RC, Pilling AB, Aisner DL, Kutateladze TG, Le AT, Weickhardt AJ, Kondo KL, Linderman DJ, Heasley LE, Franklin WA, Varella-Garcia M, Camidge DR. Mechanisms of resistance to crizotinib in patients with ALK gene rearranged non-small cell lung cancer. Clin Cancer Res. 2012;18(5):1472–82.
228. Mosse YP, Lim MS, Voss SD, Wilner K, Ruffner K, Laliberte J, Rolland D, Balis FM, Maris JM, Weigel BJ, Ingle AM, Ahern C, Adamson PC, Blaney SM. Safety and activity of crizotinib for paediatric patients with refractory solid tumours or anaplastic large-cell lymphoma: a Children's Oncology Group phase 1 consortium study. Lancet Oncol. 2013;14(6):472–80.

229. Awad MM, Shaw AT. ALK inhibitors in non-small cell lung cancer: crizotinib and beyond. Clin Adv Hematol Oncol. 2014;12(7):429–39.
230. Infarinato NR, Park JH, Krytska K, Ryles HT, Sano R, Szigety KM, Li Y, Zou HY, Lee NV, Smeal T, Lemmon MA, Mosse YP. The ALK/ROS1 inhibitor PF-06463922 overcomes primary resistance to crizotinib in ALK-driven neuroblastoma. Cancer Discov. 2015;6:96–107.
231. Carpenter EL, Haglund EA, Mace EM, Deng D, Martinez D, Wood AC, Chow AK, Weiser DA, Belcastro LT, Winter C, Bresler SC, Vigny M, Mazot P, Asgharzadeh S, Seeger RC, Zhao H, et al. Antibody targeting of anaplastic lymphoma kinase induces cytotoxicity of human neuroblastoma. Oncogene. 2012;31(46):4859–67.
232. Thiele CJ, Reynolds CP, Israel MA. Decreased expression of N-myc precedes retinoic acid-induced morphological differentiation of human neuroblastoma. Nature. 1985;313(6001):404–6.
233. Park JR, Eggert A, Caron H. Neuroblastoma: biology, prognosis, and treatment. Pediatr Clin North Am. 2008;55(1):97–120, x.
234. Prochownik EV, Vogt PK. Therapeutic targeting of Myc. Genes Cancer. 2010;1(6):650–9.
235. Zirath H, Frenzel A, Oliynyk G, Segerstrom L, Westermark UK, Larsson K, Munksgaard Persson M, Hultenby K, Lehtio J, Einvik C, Pahlman S, Kogner P, Jakobsson PJ, Henriksson MA. MYC inhibition induces metabolic changes leading to accumulation of lipid droplets in tumor cells. Proc Natl Acad Sci U S A. 2013;110(25):10258–63.
236. Puissant A, Frumm SM, Alexe G, Bassil CF, Qi J, Chanthery YH, Nekritz EA, Zeid R, Gustafson WC, Greninger P, Garnett MJ, McDermott U, Benes CH, Kung AL, Weiss WA, Bradner JE, et al. Targeting MYCN in neuroblastoma by BET bromodomain inhibition. Cancer Discov. 2013;3(3):308–23.
237. Henssen AG, Althoff K, Odersky A, Beckers A, Koche R, Speleman F, Schaefer S, Bell E, Nortmeyer M, Westermann F, De Preter K, Florin A, Heukamp L, Spruessel A, Astrahanseff K, Lindner S, et al. Targeting MYCN-driven transcription by BET-bromodomain inhibition. Clin Cancer Res. 2015;22(10):2470–81.
238. Chipumuro E, Marco E, Christensen CL, Kwiatkowski N, Zhang T, Hatheway CM, Abraham BJ, Sharma B, Yeung C, Altabef A, Perez-Atayde A, Wong KK, Yuan GC, Gray NS, Young RA, George RE. CDK7 inhibition suppresses super-enhancer-linked oncogenic transcription in MYCN-driven cancer. Cell. 2014;159(5):1126–39.
239. Hnisz D, Schuijers J, Lin CY, Weintraub AS, Abraham BJ, Lee TI, Bradner JE, Young RA. Convergence of developmental and oncogenic signaling pathways at transcriptional super-enhancers. Mol Cell. 2015;58(2):362–70.
240. Otto T, Horn S, Brockmann M, Eilers U, Schuttrumpf L, Popov N, Kenney AM, Schulte JH, Beijersbergen R, Christiansen H, Berwanger B, Eilers M. Stabilization of N-Myc is a critical function of Aurora A in human neuroblastoma. Cancer Cell. 2009;15(1):67–78.
241. Gustafson WC, Meyerowitz JG, Nekritz EA, Chen J, Benes C, Charron E, Simonds EF, Seeger R, Matthay KK, Hertz NT, Eilers M, Shokat KM, Weiss WA. Drugging MYCN through an allosteric transition in Aurora kinase A. Cancer Cell. 2014;26(3):414–27.
242. Chesler L, Schlieve C, Goldenberg DD, Kenney A, Kim G, McMillan A, Matthay KK, Rowitch D, Weiss WA. Inhibition of phosphatidylinositol 3-kinase destabilizes Mycn protein and blocks malignant progression in neuroblastoma. Cancer Res. 2006;66(16):8139–46.
243. Holzel M, Huang S, Koster J, Ora I, Lakeman A, Caron H, Nijkamp W, Xie J, Callens T, Asgharzadeh S, Seeger RC, Messiaen L, Versteeg R, Bernards R. NF1 is a tumor suppressor in neuroblastoma that determines retinoic acid response and disease outcome. Cell. 2010;142(2):218–29.
244. Jaboin J, Kim CJ, Kaplan DR, Thiele CJ. Brain-derived neurotrophic factor activation of TrkB protects neuroblastoma cells from chemotherapy-induced apoptosis via phosphatidylinositol 3'-kinase pathway. Cancer Res. 2002;62(22):6756–63.
245. Li Z, Jaboin J, Dennis PA, Thiele CJ. Genetic and pharmacologic identification of Akt as a mediator of brain-derived neurotrophic factor/TrkB rescue of neuroblastoma cells from chemotherapy-induced cell death. Cancer Res. 2005;65(6):2070–5.

246. Li Z, Zhang J, Liu Z, Woo CW, Thiele CJ. Downregulation of Bim by brain-derived neurotrophic factor activation of TrkB protects neuroblastoma cells from paclitaxel but not etoposide or cisplatin-induced cell death. Cell Death Differ. 2007;14(2):318–26.
247. Li Z, Thiele CJ. Targeting Akt to increase the sensitivity of neuroblastoma to chemotherapy: lessons learned from the brain-derived neurotrophic factor/TrkB signal transduction pathway. Expert Opin Ther Targets. 2007;11(12):1611–21.
248. Opel D, Poremba C, Simon T, Debatin KM, Fulda S. Activation of Akt predicts poor outcome in neuroblastoma. Cancer Res. 2007;67(2):735–45.
249. Izycka-Swieszewska E, Drozynska E, Rzepko R, Kobierska-Gulida G, Grajkowska W, Perek D, Balcerska A. Analysis of PI3K/AKT/mTOR signalling pathway in high risk neuroblastic tumours. Pol J Pathol. 2010;61(4):192–8.
250. Johnsen JI, Segerstrom L, Orrego A, Elfman L, Henriksson M, Kagedal B, Eksborg S, Sveinbjornsson B, Kogner P. Inhibitors of mammalian target of rapamycin downregulate MYCN protein expression and inhibit neuroblastoma growth in vitro and in vivo. Oncogene. 2008;27(20):2910–22.
251. Chanthery YH, Gustafson WC, Itsara M, Persson A, Hackett CS, Grimmer M, Charron E, Yakovenko S, Kim G, Matthay KK, Weiss WA. Paracrine signaling through MYCN enhances tumor-vascular interactions in neuroblastoma. Sci Transl Med. 2012;4(115):115ra113.
252. Westhoff MA, Faham N, Marx D, Nonnenmacher L, Jennewein C, Enzenmuller S, Gonzalez P, Fulda S, Debatin KM. Sequential dosing in chemosensitization: targeting the PI3K/Akt/mTOR pathway in neuroblastoma. PLoS One. 2013;8(12):e83128.
253. Bender A, Opel D, Naumann I, Kappler R, Friedman L, von Schweinitz D, Debatin KM, Fulda S. PI3K inhibitors prime neuroblastoma cells for chemotherapy by shifting the balance towards pro-apoptotic Bcl-2 proteins and enhanced mitochondrial apoptosis. Oncogene. 2011;30(4):494–503.
254. Li Z, Tan F, Liewehr DJ, Steinberg SM, Thiele CJ. In vitro and in vivo inhibition of neuroblastoma tumor cell growth by AKT inhibitor perifosine. J Natl Cancer Inst. 2010;102(11):758–70.
255. Li Z, Oh DY, Nakamura K, Thiele CJ. Perifosine-induced inhibition of Akt attenuates brain-derived neurotrophic factor/TrkB-induced chemoresistance in neuroblastoma in vivo. Cancer. 2011;117(23):5412–22.
256. Li Z, Yan S, Attayan N, Ramalingam S, Thiele CJ. Combination of an allosteric Akt Inhibitor MK-2206 with etoposide or rapamycin enhances the antitumor growth effect in neuroblastoma. Clin Cancer Res. 2012;18(13):3603–15.
257. Houghton PJ, Morton CL, Kolb EA, Gorlick R, Lock R, Carol H, Reynolds CP, Maris JM, Keir ST, Billups CA, Smith MA. Initial testing (stage 1) of the mTOR inhibitor rapamycin by the pediatric preclinical testing program. Pediatr Blood Cancer. 2008;50(4):799–805.
258. Kurmasheva RT, Harwood FC, Houghton PJ. Differential regulation of vascular endothelial growth factor by Akt and mammalian target of rapamycin inhibitors in cell lines derived from childhood solid tumors. Mol Cancer Ther. 2007;6(5):1620–8.
259. Zhang H, Dou J, Yu Y, Zhao Y, Fan Y, Cheng J, Xu X, Liu W, Guan S, Chen Z, Shi Y, Patel R, Vasudevan SA, Zage PE, Zhang H, Nuchtern JG. mTOR ATP-competitive inhibitor INK128 inhibits neuroblastoma growth via blocking mTORC signaling. Apoptosis. 2015;20(1):50–62.
260. Geoerger B, Kieran MW, Grupp S, Perek D, Clancy J, Krygowski M, Ananthakrishnan R, Boni JP, Berkenblit A, Spunt SL. Phase II trial of temsirolimus in children with high-grade glioma, neuroblastoma and rhabdomyosarcoma. Eur J Cancer. 2012;48(2):253–62.
261. Yan S, Li Z, Thiele CJ. Inhibition of STAT3 with orally active JAK inhibitor, AZD1480, decreases tumor growth in Neuroblastoma and Pediatric Sarcomas In vitro and In vivo. Oncotarget. 2013;4(3):433–45.
262. Hsu DM, Agarwal S, Benham A, Coarfa C, Trahan DN, Chen Z, Stowers PN, Courtney AN, Lakoma A, Barbieri E, Metelitsa LS, Gunaratne P, Kim ES, Shohet JM. G-CSF receptor posi-

tive neuroblastoma subpopulations are enriched in chemotherapy-resistant or relapsed tumors and are highly tumorigenic. Cancer Res. 2013;73(13):4134–46.

263. Agarwal S, Lakoma A, Chen Z, Hicks J, Metelitsa LS, Kim ES, Shohet JM. G-CSF promotes neuroblastoma tumorigenicity and metastasis via STAT3-dependent cancer stem cell activation. Cancer Res. 2015;75(12):2566–79.

264. Molenaar JJ, Koster J, Ebus ME, van Sluis P, Westerhout EM, de Preter K, Gisselsson D, Ora I, Speleman F, Caron HN, Versteeg R. Copy number defects of G1-cell cycle genes in neuroblastoma are frequent and correlate with high expression of E2F target genes and a poor prognosis. Genes Chromosomes Cancer. 2012;51(1):10–9.

265. Molenaar JJ, Ebus ME, Koster J, van Sluis P, van Noesel CJ, Versteeg R, Caron HN. Cyclin D1 and CDK4 activity contribute to the undifferentiated phenotype in neuroblastoma. Cancer Res. 2008;68(8):2599–609.

266. Gogolin S, Ehemann V, Becker G, Brueckner LM, Dreidax D, Bannert S, Nolte I, Savelyeva L, Bell E, Westermann F. CDK4 inhibition restores G(1)-S arrest in MYCN-amplified neuroblastoma cells in the context of doxorubicin-induced DNA damage. Cell Cycle. 2013;12(7):1091–104.

267. Rader J, Russell MR, Hart LS, Nakazawa MS, Belcastro LT, Martinez D, Li Y, Carpenter EL, Attiyeh EF, Diskin SJ, Kim S, Parasuraman S, Caponigro G, Schnepp RW, Wood AC, Pawel B, et al. Dual CDK4/CDK6 inhibition induces cell-cycle arrest and senescence in neuroblastoma. Clin Cancer Res. 2013;19(22):6173–82.

268. Cole KA, Huggins J, Laquaglia M, Hulderman CE, Russell MR, Bosse K, Diskin SJ, Attiyeh EF, Sennett R, Norris G, Laudenslager M, Wood AC, Mayes PA, Jagannathan J, Winter C, Mosse YP, et al. RNAi screen of the protein kinome identifies checkpoint kinase 1 (CHK1) as a therapeutic target in neuroblastoma. Proc Natl Acad Sci U S A. 2011;108(8):3336–41.

269. Walton MI, Eve PD, Hayes A, Valenti MR, De Haven Brandon AK, Box G, Hallsworth A, Smith EL, Boxall KJ, Lainchbury M, Matthews TP, Jamin Y, Robinson SP, Aherne GW, Reader JC, Chesler L, et al. CCT244747 is a novel potent and selective CHK1 inhibitor with oral efficacy alone and in combination with genotoxic anticancer drugs. Clin Cancer Res. 2012;18(20):5650–61.

270. Fouladi M, Park JR, Stewart CF, Gilbertson RJ, Schaiquevich P, Sun J, Reid JM, Ames MM, Speights R, Ingle AM, Zwiebel J, Blaney SM, Adamson PC. Pediatric phase I trial and pharmacokinetic study of vorinostat: a Children's Oncology Group phase I consortium report. J Clin Oncol. 2010;28(22):3623–9.

271. Mueller S, Yang X, Sottero TL, Gragg A, Prasad G, Polley MY, Weiss WA, Matthay KK, Davidoff AM, DuBois SG, Haas-Kogan DA. Cooperation of the HDAC inhibitor vorinostat and radiation in metastatic neuroblastoma: efficacy and underlying mechanisms. Cancer Lett. 2011;306(2):223–9.

272. Witt O, Milde T, Deubzer HE, Oehme I, Witt R, Kulozik A, Eisenmenger A, Abel U, Karapanagiotou-Schenkel I. Phase I/II intra-patient dose escalation study of vorinostat in children with relapsed solid tumor, lymphoma or leukemia. Klin Padiatr. 2012;224(6):398–403.

273. Jaboin J, Wild J, Hamidi H, Khanna C, Kim CJ, Robey R, Bates SE, Thiele CJ. MS-27-275, an inhibitor of histone deacetylase, has marked in vitro and in vivo antitumor activity against pediatric solid tumors. Cancer Res. 2002;62(21):6108–15.

274. Yang Q, Zage P, Kagan D, Tian Y, Seshadri R, Salwen HR, Liu S, Chlenski A, Cohn SL. Association of epigenetic inactivation of RASSF1A with poor outcome in human neuroblastoma. Clin Cancer Res. 2004;10(24):8493–500.

275. Charlet J, Schnekenburger M, Brown KW, Diederich M. DNA demethylation increases sensitivity of neuroblastoma cells to chemotherapeutic drugs. Biochem Pharmacol. 2012;83(7):858–65.

276. George RE, Lahti JM, Adamson PC, Zhu K, Finkelstein D, Ingle AM, Reid JM, Krailo M, Neuberg D, Blaney SM, Diller L. Phase I study of decitabine with doxorubicin and cyclophosphamide in children with neuroblastoma and other solid tumors: a Children's Oncology Group study. Pediatr Blood Cancer. 2010;55(4):629–38.
277. Krishnadas DK, Shusterman S, Bai F, Diller L, Sullivan JE, Cheerva AC, George RE, Lucas KG. A phase I trial combining decitabine/dendritic cell vaccine targeting MAGE-A1, MAGE-A3 and NY-ESO-1 for children with relapsed or therapy-refractory neuroblastoma and sarcoma. Cancer Immunol Immunother. 2015;64(10):1251–60.

Chapter 6
Molecular Genetics of Gastroenteropancreatic Neuroendocrine Tumours

Samuel Backman and Peyman Björklund

6.1 Introduction

The ultimate cause of tumor growth is the presence of genetic alterations that deregulate the normally tightly controlled cell division, cell growth, programmed cell death and tissue architecture [1]. In the specific case of neuroendocrine tumors (NETs), it has been clear for a long time that there is a hereditary component with, in particular pancreatic NETs (PNETs) occurring as a part of autosomal dominant syndromes. Several key genes and key pathways in neuroendocrine tumorigenesis have been identified in familial syndromes. More recently, large-scale whole-genome sequencing (WGS) and whole-exome sequencing (WES) studies, where the entire genome of a tumor or the coding fraction of it, respectively, have been resequenced, have helped shed further light on the genetic aetiology of NETs. However, much remains to be discovered, especially in non-pancreatic NETs, where the genetic drivers are still often completely unknown. This chapter attempts to provide an exposé of the current knowledge of genetics in gastroenteropancreatic neuroendocrine tumors.

6.2 Pancreatic Neuroendocrine Tumours

Pancreatic neuroendocrine tumors (PNETs) are uncommon tumors of the pancreas. PNETs are traditionally believed to arise from the pancreatic islets – the hormone-producing cell clusters that are intermixed with the exocrine pancreas and comprise

S. Backman, MB • P. Björklund, MD, PhD (✉)
Experimental Surgery, Department of Surgical Sciences, Uppsala University, Uppsala University Hospital, Building 70, 75185 Uppsala, Sweden
e-mail: samuel.backman@surgsci.uu.se; peyman.bjorklund@surgsci.uu.se

approximately 1 % of the cells in the pancreas. However, careful study of precursor lesions has suggested that at least some PNETs may be derived from non-islet structures, e.g. ductal cells [2, 3]. Significantly rarer than the more well-known and highly lethal exocrine pancreatic tumors, PNETs account for approximately 1–2 % of all pancreatic neoplasms. Pancreatic NETs may be hormonally silent, non-functioning (including tumors producing and secreting pancreatic polypeptide and or neurotensin, based on the absence of clinical symptoms), or produce any in a range of peptide hormones, including insulin, glucagon, VIP, somatostatin and gastrin as well as ectopic hormones. With the exception of insulin-producing PNETs (known as insulinomas), the tumors are often malignant, with frequent metastatic spread to the liver at the time of diagnosis [4]. The 10-year survival is currently estimated to around 34 % for functional tumors and 17 % for non-functional tumors [5].

6.2.1   Familial Syndromes

It has been known for the better part of a century that PNETs occur in familial forms as part of several inherited genetic syndromes. The syndromes include multiple endocrine neoplasia type 1 (MEN1), von Hippel-Lindau disease, tuberous sclerosis and neurofibromatosis type 1 (also known as von Recklinghausen's disease). PNETs arising in the context of inherited syndromes occur at an earlier age than sporadic tumors [6, 7]. Management of the disease can be complicated by the presence of numerous lesions in multiple organs, for example, simultaneous lesions in the anterior pituitary gland, parathyroid glands and pancreas in MEN1. The hereditary natures of these disorders breed implications not just for the individual patients but also for their families; genetic testing of offspring is warranted.

6.2.1.1   Multiple Endocrine Neoplasia Type 1

Multiple endocrine neoplasia type 1 was first described as an autosomal dominant trait by Dr. Wermer in 1954 [8]. However, concomitant hyperplasia and/or neoplasia in the classic triad of the pancreas, anterior pituitary and parathyroid glands had been described in the medical literature prior to this [9]. In addition to pancreatic, pituitary, and parathyroid lesions, affected individuals may develop other tumors including thymic carcinoids, thyroid adenomas and adrenocortical tumors [10, 11]. In 1988, the *MEN1* gene was localized by deletion mapping to the long arm of chromosome 11, and it was demonstrated that the unaffected allele is lost in pancreatic lesions from affected kindred [12]. In 1990, *MEN1* was further determined to be located in a narrow region on chromosome 11q13 [13]. In 1997 the *MEN1* gene was cloned [14]. Subsequent to this, numerous deleterious mutations (the majority leading to a truncated protein) have been found in different affected families [15]. The penetrance of the disease is nearly complete [16]. PNETs occur in about 40 % of

patients with MEN1 [10]. A hallmark of MEN1-associated PNET is multiplicity; the pancreata of MEN1 patients often show multiple microadenomas, with one or a few larger NETs [17]. This can be contrasted with sporadic cases which present with a solitary lesion [7].

6.2.1.2   Von Hippel-Lindau Disease

Von Hippel-Lindau disease (VHL) is a highly penetrant autosomal dominant trait with a prevalence of 1/36,000 live births [18]. Affected individuals may develop hemangioblastomas, pheochromocytomas and endolymphatic sack tumors, in addition to various forms of pancreatic cysts and pancreatic neuroendocrine tumors [18]. PNETs have been determined to develop in 12–17 % of patients affected by VHL [19, 20]. The tumors are most frequently non-functional [21]. The *VHL* gene was localized and cloned in 1993 [22]. The protein functions as part of an E3 ubiquitin ligase [23] that is required for the degradation of hypoxia-inducible factor (HIF) [24]. In the absence of the functional protein, a pseudo-hypoxic state occurs, which drives cellular survival and proliferation. Thus, it plays the role of a tumor suppressor. Like *MEN1, VHL* follows Knudson's two-hit hypothesis, with the inherited wild-type allele being deleted in the tumors [6].

6.2.1.3   Tuberous Sclerosis

Tuberous sclerosis complex (TSC) is an autosomal dominant genetic syndrome which may involve development of multiple benign tumors in various organ systems as well as behavioural abnormalities, seizures and developmental delay [25]. The syndrome is caused by inactivating mutations in either *TSC1* on chromosome 9 [26] or *TSC2* on chromosome 16 [27]. The two genes encode the proteins hamartin and tuberin, respectively, which form a heterodimer that acts as a negative regulator of mTOR signalling [28]. The first report of a PNET in the context of tuberous sclerosis complex was published in 1959 [29]. Since then, a number of case reports describing PNETs in patients with TSC have been published. A recent review of the association between neuroendocrine tumors pinpointed PNETs as a likely rare feature of TSC [30]. The association is further corroborated by the presence of *TSC2* mutations in a subset of sporadic PNETs [31].

6.2.1.4   Neurofibromatosis Type 1

Neurofibromatosis type 1 (also known as von Recklinghausen's disease) is a common autosomal dominant disorder affecting 1 in 2500–3000 individuals [32]. Those affected have a characteristic appearance with a large numbers of café-au-lait spots and multiple cutaneous neurofibromas [33]. Other manifestations of the disease may include cognitive deficits [34] and several forms of malignant tumors including

gastrointestinal stromal tumors [35], gliomas [36] and pheochromocytomas [37]. The *NF1* gene locates to chromosome 17 and functions as a tumor suppressor [38]. Neurofibromin, the gene product, has GAP activity [39, 40] and functions as a negative regulator of the mitogenic Ras signalling pathways [41]. PNETs producing somatostatin or insulin have been described in patients with the NF1 syndrome [42]. Single case reports have described loss of NF1 immunoreactivity in tumor tissue from NF1 patients with pancreatic NETs, supporting a causal relation between the two entities [43, 44].

6.2.1.5   Other Syndromes

There are reports of PNETs occurring in other genetic syndromes than those discussed here. Since PNETs do occur sporadically, it is difficult to determine whether there is a true causal relationship or whether co-occurrence between two conditions arises by mere chance. Of interest is a recent report of a PNET in a patient with paraganglioma syndrome due to a germline mutation in *SDHD*. The wild-type allele was lost in the tumor tissue, and the tumor lacked immunoreactivity for SDHB, compatible with a causative role of the *SDHD* mutation [45, 46]. Inactivating mutations in *SDHD* lead to oncogenesis by causing accumulation of succinate in the cell. Succinate functions as an inhibitor of alfa-ketoglutarate-dependent enzymes that degrade hypoxia-inducible factor, thus causing a pseudo-hypoxic state [47, 48].

6.2.2   Sporadic Pancreatic Neuroendocrine Tumors

Sporadic PNETs have been shown to harbour mutations in many of the same genes as familial tumors, including *MEN1*, *TSC2* and *VHL*. Whole-exome sequencing studies have identified mutations in known cancer genes as well as in a novel PNET-specific gene, *YY1* [49–51].

6.2.2.1   *MEN1*

The *MEN1* gene, which when mutated in constitutional DNA gives rise to multiple endocrine neoplasia type 1, has been found to be mutated in sporadic PNETs not associated with MEN1 [52]. Estimates of the prevalence of *MEN1* mutations vary. A whole-exome sequencing study of non-functioning PNETs found somatic *MEN1* mutations in 44 % of tumors [31]. The prevalence of *MEN1* mutations is apparently lower in insulinomas than in other PNETs. One study found a mutation in one out of seven investigated tumors [50], while another found two mutated tumors among twelve investigated tumors [53], suggesting a *MEN1* mutation prevalence of around 15 % in sporadic insulinomas.

6.2.2.2 mTOR Pathway

mTOR, the mechanistic (formerly mammalian) target of rapamycin is a serine/threonine kinase which plays an integral role in coordinating several cellular processes, including protein synthesis, cell division, cellular metabolism and mRNA synthesis. Since the discovery of the mTOR protein, it has, together with its regulators, increasingly become recognized as a key player in several human diseases, including various cancers [54]. In cancers, inactivating mutations are frequently found in negative regulators of mTOR signalling, such as *PTEN* [55], *TSC1* and *TSC2*. Activating mutations are found in the positive mTOR regulator *PIK3CA* [56] but seldom in the *MTOR* [57] gene itself. In 2011 a whole-exome sequencing study of ten non-functioning pancreatic neuroendocrine tumors (with a verification cohort of an additional 58 PNETs) found frequent mutations in several genes in the mTOR pathway: *PTEN*, *PIK3CA* and *TSC2* [31]. In total these mutations appear to occur in 14 % of sporadic pancreatic neuroendocrine tumors. Consistent with the role of the mTOR pathway in PNETs, mTOR inhibitors such as everolimus have shown efficacy in treatment of pancreatic neuroendocrine tumors [58].

6.2.2.3 *ATRX/DAXX*

The same study that found mutations affecting the mTOR pathway in PNETs also identified mutually exclusive mutations in *ATRX* and *DAXX* in 42.6 % of the analysed tumors. Several of the mutations were frameshift insertions/deletions, and the affected tumors showed loss of immunoreactivity for the affected protein, indicating that they act as tumor suppressors. The proteins encoded by *ATRX* and *DAXX* interact and participate in chromatin remodelling [59]. Subsequent studies have coupled these mutations to an alternative lengthening of telomeres (ALT) phenotype [60, 61]. Similar mutations are also found in other tumors, including pheochromocytomas [62] and glioblastomas [63]. The prognostic value of *ATRX/DAXX* mutations in PNETs is unknown, with different studies reporting discrepant results [31, 60, 64].

6.2.2.4 *YY1* Mutations in Insulinomas

Three separate studies have identified a hotspot mutation (p.T327R) in the *YY1* gene in sporadic insulinomas [49–51]. *YY1* codes for the Yin Yang 1 protein, which is a zinc finger transcription factor. The mutated Yin Yang protein has a different DNA-binding motif than the wild-type protein and causes alterations in gene expression [50]. ADCY1 and CACNA2D2 which are implicated in the regulation of insulin secretion and cell proliferation were dramatically overexpressed in *YY1*-mutated tumors compared to *YY1*-wild-type tumors and were found to neighbour binding sites for mutant YY1 [50]. Clinically, patients with *YY1*-mutated insulinomas present at a later age than those with *YY1*-wild-type tumors in two of the above-mentioned studies [49, 51]. While one study found an association between

YY1 mutation and female gender [51], the other two studies report no such association [49, 50].

6.2.3 Chromosomal Aberrations in Pancreatic Neuroendocrine Tumours

Studies of chromosomal aberrations in PNETs have identified several recurrent chromosomal aberrations. A study analysing loss of heterozygosity in non-functioning PNETs using microsatellite markers found that the most frequently deleted chromosomal arms were 6q, 11q (both deleted in >60% of cases) followed by 11p, 20q and entire chromosome 21 (deleted in approximately 50% of cases) [65]. The study also concluded that non-functioning PNETs can be divided into two groups based on chromosomal aberrations: one with few and small aberrations and another with many aberrations often involving entire chromosomes, the latter having a worse prognosis.

6.2.4 Epigenetic Aberrations in Pancreatic Neuroendocrine Tumours

The presence of mutations in genes encoding epigenetic regulators suggests that epigenetic aberrations may play an important role in PNET development and progression. It has been demonstrated that PNETs often exhibit hypomethylation of *LINE 1* elements [66, 67], a retrotransposon known to be epigenetically altered in various human cancers. *RASSF1A* hypermethylation has been suggested to be an important event in pancreatic endocrine tumorigenesis [68–70]. However, it has also been demonstrated that while RASSF1A expression is inversely correlated with *RASSF1A* methylation, its expression is not silenced in PNETs [71]. Notably, the isoform RASSF1C appears to be overexpressed [71]. Furthermore, it has been shown that tumors harbouring mutations in *DAXX* (but not tumors with *ATRX* mutations) have global dysregulation of DNA methylation [64]. Epigenetic regulation of the long non-coding RNA MEG3 expression by menin has been suggested as a partial explanation for the tumor-suppressor function of *MEN1* [72].

6.3 Neuroendocrine Tumours of the Small Intestine

Small intestinal neuroendocrine tumors (SI-NETs, previously "midgut carcinoids") are the most common tumors of the small intestine. The disease is relatively rare with an incidence of about 1/100,000 per year [73]. Epidemiological

studies report an increasing incidence during the last half-century, likely due to improved diagnostics [73, 74]. The tumors arise from enterochromaffin cells in the midgut-derived parts of the gastrointestinal canal. While SI-NETs have significantly better outcomes and longer survival than adenocarcinomas of the small intestine, they may cause significant morbidity due to their frequent production of serotonin as well as their ability to cause mesenteric fibrosis, intestinal obstruction and metastases to the liver [75]. The serotonin production may give rise to the carcinoid syndrome which includes flushing and diarrhoea. In advanced cases right-sided heart failure (carcinoid heart disease) may develop [76].

6.3.1   Genetic Drivers

Despite great efforts during the last decades, the disease-causing genetic aberrations are yet to be discovered. One study which investigated 48 small intestinal neuroendocrine tumors using whole-exome sequencing found no recurrent protein-altering mutations [77]. A subsequent study utilizing whole-exome and whole-genome sequencing found recurrent mutations in *CDKN1B* in 8 % (14/180) of investigated SI-NETs [78]. *CDKN1B* encodes p27 which is a cyclin-dependent kinase inhibitor previously implicated in endocrine neoplasia [79, 80]. An independent replication study found mutations in tumors from 8.5 % (17/200) patients. However, the mutation was noted to be present only in some lesions from these patients and, in two cases, only in some parts of the lesions [81]. This heterogeneity suggests that the mutation is disease modifying rather than disease causing. No differences between the clinical characteristics of patients with *CDKN1B*-mutated tumors and those with non-mutated tumors were detected [81].

6.3.2   Chromosomal Aberrations in SI-NETs

While driver mutations are not yet known, recurrent chromosomal aberrations have been identified in SI-NETs. The most common aberration is loss of chromosome 18 [82] which occurs in 64–88 % of SI-NETs [82, 83]. The minimal overlapping region of losses in different tumors has been observed to be 18q22-18qter [84]. No recurrent mutation has yet been identified in this region. Tumors harbouring the chromosome 18 deletion have been suggested to constitute a subgroup with superior outcome [83]. A number of other recurrent copy number aberrations have been shown to occur in lower frequencies in SI-NETs, including LOH at chromosome 11 [84], as well as amplification of chromosomes 4, 5, 14 and 20 [78].

6.3.3   Epigenetics

Unsupervised hierarchical clustering of tumors analysed using DNA methylation microarrays has identified three distinct clusters with different clinical outcomes [83, 85], suggesting a role for DNA methylation in the pathogenesis of these tumors. However, identifying epigenetic aberrations of functional importance is made difficult by the lack of easily accessible normal enterochromaffin cells usable as controls.

6.3.4   Familial SI-NETs

While SI-NETs do not show as clear patterns of heredity as do PNETs, there are reports of familial forms in the literature. Additionally, population-based studies show familial aggregation with the next of kin to affected individuals experiencing a significantly increased risk of developing SI-NETs [86, 87]. A recent study of 33 families with multiple occurrences of small intestinal neuroendocrine tumors identified one family with a loss-of-function mutation in the gene *IPMK* which encodes the enzyme inositol polyphosphate multikinase [88]. In addition to its enzymatic activity, inositol polyphosphate multikinase has been shown to promote p53-mediated apoptosis, while deletion of the *IPMK* gene has been shown to increase cell viability [89]. No *IPMK* mutations were found in the other 32 investigated families [88], suggesting that *IPMK* mutations are a very rare cause of familial SI-NETs.

6.4   Other GEP-NETs

6.4.1   Gastric NETs

Gastric NETs comprise three distinct clinical groups [90]. Type 1 tumors occur in the context of atrophic gastritis. Type 2 tumors occur in the context of multiple endocrine neoplasia type 1 and Zollinger-Ellison syndrome (ZES). Chronic hypergastrinemia has been implicated in the pathogenesis of type 1 and type 2 gastric NETs. Type 3 tumors occur in the absence of other gastric pathology. It has been shown that gastric NETs occur more frequently in patients with MEN1-related ZES than in patients with sporadic ZES in whom gastric NETs are only rarely diagnosed [91, 92]. In addition, loss of heterozygosity at the *MEN1* locus has been found in type 2 lesions [93]. Together, these results strongly support a causal role for *MEN1* aberrations in the pathogenesis of gastric NETs. Apart from the involvement of *MEN1*, little is known about the genetic causes of these tumors.

6.4.2 Duodenal NETs

Neuroendocrine tumors in the duodenum include gastrinomas, somatostatinomas, duodenal NECs, non-functioning NETs as well as gangliocytic paragangliomas [94]. The genetics of these tumors has not been well studied. What is currently known is that a subset of gastrinomas arises in the context of MEN1 syndrome [95] and that some sporadic gastrinomas harbour somatic *MEN1* mutations [53]. Additionally, duodenal somastostinomas have been described as a rare feature of neurofibromatosis type 1 [42], and there are reports of duodenal NETs as a rare manifestation of von Hippel-Lindau disease [96, 97]. Also worth noting is the recently recognized Pacak-Zhuang syndrome, which consists of somatostatinoma, paraganglioma and polycythaemia. The syndrome is caused by stabilizing mutations in the *EPAS1* gene, which encodes the HIF2α protein [98].

6.4.3 Colorectal NETs

Neuroendocrine tumors of the colon and rectum together account for approximately half of all NETs of the digestive system [99]. Despite this, little if any is known about their genetic causes.

6.4.4 Appendiceal NETs

Appendiceal neuroendocrine tumors are typically asymptomatic and diagnosed incidentally after an appendectomy for an unrelated cause [100]. Little is known about any genetic aberrations they may harbour.

6.4.5 Neuroendocrine Carcinomas

Neuroendocrine carcinomas (NECs) or grade 3 neuroendocrine tumors are NETs which have a Ki-67 of 20 % or more [101, 102]. They are poorly differentiated, rapidly growing and associated with poor clinical outcome. It is not yet known which molecular derangements distinguish NECs from lower-grade NETs. However, colorectal NECs often present together with non-neuroendocrine cancers of the colon or rectum. It has been hypothesized that synchronous colorectal NECs and adenocarcinomas may be derived from the same precursor lesion. There is some evidence suggesting that colorectal NECs are genetically more similar to their non-neuroendocrine counterparts than to lower-grade NETs [103].

6.5 Concluding Remarks

During the last few years, the widespread employment of next-generation sequencing methods and DNA hybridization arrays for copy number and gene expression analyses have allowed extensive molecular characterization of several forms of tumors. In comparison, our understanding of the genetics of gastroenteropancreatic neuroendocrine is lagging behind, with the exception of PNETs and to some extent SI-NETs.

References

1. Hanahan D, Weinberg RA. The hallmarks of cancer. Cell. 2000;100(1):57–70.
2. Vortmeyer AO, et al. Non-islet origin of pancreatic islet cell tumors. J Clin Endocrinol Metab. 2004;89(4):1934–8.
3. Perren A, et al. Multiple endocrine neoplasia type 1 (MEN1): loss of one MEN1 allele in tumors and monohormonal endocrine cell clusters but not in islet hyperplasia of the pancreas. J Clin Endocrinol Metab. 2007;92(3):1118–28.
4. Kaltsas GA, Besser GM, Grossman AB. The diagnosis and medical management of advanced neuroendocrine tumors. Endocr Rev. 2004;25(3):458–511.
5. Halfdanarson TR, et al. Pancreatic neuroendocrine tumors (PNETs): incidence, prognosis and recent trend toward improved survival. Ann Oncol. 2008;19(10):1727–33.
6. Lubensky IA, et al. Multiple neuroendocrine tumors of the pancreas in von Hippel-Lindau disease patients: histopathological and molecular genetic analysis. Am J Pathol. 1998;153(1):223–31.
7. Crippa S, et al. Surgical management of insulinomas: short- and long-term outcomes after enucleations and pancreatic resections. Arch Surg. 2012;147(3):261–6.
8. Wermer P. Genetic aspects of adenomatosis of endocrine glands. Am J Med. 1954;16(3):363–71.
9. Underdahl LO, Woolner LB, Black BM. Multiple endocrine adenomas; report of 8 cases in which the parathyroids, pituitary and pancreatic islets were involved. J Clin Endocrinol Metab. 1953;13(1):20–47.
10. Thakker RV. Multiple endocrine neoplasia type 1 (MEN1). Best Pract Res Clin Endocrinol Metab. 2010;24(3):355–70.
11. Thakker RV, et al. Clinical practice guidelines for multiple endocrine neoplasia type 1 (MEN1). J Clin Endocrinol Metab. 2012;97(9):2990–3011.
12. Larsson C, et al. Multiple endocrine neoplasia type 1 gene maps to chromosome 11 and is lost in insulinoma. Nature. 1988;332(6159):85–7.
13. Bystrom C, et al. Localization of the MEN1 gene to a small region within chromosome 11q13 by deletion mapping in tumors. Proc Natl Acad Sci U S A. 1990;87(5):1968–72.
14. Chandrasekharappa SC, et al. Positional cloning of the gene for multiple endocrine neoplasia-type 1. Science. 1997;276(5311):404–7.
15. Lemos MC, Thakker RV. Multiple endocrine neoplasia type 1 (MEN1): analysis of 1336 mutations reported in the first decade following identification of the gene. Hum Mutat. 2008;29(1):22–32.
16. Machens A, et al. Age-related penetrance of endocrine tumours in multiple endocrine neoplasia type 1 (MEN1): a multicentre study of 258 gene carriers. Clin Endocrinol (Oxf). 2007;67(4):613–22.
17. Thompson NW, et al. MEN I pancreas: a histological and immunohistochemical study. World J Surg. 1984;8(4):561–74.

18. Lonser RR, et al. von Hippel-Lindau disease. Lancet. 2003;361(9374):2059–67.
19. Libutti SK, et al. Pancreatic neuroendocrine tumors associated with von Hippel Lindau disease: diagnostic and management recommendations. Surgery. 1998;124(6):1153–9.
20. Binkovitz LA, Johnson CD, Stephens DH. Islet cell tumors in von Hippel-Lindau disease: increased prevalence and relationship to the multiple endocrine neoplasias. AJR Am J Roentgenol. 1990;155(3):501–5.
21. Blansfield JA, et al. Clinical, genetic and radiographic analysis of 108 patients with von Hippel-Lindau disease (VHL) manifested by pancreatic neuroendocrine neoplasms (PNETs). Surgery. 2007;142(6):814–8; discussion 818 e1–2.
22. Latif F, et al. Identification of the von Hippel-Lindau disease tumor suppressor gene. Science. 1993;260(5112):1317–20.
23. Iwai K, et al. Identification of the von Hippel-lindau tumor-suppressor protein as part of an active E3 ubiquitin ligase complex. Proc Natl Acad Sci U S A. 1999;96(22):12436–41.
24. Maxwell PH, et al. The tumour suppressor protein VHL targets hypoxia-inducible factors for oxygen-dependent proteolysis. Nature. 1999;399(6733):271–5.
25. Crino PB, Nathanson KL, Henske EP. The tuberous sclerosis complex. N Engl J Med. 2006;355(13):1345–56.
26. van Slegtenhorst M, et al. Identification of the tuberous sclerosis gene TSC1 on chromosome 9q34. Science. 1997;277(5327):805–8.
27. European Chromosome 16 Tuberous Sclerosis Consortium. Identification and characterization of the tuberous sclerosis gene on chromosome 16. Cell. 1993;75(7):1305–15.
28. Tee AR, et al. Tuberous sclerosis complex-1 and −2 gene products function together to inhibit mammalian target of rapamycin (mTOR)-mediated downstream signaling. Proc Natl Acad Sci U S A. 2002;99(21):13571–6.
29. Gutman A, Leffkowitz M. Tuberous sclerosis associated with spontaneous hypoglycaemia. Br Med J. 1959;2(5159):1065–8.
30. Dworakowska D, Grossman AB. Are neuroendocrine tumours a feature of tuberous sclerosis? A systematic review. Endocr Relat Cancer. 2009;16(1):45–58.
31. Jiao Y, et al. DAXX/ATRX, MEN1, and mTOR pathway genes are frequently altered in pancreatic neuroendocrine tumors. Science. 2011;331(6021):1199–203.
32. Williams VC, et al. Neurofibromatosis type 1 revisited. Pediatrics. 2009;123(1):124–33.
33. North K. Neurofibromatosis type 1. Am J Med Genet. 2000;97(2):119–27.
34. Ozonoff S. Cognitive impairment in neurofibromatosis type 1. Am J Med Genet. 1999;89(1):45–52.
35. Maertens O, et al. Molecular pathogenesis of multiple gastrointestinal stromal tumors in NF1 patients. Hum Mol Genet. 2006;15(6):1015–23.
36. Listernick R, Charrow J, Gutmann DH. Intracranial gliomas in neurofibromatosis type 1. Am J Med Genet. 1999;89(1):38–44.
37. Bausch B, et al. Germline NF1 mutational spectra and loss-of-heterozygosity analyses in patients with pheochromocytoma and neurofibromatosis type 1. J Clin Endocrinol Metab. 2007;92(7):2784–92.
38. Wallace MR, et al. Type 1 neurofibromatosis gene: identification of a large transcript disrupted in three NF1 patients. Science. 1990;249(4965):181–6.
39. Ballester R, et al. The NF1 locus encodes a protein functionally related to mammalian GAP and yeast IRA proteins. Cell. 1990;63(4):851–9.
40. Xu GF, et al. The neurofibromatosis type 1 gene encodes a protein related to GAP. Cell. 1990;62(3):599–608.
41. Xu GF, et al. The catalytic domain of the neurofibromatosis type 1 gene product stimulates ras GTPase and complements ira mutants of S. cerevisiae. Cell. 1990;63(4):835–41.
42. Anlauf M, et al. Hereditary neuroendocrine tumors of the gastroenteropancreatic system. Virchows Arch. 2007;451 Suppl 1:S29–38.
43. Perren A, et al. Pancreatic endocrine tumors are a rare manifestation of the neurofibromatosis type 1 phenotype: molecular analysis of a malignant insulinoma in a NF-1 patient. Am J Surg Pathol. 2006;30(8):1047–51.

44. Nishi T, et al. A case of pancreatic neuroendocrine tumor in a patient with neurofibromatosis-1. World J Surg Oncol. 2012;10:153.

45. Niemeijer ND, et al. Succinate dehydrogenase (SDH)-deficient pancreatic neuroendocrine tumor expands the SDH-related tumor spectrum. J Clin Endocrinol Metab. 2015;100(10):E1386–93.

46. Gill AJ, et al. Immunohistochemistry for SDHB triages genetic testing of SDHB, SDHC, and SDHD in paraganglioma-pheochromocytoma syndromes. Hum Pathol. 2010;41(6):805–14.

47. King A, Selak MA, Gottlieb E. Succinate dehydrogenase and fumarate hydratase: linking mitochondrial dysfunction and cancer. Oncogene. 2006;25(34):4675–82.

48. Jochmanova I, et al. Hypoxia-inducible factor signaling in pheochromocytoma: turning the rudder in the right direction. J Natl Cancer Inst. 2013;105(17):1270–83.

49. Cao Y, et al. Whole exome sequencing of insulinoma reveals recurrent T372R mutations in YY1. Nat Commun. 2013;4:2810.

50. Cromer MK, et al. Neomorphic effects of recurrent somatic mutations in Yin Yang 1 in insulin-producing adenomas. Proc Natl Acad Sci U S A. 2015;112(13):4062–7.

51. Lichtenauer UD, et al. Frequency and clinical correlates of somatic Ying Yang 1 mutations in sporadic insulinomas. J Clin Endocrinol Metab. 2015;100(5):E776–82.

52. Hessman O, et al. Mutation of the multiple endocrine neoplasia type 1 gene in nonfamilial, malignant tumors of the endocrine pancreas. Cancer Res. 1998;58(3):377–9.

53. Zhuang Z, et al. Somatic mutations of the MEN1 tumor suppressor gene in sporadic gastrinomas and insulinomas. Cancer Res. 1997;57(21):4682–6.

54. Guertin DA, Sabatini DM. Defining the role of mTOR in cancer. Cancer Cell. 2007;12(1):9–22.

55. Li J, et al. PTEN, a putative protein tyrosine phosphatase gene mutated in human brain, breast, and prostate cancer. Science. 1997;275(5308):1943–7.

56. Samuels Y, et al. High frequency of mutations of the PIK3CA gene in human cancers. Science. 2004;304(5670):554.

57. Sato T, et al. Single amino-acid changes that confer constitutive activation of mTOR are discovered in human cancer. Oncogene. 2010;29(18):2746–52.

58. Yao JC, et al. Everolimus for advanced pancreatic neuroendocrine tumors. N Engl J Med. 2011;364(6):514–23.

59. Lewis PW, et al. Daxx is an H3.3-specific histone chaperone and cooperates with ATRX in replication-independent chromatin assembly at telomeres. Proc Natl Acad Sci U S A. 2010;107(32):14075–80.

60. Marinoni I, et al. Loss of DAXX and ATRX are associated with chromosome instability and reduced survival of patients with pancreatic neuroendocrine tumors. Gastroenterology. 2014;146(2):453–60. e5.

61. Heaphy CM, et al. Altered telomeres in tumors with ATRX and DAXX mutations. Science. 2011;333(6041):425.

62. Fishbein L, et al. Whole-exome sequencing identifies somatic ATRX mutations in pheochromocytomas and paragangliomas. Nat Commun. 2015;6:6140.

63. Schwartzentruber J, et al. Driver mutations in histone H3.3 and chromatin remodelling genes in paediatric glioblastoma. Nature. 2012;482(7384):226–31.

64. Pipinikas CP, et al. Epigenetic dysregulation and poorer prognosis in DAXX-deficient pancreatic neuroendocrine tumours. Endocr Relat Cancer. 2015;22(3):L13–8.

65. Rigaud G, et al. High resolution allelotype of nonfunctional pancreatic endocrine tumors: identification of two molecular subgroups with clinical implications. Cancer Res. 2001;61(1):285–92.

66. Stricker I, et al. Site- and grade-specific diversity of LINE1 methylation pattern in gastroenteropancreatic neuroendocrine tumours. Anticancer Res. 2012;32(9):3699–706.

67. Choi IS, et al. Hypomethylation of LINE-1 and Alu in well-differentiated neuroendocrine tumors (pancreatic endocrine tumors and carcinoid tumors). Mod Pathol. 2007;20(7):802–10.

68. Pizzi S, et al. RASSF1A promoter methylation and 3p21.3 loss of heterozygosity are features of foregut, but not midgut and hindgut, malignant endocrine tumours. J Pathol. 2005;206(4):409–16.

69. Liu L, et al. Epigenetic alterations in neuroendocrine tumors: methylation of RAS-association domain family 1, isoform A and p16 genes are associated with metastasis. Mod Pathol. 2005;18(12):1632–40.

70. Dammann R, et al. Frequent RASSF1A promoter hypermethylation and K-ras mutations in pancreatic carcinoma. Oncogene. 2003;22(24):3806–12.

71. Malpeli G, et al. Methylation-associated down-regulation of RASSF1A and up-regulation of RASSF1C in pancreatic endocrine tumors. BMC Cancer. 2011;11:351.

72. Modali SD, et al. Epigenetic regulation of the lncRNA MEG3 and its target c-MET in pancreatic neuroendocrine tumors. Mol Endocrinol. 2015;29(2):224–37.

73. Modlin IM, et al. A three-decade analysis of 3,911 small intestinal neuroendocrine tumors: the rapid pace of no progress. Am J Gastroenterol. 2007;102(7):1464–73.

74. Yao JC, et al. One hundred years after "carcinoid": epidemiology of and prognostic factors for neuroendocrine tumors in 35,825 cases in the United States. J Clin Oncol. 2008;26(18):3063–72.

75. Akerstrom G, et al. Management of midgut carcinoids. J Surg Oncol. 2005;89(3):161–9.

76. Boudreaux JP, et al. The NANETS consensus guideline for the diagnosis and management of neuroendocrine tumors: well-differentiated neuroendocrine tumors of the Jejunum, Ileum, Appendix, and Cecum. Pancreas. 2010;39(6):753–66.

77. Banck MS, et al. The genomic landscape of small intestine neuroendocrine tumors. J Clin Invest. 2013;123(6):2502–8.

78. Francis JM, et al. Somatic mutation of CDKN1B in small intestine neuroendocrine tumors. Nat Genet. 2013;45(12):1483–6.

79. Georgitsi M, et al. Germline CDKN1B/p27Kip1 mutation in multiple endocrine neoplasia. J Clin Endocrinol Metab. 2007;92(8):3321–5.

80. Pellegata NS, et al. Germ-line mutations in p27Kip1 cause a multiple endocrine neoplasia syndrome in rats and humans. Proc Natl Acad Sci U S A. 2006;103(42):15558–63.

81. Crona J, et al. Somatic mutations and genetic heterogeneity at the CDKN1B locus in small intestinal neuroendocrine tumors. Ann Surg Oncol. 2015;22 Suppl 3:1428–35.

82. Lollgen RM, et al. Chromosome 18 deletions are common events in classical midgut carcinoid tumors. Int J Cancer. 2001;92(6):812–5.

83. Karpathakis A, et al. Prognostic impact of novel molecular subtypes of small intestinal neuroendocrine tumor. Clin Cancer Res. 2016;22(1):250–8.

84. Kytola S, et al. Comparative genomic hybridization identifies loss of 18q22-qter as an early and specific event in tumorigenesis of midgut carcinoids. Am J Pathol. 2001;158(5):1803–8.

85. Verdugo AD, et al. Global DNA methylation patterns through an array-based approach in small intestinal neuroendocrine tumors. Endocr Relat Cancer. 2014;21(1):L5–7.

86. Neklason DW, et al. Evidence for a heritable contribution to neuroendocrine tumors of the small intestine. Endocr Relat Cancer. 2016;23(2):93–100.

87. Hemminki K, Li X. Familial carcinoid tumors and subsequent cancers: a nation-wide epidemiologic study from Sweden. Int J Cancer. 2001;94(3):444–8.

88. Sei Y, et al. A hereditary form of small intestinal carcinoid associated with a Germline Mutation in inositol polyphosphate multikinase. Gastroenterology. 2015;149(1):67–78.

89. Xu R, et al. Inositol polyphosphate multikinase is a coactivator of p53-mediated transcription and cell death. Sci Signal. 2013;6(269):ra22.

90. Rindi G, et al. Three subtypes of gastric argyrophil carcinoid and the gastric neuroendocrine carcinoma: a clinicopathologic study. Gastroenterology. 1993;104(4):994–1006.

91. Bordi C, et al. The antral mucosa as a new site for endocrine tumors in multiple endocrine neoplasia type 1 and Zollinger-Ellison syndromes. J Clin Endocrinol Metab. 2001;86(5):2236–42.

92. Lehy T, et al. Influence of multiple endocrine neoplasia type 1 on gastric endocrine cells in patients with the Zollinger-Ellison syndrome. Gut. 1992;33(9):1275–9.
93. Debelenko LV, et al. The multiple endocrine neoplasia type I gene locus is involved in the pathogenesis of type II gastric carcinoids. Gastroenterology. 1997;113(3):773–81.
94. Hoffmann KM, Furukawa M, Jensen RT. Duodenal neuroendocrine tumors: classification, functional syndromes, diagnosis and medical treatment. Best Pract Res Clin Gastroenterol. 2005;19(5):675–97.
95. Pipeleers-Marichal M, et al. Gastrinomas in the duodenums of patients with multiple endocrine neoplasia type 1 and the Zollinger-Ellison syndrome. N Engl J Med. 1990;322(11):723–7.
96. Karasawa Y, et al. Duodenal somatostatinoma and erythrocytosis in a patient with von Hippel-Lindau disease type 2A. Intern Med. 2001;40(1):38–43.
97. Maddock IR, et al. A genetic register for von Hippel-Lindau disease. J Med Genet. 1996;33(2):120–7.
98. Pacak K, et al. New syndrome of paraganglioma and somatostatinoma associated with polycythemia. J Clin Oncol. 2013;31(13):1690–8.
99. Modlin IM, Lye KD, Kidd M. A 5-decade analysis of 13,715 carcinoid tumors. Cancer. 2003;97(4):934–59.
100. Stinner B, Rothmund M. Neuroendocrine tumours (carcinoids) of the appendix. Best Pract Res Clin Gastroenterol. 2005;19(5):729–38.
101. Rindi G, et al. TNM staging of foregut (neuro)endocrine tumors: a consensus proposal including a grading system. Virchows Arch. 2006;449(4):395–401.
102. Rindi G, et al. TNM staging of midgut and hindgut (neuro) endocrine tumors: a consensus proposal including a grading system. Virchows Arch. 2007;451(4):757–62.
103. Takizawa N, et al. Molecular characteristics of colorectal neuroendocrine carcinoma; similarities with adenocarcinoma rather than neuroendocrine tumor. Hum Pathol. 2015;46(12):1890–900.

Chapter 7
Current and Future Radiopharmaceuticals in Neuroendocrine Tumor Imaging

Melpomeni Fani

7.1 Introduction

Neuroendocrine tumors (NETs) comprise a heterogeneous group of hormonally active and nonactive neoplasms characterized by their histopathologic pattern and endocrine metabolism [1]. NETs range from well-differentiated and slowly growing tumors to poorly differentiated, and rather aggressive, malignancies. They derive from endocrine stem cells of the amine precursor uptake and decarboxylation (APUD) system [2, 3] that are capable of producing polypeptide hormones and biogenic amines. The currently available radiopharmaceuticals for imaging NETs are based on these two characteristics and can be divided into: (a) radiolabeled peptide analogs of the natural hormones for imaging peptide receptors that are expressed in high density on the surface of NET cells and (b) radiolabeled amine precursors that image NET metabolism. In addition, traditional PET imaging with fluorine-18-fluorodeoxyglucose (^{18}F-FDG) may as well be used in the more aggressive forms of poorly differentiated NET due to the higher glucose turnover in these tumor cells. The radionuclides that are utilized in NET imaging are summarized in Table 7.1. It is worth mentioning that, independent from the radiopharmaceutical, improvements in the overall imaging performance have been achieved by combining the strengths of functional and anatomic modalities in a synergistic way. The developments of hybrid technologies, such as SPECT/CT, PET/CT, or PET/MRI, in nuclear medicine suffice to demonstrate the utility of a multimodal approach.

This chapter summarizes the established agents used for NET imaging. The main focus is on the imaging of peptide receptors, especially somatostatin receptors, with means of radiolabeled somatostatin analogs, by far the most advanced imaging

M. Fani

Division of Radiopharmaceutical Chemistry, Clinic of Radiology and Nuclear Medicine,
University Hospital of Basel, Petersgraben 4, 4031 Basel, Switzerland
e-mail: melpomeni.fani@usb.ch

Table 7.1 Radionuclides used in neuroendocrine tumors imaging

Single Photon Emission Computed Tomography (SPECT)				
Radionuclide	$T_{1/2}$ (h)	Decay mode (%)	E_γ (keV) (%)	Production mode
^{99m}Tc	6.02	IT (100) γ	141 (91)	^{99}Mo/^{99m}Tc generator
^{111}In	67.9	EC (100) Auger γ	171 (90) 245 (94)	Cyclotron
^{123}I	13.2	EC (100) γ	159 (84) 27 (71) 31 (16)	Cyclotron
Positron Emission Tomography (PET)				
Radionuclide	$T_{1/2}$ (h)	Decay mode (%)	$E_{\beta+}$ (keV) (%)	Production mode
^{18}F	1.83	β^+ (97) EC (3)	634 (97)	Cyclotron
^{11}C	0.34	β^+ (99.79) EC (0.21)	968 (100)	Cyclotron
^{68}Ga	1.13	β^+ (89) EC (11)	1899 (88)	^{68}Ge/^{68}Ga generator
^{64}Cu	12.7	β^+ (19) β^- (40) EC (41)	656 (18)	Cyclotron

β^+ decay is always accompanied by 512-keV annihilation γ-radiation
IT isomeric transition, *EC* electron capture

probes for NETs. This chapter discusses radiopharmaceuticals that have been or are used clinically and refers only selectively to preclinical developments. The chapter is authored from the perspective of the radiopharmaceutical design and development and not from the perspective of their clinical outcome.

7.2 Current Radiopharmaceuticals

7.2.1 Somatostatin Receptor Imaging

Despite the fact that NETs are clinically and pathologically heterogeneous, they share the unique feature of overexpressing somatostatin receptors (sstr). Five somatostatin receptor subtypes are known (sstr1–sstr5) with the sstr2 being the most prominent one in differentiated NETs [4]. However, different subtypes may be expressed concomitantly and in various combinations and frequencies on pathological targets [5, 6]. The somatostatin receptors belong to the family of G-protein-coupled receptors, located on the plasma membrane of the targeted tumor cell. The natural ligand somatostatin consists of two cyclic disulfide-containing peptide hormones, one with 14 amino acids (SS-14, Table 7.2) and one with 28 amino acids (SS-28).

Table 7.2 Somatostatin analogs that have been used in humans

Code	Chemical structure
SS-14	Ala-Gly-cyclo(Cys-Lys-Asn-Phe-Phe-Trp-Lys-Thr-Phe-Thr-Ser-Cys)
Somatostatin receptor agonists	
OC	D-Phe-cyclo(Cys-Phe-D-Trp-Lys-Thr-Cys)Thr(ol)
TOC	D-Phe-cyclo(Cys-Tyr-D-Trp-Lys-Thr-Cys)Thr(ol)
TATE	D-Phe-cyclo(Cys-Tyr-D-Trp-Lys-Thr-Cys)Thr
HA-TATE	D-Phe-cyclo(Cys-3-Iodo-Tyr-D-Trp-Lys-Thr-Cys)Thr
Lanreotide	D-β-Nal-cyclo(Cys-Tyr-D-Trp-Lys-Val-Cys)-Thr-NH$_2$
NOC	D-Phe-cyclo(Cys-1-Nal-D-Trp-Lys-Thr-Cys)Thr(ol)
Somatostatin receptor antagonists	
BASS	p-NO$_2$-Phe-cyclo(D-Cys-Tyr-D-Trp-Lys-Thr-Cys)D-Tyr-NH$_2$
JR11	Cpa-cyclo[D-Cys-Aph(Hor)-D-Aph(Cbm)-Lys-Thr-Cys]-D-Tyr-NH$_2$

1-Nal 1-naphtyl-alanine, *Cpa* 4-Cl-phenylalanine, *Aph*(*Hor*) 4-amino-L-hydroorotyl-phenylalanine, d-*Aph*(*Cbm*) D-4-amino-carbamoyl-phenylalanine

Somatostatin itself turned out to be unsuitable for *in vivo* use as it has a short plasma half-life of about 3 min. Somatostatin analogs more resistant to enzymatic degradation than somatostatin itself were developed by various modifications of the natural molecule. The introduction of D-amino acids for improved *in vivo* stability, the use of the minimal chain length for conserving the biological activity of the natural hormone, the hexapeptide lead structure Cys-Phe-D-Trp-Lys-Thr-Cys, and the systematic elongation of the N and C terminals allowed the Sandoz team in 1980 to characterize the most stable and active analog known as octreotide (OC) (Table 7.2).

7.2.1.1 Somatostatin Receptor Scintigraphy and SPECT/CT

Octreotide was conjugated at the N-terminus with the acyclic chelator diethylenetriaminepentaacetic acid (DTPA, Fig. 7.1) that is able to coordinate metals such as In^{3+}. Since the mid-1990s, the radiolabeled analog [^{111}In-DTPA^0]octreotide (OctreoScan®, Covidien, Petten, The Netherlands) is commercially available for somatostatin receptor scintigraphy. OctreoScan was the first peptide-based nuclear imaging probe approved by the US Food and Drug Administration (FDA) in 1994. The procedure guidelines for tumor imaging with OctreoScan have been described by the European Association of Nuclear Medicine (EANM) [7]. OctreoScan is used mainly in midgut carcinoid, pancreatic NET, and neuroblastoma but also in growth
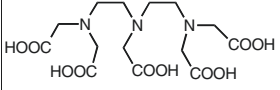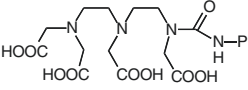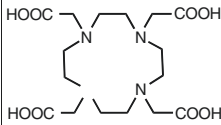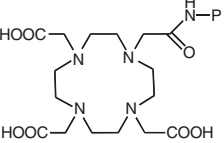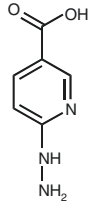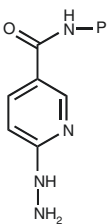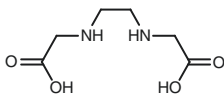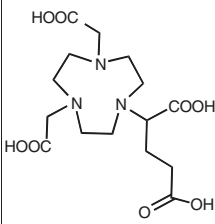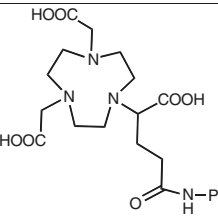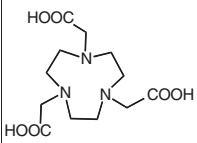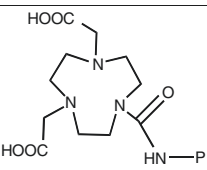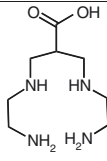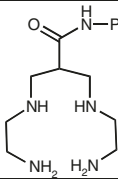
Chelator	Structure	Chelator-Peptide (P) conjugate	Radionuclide
DTPA			^{111}In
DOTA			^{111}In, ^{68}Ga, ^{64}Cu
HYNIC			^{99m}Tc
EDDA			
NODAGA			^{68}Ga
NOTA			^{68}Ga
N4			^{99m}Tc

Fig. 7.1 Chelators of clinically used radiopharmaceuticals for neuroendocrine tumors imaging

Table 7.3 Affinity profiles (IC_{50}) for human sstr1–sstr5 of a series of somatostatin analogs and their metallated conjugates that have been used clinically in neuroendocrine tumors imaging

Somatostatin analog	sstr1	sstr2	sstr3	sstr4	sstr5
Agonists					
DTPA-octreotide[a]	>10,000	12±2	376±84	>1000	299±50
In-DTPA-octreotide[a]	>10,000	22±3.6	182±13	>1000	237±52
DOTA-TOC[a]	>10,000	14±2.6	880±324	>1000	393±84
Ga-DOTA-TOC[a]	>10,000	2.5±0.5	613±140	>1000	73±21
DOTA-TATE[a]	>10,000	1.5±0.4	>1000	453±176	547±160
Ga-DOTA-TATE[a]	>10,000	0.20±0.04	>1000	300±140	377±18
DOTA-lanreotide[a]	>10,000	26±3.4	771±229	>10,000	73±12
Ga-DOTA-NOC[b]	>10,000	1.9±0.4	40.0±5.8	260±74	7.2±1.6
Antagonists					
DOTA-BASS[c]	>1000	1.5±0.4	>1000	287±27	>1000
In-DOTA-BASS[c]	>1000	9.4±0.4	>1000	380±57	>1000
DOTA-JR11[d]	>1000	0.72±0.12	>1000	>1000	>1000
In-DOTA-JR11[d]	>1000	3.8±0.7	>1000	>1000	>1000
Ga-DOTA-JR11[d]	>1000	29±2.7	>1000	>1000	>1000
Lu-DOTA-JR11[d]	>1000	0.73±0.15	>1000	>1000	>1000
NODAGA-JR11[d]	>1000	4.1±0.2	>1000	>1000	>1000
Ga-NODAGA-JR11[d]	>1000	1.2±0.2	>1000	>1000	>1000

All values are IC_{50}±SEM in n*M*

[a]Data are from Reubi et al. [10]

[b]Data are from Antunes et al. [29]

[c]Data are from Ginj et al. [72]

[d]Data are from Fani et al. [39]

hormone-secreting pituitary tumors, paraganglioma, medullary thyroid carcinoma, pheochromocytoma, meningioma, and Merkel cell tumors [8] and became an integral part of the management of NET patients [9].

[^{111}In-DTPA^0]octreotide has moderate binding affinity to sstr2 (Table 7.3). The replacement of Phe^3 in octreotide by Tyr^3 (TOC, Table 7.2) led to an improved sstr2 affinity (Table 7.3), while the C-terminal introduction of Thr^8 (TATE, Table 7.2) for Thr(ol)^8 (TOC) resulted in a further improvement of the sstr2 affinity (Table 7.3) [10]. On the other hand, DTPA is not a suitable chelator for other 3+ radiometals, such as ^{68}Ga, ^{90}Y, or ^{177}Lu. The chelator 1,4,7,10-tetraazacyclododecane-1,4,7,10-tetraacetic acid (DOTA, Fig. 7.1) has replaced DTPA, as it forms thermodynamically and kinetically stable complexes with a series of 3+ radiometals, including ^{111}In, ^{68}Ga, ^{90}Y, and ^{177}Lu. Both somatostatin conjugates DOTA-TOC and DOTA-TATE, labeled with ^{111}In, appeared to be nearly equivalent in a head-to-head comparison [11]. However, their use in SPECT imaging of NETs has been limited. To circumvent the drawbacks of ^{111}In, such as cost, limited availability, and high radiation burden, TOC was conjugated to an efficient bifunctional chelator for the generator-produced ^{99m}Tc, namely, hydrazinonicotinamide (HYNIC, Fig. 7.1). ^{99m}Tc-EDDA/HYNIC-TOC (EDDA, ethylenediamine-N,N'-diacetic acid acting as a coligand for ^{99m}Tc labeling, Fig. 7.1) was granted marketing authorization and

became commercially available in some European countries, under the commercial name 99mTc-Tektrotyd. Later on, 99mTc-EDDA/HYNIC-TATE was also developed. The two 99mTc-labeled analogs have similar performance and seem to have better or at least comparable sensitivities to OctreoScan [12–15].

Historically, the first 99mTc-based somatostatin analog was 99mTc-depreotide (NeoTect (Diatide Inc.); NeoSpect (Nycomed)), with the peptide sequence Lys-Cys-Lys-(beta-DAP)-CH$_2$CO-S-cyclo(hCys-(N-Me)Phe-Tyr-Trp-Lys-Val) that is actually a non-octreotide-based analog. FDA approved 99mTc-depreotide in 1999 for the detection of lung cancer in patients with pulmonary nodules [16]. However, its use was rather constrained, compared to OctreoScan, mainly due to the relatively high activity in the abdomen limiting its value in the diagnosis of abdominal NETs. 111In-DOTA-lanreotide (Table 7.2) is another somatostatin receptor imaging agent with a slight different affinity profile than OctreoScan (Table 7.3) [10]. In comparison with OctreoScan, it has a lower sensitivity in demonstrating neuroendocrine tumors, but it may have advantages in other tumors, for instance, in differentiated thyroid cancer [17]. 99mTc-depreotide and 111In-DOTA-lanreotide are not ideally suited for imaging abdominal NET primarily because of their diminished sensitivity compared to OctreoScan. OctreoScan has covered for many years the medical need of imaging NETs, and many clinical centers still use it, not only because it is readily available but also because it may adequately answer the question whether a patient is suitable for radionuclide therapy. However, somatostatin receptor imaging is rapidly "switching" to the use of PET tracers.

7.2.1.2   Somatostatin Receptor PET/CT

Within the last 10 years, the fast progression in NET imaging came together with the accelerated development of 68Ga radiochemistry/radiopharmacy. It combined, on one side, the advantages of PET over SPECT (100–1000-fold higher sensitivity, absolute quantitation, and shorter scanning time) and, on the other side, the advantages of using 68Ga-based radiopharmaceuticals [18–21]. 68Ga is produced from a long-lived 68Ge/68Ga generator that makes it available, rather inexpensive and independent of an on-site cyclotron or a reactor. Ultimately, 68Ga radiopharmacy is possible in each hospital. 68Ga has a short half-life of 68 min that is compatible with the relatively fast uptake mechanism of small peptides, such as the somatostatin analogs, that are transported to target tissues via the blood circulation. Thus, compared to 111In, it allows investigations to be completed within 1–3 h while decreasing the radiation dose to the patient by a factor 2–3. Impressive progress in 68Ga radiochemistry and chelation chemistry has been achieved over the last few years due to the success and high potency of the first 68Ga radiopharmaceuticals, especially the first 68Ga-labeled somatostatin analog DOTA-TOC [22, 23]. Logically, 68Ga-labeling of DOTA-TATE followed. Between these two radiopharmaceuticals, 68Ga-DOTA-TATE showed a tenfold higher affinity to sstr2 *in vitro*, compared with 68Ga-DOTA-TOC (Table 7.3) [10]. Despite its higher affinity, 68Ga-DOTA-TATE was not proven to be superior to 68Ga-DOTA-TOC in PET/CT imaging of NET patients, on the

contrary, an opposite tendency was observed [24, 25]. Very recently, the so-called high-affinity TATE (HA-TATE, a TATE analog in which Tyr[3] is iodinated, Table 7.2) labeled with ^{68}Ga has been proposed as an adequate, freely available substitute for ^{68}Ga-DOTA-TATE since its use is not governed by patent restrictions [26]. The sstr2 affinities of Ga-HA-DOTA-TATE and Ga-DOTA-TATE ($IC_{50} = 1.4 \pm 0.8$ nM and 1.2 ± 0.6 nM, respectively) were nearly identical [27].

Modifications of the octreotide at position 3 by introducing the unnatural amino acid 1-naphthyl-alanine (1-NaI) led to the analog NOC (Table 7.2), with affinity not only for the sstr2 but also for sstr3 and sstr5 (Table 7.3) [28, 29]. In theory, ^{68}Ga-DOTA-NOC may have the advantage over ^{68}Ga-DOTA-TOC and ^{68}Ga-DOTA-TATE by targeting a broader spectrum of various tumors or by increasing the tumor uptake in tumor cell coexpressing simultaneously several receptor subtypes. However, head-to-head comparative studies of ^{68}Ga-DOTA-NOC vs ^{68}Ga-DOTA-TATE have shown discrepant results [30, 31].

All three somatostatin conjugates DOTA-TOC, DOTA-TATE, and DOTA-NOC, labeled with ^{68}Ga, are routinely used for PET imaging of NET patients in many hospitals, especially in Europe [32]. The European Association of Nuclear Medicine (EANM) has currently published procedure guidelines on PET/CT tumor imaging using any of the three mentioned PET tracers [33]. Currently, there is no strong clinical evidence on the superiority of one analog over the others [34]. None of the three PET tracers is registered, and both, ^{68}Ga-DOTA-TOC and ^{68}Ga-DOTA-TATE, have received "Orphan Drug Designation" as diagnostic agents for the management of patients with neuroendocrine tumors (NETs) by the US Food and Drug Administration. It also exists a European Pharmacopeia monograph for "gallium (^{68}Ga) edotreotide injection" (N° 2482) and one for "gallium (^{68}Ga) chloride solution for radiolabeling" (N° 2464).

Recently, DOTA-TATE labeled with ^{64}Cu has been used for PET imaging of NETs [35, 36]. The rational of using ^{64}Cu, instead of ^{68}Ga, lies on delayed imaging due to longer half-life of [64]Cu (12.7 h, see also Table 7.1), better resolution, and avoiding the in-house preparation shortly before application. ^{64}Cu-DOTA-TATE was shown to be by far superior to OctreoScan in the diagnostic performance in NET patients in a head-to-head comparison [35]. Whether ^{64}Cu-labeled analogs have any advantage over the ^{68}Ga-labeled counterparts is not known since so far not head-to-head comparison has been performed. However, one could argue that DOTA is far from being an ideal chelator for ^{64}Cu, due to the possible transchelation of ^{64}Cu and therefore the rather limited *in vivo* stability of the ^{64}Cu-DOTA complex [37, 38]. Indication of the *in vivo* instability is the accumulation of radioactivity in the liver over time, as shown in many preclinical studies. That may explain the moderate to high liver uptake initially observed in patients where ^{64}Cu-DOTA-TATE was administered [36]. Nowadays, a number of chelators tailored for ^{64}Cu are available, and the *in vivo* stability of ^{64}Cu-labeled somatostatin analogs can be significantly improved, important especially when delayed images are desired. On the other hand, one should be aware that the choice of the chelator, but also of the radiometal, may influence critical properties of the radiotracer, such as affinity, pharmacokinetics, and others [10, 29, 39, 40].

There is no doubt that ^{68}Ga-labeled somatostatin analogs represent a significant evolution in somatostatin receptor imaging over OctreoScan. They have shown higher sensitivity compared with OctreoScan [41] but also with other tracers used for imaging of NETs that will be discussed later, such as ^{18}F-FDG (particularly in well-differentiated tumors) [42, 43], ^{18}F-DOPA [44–46], and also ^{123}I-MIBG [47, 48]. It seems reasonable that, if available, PET/CT with ^{68}Ga-labeled somatostatin analogs should be the image modality of choice for somatostatin receptor imaging in the future. Moreover, the preparation of ^{68}Ga radiopharmaceuticals is amenable to automation and approaches the kit-type preparation.

The success of ^{68}Ga-DOTA-somatostatin analogs also relies on the fact that the chelator DOTA forms stable complexes with important therapeutic radionuclides, such as ^{177}Lu, ^{90}Y, and others. This allows the same DOTA-conjugated analog to be used either for PET imaging, when labeled with ^{68}Ga, or for Peptide Receptor Radionuclide Therapy (PRRT), when labeled with a therapeutic radionuclide. This theranostic approach, in analogy to what has been used for decades with the various isotopes of iodine in the field of thyroid cancer, has been extremely valuable in the field of NET especially in the era of precision medicine. Somatostatin receptor imaging has paved the way for other radionuclide imaging systems and particularly in the development of different peptide-based radiopharmaceuticals (see Sects. 7.3.2 and 7.3.3).

7.2.2   Metabolic Imaging

7.2.2.1   ^{18}F-Fluorodeoxyglucose (^{18}F-FDG) PET/CT

The most widely used PET radiopharmaceutical in daily practice is 2-deoxy-2-(^{18}F) fluoro-D-glucose or ^{18}F-fluorodeoxyglucose (^{18}F-FDG), a glucose analog in which the 2' hydroxyl group (−OH) has been substituted by [18]F (Fig. 7.2). ^{18}F-FDG is taken up by glucose transporters and phosphorylated by the hexokinase enzyme. Once phosphorylated it is not further metabolized thus trapped in the cell [15]. ^{18}F-FDG was actually the first PET radiopharmaceutical to be used for detecting NETs [49]. However, in contrast to the wide use of ^{18}F-FDG in numerous types of tumors, its role in imaging of NETs is rather limited. The well-differentiated NETs (i.e., most GEP-NETs) have a normal or slightly increased glucose metabolism, and the sensitivity of ^{18}F-FDG is rather low for their detection. Therefore, ^{18}F-FDG is not routinely used for this purpose. In undifferentiated or poorly differentiated NETs that exhibit aggressive histologic features, ^{18}F-FDG PET seems to be the best choice since the expression of somatostatin receptors is less frequent, and therefore somatostatin receptor imaging is often negative [42, 43, 50]. Actually, ^{18}F-FDG PET imaging seems to have a complementary role with the first-choice diagnostic tool that is PET imaging with ^{68}Ga-labeled somatostatin analogs [42, 43, 51]. Negative ^{18}F-FDG PET results are predictive for low aggressiveness and a high survival rate, and conversely positive ^{18}F-FDG PET results identified cases with worse outcome
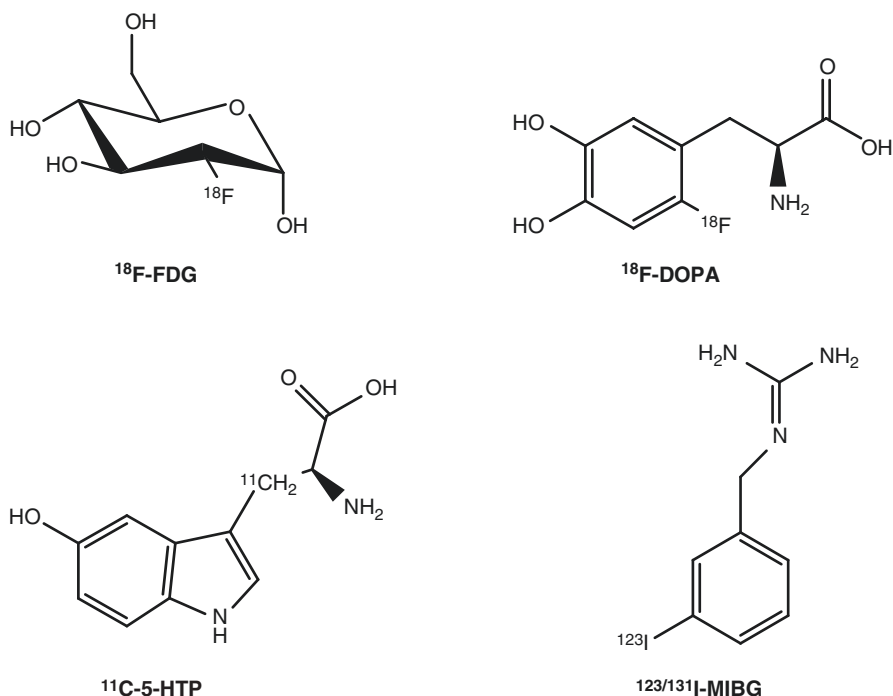
Fig. 7.2 Radiopharmaceuticals used for metabolic imaging of neuroendocrine tumors

[52–54]. Therefore, ^{18}F-FDG may retain an important role in managing NET patients mainly due to its prognostic value and its higher sensitivity in aggressive and high-grade tumors, rather than its role in the diagnosis and staging of NETs.

7.2.2.2 ^{18}F-L-Dihydroxyphenylalanine (^{18}F-DOPA) PET/CT

^{18}F-L-dihydroxyphenylalanine (^{18}F-DOPA) (Fig. 7.2) was initially introduced for studying the physiology and physiopathology of dihydroxyphenylalanine (DOPA) biodistribution in the human brain, in particular Parkinson's syndrome and then in oncology for imaging NETs or brain tumors. The use of ^{18}F-DOPA in NETs is based on the fact that neuroendocrine tumor cells take up and transport into the cytoplasm the dopamine precursor ^{18}F-DOPA via the cell membrane-bound L-type amino acid transporter (LAT) that is upregulated and highly active in these cells. Inside the cell ^{18}F-DOPA is decarboxylated (metabolized) by the aromatic acid decarboxylase (AADC) to ^{18}F-dopamine, which is transported into storage granules by vesicular monoamine transporter and trapped intracellularly [55]. ^{18}F-DOPA PET has shown very high sensitivity for both staging and restaging of NETs [56]. Compared to somatostatin receptor scintigraphy, ^{18}F-DOPA performs superior for the imaging of NETs, especially in carcinoid patients [57, 58]. Compared to PET imaging using

[68]Ga-labeled somatostatin analogs, ^{18}F-DOPA performed inferior in NET patients [44–46]. ^{18}F-DOPA PET showed relatively high sensitivity in congenital hyperinsulinism [59] and can be useful to study benign insulinomas, paragangliomas, and pheochromocytomas due to the variable expression of sstr in these tumors. Furthermore, ^{18}F-DOPA can be an option for imaging of serotonin-secreting, sstr-negative NETs.

The production of ^{18}F-DOPA by electrophilic fluorination requires modest radiochemistry expertise and is not widely established. However, nowadays, more and more centers are capable of producing ^{18}F-DOPA, and it is commercially available in several European countries. Contrary to ^{68}Ga-labeled somatostatin analogs, ^{18}F-DOPA lacks of a therapeutic counterpart.

7.2.2.3 ^{11}C-5-HTP

The PET radiopharmaceutical β-[^{11}C]-5-hydroxyl-L-tryptophan (^{11}C-5-HTP) (Fig. 7.2) is taken up via the L-amino acid transporter (LAT), it is decarboxylated by the aromatic L-amino acid decarboxylase ADCC, and the end product, serotonin, is transported via the vesicular monoamine transporter (VMAT) and stored into secretory vesicles. ^{11}C-5-HTP visualizes the serotonin pathway, which is active in many NETs. The published clinical results, even though limited, justify its use [57, 60–63]. In comparison with ^{18}F-DOPA and OctreoScan, ^{11}C-5-HTP seems to be best in pancreatic islet cell tumors, while ^{18}F-DOPA in staging of carcinoids [57], and it outperforms OctreoScan in the lesion-based detection, with high sensitivity in small NET lesions, such as primary tumor [63].

[11]C-5-HTP-PET/CT is a useful imaging technique, with higher sensitivity for pancreatic NETs, as opposed to carcinoids; however its routine clinical use is debatable. The synthesis of ^{11}C-HTP is very complex and it is only produced in a few specialized centers worldwide. Additionally, the short half-life of [11]C ($t_{1/2} = 20$ min, see also Table 7.1) demands an on-site cyclotron and production in close relation to the scan. These factors severely restrict its clinical use. Similarly to ^{18}F-DOPA, ^{11}C-5-HTP lacks of a therapeutic counterpart.

7.2.2.4 [123/131]I-Metaiodobenzylguanidine ([123/131]I-MIBG) Scintigraphy and SPECT/CT

Metaiodobenzylguanidine (MIBG) is a noradrenaline analog, containing a benzyl and a guanidine group (Fig. 7.2). MIBG labeled with ^{123}I is used for SPECT imaging of tumors that have an endocrine origin while when labeled with ^{131}I can also be used for therapy due to the concomitant beta emission. [123/131]I-MIBG is transported across the plasma membrane mainly by the human norepinephrine transporter (NET). Intracellularly, the vesicular monoamine transporters (VMATs) accumulate [123/131]I-MIBG in catecholamine-storing granules where it is not significantly metabolized [15, 64]. This mechanism provides specific accumulation of [123/131]I-MIBG in

neuroectodermally derived tumors, which made it attractive imaging method for neuroblastomas, paragangliomas, and pheochromocytomas. However, for the detection of GEP-NETs and bronchopulmonary NETs, its sensitivity is relatively low, and consequently it is not recommended for routine imaging of these tumors. The role of ^{123}I-MIBG is unsatisfactory when somatostatin receptor imaging and ^{18}F-FDG are available [65]. The main indication for ^{123}I-MIBG imaging is its use as companion diagnostics if internal radiotherapy with ^{131}I-MIGB is panned in cases of ^{123}I-MIBG-positive, sstr-negative NETs [66].

7.3   Future Radiopharmaceuticals

7.3.1   *Somatostatin Receptor Antagonists*

The radiolabeled somatostatin receptor antagonists represent the recent most favorable innovation in molecular imaging of NETs. All somatostatin analogs that are currently used in the clinic are agonists, which upon binding to the receptor are inducing internalization of the receptor-ligand complex. For years, internalization was thought to be of high importance for high- and long-lasting tumor uptake of the radioligand. However, a number of recent observations have challenged this paradigm. The *in vitro* evidence that antagonists may recognize a higher number of receptor-binding sites than agonists [67, 68] makes radiolabeled antagonists a very attractive tool for *in vivo* receptor targeting. Bass et al. published the first somatostatin-based antagonists in 1996 [69]. They found that in the hexapeptide core, disulfide cyclized, octapeptide series, the inversion of chirality at position 1 and 2 of the octreotide family converted an agonist into a potent antagonist. Later structure-activity-relationship studies by the group of Coy afforded new structures [70]. These antagonists were used as leads by J.E. Rivier (Salk Institute for Biological Studies, La Jolla, CA, USA), J.C. Reubi (University of Bern, Switzerland), and H.R. Maecke (University Hospital of Basel, Switzerland) in collaboration, for the development of new sstr antagonists, including DOTA-conjugates for radiolabeling [71, 72].

First *in vivo* preclinical studies with radiolabeled sstr2- and sstr3-selective antagonists (DOTA-BASS (Table 7.2) and sst3-ODN-8, respectively) showed that the antagonists were superior to agonists – even in case of agonists with higher receptor affinity – with regard to tumor uptake as well as tumor-to-nontumor uptake ratios [72]. *In vitro*, Scatchard analysis showed that, indeed, the radiolabeled antagonists recognize a higher number of receptor-binding sites than the agonists (higher B_{max}) [72, 73]. This was also confirmed by receptor autoradiography on human tumor tissues comparing the sstr2-antagonist DOTA-BASS and the sstr2-agonist DOTA-TATE, both labeled with [177]Lu [74]. Further studies demonstrated that this new class of compounds is extremely sensitive to modifications such as complexation with distinct radiometals or substituting a chelator by another. This may dramatically affect the affinity and pharmacokinetics of a given somatostatin receptor antagonist [39, 40].
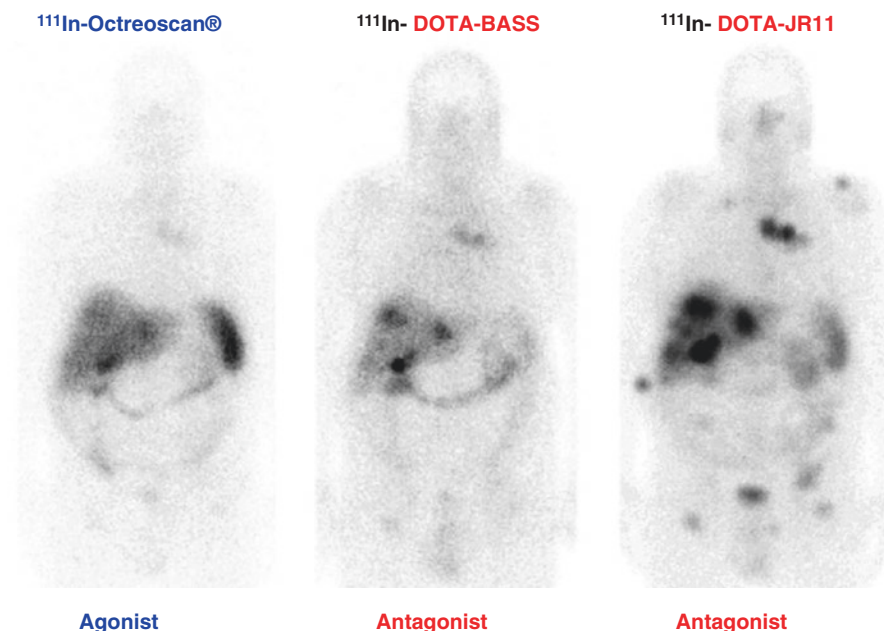
Fig. 7.3 Comparison of ^{111}In-DTPA-octreotide (OctreoScan) scintigraphy (sstr2 agonist), ^{111}In-DOTA-BASS scintigraphy (sstr2 antagonist), and ^{111}In-DOTA-JR11 scintigraphy (sstr2 antagonist), 24 h after injection in a patient with NET of unknown origin (G2). sstr2 antagonists, especially ^{111}In-DOTA-JR11, performed better than sstr2 agonist OctreoScan

The first clinical evidence that imaging of NETs with radiolabeled sstr2 antagonists is feasible was brought by a pilot study using ^{111}In-DOTA-BASS [75]. In this study the antagonist ^{111}In-DOTA-BASS had a favorable biodistribution profile – higher tumor uptake and lower normal organ uptake – than the agonist OctreoScan, resulting in a higher tumor detection rate. Further development of radiolabeled sstr2 antagonists afforded new analogs with improved affinity, compared to the first antagonist DOTA-BASS (Table 7.3), such as the analog DOTA-JR11 (Tables 7.2 and 7.3) [39]. A unique illustration of this development is given in Fig. 7.3, which shows the performance of OctreoScan (agonist), ^{111}In-DOTA-BASS (sstr2 antagonist), and the improved sstr2 antagonist ^{111}In-DOTA-JR11 in the same patient. Recently, Wild et al. brought the first clinical evidence that treatment of NETs is also clinically feasible with radiolabeled sstr2 antagonists [76] with promising results. In this pilot study, the sstr2-antagonist ^{177}Lu-DOTA-JR11 was compared in the same four patients to the agonist ^{177}Lu-DOTA-TATE and showed a favorable pharmacokinetic and increased tumor dose (due to a longer intratumoral residence time and a higher tumor uptake). Particularly encouraging, given the fact that kidneys and bone marrow are the major dose-limiting organs in PRRT [77], was that tumor-to-kidney and tumor-to-bone marrow dose ratios were several fold higher for the antagonist than for the agonist.

Based on affinity studies and preclinical results, the sstr2-antagonist JR11 conjugated with the chelator 1,4,7-triazacyclononane,1-glutaric acid-4,7-acetic acid (NODAGA, Fig. 7.1), which is ideal for ^{68}Ga-labeling, was selected for further clinical PET development (Table 7.3) [39]. A phase I/II study comparing, in the same patients, two microdoses of ^{68}Ga-NODAGA-JR11 (also named ^{68}Ga-OPS202) with ^{68}Ga-DOTA-TOC PET/CT was conducted at the University Hospital of Basel, Switzerland (ClinicalTrials.gov NCT02162446). The study indicated increased image contrast for both doses of ^{68}Ga-NODAGA-JR11, due to lower hepatic, intestinal, and pancreatic uptake, which in turn resulted in a higher sensitivity and diagnostic accuracy (overall and especially for detecting liver metastases) than ^{68}Ga-DOTA-TOC PET/CT for staging well- to moderately differentiated GEP-NET patients [78–80]. The "theranostic pair" ^{68}Ga-DOTA-JR11 (^{68}Ga-OPS202) and ^{177}Lu-DOTA-JR11 (also named ^{177}Lu-OPS201) (Table 7.3) are currently evaluated in NET patients at Memorial Sloan Kettering Cancer Center, New York, USA (ClinicalTrials.gov NCT02609737). Larger-scale multicenter clinical trials are planned for both the PET tracer ^{68}Ga-NODAGA-JR11 and the therapeutic tracer ^{177}Lu-DOTA-JR11.

7.3.2 *Glucagon-like Peptide-1 Receptor (GLP-1R) Targeting*

GLP-1R is overexpressed at a high incidence and density in almost all benign insulinomas and therefore represents an ideal target for molecular imaging [81–83]. This is clinically relevant as insulinomas can cause life-threatening hypoglycemia and are often difficult to localize with conventional imaging methods, thereby hampering the surgical intervention [84]. OctreoScan has a low sensitivity of 50–60 % in the detection of benign insulinomas [85] because sstr2 receptors are expressed by less than 70 % of insulinomas [83], while the amine precursor [^{18}F]DOPA shows controversial results with sensitivities ranging from 17 % up to 90 % [86, 87].

The natural ligand GLP-1 (30 amino acids) is unstable *in vivo* with a half-life of less than 2 min. Exendin-4 (H-His[1]-Gly[2]-Glu[3]-Gly[4]-Thr[5]-Phe[6]-Thr[7]-Ser[8]-Asp[9]-Leu[10]-Ser[11]-Lys[12]-Gln[13]-Met[14]-Glu[15]-Glu[16]-Glu[17]-Ala[18]-Val[19]-Arg[20]-Leu[21]-Phe[22]-Ile[23]-Glu[24]-Trp[25]-Leu[26]-Lys[27]-Asn[28]-Gly[29]-Gly[30]-Pro[31]-Ser[32]-Ser[33]-Gly[34]-Ala[35]-Pro[36]-Pro[37]-Pro[38]-Ser[39]-NH$_2$) is a metabolically resistant naturally occurring peptide identified in the saliva of the Gila monster lizard (*Heloderma suspectum*), and it shares 53 % homology with the human GLP-1 [88]. Exenatide, synthetic exendin-4, is an FDA-approved antidiabetic medication for the treatment of type 2 diabetes mellitus (trade name Byetta®). The introduction of a Lys residue at the C-terminal of the peptide, the conjugation with Ahx (aminohexanoic acid: a spacer and pharmacokinetic modifier) at the side chain of the Lys[40], and the coupling with chelators such as DTPA and DOTA allowed [Lys[40](Ahx-DTPA)NH$_2$]-exendin-4 to be labeled with [111]In (^{111}In-DTPA-exendin-4) and [Lys[40](Ahx-DOTA)NH$_2$]-exendin-4 to be labeled with ^{111}In or [68]Ga ([111]In-/^{68}Ga-DOTA-exendin-4) for SPECT or PET imaging.

^{111}In-DTPA-exendin-4 was the first exendin-based radiotracer used in a proof-of-concept study including only two patients, and it provided evidence of the diagnostic value of GLP-1R scintigraphy in histopathologically proven GLP-1R-expressing insulinomas [89]. ^{111}In-DOTA-exendin-4 was evaluated immediately after in six patients with biochemically proven endogenous hyperinsulinemic hypoglycemia [90]. SPECT/CT imaging successfully detected insulinomas in all six cases, which were precisely localized intraoperatively using a γ-probe allowing this way their successful removal. A prospective multicenter study including 30 patients with ^{111}In-DTPA-exendin-4 concluded on the higher sensitivity of GLP-1R imaging for the detection of benign insulinoma than CT or MRI, changing the clinical management in a substantial percentage of patients with endogeneous hyperinsulinemic hypoglycemia [91].

[99m]Tc-labeled exendin-4, [Lys^{40}(Ahx-HYNIC-^{99m}Tc/EDDA)NH_2]-exendin-4, has also been developed, and ^{99m}Tc-HYNIC-exendin-4 is being used the last few years at Jagiellonian University Medical College, Krakow, Poland, reporting very high sensitivity and specificity for the detection of benign insulinoma [92, 93].

^{68}Ga-DO3A-VS-Cys^{40}-Exendin-4 (a ^{68}Ga-labeled exendin-4 analog with Cys at position 40, coupled to DOTA via a vinylsulfonyl spacer (VS)) was the first PET exendin-based PET tracer tested in a single patient with severe hypoglycemia where several small GLP-1R-positive lesions were confirmed [94]. Very recently, the first head-to-head comparison between ^{68}Ga-DOTA-exendin-4 PET/CT and ^{111}In-DOTA-exendin-4 SPECT/CT was conducted in a pilot study including five patients [95]. ^{68}Ga-DOTA-exendin-4 PET/CT revealed higher image contrast (2.5 h after injection) than ^{111}In-DOTA-exendin-4 SPECT/CT (4 and 72 h after injection). The study's conclusion favored the use of ^{68}Ga-DOTA-exendin-4 PET/CT over ^{111}In-DOTA-exendin-4 SPECT/CT, because of a higher image contrast, a higher spatial resolution, the possibility of quantification, and a lower radiation burden. This is currently an ongoing study (ClinicalTrials.gov NCT02127541) for the localization of insulinoma and transplanted islet cells, at the University Hospital of Basel, Switzerland. In a parallel and ongoing study (ClinicalTrials.gov NCT02560376) performed at the Peking Union Medical College Hospital, China, ^{68}Ga-NOTA-MAL-Cys^{40}-exendin-4 (NOTA: 1,4,7-triazacyclononane-1,4,7-triacetic acid (Fig. 7.1) and NOTA-MAL: NOTA mono N-ethylmaleimide) PET/CT in patients with endogenous hyperinsulinemic hypoglycemia concluded on the much higher sensitivity of GLP-1R PET imaging for the detection of insulinoma than CT, MRI, endoscopic ultrasound (EUS), and somatostatin receptor scintigraphy [96]. Lately, a consortium (coordinated by the Radboud University Medical Center, Nijmegen, The Netherlands) with 17 research institutions and companies throughout Europe joined forces in order to develop an imaging and therapeutic platform for the "Personalized diagnosis and treatment of hyperinsulinemic hypoglycaemia caused by beta-cell pathology" (EU FP7 project BetaCure (http://www.betacure.eu)). Among others, the goal of the project is the development of the PET tracer [Lys^{40}(NODAGA-^{68}Ga)NH_2]-exendin-4 (^{68}Ga-NODAGA-exendin-4) and its clinical evaluation in adults and in congenital hyperinsulinism in children.

Overexpression of GLP-1 receptors not only on insulinoma cells but also on pancreatic beta cells provides further potential applications of GLP-1R imaging [82, 97, 98] in diabetes mellitus. It allows the quantification and monitoring of the β cell mass (BCM) during the course of the disease and under antidiabetic treatment. Furthermore, the method might be used for assessing islet cell graft survival after transplantation. ^{111}In-DTPA-exendin-4 was used to follow β cell viability of an islet transplantation into the forearm of a human patient [99].

7.3.3   *Cholecystokinin 2 (CCK2)/Gastrin Receptor Targeting*

Almost all medullary thyroid carcinoma (MTC) (92 %) expresses the cholecystokinin 2 (CCK2) receptor (or CCK-B or gastrin receptor), a G-protein-coupled receptor, in high density [100]. The peptide hormone gastrin binds with high affinity and specificity to CCK2. Therefore, specific targeting of CCK2 with radiolabeled gastrin analogs is a promising approach for imaging and also for systemic treatment of MTC and its metastasis.

Minigastrin (MG) Leu[1]-Glu[2]-Glu[3]-Glu[4]-Glu[5]-Glu[6]-Ala[7]-Tyr[8]-Gly[9]-Trp[10]-Met[11]-Asp[12]-Phe[13]-NH_2 is a C-terminal truncated non-sulfated form having 13 amino acid residues. The presence of the C-terminal sequence Trp-Met-Asp-Phe-NH_2 is crucial for receptor binding [101, 102]. The ^{111}In-DTPA derivative of MG, where the first amino acid Leu[1] was replaced with by D-Glu[1] resulting in an analog containing six glutamic acid chains (MG0), was the first gastrin analog to be administered in a MTC patient (^{111}In-DTPA-D-Glu-(Glu)$_5$-Ala-Tyr-Gly-Trp-Met-Asp-Phe-NH_2) [103]. Despite very encouraging accumulation at the tumor site, this preliminary study revealed also a high accumulation of radioactivity in the kidneys that are radiation-sensitive organs. High kidney uptake is a typical characteristic for this class of compounds.

Gastrins are particularly vulnerable to *in vivo* degradation by proteases. Many structure-activity relationship studies have been conducted in an attempt to circumvent this problem without diminishing the potency of *in vivo* targeting of CCK2. In a series of ^{111}In-DOTA-minigastrin analogs with reduced number of glutamic acid residues (reduced negative charge), it was shown, preclinically, that reducing the number of glutamates improved binding affinity, significantly reduced kidney uptake, and increased tumor-to-kidney ratio [104]. However, the absolute tumor uptake and the metabolic stability of the analog in which the glutamate sequence has been removed, namely, MG11 (DOTA-D-Glu-Ala-Tyr-Gly-Trp-Met-Asp-Phe-NH_2) were lower compared to MG0. The [99mTc]-labeled tetraamine (N_4)-derivatized minigastrin analogs, using a Gly spacer ([99mTc]-N_4-Gly-D-Glu-(Glu)$_5$-Ala-Tyr-Gly-Trp-Met-Asp-Phe-NH_2, where N4: 6-carboxy-1,4,7,11-tetraazaundecane, Fig. 7.1), known as demogastrin 2, appeared to be more promising diagnostic tool in preliminary clinical studies, compared to ^{111}In-DOTA-MG11 [105].

Large efforts were put into the improvement of these analogs, in terms of higher *in vivo* stability, better receptor affinity, and reduced kidney uptake. A systematic multicenter study supported by the European Cooperation in Science and Technology (COST) action BM0607 [106–108] concluded that the analog where the hexagluta-mate of the MG0 analog was replaced by hexa-D-Glu, namely, PP-F11 (DOTA-(D-Glu)$_6$-Ala-Tyr-Gly-Trp-Met-Asp-Phe-NH$_2$), was the most promising in terms of *in vitro* stability and *in vivo* performance. The analog PP-F11, labeled with ^{111}In, is currently under clinical development within the Bando ERA-net TRANSCAN JTC 2011 EU project "GRANT-T-MTC" as an imaging agent.

References

1. Klimstra DS, Modlin IR, Coppola D, Lloyd RV, Suster S. The pathologic classification of neuroendocrine tumors: a review of nomenclature, grading, and staging systems. Pancreas. 2010;39(6):707–12.
2. Ahlstrom H, Eriksson B, Bergstrom M, Bjurling P, Langstrom B, Oberg K. Pancreatic neuro-endocrine tumors: diagnosis with PET. Radiology. 1995;195(2):333–7.
3. Pearse AG. The APUD concept and hormone production. Clin Endocrinol Metab. 1980;9(2):211–22.
4. Reubi JC, Waser B, Schaer JC, Laissue JA. Somatostatin receptor sst1-sst5 expression in normal and neoplastic human tissues using receptor autoradiography with subtype-selective ligands. Eur J Nucl Med. 2001;28(7):836–46.
5. Reubi JC. Peptide receptors as molecular targets for cancer diagnosis and therapy. Endocr Rev. 2003;24(4):389–427.
6. Schaer JC, Waser B, Mengod G, Reubi JC. Somatostatin receptor subtypes sst1, sst2, sst3 and sst5 expression in human pituitary, gastroentero-pancreatic and mammary tumors: compari-son of mRNA analysis with receptor autoradiography. Int J Cancer. 1997;70(5):530–7.
7. Bombardieri E, Ambrosini V, Aktolun C, Baum RP, Bishof-Delaloye A, Del Vecchio S, et al. 111In-pentetreotide scintigraphy: procedure guidelines for tumour imaging. Eur J Nucl Med Mol Imaging. 2010;37(7):1441–8.
8. Graham MM, Menda Y. Radiopeptide imaging and therapy in the United States. J Nucl Med. 2011;52 Suppl 2:56S–63.
9. Pavel M, Baudin E, Couvelard A, Krenning E, Oberg K, Steinmuller T, et al. ENETS Consensus Guidelines for the management of patients with liver and other distant metastases from neuroendocrine neoplasms of foregut, midgut, hindgut, and unknown primary. Neuroendocrinology. 2012;95(2):157–76.
10. Reubi JC, Schar JC, Waser B, Wenger S, Heppeler A, Schmitt JS, et al. Affinity profiles for human somatostatin receptor subtypes SST1-SST5 of somatostatin radiotracers selected for scintigraphic and radiotherapeutic use. Eur J Nucl Med. 2000;27(3):273–82.
11. Forrer F, Uusijarvi H, Waldherr C, Cremonesi M, Bernhardt P, Mueller-Brand J, et al. A comparison of (111)In-DOTATOC and (111)In-DOTATATE: biodistribution and dosimetry in the same patients with metastatic neuroendocrine tumours. Eur J Nucl Med Mol Imaging. 2004;31(9):1257–62.
12. Cwikla JB, Mikolajczak R, Pawlak D, Buscombe JR, Nasierowska-Guttmejer A, Bator A, et al. Initial direct comparison of 99mTc-TOC and 99mTc-TATE in identifying sites of dis-ease in patients with proven GEP NETs. J Nucl Med. 2008;49(7):1060–5.
13. Gabriel M, Decristoforo C, Donnemiller E, Ulmer H, Watfah Rychlinski C, Mather SJ, et al. An intrapatient comparison of 99mTc-EDDA/HYNIC-TOC with 111In-DTPA-octreotide for diagnosis of somatostatin receptor-expressing tumors. J Nucl Med. 2003;44(5):708–16.

14. Hubalewska-Dydejczyk A, Fross-Baron K, Mikolajczak R, Maecke HR, Huszno B, Pach D, et al. 99mTc-EDDA/HYNIC-octreotate scintigraphy, an efficient method for the detection and staging of carcinoid tumours: results of 3 years' experience. Eur J Nucl Med Mol Imaging. 2006;33(10):1123–33.

15. Koopmans KP, Neels ON, Kema IP, Elsinga PH, Links TP, de Vries EG, et al. Molecular imaging in neuroendocrine tumors: molecular uptake mechanisms and clinical results. Crit Rev Oncol Hematol. 2009;71(3):199–213.

16. Menda Y, Kahn D. Somatostatin receptor imaging of non-small cell lung cancer with 99mTc depreotide. Semin Nucl Med. 2002;32(2):92–6.

17. Virgolini I, Britton K, Buscombe J, Moncayo R, Paganelli G, Riva P. In- and Y-DOTA-lanreotide: results and implications of the MAURITIUS trial. Semin Nucl Med. 2002;32(2):148–55.

18. Breeman WA, de Blois E, Sze Chan H, Konijnenberg M, Kwekkeboom DJ, Krenning EP. (68)Ga-labeled DOTA-peptides and (68)Ga-labeled radiopharmaceuticals for positron emission tomography: current status of research, clinical applications, and future perspectives. Semin Nucl Med. 2011;41(4):314–21.

19. Fani M, Andre JP, Maecke HR. 68Ga-PET: a powerful generator-based alternative to cyclotron-based PET radiopharmaceuticals. Contrast Media Mol Imaging. 2008;3(2):67–77.

20. Rosch F. (68)Ge/(68)Ga generators: past, present, and future. Recent Results Cancer Res. 2013;194:3–16.

21. Velikyan I. Prospective of (6)(8)Ga-radiopharmaceutical development. Theranostics. 2013;4(1):47–80.

22. Henze M, Schuhmacher J, Hipp P, Kowalski J, Becker DW, Doll J, et al. PET imaging of somatostatin receptors using [68GA]DOTA-D-Phe1-Tyr3-octreotide: first results in patients with meningiomas. J Nucl Med. 2001;42(7):1053–6.

23. Hofmann M, Maecke H, Borner R, Weckesser E, Schoffski P, Oei L, et al. Biokinetics and imaging with the somatostatin receptor PET radioligand (68)Ga-DOTATOC: preliminary data. Eur J Nucl Med. 2001;28(12):1751–7.

24. Poeppel TD, Binse I, Petersenn S, Lahner H, Schott M, Antoch G, et al. 68Ga-DOTATOC versus 68Ga-DOTATATE PET/CT in functional imaging of neuroendocrine tumors. J Nucl Med. 2011;52(12):1864–70.

25. Sandstrom M, Velikyan I, Garske-Roman U, Sorensen J, Eriksson B, Granberg D, et al. Comparative biodistribution and radiation dosimetry of 68Ga-DOTATOC and 68Ga-DOTATATE in patients with neuroendocrine tumors. J Nucl Med. 2013;54(10):1755–9.

26. Brogsitter C, Zophel K, Hartmann H, Schottelius M, Wester HJ, Kotzerke J. Twins in spirit part II: DOTATATE and high-affinity DOTATATE--the clinical experience. Eur J Nucl Med Mol Imaging. 2014;41(6):1158–65.

27. Schottelius M, Simecek J, Hoffmann F, Willibald M, Schwaiger M, Wester HJ. Twins in spirit – episode I: comparative preclinical evaluation of [(68)Ga]DOTATATE and [(68)Ga]HA-DOTATATE. EJNMMI Res. 2015;5:22.

28. Wild D, Schmitt JS, Ginj M, Macke HR, Bernard BF, Krenning E, et al. DOTA-NOC, a high-affinity ligand of somatostatin receptor subtypes 2, 3 and 5 for labelling with various radio-metals. Eur J Nucl Med Mol Imaging. 2003;30(10):1338–47.

29. Antunes P, Ginj M, Zhang H, Waser B, Baum RP, Reubi JC, et al. Are radiogallium-labelled DOTA-conjugated somatostatin analogues superior to those labelled with other radiometals? Eur J Nucl Med Mol Imaging. 2007;34(7):982–93.

30. Kabasakal L, Demirci E, Ocak M, Decristoforo C, Araman A, Ozsoy Y, et al. Comparison of (6)(8)Ga-DOTATATE and (6)(8)Ga-DOTANOC PET/CT imaging in the same patient group with neuroendocrine tumours. Eur J Nucl Med Mol Imaging. 2012;39(8):1271–7.

31. Wild D, Bomanji JB, Benkert P, Maecke H, Ell PJ, Reubi JC, et al. Comparison of 68Ga-DOTANOC and 68Ga-DOTATATE PET/CT within patients with gastroenteropancreatic neuroendocrine tumors. J Nucl Med. 2013;54(3):364–72.

32. Ambrosini V, Fani M, Fanti S, Forrer F, Maecke HR. Radiopeptide imaging and therapy in Europe. J Nucl Med. 2011;52 Suppl 2:42S–55.

33. Virgolini I, Ambrosini V, Bomanji JB, Baum RP, Fanti S, Gabriel M, et al. Procedure guide-lines for PET/CT tumour imaging with 68Ga-DOTA-conjugated peptides: 68Ga-DOTA-TOC, 68Ga-DOTA-NOC, 68Ga-DOTA-TATE. Eur J Nucl Med Mol Imaging. 2010;37(10):2004–10.

34. Johnbeck CB, Knigge U, Kjaer A. PET tracers for somatostatin receptor imaging of neuroen-docrine tumors: current status and review of the literature. Future Oncol. 2014;10(14):2259–77.

35. Pfeifer A, Knigge U, Binderup T, Mortensen J, Oturai P, Loft A, et al. 64Cu-DOTATATE PET for neuroendocrine tumors: a prospective head-to-head comparison with 111In-DTPA-octreotide in 112 patients. J Nucl Med. 2015;56(6):847–54.

36. Pfeifer A, Knigge U, Mortensen J, Oturai P, Berthelsen AK, Loft A, et al. Clinical PET of neuroendocrine tumors using 64Cu-DOTATATE: first-in-humans study. J Nucl Med. 2012;53(8):1207–15.

37. Price EW, Orvig C. Matching chelators to radiometals for radiopharmaceuticals. Chem Soc Rev. 2014;43(1):260–90.

38. Wadas TJ, Wong EH, Weisman GR, Anderson CJ. Copper chelation chemistry and its role in copper radiopharmaceuticals. Curr Pharm Des. 2007;13(1):3–16.

39. Fani M, Braun F, Waser B, Beetschen K, Cescato R, Erchegyi J, et al. Unexpected sensitivity of sst2 antagonists to N-terminal radiometal modifications. J Nucl Med. 2012;53(9):1481–9.

40. Fani M, Del Pozzo L, Abiraj K, Mansi R, Tamma ML, Cescato R, et al. PET of somatostatin receptor-positive tumors using 64Cu- and 68Ga-somatostatin antagonists: the chelate makes the difference. J Nucl Med. 2011;52(7):1110–8.

41. Gabriel M, Decristoforo C, Kendler D, Dobrozemsky G, Heute D, Uprimny C, et al. 68Ga-DOTA-Tyr3-octreotide PET in neuroendocrine tumors: comparison with somatostatin receptor scintigraphy and CT. J Nucl Med. 2007;48(4):508–18.

42. Kayani I, Bomanji JB, Groves A, Conway G, Gacinovic S, Win T, et al. Functional imaging of neuroendocrine tumors with combined PET/CT using 68Ga-DOTATATE (DOTA-DPhe1, Tyr3-octreotate) and 18F-FDG. Cancer. 2008;112(11):2447–55.

43. Simsek DH, Kuyumcu S, Turkmen C, Sanli Y, Aykan F, Unal S, et al. Can complementary Ga-68-DOTATATE and F-18-FDG PET/CT establish the missing link between histopathol-ogy and therapeutic approach in gastroenteropancreatic neuroendocrine tumors? J Nucl Med. 2014;55(11):1811–7.

44. Ambrosini V, Tomassetti P, Castellucci P, Campana D, Montini G, Rubello D, et al. Comparison between 68Ga-DOTA-NOC and 18F-DOPA PET for the detection of gastro-entero-pancreatic and lung neuro-endocrine tumours. Eur J Nucl Med Mol Imaging. 2008;35(8):1431–8.

45. Haug A, Auernhammer CJ, Wangler B, Tiling R, Schmidt G, Goke B, et al. Intraindividual comparison of 68Ga-DOTA-TATE and 18F-DOPA PET in patients with well-differenti-ated metastatic neuroendocrine tumours. Eur J Nucl Med Mol Imaging. 2009;36(5):765–70.

46. Putzer D, Gabriel M, Kendler D, Henninger B, Knoflach M, Kroiss A, et al. Comparison of (68)Ga-DOTA-Tyr(3)-octreotide and (18)F-fluoro-L-dihydroxyphenylalanine positron emis-sion tomography in neuroendocrine tumor patients. Q J Nucl Med Mol Imaging. 2010;54(1):68–75.

47. Maurice JB, Troke R, Win Z, Ramachandran R, Al-Nahhas A, Naji M, et al. A comparison of the performance of (6)(8)Ga-DOTATATE PET/CT and (1)(2)(3)I-MIBG SPECT in the diag-nosis and follow-up of phaeochromocytoma and paraganglioma. Eur J Nucl Med Mol Imaging. 2012;39(8):1266–70.

48. Naji M, Zhao C, Welsh SJ, Meades R, Win Z, Ferrarese A, et al. 68Ga-DOTA-TATE PET vs. 123I-MIBG in identifying malignant neural crest tumours. Mol Imaging Biol. 2011;13(4):769–75.

49. Bombardieri E, Seregni E, Villano C, Chiti A, Bajetta E. Position of nuclear medicine techniques in the diagnostic work-up of neuroendocrine tumors. Q J Nucl Med Mol Imaging. 2004;48(2):150–63.

50. Prasad V, Ambrosini V, Alavi A, Fanti S, Baum RP. PET/CT in neuroendocrine tumors: evaluation of receptor status and metabolism. PET Clin. 2007;2(3):351–75.

51. Naswa N, Sharma P, Gupta SK, Karunanithi S, Reddy RM, Patnecha M, et al. Dual tracer functional imaging of gastroenteropancreatic neuroendocrine tumors using 68Ga-DOTA-NOC PET-CT and 18F-FDG PET-CT: competitive or complimentary? Clin Nucl Med. 2014;39(1):e27–34.

52. Binderup T, Knigge U, Loft A, Federspiel B, Kjaer A. 18F-fluorodeoxyglucose positron emission tomography predicts survival of patients with neuroendocrine tumors. Clin Cancer Res. 2010;16(3):978–85.

53. Garin E, Le Jeune F, Devillers A, Cuggia M, de Lajarte-Thirouard AS, Bouriel C, et al. Predictive value of 18F-FDG PET and somatostatin receptor scintigraphy in patients with metastatic endocrine tumors. J Nucl Med. 2009;50(6):858–64.

54. Severi S, Nanni O, Bodei L, Sansovini M, Ianniello A, Nicoletti S, et al. Role of 18FDG PET/CT in patients treated with 177Lu-DOTATATE for advanced differentiated neuroendocrine tumours. Eur J Nucl Med Mol Imaging. 2013;40(6):881–8.

55. Jager PL, Chirakal R, Marriott CJ, Brouwers AH, Koopmans KP, Gulenchyn KY. 6-L-(18) F-fluorodihydroxyphenylalanine PET in neuroendocrine tumors: basic aspects and emerging clinical applications. J Nucl Med. 2008;49(4):573–86.

56. Kauhanen S, Seppanen M, Ovaska J, Minn H, Bergman J, Korsoff P, et al. The clinical value of [18F]fluoro-dihydroxyphenylalanine positron emission tomography in primary diagnosis, staging, and restaging of neuroendocrine tumors. Endocr Relat Cancer. 2009;16(1):255–65.

57. Koopmans KP, Neels OC, Kema IP, Elsinga PH, Sluiter WJ, Vanghillewe K, et al. Improved staging of patients with carcinoid and islet cell tumors with 18F-dihydroxy-phenyl-alanine and 11C-5-hydroxy-tryptophan positron emission tomography. J Clin Oncol. 2008;26(9): 1489–95.

58. Schiesser M, Veit-Haibach P, Muller MK, Weber M, Bauerfeind P, Hany T, et al. Value of combined 6-[18F]fluorodihydroxyphenylalanine PET/CT for imaging of neuroendocrine tumours. Br J Surg. 2010;97(5):691–7.

59. Yang J, Hao R, Zhu X. Diagnostic role of 18F-dihydroxyphenylalanine positron emission tomography in patients with congenital hyperinsulinism: a meta-analysis. Nucl Med Commun. 2013;34(4):347–53.

60. Nikolaou A, Thomas D, Kampanellou C, Alexandraki K, Andersson LG, Sundin A, et al. The value of 11C-5-hydroxy-tryptophan positron emission tomography in neuroendocrine tumor diagnosis and management: experience from one center. J Endocrinol Invest. 2010;33(11): 794–9.

61. Orlefors H, Sundin A, Ahlstrom H, Bjurling P, Bergstrom M, Lilja A, et al. Positron emission tomography with 5-hydroxytryprophan in neuroendocrine tumors. J Clin Oncol. 1998;16(7): 2534–41.

62. Orlefors H, Sundin A, Eriksson B, Skogseid B, Oberg K, Akerstrom G, et al. PET-guided surgery – high correlation between positron emission tomography with 11C-5-hydroxytryptophane (5-HTP) and surgical findings in abdominal neuroendocrine tumours. Cancers (Basel). 2012;4(1):100–12.

63. Orlefors H, Sundin A, Garske U, Juhlin C, Oberg K, Skogseid B, et al. Whole-body (11)C-5-hydroxytryptophan positron emission tomography as a universal imaging technique for neuroendocrine tumors: comparison with somatostatin receptor scintigraphy and computed tomography. J Clin Endocrinol Metab. 2005;90(6):3392–400.

64. Wafelman AR, Hoefnagel CA, Maes RA, Beijnen JH. Radioiodinated metaiodobenzylguanidine: a review of its biodistribution and pharmacokinetics, drug interactions, cytotoxicity and dosimetry. Eur J Nucl Med. 1994;21(6):545–59.

65. Binderup T, Knigge U, Loft A, Mortensen J, Pfeifer A, Federspiel B, et al. Functional imaging of neuroendocrine tumors: a head-to-head comparison of somatostatin receptor scintigraphy, 123I-MIBG scintigraphy, and 18F-FDG PET. J Nucl Med. 2010;51(5):704–12.

66. Toumpanakis C, Kim MK, Rinke A, Bergestuen DS, Thirlwell C, Khan MS, et al. Combination of cross-sectional and molecular imaging studies in the localization of gastroenteropancreatic neuroendocrine tumors. Neuroendocrinology. 2014;99(2):63–74.

67. Perrin MH, Sutton SW, Cervini LA, Rivier JE, Vale WW. Comparison of an agonist, urocortin, and an antagonist, astressin, as radioligands for characterization of corticotropin-releasing factor receptors. J Pharmacol Exp Ther. 1999;288(2):729–34.

68. Sleight AJ, Stam NJ, Mutel V, Vanderheyden PM. Radiolabelling of the human 5-HT2A receptor with an agonist, a partial agonist and an antagonist: effects on apparent agonist affinities. Biochem Pharmacol. 1996;51(1):71–6.

69. Bass RT, Buckwalter BL, Patel BP, Pausch MH, Price LA, Strnad J, et al. Identification and characterization of novel somatostatin antagonists. Mol Pharmacol. 1996;50(4):709–15.

70. Hocart SJ, Jain R, Murphy WA, Taylor JE, Coy DH. Highly potent cyclic disulfide antagonists of somatostatin. J Med Chem. 1999;42(11):1863–71.

71. Cescato R, Erchegyi J, Waser B, Piccand V, Maecke HR, Rivier JE, et al. Design and in vitro characterization of highly sst2-selective somatostatin antagonists suitable for radiotargeting. J Med Chem. 2008;51(13):4030–7.

72. Ginj M, Zhang H, Waser B, Cescato R, Wild D, Wang X, et al. Radiolabeled somatostatin receptor antagonists are preferable to agonists for in vivo peptide receptor targeting of tumors. Proc Natl Acad Sci U S A. 2006;103(44):16436–41.

73. Wadas TJ, Eiblmaier M, Zheleznyak A, Sherman CD, Ferdani R, Liang K, et al. Preparation and biological evaluation of 64Cu-CB-TE2A-sst2-ANT, a somatostatin antagonist for PET imaging of somatostatin receptor-positive tumors. J Nucl Med. 2008;49(11):1819–27.

74. Cescato R, Waser B, Fani M, Reubi JC. Evaluation of 177Lu-DOTA-sst2 antagonist versus 177Lu-DOTA-sst2 agonist binding in human cancers in vitro. J Nucl Med. 2011;52(12):1886–90.

75. Wild D, Fani M, Behe M, Brink I, Rivier JE, Reubi JC, et al. First clinical evidence that imaging with somatostatin receptor antagonists is feasible. J Nucl Med. 2011;52(9):1412–7.

76. Wild D, Fani M, Fischer R, Del Pozzo L, Kaul F, Krebs S, et al. Comparison of somatostatin receptor agonist and antagonist for peptide receptor radionuclide therapy: a pilot study. J Nucl Med. 2014;55(8):1248–52.

77. van Essen M, Krenning EP, Kam BL, de Jong M, Valkema R, Kwekkeboom DJ. Peptide-receptor radionuclide therapy for endocrine tumors. Nat Rev Endocrinol. 2009;5(7):382–93.

78. Nicolas G, Mansi R, Kaul F, Vomstein S, Kaufmann J, Bouterfa H, et al. 68Ga-OPS202/177Lu-OPS201, a high performance theranostic pair of radiolabelled somatostatin antagonists for PET imaging and radionuclide therapy: translational aspects. Eur J Nucl Med Mol Imaging. 2015;42 suppl 1:S129.

79. Nicolas G, Mansi R, Vomstein S, Kaufmann J, Bouterfa H, Maecke HR, et al., editors. Higher therapeutic index in vivo with radiolabeled somatostatin receptor antagonists may broaden the safety window of PRRT. Austin: The North American Neuroendocrine Tumor Society (NANETS); 2015.

80. Nicolas G, Mansi R, Vomstein S, Kaufmann J, Bouterfa H, Maecke H, et al. Wider safety window with radiolabeled somatostatin receptor antagonists over agonists. J Nucl Med. 2015;56(Supplement 3):335.

81. Korner M, Christ E, Wild D, Reubi JC. Glucagon-like peptide-1 receptor overexpression in cancer and its impact on clinical applications. Front Endocrinol (Lausanne). 2012;3:158.

82. Korner M, Stockli M, Waser B, Reubi JC. GLP-1 receptor expression in human tumors and human normal tissues: potential for in vivo targeting. J Nucl Med. 2007;48(5):736–43.

83. Reubi JC, Waser B. Concomitant expression of several peptide receptors in neuroendocrine tumours: molecular basis for in vivo multireceptor tumour targeting. Eur J Nucl Med Mol Imaging. 2003;30(5):781–93.

84. Placzkowski KA, Vella A, Thompson GB, Grant CS, Reading CC, Charboneau JW, et al. Secular trends in the presentation and management of functioning insulinoma at the Mayo Clinic, 1987–2007. J Clin Endocrinol Metab. 2009;94(4):1069–73.

85. Zimmer T, Stolzel U, Bader M, Koppenhagen K, Hamm B, Buhr H, et al. Endoscopic ultrasonography and somatostatin receptor scintigraphy in the preoperative localisation of insulinomas and gastrinomas. Gut. 1996;39(4):562–8.

86. Kauhanen S, Seppanen M, Minn H, Gullichsen R, Salonen A, Alanen K, et al. Fluorine-18-L-dihydroxyphenylalanine (18F-DOPA) positron emission tomography as a tool to localize an insulinoma or beta-cell hyperplasia in adult patients. J Clin Endocrinol Metab. 2007;92(4):1237–44.

87. Tessonnier L, Sebag F, Ghander C, De Micco C, Reynaud R, Palazzo FF, et al. Limited value of 18F-F-DOPA PET to localize pancreatic insulin-secreting tumors in adults with hyperinsulinemic hypoglycemia. J Clin Endocrinol Metab. 2010;95(1):303–7.

88. Eng J, Kleinman WA, Singh L, Singh G, Raufman JP. Isolation and characterization of exendin-4, an exendin-3 analogue, from Heloderma suspectum venom. Further evidence for an exendin receptor on dispersed acini from guinea pig pancreas. J Biol Chem. 1992;267(11):7402–5.

89. Wild D, Macke H, Christ E, Gloor B, Reubi JC. Glucagon-like peptide 1-receptor scans to localize occult insulinomas. N Engl J Med. 2008;359(7):766–8.

90. Christ E, Wild D, Forrer F, Brandle M, Sahli R, Clerici T, et al. Glucagon-like peptide-1 receptor imaging for localization of insulinomas. J Clin Endocrinol Metab. 2009;94(11):4398–405.

91. Christ E, Wild D, Ederer S, Behe M, Nicolas G, Caplin ME, et al. Glucagon-like peptide-1 receptor imaging for the localisation of insulinomas: a prospective multicentre imaging study. Lancet Diabetes Endocrinol. 2013;1(2):115–22.

92. Sowa-Staszczak A, Pach D, Mikolajczak R, Macke H, Jabrocka-Hybel A, Stefanska A, et al. Glucagon-like peptide-1 receptor imaging with [Lys40(Ahx-HYNIC- 99mTc/EDDA)NH2]-exendin-4 for the detection of insulinoma. Eur J Nucl Med Mol Imaging. 2013;40(4):524–31.

93. Sowa-Staszczak A, Stefańska A, Tomaszuk M, Buziak-Bereza M, Trofimiuk-Muldner M, Jabrocka-Hybel A, et al. 99mTc-Glucagon-like Peptide 1 (99mTc-GLP-1) scintigraphy – results of 3 years' experience. Eur J Nucl Med Mol Imaging. 2014;41(2):OP566.

94. Eriksson O, Velikyan I, Selvaraju RK, Kandeel F, Johansson L, Antoni G, et al. Detection of metastatic insulinoma by positron emission tomography with [(68)ga]exendin-4-a case report. J Clin Endocrinol Metab. 2014;99(5):1519–24.

95. Antwi K, Fani M, Nicolas G, Rottenburger C, Heye T, Reubi JC, et al. Localization of hidden insulinomas with (6)(8)Ga-DOTA-Exendin-4 PET/CT: a Pilot Study. J Nucl Med. 2015;56(7):1075–8.

96. Luo Y, Pan Q, Shao Y, Yu M, Wu W, Xue H, et al. Glucagon-like peptide-1 receptor PET/CT with 68Ga-NOTA-exendin-4 for detecting localized insulinoma: a Prospective Cohort Study. J Nucl Med. 2016;57(5):715–20.

97. Kieffer TJ, Habener JF. The glucagon-like peptides. Endocr Rev. 1999;20(6):876–913.

98. Tornehave D, Kristensen P, Romer J, Knudsen LB, Heller RS. Expression of the GLP-1 receptor in mouse, rat, and human pancreas. J Histochem Cytochem. 2008;56(9):841–51.

99. Pattou F, Kerr-Conte J, Wild D. GLP-1-receptor scanning for imaging of human beta cells transplanted in muscle. N Engl J Med. 2010;363(13):1289–90.

100. Reubi JC, Schaer JC, Waser B. Cholecystokinin(CCK)-A and CCK-B/gastrin receptors in human tumors. Cancer Res. 1997;57(7):1377–86.

101. Behr TM, Behe MP. Cholecystokinin-B/Gastrin receptor-targeting peptides for staging and therapy of medullary thyroid cancer and other cholecystokinin-B receptor-expressing malignancies. Semin Nucl Med. 2002;32(2):97–109.

102. Behr TM, Jenner N, Behe M, Angerstein C, Gratz S, Raue F, et al. Radiolabeled peptides for targeting cholecystokinin-B/gastrin receptor-expressing tumors. J Nucl Med. 1999;40(6): 1029–44.

103. Behe M, Becker W, Gotthardt M, Angerstein C, Behr TM. Improved kinetic stability of DTPA- dGlu as compared with conventional monofunctional DTPA in chelating indium and yttrium: preclinical and initial clinical evaluation of radiometal labelled minigastrin derivatives. Eur J Nucl Med Mol Imaging. 2003;30(8):1140–6.

104. Good S, Walter MA, Waser B, Wang X, Muller-Brand J, Behe MP, et al. Macrocyclic chelator-coupled gastrin-based radiopharmaceuticals for targeting of gastrin receptor-expressing tumours. Eur J Nucl Med Mol Imaging. 2008;35(10):1868–77.

105. Froberg AC, de Jong M, Nock BA, Breeman WA, Erion JL, Maina T, et al. Comparison of three radiolabelled peptide analogues for CCK-2 receptor scintigraphy in medullary thyroid carcinoma. Eur J Nucl Med Mol Imaging. 2009;36(8):1265–72.

106. Aloj L, Aurilio M, Rinaldi V, D'Ambrosio L, Tesauro D, Peitl PK, et al. Comparison of the binding and internalization properties of 12 DOTA-coupled and (1)(1)(1)In-labelled CCK2/gastrin receptor binding peptides: a collaborative project under COST Action BM0607. Eur J Nucl Med Mol Imaging. 2011;38(8):1417–25.

107. Laverman P, Joosten L, Eek A, Roosenburg S, Peitl PK, Maina T, et al. Comparative biodistribution of 12 (1)(1)(1)In-labelled gastrin/CCK2 receptor-targeting peptides. Eur J Nucl Med Mol Imaging. 2011;38(8):1410–6.

108. Ocak M, Helbok A, Rangger C, Peitl PK, Nock BA, Morelli G, et al. Comparison of biological stability and metabolism of CCK2 receptor targeting peptides, a collaborative project under COST BM0607. Eur J Nucl Med Mol Imaging. 2011;38(8):1426–35.

Chapter 8
SPECT/CT, PET/CT and PET/MR Principles

Stephen Walrand, Michel Hesse, and Francois Jamar

8.1 Introduction

In 1895, while studying the Crookes tube, the German physicist Wilhelm Röntgen observed that it produced an unknown kind of radiation that was able to pass through materials in a way depending on their density. Brilliantly, right after this observation, Röntgen had the idea to make the first planar radiography of his wife's hand. Next year, Henri Becquerel noted that uranium also emits a similar kind of invisible radiation able to cross opaque and dense matter. In the following years, physicists proved that these x- and γ-rays were parts of the electromagnetic spectrum described by the Maxwell equations.

Early in the beginning of radiology and of nuclear medicine, researchers tried to get free of the superimposition of the signals coming from the different depths in the patient. Johann Radon already proved in 1917 that it was mathematically possible to reconstruct a function from the knowledge of its summation over lines. However, clinical tomography studies based on this theory, namely, SPECT, PET and CT, only began in the 1970s, thanks to the continuous increasing calculation speed of the computers [40, 45].

MRI that uses the opposite part of the electromagnetic spectrum came into clinics one decade later [119]. Note that the resolution length of these electromagnetic waves is much larger than human organs. As a result, simple measurement of the radio frequency wave propagation through the patient's body is not precise enough as it is with x-rays. MRI is so based on a completely different mechanism using specific induced local resonances.

S. Walrand, PhD (✉) • M. Hesse, PhD • F. Jamar, MD, PhD
Laboratory of Molecular Imaging and Experimental Radiotherapy,
Catholic University of Louvain, Brussels, Belgium
e-mail: stephan.walrand@uclouvain.be

In oncology, emission tomography (i.e. SPECT or PET) is mainly used in four applications: disease diagnostic or staging, radionuclide post therapy check, tumor follow-up and radionuclide therapy dosimetry. The first two applications require low noise-high contrast images and the anatomical localization of the observed activity. As oncologic radiotracers are obviously designed to preferably target the tumors, the anatomical information provided by emission tomography is poor. This triggered the introduction of hybrid systems combining emission tomography with CT or MRI modality. The last two emission tomography applications require quantitative imaging and thus also benefit from the additional anatomical image that provides information about the scattering and attenuation underwent by the gamma rays in the patient.

8.2 Tomography from Projections

8.2.1 Nature of the Problem

Transmission (CT) and emission (SPECT, PET) tomography modalities originated from the work of the mathematician Johann Radon who proved in 1917 [Radon et al. [77] (translation by Parks)] that a function can be retrieved from the knowledge of its integrals along an appropriate set of lines, called lines of response (LOR). All the discussion in this section will refer only to CT, SPECT and PET tomographic modalities, magnetic resonance imaging (MRI) being a 3D probing modality.

In most applications, the LOR set is formed by the projections acquired at different angles around the patient. Basically, the appropriate number of angles is equal to the dimension of the reconstruction matrix. Besides various disturbing physical effects depending on the specific detector used in each modality (we will review them in next sections), this common tomographic acquisition geometry induces by itself several artefacts in the final reconstructed image. The understanding of these artefact productions is of prime importance in order to visually interpret the image in the right way, but also to accurately quantify the reconstructed distribution.

A major difference between planar and reconstructed images is the nature of noise. In a planar image, the noise is not correlated and follows the Poisson distribution, i.e. the standard deviation of a pixel value obtained from repeated identical acquisitions is independent of the pixel values elsewhere in the image and is simply equal to the square root of the pixel mean value, i.e. $n \pm \sqrt{n}$. In tomography, the voxel value in a transverse slice is reconstructed from different LORs passing through all the voxels of this slice. As a result, the noise in a voxel is correlated to the noise present elsewhere in the slice [79, 80], and its order of magnitude is about that of the noise present in a projection. This explains why, although tomography provides much more information by removing the activity superimposition, the
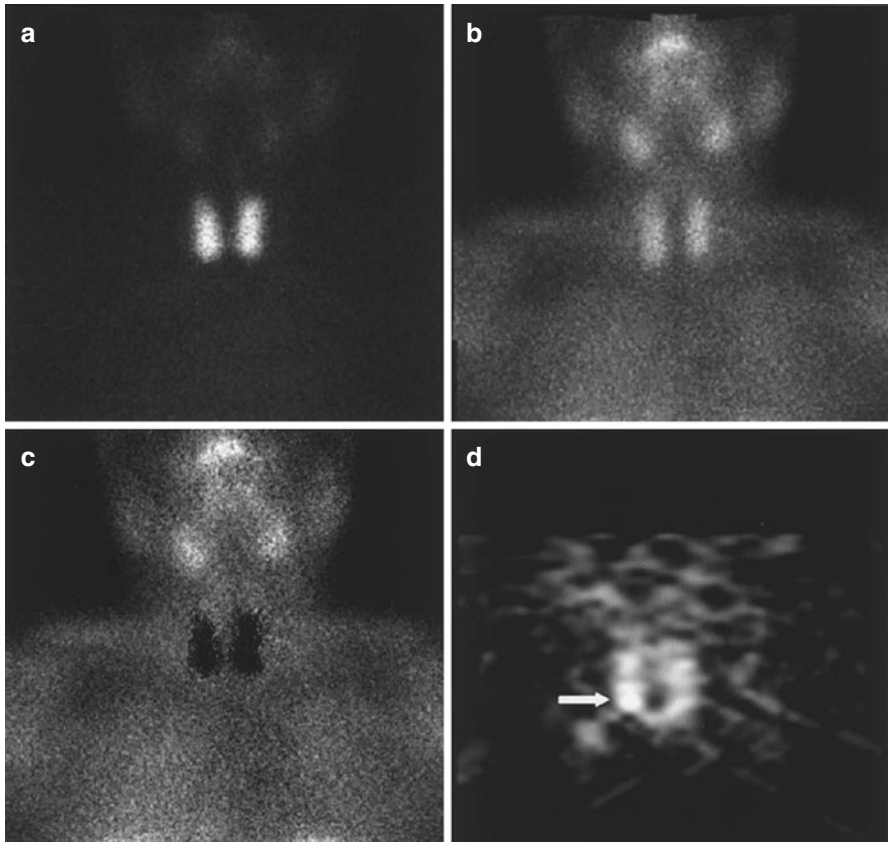
Fig. 8.1 A 55-year-old female patient affected by pHPT with small parathyroid adenoma (size, 6.1 mm; weight, 261 mg) sited behind inferior pole of right thyroid lobe, negative on planar 99mTc-pertechnetate (**a**), 99mTc-tetrofosmin (**b**) and subtraction (**c**) scintigraphy and clearly revealed (*arrow*) on coronal P-SPECT (**d**) (Reprinted from Spanu et al. [95] with permission of the Society of Nuclear Medicine)

image (Fig. 8.1d) appears less natural than planar views (Fig. 8.1a–c). This also explains why much longer acquisition time is required in tomography than in planar acquisition.

8.2.2 Tomography is an Ill-Posed Problem

Let's study the theoretical case of an ideal tomography (i.e. no disturbing physical effects) with continuous reconstruction variable (i.e. very small reconstruction voxel), with continuous detector sampling (i.e. very small projection pixel) and with projections acquired at n equidistant angles around the object. Consider the following voxel distribution $a(r,\theta)$:
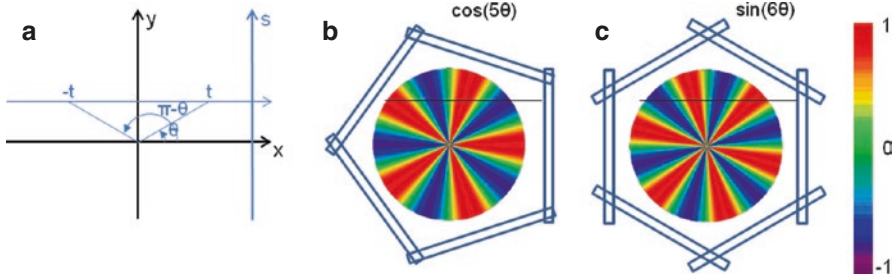
Fig. 8.2 (**a**) Schematic representation of the integration line in the transverse plane (**b**) and (**c**) invisible distributions corresponding to a tomography of five and six angles, respectively. The empty rectangles represent the detector position at the different tomography angles. Small numbers of angles were used for the sake of clarity

$$a(r,\theta) = \begin{cases} A(r)\cos\big((2k+1)\,n\theta\big) & \text{if } n \text{ is odd} \\ A(r)\sin\big(k\,n\theta\big) & \text{if } n \text{ is even} \end{cases} \tag{8.1}$$

where (r,θ) are the polar coordinates in the transverse plane (x,y), $A(r)$ is an arbitrary function and k is an integer. As the projections are acquired at the angle $i\dfrac{2\pi}{n}$ with $i=0,\ldots,n-1$, and as by construction $a(r,\theta)$ is invariant for a rotation $\theta \to \theta + \dfrac{2\pi}{n}$, all the projections are identical and it is sufficient to compute the projection for $\varphi=0$ (Fig. 8.2b, c).

Along the integration line s for the projection $\varphi=0$, the sum of $a(r,\theta)$ at the positions $-t$ and t (Fig. 8.2a) is:

$$\begin{array}{ll} A(r)\cos\big((2k+1)n(\pi-\theta)\big)+A(r)\cos\big((2k+1)\,n\theta\big) & \text{if } n \text{ is odd} \\ A(r)\sin\big(k\,n(\pi-\theta)\big)+A(r)\sin\big(k\,n\theta\big) & \text{if } n \text{ is even} \end{array} \tag{8.2}$$

Adding $n\,\pi$ with n odd changes the sign of cosine and with n even does not change the sine; thus Eq. (8.2) becomes:

$$\begin{array}{ll} A(r)\big(-\cos\big(-(2k+1)n\theta\big)+\cos\big((2k+1)\,n\theta\big)\big) & \text{if } n \text{ is odd} \\ A(r)\big(\sin\big(-k\,n\theta\big)+\sin\big(k\,n\theta\big)\big) & \text{if } n \text{ is even} \end{array} \tag{8.3}$$

As cosine is an even function and sine an odd one, both terms of Eq. (8.3) vanish.

So by symmetry the integration of the distribution $a(r,\theta)$ on lines parallel to the x-axis, i.e. all the projections $P(s,\varphi)$, is null. In other words, the non-null distribution $a(r,\theta)$ is an invisible object for the tomographic acquisition.

In the real world, the reconstruction variable and the detector sampling are discrete, i.e. transverse voxel and projection pixel have finite size. As a consequence,

the projections of the distribution (8.1) will not strictly vanish but will be very small. It is possible using more sophisticated mathematical calculus to show that the projections will be very small no matter where the distribution (8.1) is centred in the transverse slice. This means that there exist some very small perturbations of the projections that correspond to large fluctuations in the reconstruction slice. This makes the reconstruction unstable versus small perturbations induced by noise in the acquired data. Such kinds of problems are called ill-posed, or ill-conditioned, problems [10].

So, not only is the noise correlated in a transverse slice but is also structured in star patterns around intense sources, called streak artefacts (an example of such artefacts can be seen in Fig. 8.5b). Intense source refers to a dense material in CT or to a high activity in SPECT or PET. The reconstructed slice contains artefactual positive or negative values along the LORs crossing the source in order to reproduce the observed positive or negative noise contribution in the measured projection at different angles, respectively. For LORs not crossing the source, the sum of successive artefactual positive and negative values vanishes.

As a result the visualization and the quantification of low intensity sources will be significantly hampered by the artefacts originating from higher intensity sources present in the same slice. Typical issues are in CT, the tissue visualization around a metallic implant, and in emission tomography the tumor visualization and quantification around a bladder with high active content (see Fig. 8.6a). Note that in this last case, unlike PET, SPECT is additionally impacted by the fact that the content, and consequently the activity, of the bladder can increase from a projection to another one. The attenuation in tissue combined with the fact that the human body is larger than thicker favours positive artefactual values in the anterior and posterior regions of the bladder and negative artefactual values in the left and right regions of the bladder.

8.2.3 *Analytical and Iterative Reconstruction Techniques*

The meaning and the difference between analytical and iterative methods often appear quite obscure for the non-physicist. In this book mainly dedicated to the medical community, we think useless to introduce and discuss the reconstruction techniques in terms of Fourier transform, log likelihood maximization in Poisson distribution, etc. So we will discuss the principles and benefits of these reconstruction techniques through a very simple example: there is an abundant specialized literature of high level [16, 19, 20] that the medical physicist can consult. Our example will require only basic knowledges in matrix algebra that are learned in secondary school. All the numerical computations described can be easily performed using the matrix functions implemented in Microsoft Excel.

Analytical refers to an algorithm that always requires the same number of elementary operations (e.g. $+$, $-$, $\times$, $/$, cosine, sine, etc.) in order to obtain the solution. Iterative refers to an algorithm that proceeds by successive improvements (called
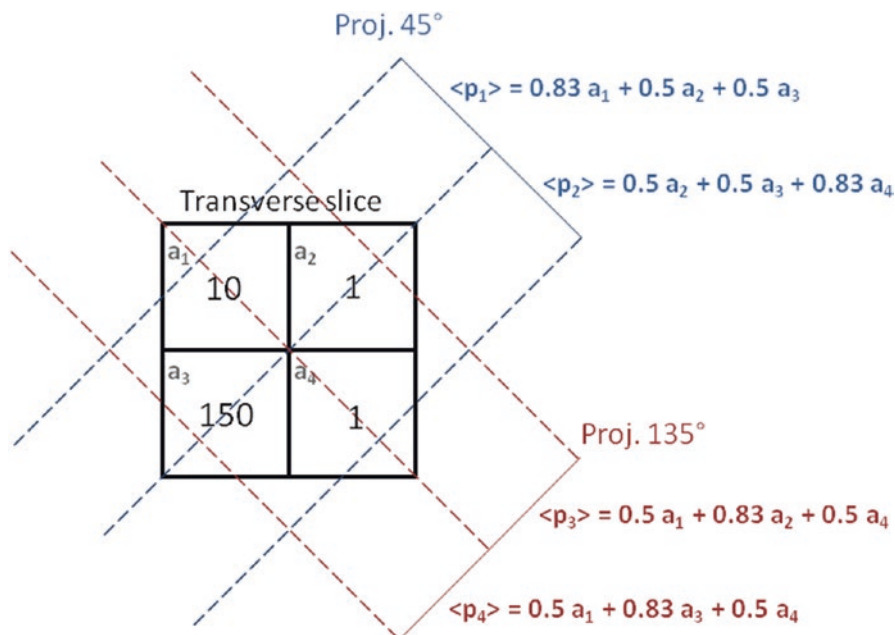
Fig. 8.3 Schematic setup in the transverse plane of a simple ideal emission 2×2 tomography with projections acquired at 45 and 135°. The numbers in the cells represent the mean counts emitted in the transverse slice voxels during a projection acquisition time. The symbols a_i and p_i are the compact labels of slice voxels and projection pixels commonly used in literature

iteration step) of an approximate solution. In this case, the number of iteration steps required to get the aimed accuracy depends on the initial approximate solution and also on the acquired data.

8.2.4 Analytical FBP Reconstruction

Consider the very simple case of an emission tomography from a 2×2 voxelated region shown in Fig. 8.3.

Typically the voxel a_1 corresponds to a tumor located close to a filled bladder modelled by the voxel a_3, the voxels a_2 and a_4 modelling some residual vascular activity. In the following computations, the reader should be attentive to the difference between p_i, i.e. the projection value obtained in one specific acquisition, and $\langle p_i \rangle$, i.e. the mean projection value obtained by repeating many times the acquisition under identical conditions.

This tomography acquisition setup can be simply written as a matrix product:

$$\langle p_i \rangle = \sum_{j=1}^{4} c_{ij} \, a_j \tag{8.4}$$

where the matrix c is:

$$c = \begin{pmatrix} 0.83 & 0.50 & 0.50 & 0.00 \\ 0.00 & 0.50 & 0.50 & 0.83 \\ 0.50 & 0.83 & 0.00 & 0.50 \\ 0.50 & 0.00 & 0.83 & 0.50 \end{pmatrix} \quad \text{with det}(c) = -0.21 \qquad (8.5)$$

giving the mean projection pixels values:

$$p = \begin{pmatrix} 83.80 \\ 76.33 \\ 6.33 \\ 130.00 \end{pmatrix} \qquad (8.6)$$

As the determinant of this matrix is non-null, the linear equation system (8.4) has a unique solution (note that using 0 and 90° in place of 45 and 135° is a degenerate case and results in a null determinant). The inverse of the matrix c can be directly computed using the minors and cofactors technique (function minverse in Excel) which gives:

$$c^{-1} = \begin{pmatrix} -0.73 & -1.94 & 1.61 & 1.61 \\ 1.61 & 1.61 & -0.73 & -1.94 \\ 1.61 & 1.61 & -1.94 & -0.73 \\ -1.94 & -0.73 & 1.61 & 1.61 \end{pmatrix} \qquad (8.7)$$

A straightforward computation (mmult in Excel) shows that our example satisfies the relation:

$$a_i = \sum_{j=1}^{4} c_{ij}^{-1} \langle p_j \rangle \qquad (8.8)$$

In other words, the reconstruction of the tomographic acquisition can be performed by computing the inverse of the matrix c and making the product of this inverse with the projection.

Even for a SPECT using a 64 by 64 transverse voxels reconstruction, the dimension of the matrix c is already 4096×4096. Direct inversion of such a matrix, even with the most powerful computer, is not compatible with clinical routine (note that in order to correct the attenuation of the gamma rays in the patient, the matrix c is in reality dependent on the patient and its inversion cannot thus be computed once for all; see next section).

Fortunately, the matrix c describing an ideal tomography, i.e. where the projection pixel values come from a single LOR (perfect collimator resolution and no

Compton scattering), has special properties resulting from the fact that the voxel integrations are performed along parallel LOR rotating around the slice. Using the Fourier transform theory, it is possible to prove that, for large dimensions (>16 × 16), the analytical computation (8.8) of a_i can be approached by two simple steps: a RAMP filtering of the projections followed by the multiplication with the transpose of the matrix c. This second operation is commonly called "back-projection", and the whole reconstruction called filtered back-projection (FBP). The RAMP filtering can be simply performed by multiplying the Fourier transform of the projection by the module of the spatial frequency, and the transpose c^T of the matrix c is just the matrix obtained by swapping of the indices, i.e.:

$$c_{ij}^T = c_{ji} \tag{8.9}$$

In a real acquisition, the mean values $\langle p_i \rangle$ will never be observed as being inevitably corrupted by Poisson noise of magnitude $\sqrt{p_i}$. Consider the following tomography typical acquisition values:

$$p = \begin{pmatrix} 93 \\ 81 \\ 4 \\ 119 \end{pmatrix} \tag{8.10}$$

p was obtained by adding a random Poisson noise to (8.6).

The computation of (8.8) using p instead of $\langle p \rangle$ gives:

$$a = \begin{pmatrix} -27 & 46 \\ 185 & -42 \end{pmatrix} \tag{8.11}$$

We can see that a small perturbation on the projection (±10) induced a larger variation in the reconstructed voxels (±40) illustrating the ill-posedness of emission tomography; see [20] for a mathematical description. As a result the tumor, modelled by the voxel a_1, is completely obscured by the streak artefact induced by the voxel a_3 modelling the filled bladder.

8.2.5　Iterative EM-ML Algorithm

A more powerful reconstruction technique can be implemented after noting that the disturbing streak artefact in (8.11) contains negative voxels which do not represent a physical emission. Rather than computing the exact solution of equation (8.4), it is preferable to compute the optimal solution containing only positive voxels. By optimal solution we mean the counts distribution a_j that minimizes the weighted

chi-square between the acquired projections p and the projections that the distribution a_i should have produced, i.e.:

$$\chi^2 = \sum_{i=1}^{n \times n} \frac{\left(p_i - \sum_{j=1}^{n \times n} c_{ij} a_j \right)^2}{p_i} \tag{8.12}$$

where n is the reconstruction matrix size. The weighting $1/p_i$ takes into account the corruption of the data by Poisson noise. Equation (8.12) is usually called the objective function to be optimized. Up to now, there is no existing analytical method minimizing Eq. (8.12) with $a_i \geq 0$. However in our simple tomography setup ($n=2$), this non-negative solution can easily be computed using the solver facility of Excel (based on the iterative Newton–Raphson algorithm) and constrained to non-negative solution. One gets:

$$a = \begin{pmatrix} 6.3 & 3.2 \\ 151.4 & 0.0 \end{pmatrix} \tag{8.13}$$

In this case the streak artefact is almost fully removed and the voxel value a_1 modelling the tumor is partially retrieved. There are numerous and fast iterative algorithms that minimize the chi-square (8.12), such as the conjugated gradient, the Levenberg–Marquardt and the Landweber [75]. However, constraining thousands of unknowns to be non-negative during the iterations dramatically hampers the convergence speed and stability of those algorithms.

An alternative of minimizing the weighted chi-square is to maximize the likelihood of the solution a_i. When the acquired data p_i are distributed as independent Poisson variables around the mean values $\langle p_i \rangle$, it can be shown that the log of the likelihood is:

$$L(a) = -\langle p_i \rangle + \sum_j c_{ij} a_j \log \langle p_i \rangle - \log \left(\left(\sum_j c_{ij} a_j \right)! \right) \tag{8.14}$$

An algorithm that at each iteration step increases the likelihood (8.14) was developed [88]. This algorithm always converges because there exists an upper bound value for the likelihood (8.14). This algorithm called expectation maximization of the maximum likelihood (EM-ML) is:

$$a_i^{n+1} = \frac{a_i^n}{\sum_k c_{ki}} \sum_k c_{ki} \frac{p_k}{\sum_j c_{kj} a_j^n} \tag{8.15}$$

Usually, the initial solution is chosen to be $a_i^0 = 1$ for all i. As all the c_{ij} are non-negative, this choice of initial solution preserves in a natural way the non-negativity of the solution. In our 2×2 example, Eq. (8.15) converges to:
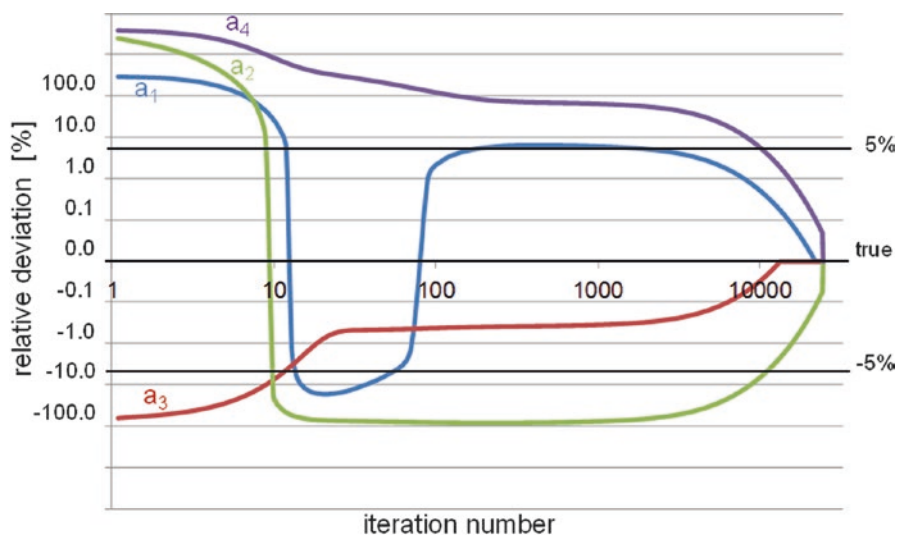
Fig. 8.4 Pseudo-log-log representation of the relative deviation (RD) as a function of the EM-ML iteration number. Although only about 11 iterations are needed to get an RD better than 5 % for the voxel a_3 (value = 150), more than 2000 and 10,000 iterations are needed for the voxel a_1 (value = 10) and the voxels a_2 and a_4 (value = 1) to get the same accuracy, respectively

$$a = \begin{pmatrix} 7.0 & 1.1 \\ 154.2 & 0.0 \end{pmatrix} \tag{8.16}$$

Note that EM-ML is a multiplicative algorithm and is thus non-linear, i.e. the sum of the reconstruction of two acquisitions is not equal to the reconstruction of the sum of the two acquisitions, i.e.:

$$\mathrm{EMML}\left(p_1\right) + \mathrm{EMML}\left(p_2\right) \neq \mathrm{EMML}\left(p_1 + p_2\right) \tag{8.17}$$

The right-hand side scenario provides the best result.

The EM-ML also has the drawback to have a very slow and non-uniform convergence speed: hundreds or even thousands of iterations are needed to come close to the solution, especially in the low count regions (Fig. 8.4).

8.2.6   FBP, EM-ML and OSEM in Clinical Studies

To reduce the computation time, an accelerated version of EM-ML called ordered subset expectation maximization (OSEM) was developed [38] and became the standard algorithm in tomographic reconstruction. Boost speed factor of about 30 can be reached; however OSEM does not overcome the non-uniform convergence speed issue.
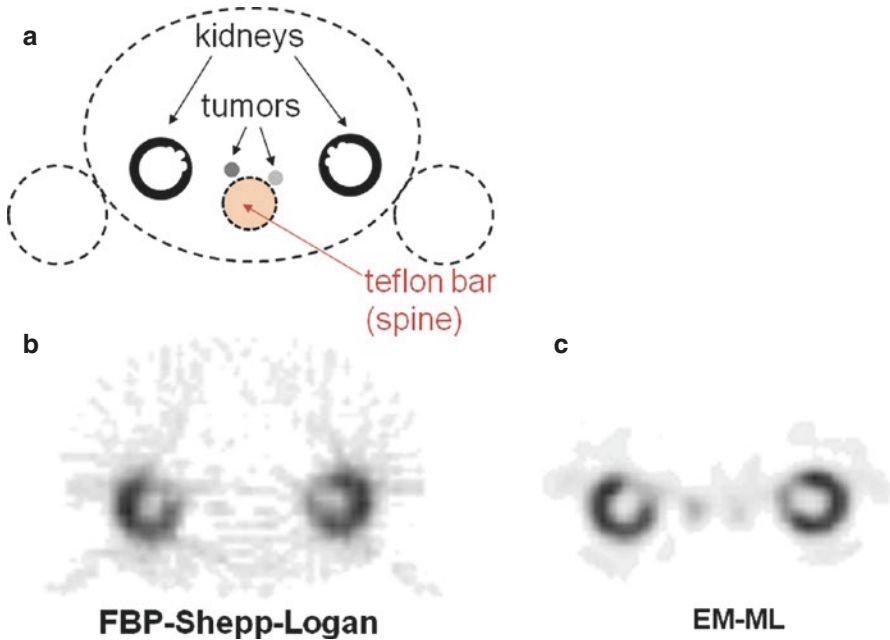
Fig. 8.5 (**a**) Drawing in the transverse plane of the phantom modelling, a typical ^{111}In-octreotate study, all compartments are filled with water, besides a Teflon bar modelling the spine attenuation. Specific ^{111}In concentrations in the two tumors were 50 and 25 % that of the modelled kidney cortex. (**b**, **c**): SPECT 30 min acquisition of the phantom performed on a Trionix Triad XLT20 camera equipped with a MEGP collimator and reconstructed in matrix 64×64 with FBP (**b**) and EM-ML (**c**), respectively. Compton scattering [114] and collimator PSF were included in the EM-ML reconstruction. Note the clear visualization of the modelled tumors in the EM-ML reconstruction, while in FBP they are overshadowed by the streak artefact originating from the kidneys

Physically, c_{ij} represents the probability that a photon emitted in the voxel a_j will be detected in the pixel p_i. When physical effects such as non-uniform attenuation, Compton scattering and detector response are included in the modelling of this probability c_{ij}, it is no longer possible to reconstruct the tomography using analytical methods such as FBP. On the other hand, iterative algorithms like EM-ML (Eq. 8.15) naturally compensate these disturbing physical effects during the reconstruction. This further explains why since a decade EM-ML or OSEM have superseded the historical FBP reconstruction in most SPECT and PET routines.

Figure 8.5 shows reconstructions of a phantom modelling, a typical ^{111}In-octreotate SPECT study. Conventional FBP reconstruction using a Shepp–Logan filter does not allow visualizing the two modelled tumors that are overshadowed by the streak artefact originating by the active kidney cortices. The EM-ML reconstruction clearly reveals the presence of the modelled tumors. Note also the better cortex delineation and contrast with the kidney pelvis as a result of the inclusion of the Compton scattering and of the collimator response in the EM-ML algorithm.

In contrary, most CT studies are still reconstructed with FBP. This results from two major features. First, CT scan requires reconstruction matrix size much larger than in SPECT or PET which dramatically increases the reconstruction time when using EM-ML-based algorithms. Secondly, as the dose is delivered to the patient only during the acquisition time, and not during several hours such as in SPECT and PET, CT can benefit from higher acquisition counting rates. This reduces the noise present in the acquired data and the need to use EM-ML-based algorithms. However, due to the endless increasing concern about patient radioprotection, all CT manufacturers are now proposing iterative reconstruction algorithm with their systems in order to reduce the patient irradiation [8, 39, 70, 71].

8.2.7   EM-ML and OSEM Regularization

Although the non-negativity of EM-ML well overcomes the streak artefact issues in low count region, EM-ML does not succeed as well in large count regions where the ill-posed nature of tomography induces high negative–positive fluctuations around the actual counts. The amplitude and the frequency of these fluctuations increase with the number of iterations. A simple method to address this issue is to limit the number of iterations, which in some way regularizes the problem. However, due to the non-uniform convergence speed, this approach cannot be recommended when the target tissue is located close to a more active tissue, which is often the case in nuclear medicine.

A popular way to regularize the problem is to add some penalty function P to the likelihood and to maximize the cost function:

$$Q(a) = L(a) - \lambda \ P(a) \tag{8.18}$$

The goal is now to find the solution a_j that maximizes $Q(a)$. The penalty function $P(a)$ is constructed such that $P(a)$ increases with fluctuations in a_i. In other words, the first term in (8.18) penalizes solutions which do not fit well the acquired data, while the second penalizes solutions containing unphysical variations. Note that Eq. (8.18) contains an adjustable parameter λ. A very simple penalty function is:

$$P(a) = \sum_i a_i^2 \tag{8.19}$$

It is very simple to check that for a constant total count $C = \sum_i a_i$, the solution that maximizes $-P(a)$ is the uniform solution $a_i = \dfrac{C}{n}$, i.e. the smoothest solution (e.g. if $n = 2$ and $C = 8$, $5^2 + 3^2 > 4^2 + 4^2$). Obviously, this simple penalty function has the drawback to also smooth the actual activity transition at the tissue boundaries.

There is a very abundant literature about regularization methods [10, 20, 24, 62–64]. Popular regularization methods are:

- The use of various sophisticated penalty functions or Bayesian prior designed to better preserve the actual edge transitions, such as the promising total variation method [14].
- Blob-based reconstruction, where the reconstruction is not performed on adjacent voxels but on overlapping voxels (called blobs) of various shapes and diameters playing the role of regularization parameter λ. The inter-blobs coupling due to the overlapping stabilizes the reconstruction and avoids excessive fluctuations.
- Relaxation method, where the next iteration is not obtained purely using Eq. (8.15), but by performing a weighted sum of Eq. (8.15) with the previous iteration, i.e. $\lambda a^n + (1-\lambda) a^{n+1}$. When the relaxation parameter λ vanishes, one gets back the standard EM-ML algorithm.

Combinations of these different regularization methods are also proposed. Once in a while, one manufacturer claims to have succeeded in implementing the ultimate reconstruction algorithm that provides a noise-free image without any compromising of the resolution, giving self-important and attractive name to their reconstruction software. The reality is that despite intense works performed by mathematicians during the last two decades, this ideal regularization has not yet been found. Current regularizations still include some trade-off between noise reduction and resolution smoothing through the regularization parameter λ which in practice depends in an obscure way on the acquired data. Manufacturers continuously improve empirical relations giving the regularization parameter as a function of the tracers used, tissue studied and patient size. All these considerations advise the clinician to pay attention to the image rendering.

8.2.8   Conditioning Improvement in Emission Tomography

Although during 40 years the ill-posed nature of emission tomography was only addressed in the reconstruction process and only intensively for the last two decades, a major breakthrough was initiated in 2006 with the launching of the first successful commercial time-of-flight (TOF) PET system [102]. Indeed, by measuring the arrival delay between the two 511 keV γ-rays on the detector ring, it is possible to get information about the decay location on the LOR. Current TOF-PET systems have a TOF resolution of about 320 ps [101] which corresponds to a spatial resolution of about 5 cm on the decay location on the LOR. Using such a system, two decays occurring at two positions $-t$ and t on the LORs (see Fig. 8.2a) more than 5 cm apart will be counted in two different TOF projections. As a result negative and positive offset around the actual counts will no longer cancel each other. In other words, the distribution (8.1) is now a visible object for a TOF-PET system, and only the distribution (8.1) truncated inside the radius $r = 2.5$ cm will remain an invisible object. TOF information really reduces the ill-posed nature of the tomography acquisition [4, 18] rather than lowering its impact on the reconstructed data. As a
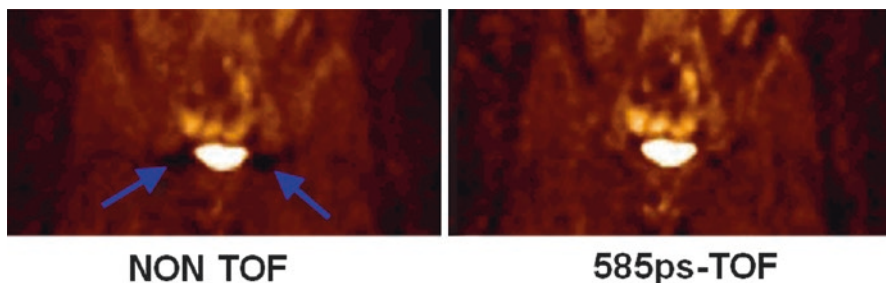
Fig. 8.6 Reduction of the artefacts present around the bladder in non-TOF reconstruction (Courtesy of Dr. Joel Karp)

result TOF significantly reduces noise artefact (Fig. 8.6), especially in corpulent patient where the higher attenuation reduces the count rate and thus increases the noise in acquired data [50].

Since a decade an intense race is engaged between physics labs in order to reach a TOF resolution of 25 ps corresponding to a decay localisation resolution of 4 mm [111]. When reached, this TOF resolution will allow the direct positioning of the decay in the appropriate 4 mm transverse voxel without any reconstruction process: TOF-PET will become a full well-posed problem. In consequence, all the noise artefacts will disappear; noise will no longer be correlated in the transverse slice and will follow the Poisson distribution such as in planar view. From 2006 to 2015, the TOF resolution of commercial systems improved from 650 ps to 320 ps [60, 101, 103]. In physics labs, TOF resolution of 75 ps was reached, but using a simple two-arm detectors equipped with pure thin CsBr crystal [89].

A similar breakthrough for SPECT is in preparation in physics labs with the development of recoil electron-tracking Compton camera using pressurized gas chamber [46, 47]. With this camera, the LOR of the decay is determined without the use of a collimator. Surrounding the patient with such cameras and using multi γ-rays emitters, such as ^{111}In, ^{67}Ga or ^{95}Tc, the decay location will directly be obtained without any reconstruction process [111].

8.3   CT

8.3.1   Principles

In CT, an anatomical image is derived from the total attenuation underwent by x-rays along different angles around the patient. The radiation intensity reaching the detector is given by

$$I(s,\theta) = I_0\, e^{-\sum_l R_\theta \mu(s,l)} \tag{8.20}$$

where I_0 is the source intensity, $\mu(x,y)$ is the patient attenuation coefficient and R_θ is the rotation by an angle θ. Taking the logarithm gives:

$$p(s,\theta) = -\ln\left(\frac{I(s,\theta)}{I_0}\right) = \sum_l R_\theta \mu(s,l) \qquad (8.21)$$

Projections p are the sum of the attenuation coefficients along the LORs and can thus be reconstructed in the same way that emission tomography where the projections are the sum of the activity. For a specific photon energy, regarding that mammalians are mainly made of low atomic number Z elements ($Z \leq 8$), the attenuation coefficient mainly depends on the crossed tissues density.

CT reconstructed images are usually displayed in Hounsfield units, defined as

$$HU(x,y) = 1000\frac{\mu(x,y) - \mu_w}{\mu_w} \qquad (8.22)$$

where μ_w is the attenuation coefficient of water at the x-ray beam energy used.

Clinical CT developed in [36] is still in continuous improvement [22, 48]. The first CT generation was composed of only one x-ray source and one detector cell translating and rotating together around the patient (Fig. 8.7a). Next, the number of detector cells was increased in order to reduce the acquisition time (Fig. 8.7b). Most current CT scanners are from the third generation where an x-ray fan beam is detected by many cells forming an arc or a flat panel [29, 30] (Fig. 8.7c). In some systems, the source-detector couple rotates around the patient while the patient table translates, resulting in a helical acquisition, often called spiral. There exists a fourth generation of CT scanner where the detector is a full stationary ring around the patient (Fig. 8.7d).

Note that similarly to PET, no mechanical collimation is needed, the LOR being the line going from the x-ray point source to the detector cell reached.

The development of fast spiral CT scanner in the 1980s gave a boost to the use of CT in medical imaging. Shorter scans make it possible for patients to hold their breath during the scan which reduces motion artefacts. Spiral CT scans are characterized by the pitch factor, equal to the ratio of the distance covered by the table in one source revolution over the detector axial width (or slice thickness). In practice the pitch factor is chosen between 1 and 1.8. A higher pitch corresponds to faster volume coverage, but also to fewer data samples as the gap between samples increases [37]. Note that with the introduction of multi-row detector, some controversies and discrepancies appeared in the definition of the pitch [91].

Although CT reconstruction used the same methods than in emission tomography, the different detection technique used results in specific reconstruction artefacts that are important to know and to identify [7, 12, 37].
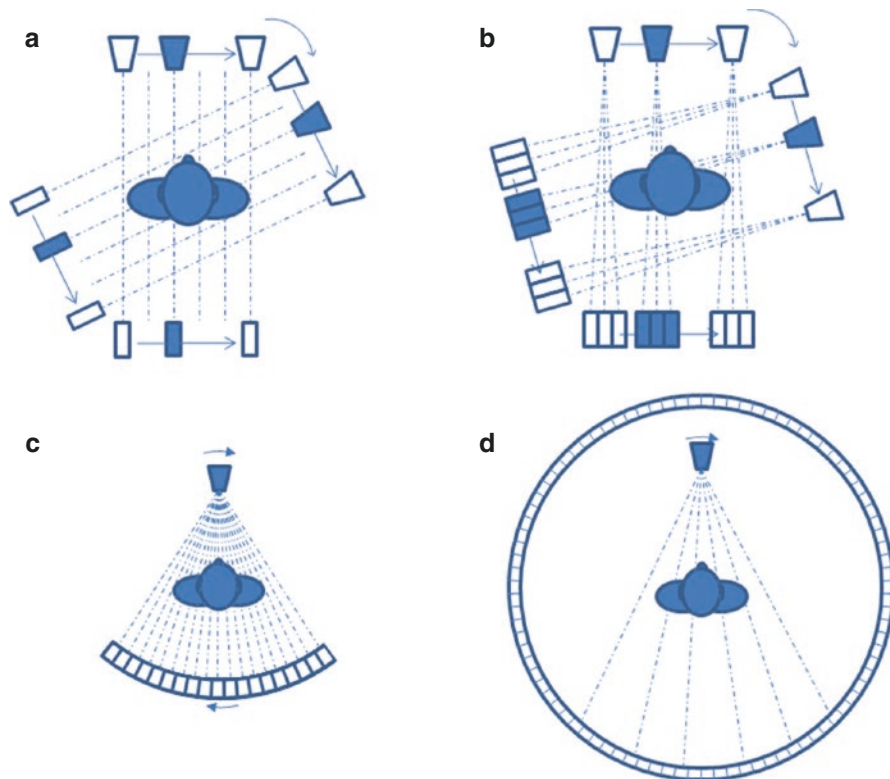
Fig. 8.7 Four generations of CT scan. (**a**, **b**) First and second generation: one beam source and detector(s) couple translating and rotating around the patient. (**c**) Third generation: fan beam source and arc-shaped detector couple rotating around the patient. (**d**) Fourth generation: fan beam source rotating around the patient surrounded by a full-ring static detector

8.3.2   Beam-Hardening Artefacts

Beam-hardening artefacts are due to the non-monochromatic nature of the x-ray beam source which is produced by fast electrons colliding with a solid metal anode. This generates a continuous energy spectrum up to a maximum energy fixed by the high voltage applied between the cathode and anode, i.e. the "kV" value. When travelling into the patient's body, the low-energy part of the spectrum is more attenuated making the beam harder and harder. As a result, the beam is less and less attenuated by the tissue, resulting in an underestimation of the tissue density in the reconstruction image (Fig. 8.8).

A simple correction, implemented in all modern CT scanner to reduce the beam-hardening artefacts, consists in adding an aluminium or copper plate between the source and the patient to filter the low energetic photons.
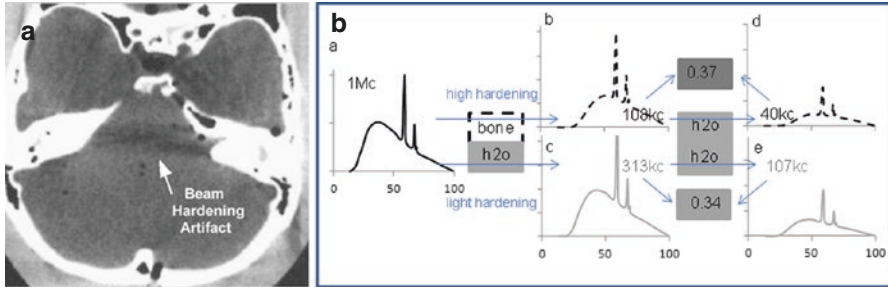
Fig. 8.8 (**a**) Beam-hardening artefact due to the stronger attenuation of bone tissues (Reprinted from [27] with permission of the society of nuclear medicine). (**b**) Schematic explanation. *a*: Typical CT energy spectrum. *b* and *c*: Hardened energy spectra after crossing 5 cm of bone and water, respectively. *d* and *e*: Resulting energy spectra after crossing an additional 5 cm of water. Due to the higher hardening by bone, the ratio of the total counts between spectra d and b (i.e. $0.37 = 40/108$) corresponds to a pseudo less attenuating additional tissue than the one exhibited by the ratio of spectra e and c (i.e. $0.34 = 107/313$)

The beam-hardening of the x-ray spectrum also induces errors in the reconstructed image in the form of under-evaluated attenuation coefficients in the central region of the patient. These are called cupping artefacts. Most CT scanners include software corrections for these artefacts based on a calibration of the system with a water phantom. Of course these corrections are not adapted for bone tissues as these attenuate the x-ray beam a lot more than water or soft tissues. In that case more sophisticated techniques are needed to correct for beam-hardening artefacts. One solution is to combine CT scans acquired with two different energies, i.e. two different maximum high voltages [44]. By combining the projections obtained with the two scans, it is possible to reconstruct the image without beam-hardening artefacts [15].

8.3.3 Motion Artefacts

The reconstruction theory assumed that the object did not change during the CT scan. In clinics, this assumption may not hold as breathing, cardiac beating and peristalsis induce motions. Object changes can also result from the administration of contrast agent. As a result, the projections acquired at different time become inconsistent and produce motion artefacts in the reconstructed image. These artefacts can be reduced by decreasing the scan duration below the typical motion. The drawback is the associated reduction of the signal to noise ratio. In the case of respiratory motion, artefacts can be reduced if the patient is able to hold his breath during the scan.

Optimal solutions to avoid breathing and beating artefacts make use of gating acquisitions [51, 96]. Different parts of the cycle are then reconstructed resulting in

4D images. These 4D modes not only reduce motion artefacts but also make it possible to study the organs in motion. Alternative methods are also developed in order to extract motion information from the projection data only directly into the iterative reconstruction algorithms [39].

8.3.4 Sampling Artefacts

Sampling artefacts, also known as aliasing, arise when the Nyquist–Shannon sampling theorem is not satisfied. The theorem states that, to be able to correctly reconstruct, the number of sampling points per distance unit must be at least twice the highest spatial frequency in the imaged object. Thus in order to fully profit of the resolution of the detector cells, at least two sampling points should be obtained per detector cell [37].

Two oversampling methods exist. (1) The quarter detector shift consists in shifting the detector array from one quarter of a cell with respect to the x-ray focal spot (Fig. 8.9a). Projections at 180° from each other are no more equivalent, and scans over 360° allow to double the sampling points. However, this technique is only partially effective as the double sampling property, exact for the centre rays, is only approximate for other rays. (2) In the focal spot wobble approach, the doubling of the sampling is obtained by taking additional measurements after a small displacement of the focal spot. For each projection data, an additional projection is performed when the detector has rotated, so that the detector cells straddle their previous position, and the focal spot was moved close to its previous location (Fig. 8.9b,c).

8.3.5 Detector-Induced Artefacts

It is well known that defects in the detector produce artefacts in the reconstructed image. In third-generation CT scanner, the failure of a detector channel is at the origin of ring artefacts as to a given detector channel corresponds a circle in the object space [15].

Afterglow photons can be detected too late and then associated to wrong projections resulting in blurred tissue boundaries in the images. However, modern ceramic scintillators, such as the popular gadolinium oxysulfide, have significantly overcome this issue with their very short afterglow.

8.3.6 Metal Artefacts

Metal artefacts are very problematic for patient diagnosis. Because of their high-density and high atomic number compared to soft and bone tissues, metal implants produce strong beam-hardening artefacts. Furthermore, as the borders of metal parts
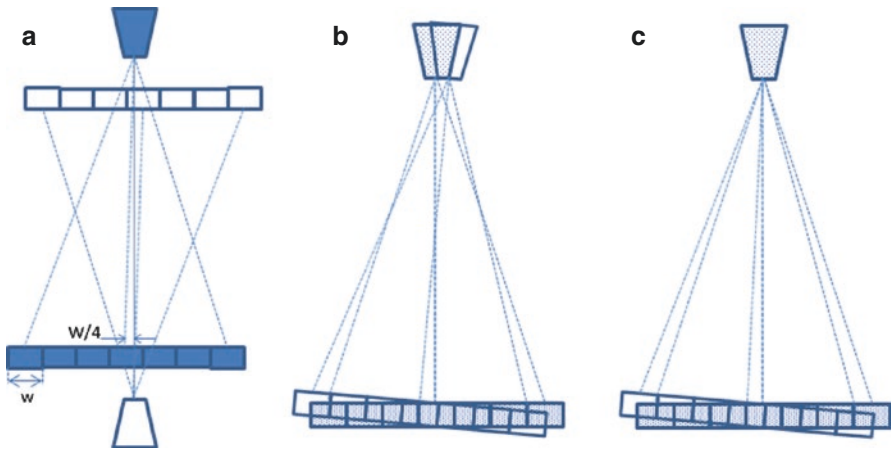
Fig. 8.9 (**a**) Quarter shift detector technique to double the sampling in 360° CT scans. Opposite projections are no more equivalent. (**b**, **c**): Focal spot wobble technique to double the sampling. The couple formed by the x-ray source and the detector are rotated by a small angle so that the detector cells straddle their previous positions (**b**), and then the focal spot is moved to its previous location (**c**)
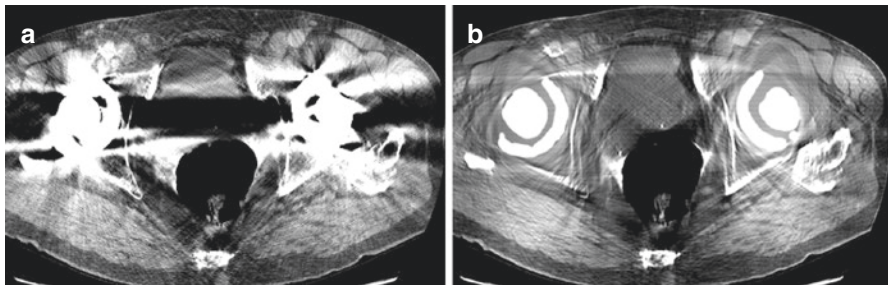
Fig. 8.10 (**a**) Metal artefact as dark streak between hip replacements. (**b**) Same image after use of the metal deletion technique (Reprinted from Boas et al. [8] with permission of Future Medicine)

are usually very sharp, partial volume and aliasing artefacts are also common in the reconstructed image. Metal implants not only strongly attenuates the primary beam, they also produce a lot of scattered rays. This induces a low signal to noise ratio behind the metal object. Metal objects also introduce inconsistencies in the projections data, which produces especially dark and light stripes in the CT image (Fig. 8.10).

Solutions to beam-hardening and partial volume artefacts are also adequate to reduce metal artefacts. Additional techniques replace projections data due to the metal objects by some interpolation of the neighbouring projection data. This greatly improves the image quality around the metal objects, but these objects and the nearest tissues are missing from the reconstructed image. Dedicated iterative reconstructions allow a better compensation of projection inconsistencies and are now proposed by CT manufacturers [105].

8.3.7   Scatter Radiation Artefacts

In addition to be absorbed by the tissue by photoelectric effect, x-rays are also scattered. These scattered photons can then reach other detector cells and increase the corresponding measured signals. This is an issue when strongly attenuating objects are scanned (like shoulder, abdomen, pelvis or metal implants), because in that case the scattered signal may become larger than the direct signal. In the third CT generation, the contribution of scattered rays is reduced by setting a collimator, or anti-scatter grid, in front of the detector and focusing to the x-ray source [15, 37]. Correcting software algorithms are also developed [90, 122].

8.3.8   Specific Spiral CT Artefacts

Artefacts specific to spiral CT scans are related to the pitch factor. When the pitch increases, or equivalently when the distance travelled by the table during one gantry rotation increases, less information are collected per scan volume. This induces inconsistencies in the data because of the interpolation needed in spiral CT reconstruction which results in shading artefacts.

8.3.9   Noise

The noise in reconstructed images has two origins. (1) The detector noise is the thermal noise produced by the electrons in the detector and is independent of the x-ray flux. (2) The quantum noise comes from the stochastic fluctuations in the number of photons (quanta) reaching the detector and can produce streak artefacts in reconstructed images (Fig. 8.11). Typically, noise reduction is obtained by increasing the number of photons measured on the detector. This can be done by increasing the detector size or the x-ray tube intensity, expressed in mAs, i.e. the product of the current by the exposition time. Noise reduction techniques are also implemented in recent iterative reconstruction algorithm, so as to preserve the image quality together with a dose reduction for the patient (see below).

8.3.10   Dose Reduction

Because of its performance as a diagnostic tool, the use of CT scans has known a tremendous growth since a few decades [58] resulting in concerns about radiation doses. Moreover, scanning protocols were initially derived for adults which leads to an overexposure in the case of paediatric CT study. Several techniques have been developed in order to reduce the patient dose from CT scans [49, 57, 120, 121].

A 60 mA, 120 kVp, slice thickness 5 mm   A 440 mA, 120 kVp, slice thickness 5 mm
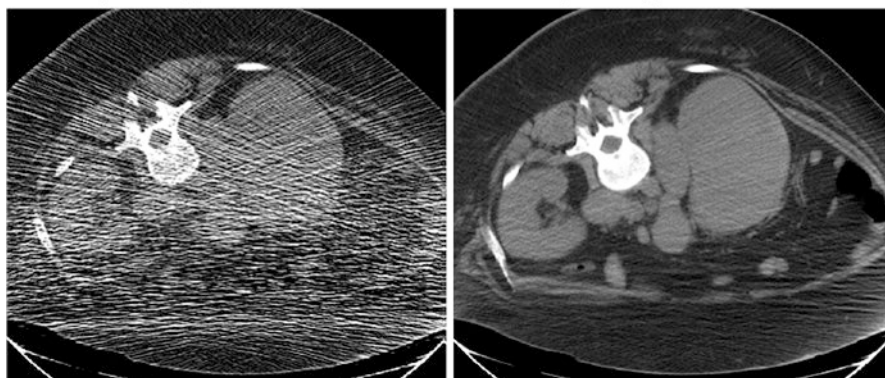
Fig. 8.11 Illustration of quantum noise related to the mA intensity. (**a**) Low-dose CT image shows streak artefacts. (**b**) CT image obtained at a 7.3 times higher dose displays much less quantum noise (Reprinted from Boas and Fleischmann [12] with permission of Future Medicine)

The first way to reduce the dose is to use a low x-ray intensity, i.e. low mAs, that ensures a sufficient image quality regarding the study purpose. In this perspective use of iterative reconstruction algorithms is promising and is now proposed by CT manufacturers [72]. In hybrid use, i.e. with SPECT or PET, the goal is often to obtain the attenuation map in order to correct the associated emission tomography and to anatomically locate the tumors. These two purposes do not require very high-resolution imaging. CT scans performed in hybrid studies usually used about 5 times lower mAs than in diagnostic studies and are thus often called low-dose CT scan.

The acquired photons depend on the initial x-ray intensity and on the patient attenuation along the LOR. So it makes sense to reduce the initial intensity for the detector position where the beam is less attenuated in the patient. This is the principle of the dose modulation [49]. The longitudinal dose modulation corresponds to a current modulation according to the detector position along the patient's body in which smaller current intensities are used in the lung region. In angular dose modulation, the tube current is reduced from anterior or posterior detector position as patient section is rather oval than circular. A temporal dose modulation is also possible during gated scans, i.e. the tube current is switch on and off according to the phase in the gated cycle.

As low-energy x-rays are strongly attenuated by matter, they contribute a lot to the dose but have a low impact on the measured signal. It is so of interest to limit the part of low-energy x-rays in the beam produced by the CT tube. This is generally done by adding a filter plate made of aluminium and/or copper in front of the CT tube. From the same idea of filtering the x-ray beam, specially shaped filters, called bowtie filters, may be used to take into account the fact that x-rays at the beam centre must go through more tissues than rays on the beam border [15, 37].

8.4   SPECT/CT and PET/CT

As attenuation depends on the photon energy, some conversion is needed in order to rescale the attenuation coefficients to the gamma rays energy used in SPECT and PET. The basic approach is to scale the attenuation coefficients by the ratio of the attenuation coefficient of water at the CT energy and at the emission energy. This gives relatively good results for soft tissues, but does not work very well for denser tissues like bones [5, 53].

Not only breathing blurred the image in SPECT and PET [11, 65, 67, 93], but it can induce a mismatch between the attenuation map obtained in CT with breathing hold (to avoid CT artefact) and the mean location of tissues in the emission tomography. This can produce an inaccurate attenuation correction and artefacts in the emission tomography [86]. These errors impact the reliability of the resulting images, and this is especially problematic in the follow-up of patient lesions in PET/CT [67]. The breath-holding technique has been adapted for PET and SPECT in the form of repeated breath-holds [11, 59, 99, 118]. Breath gating is a preferable option to overcome these issues [67, 68, 100]. Other techniques are being developed to take into account the respiratory motion directly into the iterative reconstruction algorithm [82, 83].

8.5   MRI (Magnetic Resonance Imaging)

8.5.1   Principles

MRI is based on the spin, or magnetic moment, of the hydrogen nucleus (noted here H^+). The classical representation of the spin is a top; the spinning speed of which being defined by the spin value, i.e. $S = 1/2$ for the hydrogen nucleus. In the presence of a static external magnetic field $\vec{B}_0$, the mean proton spin over time $\vec{M}$ is parallel with the magnetic field axis although precessing around it at the Larmor frequency ω_0 which is proportional to $\left|\vec{B}_0\right|$. Animations of the Larmor precession and of the different MRI sequences are freely accessible in [35].

Quantum mechanics (QM) shows that the Larmor precession has $2S + 1$ steady states, i.e. for H^+ two states corresponding to $\vec{M}$ anti-aligned or aligned with $\vec{B}_0$, this last state being the fundamental state of lowest energy. Even with magnetic fields of a few teslas, due to the weakness of magnetic interaction versus the thermal collisions, at room temperature the number of H^+ spin aligned with $\vec{B}_0$ only exceeds by a very small amount that of anti-aligned. Regarding that only this small amount induces a macroscopic field, it is common to represent and discuss only the behaviour of this small amount.

In a non-uniform magnetic field $\vec{B}(x,,y,,z)$, the H^+ will obviously precess with different Larmor frequencies $\omega_B(x, y, z)$. By applying a radiofrequency (RF) pulse of

frequency ω during an appropriate time, it is possible to rotate by a specific angle only the H$^+$ precessing at a frequency close to that frequency ω (resonance effect). After the RF pulse, as they are not longer in a QM steady state, the rotated spins will move back to a steady state by emitting a RF signal proportional to the H$^+$ density and during a time depending on the surrounding tissue environment (relaxation).

In MRI system, a static magnetic field $\vec{B}_0$ of several teslas is set parallel to the patient table. By convention the z-axis is parallel to the table, x-axis is horizontal and y-axis is vertical. The simplest imaging sequence is made of three steps.

$\vec{B}_0$ is transformed to a new static field $\vec{B}_0(z)$ by adding a gradient Gz along the direction z. As a result, the Larmor frequency ω_0 becomes $\omega_0(z)$. During the application of this gradient Gz, an RF pulse of frequency $\omega_0(Z)$ during an appropriate time forces the spins of the H$^+$ located in the slice $z = Z$ to align perpendicularly to the z-axis. Just after switching off the gradient Gz, the spins are precessing in phase (coherent state) with the precession axis nutating to the z-axis (relaxation).

A gradient Gy is then applied along the y-axis during a short time, as the precession speed is different along y during the gradient application, after switching off the gradient the precession is in different phase along y (phase encoding).

Lastly, a gradient Gx is applied along the x-axis giving a precession frequency depending on the coordinate x. During the application of Gx, the measured macroscopic RF signal has a phase and a frequency depending on the y and x coordinates, respectively. This corresponds thus on the direct measurement of the 2D Fourier transform of the slice Z.

These three steps are repeated for all the slices z to be imaged and were the core of the early MRI. With time, numerous imaging sequences have been developed in order to improve the measured signal or to assess other parameters than the H$^+$ density, such as the different relaxation times which depend on the chemical composition. Description of all the imaging sequence is far beyond the scope of this section and can be found in [35, 98].

The major point is that MRI does not proceed as the measurement of projections, but more as a spatial probing. As a result, performance and artefact in MRI will be peculiar to this modality.

8.5.2 Artefacts

MR images may be subject to different kinds of artefacts [9].

The frequency of the radio waves used in MRI lies in the FM band. If the scanner room is not properly shielded, e.g. if a door remains open, TV and radio communications can produce artefacts in the image. They typically take the form of zipper artefacts, i.e. spurious bands of noise, oriented perpendicularly to the axis of the frequency encoding [31].

Hardware defects with the field gradients or RF antennas may produce local non-uniformity in the magnetic field that would result in image artefacts.

The reconstruction technique of the MRI image is based on the assumption that all frequency differences are due to the linear imaging gradients. Any violation of that assumption results in image artefacts. These artefacts appear as relative displacements of nuclei in the image slice. Similar differences in phase induced by other factors than the linear gradients produce distortion artefacts in the image slice.

As the k-space imaging is a Fourier technique, it presents the same artefacts if the underlying assumptions are not met. For example, if the sampling of the k-space is not dense enough relatively to the signal variations, aliasing artefacts may appear, giving rise to misplaced and overlapping signals. Techniques, referred as parallel imaging, have been developed to avoid aliasing artefacts. They are based on the use of multiple antennas to measure the signal and the combination of their data to produce a un-aliased image [76, 94].

Artefacts may also be produced by metal implants due to the large differences in the magnetic properties of metal parts and tissues. The difference in magnetic susceptibilities between the metal implant and the surrounding tissues may induce local inhomogeneities in the magnetic field. This results in variations in the phase and frequency of local spins, which translates to misplacement (possibly coupled with signal loss) and distortion artefacts in the image. Such metal artefacts may be reduced by proper selection of the scan sequence parameters [32, 97].

8.5.3   Attenuation Map

A few years ago, PET/MR hybrid systems have been introduced in the clinical frame. At the beginning the two modalities were located in separate gantries because of electromagnetic interferences, with a common bed moved from one modality to the other during patient studies. Recent technological advances, especially in solid-state detectors (SiPM) for PET, allowed companies to develop PET/MR systems with both modalities integrated in the same gantry. This enables simultaneous PET and MR acquisitions. One of the challenges of such PET/MR hybrid systems is to determine an attenuation map for the PET image reconstruction in the absence of a CT scan or a PET transmission scan [106].

MR has the advantage over CT to offer better contrast between soft tissues. However deriving an attenuation map from the MR image is less straightforward than from the CT image. Indeed unlike the CT scan that provides the distribution of the electron density in the image volume, MR image reflects the distribution of hydrogen nuclei in tissues and tissue relaxation properties. In particular MR is typically unable to delineate cortical bones because hydrogen nuclei are somewhat frozen in the corresponding structure and so, like air cavities, emit no signal when excited by RF pulses. Cortical bone structures then appear like air cavities on MR images. Different approaches have been explored to construct an attenuation map from the MR image, but this is still a work in progress [34]. The ideal method would provide automatically, i.e. without any intervention of the operator, an attenuation map accurate enough to enable the reconstruction of PET images of quality.

There are mainly two approaches to obtain an attenuation map from MR: image segmentation and atlas/template matching [52]. Segmentation techniques of the MR image have been successfully applied for brain imaging. MR images are typically segmented in three to five classes (air, soft tissues, lungs+fat+bone), each one associated to an appropriate attenuation coefficient value at 511 keV [2, 85]. Classification can be improved by using additional anatomical information to distinguish between regions showing similar MR intensities but corresponding to different attenuation properties. Classification schemes based on fused MR and uncorrected PET images may also improve the classification accuracy and the corrected PET image quality [117].

The atlas-matching method is based on some atlas co-registration [3]. An atlas is composed of a template MR image co-registered to an attenuation label image. The template image can be formed by the average of several co-registered MR patient images. The label image can be derived from an image segmented into different tissue classes or a co-registered attenuation map obtained from a CT scan. The template MR is distorted to match the patient-specific MR image volume. The same transformation is then applied to the atlas attenuation image to obtain a patient-specific attenuation map for the PET reconstruction. Atlas methods may prove challenging in whole body imaging because of the strong anatomic variability between patients. A general spatial transformation to transform the template to the patient-specific image may thus be difficult to obtain [34].

The estimation of the attenuation map from the MR image presents additional specific difficulties [34]. As stated before MR imaging usually does not represent bones. A combination of dedicated MR sequences, like ultrashort echo time (UTE) and late echo, may enable the delineation of cortical bones from soft tissues [1, 52, 84]. The drawback is the longer acquisition time required by these sequences. As the field of view of the MR modality is usually reduced compared to PET, parts of the patient's body, especially its arms, may be truncated on the MR image [21]. However, these parts contribute to the attenuation of the gammas in the PET acquisition and so have to be accounted for. One possible solution would be to use the uncorrected PET image to identify these structures unseen on the MR image.

There are other structures unseen on the MR image but whose attenuation has to be taken into account: MR coils. On one hand, some fixed coils, like head coils, can be identified and assigned an attenuation value through some basic CT scan. On the other hand, flexible surface coils cannot be located easily because of their elasticity. However, they might probably be localized by using some specific UTE MR sequences.

Respiratory motion may also impact the quality of the attenuation map when used for PET reconstruction. Indeed MR acquisition durations are relatively long (counting in dozen minutes), especially if specific RF sequences are combined. So these acquisitions span many breathing cycles, and the corresponding MR image can only be used to construct an average attenuation map that could be badly correlated to the PET image. To lessen the impact of breath averaging, some studies are focusing on the creation of attenuation maps from 4D MR acquisitions [13].

The use of predefined attenuation coefficients in the map may pose problem in regions showing strong inter-patient variability, like for lungs. This may lead to non-negligible errors in the PET reconstruction. Similarly the number of classes used in the segmentation approaches may impact quantitative PET results. Some studies indicate that at least air, lung and soft tissue, spongious bone and cortical bone should be distinguished for attenuation correction in order to maintain errors below 5 % [52].

8.6   SPECT

8.6.1   Dead Time Issue

Large FOV SPECT are still routinely performed using conventional NaI gamma camera (developed by Hal Anger in 1958) equipped with parallel hole collimator. Originally, all the analogue PMT signals were combined together by a resistor matrix in order to compute the position and the energy of the photoelectric effect. As a result, photoelectric effects occurring anywhere on the crystal impact the detector dead time, and the camera count rate starts to quickly saturate above 20 kcps. Although, this count rate capacity was sufficient for most diagnostic studies, it was a real limitation in post-radionuclide therapy imaging.

A major improvement occurred in the 1990s with the individualized digitalization of the PMT signals. Thanks to the digitalization, only the signals of the PMTs in front of the photoelectric effect are used to characterize the effect. As a result, several photoelectric effects occurring at the same time in sufficient distant regions of the crystal can be simultaneously treated allowing the maximal count rate of modern camera to exceed 500 kcps. This is a significant improvement when performing quantitative ^{777}Lu-DOTATATE or ^{131}I-MIBG early post therapy imaging that can still require some dead time correction. Obviously, maximal camera count rate capacity can be reached only if the count rate is uniformly spread on the crystal. High non-uniform activity uptake can require non-uniform dead time correction.

In contrary, the energy and spatial resolution that mainly depend on the crystal and on the collimator, respectively, have little improved.

8.6.2   Spatial Resolution

The spatial resolution of the detector is mainly that of the collimator and thus linearly increased with the distance. It is thus of prime importance to keep the collimator as close as possible to the patient during the SPECT orbit. Most modern cameras have automatic detector radial motion following the patient surface. At 15 cm away from the collimator, the spatial resolution of the system is typically ≈ 10 mm using a low-energy (LE) high-resolution collimator and ≈ 15 mm using a middle energy (ME) collimator. Note that these are the optimal theoretical

resolutions; the clinical resolution is still worsened by the presence of noise requiring some smoothing of the reconstruction (see first section of the chapter).

8.6.3 Attenuation Issue

Attenuation of gamma rays of energy E in a uniform medium is described by the simple law:

$$N(x) = N_0\, e^{-\mu(E)x} \tag{8.23}$$

where N_0 is the initial number of photons, $N(x)$ the number after crossing a length x in the medium and μ is the attenuation coefficient of the medium. μ decreases when the energy of the photons increases, i.e. high-energy gamma rays are less attenuated. When different media are successively crossed by the gamma rays, the final number of photons is obtained by successively multiplying the initial number by the exponential terms corresponding to each voxel crossed, i.e.:

$$N = N_0\, e^{-h\sum_i \mu_i(E)} \tag{8.24}$$

where $\mu_i(E)$ is the attenuation coefficient of the crossed voxel i and h the width of the voxel.

For water, $\mu = 0.15$ cm^{-1} meaning that 5 cm of water reduces by a factor 2 the number of photons. Air attenuation is negligible for any energy. With regard to the limited energy resolution of gamma camera, all natural tissues, besides the lung and bones, can be considered as water regarding the attenuation.

Analytical reconstruction algorithm correcting a non-uniform attenuation has been recently found [28, 69]. In iterative reconstruction, the correction simply consists to include the attenuation (8.23) in the matrix c used in the algorithm (8.15). Obviously, this requires the prior knowledge of the coefficients $\mu_i(E)$ that can be derived from a CT or a MR scan.

8.6.4 Energy Resolution and Compton Scatter Issue

The NaI energy resolution ($\approx 10\,\%$) forbids simultaneous clinical acquisition of isotopes having close gamma emission energies, such as ^{177}Lu (113 & 200 keV) and ^{111}In (171 & 245 keV). Furthermore, acquisitions are corrupted by a significant amount of gamma rays undergoing Compton scattering inside the patient. This amount is about 40 % in standard patient size and increases with the patient corpulence due to the attenuation of the primary gamma rays by the tissue. Typically, 14 cm of soft tissue corresponds to attenuation by a factor 2 at 200 keV that is the main emission of ^{177}Lu. Giving wrong information on the decay location, these scattered gamma rays hamper both the image contrast and the activity quantification.

The simplest method to correct scattering is to perform the attenuation correction using effective attenuation factors that are lower than the actual ones in order to take into account the extra amount of detected events induced by the scattering. Although this method improves in some way the quantification, it has no impact on the loss of contrast induced by the wrong decay location information carried by the scattered gamma rays.

A better and popular method is to subtract from the primary acquisition energy window a fraction of the events recorded in a lower energy window that mainly contains scattered gamma rays [41]. Although not perfect, due to the fact that the events detected in the lower energy windows correspond to scattering angles larger than those in the primary energy window, this method has the benefits to also improve the image contrast and has been implemented in most commercial systems.

More sophisticated and more accurate models consider an effective path of the photon between its emission and its last scattering position; at this last position a function takes into account the angular scattering probability. This can be done by introducing at each iteration step an additional 3D integration on the last scattering position [114] or by performing three simple conventional convolutions [26].

8.6.5 Collimator Choice

The choice of the right collimator is of prime importance, both for the visual quality and quantitative accuracy of SPECT imaging. Within its nominal energy range, a collimator will behave accordingly to the sensitivity and spatial resolution specifications provided by the manufacturer. In contrary, just above the nominal energy range, the collimator behaviour can appear unpredictable. For example, low-energy (LE) collimators with 0.3-mm-thick septa (usually old ones) rightly behave up to 200 keV, while LE collimators with 0.015-mm-thick septa (usually modern ones) suffer from penetration above 160 keV. As a result, one should always use medium energy (ME) collimator for ^{177}Lu [54] and for ^{111}In. High-energy (HE) collimator is required for ^{131}I due to the presence of small peaks around 700 keV that even if not imaged can easily penetrate an ME collimator and afterwards scatter down to the 360 keV acquisition window.

For ^{111}In and ^{131}I, if available, the use of a camera with thicker crystal is preferable: not only the sensitivity will increase, but the penetration of the high-energy gamma rays through the crystal will decrease, by the way reducing their backscattering down into the acquisition energy window by the PMTs.

8.6.6 Bremsstrahlung SPECT

Quantitative bremsstrahlung SPECT of ^{90}Y is one of the most challenging tasks in nuclear medicine imaging: high-energy x-rays (up to 2.3 MeV) activate the K-edge fluorescence of lead [around 80 keV], penetrate the collimator and the crystal and

finally backscatter down [around 200 keV] into the energy range usable by the camera [108]. The use of an ME or HE collimator is absolutely required. The acquisition energy windows giving the best geometric to scatter photons ratio is [100, 150] keV [33]. Note that, even in this window, the primary photons represent only about 15 % of all the photons detected resulting in very poor imaging resolution and quantification.

Unfortunately, no commercial and effective correction method is available. Sophisticated correction methods [61, 78], helical SPECT using high-energy pinhole collimator [107–110], have been developed. Although providing nice quantification accuracy, these methods required the involvement of a local physicist for their implementation.

8.7 PET

8.7.1 Sensitivity and Spatial Resolution

The major benefit of 3D PET versus SPECT is the replacement of the mechanical collimator by an electronic collimation that uses the colinearity of the two annihilation 511 keV gamma rays (Fig. 8.12). In older BGO PET systems acquiring in 2D mode, a mechanical collimation is still performed in the longitudinal direction in
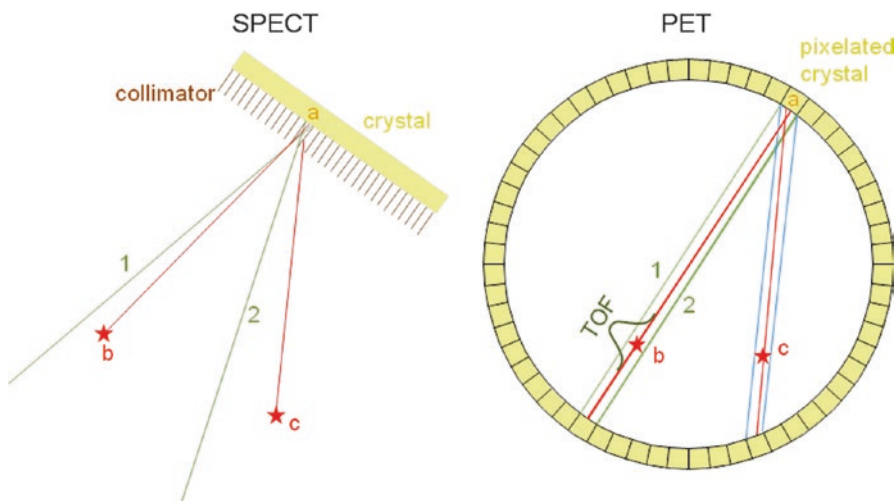
Fig. 8.12 Unscaled transverse section illustrating the spatial resolution and sensitivity improvement obtained in PET by the replacement of the mechanical collimator by an electronic collimation. Sensitivity: in SPECT, gamma rays going from the decay position *c* to the crystal position *a* are ruled out by the collimator, while they are detected in PET. Spatial resolution: lines 1 and 2 show the accuracy limits on the decay position *b* when the gamma ray is detected at the crystal position *a*, note that in SPECT this accuracy worsens when moving away from the collimator while it is almost uniform in PET. TOF-PET still goes a step beyond by giving the probability of the decay location along the LOR

order to reduce the significant scatter gamma rays detection resulting from the poor energy resolution of BGO.

Contrary to mechanical collimator, the electronic collimation does not determine the decay direction by ruling out all oblique gamma rays, but by measuring the location of the two 511 keV photoelectric effects on the crystal ring. This results in a sensitivity improvement of a factor higher than 100 for 3D PET versus SPECT.

As a result, the spatial resolution of the system is mainly fixed by the crystal pixilation width, i.e. typically ≈ 4 mm. Contrary to SPECT, the spatial resolution is optimal in the FOV centre and worsens a little bit moving to the crystal ring. Note that usually an aluminium ring prevents setting the patient closer than 10 cm from the crystal ring. The much better sensitivity compared to SPECT reduces the noise present in acquired data and by the way also reduces the needed reconstruction smoothing. This results in less degradation of the theoretical resolution in clinical studies.

8.7.2   Attenuation Issue

Attenuation coefficients are lower in PET compared to those in SPECT for which energy is significantly lower than 511 keV. However, as the detection of coincidence requires that both 511 keV photons reach the detector, the effective attenuation corresponds to the total length of the patient's body intercepted by the LOR. As a result, attenuation is in reality higher in PET. In iterative reconstruction, the attenuation is implemented in the same way as in SPECT.

8.7.3   Compton Scatter Issue

Accurate scatter correction is much easier to perform in PET than in SPECT. Indeed, by breaking the colinearity of the two 511 keV gamma rays, the scattering in the patient induces the detection of LORs which do not intercept the patient's body. These counts detected outside the patient's body in the sinogram are used to estimate those that are coming from the patient's body and are mixed with the primary 511–511 keV coincidences. Originally this estimation was performed using a linear or quadratic interpolation of the outside-body counts located in the sinogram tails. Current state-of-the-art estimations use a prediction of the scatter using the analytic single scatter simulation algorithm [74]. In order to take into account the multiple scattering, the simulation is then normalized to fit the outside-body counts.

8.7.4   Yttrium-86 PET Imaging

As peptides labelled with different metals exhibit different receptor affinities [81], the positron emitter ^{86}Y has been used as a perfect chemical surrogate of ^{90}Y [42]. However, its positron branching fraction is only 30 %, and ^{86}Y also emits about 300 %

of prompt high-energy single gamma rays. A fraction of these gamma rays are scattered in the patient down to ≈ 511 keV inducing acquisition of spurious coincidences. The prompt single gamma rays, being simultaneously emitted with the positron, cannot be removed by the delayed window method. Sophisticated correction methods are required to rule out these spurious coincidences and achieve accurate quantification [108, 112]. Corrected [86]Y-DOTATOC PET-based dosimetry study provided convincing tumor dose–response correlation in ^{90}Y-DOTATOC therapy [73]. Kidney dose–toxicity correlation in good agreement with that observed in external beam radiotherapy was also obtained [6, 115].

Due to the absence of correction method commercially available, [86]Y is rarely used in clinical imaging, in contrary to preclinical studies [66] where the small size of the animals prevents the scattering of the single prompt high-energy gamma rays down to the acquisition energy window.

8.7.5   *Yttrium-90 PET Imaging*

Up to recently, the nuclear medicine community assumed that ^{90}Y was a pure beta emitter. But it is not! Early in 1955, Ford theoretically proved the existence of a low positron emission in the ^{90}Y decay [25] that was observed the same year [43]. The positron branching factor is very low: 32 positron emissions out of one million decays [87]. In 2009 our team performed the first human ^{90}Y PET imaging after a liver radioembolization with resin spheres [55]. Due to the high ^{90}Y activity (typically $0.8 \rightarrow 4$GBq) present in the liver, TOF-PET imaging displays a good spatial resolution, is quantitative [56, 116] and is becoming the standard in post liver radioembolization imaging.

Unfortunately, the situation is not so favourable in ^{90}Y-PRRT where activities in tissues are much lower: typically less than 0.05 GBq in the kidney. A phantom study modelling ^{90}Y-PRRT shows that ^{90}Y PET imaging was feasible in tumors and in kidneys [113]. In this study, an old BGO PET system performed better than a 650 ps-TOF LYSO PET system. This can be explained by the random coincidences rate, induced by the natural radioactivity of lutetium-based crystal. The correction of the random coincidences induces noise and bias that are significant compared to the low true coincidence count rate [104].

A recent phantom and patient study using a 545 ps-TOF LYSO PET system confirmed the quantification feasibility [23]. Patient imaging exhibits spatial resolution clearly surpassing that of bremsstrahlung SPECT (Fig. 8.13). TOF does not only better condition tomography (see first section of the chapter) but also reduce the negative impact of the random coincidences on the signal to noise ratio [17]. No doubt that the emerging new generation of SiPM-based TOF-PET systems with their TOF resolution reaching 320 ps [60, 92] will further improve the quantification accuracy in these low count rate studies.

^{90}Y-PRRT imaging by PET allows computing the tumors and kidneys absorbed dose after each therapy cycle. Afterwards, the delivered activity in the following cycles can be tuned in order to optimize the therapy. Compared to bremsstrahlung,
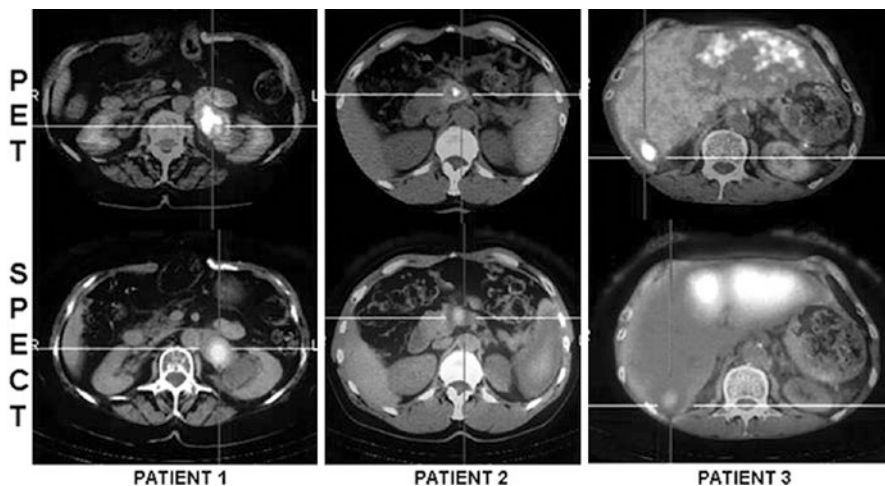
Fig. 8.13 ^{90}Y PET/CT (first line) and SPECT/CT (second line) imaging of three patients after administration of peptide receptor radionuclide therapy (PRRT). SPECT/CT and PET/CT scans were acquired at 4 and 6 h p.i., respectively. *Patient 1*, injected with 1424 MBq of ^{90}Y-DOTATATE (second cycle), shows a consistent accumulation of activity in the suprarenal lesion. *Patient 2*, suffering from inoperable pancreatic tumor, was administered with 2834 MBq of ^{90}Y-PRRT (seventh cycle). *Patient 3*, at his eighth cycle of PRRT (1426 MBq), presents wide areas of radiopharmaceutical uptake within the liver at the level of the third and fourth hepatic segment (Reprinted from Fabbri et al. [23] with permission of Mary Ann Liebert, Inc)

PET has the benefit to provide a better spatial resolution and a better quantification accuracy without the need to implement additional correction methods and, last, can be performed in patient receiving a ^{177}Lu-^{90}Y cocktail.

References

1. Aitken AP, Giese D, Tsoumpas C, Schleyer P, Kozerke S, Prieto C, Schaeffter T. Improved UTE-based attenuation correction for cranial PET-MR using dynamic magnetic field monitoring. Med Phys. 2014;41:012302.
2. Arabi H, Rager O, Alem A, Varoquaux A, Becker M, Zaidi H. Clinical assessment of MR-guided 3-class and 4-class attenuation correction in PET/MR. Mol Imaging Biol. 2015;17:264–76.
3. Arabi H, Zaidi H. Magnetic resonance imaging-guided attenuation correction in whole-body PET/MRI using a sorted atlas approach. Med Image Anal. 2016;31:1–5.
4. Asma E, Ahn S, Manjeshwar RM. Object size dependency of noise strength and correlation patterns for TOF and non-TOF PET. Symposium and Medical Imaging Conference (NSS/MIC), IEEE. 2011;3812–5.
5. Bai C, Shao L, Da Silva AJ, Zhao Z. A generalized model for the conversion from CT numbers to linear attenuation coefficients. IEEE Trans Nucl Sci. 2003;50:1510–5.
6. Barone R, Borson-Chazot F, Valkema R, Walrand S, Chauvin F, Gogou L, Kvols LK, Krenning EP, Jamar F, Pauwels S. Patient-specific dosimetry in predicting renal toxicity with 90Y-DOTATOC: relevance of kidney volume and dose rate in finding a dose–effect relationship. J Nucl Med. 2005;46:99S–106.

7. Barrett JF, Keat N. Artifacts in CT: recognition and avoidance 1. Radiographics. 2004;24: 1679–91.

8. Beister M, Kolditz D, Kalender WA. Iterative reconstruction methods in X-ray CT. Phys Med. 2012;28:94–108.

9. Bellon EM, Haacke EM, Coleman PE, Sacco DC, Steiger DA, Gangarosa RE. MR artifacts: a review. AJR Am J Roentgenol. 1986;147:1271–81.

10. Bertero M, Boccacci P. Introduction to inverse problems in imaging. London: IOP Publishing Ltd; 1998.

11. Beyer T, Antoch G, Blodgett T, Freudenberg LF, Akhurst T, Mueller S. Dual-modality PET/CT imaging: the effect of respiratory motion on combined image quality in clinical oncology. Eur J Nucl Med Mol Imaging. 2003;30:588–96.

12. Boas FE, Fleischmann D. CT artifacts: causes and reduction techniques. Imaging Med. 2012; 4:229–40.

13. Buerger C, Aitken A, Tsoumpas C, King AP, Schulz V, Marsden P, Schaeffter T. Investigation of 4D PET attenuation correction using ultra-short echo time MR. IEEE Nucl Sci Symp Med Imaging Conf. 2011;3558–3561.

14. Burger M, Mennucci AC, Osher S, Rumpf M. Level set and PDE based reconstruction methods in imaging. Cham: Springer; 2013.

15. Buzug TM. Computed tomography: from photon statistics to modern cone-beam CT. Berlin/Heidelberg: Springer; 2008.

16. Clackdoyle R, Defrise M. Tomographic reconstruction in the 21st century. IEEE Signal Process Mag. 2010;27:60–80.

17. Conti M. Effect of randoms on signal-to-noise ratio in TOF PET. IEEE Trans Nucl Sci. 2006;53:1188–93.

18. Conti M. Focus on time-of-flight PET: the benefits of improved time resolution. Eur J Nucl Med Mol Imaging. 2011;38:1147–57.

19. Defrise M, Gullberg GT. Image reconstruction. Phys Med Biol. 2006;51:R139.

20. Defrise M, Kinahan PE, Michel CJ. Image reconstruction algorithms in PET. In: Positron emission tomography. London: Springer; 2005. p. 63–91.

21. Delso G, Martinez-Möller A, Bundschuh RA, Nekolla SG, Ziegler SI. The effect of limited MR field of view in MR/PET attenuation correction. Med Phys. 2010;37:2804–12.

22. Doty FP, Friesenhahn SJ, Butler JF, Hink PL. X-ray and gamma-ray imaging with monolithic CdZnTe detector arrays. Proc SPIE. 1945. doi:10.1117/12.158756.

23. Fabbri C, Bartolomei M, Mattone V, Casi M, De Lauro F, Bartolini N, Gentili G, Amadori S, Agostini M, Sarti G. 90Y-PET/CT imaging quantification for dosimetry in peptide receptor radionuclide therapy: analysis and corrections of the impairing factors. Cancer Biother Radiopharm. 2015;30:200–10.

24. Fessler J. 2004 NSS/MIC statistical image reconstruction short course notes. http://web.eecs.umich.edu/~fessler/papers/files/talk/04/mic,notes.pdf. Accessed 15 Feb 2016.

25. Ford K. Predicted 0+ level of Zr90. Phys Rev. 1955;98:1516.

26. Frey EC, Tsui BM. A new method for modeling the spatially-variant, object-dependent scatter response function in SPECT. IEEE Nucl Sci Symp. 1996;2:1082–6.

27. Goldman LW. Principles of CT; radiation dose and image quality. J Nucl Med Technol. 2007;35:213–25.

28. Guillement JP, Jauberteau F, Kunyansky L, Novikov R, Trebossen R. On single-photon emission computed tomography imaging based on an exact formula for the nonuniform attenuation correction. Inv Prob. 2002;18:L11.

29. Gupta R, Cheung AC, Bartling SH, Lisauskas J, Grasruck M, Leidecker C, Schmidt B, Flohr T, Brady TJ. Flat-Panel CT Volume: fundamental principles, technology, and applications. Radiographics. 2008;28:2009–22.

30. Gupta R, Grasruck M, Suess C, Bartling SH, Schmidt B, Stierstorfer K, Popescu S, Brady T, Flohr T. Ultra-high resolution flat-panel volume CT: fundamental principles, design architecture, and system characterization. Eur Radiol. 2006;16:1191–205.

31. Hakky M, Pandey S, Kwak E, Jara H, Erbay SH. Application of basic physics principles to clinical neuroradiology: differentiating artifacts from true pathology on MRI. AJR Am J Roentgenol. 2013;201:369–77.
32. Hargreaves BA, Worters PW, Pauly KB, Pauly JM, Koch KM, Gold GE. Metal-induced artifacts in MRI. Am J Roentgenol. 2011;197:547–55.
33. Heard S, Flux GD, Guy MJ, Ott RJ. Monte Carlo simulation of 90Y bremsstrahlung imaging. IEEE Nucl Sci Symp. 2004;6:3579–83.
34. Hofmann M, Pichler B, Schölkopf B, Beyer T. Towards quantitative PET/MRI: a review of MR-based attenuation correction techniques. Eur J Nucl Med Mol Imaging. 2009;36: 93–104.
35. Hornak JP. 2011. http://www.cis.rit.edu/htbooks/nmr/inside.htm. Accessed 21 Mar 2016.
36. Hounsfield GN. Computerized transverse axial scanning (tomography): I. Description of system *Br*. J Radiol. 1973;46:1016–22.
37. Hsieh J. Computed tomography: principles, design, artifacts, and recent advances. Bellingham: SPIE; 2009.
38. Hudson HM, Larkin RS. Accelerated image reconstruction using ordered subsets of projection data. IEEE Trans Med Imaging. 1994;13:601–9.
39. Hutton BF. Recent advances in iterative reconstruction for clinical SPECT/PET and CT. Acta Oncol. 2011;50:851–8.
40. Hutton BF. The origins of SPECT and SPECT/CT. Eur J Nucl Med Mol Imaging. 2014; 41:S3–16.
41. Hutton BF, Buvat I, Beekman FJ. Review and current status of SPECT scatter correction. Phys Med Biol. 2011;56:R85.
42. Jamar F, Barone R, Mathieu I, Walrand S, Labar D, Carlier P, De Camps J, Schran H, Chen T, Smith MC, Bouterfa H. 86Y-DOTA0-D-Phe1-Tyr3-octreotide (SMT487)—a phase 1 clinical study: pharmacokinetics, biodistribution and renal protective effect of different regimens of amino acid co-infusion. Eur J Nucl Med Mol Imaging. 2003;30:510–8.
43. Johnson OE, Johnson RG, Langer LM. Evidence for a 0+ first excited state in Zr 90. Phys Rev. 1955;98:1517.
44. Johnson TR. Dual-energy CT: general principles. Am J Roentgenol. 2012;199:S3–8.
45. Jones T, Price P. Development and experimental medicine applications of PET in oncology: a historical perspective. Lancet Oncol. 2012;13:e116–25.
46. Kabuki S, Hattori K, Kohara R, Kunieda E, Kubo A, Kubo H, Miuchi K, Nakahara T, Nagayoshi T, Nishimura H, Okada Y. Development of electron tracking Compton camera using micro pixel gas chamber for medical imaging. Nucl Inst Meth Phys Res Section A. 2007;580:1031–5.
47. Kabuki S, Kimura H, Amano H, Nakamoto Y, Kubo H, Miuchi K, Kurosawa S, Takahashi M, Kawashima H, Ueda M, Okada T. Imaging study of a phantom and small animal with a two-head electron-tracking Compton gamma-ray camera. IEEE Nucl Sci Symp Conf Rec. 2010;30:2844–7.
48. Kalender WA. X-ray computed tomography. Phys Med Biol. 2006;51:R29–43.
49. Kalra MK, Maher MM, Toth TL, Schmidt B, Westerman BL, Morgan HT, Saini S. Techniques and applications of automatic tube current modulation for CT 1. Radiology. 2004;233: 649–57.
50. Karp JS, Surti S, Daube-Witherspoon ME, Muehllehner G. Benefit of time-of-flight in PET: experimental and clinical results. J Nucl Med. 2008;49:462–70.
51. Keall P. 4-dimensional computed tomography imaging and treatment planning. Semin Radiat Oncol. 2004;14:81–90.
52. Keereman V, Vandenberghe S, De Deene Y, Luypaert R, Broux T, Lemahieu I. MR-based attenuation correction for PET using an Ultrashort Echo Time (UTE) sequence. IEEE Nucl Sci Symp Conf Rec. 2008:4656–61.
53. LaCroix KJ, Tsui BM, Hasegawa BH, Brown JK. Investigation of the use of X-ray CT images for attenuation compensation in SPECT. IEEE Trans Nucl Sci. 1994;41:2793–9.

54. Ljungberg M, Celler A, Konijnenberg MW, Eckerman KF, Dewaraja YK, Sjögreen-Gleisner K. MIRD pamphlet No. 26: joint EANM/MIRD guidelines for quantitative 177Lu SPECT applied for dosimetry of radiopharmaceutical therapy. J Nucl Med. 2016;57:151–62.

55. Lhommel R, Goffette P, Van den Eynde M, Jamar F, Pauwels S, Bilbao JI, Walrand S. Yttrium-90 TOF PET scan demonstrates high-resolution biodistribution after liver SIRT. Eur J Nucl Med Mol Imaging. 2009;36:1696.

56. Lhommel R, Van Elmbt L, Goffette P, Van den Eynde M, Jamar F, Pauwels S, Walrand S. Feasibility of 90Y TOF PET-based dosimetry in liver metastasis therapy using SIR-spheres. Eur J Nucl Med Mol Imaging. 2010;37:1654–62.

57. McCollough CH, Primak AN, Braun N, Kofler J, Yu L, Christner J. Strategies for reducing radiation dose in CT. Radiol Clin of North Am. 2009;47:27–40.

58. Meeson S, Patel R, Golding S, Clinical Expansion of CT and Radiation Dose, D. Tack et al., editors. Radiation dose from multidetector CT, medical radiology. Diagnostic imaging. doi:10.1007/174_2012_541. Berlin/Heidelberg: Springer; 2012.

59. Meirelles GS, Erdi YE, Nehmeh SA, Squire OD, Larson SM, Humm JL, Schöder H. Deep-inspiration breath-hold PET/CT: clinical findings with a new technique for detection and characterization of thoracic lesions. J Nucl Med. 2007;48:712–9.

60. Miller M, Zhang J, Binzel K, Griesmer J, Laurence T, Narayanan M, et al. Characterization of the vereos digital photon counting PET system. J Nucl Med. 2015;56:434.

61. Minarik D, Sjögreen Gleisner K, Ljungberg M. Evaluation of quantitative (90)Y SPECT based on experimental phantom studies. Phys Med Biol. 2008;53:5689–703.

62. Morozov VA. Regularization methods for ill-posed problems. Boca Raton: CRC Press; 1993.

63. Morozov VA. Methods for solving incorrectly posed problems. New York: Springer Science & Business Media; 2012.

64. Morozov VA, Grebennikov AI. Methods for solution of Ill-posed problems: algorithmic aspects. Moscow: University Pres; 2005.

65. Murase K, Ishine M, Kataoka M, Itoh H, Mogami H, Iio A, Hamamoto K. Simulation and experimental study of respiratory motion effect on image quality of single photon emission computed tomography (SPECT). Eur J Nucl Med. 1987;13:244–9.

66. Nayak TK, Brechbiel MW. 86Y based PET radiopharmaceuticals: radiochemistry and biological applications. Med Chem. 2011;7:380–8.

67. Nehmeh SA, Erdi YE. Respiratory motion in positron emission tomography/computed tomography: a review. Semin Nucl Med. 2008;38:167–76.

68. Nehmeh SA, Erdi YE, Pan T, Pevsner A, Rosenzweig KE, Yorke E, Mageras GS, Schoder H, Vernon P, Squire O, Mostafavi H. Four-dimensional (4D) PET/CT imaging of the thorax. Med Phys. 2004;31:3179–86.

69. Novikov RG. An inversion formula for the attenuated X-ray transformation. Ark Mat. 2002;40:145–67.

70. Nuyts J, De Man B, Fessler JA, Zbijewski W, Beekman FJ. Modelling the physics in the iterative reconstruction for transmission computed tomography. Phys Med Biol. 2013;58:R63–96.

71. Padole A, Ali Khawaja RD, Kalra MK, Singh S. CT radiation dose and iterative reconstruction techniques. Am J Roentgenol. 2015;204:W384–92.

72. Patino M, Fuentes JM, Singh S, Hahn PF, Sahani DV. Iterative reconstruction techniques in abdominopelvic CT: technical concepts and clinical implementation. Am J Roentgenol. 2015;205:W19–31.

73. Pauwels S, Barone R, Walrand S, Borson-Chazot F, Valkema R, Kvols LK, Krenning EP, Jamar F. Practical dosimetry of peptide receptor radionuclide therapy with 90Y-labeled somatostatin analogs. J Nucl Med. 2005;46:92S–8.

74. Polycarpou I, Thielemans K, Manjeshwar R, Aguiar P, Marsden PK, Tsoumpas C. Comparative evaluation of scatter correction in 3D PET using different scatter-level approximations. Ann Nucl Med. 2011;25:643–9.

75. Press WH, Tuekolsky SA, Vetterling WT, Flannery BP. Numerical recipes in C++. Cambridge University Press; 2007.

76. Pruessmann KP, Weiger M, Scheidegger MB, Boesiger P. SENSE: sensitivity encoding for fast MRI. Magn Reson Med. 1999;42:952–62.

77. Radon J, Parks PC (translator). On the determination of functions from their integral values along certain manifolds. IEEE Trans Med Imag. 1986;5:170–6.

78. Rault E, Vandenberghe S, Staelens S, Lemahieu I. Optimization of yttrium-90 bremsstrahlung imaging with Monte Carlo simulations. IFMBE Proc. 2009;22:500–4.

79. Razifar P, Lubberink M, Schneider H, Långström B, Bengtsson E, Bergström M. Non-isotropic noise correlation in PET data reconstructed by FBP but not by OSEM demonstrated using autocorrelation function. BMC Med Imaging. 2005;5:3. DOI:10.1186/1471-2342-5-3.

80. Razifar P, Sandström M, Schnieder H, Långström B, Maripuu E, Bengtsson E, Bergström M. Noise correlation in PET, CT, SPECT and PET/CT data evaluated using autocorrelation function: a phantom study on data, reconstructed using FBP and OSEM. BMC Med Imaging. 2005;5:5. DOI:10.1186/1471-2342-5-5.

81. Reubi JC, Schär JC, Waser B, Wenger S, Heppeler A, Schmitt JS, Mäcke HR. Affinity profiles for human somatostatin receptor subtypes SST1-SST5 of somatostatin radiotracers selected for scintigraphicand radiotherapeutic use. Eur J Nucl Med. 2000;27:273–82.

82. Reyes M, Malandain G, Koulibaly PM, Ballester MA, Darcourt J. Respiratory motion correction in emission tomography image reconstruction. Medical image computing and computer-assisted intervention–MICCAI . Berlin/Heidelberg: Springer; 2005. p. 369–76.

83. Reyes M, Malandain G, Koulibaly PM, Gonzalez-Ballester MA, Darcourt J. Model-based respiratory motion compensation for emission tomography image reconstruction. Phys Med Biol. 2007;52:3579.

84. Robson MD, Gatehouse PD, Bydder M, Bydder GM. Magnetic resonance: an introduction to ultrashort TE (UTE) imaging. J comput Assist Tomoqr. 2003;27:825–46.

85. Schulz V, Torres-Espallardo I, Renisch S, Hu Z, Ojha N, Börnert P, Perkuhn M, Niendorf T, Schäfer WM, Brockmann H, Krohn T. Automatic, three-segment, MR-based attenuation correction for whole-body PET/MR data. Eur J Nucl Med Mol Imaging. 2011;38:138–52.

86. Segars WP, Tsui BMW. Effect of respiratory motion in CT-based attenuation correction in SPECT using different CT scanners and protocols. IEEE Nucl Sci Symp Conf Rec. 2005;4:2413–7.

87. Selwyn RG, Nickles RJ, Thomadsen BR, DeWerd LA, Micka JA. A new internal pair production branching ratio of 90Y: the development of a non-destructive assay for 90Y and 90Sr. Appl Radiat Isot. 2007;65:318–27.

88. Shepp LA, Vardi Y. Maximum likelihood reconstruction for emission tomography. IEEE Trans Med Imaging. 1982;1:113–22.

89. Shibuya K, Saito H, Koshimizu M, Asai K. Outstanding timing resolution of pure CsBr scintillators for coincidence measurements of positron annihilation radiation. Appl Phys Express. 2010;3:086401.

90. Siewerdsen JH, Daly MJ, Bakhtiar B, Moseley DJ, Richard S, Keller H, Jaffray DA. A simple, direct method for x-ray scatter estimation and correction in digital radiography and cone-beam CT. Med Phys. 2006;33:187–97.

91. Silverman PM, Kalender WA, Hazle JD. Common terminology for single and multislice helical CT. Am J Roentgenol. 2001;176:1135–6.

92. Slomka PJ, Pan T, Germano G. Recent advances and future progress in PET instrumentation. Semin Nucl Med. 2016;46:5–19.

93. Smyczynski MS, Gifford HC, Lehovich A, McNamara JE, Segars WP, Tsui BM, King MA. Impact of respiratory motion on the detection of small pulmonary nodules in SPECT imaging. IEEE Nucl Sci Symp Conf Rec. 2007;5:3241–5.

94. Sodickson DK, Manning WJ. Simultaneous acquisition of spatial harmonics (SMASH): fast imaging with radiofrequency coil arrays. Magn Reson Med. 1997;38:591–603.

95. Spanu A, Falchi A, Manca A, Marongiu P, Cossu A, Pisu N, Chessa F, Nuvoli S, Madeddu G. The usefulness of neck pinhole SPECT as a complementary tool to planar scintigraphy in primary and secondary hyperparathyroidism. J Nucl Med. 2004;45:40–8.

96. Starkschall G, Desai N, Balter P, Prado K, Luo D, Cody D, Pan T. Quantitative assessment of four-dimensional CT image acquisition quality. J Appl Clin Med Phys. 2007;8.

97. Stradiotti P, Curti A, Castellazzi G, Zerbi A. Metal-related artifacts in instrumented spine. Techniques for reducing artifacts in CT and MRI: state of the art. Eur Spine J. 2009; 18:102–8.

98. Stuart C. 1997. http://users.fmrib.ox.ac.uk/~stuart/thesis/chapter_2/chapter2.html. Accessed 21 Mar 2016.

99. Suga K, Kawakami Y, Iwanaga H, Tokuda O, Matsunaga N. Automated breath-hold perfusion SPECT/CT fusion images of the lungs. Am J Roentgenol. 2007;189:455–63.

100. Sun T, Mok GS. Techniques for respiration-induced artifacts reductions in thoracic PET/CT. Quant Imaging Med Surg. 2012;2:46.

101. Surti S, Karp JS. Advances in time-of-flight PET. Phys Med. 2016;32:12–22.

102. Surti S, Kuhn A, Werner ME, Perkins AE, Kolthammer J, Karp JS. Performance of Philips Gemini TF PET/CT scanner with special consideration for its time-of-flight imaging capabilities. J Nucl Med. 2007;48:471–80.

103. Vandenberghe S, Mikhaylova E, D'Hoe E, Mollet P, Karp JS. Recent developments in time-of-flight PET. EJNMMI Phys. 2016;3:1–30.

104. Van Elmbt L, Vandenberghe S, Walrand S, Pauwels S, Jamar F. Comparison of yttrium-90 quantitative imaging by TOF and non-TOF PET in a phantom of liver selective internal radiotherapy. Phys Med Biol. 2011;56:6759.

105. Wagenaar D, van der Graaf ER, van der Schaaf A, Greuter MJ. Quantitative comparison of commercial and Non-commercial metal artifact reduction techniques in computed tomography. PLoS One. 2015;10, e0127932.

106. Wagenknecht G, Kaiser HJ, Mottaghy FM, Herzog H. MRI for attenuation correction in PET: methods and challenges. MAGMA. 2013;26:99–113.

107. Walrand S. Bremsstrahlung SPECT/CT. In: Ahmadzadehfar H, Biersack HJ, editors. Clinical applications of SPECT-CT. Heidelberg: Springer; 2014.

108. Walrand S, Flux GD, Konijnenberg MW, Valkema R, Krenning EP, Lhommel R, Pauwels S, Jamar F. Dosimetry of yttrium-labelled radiopharmaceuticals for internal therapy: 86Y or 90Y imaging? Eur J Nucl Med Mol Imaging. 2011;38:57–68.

109. Walrand S, Hesse M, Demonceau G, Pauwels S, Jamar F. Yttrium-90-labeled microsphere tracking during liver selective internal radiotherapy by bremsstrahlung pinhole SPECT: feasibility study and evaluation in an abdominal phantom. EJNMMI Res. 2011;1:1186.

110. Walrand S, Hesse M, Wojcik R, Lhommel R, Jamar F. Optimal design of Anger camera for bremsstrahlung imaging: Monte Carlo evaluation. Front Oncol. 2014;4:149.

111. Walrand S, Jamar F. Perspectives in nuclear medicine tomography: a physicist's point of view. In: Giussani A, Hoeschen C, Giussani A, Hoeschen C, editors. Imaging in nuclear medicine. Heidelberg: Springer; 2013.

112. Walrand S, Jamar F, Mathieu I, De Camps J, Lonneux M, Sibomana M, et al. Quantitation in PET using isotopes emitting prompt single gammas: application to yttrium-86. Eur J Nucl Med Mol Imaging. 2003;30:354–61.

113. Walrand S, Jamar F, van Elmbt L, Lhommel R, Bekonde EB, Pauwels S. 4-Step renal dosimetry dependent on cortex geometry applied to 90Y peptide receptor radiotherapy: evaluation using a fillable kidney phantom imaged by 90Y PET. J Nucl Med. 2010;51:1969–73.

114. Walrand S, van Elmbt L, Pauwels S. Quantitation in SPECT using an effective model of the scattering. Phys Med Biol. 1994;39:719.

115. Wessels BW, Konijnenberg MW, Dale RG, Breitz HB, Cremonesi M, Meredith RF, Green AJ, Bouchet LG, Brill AB, Bolch WE, Sgouros G. MIRD pamphlet No. 20: the effect of model assumptions on kidney dosimetry and response–implications for radionuclide therapy. J Nucl Med. 2008;49:1884–99.

116. Willowson KP, Tapner M, Bailey DL. A multicentre comparison of quantitative 90Y PET/CT for dosimetric purposes after radioembolization with resin microspheres. Eur J Nucl Med Mol Imaging. 2015;42:1202–22.

117. Yang Z, Choupan J, Sepehrband F, Reutens D, Crozier S. Tissue classification for PET/MRI attenuation correction using conditional random field and image fusion. Int J Mach Learn Comput. 2013;3:87.
118. Yonezawa T, Koike M, Oishi Y, Iwanaga H. Application of breath-holding SPECT with high-speed-rotation technique in hepatic-function scintigraphy. Radiol Phys Technol. 2008;1:234–7.
119. Young IR. Significant events in the development of MRI. J Magn Reson Imaging. 2004;20:183–6.
120. Yu L, Bruesewitz MR, Thomas KB, Fletcher JG, Kofler JM, McCollough CH. Optimal tube potential for radiation dose reduction in pediatric CT: principles, clinical implementations, and pitfalls. Radiographics. 2011;31:835–48.
121. Yu L, Liu X, Leng S, Kofler JM, Ramirez-Giraldo JC, Qu M, Christner J, Fletcher JG, McCollough CH. Radiation dose reduction in computed tomography: techniques and future perspective. Imaging Med. 2009;1:65–84.
122. Zhu L, Bennett NR, Fahrig R. Scatter correction method for x-ray CT using primary modulation: theory and preliminary results. IEEE Trans Med Imaging. 2006;25:1573–87.

Chapter 9
Internal Dosimetry: Principles and Applications to NET

Uta Eberlein and Michael Lassmann

Abbreviations

PRRT   Peptide receptor radionuclide therapy
RIF/cell   Radiation-induced foci per cell

9.1 Introduction

In recent years few reports on the dosimetry of diagnostically used ^{68}Ga-labeled compounds (see the review by Eberlein and Lassmann [1]) and numerous reports describing dosimetry in molecular radiotherapies using ^{177}Lu-labeled [2–10] and ^{90}Y-labeled compounds have been published. The purpose of this chapter is to familiarize the reader with the concepts of internal dosimetry in nuclear medicine, provide data on dosimetry after treatment of neuroendocrine tumors, and show dose-response relationships.

U. Eberlein, Dr. rer. nat • M. Lassmann, Dr. rer. nat (✉)

Klinik und Poliklinik für Nuklearmedizin, Universitätsklinikum Würzburg,
Oberdürrbacher Str. 6, D – 97080 Würzburg, Germany
e-mail: eberlein_u@ukw.de; lassmann_m@ukw.de

9.2   Internal Dosimetry

9.2.1   Basic Quantities and Definitions[1]

9.2.1.1   Absorbed Dose (*D*)

In a lot of publications in nuclear medicine, the term "dose" is used for describing the administered activity as well as the "absorbed dose." It is, however, mandatory to distinguish between these two terms. The appropriate term for the quantity of interest in radiation protection and dosimetry, however, is "absorbed dose" (*D*), expressed in units of gray (Gy) [11].

According to ICRP103 [11], the absorbed dose is defined as the mean energy $d\varepsilon$ imparted to matter of mass dm by ionizing radiation:

$$D = \frac{d\varepsilon}{dm}$$

The SI unit for absorbed dose is joule per kilogram (J kg^{-1}) and its special name is gray (Gy) [11]. In nuclear medicine $d\varepsilon$ represents the number of radionuclide disintegrations in a particular volume multiplied by the energy emitted per disintegration of the radionuclide and multiplied by the fraction of emitted energy that is absorbed by a particular (target) mass.

The concept of absorbed dose is only applicable in a macroscopic scale as it is generally done in nuclear medicine dosimetry. In "macrodosimetry," one considers mean parameters (mean doses). It should be noted that the mean absorbed dose can be calculated for a large (i.e., organ) volume or at the microscopic level, as long as the criteria applicable to macrodosimetry are met. The energy deposition, however, is a stochastic process and shows inherent statistical fluctuations. If particle flux – and energy deposition – is large enough, then the mean absorbed dose is relevant as the standard deviation due to stochastic fluctuations is small.

9.2.1.2   Effective Dose (E)

For a risk assessment of medical diagnostic procedures involving ionizing radiation and radiation protection, the concept of the effective dose (*E*) has been widely adapted [11, 12]. The risk associated with the effective dose is based on assumptions such as the concept of considering the risk to the general public or to workers. This does not necessarily reflect the situation for patients in nuclear medicine as,

---

[1] Parts of this chapter have been taken from Lassmann M, Eberlein U. Radiation safety and dosimetry. In: Herrmann K, Nieweg EO, Povoski PS, editors. Radioguided surgery: current applications and innovative directions in clinical practice. Cham: Springer International Publishing; 2016. p. 103–11 with permission of Springer.

Table 9.1 Tissue weighting factors according to ICRP103 [11]

Tissue	ω_T	$\Sigma_T\,\omega_T$
Bone marrow (red), colon, lung, stomach, breast, remainder tissues[a]	0.12	0.72
Gonads	0.08	0.08
Bladder, esophagus, liver, thyroid	0.04	0.16
Bone surface, brain, salivary glands, skin	0.01	0.04
Total		1.00

[a]Remainder tissues: Adrenals, extrathoracic (ET) region, gall bladder, heart, kidneys, lymphatic nodes, muscle, oral mucosa, pancreas, prostate (male), small intestine, spleen, thymus, uterus/cervix (female)

particularly in patients with cancer, the life expectancy is likely to be different of that of the general public or of workers. Another aspect is the strong age and sex dependency of the radiation risk, which is not included in the effective dose. Therefore, the effective dose should not be used for individual risk-benefit assessments in patients; instead, the relevant quantity is the equivalent dose or the absorbed dose to irradiated organs. E is defined as

$$E = \sum_T \omega_T H_T$$

ω_T is the tissue weighting factor for the tissue T and represents the radiation sensitivity for stochastic radiation damage of each tissue considered. The sum over all tissue weighting factors is 1: $\sum_T \omega_T = 1$. H_T is the organ dose (unit: Sv) caused by internal or external exposure. For nuclear medicine applications using beta and gamma emitters, the organ doses are calculated by multiplying the absorbed dose (unit: Gy) by the radiation weighting factor for photons and electrons (=1 Sv/Gy). According to ICRP103 [11], the effective dose E is then the arithmetic mean of the gender-specific organ doses H_T^M (male) and H_T^F (female):

$$E = \sum_T \omega_T \cdot \frac{H_T^M + H_T^F}{2}$$

Table 9.1 summarizes the tissue weighting factors according to ICRP103.

The term effective dose is, according to ICRP103 [11], only a protection quantity which provides a dose value that is related to the probability of health detriment to a reference person due to stochastic effects from exposure to low doses of ionizing radiation [11–13] and should not be used for an individual risk analysis. For comparing both different diagnostic procedures and similar procedures in different hospitals and countries, the effective dose can be very useful. Furthermore, it is a good quantity to compare the use of different technologies for the same medical examination. But one has to consider that this only holds for patient populations with the same age and sex distribution [11].

9.2.2 Dosimetry in Nuclear Medicine

Methods for calculating the absorbed dose from administration of a radiopharmaceutical were first standardized in the 1960s by the Medical Internal Radiation Dosimetry (MIRD) committee, with the initial aim of estimating average doses to critical organs resulting from diagnostic procedures [14]. Essentially this methodology allows the calculation of absorbed dose using the *simplified* version of the basic equation [15]:

$$\bar{D}(r_k \leftarrow r_h) = \tilde{A}_h \, S(r_k \leftarrow r_h)$$

$\bar{D}(r_k \leftarrow r_h)$:   the mean absorbed dose to a target region r_k from the cumulated activity in source region r_h.

$\tilde{A}_h$:   the cumulated activity (i.e., the integral of the activity-time curve from zero to infinity) in a given target region r_h.

$S(r_k \leftarrow r_h)$:   the radionuclide-specific S factor for target region r_k and source region r_h per unit cumulated activity in source region r_h.

$\tilde{A}$ denotes the total number of radioactive decays occurring within an organ in which a radiopharmaceutical accumulates (the "source organ"). The MIRD S factor accounts for the energy released from each radioactive decay and the relative geometry of the source organ and the organ for which the absorbed dose is to be calculated. Thus, the cumulated activity is dependent on biological parameters, while the S factor deals with the physical components of the absorbed dose.

There is no assumption made concerning the source or target, other than that the radioactive distribution is homogeneous in the source *h*: the source and target can be of any size or composition. Theoretically, if the activity in the source is heterogeneously distributed, it is possible to subdivide the source into smaller volumes in which the activity can be considered homogeneous.

For determining $\tilde{A}$, quantitative imaging of the biokinetics of the administered radiolabeled substance is a prerequisite followed by absorbed dose calculation. This comprises the following steps [16, 17]:

1. The percentage of administered activity of the radiopharmaceutical must be determined for the accumulating organs. This step mainly requires the implementation of quantitative imaging procedures and/or blood sampling. The established method for quantitative imaging for dosimetry relies on the measurement of the biokinetics by serial gamma-camera scans, if possible, including SPECT/CT and/or PET/CT to increase dosimetric accuracy. The quantitative accuracy depends on these different settings and needs to be carefully checked. If organ or lesion dosimetry is performed, precise determination of organ/lesion volumes is necessary, as the use of standard organ volumes may be severely incorrect

leading to serious under- or overdosing in targeted radiotherapy. Dosimetry based on quantitative 3-dimensional data is more accurate, provided that all effects that degrade the quantitative content of the images have been corrected for, and allows a more individualized dosing approach. In addition, inhomogeneous organ accumulation of the radionuclide can be detected and possibly taken into account. Blood samples can be measured easily using a calibrated well counter in order to provide time-activity curves for the disappearance of the radiolabeled pharmaceutical from the blood. These measurements can be performed either pre-therapeutically for assessing the activity to be administered or post-therapeutically for verification of the absorbed doses.

2. The previous step needs to be repeated at different time points in order to assess the pharmacokinetics of the radiopharmaceutical. This requires the determination of a correct temporal sampling and the use of ad hoc procedures to integrate the activity over time to obtain the total number of decays occurring in the source organs or the residence times. A proposal for choosing optimal time points is provided by MIRD pamphlet 16 [18] and for obtaining optimized fit procedures for nuclear medicine by Kletting et al. [19].

As the cumulated activity constitutes the sum of all radioactive emissions during the time considered, the energy deposition rate with time is not taken into account, although the absorbed dose rate (Gy s^{-1}) is known to impact on the biological consequences of the irradiation. The relevance of this is indicated by the fact that the aim of most dosimetric studies is to relate a physical parameter (i.e., energy absorbed per unit mass) to the observed biological effect: the relation between these two parameters may not be simple, and scientifically sound dosimetric protocols are simply a prerequisite for subsequent radiobiological studies.

Radionuclide *S*-values for all combinations of source and target tissues, as needed for internal dosimetry in *diagnostic* nuclear medicine, should be based upon internationally accepted reference anatomic phantoms as defined by the International Commission on Radiological Protection [20]. In this way, organ dose estimates may be harmonized across all imaging modalities for the purpose of quantifying stochastic risk.

In *therapeutic* applications, the absorbed doses of critical organs must be determined. This is usually obtained for an anthropomorphic computational model using adequate knowledge about radiation transport. A variety of methods exists for the calculation of the absorbed doses. As a basis for the calculation of absorbed doses, the number of decays per administered activity must be determined. This can be done for whole body only, for each accumulating organ, for each voxel, or even on a cellular level. Different dose calculation approaches exist, and these may be based on absorbed dose rates per unit activity (with mass correction) of anthropomorphic phantoms, convolution kernels, or on Monte Carlo simulations [21]. Figure 9.1 shows, in a schematic drawing, a flowchart denoting the single steps needed for dosimetry.
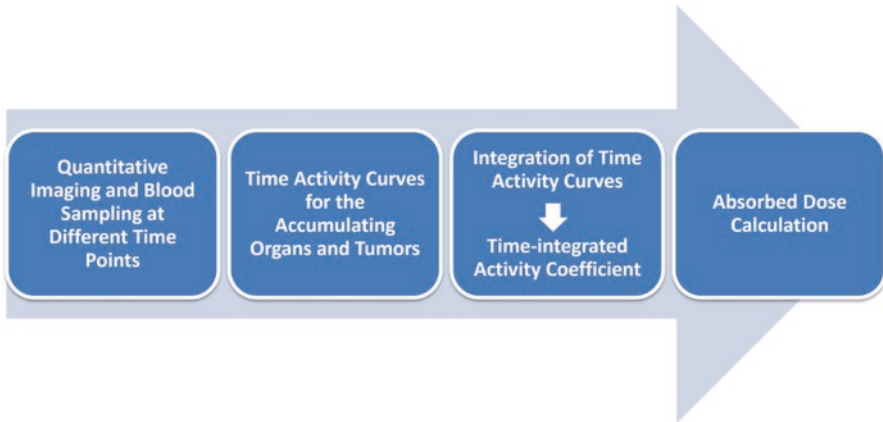
Fig. 9.1 Dosimetry flowchart

9.2.3 Radiobiology

9.2.3.1 Linear Quadratic Model and Biological Effective Dose

During internal or external irradiation, patients are exposed to ionizing radiation, which does not only destroy the malignant cells but also damages healthy tissue and cells. This is mainly caused by direct and indirect interaction of the radiation with the DNA which damages the DNA structure. Most frequently, there are single-strand breaks and base damages. DNA double-strand breaks (DSBs) are rare; nevertheless, they are the most critical lesions for cells as repairing the damage is difficult. Unrepaired or misrepaired DNA could cause mutations and chromosomal aberrations or lead to cell death.

It is assumed that there are two different ways of producing a DSB [22]:

Type A damage: adjacent DNA strands are broken by a single ionizing event.
Type B damage: two different ionizing events destroy adjacent DNA strands. They can be considered as two individual single-strand breaks and are therefore assumed as potentially repairable because the first single-strand break could be repaired before the second occurs. They are also called sublethal damages. This effect depends on the dose rate.

During radionuclide therapy, the radioactive decay of the nuclide and its biokinetics cause the dose rate to be time dependent and decreasing. The influence of the time dependence of the dose rate on the biological effects should, therefore, not be neglected. An important point is the influence of repair mechanisms taking place during the continuous irradiation.

The survival of cells after irradiation is usually expressed by survival curves, which are represented by the linear quadratic model (LQ)

$$F_S = \exp\left(-\alpha D - \beta D^2\right)$$

Whereas F_S is the survival fraction of the cells, D *is the* absorbed dose, and α and β are tissue-specific cell parameters.

It is assumed that the first part of the equation describes the type A damage because those are linearly increasing with the absorbed dose and, therefore, the cell survival decreases with increasing absorbed dose. The second part represents the type B damage, which increases quadratically with the absorbed dose [23].

During internal irradiation in nuclear medicine, the cells and organs not only are irradiated for seconds or minutes but are continuously irradiated over a longer period with permanently changing dose rate. This is in contrast to external irradiation, for example, in radiotherapy. This fact potentially alters the impact of the ionizing radiation, although the same absorbed dose is delivered. Therefore, the sparing effect in nuclear medicine already occurs during the therapy.

To compare therapies with different dose rates and fractionation, the concept of the biological effective dose (BED) is used [22, 24]:

$$\mathrm{BED}(D) = D \cdot \mathrm{RE}(D)$$

$\mathrm{RE}(D)$ defines the relative effectiveness and has to be modified for nuclear medicine by a factor G which takes the repair of sublethal damage taking place during the therapy into account:

$$\mathrm{RE}(D) = 1 + G\frac{\beta}{\alpha}D$$

with

$$G = \frac{\lambda}{\lambda + \mu}$$

and

$$\lambda = \frac{\ln(2)}{T_{1/2}}$$

while λ is the effective decay rate of the nuclide from the organ of question, $T_{1/2}$ is the effective half-life and μ is the damage recovery constant.

For more than one therapy cycle, the BEDs can be summed, if one assumes that there is no activity left and the sublethal damage is repaired.

With those formulas, the adjusted linear quadratic model for nuclear medicine treatments is written as
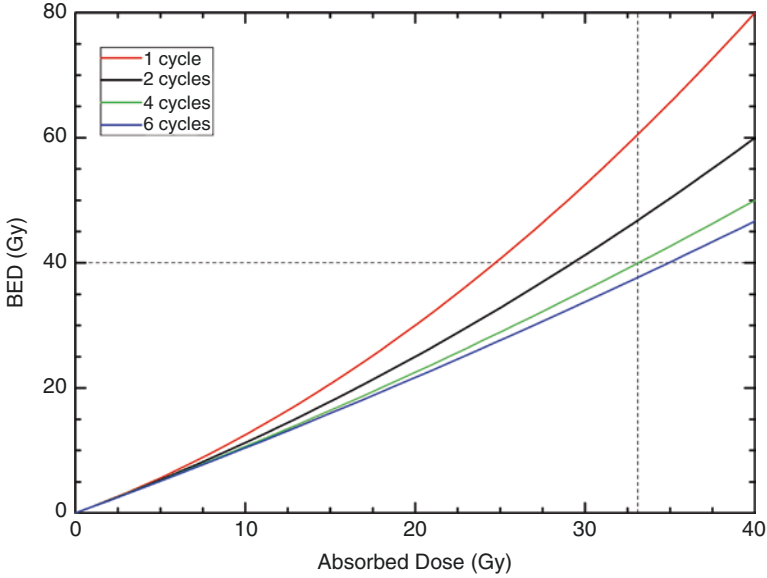
Fig. 9.2 BED as a function of the absorbed dose for healthy kidneys after PRRTs with ^{90}Y-labeled compounds. The fractionation schemes were one cycle (*red*), two cycles (*black*), four cycles (*green*), and six cycles (*blue*). The dotted lines denote, for four therapy cycles, the intersection of a BED of 40 Gy and an absorbed dose to the kidney of 33 Gy

$$F_S = \exp\left(-\alpha D\left(1 + G\frac{\beta}{\alpha}D\right)\right) = \exp\left(-\alpha \cdot \text{BED}(D)\right)$$

F_s describes the surviving fraction of the cells as a function of the absorbed dose D. The alpha/beta ratios are individual parameters for each organ, tumors, and healthy tissue.

How this concept can be applied to kidney dosimetry in PRRTs with ^{90}Y-labeled compounds is illustrated in Fig. 9.2. Data for the kidney alpha/beta ratios, the repair half-life, and the effective half-life were taken from MIRD pamphlet 20 [25]. The dotted lines denote the intersection of a BED of 40 Gy and an absorbed dose to the kidney of 33 Gy for 4 therapy cycles. This graph shows that the normally accepted tolerance dose of healthy kidneys (23 Gy [26]) can be exceeded if the therapy is fractionated. It also shows that increasing the number of cycles to more than four does not lead to a substantial increase in the tolerance dose.

9.2.3.2 Biodosimetry

Specific biomarkers representing DSBs also provide additional information after irradiation. Well-known biomarkers used for this purpose are γ-H2AX and 53BP1.
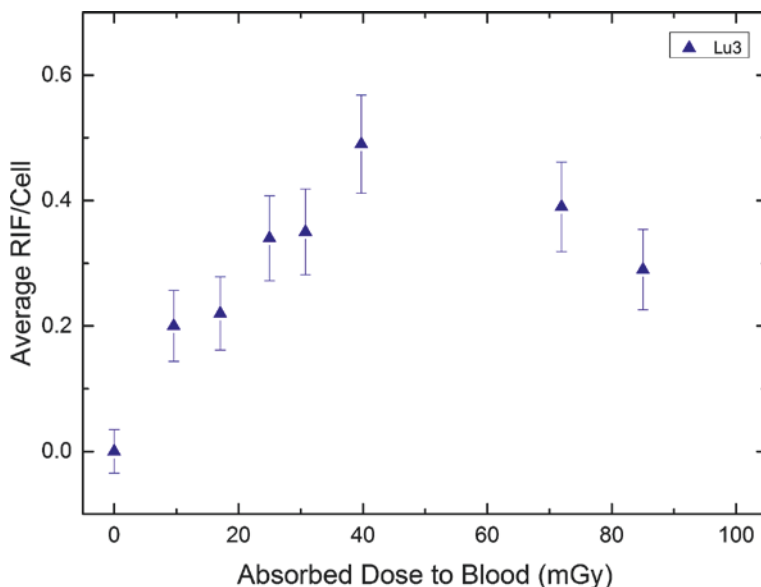
Fig. 9.3 Average RIF per cell in lymphocytes after PRRT as a function of the absorbed dose to the blood in an example patient (Lu3). The blood sampling times were 0, 0.6, 1.1, 1.7, 2.3, 3.6, 24.1, and 44.7 h. The graph was taken from the work of Eberlein et al. [28] (Copyright with the authors)

The formation of a DNA DSB in nuclear chromatin results in the rapid phosphorylation of the histone H2 variant H2AX, which then called γ-H2AX. Furthermore, DSBs also recruit the damage sensor 53BP1 to the chromatin surrounding the DSBs, which leads to 53BP1 and γ-H2AX co-localization in the chromatin surrounding a DSB. By immunofluorescence staining with γ-H2AX and 53BP1 antibodies, those biomarkers can be addressed by microscopically visible DNA damage protein foci; this is also known as the DNA damage focus assay [27–29].

For PRRT, there are two studies that addressed the absorbed dose to the blood and the number and temporal behavior of radiation-induced DNA double-strand breaks in peripheral blood samples [28, 30]. Only the study by Eberlein et al. [28] could establish, for the first time, a linear correlation between the average numbers of radiation-induced foci per cell (RIF/cell) and the absorbed dose to the blood up to 5 h after ^{177}Lu administration. Thereafter, the number of RIF/cell is no longer linearly dependent on the absorbed dose. The time- and dose-dependent increase and decay of the number of RIF/cell could best be described by a linear increase and an exponential decay.

Figure 9.3 illustrates this finding for one of the study patients (after administration of 7.9 GBq ^{177}Lu-DOTATATE). There is a linear increase of the foci number up to 5 h as a function of the absorbed dose to the blood (left panel); the later time points are characterized by a decreasing number of radiation-induced foci which is in accordance with the progression of DNA repair and the declining dose rates (right panel, solid line). 120 h after therapy, the number of RIF/cell are almost back to the pretreatment level.

Table 9.2 Effective dose coefficients (mSv/MBq)

	^{68}Ga-DOTATATE Sandström et al. [33]	^{68}Ga-DOTATOC Sandström et al. [33]	^{68}Ga-DOTATOC Hartmann et al. [34]	^{111}In-octreotate Eberlein et al. [32]
Adult	2.0E-02	1.9E-02	2.3E-02	5.4E-2

In the future, mores studies like this will help us better understanding the biological effects of nuclear medicine therapies.

9.3 Applications

9.3.1 Diagnostic Procedures

Two papers by Eberlein et al. [1] and by Machado et al. [31] summarize the most recent data on dosimetry for ^{68}Ga-labeled compounds. For ^{111}In-octreotate, the data are taken from the review on the dosimetry of diagnostic compounds by Eberlein et al. [32]. The results are compiled in Table 9.2.

For most of the Ga-labeled compounds, the effective dose for typically administered activities of 150 MBq is less than 3 mSv, whereas the effective dose for ^{111}In-octreotate is in the order of some 10 mSv for an administered activity of 200 MBq.

For diagnostic pediatric applications, Machado et al. published a recommendation how to modify the administered activities based on body weight [31].

9.3.2 Therapy with [177]Lu

For ^{177}Lu data dosimetry, data are summarized in the review article by Lassmann and Eberlein [34]. Table 9.3 shows most of the data published so far and the respective absorbed doses to the red marrow, the kidneys, and the tumor.

Red marrow doses and hematological toxicity
The ^{177}Lu-labeled compounds show a rapid clearance from the blood [7]. The calculated absorbed doses using blood-based methods result in low specific absorbed doses of <0.1Gy/GBq. Consequently, hematological toxicity has not been observed in patients receiving ^{177}Lu-DOTATATE/TOC apart from one grade 3 leukopenia and thrombocytopenia [6]. An interesting observation was reported by Forrer et al. [4]. In their study, the authors observed a strong linear correlation and high agreement between the measured radioactivity in the bone marrow aspirates and in the blood.

Table 9.3 Absorbed dose values for tumors and organs at risk for one treatment cycle

Organ/lesion	Absorbed dose (median) Gy/GBq	Reference
Red marrow	0.07	Kwekkeboom et al. [2]
	0.01	Forrer et al. [4]
	0.03	Bodei et al. [6]
	0.02	Sandström et al. [7]
	≤0.07 (pre-therapeutic) ≤0.08 (post-therapeutic)	Kairemo et al. [9]
Kidney	0.88	Kwekkeboom et al. [2]
	0.90	Wehrmann et al. [3]
	0.97 (planar) 0.81 (SPECT)	Garkavij et al. [5]
	0.68	Bodei et al. [6]
	0.63	Sandström et al. [7]
	0.57	Gupta et al. [8]
	1.15 (pre-therapeutic) 0.68 (post-therapeutic)	Kairemo et al. [9]
Tumor	3.9–37.9	Kwekkeboom et al. [2]
	9.7 (mean)	Wehrmann et al. [3]
	0.1–20	Garkavij et al. [5]
	1.3–4.8	Gupta et al. [8]
	0.6–56	Cremonesi et al [38]
	2–11 (pre-therapeutic) 1–11 (post-therapeutic)	Kairemo et al. [9]

Kidney doses and kidney toxicity

The kidney doses varied between 0.62 and 0.97 Gy/GBq, and the variability was evidently mostly caused by methodological issues (higher values in planar scans as compared to SPECT/CT-based scans; see comments by Lassmann et al. [35]).

Although similar conditions were applied for kidney protection before diagnostic imaging and therapy, differences between pre-therapeutic dosimetry using 200 MBq of ^{177}Lu-DOTATATE and post-therapeutic dosimetry were observed, the absorbed dose estimates being higher by almost a factor of two [9]. The authors, however, do not discuss potentials reasons for these differences.

In therapies using ^{177}Lu-labeled peptides, no major acute or delayed renal toxicity has been observed. Therefore, the maximum tolerable absorbed dose with ^{177}Lu remains unknown, and this therapy is in most cases routinely performed without dosimetry.

Tumor absorbed doses

The absorbed doses to the tumors per treatment cycle show a wide variability and range from 0.1 to 56 Gy/GBq (see Table 9.3).

Table 9.4 Absorbed doses for ^{90}Y

Organ/lesion	Absorbed (median) Gy/GBq	Reference
Red marrow	0.03	Bodei et al. [36]
	0.17	Forrer et al. [39]
	0.05	Forster et al. [42]
	0.06	Helisch et al. [43]
Kidney	6.1	Kwekkeboom et al. [44]
	3.7–4.3	Hindorf et al. [41]
	3.8	Cremonesi et al. [38]
	2.8	Forrer et al. [39]
	1.7	Jamar et al. [40]
	2.7	Helisch et al. [43]
Tumor (range)	2.1–29.5	Helisch et al. [43]
	2.4–41.7	Forrer et al. [39]
	1.4–31	Cremonesi et al. [36]
	0.9–5.4	Hindorf et al. [41]

9.3.3   Therapy with ^{90}Y

Data on absorbed doses after therapy with ^{90}Y-labeled compounds are sparse and are mostly based on pre-therapeutic quantitative imaging using either ^{111}In- or ^{86}Y-labeled peptides [6, 37–43].

Red marrow doses
There are only a few studies on the absorbed doses to the red bone marrow. Absorbed doses varied between 0.03 and 0.17 Gy/GBq (see Table 9.4).

Kidney doses and kidney toxicity
The kidney doses varied between 1.7 and 6.1 Gy/GBq, and the variability was evidently mostly caused by methodological issues (higher values in ^{111}In scans as compared to ^{86}Y-based PET scans). Although data are available on toxicity thresholds, therapy with ^{90}Y-labeled peptides is, in most cases, routinely performed without dosimetry.

Tumor absorbed doses
The absorbed doses to the tumors per treatment cycle show a wide variability and range from 0.9 to 41.7 Gy/GBq (see Table 9.4).

9.4   Therapy-Related Dose-Effect Relationships

In a recent paper Strigari et al. [45] analyzed therapy-related dose-effect relationships for radionuclide therapy. For neuroendocrine tumors, their review concentrated on absorbed dose effects concerning bone marrow and kidney toxicity. The corresponding studies are summarized in Table 9.5.

Table 9.5 Studies showing dose-effect relationships for kidneys and bone marrow in PRRTs after therapy with ^{90}Y

End point	Threshold dose	Reference
>20 % decline per year in creatinine clearance	35 Gy BED (kidneys)	Barone et al. [37]
50 % reduction in platelets	2 Gy (bone marrow)	Walrand et al. [46]
Creatinine toxicity more than grade 1	28 Gy BED (kidney risk factors) 40 Gy (no kidney risk factors)	Bodei et al. [47]

In a patient-specific dosimetry study with the aim of predicting renal toxicity with ^{90}Y-DOTATOC, Barone et al. [37] found a therapy-related dose-effect relationship for renal failure. The endpoint was a reduction in creatinine clearance of >20 % per year, as not all patients developed G3 or G4 nephrotoxicity. This value was obtained only when individual kidney masses were considered and the biologically effective dose (BED) was used as dosimetric descriptor, accounting for different dosing schemes. Bodei et al. [47] observed two dose limits for kidneys after treatment with ^{90}Y: 28 Gy BED was a threshold for toxicity in patients with risk factors (mainly hypertension and diabetes), while 40 Gy was the limit in patients without risk factors.

This finding has been confirmed by a prospective phase II dosimetry trial in which a 37 Gy BED threshold for kidney toxicity was found to be a good guide for ^{90}Y-DOTATOC PRRT [48].

These important findings were not experimentally reproduced with ^{177}Lu-DOTATATE, with which no major acute or delayed renal or hematological toxicity occurred in 51 patients (apart from one G3 leukopenia and thrombocytopenia) [6]. With an administered activity up to 30 GBq, the BED remained under 40 Gy. Consequently, the maximum tolerable BED with ^{177}Lu remains unknown.

With respect to hematological toxicity in 21 patients with NET treated with ^{90}Y-DOTATOC showing recovery of platelet counts to normal, Walrand et al. [46] found a strong correlation ($r = 0.96$) between red marrow-absorbed doses and the platelet count reduction at nadir in nine a posteriori selected patients without prior chemotherapy who had spontaneous red marrow recovery. A reduction of 50 % in the platelet counts was observed at a red marrow dose of 2 Gy.

Bergsma et al. [49] reported on subacute hematotoxicity after PRRT with ^{177}Lu-DOTA-octreotate. The authors found, in a subgroup of patients, the mean bone marrow dose per administered activity in 23 evaluable patients was 67 ± 7 mGy/GBq, resulting in a mean bone marrow dose of 2 Gy in patients who received four cycles of 7.4 GBq ^{177}Lu-DOTATATE. Significant correlations between (cumulative) bone marrow dose and platelet and WBC counts were found in a selected group of patients, however, less toxicity was observed than anticipated. Their conclusion is that the often-adopted bone marrow dose limit of 2 Gy, adopted from data on thyroid cancer treatment with ^{131}I, may be too low for PRRTs with ^{177}Lu-DOTATATE.

9.5 Conclusion

The application of dosimetry to PRRT leads to several important conclusions:

(a) Biodosimetry linked to physical dosimetry might bring new insights in the radiation risk associated with PRRT.

(b) Effective doses after the diagnostic use of ^{68}Ga-labeled compounds are considerably lower than those for ^{111}In-labeled compounds.

(c) There is evidence for a threshold value of 40 Gy BED for kidney damages after PRRT with ^{90}Y-labeled compounds for healthy kidneys. Lower values should be applied for patients with kidney risk factors.

(d) A dose limit to the kidneys based on patient data has not been established yet for PRRT with ^{177}Lu-labeled compounds.

(e) Reported absorbed doses to tumors vary considerably. More data on dose-response relationships are needed.

(f) Hematological complications play a minor role after PRRT.

References

1. Eberlein U, Lassmann M. Dosimetry of [Ga-68]-labeled compounds. Appl Radiat Isot. 2013;76:70–4.
2. Kwekkeboom DJ, Bakker WH, Kooij PP, Konijnenberg MW, Srinivasan A, Erion JL, et al. [177Lu-DOTAOTyr3]octreotate: comparison with [111In-DTPAO]octreotide in patients. Eur J Nucl Med. 2001;28:1319–25.
3. Wehrmann C, Senftleben S, Zachert C, Muller D, Baum RP. Results of individual patient dosimetry in peptide receptor radionuclide therapy with 177Lu DOTA-TATE and 177Lu DOTA-NOC. Cancer Biother Radiopharm. 2007;22:406–16. doi:10.1089/cbr.2006.325.
4. Forrer F, Krenning EP, Kooij PP, Bernard BF, Konijnenberg M, Bakker WH, et al. Bone marrow dosimetry in peptide receptor radionuclide therapy with [177Lu-DOTA(0), Tyr(3)] octreotate. Eur J Nucl Med Mol Imaging. 2009;36:1138–46. doi:10.1007/s00259-009-1072-6.
5. Garkavij M, Nickel M, Sjogreen-Gleisner K, Ljungberg M, Ohlsson T, Wingardh K, et al. 177Lu-[DOTA0, Tyr3] octreotate therapy in patients with disseminated neuroendocrine tumors: analysis of dosimetry with impact on future therapeutic strategy. Cancer. 2010;116:1084–92. doi:10.1002/cncr.24796.
6. Bodei L, Cremonesi M, Grana CM, Fazio N, Iodice S, Baio SM, et al. Peptide receptor radionuclide therapy with 177Lu-DOTATATE: the IEO phase I-II study. Eur J Nucl Med Mol Imaging. 2011;38:2125–35. doi:10.1007/s00259-011-1902-1.
7. Sandström M, Garske-Román U, Granberg D, Johansson S, Widstrom C, Eriksson B, et al. Individualized dosimetry of kidney and bone marrow in patients undergoing 177Lu-DOTA-octreotate treatment. J Nucl Med. 2013;54:33–41. doi:10.2967/jnumed.112.107524.
8. Gupta SK, Singla S, Thakral P, Bal CS. Dosimetric analyses of kidneys, liver, spleen, pituitary gland, and neuroendocrine tumors of patients treated with 177Lu-DOTATATE. Clin Nucl Med. 2013;38:188–94. doi:10.1097/RLU.0b013e3182814ac1.
9. Kairemo K, Kangasmaki A. 4D SPECT/CT acquisition for 3D dose calculation and dose planning in 177Lu-peptide receptor radionuclide therapy: applications for clinical routine. Recent Results Cancer Res. 2013;194:537–50. doi:10.1007/978-3-642-27994-2_31.

10. Forrer F, Oechslin-Oberholzer C, Campana B, Herrmann R, Maecke HR, Mueller-Brand J, et al. Radioimmunotherapy with ^{177}Lu-DOTA-rituximab: final results of a phase I/II Study in 31 patients with relapsing follicular, mantle cell, and other indolent B-cell lymphomas. J Nucl Med. 2013;54:1045–52. doi:10.2967/jnumed.112.115170.
11. ICRP publication 103: the 2007 recommendations of the International Commission of Radiological Protection. Ann ICRP 2007;37:2–4.
12. ICRP publication 60: 1990 recommendations of the International Commission on Radiological Protection. Ann ICRP 1991;21:1–3.
13. Martin CJ. Effective dose: how should it be applied to medical exposures? Br J Radiol. 2007;80:639–47. doi:10.1259/bjr/25922439.
14. Loevinger R, Budinger TF, Watson EE. MIRD primer for absorbed dose calculations. New York: The Society of Nuclear Medicine; 1989.
15. Bolch WE, Eckerman KF, Sgouros G, Thomas SR. MIRD pamphlet No. 21: a generalized schema for radiopharmaceutical dosimetry – standardization of nomenclature. J Nucl Med. 2009;50:477–84. doi:10.2967/jnumed.108.056036.
16. Glatting G, Bardiès M, Lassmann M. Treatment planning in molecular radiotherapy. Z Med Phys. 2013;23:262–9. doi:10.1016/j.zemedi.2013.03.005.
17. Glatting G, Lassmann M. Nuclear medicine dosimetry: quantitative imaging and dose calculations. Z Med Phys. 2011;21:246–7. doi:10.1016/j.zemedi.2011.07.005.
18. Siegel JA, Thomas SR, Stubbs JB, Stabin MG, Hays MT, Koral KF, et al. MIRD pamphlet no. 16: techniques for quantitative radiopharmaceutical biodistribution data acquisition and analysis for use in human radiation dose estimates. J Nucl Med. 1999;40:37S–61.
19. Kletting P, Schimmel S, Kestler HA, Hänscheid H, Luster M, Fernández M, et al. Molecular radiotherapy: the NUKFIT software for calculating the time-integrated activity coefficient. Med Phys. 2013;40:102504. doi:10.1118/1.4820367.
20. ICRP publication 110: adult reference computational phantoms. Ann ICRP. 2009;39(2).
21. Bardiès M, Lassmann M. Monte carlo methods in nuclear medicine. In: Baum PR, editor. Therapeutic nuclear medicine. Berlin/Heidelberg: Springer Berlin Heidelberg; 2014. p. 759–68. Available: http://dx.doi.org/10.1007/174_2012_713.
22. Dale R, Carabe-Fernandez A. The radiobiology of conventional radiotherapy and its application to radionuclide therapy. Cancer Biother Radiopharm. 2005;20:47–51.
23. Strigari L, Benassi M, Chiesa C, Cremonesi M, Bodei L, D'Andrea M. Dosimetry in nuclear medicine therapy: radiobiology application and results. Q J Nucl Med Mol Imaging. 2011;55:205–21. doi:R39112324 [pii].
24. Lassmann M. Dosimetry of short-ranged radionuclides. Nuklearmedizin. 2010;49:S46–9. doi:10610046 [pii].
25. Wessels BW, Konijnenberg MW, Dale RG, Breitz HB, Cremonesi M, Meredith RF, et al. MIRD pamphlet No. 20: the effect of model assumptions on kidney dosimetry and response – implications for radionuclide therapy. J Nucl Med. 2008;49:1884–99. doi:jnumed.108.053173 [pii].
26. Emami B, Lyman J, Brown A, Coia L, Goitein M, Munzenrider JE, et al. Tolerance of normal tissue to therapeutic irradiation. Int J Radiat Oncol Biol Phys. 1991;21:109–22.
27. Eberlein U, Peper M, Fernandez M, Lassmann M, Scherthan H. Calibration of the gamma-H2AX DNA double strand break focus assay for internal radiation exposure of blood lymphocytes. PLoS One. 2015;10:e0123174. doi:10.1371/journal.pone.0123174.
28. Eberlein U, Nowak C, Bluemel C, Buck AK, Werner RA, Scherthan H, et al. DNA damage in blood lymphocytes in patients after ^{177}Lu peptide receptor radionuclide therapy. Eur J Nucl Med Mol Imaging. 2015;42:1739–49. doi:10.1007/s00259-015-3083-9.
29. Eberlein U, Scherthan H, Bluemel C, Peper M, Lapa C, Buck AK, et al. DNA damage in peripheral blood lymphocytes of thyroid cancer patients after radioiodine therapy. J Nucl Med. 2016;57:173–9. doi:10.2967/jnumed.115.164814.
30. Denoyer D, Lobachevsky P, Jackson P, Thompson M, Martin OA, Hicks RJ. Analysis of ^{177}Lu-DOTA-octreotate therapy-induced DNA damage in peripheral blood lymphocytes of

patients with neuroendocrine tumors. J Nucl Med. 2015;56:505–11. doi:10.2967/jnumed.114.145581.

31. Machado JS, Beykan S, Herrmann K, Lassmann M. Recommended administered activities for ^{68}Ga-labelled peptides in paediatric nuclear medicine. Eur J Nucl Med Mol Imaging. 2016;43(11):2036–9. doi:10.1007/s00259-015-3289-x.

32. Eberlein U, Broer JH, Vandevoorde C, Santos P, Bardies M, Bacher K, et al. Biokinetics and dosimetry of commonly used radiopharmaceuticals in diagnostic nuclear medicine – a review. Eur J Nucl Med Mol Imaging. 2011;38:2269–81. doi:10.1007/s00259-011-1904-z.

33. Sandström M, Velikyan I, Garske-Román U, Sorensen J, Eriksson B, Granberg D, et al. Comparative biodistribution and radiation dosimetry of ^{68}Ga-DOTATOC and ^{68}Ga-DOTATATE in patients with neuroendocrine tumors. J Nucl Med. 2013;54:1755–9. doi:10.2967/jnumed.113.120600.

34. Hartmann H, Zophel K, Freudenberg R, Oehme L, Andreeff M, Wunderlich G, et al. Radiation exposure of patients during ^{68}Ga-DOTATOC PET/CT examinations. Nuklearmedizin. 2009;48:201–7. doi:10.3413/nukmed-0214.

35. Lassmann M, Eberlein U. Radiation dosimetry aspects of [177]Lu. Curr Radiopharm. 2015;8:139–44.

36. Cremonesi M, Ferrari M, Bodei L, Tosi G, Paganelli G. Dosimetry in peptide radionuclide receptor therapy: a review. J Nucl Med. 2006;47:1467–75. doi:47/9/1467 [pii].

37. Barone R, Borson-Chazot F, Valkema R, Walrand S, Chauvin F, Gogou L, et al. Patient-specific dosimetry in predicting renal toxicity with ^{90}Y-DOTATOC: relevance of kidney volume and dose rate in finding a dose-effect relationship. J Nucl Med. 2005;46 Suppl 1:99S–106.

38. Cremonesi M, Botta F, Di Dia A, Ferrari M, Bodei L, De Cicco C, et al. Dosimetry for treatment with radiolabelled somatostatin analogues. A review. Q J Nucl Med Mol Imaging. 2010;54:37–51. doi:R39102235 [pii].

39. Forrer F, Uusijarvi H, Waldherr C, Cremonesi M, Bernhardt P, Mueller-Brand J, et al. A comparison of ^{111}In-DOTATOC and ^{111}In-DOTATATE: biodistribution and dosimetry in the same patients with metastatic neuroendocrine tumours. Eur J Nucl Med Mol Imaging. 2004;31:1257–62. doi:10.1007/s00259-004-1553-6.

40. Jamar F, Barone R, Mathieu I, Walrand S, Labar D, Carlier P, et al. [86]Y-DOTA0)-D-Phe1-Tyr3-octreotide (SMT487) – a phase 1 clinical study: pharmacokinetics, biodistribution and renal protective effect of different regimens of amino acid co-infusion. Eur J Nucl Med Mol Imaging. 2003;30:510–8. doi:10.1007/s00259-003-1117-1.

41. Hindorf C, Chittenden S, Causer L, Lewington VJ, Macke HR, Flux GD. Dosimetry for ^{90}Y-DOTATOC therapies in patients with neuroendocrine tumors. Cancer Biother Radiopharm. 2007;22:130–5. doi:10.1089/cbr.2007.306.

42. Forster GJ, Engelbach MJ, Brockmann JJ, Reber HJ, Buchholz HG, Macke HR, et al. Preliminary data on biodistribution and dosimetry for therapy planning of somatostatin receptor positive tumours: comparison of [86]Y-DOTATOC and (111)In-DTPA-octreotide. Eur J Nucl Med. 2001;28:1743–50. doi:10.1007/s002590100628.

43. Helisch A, Forster GJ, Reber H, Buchholz HG, Arnold R, Goke B, et al. Pre-therapeutic dosimetry and biodistribution of [86]Y-DOTA-Phe1-Tyr3-octreotide versus 111In-pentetreotide in patients with advanced neuroendocrine tumours. Eur J Nucl Med Mol Imaging. 2004;31:1386–92. doi:10.1007/s00259-004-1561-6.

44. Kwekkeboom DJ, Kooij PP, Bakker WH, Macke HR, Krenning EP. Comparison of ^{111}In-DOTA-Tyr3-octreotide and ^{111}In-DTPA-octreotide in the same patients: biodistribution, kinetics, organ and tumor uptake. J Nucl Med. 1999;40:762–7.

45. Strigari L, Konijnenberg M, Chiesa C, Bardies M, Du Y, Gleisner KS, et al. The evidence base for the use of internal dosimetry in the clinical practice of molecular radiotherapy. Eur J Nucl Med Mol Imaging. 2014;41:1976–88. doi:10.1007/s00259-014-2824-5.

46. Walrand S, Barone R, Pauwels S, Jamar F. Experimental facts supporting a red marrow uptake due to radiometal transchelation in ^{90}Y-DOTATOC therapy and relationship to the decrease of platelet counts. Eur J Nucl Med Mol Imaging. 2011;38:1270–80. doi:10.1007/s00259-011-1744-x.
47. Bodei L, Cremonesi M, Ferrari M, Pacifici M, Grana CM, Bartolomei M, et al. Long-term evaluation of renal toxicity after peptide receptor radionuclide therapy with ^{90}Y-DOTATOC and ^{177}Lu-DOTATATE: the role of associated risk factors. Eur J Nucl Med Mol Imaging. 2008;35:1847–56. doi:10.1007/s00259-008-0778-1.
48. Van Binnebeek S, Baete K, Vanbilloen B, Terwinghe C, Koole M, Mottaghy FM, et al. Individualized dosimetry-based activity reduction of ^{90}Y-DOTATOC prevents severe and rapid kidney function deterioration from peptide receptor radionuclide therapy. Eur J Nucl Med Mol Imaging. 2014;41:1141–57. doi:10.1007/s00259-013-2670-x.
49. Bergsma H, Konijnenberg MW, Kam BL, Teunissen JJ, Kooij PP, de Herder WW, et al. Subacute haematotoxicity after PRRT with Lu-DOTA-octreotate: prognostic factors, incidence and course. Eur J Nucl Med Mol Imaging. 2015. doi:10.1007/s00259-015-3193-4.

Chapter 10
Principles and Application of Molecular Imaging for Personalized Medicine and Guiding Interventions in Neuroendocrine Tumors

Michael S. Hofman

10.1 Introduction

Management of patients with neuroendocrine tumors is being significantly altered by integration of molecular imaging into routine patient care. Multi-slice computed tomography (CT) and magnetic resonance imaging (MRI) provide astonishing anatomic detail with submillimeter resolution on modern devices but limited ability to characterise disease. Molecular imaging with single photon emission tomography (SPECT) or positron emission tomography (PET) are complementary with its strength lying in the radiotracer principle where a particular pathway can be interrogated by labeling a molecule with a radioactive isotope enabling visualization and noninvasive quantification of specific metabolic or biochemical pathways. For neuroendocrine tumors, the high expression of somatostatin receptors (SSTRs) on the cell surface of tumors provides a highly specific target for nuclear medicine. The gamma camera and PET/CT have an extraordinary sensitivity for detecting substances, with the ability to detect femtomolar concentrations of substances, several orders of magnitude greater than detection of iodinated or paramagnetic contrast used with CT or MRI (see Fig. 10.1). Moreover, for both SPECT and PET, radiotracers are administered in microgram dosages which do not have any adverse effects. Nowadays, both SPECT and PET are combined with anatomic imaging providing integration of functional and anatomic assessment in a single study.

In the conventional cancer imaging paradigm, anatomic imaging is used to define the number and size of lesions. From these, a tumor stage can be derived, typically using the American Joint Committee on Cancer (AJCC) staging system which classifies tumors into different groups depending on the extent of the primary tumor

M.S. Hofman, MBBS, FRACP, FAANMS
Centre for Molecular Imaging, Peter MacCallum Cancer Centre, Melbourne, Australia

Sir Peter MacCallum Department of Oncology, The University of Melbourne, Melbourne, Australia
e-mail: Michael.hofman@petermac.org
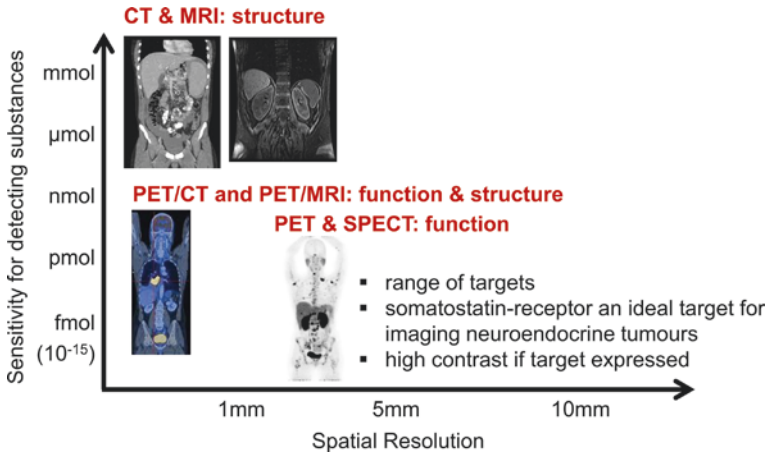
Fig. 10.1 Contrasting strengths and weaknesses of both anatomic and molecular imaging. The fusion of both modalities with hybrid PET/CT or PET/MRI enables the evaluation of function and anatomy contemporaneously with precise co-registration between the two modalities

(T stage), nodal spread (N stage), and distant metastatic disease (M stage). To define whether there is nodal disease involvement, arbitrary size criteria are utilized with anatomically enlarged nodes considered likely malignant.

The molecular imaging paradigm for tumor imaging is contrasted by focusing on MNT stage emphasizing that once distant metastases are identified, the locoregional staging is less important (Fig. 10.2). Molecular imaging also performs well in the conventional paradigm of identifying lesions and measuring them, particularly given the high tumor-to-background contrast that is frequently observed. The high tumor-to-background contrast seen with PET/CT also ensures high reporter agreement. There is less reliance on size, since normal size structures that have abnormal uptake can be characterized as malignant. With highly specific radiotracers and modern generation PET equipment, structures smaller than 5 mm can be confidently identified as malignant if they have high uptake. Given the advantages of PET/CT, we advocate that it should be utilized early in the patient workup as the first rather than last imaging modality [1].

The paradigm shift and advantages of molecular imaging, however, go beyond its ability to identify, count, and measure lesions. Through its ability to characterize tumor biology, it provides powerful prognostic information [2]. This was previously the realm of histopathology, but with the insights of PET/CT imaging, the limitations of relying on characteristics of biopsy from a single site are becoming clear. This is particularly true for metastatic neuroendocrine tumors where their inter-tumor heterogeneity may be observed with varying degrees of tumor differentiation at different sites. In addition to its prognostic power is the predictive power of molecular imaging. This is particularly well demonstrated in theranostic treatments, in which the same molecule is labeled to a therapeutic beta emitter rather than a gamma or positron emitter. The diagnostic scan thereby serves as a predictive biomarker to determine suitability for targeted therapy. This is a well-grounded principle that has been used to successfully treat patients with thyroid cancer for more than 75 years.
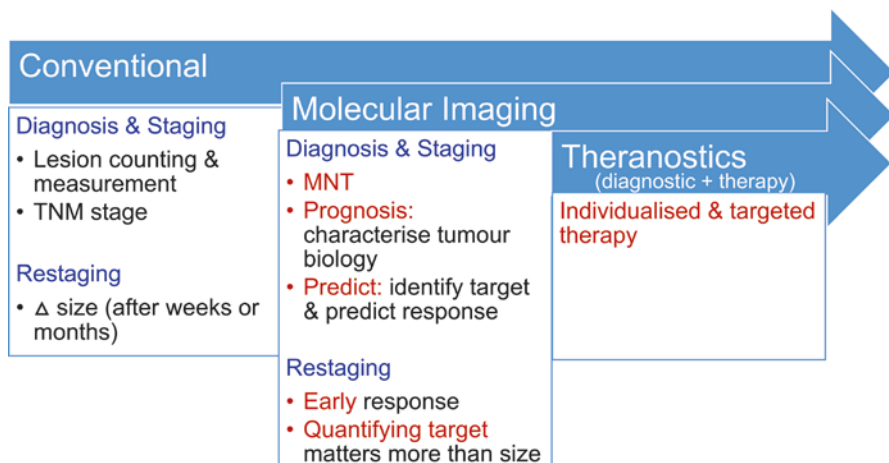
Fig. 10.2 The changing cancer imaging paradigm with the use of molecular imaging. This archetype is particularly well demonstrated for neuroendocrine tumors where somatostatin receptor (SSTR) expression assessed with imaging serves as a predictive biomarker for likely response to somatostatin analogue (SSA) therapy or peptide receptor radionuclide therapy (PRRT). FDG retains a pivotal role for assessing tumor biology with dedifferentiated tumors having high glycolytic activity and poor prognosis

10.2 PET Versus SPECT and Selection of Radiotracer

For diagnostic imaging, PET has clear technical superiority compared to SPECT including higher sensitivity for detecting radioactive decay, higher spatial resolution, higher temporal resolution, quantitative capability, and, often, lower radiation dose to the patient owing to the use of short half-life radiotracers [3]. In our center, PET has become the dominant modality for cancer imaging. For imaging neuroendocrine tumors, we employ a variety of radiotracers predominantly using fluorine-18 (^{18}F) and gallium-68 (^{68}Ga) labeled to fluorodeoxyglucose (FDG) and peptides that bind to SSTR, respectively. The latter including DOTATATE, DOTATOC and DOTANOC, which have variable affinity for different subtypes of SSTR, but in clinical practice have similar performance [4]. We have a preference to use DOTATATE as we also treat patients with Lu-177 (^{177}Lu)- and Y-90 (^{90}Y)-radiolabeled DOTATATE, and it therefore serves as a theranostic pair. The short half-life of ^{68}Ga of 68 minutes means that imaging must be perform within a few hours of injection, negating the ability to perform delayed imaging (e.g., at 24 h) that can be readily performed with Indium-111 (^{111}In)- or Technetium-99m (^{99m}Tc)-radiolabeled octreotide with SPECT imaging. The early time-point imaging with ^{68}Ga is not suitable for performing prospective dosimetry where imaging at 24-h or later time-points are required. Positron emitters with longer half-life such as Copper-64 (^{64}Cu) are better suited for prospective dosimetry but are not in widespread use. Carbon-11 (^{11}C) labeled to 5-hydroxytryprophan can also be used to image neuroendocrine tumors [5], but their clinical implementation is not widespread beyond the research setting owing to the short half-life of 20 min.

10.3   Diagnosis

Definitive diagnosis has traditionally been the realm of histopathology, but as PET imaging evolves with specific radiotracers including SSTR PET/CT, one can consider it a form of "imaging histopathology," in some cases obviating the need for invasive biopsy. In the era of multi-slice CT and MRI being more widely performed, incidental neuroendocrine tumors in the pancreas, small bowel, and lung are being identified. These may have anatomic features that favor neuroendocrine etiology such desmoplastic changing surrounding mesenteric lymphadenopathy or arterial enhancement of the primary, but these features are not sufficiently specific to establish a diagnosis. While biopsy remains the first-line diagnostic choice, this cannot singularly be regarding as a gold standard as it is subject to sampling error. There is also morbidity associated with endoscopic or percutaneous biopsy, and depending on patient comorbidities and anatomic location, it may not be feasible. We now utilize SSTR PET/CT to confirm the diagnosis of NET in selected patients. If very intense uptake is demonstrated at site anatomically consistent with a neuroendocrine tumor, diagnosis can be established with a high degree of certainty on imaging alone.

Patients presenting with symptoms due to hormone secretion and elevation of specific hormones and clinical symptoms are another group where SSTR PET/CT is useful to localize the primary site of disease and confirm the diagnosis. This includes patients with carcinoid tumors, insulinoma, glucagonoma, gastrinoma, and VIPoma. We now utilize SSTR PET/CT as the first-line imaging investigation as CT and MRI have a relatively low yield and specificity (see Fig. 10.3). The use of SSTR PET/CT may also obviate the need for endoscopic assessment or direct the endoscopy in cases where histopathologic correlation is required. While most well-differentiated NETs have high SSTR expression making SSTR PET/CT the investigation of choice, this is not universally true. In particular, a proportion of insulinomas do not have SSTR expression. In these patients, we perform ^{68}Ga-Exendin-4 PET/CT which targets the glucagon-like peptide-1 receptor (GLP-1) which is highly expressed in SSTR-negative insulinomas [6, 7].

10.4   Tumor Grade and Tumor Heterogeneity

Establishing the grade of neuroendocrine tumor is pivotal for selecting the appropriate therapy for an individual patient. Molecular imaging complements histopathologic analysis of individual sites by enabling a whole-body assessment of tumor phenotype. High uptake on DOTATATE and low uptake on FDG PET/CT are seen in patients with well-differentiated NETs commensurate with the high SSTR expression and low proliferative rate. The converse is seen in poorly differentiated tumors. In patients with advanced disease and particular in patients with intermediate or high-grade neuroendocrine tumors, we utilize molecular imaging to guide
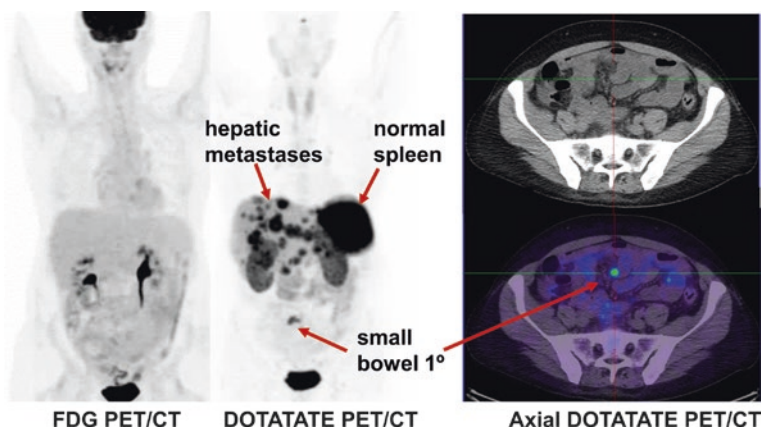
Fig. 10.3 Middle-aged man who presented with carcinoid syndrome, confirmed by the biopsy of hepatic metastatic disease which demonstrated well differentiated tumor with Ki-67 less than 1 %. FDG PET/CT shows no abnormal uptake. In the conventional imaging paradigm, this would be considered a false negative, but the absence of uptake is concordant with the biopsy and supports all sites of disease being indolent Grade I neuroendocrine tumor. DOTATATE PET/CT demonstrates intense uptake in the hepatic metastases indicative of high somatostatin cell surface expression and serving as a predictive biomarker of response to SSA therapy. The primary site of disease which is not visualized on conventional imaging is localized with confidence to the small bowel

biopsy as tumor heterogeneity is frequently observed (see Fig. 10.4). In the conventional paradigm, biopsy typically targets the site that is most accessible. Such blinded biopsy may yield tumor specimen that is not reflective of disease at other sites. This can misguide management, particularly if biopsy demonstrates low-grade disease in a patient with occult high-grade disease at other sites. Such patients may be erroneously reassured that they will follow an indolent course only to unexpectedly progress. We utilize both FDG and SSTR PET/CT to image sites of poorly differentiated and well-differentiated disease, respectively (see Fig. 10.5). Biopsy is targeted at sites of most FDG-avid disease which are likely the more aggressive sites that will determine the patients' prognosis.

10.5 Using Molecular Imaging to Guide Management

In the conventional cancer imaging paradigm with anatomic imaging, prognosis can be inferred from the stage of disease determined by the extent of the primary tumor, nodal spread, and distant metastatic disease according to the TNM staging system. In this paradigm, histopathologic features, in particular the proliferative rate measured using Ki-67, are further used to characterize the grade of the tumor. In the molecular imaging paradigm, information from PET/CT is independently valued for establishing the grade and prognosis of the patient which is pivotal in directing therapy, as more aggressive treatment is needed in patients with poorer prognosis,
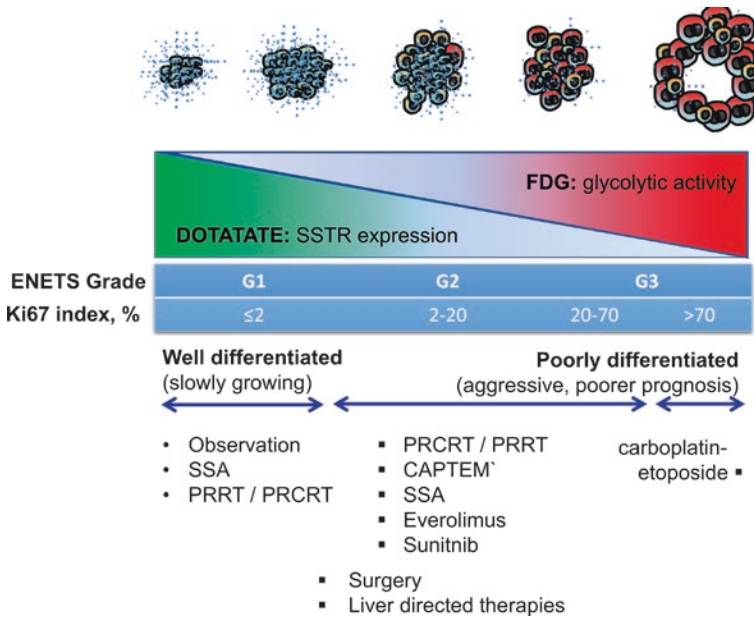
Fig. 10.4 The "flip-flop" phenomenon of high DOTATATE and low FDG uptake in well-differentiated tumors and the opposite imaging phenotype in poorly differentiated tumors. Inter-tumoral heterogeneity may be present with different grade tumors at different sites. Using the prognostic and predictive power of FDG and DOTATATE enables better selection of management for an individual patient. It should be noted, however, that the pattern is not universal as some highly differentiated tumors do not express somatostatin receptors (e.g., insulinomas) and not all aggressive tumors use glycolytic metabolism for growth

whereas patients with very indolent disease on the other end of the spectrum can sometimes be observed.

In a prospective study of 98 patients with neuroendocrine tumors, 58 % of FDG PET were positive, and in multivariate analysis, SUVmax > 3 was the only predictor of progression-free survival [8] (Fig. 10.6). The study demonstrated that FDG PET/CT provides strong prognostic information which exceeded traditional markers such as Ki-67, chromogranin A, or the presence of hepatic metastases. Other studies have confirmed these results [9, 10]. Conversely, high uptake on SSTR PET indicative of a well-differentiated phenotype confers a favorable prognosis [11]. These studies highlight the ability of whole-body PET imaging to characterize all sites of disease in a given patient, minimizing the sampling error inherent with histopathologic sampling of a random biopsy site. Based on these results, we integrate PET phenotype as a critical factor when stratifying patient risk and deciding on therapy in conjunction with the European Neuroendocrine Tumor Society (ENETS) pathologic grading system [12].

The improved accuracy obtained when imaging patients with SSTR PET/CT confers a high management impact with an inter-modality change of therapeutic strategy in 19 to 71 % demonstrated in several retrospective studies [13–19]. Most
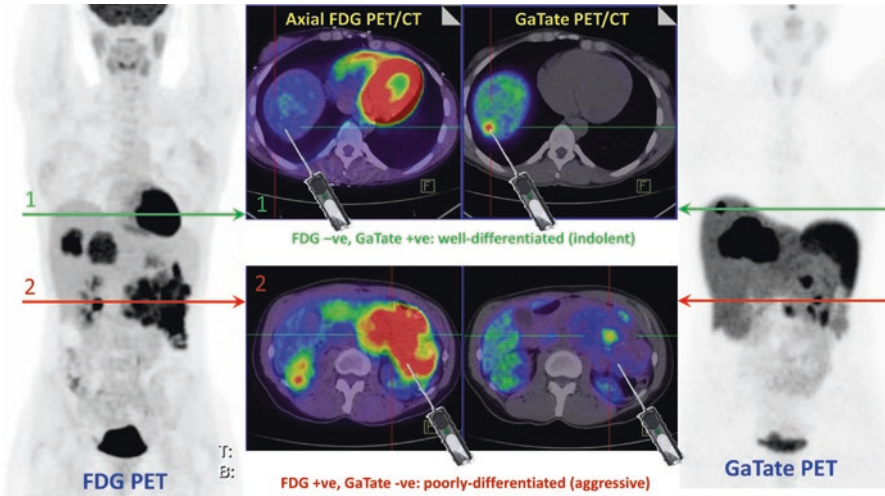
Fig. 10.5 Patient with insulinoma and CT/MRI demonstrating a large pancreatic tail primary with locoregional nodal and multiple hepatic metastases. FDG and DOTATATE (GaTate) PET/CT demonstrate different grade tumors at different sites. Without the knowledge of the PET findings, random core biopsy on the basis of CT or MRI could reveal either subtype, which might misinform decision-making. The PET studies demonstrate tumor heterogeneity suggesting both well- and poorly differentiated disease at different sites (Modified with permission from [2])
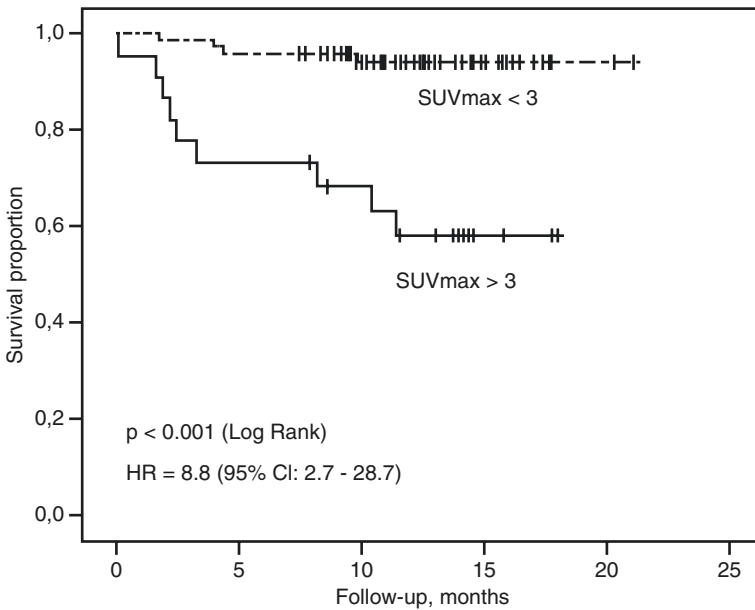
Fig. 10.6 Kaplan–Meier survival curves in a prospective cohort of patients with neuroendocrine tumors. FDG PET provided superior prognostication with overall survival compared to histopathologic Ki-67 (Reproduced with permission from [8])

recently, a prospective study of 78 patients demonstrated significant management impact of 36%, with SSTR PET/CT being equivalent or superior to ^{111}In-octreotide in all patients [20]. In recent years, there are an increasing number of therapeutic options for patients with neuroendocrine tumors. Selecting the optimal therapy or sequence of therapies for an individual patient can be challenging. In our center, molecular imaging staging and characterization play a key role in selection and sequencing of therapy as detailed below.

10.6   Surgery

Surgery remains the cornerstone of curative management of patients with localized neuroendocrine tumors. As detailed above, the use of SSTR PET/CT usually enables confident localization of the primary site which can direct patients to curative surgery, especially those with localized disease. In patients with incidental small well-differentiated tumor discovered on imaging performed for other reasons, observation may be appropriate in a select population. The strongest evidence of such a conservative approach is for incidental well-differentiated pancreatic NET less than 2 cm in size [21]. This may also be true for small incidental lesions in the small bowel and lung. Debulking surgery in patients with metastatic disease can be useful, particularly in patients with symptoms due to secretion of hormones, in whom quality of life can be improved. The role of non-curative debulking surgery is, however, diminishing due to more sensitive imaging with SSTR PET/CT which often demonstrates more extensive disease than conventional anatomic imaging (see Fig. 10.7) and with the availability of new systemic therapeutic options as detailed below. In patients with disease confined to the liver who are being considered for surgery, additional imaging with MRI should be performed to complete staging as this modality can identify small metastases below PET/CT resolution which may modify management.

10.7   Somatostatin Analogue (SSA) Therapy

Somatostatin analogues (SSA) such as lanreotide or octreotide LAR are now commonly used to treat patients with unresectable NET. This was originally used for patients with symptoms due to hormonal secretion but is now also used to slow progression in selected patients. A key selection criteria for commencing SSA are adequate SSTR expression in the tumor, which is defined by imaging. In the CLARINET trial [22], this was defined by a Krenning score of Grade II or higher on ^{111}In-octreotide scintigraphy. In this semiquantitative scale [23], there are five scores ranging from 0 to 4 defined as no uptake, very low-intensity uptake, uptake intensity less than or equal to the liver, uptake intensity greater than the liver, and uptake intensity greater than the spleen, respectively. Although this scale was designed for planar scintigraphy, we continue to use this scale for reporting SSTR PET/CT.
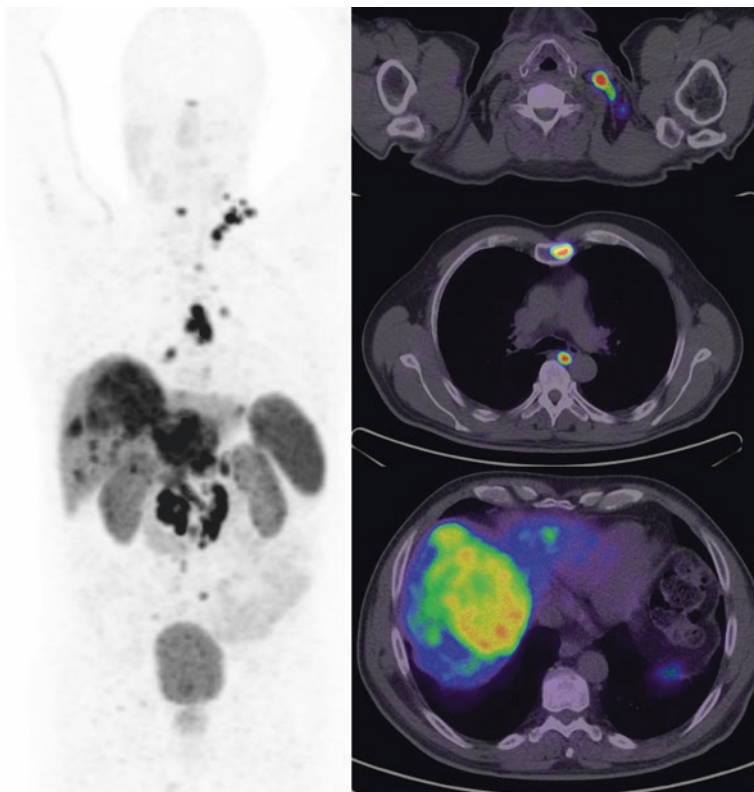
Fig. 10.7 Middle-aged man with metastatic ENETS Grade II pancreatic tumor of unknown primary and documented disease progression despite treatment with somatostatin analogue therapy. Following workup with CT and MRI, the patient was scheduled to undergo hepatic debulking surgery on the basis that more than 90 % of disease could be excised. DOTATATE PET/CT demonstrated additional disease within the bone and lymph nodes on both sides of the diaphragm. In the setting of significant burden of extrahepatic disease not appreciated on conventional imaging with all sites of disease demonstrating high SSTR expression, management was changed to peptide receptor radionuclide therapy (PRRT)

10.8   Radionuclide Therapy

Labeling SSA with therapeutic beta emitters enables targeted treatment of non-resectable neuroendocrine tumors. Peptide receptor radionuclide therapy (PRRT) with ^{177}Lu was pioneered by the Erasmus group who demonstrated highly favorable results in a large cohort of patients back in 2005 [24]. Since this time, the treatment has evolved [24–34] with additional use of ^{90}Y-radiolabeled SSA and combining PRRT with chemotherapy, the so-called peptide receptor chemoradionuclide therapy (PRCRT) [27, 35, 36]. Similar to SSA therapy, the use of SSTR scintigraphy or SSTR PET/CT is essential for selection of patients that may benefit from PRRT. Studies to date have required uptake intensity greater than the liver corresponding to a Krenning

Table 10.1 Our recommendation for indications of selective use FDG PET/CT in addition to SSTR PET/CT

Ki-67 ≥ 5 %
Lesions of concern on the CT component of SSTR PET/CT with low or no activity
Clinical or radiologic evidence of disease progression within a time frame less than 6 months despite a Ki-67 < 5 %

score of 3 to indicate potential benefit and suitability for PRRT. While SSTR PET/CT is generally superior to SSTR planar or SPECT imaging, there are a minority of patients where early time-point imaging performed with ^{68}Ga has lower intensity uptake compared with more delayed imaging performed with ^{99m}Tc or ^{111}In-SSTR SPECT/CT.

We additionally employ FDG PET/CT in selected patients, usually those with ENETS Grade II or higher tumors, to further enrich the selection for patients likely to benefit from PRRT (see Table 10.1). For patients with sites of FDG+/SSTR- disease, we usually do not recommend PRRT as these patients have sites of aggressive NET that cannot be targeted (see Fig. 10.8). This recommendation is not universal as the addition of concomitant chemotherapy with PRCRT may target these sites, while patients with symptoms due to hormonal secretion may still derive symptomatic benefit by treating the well-differentiated disease components (see Fig. 10.9).

Our application of PRRT and PRCRT is highly individualized [38]. In general, for patients with ENETS Grade I tumor, we only use radionuclide therapy for patients who, despite SSA therapy, have objective evidence of disease progression or have ongoing symptoms. For patients with more aggressive ENETS Grade II or higher tumors, we now routinely use PRCRT as the first-line treatment [39] given the significantly greater response rates and survival rates seen with the individualized theranostic approach compared to other therapeutic options [40]. For patients with tumors greater than 4 cm in size, we generally administer one or two cycles with ^{90}Y-DOTATATE followed by further cycles of ^{177}Lu-DOTATATE up to a total of four cycles. For patients with very large burdens of disease, we consider early consolidation with one to two further cycles of PRRT. We individualize the administered activity according to tumor burden seen on SSTR PET/CT, body weight, and renal function [38].

The adverse prognosis associated with FDG-avid NET as described above was described in the pre-PRRT era. We have recently published data regarding the efficacy of peptide receptor chemoradionuclide therapy (PRCRT) with Lutetium-177 DOTATATE (LuTate) combined with 5-fluorouracil (5FU) in a cohort of 52 patients with FDG-avid NET [41]. Despite the anticipated poor prognosis of this cohort, we demonstrated an unexpectedly long progression-free survival (PFS) of 48 months, with median overall survival of 55 months [40]. While retrospectively, our results have a lead-time bias which is disadvantageous to our analysis, as survival was measured not from diagnosis but from the time of PRCRT in a population who were previously treated with conventional therapeutic regimens including at least one line of chemotherapy in 67 %. We believe these favorable results demonstrate how
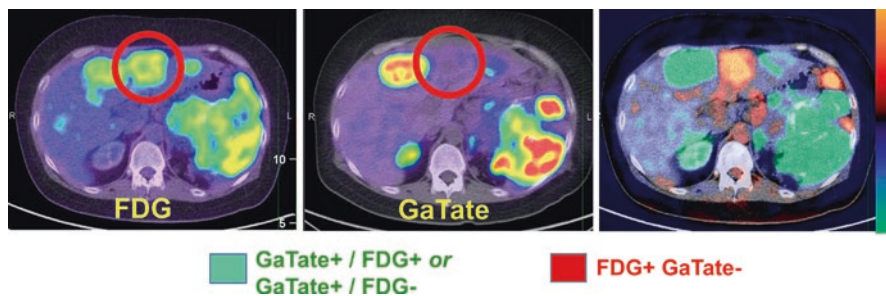
Fig. 10.8 This patient with metastatic neuroendocrine tumor and known hepatic metastases was evaluated for suitability for peptide receptor radionuclide therapy (PRRT). FDG and DOTATATE PET/CT demonstrated several sites of discordant FDG+ DOTATATE- (*orange/red color*) disease, although the majority sites were DOTATATE+ FDG+ or DOTATATE+ FDG- (*green color*). This patient is not an ideal candidate for PRRT as discordant FDG+ sites will not be targeted with PRRT but represent the sites of most aggressive disease that more likely determine patient prognosis and outcome
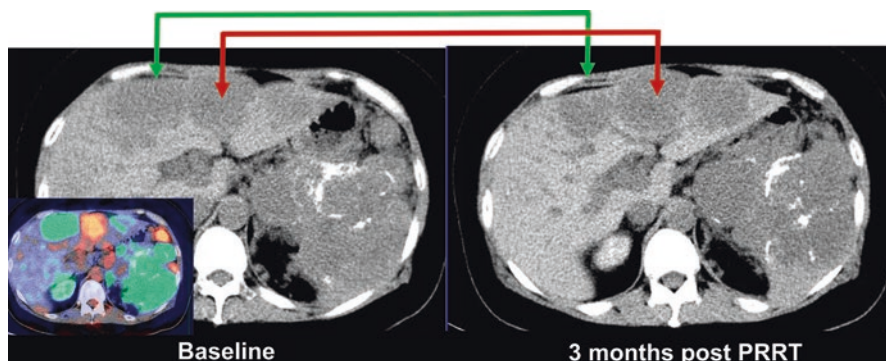
Fig. 10.9 The patient in Fig. 10.8 had intractable hypercalcemia due to PTHrP secretion from the neuroendocrine tumor. In view of likely hormone secretion from the well-differentiated disease, the patient was treated with PRRT [37] despite the presence of FDG+ DOTATATE- sites of disease. As predicted by the baseline molecular imaging phenotype, sites of DOTATATE+ disease (whether FDG+ or FDG-) responded to PRRT (*green arrow*), but sites of discordant FDG+ disease progressed (*red arrow*)

PRCRT can successfully treat sites of poorly differentiated disease, "converting" some patients with aggressive NET back to a more indolent phenotype.

Post-therapy imaging is routinely performed which enables visualization of the actual radiotracer delivery. Dosimetry can be performed using a variety of techniques but is beyond the scope of this chapter. Our preference is to perform quantitative SPECT/CT for ^{177}Lu [42] or PET/CT for ^{90}Y, followed by voxel-based lesional dosimetry [43]. Knowledge of the actual dose of radiation delivered to sites of tumor and normal tissues is informative, but it can be challenging to use this information to inform future therapy.

DOTATATE PET/CT   FDG PET/CT
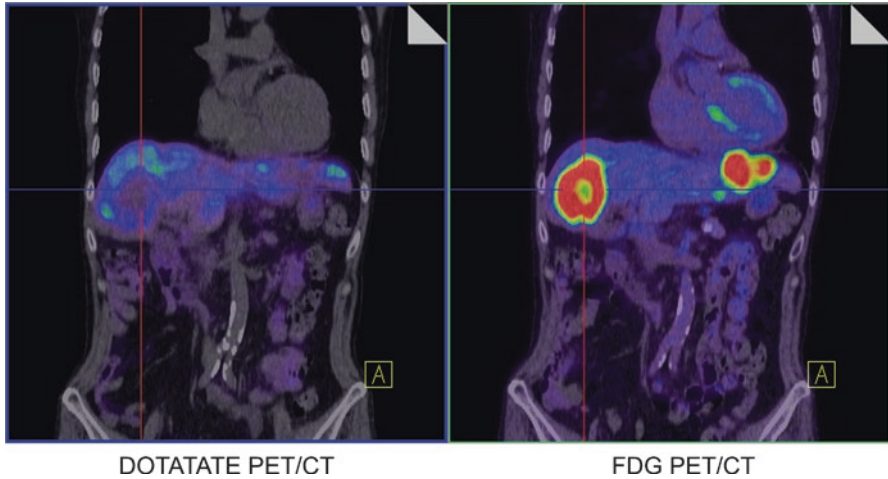
Fig. 10.10 Patient with metastatic pancreatic islet cell tumor. He previously had a highly favorable response to Lutate PRCRT over a 6-year period but then progressed with several sites of discordant FDG+ DOTATATE- disease. As these were confined to hepatic segment II and VIII, the patient proceeded to have treatment with selective transarterial chemoembolization (TACE)

10.9   Liver-Directed Therapy

For patients with metastatic disease confined to the liver, transarterial chemoembolization (TACE), microwave or other ablative therapies, or administration of radiolabeled-^{90}Y microspheres such as SIR-Spheres® are therapeutic options. As detailed above for surgery, the use of SSTR PET/CT for selection of patients is pivotal as conventional imaging may significantly underestimate the burden of extrahepatic disease, particularly within the bone. In patients with hepatic-confined disease and high SSTR expression, intra-arterial PRRT is another therapeutic option, although data is lacking to demonstrate superiority to intravenous PRRT. We generally reserve liver-directed therapies for patients who are not suitable for PRRT (see Fig. 10.10).

10.10   Cytotoxic Chemotherapy and Targeted Therapy

A range of systemic chemotherapy are available for treating NET include SSA + 5,fluorouracil (5FU) [44, 45], 5FU/streptozocin [46], capecitabine/temozolomide [47, 48] and noncytotoxic therapies including everolimus [49, 50] and sunitinib [51]. To select patients for these therapies, we generally mandate that they have FDG-avid disease signifying tumors in the ENETS Grade II or III range (see Fig. 10.11). We use FDG PET/CT as the primary modality of assessing response to these therapies, and repeat DOTATATE PET/CT if consideration is still being given to PRRT.

baseline   +3 months everolimus
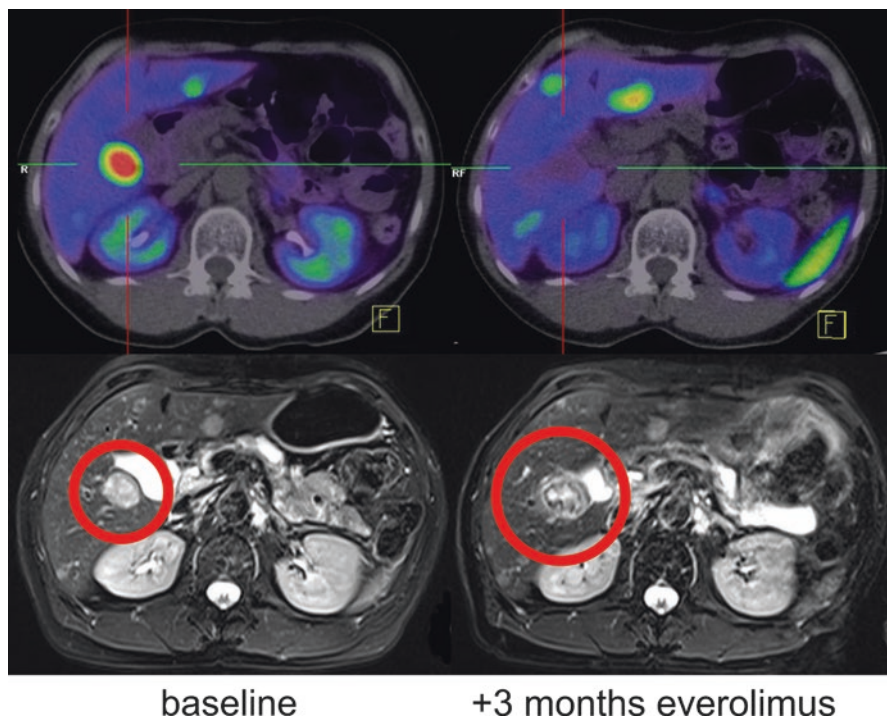
Fig. 10.11 Patient with ENETS Grade II metastatic pancreatic neuroendocrine tumor with multiple hepatic metastases. The patient was restaged after three months of everolimus treatment. MRI demonstrated enlargement of the dominant hepatic metastases, including a segment 5/6 lesion which increased from 23 × 20 mm (left) to 31 × 25 mm (right), with similar enlargement of a further dominant metastasis (not shown). DOTATATE and FDG PET/CT (not shown) demonstrated a complete functional response in both these metastases. While MRI defined progression by RECIST criteria, functional imaging confirms that this was due to cystic necrosis. By inaccurately defining progression, the use of anatomic imaging alone may misinform management as consideration may be given to cessation of the effective agent (Reproduced with permission from [4])

10.11 Response Assessment

In the conventional cancer imaging paradigm, CT and MRI are repeated several months after a therapy with changes in size used to measure effectiveness. The anatomic end point of progression-free survival (PFS) using the Response Evaluation Criteria in Solid Tumors (RECIST) [52] is used in most oncologic studies. This, however, is a surrogate imaging end point since there is an assumption that prolonged PFS is a patient relevant end point and a marker of prolonged overall survival. The use of PET/CT for restaging frequently highlights the limitations of relying on anatomic assessment (see Fig. 10.11, Table 10.2).

Table 10.2 Limitations of anatomic assessment alone for restaging and advantages of molecular imaging

Many target lesions seen with PET are occult on baseline imaging
Change in size is only a surrogate of true response: size may increase with cystic necrosis or remain unchanged with cytostatic therapies despite favorable response
Change in size occurs slowly, potentially mandating longer trial of ineffective therapy
Differences in contrast enhancement due to technique, equipment, or physiology can confound measurement (e.g., worsening carcinoid heart disease)
Substantial reporter variability in measurement
Selecting erroneous (i.e., benign) target lesion in patients with multiple metastases
Inability to quantify change in function such as SSTR expression or glycolytic metabolism, reflecting changes in well- and poorly differentiated disease components

baseline DOTATATE | + 3 cycles carbo-etoposide | + 4 cycles LuTate PRCRT
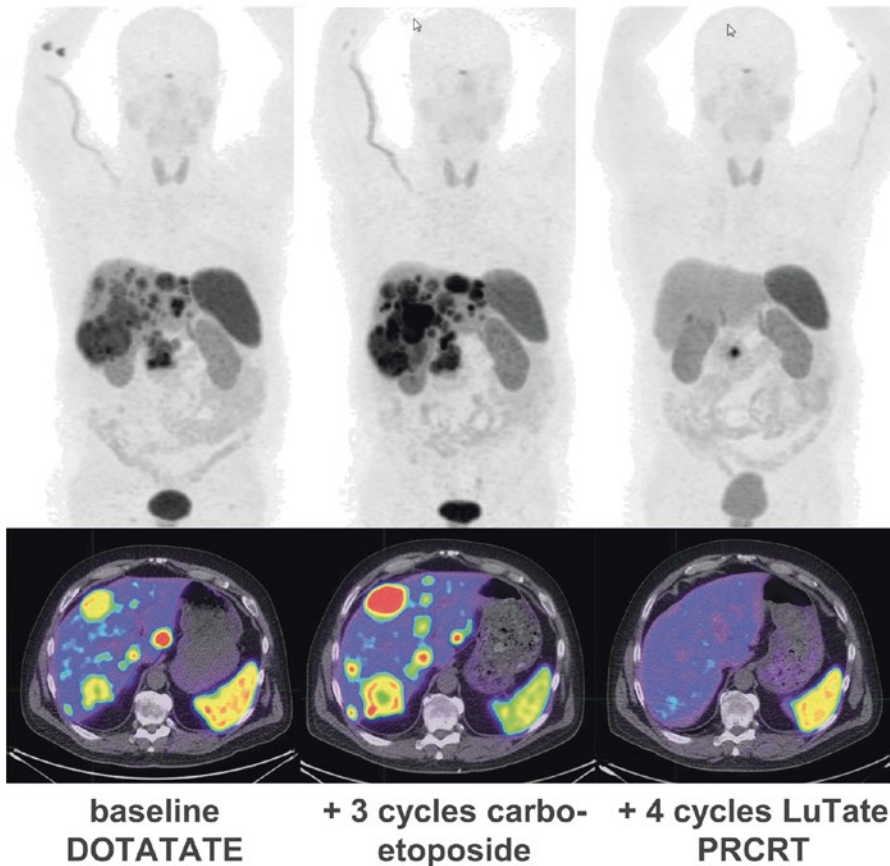
Fig. 10.12 Patient with high-grade metastatic pancreatic neuroendocrine tumor, ENETS Grade III, Ki-67 50%. The patient had rapidly progressive disease and was treated with carboplatin–etoposide chemotherapy. After three cycles, a repeat FDG PET/CT demonstrated increase in tumor burden by 55%. On the basis of chemorefractory disease and high SSTR expression, management was changed to peptide receptor chemoradionuclide therapy (PRCRT), with Lu-177 DOTATATE combined with 5FU. There was a dramatic response following PRCRT which has been durable for over 3 years at the time of publication
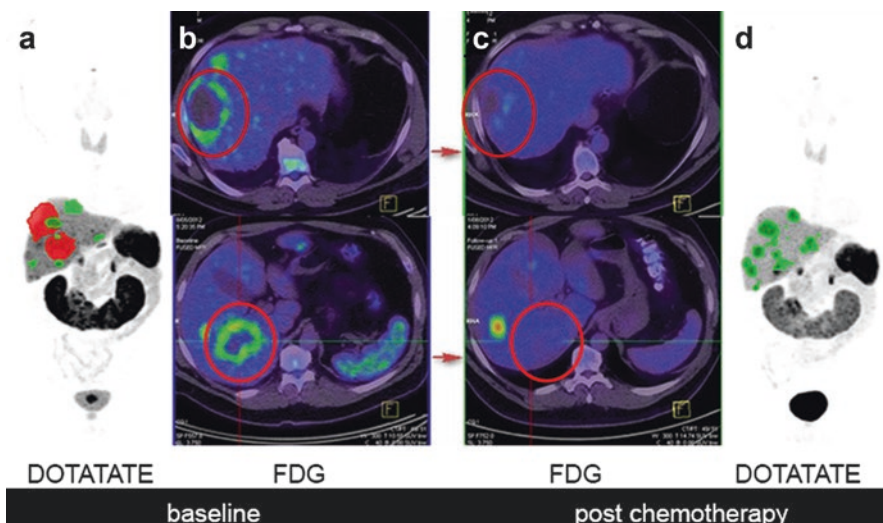
Fig. 10.13 Patient with metastatic renal neuroendocrine tumor and rapidly progressive disease, biopsy demonstrating Ki-67 of 15 %. CT demonstrated multiple hepatic metastases, but FDG and DOTATATE demonstrate different patterns of uptake consistent with significant tumor heterogeneity. There were two dominant sites of FDG+/DOTATATE- disease (*red*) and multiple sites of DOTATATE+/FDG+ or DOTATATE+/FDG- disease (*green*). The patient was treated with six cycles of cisplatin–etoposide chemotherapy. On anatomic imaging, there was a "mixed response" with some hepatic metastases smaller and others larger. Restaging FDG and DOTATATE PET better characterizes this by demonstrating a complete response at sites of baseline FDG+ discordant disease (*red*) which represented the sites of most aggressive disease that were most chemosensitive and progression of GaTate + (*green*) disease representing sites of more well-differentiated phenotype that were less sensitive to chemotherapy. The results of PET/CT could be summarized as complete response of poorly differentiated disease and progression of more well-differentiated disease, elegantly explaining the mixed response on anatomic imaging. As all sites of disease now demonstrated high SSTR expression, the patient was subsequently treated with PRCRT. He had a highly favorable response but relapsed within 12 months highlighting the poor prognosis associated with this pattern of discordant disease (Reproduced with permission from [55])

In the molecular imaging paradigm, earlier response is feasible as changes, such as reduction in glycolytic metabolism, occur faster than anatomic changes after initiation of therapy. This may enable restaging after a shorter course of therapy and enable a change in therapy if there is an inadequate response (see Fig. 10.12). Formalized criteria such as the EORTC criteria [53] and the PET Evaluation Response Criteria In Solid Tumors (PERCIST) [54] have not been validated in neuroendocrine tumors. With DOTATATE PET/CT, changes in SSTR cell surface expression can occur following treatment, and therefore change in intensity of uptake alone should be interpreted with caution. For patients with metastatic disease and tumor heterogeneity, the combined use of FDG and DOTATATE PET/CT can be informative in assessing response of poorly differentiated and well-differentiated disease, respectively (Fig. 10.13).

10.12 Conclusion

There are a growing range of therapeutic options for patients with neuroendocrine tumors. A large number of ongoing clinical trials will further inform the efficacy of specific therapeutic modalities. The optimal sequencing and fine tuning of therapy, however, will remain a challenge. We believe that a personalized approach which incorporates predictive and prognostic markers obtained from molecular imaging will remain key to optimal treatment of patients.

References

 1. Hicks RJ. Should positron emission tomography/computed tomography be the first rather than the last test performed in the assessment of cancer? Cancer Imaging. 2012;12:315–23. doi:10.1102/1470-7330.2012.9005.
 2. Hofman MS, Hicks RJ. Changing paradigms with molecular imaging of neuroendocrine tumors. Discov Med. 2012;14(74):71–81.
 3. Hicks RJ, Hofman MS. Is there still a role for SPECT-CT in oncology in the PET-CT era? Nat Rev Clin Oncol. 2012;9(12):712–20. doi:10.1038/nrclinonc.2012.188.
 4. Hofman MS, Lau WF, Hicks RJ. Somatostatin receptor imaging with 68Ga DOTATATE PET/CT: clinical utility, normal patterns, pearls, and pitfalls in interpretation. Radiographics. 2015;35(2):500–16. doi:10.1148/rg.352140164.
 5. Orlefors H, Sundin A, Ahlstrom H, Bjurling P, Bergstrom M, Lilja A, Langstrom B, Oberg K, Eriksson B. Positron emission tomography with 5-hydroxytryprophan in neuroendocrine tumors. J Clin Oncol. 1998;16(7):2534–41.
 6. Luo Y, Pan Q, Yao S, Yu M, Wu W, Xue H, Kiesewetter DO, Zhu Z, Li F, Zhao Y, Chen X. Glucagon-like peptide-1 receptor PET/CT with 68Ga-NOTA-Exendin-4 for detecting localized insulinoma: a prospective cohort study. J Nucl Med. 2016;57(5):715–20. doi:10.2967/jnumed.115.167445.
 7. Wild D, Wicki A, Mansi R, Behe M, Keil B, Bernhardt P, Christofori G, Ell PJ, Macke HR. Exendin-4-based radiopharmaceuticals for glucagonlike peptide-1 receptor PET/CT and SPECT/CT. J Nucl Med. 2010;51(7):1059–67. doi:10.2967/jnumed.110.074914.
 8. Binderup T, Knigge U, Loft A, Federspiel B, Kjaer A. 18F-fluorodeoxyglucose positron emission tomography predicts survival of patients with neuroendocrine tumors. Clin cancer Res Off J Am Ass Cancer Res. 2010;16(3):978–85. doi:10.1158/1078-0432.CCR-09-1759.
 9. Bahri H, Laurence L, Edeline J, Leghzali H, Devillers A, Raoul JL, Cuggia M, Mesbah H, Clement B, Boucher E, Garin E. High prognostic value of 18F-FDG PET for metastatic gastroenteropancreatic neuroendocrine tumors: a long-term evaluation. J Nucl Med Official Publ Soc Nucl Med. 2014;55(11):1786–90. doi:10.2967/jnumed.114.144386.
10. Garin E, Le Jeune F, Devillers A, Cuggia M, de Lajarte-Thirouard AS, Bouriel C, Boucher E, Raoul JL. Predictive value of 18F-FDG PET and somatostatin receptor scintigraphy in patients with metastatic endocrine tumors. J Nucl Med Off Publ Soc Nucl Med. 2009;50(6):858–64. doi:10.2967/jnumed.108.057505.
11. Ambrosini V, Campana D, Polverari G, Peterle C, Diodato S, Ricci C, Allegri V, Casadei R, Tomassetti P, Fanti S. Prognostic value of 68Ga-DOTANOC PET/CT SUVmax in patients with neuroendocrine tumors of the pancreas. J Nucl Med. 2015;56(12):1843–8. doi:10.2967/jnumed.115.162719.
12. Klimstra DS, Modlin IR, Coppola D, Lloyd RV, Suster S. The pathologic classification of neuroendocrine tumors: a review of nomenclature, grading, and staging systems. Pancreas. 2010;39(6):707–12. doi:10.1097/MPA.0b013e3181ec124e.

13. Hofman MS, Kong G, Neels OC, Eu P, Hong E, Hicks RJ. High management impact of Ga-68 DOTATATE (GaTate) PET/CT for imaging neuroendocrine and other somatostatin expressing tumours.JMedImagingRadiatOncol.2012;56(1):40–7.doi:10.1111/j.1754-9485.2011.02327.x.

14. Ambrosini V, Campana D, Bodei L, Nanni C, Castellucci P, Allegri V, Montini GC, Tomassetti P, Paganelli G, Fanti S. 68Ga-DOTANOC PET/CT clinical impact in patients with neuroendocrine tumors. J Nucl Med. 2010;51(5):669–73. doi:10.2967/jnumed.109.071712.

15. Srirajaskanthan R, Kayani I, Quigley AM, Soh J, Caplin ME, Bomanji J. The role of 68Ga-DOTATATE PET in patients with neuroendocrine tumors and negative or equivocal findings on 111In-DTPA-octreotide scintigraphy. J Nucl Med. 2010;51(6):875–82. doi:10.2967/jnumed.109.066134.

16. Frilling A, Sotiropoulos GC, Radtke A, Malago M, Bockisch A, Kuehl H, Li J, Broelsch CE. The impact of 68Ga-DOTATOC positron emission tomography/computed tomography on the multimodal management of patients with neuroendocrine tumors. Ann Surg. 2010;252(5): 850–6. doi:10.1097/SLA.0b013e3181fd37e8.

17. Kumar R, Sharma P, Garg P, Karunanithi S, Naswa N, Sharma R, Thulkar S, Lata S, Malhotra A. Role of (68)Ga-DOTATOC PET-CT in the diagnosis and staging of pancreatic neuroendocrine tumours. Eur Radiol. 2011;21(11):2408–16. doi:10.1007/s00330-011-2199-y.

18. Ruf J, Heuck F, Schiefer J, Denecke T, Elgeti F, Pascher A, Pavel M, Stelter L, Kropf S, Wiedenmann B, Amthauer H. Impact of Multiphase 68Ga-DOTATOC-PET/CT on therapy management in patients with neuroendocrine tumors. Neuroendocrinology. 2010;91(1):101–9. doi:10.1159/000265561.

19. Skoura E, Michopoulou S, Mohmaduvesh M, Panagiotidis E, Al Harbi M, Toumpanakis C, Almukhailed O, Kayani I, Syed R, Navalkissoor S, Ell PJ, Caplin ME, Bomanji J. The impact of 68Ga-DOTATATE PET/CT imaging on management of patients with neuroendocrine tumors: experience from a national referral center in the United Kingdom. J Nucl Med. 2016;57(1):34–40. doi:10.2967/jnumed.115.166017.

20. Deppen SA, Liu E, Blume JD, Clanton J, Shi C, Jones-Jackson LB, Lakhani V, Baum RP, Berlin J, Smith GT, Graham M, Sandler MP, Delbeke D, Walker RC. Safety and efficacy of 68Ga-DOTATATE PET/CT for diagnosis, staging, and treatment management of neuroendocrine tumors. J Nucl Med. 2016;57(5):708–14. doi:10.2967/jnumed.115.163865.

21. Gaujoux S, Partelli S, Maire F, D'Onofrio M, Larroque B, Tamburrino D, Sauvanet A, Falconi M, Ruszniewski P. Observational study of natural history of small sporadic nonfunctioning pancreatic neuroendocrine tumors. J Clin Endocrinol Metab. 2013;98(12):4784–9. doi:10.1210/jc.2013-2604.

22. Caplin ME, Pavel M, Cwikla JB, Phan AT, Raderer M, Sedlackova E, Cadiot G, Wolin EM, Capdevila J, Wall L, Rindi G, Langley A, Martinez S, Blumberg J, Ruszniewski P, Investigators C. Lanreotide in metastatic enteropancreatic neuroendocrine tumors. N Engl J Med. 2014;371(3):224–33. doi:10.1056/NEJMoa1316158.

23. Krenning EP, Valkema R, Kooij PP, Breeman WA, Bakker WH, deHerder WW, vanEijck CH, Kwekkeboom DJ, deJong M, Pauwels S. Scintigraphy and radionuclide therapy with [indium-111-labelled-diethyl triamine penta-acetic acid-D-Phe1]-octreotide. Ital J Gastroenterol Hepatol. 1999;31 Suppl 2:S219–23.

24. Kwekkeboom DJ, de Herder WW, Kam BL, van Eijck CH, van Essen M, Kooij PP, Feelders RA, van Aken MO, Krenning EP. Treatment with the radiolabeled somatostatin analog [177 Lu-DOTA 0, Tyr3]octreotate: toxicity, efficacy, and survival. J Clin Oncol Official J Am Soc Clin Oncol. 2008;26(13):2124–30. doi:10.1200/JCO.2007.15.2553.

25. Krenning EP, Kooij PP, Pauwels S, Breeman WA, Postema PT, De Herder WW, Valkema R, Kwekkeboom DJ. Somatostatin receptor: scintigraphy and radionuclide therapy. Digestion. 1996;57 Suppl 1:57–61.

26. Kong G, Johnston V, Ramdave S, Lau E, Rischin D, Hicks RJ. High-administered activity In-111 octreotide therapy with concomitant radiosensitizing 5FU chemotherapy for treatment of neuroendocrine tumors: preliminary experience. Cancer Biother Radiopharm. 2009;24(5): 527–33. doi:10.1089/cbr.2009.0644.

27. Claringbold PG, Brayshaw PA, Price RA, Turner JH. Phase II study of radiopeptide 177Lu-octreotate and capecitabine therapy of progressive disseminated neuroendocrine tumours. Eur J Nucl Med Mol Imaging. 2011;38(2):302–11. doi:10.1007/s00259-010-1631-x.

28. Claringbold PG, Price RA, Turner JH. Phase I-II study of radiopeptide 177Lu-octreotate in combination with capecitabine and temozolomide in advanced low-grade neuroendocrine tumors. Cancer Biother Radiopharm. 2012;27(9):561–9. doi:10.1089/cbr.2012.1276.

29. Cwikla JB, Sankowski A, Seklecka N, Buscombe JR, Nasierowska-Guttmejer A, Jeziorski KG, Mikolajczak R, Pawlak D, Stepien K, Walecki J. Efficacy of radionuclide treatment DOTATATE Y-90 in patients with progressive metastatic gastroenteropancreatic neuroendocrine carcinomas (GEP-NETs): a phase II study. Ann Oncol Off J Eur Soc Med Oncol. 2010;21(4):787–94. doi:10.1093/annonc/mdp372.

30. Horsch D, Ezziddin S, Haug A, Gratz KF, Dunkelmann S, Krause BJ, Schumichen C, Bengel FM, Knapp WH, Bartenstein P, Biersack HJ, Plockinger U, Schwartz-Fuchs S, Baum RP. Peptide receptor radionuclide therapy for neuroendocrine tumors in Germany: first results of a multi-institutional cancer registry. Recent Results Cancer Res Fortschritte der Krebsforschung Progres dans les recherches sur le cancer. 2013;194:457–65. doi:10.1007/978-3-642-27994-2_25.

31. Romer A, Seiler D, Marincek N, Brunner P, Koller MT, Ng QK, Maecke HR, Muller-Brand J, Rochlitz C, Briel M, Schindler C, Walter MA. Somatostatin-based radiopeptide therapy with [177Lu-DOTA]-TOC versus [90Y-DOTA]-TOC in neuroendocrine tumours. Eur J Nucl Med Mol Imaging. 2014;41(2):214–22. doi:10.1007/s00259-013-2559-8.

32. Villard L, Romer A, Marincek N, Brunner P, Koller MT, Schindler C, Ng QK, Macke HR, Muller-Brand J, Rochlitz C, Briel M, Walter MA. Cohort study of somatostatin-based radio-peptide therapy with [(90)Y-DOTA]-TOC versus [(90)Y-DOTA]-TOC plus [(177)Lu-DOTA]-TOC in neuroendocrine cancers. J Clin Oncol Off J Am Soc Clin Oncol. 2012;30(10):1100–6. doi:10.1200/JCO.2011.37.2151.

33. Imhof A, Brunner P, Marincek N, Briel M, Schindler C, Rasch H, Macke HR, Rochlitz C, Muller-Brand J, Walter MA. Response, survival, and long-term toxicity after therapy with the radiolabeled somatostatin analogue [90Y-DOTA]-TOC in metastasized neuroendocrine cancers. J Clin Oncol Off J Am Soc Clin Oncol. 2011;29(17):2416–23. doi:10.1200/JCO.2010.33.7873.

34. Kong G, Thompson M, Collins M, Herschtal A, Hofman MS, Johnston V, Eu P, Michael M, Hicks RJ. Assessment of predictors of response and long-term survival of patients with neuroendocrine tumour treated with peptide receptor chemoradionuclide therapy (PRCRT). Eur J Nucl Med Mol Imaging. 2014;41(10):1831–44. doi:10.1007/s00259-014-2788-5.

35. van Essen M, Krenning EP, Kam BL, de Herder WW, van Aken MO, Kwekkeboom DJ. Report on short-term side effects of treatments with 177Lu-octreotate in combination with capecitabine in seven patients with gastroenteropancreatic neuroendocrine tumours. Eur J Nucl Med Mol Imaging. 2008;35(4):743–8. doi:10.1007/s00259-007-0688-7.

36. Hubble D, Kong G, Michael M, Johnson V, Ramdave S, Hicks RJ. 177Lu-octreotate, alone or with radiosensitising chemotherapy, is safe in neuroendocrine tumour patients previously treated with high-activity 111In-octreotide. Eur J Nucl Med Mol Imaging. 2010;37(10):1869–75. doi:10.1007/s00259-010-1483-4.

37. Teng J, Abell S, Hicks RJ, Hofman MS, Sachithanandan N, McKelvie P, MacIsaac RJ. Protracted hypocalcaemia following a single dose of denosumab in humoral hypercalcaemia of malignancy due to PTHrP-secreting neuroendocrine tumour. Clin Endocrinol (Oxf). 2014;81(6):940–2. doi:10.1111/cen.12519.

38. Hofman MS, Hicks RJ. Peptide receptor radionuclide therapy for neuroendocrine tumours: standardized and randomized, or personalized? Eur J Nucl Med Mol Imaging. 2014;41(2):211–3. doi:10.1007/s00259-013-2621-6.

39. Hofman MS, Michael M, Kashyap R, Hicks RJ. Modifying the poor prognosis associated with 18F-FDG-Avid NET with Peptide Receptor Chemo-Radionuclide Therapy (PRCRT). J Nucl Med. 2015;56(6):968–9. doi:10.2967/jnumed.115.154500.

40. Kashyap R, Hofman MS, Michael M, Kong G, Akhurst T, Eu P, Zannino D, Hicks RJ. Favourable outcomes of (177)Lu-octreotate peptide receptor chemoradionuclide therapy in

patients with FDG-avid neuroendocrine tumours. Eur J Nucl Med Mol Imaging. 2015;42(2):176–85. doi:10.1007/s00259-014-2906-4.

41. Kashyap R, Hofman MS, Michael M, Kong G, Akhurst T, Eu P, Zannino D, Hicks RJ. Favourable outcomes of Lu-octreotate peptide receptor chemoradionuclide therapy in patients with FDG-avid neuroendocrine tumours. Eur J Nucl Med Mol Imaging. 2014. doi:10.1007/s00259-014-2906-4.

42. Beauregard JM, Hofman MS, Pereira JM, Eu P, Hicks RJ. Quantitative (177)Lu SPECT (QSPECT) imaging using a commercially available SPECT/CT system. Cancer Imaging. 2011;11:56–66. doi:10.1102/1470-7330.2011.0012.

43. Jackson PA, Beauregard JM, Hofman MS, Kron T, Hogg A, Hicks RJ. An automated voxelized dosimetry tool for radionuclide therapy based on serial quantitative SPECT/CT imaging. Med Phys. 2013;40(11):112503. doi:10.1118/1.4824318.

44. Rinke A, Muller HH, Schade-Brittinger C, Klose KJ, Barth P, Wied M, Mayer C, Aminossadati B, Pape UF, Blaker M, Harder J, Arnold C, Gress T, Arnold R, Group PS. Placebo-controlled, double-blind, prospective, randomized study on the effect of octreotide LAR in the control of tumor growth in patients with metastatic neuroendocrine midgut tumors: a report from the PROMID Study Group. J Clin Oncol Off J Am Soc Clin Oncol. 2009;27(28):4656–63.

45. Brizzi MP, Berruti A, Ferrero A, Milanesi E, Volante M, Castiglione F, Birocco N, Bombaci S, Perroni D, Ferretti B, Alabiso O, Ciuffreda L, Bertetto O, Papotti M, Dogliotti L. Continuous 5-fluorouracil infusion plus long acting octreotide in advanced well-differentiated neuroendocrine carcinomas. A phase II trial of the Piemonte oncology network. BMC Cancer. 2009;9:388. doi:10.1186/1471-2407-9-388.

46. Sun W, Lipsitz S, Catalano P, Mailliard JA, Haller DG, Eastern Cooperative Oncology G. Phase II/III study of doxorubicin with fluorouracil compared with streptozocin with fluorouracil or dacarbazine in the treatment of advanced carcinoid tumors: Eastern Cooperative Oncology Group Study E1281. J Clin Oncol Off J Am Soc Clin Oncol. 2005;23(22):4897–904. doi:10.1200/JCO.2005.03.616.

47. Strosberg JR, Fine RL, Choi J, Nasir A, Coppola D, Chen DT, Helm J, Kvols L. First-line chemotherapy with capecitabine and temozolomide in patients with metastatic pancreatic endocrine carcinomas. Cancer. 2011;117(2):268–75. doi:10.1002/cncr.25425.

48. Fine RL, Gulati AP, Krantz BA, Moss RA, Schreibman S, Tsushima DA, Mowatt KB, Dinnen RD, Mao Y, Stevens PD, Schrope B, Allendorf J, Lee JA, Sherman WH, Chabot JA. Capecitabine and temozolomide (CAPTEM) for metastatic, well-differentiated neuroendocrine cancers: the Pancreas Center at Columbia University experience. Cancer Chemother Pharmacol. 2013;71(3):663–70. doi:10.1007/s00280-012-2055-z.

49. Yao JC, Shah MH, Ito T, Bohas CL, Wolin EM, Van Cutsem E, Hobday TJ, Okusaka T, Capdevila J, de Vries EG, Tomassetti P, Pavel ME, Hoosen S, Haas T, Lincy J, Lebwohl D, Oberg K, Rad001 in Advanced Neuroendocrine Tumors TTSG . Everolimus for advanced pancreatic neuroendocrine tumors. N Engl J Med. 2011;364(6):514–23. doi:10.1056/NEJMoa1009290.

50. Yao JC, Phan AT, Chang DZ, Wolff RA, Hess K, Gupta S, Jacobs C, Mares JE, Landgraf AN, Rashid A, Meric-Bernstam F. Efficacy of RAD001 (everolimus) and octreotide LAR in advanced low- to intermediate-grade neuroendocrine tumors: results of a phase II study. J Clin Oncol Off J Am Soc Clin Oncol. 2008;26(26):4311–8. doi:10.1200/JCO.2008.16.7858.

51. Raymond E, Dahan L, Raoul JL, Bang YJ, Borbath I, Lombard-Bohas C, Valle J, Metrakos P, Smith D, Vinik A, Chen JS, Horsch D, Hammel P, Wiedenmann B, Van Cutsem E, Patyna S, Lu DR, Blanckmeister C, Chao R, Ruszniewski P. Sunitinib malate for the treatment of pancreatic neuroendocrine tumors. N Engl J Med. 2011;364(6):501–13. doi:10.1056/NEJMoa1003825.

52. Therasse P, Arbuck SG, Eisenhauer EA, Wanders J, Kaplan RS, Rubinstein L, Verweij J, Van Glabbeke M, van Oosterom AT, Christian MC, Gwyther SG. New guidelines to evaluate the response to treatment in solid tumors. European Organization for Research and Treatment of Cancer, National Cancer Institute of the United States National Cancer Institute of Canada. J Natl Cancer Inst. 2000;92(3):205–16.

53. Young H, Baum R, Cremerius U, Herholz K, Hoekstra O, Lammertsma AA, Pruim J, Price P. Measurement of clinical and subclinical tumour response using [18F]-fluorodeoxyglucose

and positron emission tomography: review and 1999 EORTC recommendations. European Organization for Research and Treatment of Cancer (EORTC) PET Study Group. Eur J Cancer. 1999;35(13):1773–82.

54. Wahl RL, Jacene H, Kasamon Y, Lodge MA. From RECIST to PERCIST: evolving considerations for PET response criteria in solid tumors. J Nucl Med. 2009;50 Suppl 1:122S–50. doi:10.2967/jnumed.108.057307.

55. Pattison DA, Hofman MS. Role of fluorodeoxyglucose PET/computed tomography in targeted radionuclide therapy for endocrine malignancies. PET Clin. 2015;10(4):461–76. doi:10.1016/j.cpet.2015.05.005.

Chapter 11
Tumor Metabolism and Metabolomics of Pheochromocytomas and Paragangliomas

Susan Richter and Graeme Eisenhofer

Abbreviations

ATP	Adenosine triphosphate
FH	Fumarate hydratase
HIF	Hypoxia-inducible factor
MAX	Myc-associated factor X
MDH2	Mitochondrial malate dehydrogenase
MYCV	Myc avian myelocytomatosis viral oncogene homolog
NF1	Neurofibromin 1
NMR	Nuclear magnetic resonance
PET	Positron emission tomography
PHDs	Prolyl hydroxylases
PPGL	Pheochromocytoma and paraganglioma
RCC	Renal cell carcinoma
RET proto-oncogene	Rearranged during transfection proto-oncogene
ROS	Reactive oxygen species
SDH	Succinate dehydrogenase
VHL	Von Hippel–Lindau

S. Richter, PhD (✉) • G. Eisenhofer, PhD
Institute of Clinical Chemistry and Laboratory Medicine, University Hospital Carl Gustav Carus, Medical Faculty Carl Gustav Carus, Technische Universität Dresden, Fetscherstrasse 74, 01307 Dresden, Germany
e-mail: susan.richter@uniklinikum-dresden.de; graeme.eisenhofer@uniklinikum-dresden.de

11.1 Introduction

The research field of tumor metabolism can be traced back to discoveries made in the 1920s by Otto Warburg, with recent renewed focus following discoveries of tumor susceptibility genes with key roles in mitochondrial energy metabolism. In 2011, Hanahan and Weinberg updated their hallmarks of cancer to include metabolic reprogramming of tumor cells, emphasizing the importance of considering metabolic changes in tumor development, progression, and therapeutic interventions [24]. To maintain high proliferative capacities, tumor cells must satisfy their energetic and anabolic requirements through changes in substrate utilization and pathway activities. This metabolic switch often results from mutations in genes involved in the regulation of metabolism.

With the discovery of *SDHB*, *SDHC*, and *SDHD* mutations as a cause of familial paraganglioma syndromes, the involvement of metabolism in the pathogenesis of chromaffin cell tumors became recognized [2, 4, 38]. More recently, mutations of other Krebs cycle-related genes, *SDHA*, *SDHAF2*, *FH*, and *MDH2*, have been identified as causes of hereditary PPGL [3, 6, 8, 34]. Together with recent advances in small molecule analysis by mass spectrometry, these findings have sparked interest in PPGL metabolomics.

This chapter reviews the current state of the field focusing on metabolic processes during PPGL tumorigenesis and developments in diagnostics and therapeutic approaches based on metabolic aberrations in tumor cells.

11.2 The Warburg Effect in Pheochromocytoma and Paraganglioma

In 1924 Warburg and coworkers published their landmark paper about the metabolism of cancer cells describing that thin tumor slices, in comparison to non-transformed tissue, produce an excess of lactate even in the presence of oxygen [55]. Warburg believed mitochondrial deficiency to be the reason for this phenotype. It has since been demonstrated that this is only the case for a small proportion of tumors; more often mechanisms dysregulating glycolysis are the cause, including p53 inactivation and activation of Akt/mTOR, hypoxia-inducible factor (HIF), and MYC signaling pathways.

Today the terms "Warburg effect" and aerobic glycolysis refer to tumor features of increased glucose uptake and subsequent pyruvate reduction to lactate [30]. This is suggested to provide a general growth advantage for proliferating cells via several mechanisms: (i) use of the most abundant extracellular nutrient, glucose, which has the potential to generate ATP faster than oxidative phosphorylation; (ii) provision of intermediate metabolites for biosynthesis; (iii) maximization of flux through pathways branching from glycolysis; and (iv) reduction in production of reactive oxygen species (ROS) by decreased respiratory demands [14, 53].

Warburg's hypothesis of mitochondrial defects causing increased glycolytic activity holds partly true for PPGLs. ¹⁸F-Fluorodeoxyglucose (¹⁸F-FDG)-PET allows for detection of tissues with increased glucose uptake. Consequently, PPGLs due to germline von Hippel–Lindau (*VHL*) or *SDHx* mutations show strong uptake of ¹⁸F-FDG, whereas PPGLs with germline Rearranged during transfection (*RET*) proto-oncogene or neurofibromin 1 (*NF1*) mutations show lower ¹⁸F-FDG uptake [50–52]. Sporadic PPGLs present as a heterogeneous group, where ¹⁸F-FDG uptake is likely dependent on underlying somatic mutations and the affected signaling pathways.

Expression profiling studies in PPGL tumors with four genetic backgrounds (*NF1*, *RET*, *VHL*, and *SDHx* mutation) showed mutation-dependent differences in Warburg gene signatures. *VHL*-mutated PPGLs showed elevated expression of glucose and lactate transporters and glycolytic genes compared to tumors due to *NF1* or *RET* mutations [18]. In contrast, *SDHx*-mutated PPGLs showed an intermediate expression profile with some elevation of glucose transporter 3 and hexokinase 2, but not of other glycolysis-related genes. In another study expression of lactate dehydrogenase A was increased in *SDHB*-mutated PPGLs compared to *VHL* tumors and normal medulla [19]. On the metabolite level, however, no differences in lactate or pyruvate were measured in PPGL tissue with different mutational backgrounds [42, 45]. Enzymatic activity of respiratory chain complexes was decreased not only in PPGLs with impairment of complex II (*SDHx* mutations) but also in *VHL* tumors, albeit to a lesser extent [18, 41].

In summary, PPGLs due to mutations impacting hypoxia-signaling pathways (*VHL* and *SDHx*) display a Warburg-like metabolic phenotype with increased glucose uptake, but appear to be distinct in their level of glycolytic activation and most likely also in their dependence on other metabolic pathways.

VHL tumors have been studied extensively in the context of renal cell carcinoma (RCC), where 70–90 % of clear cell RCC have a VHL deficiency caused by either a mutation or hypermethylation. The inactivation of the VHL protein has well-documented effects on hypoxia-signaling pathways leading to a HIF1-induced Warburg effect [47]. Introduction of *VHL* in *VHL*-mutated RCC cell lines reversed the Warburg phenotype by reducing glucose uptake and glycolytic flux to lactate [32]. VHL-deficient cancer cells are further known to heavily depend on glutamine as a carbon source [21]. In this case reductive carboxylation of α-ketoglutarate replenishes citrate for subsequent generation of lipids.

11.3 Pheochromocytoma and Paraganglioma due to Germline Mutations in Krebs Cycle Genes

PPGLs have a particularly rich hereditary background with every third patient testing positive for a germline mutation in one of the currently known susceptibility genes: *NF1*, *RET*, transmembrane protein 127, myc-associated factor X (*MAX*), *VHL*, *SDHA*, *SDHB*, *SDHC*, *SDHD*, *SDHAF2*, prolyl hydroxylases (*PHD1* and

PHD2), kinesin *KIF1β*, *FH* [13], and *MDH2* [8]. Somatic mutations in many of the above genes are also now established to contribute to sporadic PPGLs indicating involvement of these genes in 50 % or more of all PPGLs. Additionally somatic mutations of the Harvey rat sarcoma viral oncogene homolog (*HRAS*) play a role in a subset of patients [12]. Recently epigenetic aberrations in the *SDHC* promoter have also been shown to occur in PPGLs [23, 44]. Finally, findings of mosaic somatic mutations of *EPAS1* (also known as HIF2α) as a cause of PPGLs, polycythemia, and somatostatinomas support a central role of this hypoxia pathway driver in both tumorigenesis and as a determinant of phenotypic features of PPGLs [5, 11, 58, 59].

Generally PPGLs are benign tumors; however 10–15 % develops metastases to distant organs including the bone, liver, lungs, and lymph nodes. The highest risk for recurrence after surgery and/or metastasis lies with patients carrying *SDHB* mutations. Mutations in other Krebs cycle genes such as *FH* and *MDH2* also appear to predispose to malignancy [8, 9].

Disruption of SDH, FH, and MDH, which are involved in central carbon metabolism, causes accumulation of the Krebs cycle intermediates, succinate or fumarate [8, 33, 45]. Similar to the oncometabolite 2-hydroxyglutarate, succinate and fumarate are competitive inhibitors of α-ketoglutarate-dependent dioxygenases that impact two major signaling pathways [37] (Fig. 11.1). Through inhibition of PHDs, HIF transcription factors are stabilized under oxygenated conditions leading to activation of genes responsible for angiogenesis, growth, survival, energy metabolism, pH regulation, and invasion. Another group of α-ketoglutarate-dependent enzymes include DNA and histone demethylases of the TET (ten-eleven translocation) family of 5-methlycytosine hydroxylases and the Jumonji C-domain-containing protein family. Inhibition of these enzymes results in changes of DNA methylation, which in turn cause profound alterations in gene expression [10, 34, 57]. Activation of these pathways was shown to drive metastatic transformation of tumor cells by activation of epithelial-mesenchymal transition in different cell models, including chromaffin, ovarian, and lung cancer cells [1, 34, 35]. It has also been demonstrated that hypoxia acts synergistically with succinate accumulation to inhibit α-ketoglutarate-dependent dioxygenases, potentially leading to a more aggressive phenotype in hypoxic tumor areas [25].

Succinate dehydrogenase not only participates in the metabolism of carbon but is also a component of the electron transport chain located in the mitochondrial membrane (complex II) that is required for ATP generation through oxidative phosphorylation. Inhibition of complex II is known to induce oxidative stress in cell culture models [22, 28]. ROS, dependent on their equilibrium to antioxidants, can cause damage to intracellular molecules, including nucleic acids, proteins, and lipids [49]. DNA oxidation generates 8-hydroxy-2′-deoxyguanosine, a compound capable of inducing mutations and essentially leading to genomic instability. Oxidation of proteins may lead to functional impairment due to structural changes. ROS have been shown to promote different aspects of tumor development and progression, including proliferation, invasion and metastasis, and angiogenesis.
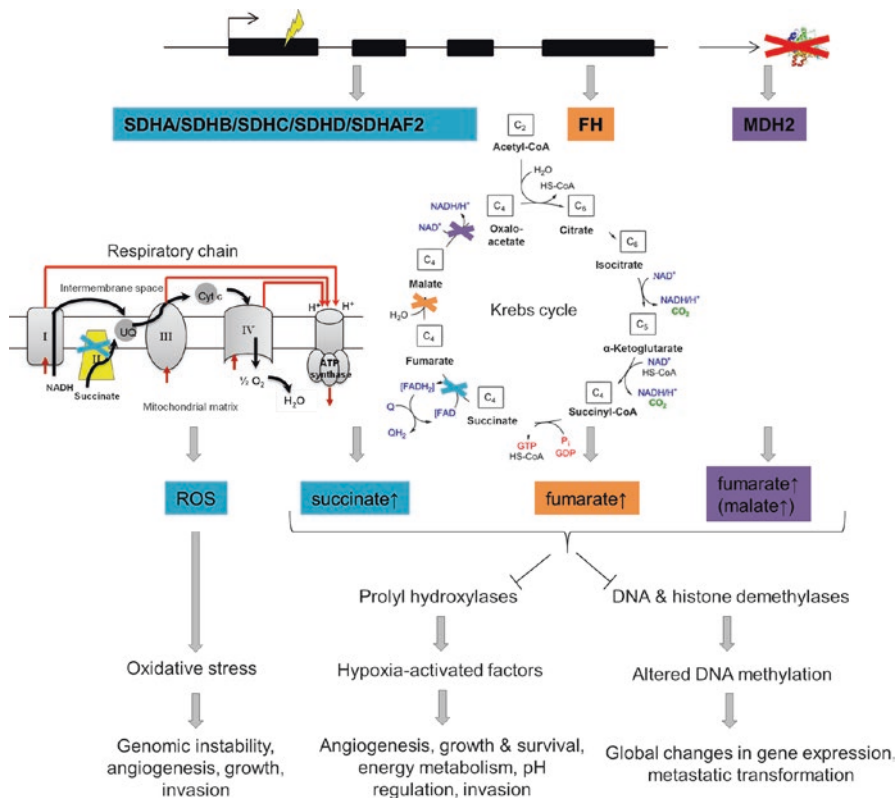
Fig. 11.1 Krebs cycle gene mutations in pheochromocytoma and paraganglioma and their downstream cellular effects. Mutations in succinate dehydrogenase (*SDH*) subunit and assembly factor genes, fumarate hydratase (*FH*), and mitochondrial malate dehydrogenase (*MDH2*) have been shown to predispose to chromaffin cell tumors. Due to their disruptive effect on central carbon metabolism, intracellular metabolites are altered leading to profound changes in downstream signaling pathways. Succinate and fumarate are known to inhibit α-ketoglutarate-dependent dioxygenases, including prolyl hydroxylases and histone and DNA demethylases. Succinate dehydrogenase also participates in the respiratory chain, where complex disruption can increase reactive oxygen species (*ROS*) production

11.4   Tumor Microenvironment and Metabolism

An important component of solid tumors is the stromal microenvironment consisting of several cell types, such as fibroblasts, endothelial cells, and immune cells. Immunological staining studies of colorectal tumor tissue section for different metabolic enzymes (lactate dehydrogenase, pyruvate dehydrogenase, pyruvate-dependent kinase) and lactate and glucose transporters have indicated that fibroblasts and untransformed colorectal cells favor aerobic metabolism of pyruvate, whereas tumor cells have a suppressed aerobic metabolism aiding in survival under low oxygen conditions [31]. Based on these findings, the authors proposed a model of

complementary metabolic pathways between highly glycolytic cancer cells, tumor-associated fibroblasts with strong lactate uptake and oxidation fueling aerobic metabolism, and tumor-associated endothelial cells with a high capacity for glucose uptake and aerobic pyruvate metabolism, but resistance to lactate intrusion. Other studies have demonstrated a metabolic symbiosis of tumor cells along oxygen and nutrient gradients with hypoxic cells being highly glycolytic and excreting lactate, which is then taken up as a carbon source by oxygenated cells [48]. Such cell-cell lactate shuttles have also been described in normal physiological tissues, including between neurons and astrocytes in the brain [15].

In further support of the aforementioned tumor microenvironment intercellular shuttling mechanisms, it has also been shown that *SDHB* silencing in a neuroblastoma model leads to increased proliferation, decreased glucose uptake, and increased lactate uptake compared to control [43]. Co-culturing these tumor cells with fibroblasts resulted in an additional increase in proliferation and lactate uptake, but also in a further decrease in glucose uptake.

11.5   Metabolic Biomarkers for Patient Stratification

Different underlying mutations in patients with PPGL result in tumors with distinct metabolic fingerprints. In PPGL, profiles of catecholamines and their metabolites, metanephrines, are characteristic for certain patient groups. Mutations affecting the Ras-Raf-MEK-ERK pathway, such as *RET* and *NF1*, lead to generally high tumor catecholamine contents and a relatively high proportion of epinephrine, whereas tumors due to *VHL* or *SDHx* aberrations predominantly produce norepinephrine with an additional high proportion of dopamine in those with *SDHx* mutations [16]. Patients with *MAX* mutations on the other hand present with an intermediate catecholamine phenotype [40]. *SDHx*-mutated tumors, which have a high risk of metastasis and recurrence, can be further distinguished by high levels of the dopamine metabolite 3-methoxytyramine [39]. Quantification of catecholamines and metanephrines by liquid chromatography tandem mass spectrometry (LC-MS/MS) therefore not only is crucial for the diagnosis of patients with PPGLs but also delivers information for stratification of patients [17].

Other biomarkers have been identified within the intermediates of the central carbon metabolism. Due to the blockade of the Krebs cycle at the site of SDH, PPGLs with disruptions in one of the SDH subunits have high levels of succinate and corresponding low levels of other Krebs cycle intermediates, including fumarate, citrate, isocitrate, and *cis*-aconitate [33, 45]. Measurements of the succinate-to-fumarate ratio by LC-MS/MS reliably identify tumors from patients with *SDHx* mutations making this a useful test for assessing the functional impact of mutational variants of unknown significance identified during genetic testing. In the same study, *VHL*-mutated tumors were also shown to have lower levels of fumarate, citrate, isocitrate, and *cis*-aconitate indicating increased requirements for

biosynthesis leading to depletion of Krebs cycle intermediates. Citrate, a precursor for lipids, is known to be especially depleted in VHL-deficient RCC [21].

NMR-based studies identified a reduction of adenine nucleotides, glutamate, and N-acetylaspartate in *SDHx*-mutated PPGLs, as well as increased levels of glutathione and decreased levels of creatine in *VHL*-mutated PPGLs [27, 42]. Other metabolites altered in *SDHx* versus non-*SDHx* tumors include elevated methionine, glutamine, and taurine [26]. Recently, proton magnetic resonance spectroscopy was successfully employed to identify high succinate levels in patients' tumors *in vivo* [54]. This technique can provide metabolic information in inoperable tumors, which could be used to predict tumor aggressiveness and guide therapeutic decision making and monitor therapeutic response.

11.6 Tumor Metabolism as a Therapeutic Target

Similar to cellular signaling cascades, the metabolism of tumor cells is distinct from that of healthy untransformed cells providing possibilities for targeted treatments. The Warburg phenotype of increased glucose uptake and utilization is one possible metabolic target. Gene silencing approaches and small molecule inhibitors were successfully used to inhibit different glycolytic steps in several cancer types leading to growth delay and apoptosis; however, due to lack of specificity, preclinical development of small molecule inhibitors is still ongoing [29]. Glutamine is another major carbon source used for oxidative phosphorylation and lipid biosynthesis or to replenish Krebs cycle intermediates. Glutamine dependence has been shown in different cancers, including *VHL*-mutated RCC and *MYC*-transformed tumors [21, 56]. Targeting glutamine uptake and metabolism through glutaminase is another proven concept for metabolic intervention.

A targeted treatment for *SDHx*-mutated tumor cells has been suggested by employing a genome-scale model of cancer metabolism [20]. This model predicted synthetic lethality for inhibition of pyruvate carboxylase (PC) in SDH- and FH-deficient cells. In the latter case, separate inhibition of nine other proteins was predicted to also selectively kill *FH*-mutated cells; these include seven enzymes involved in heme biosynthesis and two transporters. PC replenishes Krebs cycle intermediates by carboxylating pyruvate to oxaloacetate, which is essential for aspartate biosynthesis, a precursor for proteins, nucleotides, and other nonessential amino acids (Fig. 11.2). An alternative source of oxaloacetate is glutamine feeding into the Krebs cycle via α-ketoglutarate. The oxidative metabolic route is however blocked in *SDHx*-, *FH*-, and also *MDH2*-mutated tumor cells.

Cell culture models have since established that *SDHB* knockout cells are dependent on extracellular pyruvate to sustain maximal glycolytic flux. Pyruvate deprivation or PC knockdown results in a selective growth delay of *SDHB* knockout cells compared to wild type *in vitro* and as xenografts [7, 36]. PC protein levels were also found to be upregulated in *SDHB*-mutated compared to *SDHB* wild-type PPGLs. Experiments with 13C labels demonstrated that pyruvate carbons replenish
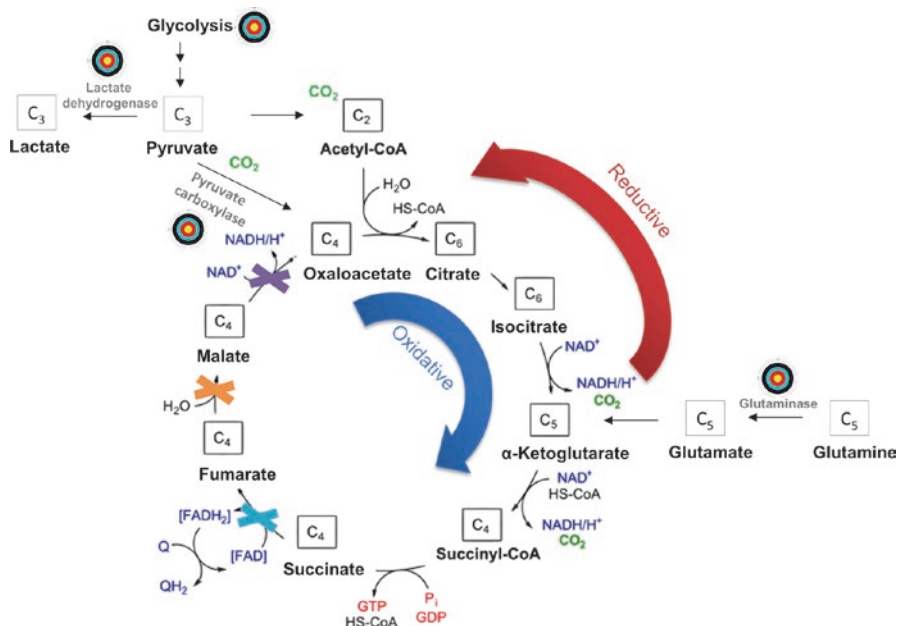
Fig. 11.2 Targeting tumor metabolism in pheochromocytoma and paraganglioma. There are several possible points of intervention in the central carbon metabolism (marked by bull's eye). Glycolysis can be inhibited by restriction of glucose import via glucose transporters or by inhibition of specific enzymes, including lactate dehydrogenase. Tumors with mutations in succinate dehydrogenase, fumarate hydratase, or mitochondrial malate dehydrogenase (*marked as crosses*) are dependent on additional carbon sources to replenish Krebs cycle intermediates. Those could be pyruvate metabolized by pyruvate carboxylase or glutamine metabolized by glutaminase. Due to the blockade of oxidative α-ketoglutarate metabolism, tumors with the abovementioned mutations use reductive metabolism to replenish citrate and oxaloacetate pools. Hence, pyruvate carboxylase and glutaminase may be suitable targets for small molecule inhibitors

oxaloacetate pools in *SDHB* knockout cells to maximize the glycolytic flux into the Krebs cycle via acetyl-CoA. This process supports the biosynthesis of aspartate from oxaloacetate. Glutamine is the major source of aspartate in *SDHB* wild-type cells, but only contributes to 20% in *SDHB*-mutated cells. Compared to wild-type chromaffin cells, which preferably utilize oxidative glutamine metabolism, reductive carboxylation of glutamine is increased in *SDHB* knockouts indicating another potential point of intervention for targeted therapy.

Cardaci *et al.* furthermore showed that the respiratory chain in SDH-deficient kidney cells operates close to the bioenergetic limit and that these cells have a reduced coupling efficiency resulting in ATP being predominantly produced by glycolysis rather than oxidative phosphorylation. Inhibition of lactate dehydrogenase, a key glycolytic player, with oxamate selectively inhibited proliferation in *SDHB*-mutated cells by 40%. By using 13C-labeled substrates, reduced entry of glucose carbons in the Krebs cycle was demonstrated leading to reduced citrate levels, which correlated with findings in PPGL tumor tissue.

Targeting the metabolism of tumors can be an effective way to selectively kill cancer cells by limiting their biosynthetic capacity. Clinical trials with metabolic inhibitors as single agents or in combination had varying successes, and many trials are still ongoing [46]. There is a strong need for the development of more specific agents targeting different metabolic pathways; a careful selection process to match certain drugs or drug combinations to specific patients will also be of importance to success of any therapies targeting tumor metabolism.

References

1. Aspuria PJ, Lunt SY, Varemo L, Vergnes L, Gozo M, Beach JA, et al. Succinate dehydrogenase inhibition leads to epithelial-mesenchymal transition and reprogrammed carbon metabolism. Cancer Metab. 2014;2:21.
2. Astuti D, Latif F, Dallol A, Dahia PL, Douglas F, George E, et al. Gene mutations in the succinate dehydrogenase subunit SDHB cause susceptibility to familial pheochromocytoma and to familial paraganglioma. Am J Hum Genet. 2001;69(1):49–54.
3. Bayley JP, Kunst HP, Cascon A, Sampietro ML, Gaal J, Korpershoek E, et al. SDHAF2 mutations in familial and sporadic paraganglioma and phaeochromocytoma. Lancet Oncol. 2010;11(4):366–72.
4. Baysal BE, Ferrell RE, Willett-Brozick JE, Lawrence EC, Myssiorek D, Bosch A, et al. Mutations in SDHD, a mitochondrial complex II gene, in hereditary paraganglioma. Science. 2000;287(5454):848–51.
5. Buffet A, Smati S, Mansuy L, Menara M, Lebras M, Heymann MF, et al. Mosaicism in HIF2A-related polycythemia-paraganglioma syndrome. J Clin Endocrinol Metab. 2014;99(2):E369–73.
6. Burnichon N, Briere JJ, Libe R, Vescovo L, Riviere J, Tissier F, et al. SDHA is a tumor suppressor gene causing paraganglioma. Hum Mol Genet. 2010;19(15):3011–20.
7. Cardaci S, Zheng L, MacKay G, van den Broek NJ, MacKenzie ED, Nixon C, et al. Pyruvate carboxylation enables growth of SDH-deficient cells by supporting aspartate biosynthesis. Nat Cell Biol. 2015;17(10):1317–26.
8. Cascon A, Comino-Mendez I, Curras-Freixes M, de Cubas AA, Contreras L, Richter S, et al. Whole-exome sequencing identifies MDH2 as a new familial paraganglioma gene. J Natl Cancer Inst. 2015;107(5).
9. Castro-Vega LJ, Buffet A, De Cubas AA, Cascon A, Menara M, Khalifa E, et al. Germline mutations in FH confer predisposition to malignant pheochromocytomas and paragangliomas. Hum Mol Genet. 2014;23(9):2440–6.
10. Cervera AM, Bayley JP, Devilee P, McCreath KJ. Inhibition of succinate dehydrogenase dysregulates histone modification in mammalian cells. Mol Cancer. 2009;8:89.
11. Comino-Mendez I, de Cubas AA, Bernal C, Alvarez-Escola C, Sanchez-Malo C, Ramirez-Tortosa CL, et al. Tumoral EPAS1 (HIF2A) mutations explain sporadic pheochromocytoma and paraganglioma in the absence of erythrocytosis. Hum Mol Genet. 2013;22:2169.
12. Crona J, Delgado Verdugo A, Maharjan R, Stalberg P, Granberg D, Hellman P, et al. Somatic mutations in H-RAS in sporadic pheochromocytoma and paraganglioma identified by exome sequencing. J Clin Endocrinol Metab. 2013;98(7):E1266–71.
13. Dahia PL. Pheochromocytoma and paraganglioma pathogenesis: learning from genetic heterogeneity. Nat Rev Cancer. 2014;14(2):108–19.
14. DeBerardinis RJ, Lum JJ, Hatzivassiliou G, Thompson CB. The biology of cancer: metabolic reprogramming fuels cell growth and proliferation. Cell Metab. 2008;7(1):11–20.
15. Draoui N, Feron O. Lactate shuttles at a glance: from physiological paradigms to anti-cancer treatments. Dis Model Mech. 2011;4(6):727–32.

16. Eisenhofer G, Pacak K, Huynh TT, Qin N, Bratslavsky G, Linehan WM, et al. Catecholamine metabolomic and secretory phenotypes in phaeochromocytoma. Endocr Relat Cancer. 2011;18(1):97–111.
17. Eisenhofer G, Peitzsch M. Laboratory evaluation of pheochromocytoma and paraganglioma. Clin Chem. 2014;60(12):1486–99.
18. Favier J, Briere JJ, Burnichon N, Riviere J, Vescovo L, Benit P, et al. The Warburg effect is genetically determined in inherited pheochromocytomas. PLoS One. 2009;4(9):e7094.
19. Fliedner SM, Kaludercic N, Jiang XS, Hansikova H, Hajkova Z, Sladkova J, et al. Warburg effect's manifestation in aggressive pheochromocytomas and paragangliomas: insights from a mouse cell model applied to human tumor tissue. PLoS One. 2012;7(7):e40949.
20. Folger O, Jerby L, Frezza C, Gottlieb E, Ruppin E, Shlomi T. Predicting selective drug targets in cancer through metabolic networks. Mol Syst Biol. 2011;7:501.
21. Gameiro PA, Yang J, Metelo AM, Perez-Carro R, Baker R, Wang Z, et al. In vivo HIF-mediated reductive carboxylation is regulated by citrate levels and sensitizes VHL-deficient cells to glutamine deprivation. Cell Metab. 2013;17(3):372–85.
22. Guzy RD, Sharma B, Bell E, Chandel NS, Schumacker PT. Loss of the SdhB, but Not the SdhA, subunit of complex II triggers reactive oxygen species-dependent hypoxia-inducible factor activation and tumorigenesis. Mol Cell Biol. 2008;28(2):718–31.
23. Haller F, Moskalev EA, Faucz FR, Barthelmess S, Wiemann S, Bieg M, et al. Aberrant DNA hypermethylation of SDHC: a novel mechanism of tumor development in Carney triad. Endocr Relat Cancer. 2014;21(4):567–77.
24. Hanahan D, Weinberg RA. Hallmarks of cancer: the next generation. Cell. 2011;144(5):646–74.
25. Her YF, Nelson-Holte M, Maher 3rd LJ. Oxygen concentration controls epigenetic effects in models of familial paraganglioma. PLoS One. 2015;10(5):e0127471.
26. Imperiale A, Moussallieh FM, Roche P, Battini S, Cicek AE, Sebag F, et al. Metabolome profiling by HRMAS NMR spectroscopy of pheochromocytomas and paragangliomas detects SDH deficiency: clinical and pathophysiological implications. Neoplasia. 2015;17(1):55–65.
27. Imperiale A, Moussallieh FM, Sebag F, Brunaud L, Barlier A, Elbayed K, et al. A new specific succinate-glutamate metabolomic hallmark in sdhx-related paragangliomas. PLoS One. 2013;8(11):e80539.
28. Ishii T, Yasuda K, Akatsuka A, Hino O, Hartman PS, Ishii N. A mutation in the SDHC gene of complex II increases oxidative stress, resulting in apoptosis and tumorigenesis. Cancer Res. 2005;65(1):203–9.
29. Kishton RJ, Rathmell JC. Novel therapeutic targets of tumor metabolism. Cancer J. 2015;21(2):62–9.
30. Koppenol WH, Bounds PL, Dang CV. Otto Warburg's contributions to current concepts of cancer metabolism. Nat Rev Cancer. 2011;11(5):325–37.
31. Koukourakis MI, Giatromanolaki A, Harris AL, Sivridis E. Comparison of metabolic pathways between cancer cells and stromal cells in colorectal carcinomas: a metabolic survival role for tumor-associated stroma. Cancer Res. 2006;66(2):632–7.
32. Leisz S, Schulz K, Erb S, Oefner P, Dettmer K, Mougiakakos D, et al. Distinct von Hippel-Lindau gene and hypoxia-regulated alterations in gene and protein expression patterns of renal cell carcinoma and their effects on metabolism. Onc Otarget. 2015;6(13):11395–406.
33. Lendvai N, Pawlosky R, Bullova P, Eisenhofer G, Patocs A, Veech RL, et al. Succinate-to-fumarate ratio as a new metabolic marker to detect the presence of SDHB/D-related paraganglioma: initial experimental and ex vivo findings. Endocrinology. 2014;155(1):27–32.
34. Letouze E, Martinelli C, Loriot C, Burnichon N, Abermil N, Ottolenghi C, et al. SDH mutations establish a hypermethylator phenotype in paraganglioma. Cancer Cell. 2013;23(6):739–52.
35. Liu J, Gao L, Zhang H, Wang D, Wang M, Zhu J, et al. Succinate dehydrogenase 5 (SDH5) regulates glycogen synthase kinase 3beta-beta-catenin-mediated lung cancer metastasis. J Biol Chem. 2013;288(41):29965–73.

36. Lussey-Lepoutre C, Hollinshead KE, Ludwig C, Menara M, Morin A, Castro-Vega LJ, et al. Loss of succinate dehydrogenase activity results in dependency on pyruvate carboxylation for cellular anabolism. Nat Commun. 2015;6:8784.

37. Morin A, Letouze E, Gimenez-Roqueplo AP, Favier J. Oncometabolites-driven tumorigenesis: from genetics to targeted therapy. Int J Cancer. 2014;135(10):2237–48.

38. Niemann S, Muller U. Mutations in SDHC cause autosomal dominant paraganglioma, type 3. Nat Genet. 2000;26(3):268–70.

39. Peitzsch M, Prejbisz A, Kroiss M, Beuschlein F, Arlt W, Januszewicz A, et al. Analysis of plasma 3-methoxytyramine, normetanephrine and metanephrine by ultraperformance liquid chromatography-tandem mass spectrometry: utility for diagnosis of dopamine-producing metastatic phaeochromocytoma. Ann Clin Biochem. 2013;50(Pt 2):147–55.

40. Qin N, de Cubas AA, Garcia-Martin R, Richter S, Peitzsch M, Menschikowski M, et al. Opposing effects of HIF1alpha and HIF2alpha on chromaffin cell phenotypic features and tumor cell proliferation: Insights from MYC-associated factor X. Int J Cancer. 2014;135(9):2054–64.

41. Rao JU, Engelke UF, Rodenburg RJ, Wevers RA, Pacak K, Eisenhofer G, et al. Genotype-specific abnormalities in mitochondrial function associate with distinct profiles of energy metabolism and catecholamine content in pheochromocytoma and paraganglioma. Clin Cancer Res. 2013;19(14):3787–95.

42. Rao JU, Engelke UF, Sweep FC, Pacak K, Kusters B, Goudswaard AG, et al. Genotype-specific differences in the tumor metabolite profile of pheochromocytoma and paraganglioma using untargeted and targeted metabolomics. J Clin Endocrinol Metab. 2015;100(2):E214–22.

43. Rapizzi E, Fucci R, Giannoni E, Canu L, Richter S, Cirri P, et al. Role of microenvironment on neuroblastoma SK-N-AS SDHB silenced cell metabolism and function. Endocr Relat Cancer. 2015;22:409.

44. Richter S, Klink B, Nacke B, de Cubas AA, Mangelis A, Rapizzi E, et al. Epigenetic mutation of the succinate dehydrogenase C promoter in a patient with two paragangliomas. J Clin Endocrinol Metab. 2016;101(2):359–63.

45. Richter S, Peitzsch M, Rapizzi E, Lenders JW, Qin N, de Cubas AA, et al. Krebs cycle metabolite profiling for identification and stratification of pheochromocytomas/paragangliomas due to succinate dehydrogenase deficiency. J Clin Endocrinol Metab. 2014;99(10):3903–11.

46. Sborov DW, Haverkos BM, Harris PJ. Investigational cancer drugs targeting cell metabolism in clinical development. Expert Opin Investig Drugs. 2015;24(1):79–94.

47. Semenza GL. HIF-1 mediates the Warburg effect in clear cell renal carcinoma. J Bioenerg Biomembr. 2007;39(3):231–4.

48. Sonveaux P, Vegran F, Schroeder T, Wergin MC, Verrax J, Rabbani ZN, et al. Targeting lactate-fueled respiration selectively kills hypoxic tumor cells in mice. J Clin Invest. 2008;118(12):3930–42.

49. Sosa V, Moline T, Somoza R, Paciucci R, Kondoh H, ME LL. Oxidative stress and cancer: an overview. Ageing Res Rev. 2013;12(1):376–90.

50. Taïeb D, Sebag F, Barlier A, Tessonnier L, Palazzo FF, Morange I, et al. 18F-FDG avidity of pheochromocytomas and paragangliomas: a new molecular imaging signature? J Nucl Med. 2009;50(5):711–7.

51. Timmers HJ, Chen CC, Carrasquillo JA, Whatley M, Ling A, Eisenhofer G, et al. Staging and functional characterization of pheochromocytoma and paraganglioma by 18F-fluorodeoxyglucose (18F-FDG) positron emission tomography. J Natl Cancer Inst. 2012;104(9):700–8.

52. van Berkel A, Rao JU, Kusters B, Demir T, Visser E, Mensenkamp AR, et al. Correlation between in vivo 18F-FDG PET and immunohistochemical markers of glucose uptake and metabolism in pheochromocytoma and paraganglioma. J Nucl Med. 2014;55(8):1253–9.

53. Vander Heiden MG, Cantley LC, Thompson CB. Understanding the Warburg effect: the metabolic requirements of cell proliferation. Science. 2009;324(5930):1029–33.

54. Varoquaux A, le Fur Y, Imperiale A, Reyre A, Montava M, Fakhry N, et al. Magnetic resonance spectroscopy of paragangliomas: new insights into in vivo metabolomics. Endocr Relat Cancer. 2015;22(4):M1–8.
55. Warburg O, Posener K, Negelein E. Über den Stoffwechsel der Carcinomzelle. Biochem Zeitschr. 1924;152:309–44.
56. Wise DR, DeBerardinis RJ, Mancuso A, Sayed N, Zhang XY, Pfeiffer HK, et al. Myc regulates a transcriptional program that stimulates mitochondrial glutaminolysis and leads to glutamine addiction. Proc Natl Acad Sci U S A. 2008;105(48):18782–7.
57. Xiao M, Yang H, Xu W, Ma S, Lin H, Zhu H, et al. Inhibition of alpha-KG-dependent histone and DNA demethylases by fumarate and succinate that are accumulated in mutations of FH and SDH tumor suppressors. Genes Dev. 2012;26(12):1326–38.
58. Yang C, Sun MG, Matro J, Huynh TT, Rahimpour S, Prchal JT, et al. Novel HIF2A mutations disrupt oxygen sensing leading to polycythemia, paragangliomas and somatostatinomas. Blood. 2013;121:2563.
59. Zhuang Z, Yang C, Lorenzo F, Merino M, Fojo T, Kebebew E, et al. Somatic HIF2A gain-of-function mutations in paraganglioma with polycythemia. N Engl J Med. 2012;367(10):922–30.

Chapter 12
Radionuclide Imaging of Pheochromocytoma and Paraganglioma in the Era of Multi-omics

Henri J.L.M. Timmers

Abbreviations

[123/131]I-MIBG	[[123/131]I]-metaiodobenzylguanidine
^{18}F-DOPA	6-[^{18}F]-fluoro-L-3,4-dihydroxyphenylalanine
^{18}F-FDA	6-[^{18}F]-fluorodopamine
^{18}F-FDG	2-[^{18}F]-Fluoro-2-deoxy-D-glucose
^{1}H-NMR	Proton nuclear magnetic resonance
FH	*fumarate hydratase*
GLUT	Glucose transporter
HIF	hypoxia-inducible factor
HK	Hexokinase
HNPGL	Head and neck paraganglioma
LC-MS	Liquid chromatography-mass spectrometry
MAX	*myc-associated factor X*
MCT-4	monocarboxylate transporter type 4
MDH2	*malate dehydrogenase 2*
NF-1	*neurofibromatosis type 1*
PET	Positron emission tomography
PPGL	Pheochromocytoma and paraganglioma
RET	Rearranged during transfection
SDHA/B/C/D/AF2	Succinate dehydrogenase subunits A/B/C/D/assembly factor 2
SPECT	Single-photon emission computed tomography
SUV	Standard uptake values

H.J.L.M. Timmers, MD, PhD
Department of Internal Medicine, section of Endocrinology (471), Radboud University Medical Centre, PO Box 9101 6500 HB, Nijmegen, The Netherlands
e-mail: henri.timmers@radboudumc.nl

TMEM127	*transmembrane protein 127*
VEGF	Vascular endothelial growth factor
VHL	von Hippel-Lindau

12.1 Pheochromocytoma and Paraganglioma

Pheochromocytomas and paragangliomas (PPGLs) are rare catecholamine-producing neuroendocrine tumors that derive from sympathetic chromaffin tissue in adrenal and extra-adrenal abdominal or thoracic locations [1]. PPGLs arising from the adrenal medulla are commonly referred to as pheochromocytomas. Typical locations for extra-adrenal PPGLs are (1) the Zuckerkandl body, a sympathetic ganglion located at the root of the inferior mesenteric artery, (2) the sympathetic plexus of the urinary bladder, the kidneys, and the heart, and (3) the sympathetic ganglia in the mediastinum. Head and neck paragangliomas (HNPGLs), also called glomus tumors, arise from parasympathetic paraganglia, mainly from the glomus caroticum, glomus (jugulo-)tympanicum, and glomus vagale.

Most PPGLs are benign, but 10–15 % are defined as malignant based on the development of metastases in nonchromaffin tissues such as the lymph nodes, lung, liver, and bone. For pediatric PPGL, malignancy rates between 2 and 47 % have been described. Currently there are no reliable pathological or molecular markers for malignancy. The strongest predictors for the developments of metastases are *succinate dehydrogenase subunits B* (*SDHB*) mutations (see below), young age, large tumors (>5 cm), extra-adrenal tumor location, and elevated plasma 3-methoxytyramine [2]. The prevalence of an underlying *SDHB* mutation among patients with metastatic PPGL is 30 % and up to 90 % if the tumor originates from an extra-adrenal location. Survival is highly variable. The overall 5-year survival rate varies between 34 and 60 % [3]. The survival of patients with metastatic disease due to an underlying *SDHB* mutation is lower than in non-*SDHB* patients [4].

In the context of a tumor that is highly variable in its genotype, biochemical phenotype, tumor location, growth and malignancy rate, and prognosis, a multi-omics approach is being applied to better stratify PPGLs and guide tailor-made diagnostic and therapeutic strategies. As will be reviewed in this chapter, radionuclide imaging is a very valuable tool to recognize the different molecular signatures of these tumors and can be regarded as a method for *in vivo* omics.

12.2 The PPGL Genome, Transcriptome, and Methylome

Nearly 40 % of the PPGLs are caused by germline mutations in tumor susceptibility genes which include *VHL* (*von Hippel-Lindau*), *RET* (*rearranged during transfection*), *NF-1* (*neurofibromatosis type 1*), *SDHA/B/C/D/AF2* (*succinate dehydrogenase subunits A, B, C, and D and assembly factor 2*), *TMEM127* (*transmembrane*

protein 127), *MAX* (*myc-associated factor X*) [5], and more recently discovered *HIF2α* (*hypoxia-inducible factor 2 α*) [6], *FH* (*fumarate hydratase*) [7], and *MDH2* (*malate dehydrogenase 2*) [8]. In addition to hereditary cases, in at least 17 % of sporadic tumors, somatic mutations in especially *NF1*, but also *RET*, *VHL*, *MAX*, and in rare cases *SDHx* and *HIF2α*, have been reported [9–14].

Based on transcriptional profiling studies, PGLs can be classified into two clusters [15, 16]. Cluster 1 tumors (1a, *SDH* and *FH*; 1b, *VHL* and *HIF2α)* are characterized by increased expression of genes involved in (pseudo)hypoxia, cell proliferation, angiogenesis, electron transport chain and the Krebs cycle, and abnormal function of oxidoreductases. Cluster 2 tumors (*RET*, *NF1*, *TMEM127*, *MAX*) show an increased expression of genes involved in protein synthesis, kinase signaling, endocytosis, and maintenance of a differentiated chromaffin cell catecholamine biosynthetic and secretory phenotype. Sporadic PGLs are distributed between the two major clusters based on their gene expression pattern and catecholamine phenotype [15].

SDHB mutations are of particular interest, because they have been associated with large-sized aggressive tumors and increased risk of malignancy. SDH is an important component of the mitochondrial electron transport chain. In tumors with *SDHx* mutations, the ability of cells for oxidative phosphorylation is compromised [16–19]. Also, it has been demonstrated *in vitro* that accumulation of succinate in cells silenced for SDH causes inhibition of prolyl hydroxylase activity resulting in stabilization of hypoxia-inducible factors (HIF)-1α and -2α [20, 21]. HIF-1α and -2α then translocate to the nucleus where, together with aryl hydrocarbon receptor nuclear translocator, they form an active HIF complex that induces the expression of genes with hypoxia response elements that support tumor progression via different signaling pathways. Thus, in cluster 1 tumors, the pseudo-hypoxic drive is hypothesized to mediate an increase in aerobic glycolysis, also known as the Warburg effect. This is supported by increased HIF-α protein level combined with lower SDH activity and increased glycolysis as indicated by lactate dehydrogenase activity [16].

DNA methylation profiling revealed that SDH-deficient PPGLs are characterized by a pattern of global histone and DNA hypermethylation that results in a decrease in gene expression [22, 23]. These epigenetic changes are induced by succinate through inactivation of histone demethylases and account for several of the characteristics of this subset of tumors, including catecholamine secretory profile and cell migration/metastatic capacity. A pattern of global histone and DNA hypermethylation was also found in FH-related paraganglioma. In this case, fumarate rather than succinate acts as an oncometabolite.

12.3 The PPGL Metabolome

Mitochondria are the metabolic hubs of the tumor which, in addition to providing energy, generate reducing equivalents (NADH and NADPH) and intermediates for anabolic reactions. Thus, genotype-specific differences in the mitochondrial function have a strong impact on intermediary metabolism of PPGLs [16, 24, 25].

In comparison with other genotypes, *VHL* tumors show an overall decrease in respiratory chain enzyme function, while *SDHx* tumors demonstrate a decreased complex II and an attempted compensatory increase in the complex I, III, and IV activities, indicative of impaired mitochondrial function [24].

Simultaneous detection of several metabolites is called metabolomics and can improve our understanding of the pathophysiology of PPGL. Targeted and untargeted metabolomic analyses in PPGL tumor tissues have clearly indicated profound genotype-specific differences in the tumor metabolite profile related to differences in mitochondrial function [24, 26, 27]. This was achieved by proton nuclear magnetic resonance (^{1}H-NMR) spectroscopy, a leading technology for untargeted metabolomics [24] and liquid chromatography-mass spectrometry (LC-MS). With ^{1}H-NMR on homogenized tumor tissue, vast accumulation of succinate was found in SDH-deficient tumors, together with a decrease in energy-rich phosphates ATP/ADP/AMP when compared to cluster 2 and sporadic PGLs [24]. Positive correlations were observed between respiratory chain complex II activity, catecholamine content, and ATP/ADP/AMP suggesting that genotype-specific differences in the energy metabolism contribute to genotype-specific differences in tumor catecholamine phenotypic features. Furthermore, ^{1}H-NMR studies exhibited reduced levels of *N*-acetylaspartic acid in *SDHx* tumors and reduced total creatine in *VHL* tumors, as well as increased lactate in a subset of cluster 1 tumors, all of which are probably related to altered energy metabolism. These findings were confirmed by ^{1}H high-resolution magnetic-angle spinning (HRAS) on small intact tissue samples (solid-state NMR). In addition, *SDHx* tumors exhibited a specific metabolic signature characterized by low glutamate and high glutamine, myoinositol, glutathione, and methionine levels [28, 29], the latter being consistent with the hypermethylation pattern of these tumors. Apparently, cell metabolism is affected beyond the Krebs cycle, involving purine and amino acid metabolism, energy storage, and oxidative stress response. The full significance of these metabolomic findings requires further exploration.

By applying principal component analysis and other unsupervised statistical methods for interpretation of magnetic resonance spectra, PPGL tissues could be classified in genotype-specific groups on the basis of their metabolite profile [27, 29]. ^{1}H-NMR can therefore also serve to assess the relevance of *SDHx* variants of unknown significance. This is certainly also true for targeted metabolomics using mass spectrometric analysis, which allows identification of metabolites at much lower concentrations than ^{1}H-NMR [27]. Measurement of Krebs cycle intermediates by LC-MS identified 25-fold higher succinate and 80 % lower fumarate, cis-aconitate and isocitrate levels in *SDHx* PPGLs. Succinate:fumarate ratios were shown to be highly discriminative for SDH deficiency, providing a sensitivity of 100 % in PPGL. Succinate:fumarate ratios were higher in *SDHB* than *SDHC/D* tumors, linking specific *SDH* mutations to tumor aggressiveness through different

extents of succinate-induced hypermethylation and related tumorigenesis. Metabolomic profiling is thereby suggested to have prognostic value for assessing the likelihood of malignancy.

12.4 Localization of PPGL by Radionuclide Imaging

In patients with a biochemically established diagnosis of PPGL, anatomical and functional imaging are critical for primary tumor localization and detection of multiple primary tumors and metastases, guiding the optimal choice between curative surgery and palliative treatment options. CT and MRI provide a high sensitivity and allow precise tumor delineation. Lesions detected by anatomical imaging can be specifically identified as PPGL by functional imaging agents that target the catecholamine synthesis, storage, and secretion pathways of chromaffin tumor cells [30]. These techniques include [123/131I]-metaiodobenzylguanidine (123/131I-MIBG) single-photon emission computed tomography (SPECT) and 6-[18F]-fluorodopamine (18F-FDA) positron emission tomography (PET). 123/131I-MIBG and 18F-FDA target the norepinephrine transporter of the PPGL cell membrane and the vesicular monoamine transporters in the membrane of intracellular vesicles. These transporters facilitate the reuptake and storage of catecholamines, respectively. The PET tracers 11C-epinephrine and 11C-hydroxyephedrine are alternatives that accumulate in tumor cells through the same mechanisms but are of limited use for clinical imaging because of their (very) short half-life. 6-[18F]-fluoro-L-3,4-dihydroxyphenylalanine (18F-DOPA) PET can be used for the imaging of the striatal system and neuroendocrine tumors such as carcinoids but also for PPGL and HNPGL. The target of 18F-DOPA is the large amino acid transporter involved in the uptake of amine precursors.

Other targets for PPGL imaging are the somatostatin receptors and glucose transporters (GLUTs). For somatostatin receptor-based imaging, 11In-Pentetreotide is available for SPECT and 68Ga-/111In-DOTATATE/DOTANOC/DOTATOC for PET. 2-[18F]-fluoro-2-deoxy-D-glucose (18F-FDG) PET provides an index of intracellular glucose metabolism and is taken up by the tumor cell through the GLUTs [6–8]. 18F-FDG PET has been successfully applied in the localization of primary non-metastatic PPGL, yielding a high sensitivity similar to 123I-MIBG [31]. In malignant PPGL and especially in *SDHB*-related PPGL, metastases are more accurately detected by 18F-FDG PET than by 123I-MIBG SPECT [31–34]. A large NIH study indicated sensitivities of 80% versus 49% with 18F-FDG PET and 123I-MIBG SPECT, respectively [34]. One third of patients with metastatic PPGL even had completely false-negative 123I-MIBG scans. Moreover, for the localization of metastases of the bone, a frequent site of involvement in malignant PPGL, 18F-FDG PET was superior to whole-body CT and/or MRI (sensitivity 94% vs. 79%), whereas for soft tissue metastases, the performance was similar.

12.5   Characterization of PPGL by Radionuclide Imaging

Different genotypes are associated with differences in PPGL features such as catecholamine profile, tumor location, and malignant potential [35]. Similarly, the results of radionuclide imaging appear to be largely determined by the underlying mutations and related tumor cell characteristics. For example, there is evidence of differential expression of cellular targets for radiopharmaceuticals across genotypes. There is lower expression of the cell membrane norepinephrine transporter system in *VHL*-related PPGL cells than in *RET*-related tumor cells [36]. Considering a higher affinity of ^{18}F-FDA than ^{123}I-MIBG for these transporters, it is no surprise that ^{18}F-FDA PET is superior to ^{123}I-MIBG SPECT in the specific context of the VHL syndrome [37].

Profound effects among PPGLs with different molecular signatures have also been observed with ^{18}F-FDG PET. It has been well established that ^{18}F-FDG PET is superior to ^{123}I-MIBG SPECT, ^{18}F-FDA PET, and ^{18}F-FDOPA PET for localizing metastatic PPGL, particularly with an underlying *SDHB* mutation [31, 32, 34]. The detection rate for metastases was 92.0 % in *SDHB* versus 67.3 % in non-*SDHB* [34]. Regarding non-metastatic PPGLs, ^{18}F-FDG uptake varies considerably among PPGLs of different genotypes, with the highest standard uptake values (SUVs) being observed in *SDHx*- and *VHL*-related tumors [34]. In the same study, *SDHx*- and *VHL*-related tumors were without exception detected by ^{18}F-FDG PET, whereas the majority of *RET*-related PPGLs were ^{18}F-FDG PET negative. Similarly, in HNPGLs ^{18}F-FDG PET can help to distinguish between SDHx and non-SDHx tumors [38]. Apparently, genotype-specific tumor cell biology translates into distinct patterns of radiotracer uptake and accumulation. These observations suggest that ^{18}F-FDG PET can be used along with syndromal features, family history, age, tumor location, and catecholamine phenotype [39] to guide the genetic testing strategy in individual patients, prioritizing *SDH* and *VHL* testing in those with prominent ^{18}F-FDG uptake (SUV > 5).

Besides ^{18}F-FDG, other PET radiotracers have been shown to exhibit differential uptake among genotypes. For unknown reasons, the sensitivity of ^{18}F-FDOPA PET for the detection of *SDHB*-related metastases appears to be lower than in non-*SDHB* metastases (20 vs 93 %) [31], although this awaits confirmation in a larger study. In another study in non-metastatic PPGLs and HNPGLs, false-negative ^{18}F-FDOPA PET scans were predominantly encountered in *SDHx* PPGLs [40]. On the other hand, no difference in quantitative uptake was found by others [41], excluding the possibility to reliably identify genotypes by ^{18}F-FDOPA SUVs. Very recently, the superiority of ^{68}Ga-DOTATATE PET/CT to other functional imaging modalities in the localization of *SDHB*-associated metastatic PPGL has been reported [42]. Its lesion-based detection rate was 98.6 %, which was higher than that of ^{18}F-FDG PET (85.8 %), ^{18}F-FDOPA PET (61.4 %), and ^{18}F-FDA PET (51.9 %). Whether

^{68}Ga-DOTATATE PET/CT can facilitate the identification of *SDHx* versus non-*SDHx* PPGLs remains to be established. Although ^{123}I-MIBG is still considered the gold standard for PPGL functional imaging, there seems to be no role for genetically characterizing PPGLs by semiquantitative ^{123}I-MIBG uptake measurements [43]. Taking into account the fact that the diagnostic accuracy of different functional imaging modalities for PPGL is largely determined by the underlying genotypes, a tailored approach regarding the choice of the most appropriate tracer is advocated in recent guidelines [44, 45].

12.6   Determinants of ^{18}F-FDG Avidity in PPGL

Enhanced uptake of glucose by tumor cells compared to normal cells is the hallmark of *in vivo* cancer imaging with ^{18}F-FDG PET. However, prominent ^{18}F-FDG uptake by subsets of PPGLs has been suggested to be a specific hallmark of altered glucose metabolism related to genotype-specific tumor cell metabolism. Similar to glucose, ^{18}F-FDG is taken up by tumor cells mostly via facilitative transport by GLUTs. After cell entry, ^{18}F-FDG is phosphorylated by cytosolic hexokinase (HK) enzymes into ^{18}F-FDG-6-P which, in contrast to glucose-6-P, cannot be further metabolized along the glycolytic pathway. The cell membrane is impermeable to ^{18}F-FDG-6P so it accumulates within cells directly proportionate to their metabolic activity. ^{18}F-FDG-6P can theoretically escape from the cell by dephosphorylation back to ^{18}F-FDG by glucose-6-phosphatase. In general, this process is negligible because of the low intracellular levels of the dephosphorylating enzyme. Therefore, ^{18}F-FDG uptake and accumulation of any cell is determined by expression of GLUTs and activity of HKs. Another possible determinant is tumoral blood flow which brings ^{18}F-FDG to the cell and reasonably increases its metabolism in parallel.

High uptake of ^{18}F-FDG by *SDHx*-related tumors has been suggested to be a reflection of the Warburg effect. Various mechanisms for accelerated glucose use by tumor cells have been described. Enhanced influx of glucose via GLUTs is considered to be the most important. Overexpression of GLUT isoforms GLUT-1 and GLUT-3 is closely related to ^{18}F-FDG uptake in tumor cells [46]. In addition, accelerated glucose phosphorylation by the HK enzymes results in enhanced ^{18}F-FDG accumulation. HK-2 is predominantly expressed in tumor cells that exhibit the Warburg effect [47] and is associated with elevated ^{18}F-FDG uptake in malignant conditions [48, 49]. Upregulation of both GLUTs and HK is frequently associated with malignant transformation of cells [50]. Furthermore, activity of HK-3 and monocarboxylate transporter type 4 (MCT-4), which facilitates the cellular lactate transport, possibly is regulated by hypoxia [16, 51]. In addition, hypoxia also promotes anaerobic glycolysis, and several studies have demonstrated that ^{18}F-FDG uptake is an indirect reflection of tumor hypoxia [52, 53].

The relationship between markers of the hypoxia-angiogenesis pathway and ^{18}F-FDG uptake in PPGL was investigated by comparing preoperative ^{18}F-FDG PET scans with the immunohistochemical expression of relevant markers in the same tumors. The expression of both HK-2 and HK-3 was significantly higher in *SDHx*-related PPGLs compared to sporadic and cluster 2 tumors [54]. Also, expression of vascular endothelial growth factor (VEGF), a downstream target of HIF, was significantly higher in *SDHx*-related PPGLs compared to cluster 2 PPGLs. Quantitative uptake of ^{18}F-FDG significantly correlated with the expression of HK-2, HK-3, VEGF, and MCT-4. VEGF activated in endothelial vascular cells within tumors can significantly contribute to ^{18}F-FDG uptake [55]. The immunohistochemical expression of GLUT-1 and GLUT-3, however, did not differ between cluster 1 and cluster 2 PPGL, nor did it correlate with ^{18}F-FDG uptake. So taken together these observations suggest that activation of aerobic glycolysis in SDHx-related PPGLs is associated with increased ^{18}F-FDG accumulation due to accelerated glucose phosphorylation by hexokinases rather than increased expression of glucose transporters. Differences in tumor vasculature and the activity of transporter systems may also contribute to genotype-related SUVs.

12.7 Dynamic ^{18}F-FDG PET Scanning

Routinely, ^{18}F-FDG avidity is calculated as SUVs from static PET images acquired at least 60 min after tracer injection. However, using ^{18}F-FDG SUV as a measure of glucose uptake and metabolism is hampered by several assumptions and simplifications. For example, it is assumed that the unmetabolized component of a radiopharmaceutical (e.g., in blood within a tumor, in intercellular spaces, and within tumor cells per se) is negligible relatively soon after its administration. Theoretically, however, high SUVs in *SDHx* PPGLs may reflect a high proportion of unmetabolized (unphosphorylated) ^{18}F-FDG located in the extracellular and intracellular spaces rather than a high actual glycolytic rate of the tumor. To overcome this, specific determinants of ^{18}F-FDG avidity can be identified by dynamic ^{18}F-FDG-PET acquisition and pharmacokinetic analysis of tracer distribution within the first hour after injection [56]. Time-activity curves can be created for a volume of interest over the tumor and a reference area such as the abdominal aorta. A two-tissue compartment tracer kinetic model can be used to estimate transfer rates of ^{18}F-FDG between the vascular/extravascular extracellular space and non-metabolized and metabolized tissue compartments. The derived transfer rates for transmembranous glucose flux (K1 (in), k2 (out)) and intracellular phosphorylation (k3) along with the fractional blood volume can be analyzed using nonlinear regression analysis. Glucose metabolic rate can be calculated using Patlak pharmacokinetic linear regression analysis [57] and can be displayed quantitatively in a metabolic rate map. Preliminary results of dynamic ^{18}F-FDG PET in patients with PPGL suggest that this approach, rather than calculating SUVs from static PET, further facilitates the *in vivo* identification of SDH-deficient tumors.

12.8   Magnetic Resonance Spectroscopy

The *in vivo* counterpart of ^{1}H-NMR is proton magnetic resonance spectroscopy (^{1}H-MRS), a non-radionuclide imaging technique by which several aspects of the metabolic composition of tissues can be studied in humans and whole animals. For example, in the specific context of mitochondrial disease, ^{1}H-MRS of the brain was applied in patients with Leigh syndrome, a neurodegenerative disorder caused by germline *SDHA* mutations. ^{1}H-MRS displayed a typical pattern of increased lactate and succinate in cerebral and cerebellar white matter areas [58, 59].

So far on a very limited scale, ^{1}H-MRS has also been successfully applied to characterize PPGL and HNPGL. The feasibility of ^{1}H-MRS to distinguish between PPGL and adrenocortical adenomas was investigated [60]. PPGLs appear to exhibit a unique spectral signature, showing a 6.8 ppm resonance that is not seen in adenomas. This peak, together with other resonances, was attributed to the presence of catecholamines and their metabolites metanephrines. Very recently, ^{1}H-MRS was shown to enable the distinction between *SDHx* and non-*SDHx* tumors, both in humans and in a mouse xenograft model [29, 61]. A succinate peak was observed by ^{1}H-NMR in all Sdhb$^{-/-}$-derived tumors in mice and in all paragangliomas of patients carrying an *SDHx* gene mutation, but neither in wild-type mouse tumors nor in patients exempt of *SDHx* mutation. In parallel to radionuclide imaging, this technique holds great promise for further *in vivo* metabolic characterization of PPGLs.

12.9   *In Vivo* "Radionuclide-omics"

In this era of ex vivo multi-omics, tumor characteristics at the (epi)genetic and metabolite level can be analyzed in detail, but not until after invasive surgical tumor resection or biopsy has been performed. There is a strong need to determine specific features of neuroendocrine tumors such as PPGL at an earlier stage and in a noninvasive way, so that tailor-made and personalized treatment can be planned. This purpose can be served by functional imaging, which can identify biomarkers of malignancy, growth rate, prognosis, and therapeutic targets. With the rapid development of new radiopharmaceuticals and imaging techniques, a new era of *in vivo* tumor characterization has arrived. In parallel to precise localization and delineation by anatomical imaging, radionuclide imaging of PPGL can serve to predict the underlying genotype and can detect important aspects of tumor cell metabolism, as reviewed here. In addition, if germline variants in *SDHB* or other PPGL susceptibility genes are encountered that are of unknown significance, functional imaging can be useful to assess the functionality of such mutations, providing information that is very valuable to determine the risk of malignancy in the individual patient.

In other cancers, functional imaging has been applied successfully to assess angiogenesis [62], hypoxia [63], apoptosis [64], and other mechanisms involved in tumorigenesis that are also highly relevant for neuroendocrine tumors and may
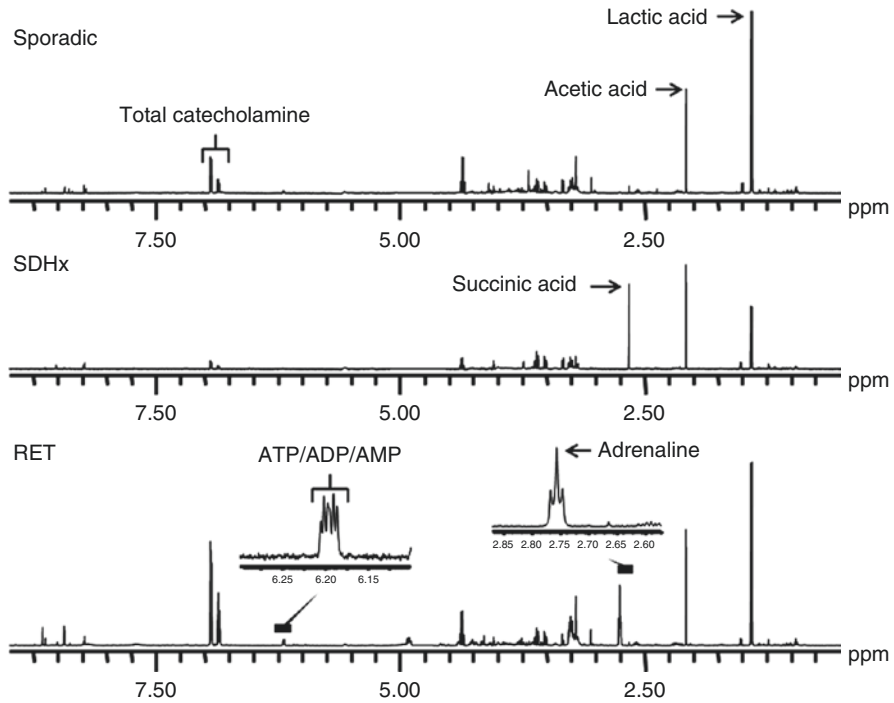
Fig. 12.1 ¹H-NMR spectra of PPGLs. One-dimensional 500 MHz ¹H-NMR spectra of PPGL tumor tissues at pH 2.50. *Upper panel*, sporadic tumor showing normal tumor metabolites like lactic acid, acetic acid, and catecholamines. *Middle panel*, *SDHB* tumor showing a high concentration of succinic acid (9.89 nmol/mg tissue). *Lower panel*, *RET* tumor showing high resonance of epinephrine and the overlap of the three doublets deriving from ATP/ADP/AMP

point toward more specific treatment. This warrants further investigation in PPGL. Obviously, the results of diagnostic ¹²³I-MIBG and somatostatin receptor scanning can lead the way to ¹³¹I-MIBG treatment and peptide receptor radiotherapy with [¹⁷⁷Lutetium]-octreotate, respectively. On top of this, however, in the near future, functional imaging may help to determine the metabolic Achilles heel and/or specific therapeutic targets in individual patients and serve to choose the appropriate drug regimen, depending on which "targeted" pathway is affected. In addition, radionuclide imaging can be used for treatment monitoring, detecting (absence of) an antitumor effect at an early stage, when tumor shrinkage is not yet anticipated. This could prevent unnecessary further exposure to systemic drugs with potential adverse effects. Stratification of PPGLs and other neuroendocrine tumors by "radionuclide-omics" is expected to further facilitate optimal and personalized management of these tumors (Figs. 12.1, 12.2, 12.3, 12.4, 12.5, 12.6, and 12.7).
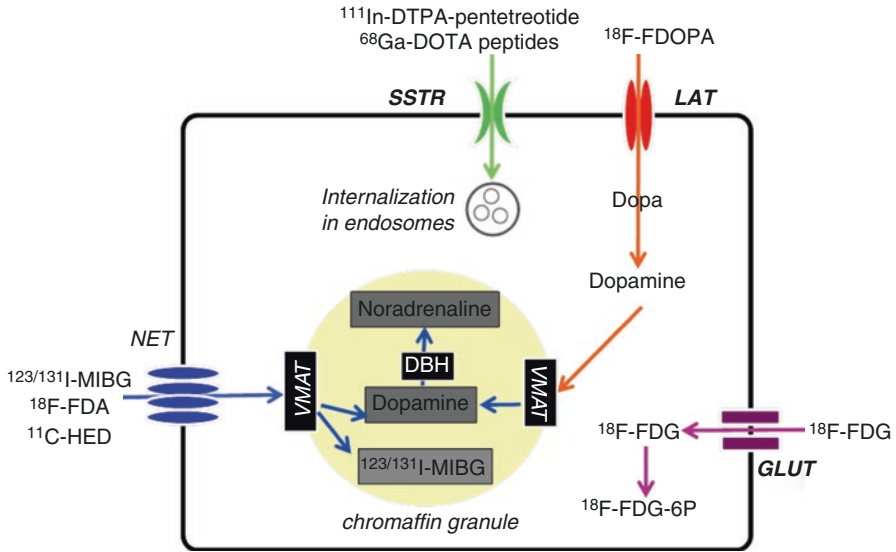
Fig. 12.2 Radionuclide transporters in PPGL tumor cell. *GLUT* glucose transporter, *LAT* large amino acid transporter, *NET* norepinephrine transporter, *SSTR* somatostatin receptor, *VMAT* vesicular monoamine transporter
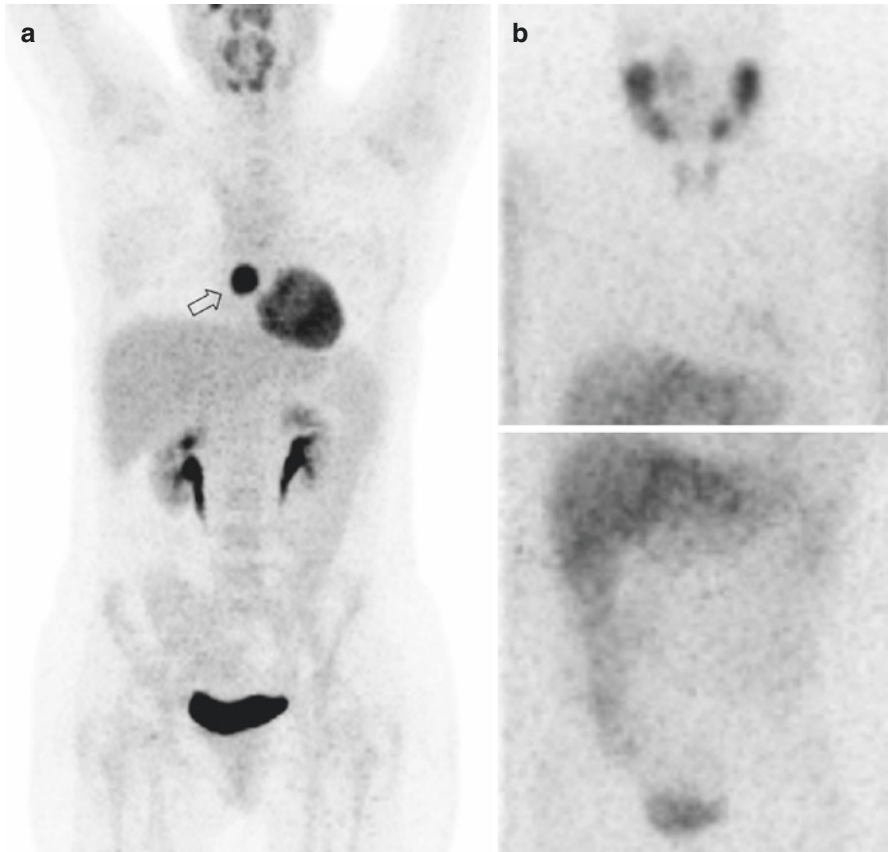
Fig. 12.3 Radionuclide imaging of *SDHB* PPGL. ^{18}F-FDG PET (panel **a**) and ^{123}I-MIBG SPECT (panel **b**) images of patients with a mediastinal PPGL due to a succinate dehydrogenase subunit B (*SDHB*) mutation. ^{123}I-MIBG fails to detect the tumor (Adapted from Timmers et al. [34])
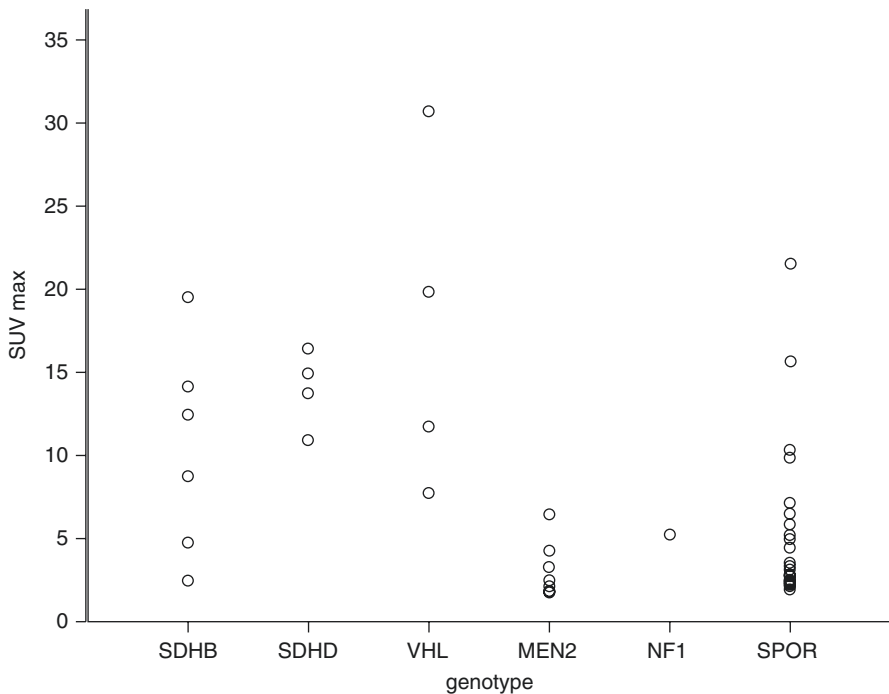
Fig. 12.4 ^{18}F-FDG uptake across genotypes. ^{18}F-FDG PET standardized uptake values in non-metastatic PPGLs across genotypes. *MEN2* multiple endocrine neoplasia type 2, *SPOR* sporadic, *SUVmax* maximum standard uptake value (Adapted from Timmers et al. [34])
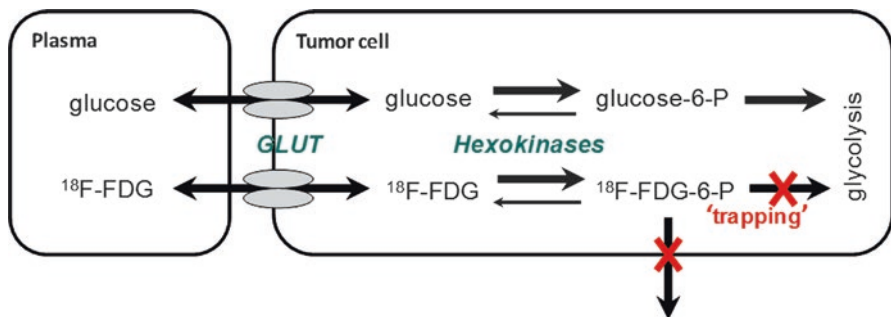
Fig. 12.5 ^{18}F-FDG uptake and metabolism in PPGL tumor cell
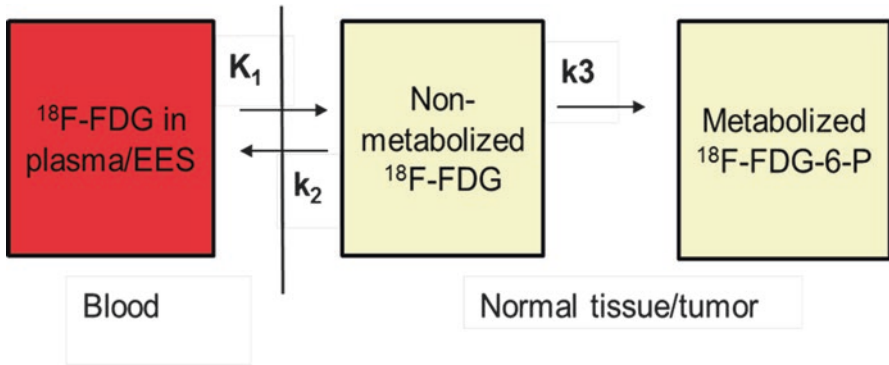
Fig. 12.6 Two-tissue compartment ^{18}F-FDG kinetic model. Transfer rates for transmembranous glucose flux (K1 (in), k2 (out)) and intracellular phosphorylation (k3). *EES* extravascular extracellular space
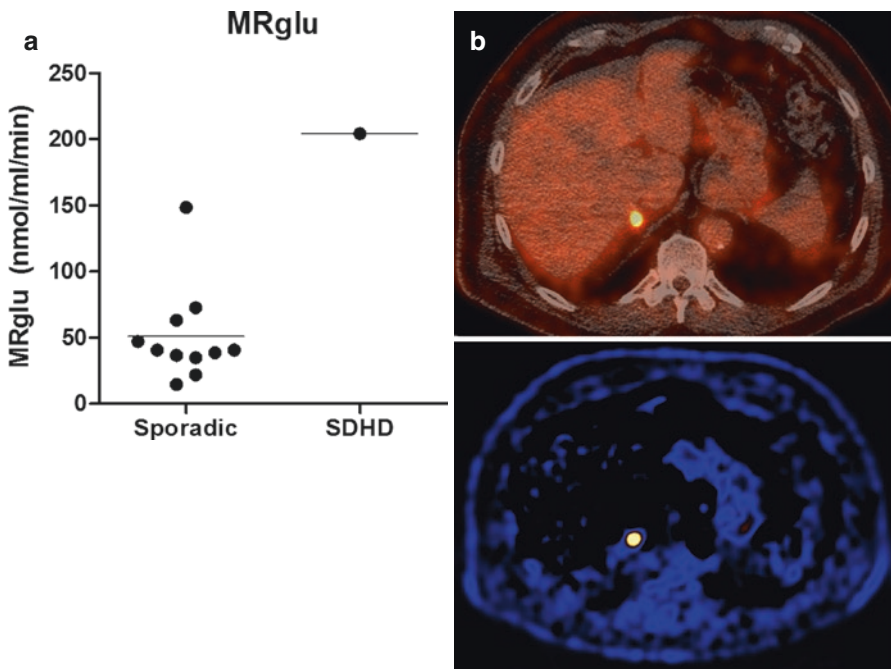
Fig. 12.7 Dynamic ^{18}F-FDG PET scanning. Panel **a**: the *SDHD (succinate dehydrogenase subunit D)*-related PPGL stands out from sporadic tumors in regards to metabolic rate of glucose (MRglu). Panel **b**: ^{18}F-FDG PET-CT fusion image (*upper* image) and metabolic rate map (lower image) of *SDHD*-related right adrenal pheochromocytoma (corresponding with *SDHD* case in panel **a**)

References

1. Lenders JW, Eisenhofer G, Mannelli M, Pacak K. Phaeochromocytoma. Lancet. 2005;366(9486):665–75.
2. Eisenhofer G, Goldstein DS, Sullivan P, Csako G, Brouwers FM, Lai EW, et al. Biochemical and clinical manifestations of dopamine-producing paragangliomas: utility of plasma methoxytyramine. J Clin Endocrinol Metab. 2005;90:2068–75.
3. Plouin PF, Fitzgerald P, Rich T, Ayala-Ramirez M, Perrier ND, Baudin E, et al. Metastatic pheochromocytoma and paraganglioma: focus on therapeutics. Horm Metab Res. 2012;44(5):390–9.
4. Amar L, Baudin E, Burnichon N, Peyrard S, Silvera S, Bertherat J, et al. Succinate dehydrogenase B gene mutations predict survival in patients with malignant pheochromocytomas or paragangliomas. J Clin Endocrinol Metab. 2007;92(10):3822–8.
5. Welander J, Soderkvist P, Gimm O. Genetics and clinical characteristics of hereditary pheochromocytomas and paragangliomas. Endocr Relat Cancer. 2011;18(6):R253–76.
6. Lorenzo FR, Yang C, Ng Tang Fui M, Vankayalapati H, Zhuang Z, Huynh T, et al. A novel EPAS1/HIF2A germline mutation in a congenital polycythemia with paraganglioma. J Mol Med. 2013;91(4):507–12.
7. Castro-Vega LJ, Buffet A, De Cubas AA, Cascon A, Menara M, Khalifa E, et al. Germline mutations in FH confer predisposition to malignant pheochromocytomas and paragangliomas. Human molecular genetics. 2014; 23(9):2440–6.
8. Cascon A, Comino-Mendez I, Curras-Freixes M, de Cubas AA, Contreras L, Richter S, et al. Whole-exome sequencing identifies MDH2 as a new familial paraganglioma gene. J Natl Cancer Inst. 2015;107(5):1–5.
9. Burnichon N, Vescovo L, Amar L, Libe R, de Reynies A, Venisse A, et al. Integrative genomic analysis reveals somatic mutations in pheochromocytoma and paraganglioma. Hum Mol Genet. 2011;20(20):3974–85.
10. Burnichon N, Buffet A, Parfait B, Letouze E, Laurendeau I, Loriot C, et al. Somatic NF1 inactivation is a frequent event in sporadic pheochromocytoma. Hum Mol Genet. 2012;21(26):5397–405.
11. Zhuang Z, Yang C, Lorenzo F, Merino M, Fojo T, Kebebew E, et al. Somatic HIF2A gain-of-function mutations in paraganglioma with polycythemia. N Engl J Med. 2012;367(10):922–30.
12. van Nederveen FH, Korpershoek E, Lenders JW, de Krijger RR, Dinjens WN. Somatic SDHB mutation in an extraadrenal pheochromocytoma. N Engl J Med. 2007;357(3):306–8.
13. Welander J, Larsson C, Backdahl M, Hareni N, Sivler T, Brauckhoff M, et al. Integrative genomics reveals frequent somatic NF1 mutations in sporadic pheochromocytomas. Hum Mol Genet. 2012;21(26):5406–16.
14. Crona J, Delgado Verdugo A, Maharjan R, Stalberg P, Granberg D, Hellman P, et al. Somatic mutations in H-RAS in sporadic pheochromocytoma and paraganglioma identified by exome sequencing. J Clin Endocrinol Metab. 2013;98(7):E1266–71.
15. Dahia PL. Transcription association of VHL and SDH mutations link hypoxia and oxidoreductase signals in pheochromocytomas. Ann N Y Acad Sci. 2006;1073:208–20.
16. Favier J, Briere JJ, Burnichon N, Riviere J, Vescovo L, Benit P, et al. The Warburg effect is genetically determined in inherited pheochromocytomas. PLoS One. 2009;4(9):e7094.
17. Gimenez-Roqueplo AP, Favier J, Rustin P, Mourad JJ, Plouin PF, Corvol P, et al. The R22X mutation of the SDHD gene in hereditary paraganglioma abolishes the enzymatic activity of complex II in the mitochondrial respiratory chain and activates the hypoxia pathway. Am J Hum Genet. 2001;69(6):1186–97.
18. Gimenez-Roqueplo AP, Favier J, Rustin P, Rieubland C, Kerlan V, Plouin PF, et al. Functional consequences of a SDHB gene mutation in an apparently sporadic pheochromocytoma. J Clin Endocrinol Metab. 2002;87(10):4771–4.
19. Rapizzi E, Ercolino T, Canu L, Giache V, Francalanci M, Pratesi C, et al. Mitochondrial function and content in pheochromocytoma/paraganglioma of succinate dehydrogenase mutation carriers. Endocr Relat Cancer. 19(3):261–9.

20. Selak MA, Armour SM, MacKenzie ED, Boulahbel H, Watson DG, Mansfield KD, et al. Succinate links TCA cycle dysfunction to oncogenesis by inhibiting HIF-alpha prolyl hydroxylase. Cancer Cell. 2005;7(1):77–85.

21. Lee S, Nakamura E, Yang H, Wei W, Linggi MS, Sajan MP, et al. Neuronal apoptosis linked to EglN3 prolyl hydroxylase and familial pheochromocytoma genes: developmental culling and cancer. Cancer Cell. 2005;8(2):155–67.

22. Letouze E, Martinelli C, Loriot C, Burnichon N, Abermil N, Ottolenghi C, et al. SDH mutations establish a hypermethylator phenotype in paraganglioma. Cancer Cell. 2013;23(6):739–52.

23. Favier J, Amar L, Gimenez-Roqueplo AP. Paraganglioma and phaeochromocytoma: from genetics to personalized medicine. Nat Rev Endocrinol. 2015;11(2):101–11.

24. Rao JU, Engelke UF, Rodenburg RJ, Wevers RA, Pacak K, Eisenhofer G, et al. Genotype-specific abnormalities in mitochondrial function associate with distinct profiles of energy metabolism and catecholamine content in pheochromocytoma and paraganglioma. Clin Cancer Res. 2013;19(14):3787–95.

25. Rapizzi E, Ercolino T, Canu L, Giache V, Francalanci M, Pratesi C, et al. Mitochondrial function and content in pheochromocytoma/paraganglioma of succinate dehydrogenase mutation carriers. Endocr Relat Cancer. 2012;19(3):261–9.

26. Rao JU, Engelke UF, Sweep FC, Pacak K, Kusters B, Goudswaard AG, et al. Genotype-specific differences in the tumor metabolite profile of pheochromocytoma and paraganglioma using untargeted and targeted metabolomics. J Clin Endocrinol Metab. 2015;100(2): E214–22.

27. Richter S, Peitzsch M, Rapizzi E, Lenders JW, Qin N, de Cubas AA, et al. Krebs cycle metabolite profiling for identification and stratification of pheochromocytomas/paragangliomas due to succinate dehydrogenase deficiency. J Clin Endocrinol Metab. 2014;99(10):3903–11.

28. Imperiale A, Moussallieh FM, Sebag F, Brunaud L, Barlier A, Elbayed K, et al. A new specific succinate-glutamate metabolomic hallmark in SDHx-related paragangliomas. PLoS One. 2013;8(11):e80539.

29. Imperiale A, Moussallieh FM, Roche P, Battini S, Cicek AE, Sebag F, et al. Metabolome profiling by HRMAS NMR spectroscopy of pheochromocytomas and paragangliomas detects SDH deficiency: clinical and pathophysiological implications. Neoplasia. 2015;17(1):55–65.

30. Ilias I, Shulkin B, Pacak K. New functional imaging modalities for chromaffin tumors, neuroblastomas and ganglioneuromas. Trends Endocrinol Metabol TEM. 2005;16(2):66–72.

31. Timmers HJ, Chen CC, Carrasquillo JA, Whatley M, Ling A, Havekes B, et al. Comparison of 18F-fluoro-L-DOPA, 18F-fluoro-deoxyglucose, and 18F-fluorodopamine PET and 123I-MIBG scintigraphy in the localization of pheochromocytoma and paraganglioma. J Clin Endocrinol Metab. 2009;94(12):4757–67.

32. Timmers HJ, Kozupa A, Chen CC, Carrasquillo JA, Ling A, Eisenhofer G, et al. Superiority of fluorodeoxyglucose positron emission tomography to other functional imaging techniques in the evaluation of metastatic SDHB-associated pheochromocytoma and paraganglioma. J Clin Oncol. 2007;25(16):2262–9.

33. Taïeb D, Sebag F, Barlier A, Tessonnier L, Palazzo FF, Morange I, et al. 18F-FDG avidity of pheochromocytomas and paragangliomas: a new molecular imaging signature? J Nucl Med. 2009;50(5):711–7.

34. Timmers HJ, Chen CC, Carrasquillo JA, Whatley M, Ling A, Eisenhofer G, et al. Staging and functional characterization of pheochromocytoma and paraganglioma by 18F-fluorodeoxyglucose (18F-FDG) positron emission tomography. J Natl Cancer Inst. 2012;104(9):700–8.

35. Eisenhofer G, Pacak K, Huynh TT, Qin N, Bratslavsky G, Linehan WM, et al. Catecholamine metabolomic and secretory phenotypes in phaeochromocytoma. Endocr Relat Cancer. 18(1):97–111.

36. Huynh TT, Pacak K, Brouwers FM, Abu-Asab MS, Worrell RA, Walther MM, et al. Different expression of catecholamine transporters in phaeochromocytomas from patients with von Hippel-Lindau syndrome and multiple endocrine neoplasia type 2. Eur J Endocrinol Eur Feder Endocrine Soc. 2005;153(4):551–63.

37. Kaji P, Carrasquillo JA, Linehan WM, Chen CC, Eisenhofer G, Pinto PA, et al. The role of 6-[18F]fluorodopamine positron emission tomography in the localization of adrenal pheochromocytoma associated with von Hippel-Lindau syndrome. Eur J Endocrinol Eur Feder Endocrine Soc. 2007;156(4):483–7.

38. Blanchet EM, Gabriel S, Martucci V, Fakhry N, Chen CC, Deveze A, et al. 18F-FDG PET/CT as a predictor of hereditary head and neck paragangliomas. Eur J Clin Invest. 2014;44(3):325–32.

39. Gimenez-Roqueplo AP, Lehnert H, Mannelli M, Neumann H, Opocher G, Maher ER, et al. Phaeochromocytoma, new genes and screening strategies. Clin Endocrinol (Oxf). 2006;65(6):699–705.

40. Gabriel S, Blanchet EM, Sebag F, Chen CC, Fakhry N, Deveze A, et al. Functional characterization of nonmetastatic paraganglioma and pheochromocytoma by (18) F-FDOPA PET: focus on missed lesions. Clin Endocrinol (Oxf). 2013;79(2):170–7.

41. Rischke HC, Benz MR, Wild D, Mix M, Dumont RA, Campbell D, et al. Correlation of the genotype of paragangliomas and pheochromocytomas with their metabolic phenotype on 3,4-dihydroxy-6-18F-fluoro-L-phenylalanin PET. J Nucl Med. 2012;53(9):1352–8.

42. Janssen I, Blanchet EM, Adams K, Chen CC, Millo CM, Herscovitch P, et al. Superiority of [68Ga]-DOTATATE PET/CT to Other Functional Imaging Modalities in the Localization of SDHB-Associated Metastatic Pheochromocytoma and Paraganglioma. Clin Cancer Res. 2015;21(17):3888–95.

43. van Berkel A, Rao JU, Lenders JW, Pellegata NS, Kusters B, Piscaer I, et al. Semiquantitative 123I-Metaiodobenzylguanidine Scintigraphy to Distinguish Pheochromocytoma and Paraganglioma from Physiologic Adrenal Uptake and Its Correlation with Genotype-Dependent Expression of Catecholamine Transporters. J Nucl Med. 2015;56(6):839–46.

44. Lenders JW, Duh QY, Eisenhofer G, Gimenez-Roqueplo AP, Grebe SK, Murad MH, et al. Pheochromocytoma and paraganglioma: an endocrine society clinical practice guideline. J Clin Endocrinol Metab. 2014;99(6):1915–42.

45. Taïeb D, Timmers HJ, Hindie E, Guillet BA, Neumann HP, Walz MK, et al. EANM 2012 guidelines for radionuclide imaging of phaeochromocytoma and paraganglioma. Eur J Nucl Med Mol Imaging. 2012;39(12):1977–95.

46. Macheda ML, Rogers S, Best JD. Molecular and cellular regulation of glucose transporter (GLUT) proteins in cancer. J Cell Physiol. 2005;202(3):654–62.

47. Mathupala SP, Ko YH, Pedersen PL. Hexokinase-2 bound to mitochondria: cancer's stygian link to the "Warburg Effect" and a pivotal target for effective therapy. Semin Cancer Biol. 2009;19(1):17–24.

48. Ahn KJ, Hwang HS, Park JH, Bang SH, Kang WJ, Yun M, et al. Evaluation of the role of hexokinase type II in cellular proliferation and apoptosis using human hepatocellular carcinoma cell lines. J Nucl Med. 2009;50(9):1525–32.

49. Yamada T, Uchida M, Kwang-Lee K, Kitamura N, Yoshimura T, Sasabe E, et al. Correlation of metabolism/hypoxia markers and fluorodeoxyglucose uptake in oral squamous cell carcinomas. Oral Surg Oral Med Oral Pathol Oral Radiol. 2012;113(4):464–71.

50. de Geus-Oei LF, van Krieken JH, Aliredjo RP, Krabbe PF, Frielink C, Verhagen AF, et al. Biological correlates of FDG uptake in non-small cell lung cancer. Lung Cancer. 2007;55(1):79–87.

51. Wyatt E, Wu R, Rabeh W, Park HW, Ghanefar M, Ardehali H. Regulation and cytoprotective role of hexokinase III. PLoS One. 2010;5(11):e13823.

52. Dierckx RA, Van de Wiele C. FDG uptake, a surrogate of tumour hypoxia? Eur J Nucl Med Mol Imaging. 2008;35(8):1544–9.

53. Clavo AC, Brown RS, Wahl RL. Fluorodeoxyglucose uptake in human cancer cell lines is increased by hypoxia. J Nucl Med. 1995;36(9):1625–32.

54. van Berkel A, Rao JU, Kusters B, Demir T, Visser E, Mensenkamp AR, et al. Correlation Between In Vivo 18F-FDG PET and Immunohistochemical Markers of Glucose Uptake and Metabolism in Pheochromocytoma and Paraganglioma. J Nucl Med. 2014;55(8):1253–9.

55. Maschauer SPO, Hoffmann M, Deichen JT, Kuwert T. Characterization of 18F-FDG uptake in human endothelial cells in vitro. J Nucl Med. 2004;45(3):455–60.

56. Willemsen AT, van den Hoff J. Fundamentals of quantitative PET data analysis. Curr Pharm Des. 2002;8(16):1513–26.
57. Patlak CSBR, Fenstermacher JD. Graphical evaluation of blood-to-brain transfer constants from multiple-time uptake data. J Cereb Blood Flow Metab. 1983;3:1–7.
58. Sijens PE, Smit GP, Rodiger LA, van Spronsen FJ, Oudkerk M, Rodenburg RJ, et al. MR spectroscopy of the brain in Leigh syndrome. Brain Dev. 2008;30(9):579–83.
59. Brockmann K, Bjornstad A, Dechent P, Korenke CG, Smeitink J, Trijbels JM, et al. Succinate in dystrophic white matter: a proton magnetic resonance spectroscopy finding characteristic for complex II deficiency. Ann Neurol. 2002;52(1):38–46.
60. Kim S, Salibi N, Hardie AD, Xu J, Lim RP, Lee VS, et al. Characterization of adrenal pheochromocytoma using respiratory-triggered proton MR spectroscopy: initial experience. AJR Am J Roentgenol. 2009;192(2):450–4.
61. Lussey-Lepoutre C, Bellucci A, Morin A, Buffet A, Amar L, Janin M, et al. In Vivo Detection of Succinate by Magnetic Resonance Spectroscopy as a Hallmark of SDHx Mutations in Paraganglioma. Clin Cancer Res. 2015.
62. Battle MR, Goggi JL, Allen L, Barnett J, Morrison MS. Monitoring tumor response to antiangiogenic sunitinib therapy with 18F-fluciclatide, an 18F-labeled alphaVbeta3-integrin and alphaV beta5-integrin imaging agent. J Nucl Med. 52(3):424–30.
63. Hendrickson K, Phillips M, Smith W, Peterson L, Krohn K, Rajendran J. Hypoxia imaging with [F-18] FMISO-PET in head and neck cancer: Potential for guiding intensity modulated radiation therapy in overcoming hypoxia-induced treatment resistance. Radiother Oncol. 2011;101(3):369–75.
64. Blankenberg FG. In vivo detection of apoptosis. J Nucl Med. 2008;49 Suppl 2:81S–95.

Chapter 13
Radionuclide Imaging of Head and Neck Paragangliomas

David Taïeb, Arthur Varoquaux, Ingo Janssen, and Karel Pacak

13.1 Epidemiology and Natural History

Head and neck paragangliomas (HNPGLs, often referred to as "glomus tumors") belong to the pheochromocytoma/paraganglioma (PHEO/PGL) family. They are usually located in specific areas of the head and neck, and more rarely in the anterior or middle mediastinum. Like their retroperitoneal counterparts, they exhibit a typical endocrine pattern with chief cell nests (i.e., zellballen pattern).

HNPGLs account for approximately 20 % of PGLs in an unselected series [1], 0.6 % of head and neck tumors, and 0.03 % of all tumors [2]. The overall incidence of HNPGLs ranges from 1 in 30,000 to 1 in 100,000, with carotid body PGL (CBP) making up nearly 60 % of all HNPGL cases, followed by jugular PGL (JP), vagal PGL (VP), and tympanic PGL (TP) [3]. It has now been established that 35 % or more of HNPGLs are associated with recognized genetic defects. The reported malignancy risks are variable and probably overestimated by cancer registries (due to unregistered un-resected tumors) [4] or old literature (under diagnosis). In a more recent series, malignant cases were present in less than 7 % [5]. In patients with

D. Taïeb, MD, PhD (✉)
Department of Nuclear Medicine, La Timone University Hospital, CERIMED, Aix-Marseille University, Marseille, France
e-mail: david.Taïeb@ap-hm.fr

A. Varoquaux, MD, PhD
Department of Medical Imaging, Conception Hospital, Aix-Marseille University, 13005 Marseille, France

I. Janssen, MD • K. Pacak, MD, PhD, DSc, FACE
Section on Medical Neuroendocrinology, Eunice Kennedy Shriver National Institute of Child Health and Human Development (NICHD), National Institutes of Health (NIH), Bethesda, MD, USA
e-mail: karel@mail.nih.gov

HNPGLs, data suggests little to no growth over time in most cases. To our knowledge, only two studies have specifically examined the natural history of HNPGLs (for a total of 95 tumors) [6, 7]. The authors did not find any patients with clinically meaningful tumor growth during the 4–5-year follow-up period. Among the tumors that grew, the mean growth ranged from 1 to 2 mm/year.

13.2 Tumor Origin

Embryogenesis of paraganglial cells has received considerable attention over the last century. Evidence for the origin of sympathetic ganglia, adrenal medulla, and carotid body was pursued by a number of labs, but it was largely the work of Le Douarin and colleagues using quail/chick chimeras that led to the resolution of their neural crest (NC) origin [8]. Later, immunohistochemical, in situ hybridization, transgenic animal studies, and single-cell electroporation methods using fluorescent NC progenitors signficantly added to the knowledge of the mechanisms required for the correct specification, migration, and differentiation of multipotent NC progenitors during development [9]. Beyond the carotid body, little data is available on the embryology of other paraganglionic cells associated with the parasympathetic system, probably because these cells are relatively late in differentiating. However, these peripheral cells produce a selection of neurotransmitter-like compounds, which are common to other NC derivatives. They are embedded in several sensory ganglia whose neurons may be of NC or placodal origin, but whose supporting cells are crest derived. Therefore, it is widely assumed that these cells are also of NC origin. Head and neck paraganglia are closely aligned with the distribution of the parasympathetic nervous system and act as chemoreceptors. The carotid body is a prime example of a chemoreceptor organ that mediates reflex hyperventilation during hypoxemia via activation of the respiratory center. Long-term exposure to altitude induces carotid body hypertrophy necessary for acclimatization to chronic hypoxemia [10].

13.3 Clinical Presentation

HNPGLs range in spectrum from small lesions (usually detected in PGL mutation carriers) to large unresectable masses, often invading cranial nerves and sometimes the brainstem. HNPGLs are often discovered on imaging studies or revealed by symptoms of cervical mass and/or compression or infiltration of adjacent structures (e.g., hearing loss, pulsatile tinnitus, pain, cervical mass, dysphagia, or cranial nerve palsies often presenting with vocal cord paralysis). HNPGLs are distinguished from other tumors by a newly introduced biochemical marker, 3-methoxy-tyramine (a dopamine metabolite), that is elevated in almost one third of patients

with a HNPGL in contrast to plasma or urine metanephrines, which are very rarely elevated [11–14].

13.4 Diagnosis

In the presence of a non-secreting tumor mass, accurate diagnosis of a HNPGL can be made by the following criteria:

1. Typical anatomical location
2. Typical imaging finding on CT and/or MRI
3. Tumor uptake using specific radiopharmaceuticals
4. Presence of a germline mutation in HNPGL susceptibility genes and/or family history of PHEO/PGL

13.4.1 Typical Anatomical Location

HNPGLs are usually located in specific areas of the head and neck and more rarely in the anterior or middle mediastinum. Tumor sizes range from small lesions (usually detected in PGL mutation carriers) to very large invasive masses.

Jugular PGLs arise within the adventitia of the dome of the jugular bulb (glomus jugulare PGLs, JP), in the middle part of the petro-occipital fissure, posteriorly and inferiorly to the middle ear, and in the labyrinthine structure (Fig. 13.1). They may extend into the middle ear and mastoid space, inferiorly into the jugular vein and the jugular foramen, and medially into the posterior cerebellar fossa and cerebellopontine angle.

Tympanic PGLs commonly arise from paraganglia adjacent to the tympanic plexus of Jacobson's nerve on the cochlear promontory (glomus tympanicum PGLs, TP) (Fig. 13.2). They can occlude the Eustachian tube or protrude through the tympanic membrane into the external auditory canal.

Vagal PGLs arise from paraganglia associated with the vagus nerve, most often at the level of the inferior (nodose) ganglion (glomus vagale PGL, VP) (Fig. 13.3). They may extend upward into the skull base through the jugular foramen, inferiorly into the cervical area, and laterally surrounding the internal carotid artery and lower nerves. Moreover, they can compress the pharyngeal wall.

Carotid PGLs arise from the carotid body at the bifurcation of the common carotid artery (glomus caroticum PGLs, CBP) (Fig. 13.4). They may extend laterally surrounding carotid vessels and lower nerves and upward into the retrostyloid parapharyngeal space.

PGLs may also develop in the anterior and middle mediastinum. They have the same embryologic origin as HNPGLs, and are therefore considered within the same entity.
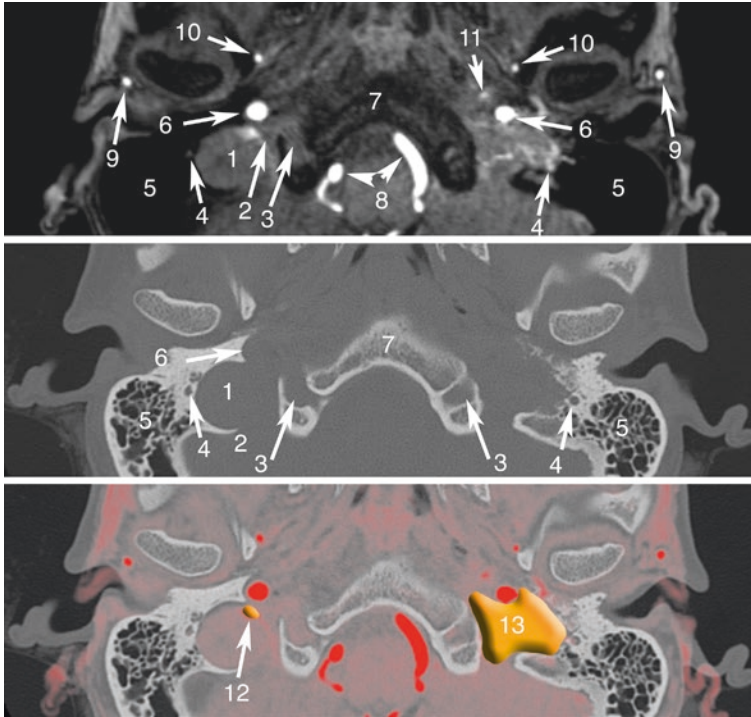
Fig. 13.1 Jugular PGL. Co-registered axial planes in MR TOF (time of flight) without gadolinium, CT (bone kernel), and MR TOF—CT rigid fusion with PGLs drawn in orange. *1* Jugular bulb, pars vascularis; *2* Jugular bulb, pars nervosa; *3* Hypoglossal nerve in the hypoglossal canal; *4* Facial nerve, mastoid part; *5* Mastoid cells; *6* Internal carotid artery; *7* Basilar process of occipital bone; *8* Vertebral artery (V4); *9* Occipital artery; *10* Middle meningeal artery before entering in foramen spinosum; *11* Ascending pharyngeal artery, neuromeningeal trunk; *12* Right jugular PGL (confirmed with focal uptake of ^{18}F-FDOPA and ^{68}Ga-DOTATATE) located in the anterior wall of jugular vein (pars vascularis of the jugular foramen); *13* Left jugular PGL extending to pars vascularis and nervosa and responsible of "wet sugar" bone erosion

Unusual or exceptional locations have also been reported, such as PGLs of the larynx, thyroid, sinonasal region, nasopharynx, orbit, and tongue. Exceptional cases of PGLs of the cervical sympathetic chain have been reported.

13.4.2 Typical Imaging Finding on CT and/or MRI

HNPGLs usually demonstrate marked enhancement of intra-tumoral vessels following contrast administration on CT, a low signal on T1-weighted images, and an intermediate to high signal on T2-weighted MRI images. They also often enhance intensely after gadolinium injection on MRI. Flow signal voids in the tumor are typical of PGL, with a "salt and pepper" appearance on spin-echo sequences. These
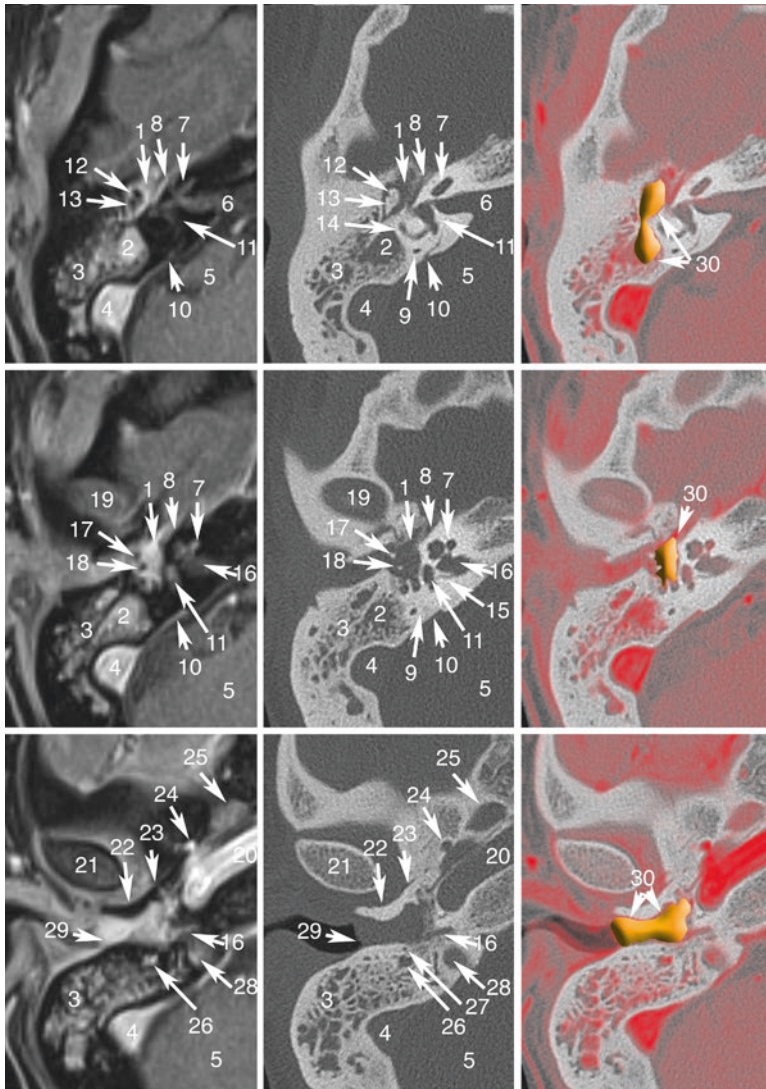
Fig. 13.2 Tympanic PGL. Co-registered axial planes in MR 3D T1 weighted with fat saturation (VIBE, Siemens) with gadolinium, CT (bone kernel), and MR T1 VIBE gadolinium—CT rigid fusion with PGLs drawn in orange. *1* Attic, filled by PGL; *2* Mastoid antrum filled by PGL; *3* Mastoid cells filled by serohemorrhagic fluid; *4* Sigmoid sinus, tumor-free and permeable; *5* Posterior fossa; *6* Internal auditory meatus opening (porus acusticus internus); *7* Cochlea; *8* Labyrinthic portion of facial nerve; *9* Posterior semicircular canal; *10* Endolymphatic sac (internal blind pouch of endolymphatic duct); *11* Vestibule, *12* Head of malleus; *13* Incus, body and short crus; *14* Lateral semicircular canal; *15* Utricularis and ampullaris posterior nerve canal; *16* Fundus of internal acoustic meatus; *17* Handle of malleus; *18* Incus, long crus; *19* Mandibular fossa of the temporal bone; *20* Carotid canal; *21* Mandibular condyle; *22* Tympanic part of temporal bone; *23* Anterior tympanosquamous fissure (Glaser's fissure); *24* Foramen spinosum-middle meningeal artery; *25* Foramen ovale; *26* Mastoid segment of facial nerve; *27* Chorda tympani; *28* Jugular bulb (*upper part*); *29* Tympanic membrane (bulging); *30* Tympanic PGL
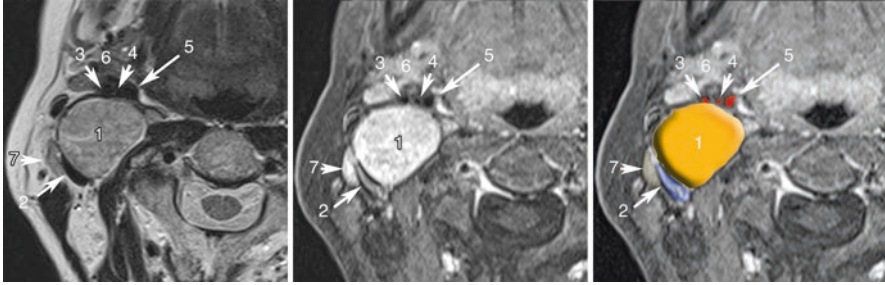
Fig. 13.3 Vagal PGL. Co-registered axial planes in MR T2 WI (**a**), 3D T1 weighted with fat saturation (VIBE, Siemens) with gadolinium (**b**). Drawn layer (**c**) of surrounding arteries (in *red*) and veins (in *blue*) around the PGL drawn in orange. *1* Vagal PGL, *2* Jugular vein, *3* External carotid artery, *4* Ascending pharyngeal artery, *5* Internal carotid artery, *6* submandibular gland, *7* normal node. Note that vagal nerve PGLs splay jugular veins away from the carotid arteries

flow voids correspond to intra-tumoral arterial vessels on MR angiography [15–19]. These MR angiography sequences can be achieved without gadolinium (3D time of flight) or with gadolinium injection (3D time-resolved gadolinium). These sequences have been shown to be highly informative, with sensitivities and specificities of 90 % and 94 % [16] and 100 % and 94 % [17], respectively. There is a recent trend of using time-resolved 4D gadolinium MR angiography [19]. The 4D time-resolved imaging of contrast kinetics (TRICKS) technique enables evaluation of both intra-tumoral vessels (early arterial phase) and tumor perfusion, including capillary permeability. Fusion images between 3D volumetric interpolated fat-saturated (FATSAT) T1-weighted (VIBE) and 4D MR angiography are particularly informative. Diffusion-weighted imaging (DWI), which is dependent on tissue cellularity, may be useful in preoperative characterization and prognosis assessment of PGL, but further evaluation is needed [20].

13.4.3   Tumor Uptake Using Specific Radiopharmaceuticals

Radionuclide imaging techniques now play a crucial role in the evaluation of HNPGLs. Several excellent studies have demonstrated the superiority of Octreoscan for HNPGLs compared to metaiodobenzylguanidine ($^{123/131}$I-MIBG), with sensitivities of 89–100 % and 18–50 %, respectively [21–26]. However, the sensitivity of this imaging modality needs to be revised downward, because some lesions are only a few millimeters in size, and are therefore not detectable by available cameras [27]. The recently introduced hybrid SPECT/CT cameras have increased diagnostic confidence in image interpretation and enhanced sensitivity, but practical constraints such as long imaging times remain important limitations. PET imaging is a highly sensitive functional imaging technique for HNPGLs.
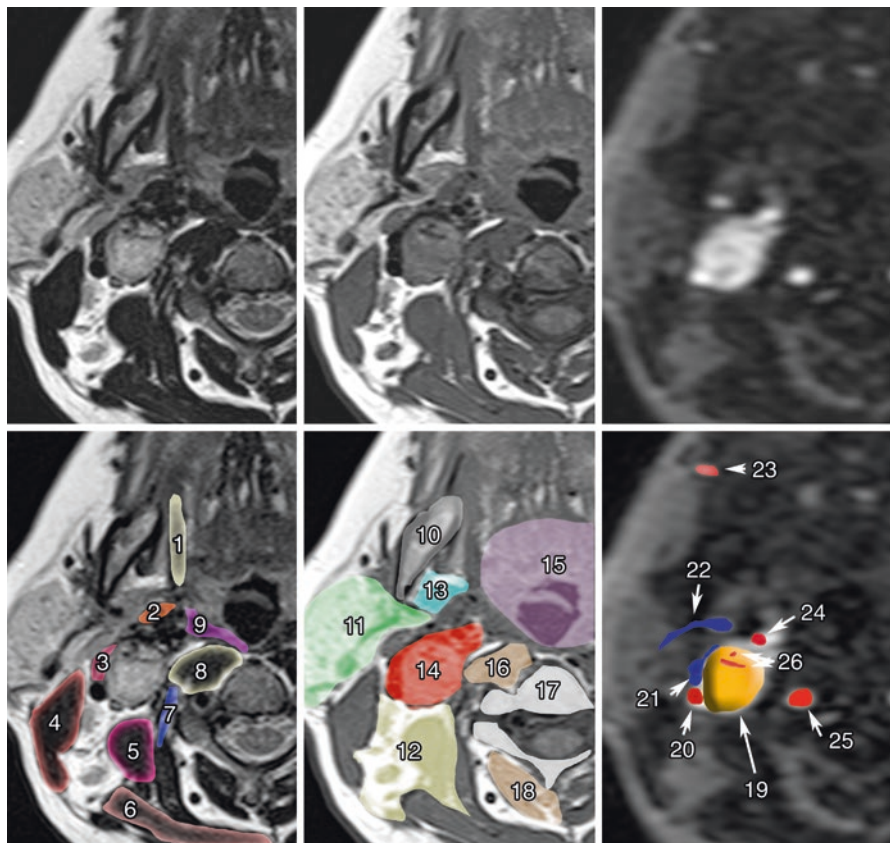
Fig. 13.4 Carotid body PGL. Co-registered axial planes in MR T2 WI (**a**), MR T1 WI (**b**), and time-resolved 4D MRA at an early arterial phase of gadolinium injection (**c**). Drawn layers of surrounding muscle (**d**), deep spaces of the neck (**e**), and vascular structures (**f**) around the carotid PGL. *1* Styloglossus muscles; *2* Stylopharyngeus muscles; *3* Digastric muscle, posterior belly; *4* Sternocleidomastoid muscle; *5* Scalene muscles; *6* Trapezius muscle; *7* Longus capitis muscle; *8* Longus colli muscle; *9* Middle pharyngeal constrictor muscle; *10* Mandible; *11* Parotid space; *12* Posterior triangle of the neck; *13* Parapharyngeal space, prestyloid; *14* Parapharyngeal space, poststyloid (vascular space); *15* Mucosal space (visceral); *16* Retropharyngeal and revertebral spaces; *17* Vertebrae; *18* Paravertebral space; *19* Carotid body PGL; *20* Internal carotid artery; *21* Jugular vein; *22* Retromandibular vein; *23* Facial artery; *24* External carotid artery; *25* Vertebral artery; *26* Internal arterial feeders (flow voids). Note that carotid body PGL (glomus) splays external carotid away from the internal carotid artery

13.4.3.1 ^{18}F-Fluorodihydroxyphenylalanine

^{18}F-fluorodihydroxyphenylalanine (^{18}F-fluorodopa, ^{18}F-FDOPA) is taken up through neutral amino acid transporters (mainly LAT1/LAT2), decarboxylated into ^{18}F-fluorodopamine by aromatic L-amino acid decarboxylase, and concentrated in intracellular vesicles. ^{18}F-FDOPA PET/CT was found to be a highly sensitive

(>90 % for HNPGLs) and specific (95–100 %) imaging modality for PGL detection, especially for HNPGLs [28–32]. ^{18}F-FDOPA PET was also found to be superior to octreoscan [28, 30] in the detection of HNPGLs, mainly due to increased sensitivity to PET cameras. However, ^{18}F-FDOPA is not routinely available at most imaging centers worldwide.

13.4.3.2   ^{18}F-Fluorodopamine

[18]F-fluorodopamine (^{18}F-FDA), which uses the cellular norepinephrine transporter system expressed on PGL cells, is not recommended for the evaluation of these tumors due to its suboptimal sensitivity.

13.4.3.3   ^{68}Ga-Labeled Somatostatin Analogues

More recently, PET/CT imaging with ^{68}Ga-labeled somatostatin analogues (^{68}Ga-DOTA-SSAs) has rapidly evolved, since it does not require a cyclotron to make the radiotracer. All ^{68}Ga-DOTA-SSAs (DOTATOC, DOTATATE, and DOTANOC) effectively target somatostatin receptor subtype 2 (SST2) (IC50: 2.5 nM, 0.2 nM, and 1.9 nM, respectively), which is the most overexpressed subtype in PGLs. The low expression of SST5 observed in PGLs constitutes a major difference with GEP-NETs.

Moreover, a special advantage of labeled SSAs is that, unlike ^{18}F-FDOPA, they can be used in the radioactive treatment of these tumors (as theranostic agents). In 2014, ^{68}Ga-DOTATATE was approved with an orphan drug status by both the US Food and Drug Administration (FDA) and the European Medicines Agency (EMA) in the imaging of gastroenteropancreatic neuroendocrine tumors. The use of ^{68}Ga-DOTA-SSA in the context of PHEO/PGLs has been less studied but has shown excellent preliminary results in localizing these tumors [33–38]. Head-to-head comparison between ^{68}Ga-DOTA-SSA and ^{18}F-FDOPA PET has been performed in only four studies: one retrospective study from Innsbruck Medical University (^{68}Ga-DOTATOC in 20 patients with unknown genetic background) [39], two prospective studies from the NIH (^{68}Ga-DOTATATE in 17 and 20 patients) [40–42], and one prospective study from La Timone University Hospital (^{68}Ga-DOTATATE in 30 patients) [43]. In these studies, ^{68}Ga-DOTA-SSA PET/CT detected more primary head and neck PGLs as well as *SDHx*-associated PGLs than ^{18}F-FDOPA PET/CT. The performances of the different imaging techniques are detailed in Table 13.1. In the context of sporadic cases, ^{68}Ga-DOTATATE and ^{18}F-FDOPA PET/CT have similar sensitivities with higher uptake values and metabolic tumor volumes with ^{68}Ga-DOTATATE compared to ^{18}F-FDOPA (Fig. 13.5).

It should be noted that SST-based imaging may be somewhat less specific than ^{18}F-FDOPA in the evaluation of these tumors and could be falsely positive in metastatic lymph nodes due to various cancers; meningiomas; other central nervous, inflammatory processes; and some rare conditions such as fibrous dysplasia [43].

Table 13.1 Comparison of different imaging techniques for the localization and staging of HNPGLs

	Sensitivity	Specificity	Locoregional staging (delineation)	Malignancy prediction	Advantages and drawbacks	Mean estimated effective dose equivalent
CT	80–90%	90%	High	Unreliable[a]	High spatial resolution Low-motion artifacts Accurately delineates temporal bone extension	3 mSv for unenhanced CT and 5 mSv for CT angiogram
MR	80–90%	90%	High	Unreliable[a]	No iodinated media No radiation exposure Accurately delineates soft tissue extension	None
PET/CT ^{18}F-FDOPA	90%	>95%	Low	Unreliable[a]	Decreased sensitivity in *SDHx*-related PGL (especially sympathetic ones) Very high sensitivity for PHEO detection	0.025 mSv/MBq for ^{18}F-FDOPA and 3 mSv for low-dose CT
PET/CT ^{18}F-FDG	60–70%	80–90%	Low	Unreliable[a]	Increased sensitivity in *SDHx* tumors[b] Accurately detects concomitant abdominal PGLs that can be missed by ^{18}F-FDOPA	0.019 mSv/Mbq for ^{18}F-FDG and 3 mSv for low-dose CT
PET/CT ^{68}Ga-DOTATATE	100%	90%	Low	Unreliable[a]	Highly sensitive in HNPGLs, regardless of genotype High TBR Extemporaneously prepared	0.021 mSv/Mbq for ^{68}Ga-DOTATATE and 3 mSv for low-dose CT

[a]In the absence of metastases, there is no reliable assessment tool for distinguishing benign from malignant PGLs
[b]Low tumor ^{18}F-FDG uptake has an excellent negative predictive value for SDHx mutations
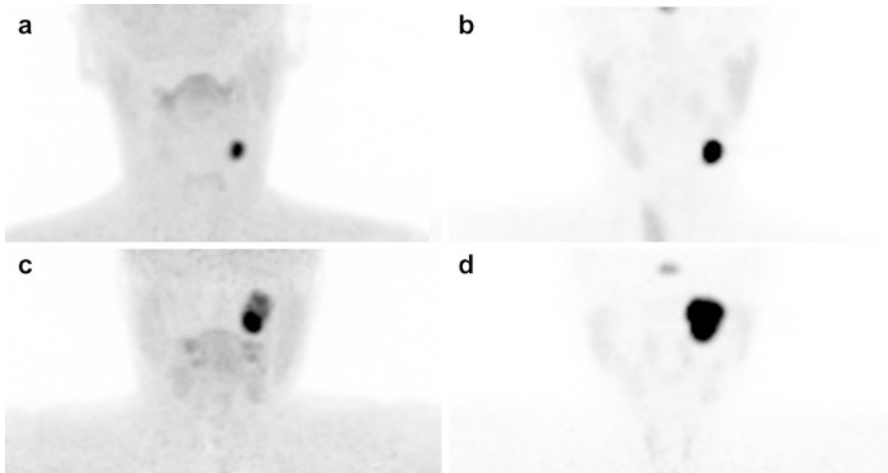
Fig. 13.5 Examples of ^{18}F-FDOPA and ^{68}Ga-DOTATATE tumor uptake patterns in sporadic HNPGLs. (**a**, **b**) Left CBP, (**c**, **d**) left jugular PGL. (**a**, **c**) ^{18}F-FDOPA PET/CT (MIP image), (**b**, **d**) ^{18}F-FDG PET/CT (MIP image)

Nevertheless, this is often not a serious issue, since HNPGLs have a specific location and exhibit highly elevated uptake values [38].

13.4.4 Presence of Germline Mutation in HNPGL Susceptibility Genes and/or Family History of PGL/ PHEOs

HNPGLs can be sporadic or can occur as components of hereditary syndromes in up to 30–40% with variable penetrance and increased risk for recurrent behavior and tumor multiplicity. Of all the known genetic mutations, mutations in *SDHD* are currently the leading cause of hereditary HNPGLs (>50%), followed by *SDHB* (20–35%) and *SDHC* (15%) mutations [44–46]. Some correlations between the gene(s) involved and tumor location have been found. *SDHD*-linked patients have a 75% risk of developing HNPGLs throughout their life, with concomitant thoracoabdominal PGLs in about 10% of cases [27]. *SDHB*-linked PGL syndrome is characterized by a high rate of retroperitoneal PGL or HNPGLs, but a combination of sympathetic and parasympathetic PGLs is found less frequently [27]. Furthermore, it should be noted that multiple PGLs at a very young age found in several family members may be related to *SDHAF2* mutations [47]. So far, only HNPGLs have been reported in these rare families. The inheritance pattern of the *SDHB* and *SDHC* genes is autosomal dominant, whereas for *SDHD* and *SDHAF2* genes, the disease occurs only when the mutations are inherited from the father, which is consistent with maternal imprinting [48]. Until present, mutations in *SDHA* have been described in several isolated cases. Major predictors for hereditary HNPGLs are a

family history of PGL (especially those related to *SDHD* mutations), a previous personal history of HNPGLs or sympathetic PGL, and multifocality or a characteristic syndromic presentation [5, 46]. Currently, a well-characterized syndromic presentation includes the existence of other tumor types associated with the presence of a PGL (e.g., renal cell carcinoma, gastrointestinal stromal tumor, and pituitary adenomas can also be related to *SDHx* mutations) [49, 50].

Imaging phenotypes may vary across genotypes. Although ^{18}F-FDG is not specific, this imaging modality has clearly shown a higher sensitivity over CT/MRI, [123/131]I-MIBG, ^{18}F-FDA, and ^{18}F-FDOPA [32, 51, 52]. More recently, ^{68}Ga-DOTATATE PET/CT detected more *SDHx*-associated PGLs than ^{18}F-FDOPA PET/CT [39–41, 43]. It is expected that ^{68}Ga-DOTA-SSA PET/CT will become the preferred functional imaging modality for HNPGLs in the near future.

13.4.5   Differential Diagnosis

There are several potential causes to consider in the differential diagnosis (Tables 13.2 and 13.3).

13.5   Role of Imaging and Clinical Impact

The aim of pre-therapeutic imaging is to provide the most complete staging of the disease. In this way, treatment can be tailored to each specific situation. The initial staging of a HNPGL is currently based on the use of anatomical and functional imaging approaches in order to determine the tumor extension into the bone and surrounding soft tissue; to determine tumor multiplicity, not only in the head and neck area but elsewhere in the body; and finally to exclude any metastases.

13.5.1   Detection of Multifocal/Metastatic Disease

To determine whether additional HNPGLs are present, MRI is inferior to ^{18}F-FDOPA PET/CT and ^{68}Ga-DOTA-SSA. Therefore, it is currently recommended that all patients with HNPGLs, especially *SDHx* mutation carriers, be assessed by ^{68}Ga-DOTA-SSA PET/CT. Although both functional imaging modalities are relatively new and more studies are needed, the published results are strongly supportive [33–35, 39, 41, 43, 53] (Figs. 13.6 and 13.7). In absence of available ^{68}Ga-DOTA-SSA, a combination of ^{18}F-FDOPA and ^{18}F-FDG PET/CT is recommended, especially for patients with multifocal tumors [29, 54] (Fig. 13.8). One of the main drawbacks of ^{68}Ga-DOTA-SSA is the very high physiological uptake by healthy adrenal glands [55]. This could be a critical problem for detecting small PHEOs in hereditary syndromes.

Table 13.2 Classification of HNPGLs and their main clinical and radiological differential diagnoses

Type	Differential diagnoses
Jugular PGL	Schwannoma
	Neurofibroma
	Meningioma
	Carcinoma (primary and metastatic) and tumor extension from nasopharyngeal carcinoma
	Angiosarcoma and chondrosarcoma
	Plasmacytoma, hemangiopericytoma
	Endolymphatic sac tumor
	Miscellaneous lesions (i.e., internal jugular vein thrombosis, Langerhans cell histiocytosis)
Tympanic PGL	Middle ear adenoma (carcinoid)
	Meningioma
	Hemangioma of geniculate ganglion
	Schwannoma
	Neurofibroma
	Miscellaneous lesions (i.e., aberrant internal carotid artery, mega bulb jugular, dehiscent jugular bulb, Langerhans cell histiocytosis)
Vagal PGL	Schwannoma
	Neurofibroma
	Lymph node metastasis (nasopharynx/oropharynx, thyroid cancer)
	Lymphoma
	Ganglioneuroma
	Hemangiopericytoma
	Miscellaneous lesions (i.e., abscess, internal carotid artery aneurysm, internal jugular vein thrombosis, vascular malposition, organizing hematoma)
Carotid body PGL	Carotid artery aneurysm
	Vasculitis of the carotid artery
	Lymphadenopathy
	Schwannoma
	Neurofibroma
	Branchial cleft cyst
	Accessory thyroid gland

Although rare, malignancy often requires dramatically different patient management. When metastases are present, the goal of imaging is to precisely assess the anatomy of these tumors in order to carefully select patients who could benefit from aggressive but complete surgical resection with the intent to cure as opposed to "debulking" strategies [56]. To this end, ^{68}Ga-DOTA-SSA is superior to ^{18}F-FDG PET/CT and ^{18}F-FDOPA PET/CT in *SDHB* patients [40] (Figs. 13.9 and 13.10).

13.5.2 Assessment of Locoregional Extension

Anatomic imaging serves as the first-line modality in the locoregional staging of these tumors. CT offers several advantages over MRI (e.g., better spatial resolution and less motion artifacts) and enables better evaluation of the temporal bone extension of JP and TP. MRI provides better soft tissue contrast than CT, and thus, it

Table 13.3 Differential diagnosis of post-styloid retropharyngeal masses: imaging features on MRI and molecular imaging

	Paraganglioma	Nodal metastasis	Schwannoma	Neurofibroma
MRI	Numerous arterial feeders Spin echo: flow void ("salt and pepper" appearance on T1- and T2-weighted images) TOF: hyperintense vessels within the lesion 3D (or 4D) gadolinium angiograms: avid enhancement	Variable appearance Well-defined margins Moderate signal in T2 Restricted diffusion Heterogeneous enhancement usual	Well-defined margins Moderate to high signal intensity on T2 No restriction of diffusion Heterogeneous enhancement seen in large tumors with degenerative changes (cystic, pseudocystic)	IDEM schwannoma Central low signal on T2 may be seen ("target sign")
PET/CT ^{18}F-FDG	Moderate to high uptake (highly elevated in SDHx)	Low to high uptake depending on the primary tumor	Low to high uptake (even in benign cases)	Low uptake (high uptake values in malignant forms)
PET/CT ^{18}F-FDOPA	High uptake	No significant uptake	No significant uptake	No significant uptake
PET/CT ^{68}Ga-SSA	High uptake	No significant uptake (possible high uptake in nodal metastases from thyroid cancers or nasopharyngeal cancers)	No significant uptake	No significant uptake

offers unique information for tumor delineation. MRI is also preferred if radiotherapy or stereotactic radiosurgery (SRS) is considered. Several classifications (i.e., Fisch and Mattox's or Glasscock and Jackson's for TP and JP, Netterville's for VP, Shamblin's for CBP) help predict surgical outcome and should be used in the evaluation of these patients [57–60] (Table 13.4, Figs. 13.11 and 13.12).

13.5.3 Tumor Characterization

Beyond its localization value, radionuclide imaging provides unique opportunities for characterizing these tumors at molecular levels (e.g., catecholamine synthesis, specific receptor and transporter expression) and mirroring ex vivo histological classification on a whole-body, *in vivo*, scale [61]. This opportunity has more recently
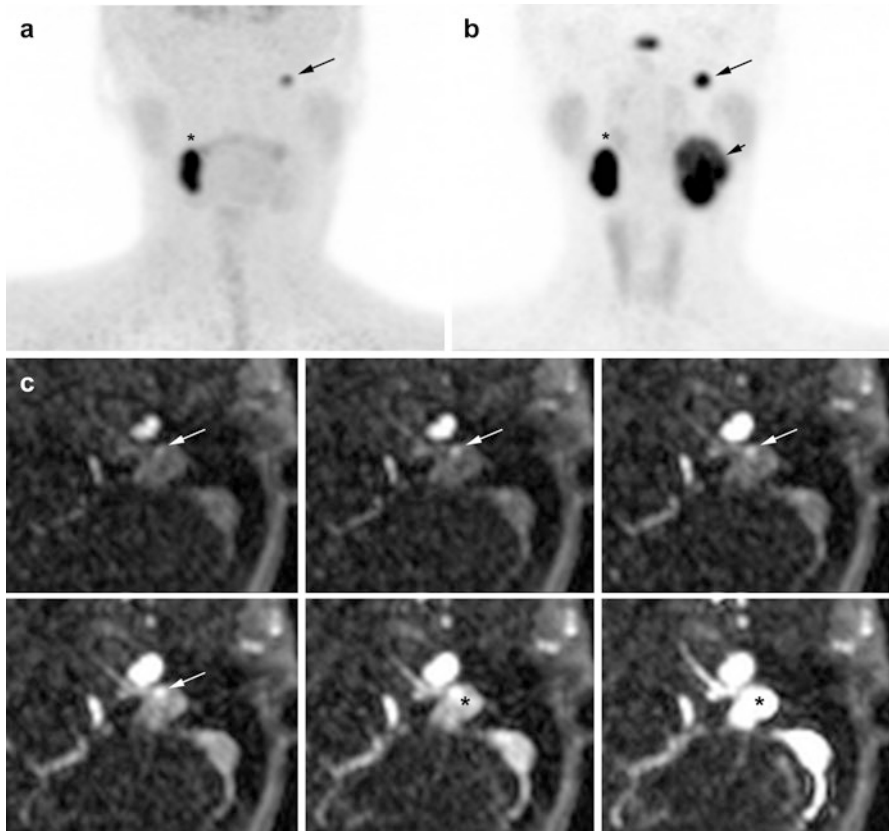
Fig. 13.6 Superiority of ^{68}Ga-DOTATATE to ^{18}F-FDOPA PET/CT and MRI in an *SDHD* patient. (**a**) ^{18}F-FDOPA PET (MIP) missed the large left VP (*long arrow*). (**b**) ^{68}Ga-DOTATATE (maximal intensity projection (MIP)) showing three PGLs (right VP = *asterisk*, left VP = *small arrow*, left JP = *long arrow*). (**c**) Contrast-enhanced time-resolved 4D MRA at 3 tesla showing a small nodule located in the wall of the jugular bulb with an early arterial enhancement (*white arrow*), prior to jugular vein and sigmoid sinus lumen contrast media injection filling (*). This lesion was detected only upon knowledge of the PET results

been augmented by a number of excellent radiopharmaceuticals, which target different functional and molecular pathways that often reflect the diverse genetic landscape of PGL. Based on these characteristics, nuclear imaging provides a means of linking imaging phenotype to genotype and can be considered a member of the multi-omics approach. For example, an intense ^{18}F-FDG uptake by a PGL is mostly associated with mutations involving one of the genes encoding the succinate dehydrogenase (*SDH*) complex. Conversely, a low uptake can often rule out a classic SDH deficiency linked to *SDH* mutations [62]. The ^{18}F-FDG uptake pattern *SDHx* PGLs reflects metabolic reprogramming, a hypermethylator phenotype, and abnormal mitochondrial respiratory function [63] and is predominantly linked with high succinate metabolomic pattern [64–66]. Such tumors are classified as exhibiting "pseudohypoxia" [67]. There are further differences based on the site of origin.
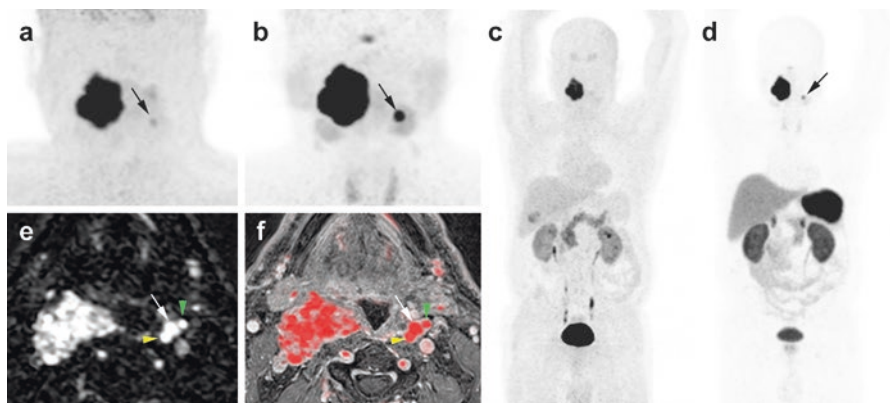
Fig. 13.7 Superiority of ^{68}Ga-DOTATATE to ^{18}F-FDOPA PET/CT and MRI in an *SDHD* patient. Multicentric *SDHD*-related PGL syndrome. (**a**) Craniocervical ^{18}F-FDOPA PET image (MIP) showing the two lesions but was slightly positive on the left side (*arrow*). (**b**) Craniocervical ^{68}Ga-DOTATATE image (MIP) showing two VP. (**c**) WB ^{18}F-FDOPA PET (MIP) which failed to demonstrate the left VP. (**d**) WB ^{68}Ga-DOTATATE (MIP) image showing the known two lesions. (**e**) Early arterial phase of contrast-enhanced time-resolved 4D MRA at 3 tesla. (**f**) 4D MRA fused with 3D gadolinium-enhanced sequences T1 fat-saturated post-gadolinium (3D VIBE) image. Both images show the early arterial enhancement pattern of the two VPs (*white arrows* showing the left VP). Note the discrete splaying between internal carotid artery (*yellow arrowhead*) and external carotid artery (*green arrowhead*)

More recently, MR spectroscopy (MRS) was found to be a valuable tool for *in vivo* quantifying metabolic abnormalities associated to cancer. Technical developments including high and ultrahigh field are providing increased sensitivity and specificity for probing *in vivo* tissue metabolites. *In vivo* proton MRS has shown promising results for characterizing PGLs/PHEOs with detection of succinate and other metabolites in *SDHx*-related PGLs [67, 68]. There are some specific technical difficulties for imaging of HNPGLs since they are located in very challenging regions for MRS (with the bone, lipids, air) making difficult the automatic shim procedures. Furthermore, tumor volumes may be small, and MRS requires a number of acquisitions to get an acceptable signal-to-noise ratio without any motion. It is proposed to get raw data before summation to be able to correct any phase or frequency shift induced by weak motion and to exclude useless spectra due to significant motion. Automatic procedures are available for this purpose by using the water signal as a reference.

13.5.4   *Clinical Impact*

The clinical impact of detecting additional PGL is multiple.

(i) Complete surgical resection is curative for patients with HNPGLs. However, for many tumors, e.g., large and locally advanced JPs, complete resection is
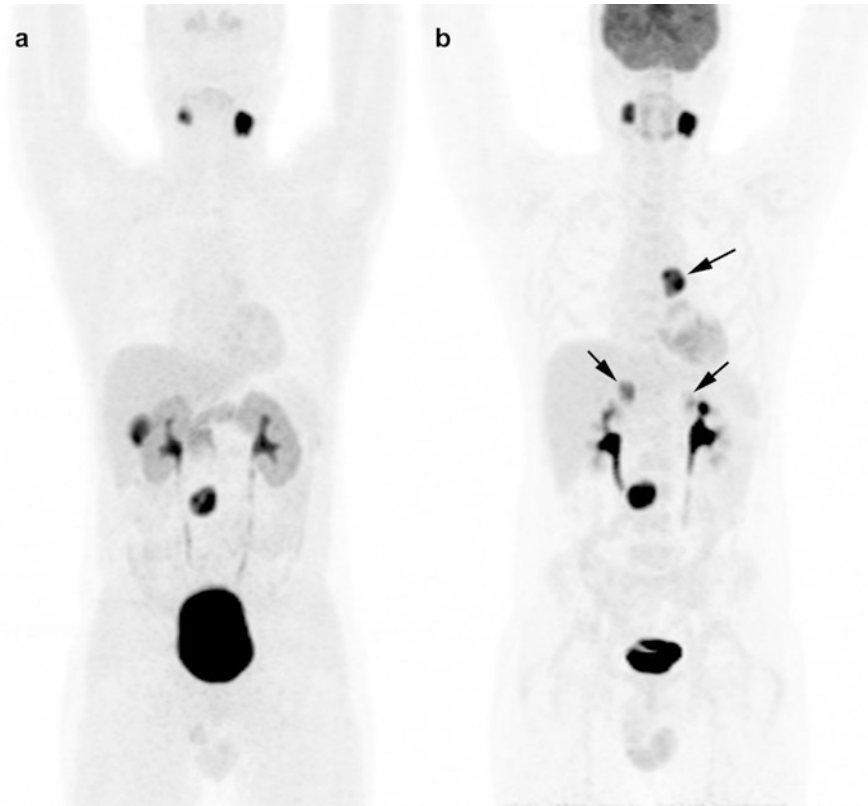
Fig. 13.8 Superiority of ^{18}F-FDG PET/CT to ^{18}F-FDOPA PET/CT in the detection of additional PGL of sympathetic origin in an *SDHD* patient. (**a**) ^{18}F-FDOPA PET/CT (MIP image), (**b**) ^{18}F-FDG PET/CT (MIP image). *Arrows* mark the false-negative ^{18}F-FDOPA tumors

    inadvisable due to their specific anatomical location. It is expected that early detection of JP with functional imaging may minimize complications related to mass effect and facilitate curative treatment of these tumors.

(ii) For tumors that are good candidates for tumor resection, lower cranial nerve injury represents a major risk in the surgical resection of HNPGLs—up to 20 % for CBP (especially for Shamblin class III) and quasi 100 % for VP. In patients with an apparently single tumor, cranial nerve palsy may significantly compromise additional surgery to the contralateral side. Therefore, identification of an additional tiny tumor may change the management strategy from surgery to follow-up or radiation therapy.

(iii) It is widely accepted that tumors with an underlying *SDHB* mutation are associated with a higher risk of aggressive behavior. It is therefore expected that the early detection and treatment of *SDHB*-related tumors may potentially reduce the occurrence of metastases.

(iv) Detection of these lesions by functional imaging facilitates their evaluation by anatomical imaging and subsequent follow-up.
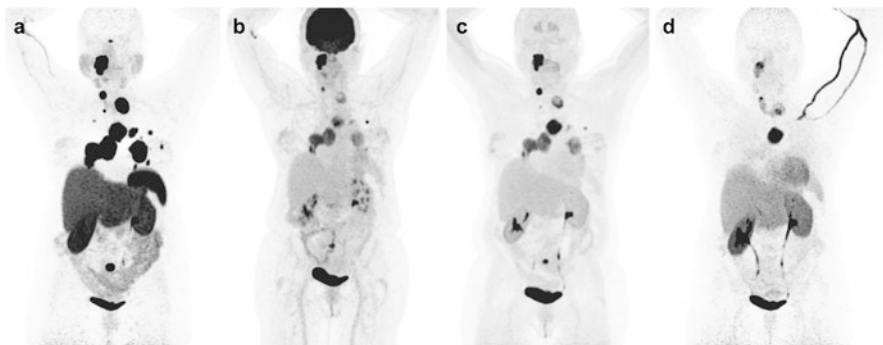
Fig. 13.9 Superiority of ^{68}Ga-DOTATATE to other molecular imaging modalities in *SDHB*-related metastatic HNPGL. Imaging of metastatic head and neck PGL with ^{68}Ga-DOTATATE (**a**), ^{18}F-FDG (**b**), ^{18}F-FDOPA (**c**), and ^{18}F-FDA PET/CT (**d**) in a 63-year-old female patient with *SDHB* mutation. First diagnosed with CB tumor on the right side at the age of 27. Recurrence of CB tumor as well as glomus vagale tumor and diagnosis of metastatic disease to the neck, mediastinum, lungs, and bones at the age of 49
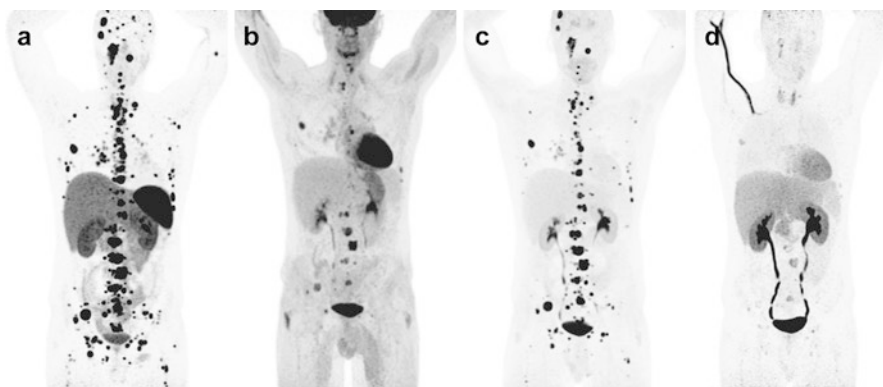
Fig. 13.10 Superiority of ^{68}Ga-DOTATATE to other molecular imaging modalities in *SDHB*-related metastatic HNPGL. Imaging of metastatic head and neck PGL with ^{68}Ga-DOTATATE (**a**), ^{18}F-FDG (**b**), ^{18}F-FDOPA (**c**), and ^{18}F-FDA PET/CT (**d**) in a 36-year-old male patient with *SDHB* mutation, first diagnosed with a paraganglioma of the right foramen jugulare at the age of 19 with partial resection. First diagnosis of widespread bone metastatic disease in 2012

(v) Functional imaging also enables the localization of extra-cervical PGLs/
    PHEOs that could justify surgery prior to the management of HNPGLs.

13.5.5 Imaging Follow-Up of Mutation Carriers

Mutation carriers, especially those with *SDHD* mutations, may develop asymptomatic HNPGLs during their lifespan [69]. The penetrance of *SDHD*-related PGLs is modulated by genomic imprinting, resulting in an almost complete absence of

Table 13.4 Classifications of HNPGLs

Shamblin's	Carotid body PGL	I: Splaying of the carotid bifurcation with little attachment to the carotid vessels	II: Partial involvement of the carotid vessels	III: Complete involvement of the carotid vessels
Netterville's	Vagal PGL	A: Confined to the neck	B: In contact with the jugular foramen	C: Extended into or beyond the jugular foramen with or without intracranial extension
Fisch and Mattox's	Tympanic PGL	A: Limited to the middle ear cleft	B: Limited to the tympanomastoid compartment	
	Jugular PGL	C1: Located in the jugular foramen, erosion of the carotid foramen	C2: Vertical segment of the carotid canal involved C3: Horizontal segment of the carotid canal involved C4: Foramen lacerum and cavernous sinus involved	De: Intracranial extradural extension (De$_{1/2}$ depending on the displacement of the dura) Di: Intracranial intradural extension (Di$_{1/2/3}$ depending on the depth of invasion into the posterior cranial fossa)

disease following maternal transmission [48]. Paternal transmission is associated with incomplete penetrance (43–100%) [27, 69, 70]. In contrast to *SDHD*, *SDHB* mutations are responsible for a lower risk of asymptomatic PGLs in mutation carriers, consistent with a lower penetrance of the disease [71].

The optimal follow-up algorithm has not yet been validated in hereditary HNPGLs but most likely requires a more frequent and complete imaging workup than for their sporadic counterparts. MRI offers several physical advantages over CT and does not expose patients to ionizing radiation, which is critical in a patient population submitted to lifelong imaging surveillance. Follow-up should include annual biochemical screening, and MRI can be delayed to 3-year intervals. Indications for PET imaging studies should be discussed on an individual basis [72].

13.5.6 *Current Proposed Imaging Algorithm in the Diagnosis and Localization of HNPGLs*

Based on the currently available imaging techniques for the diagnosis and staging of PGLs, we propose the following approach to investigate a patient with HNPGL:
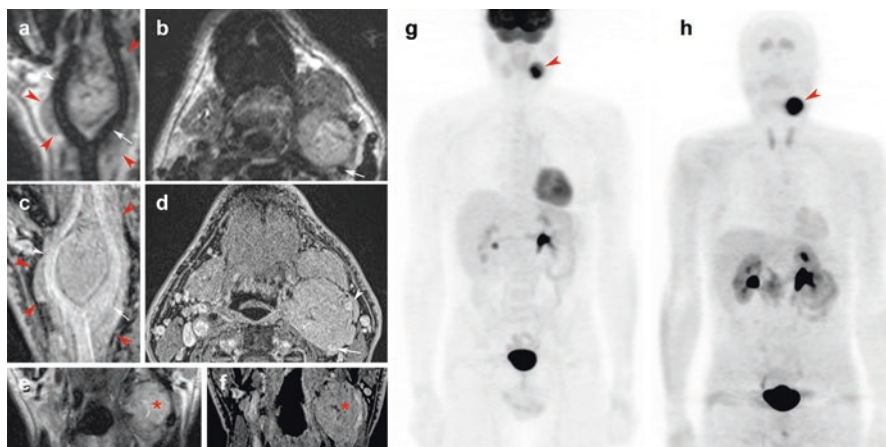
Fig. 13.11 Shamblin III carotid body PGL. T2-weighted 3D fast spin echo imaging sagittal (**a**), axial (**b**), and coronal (**e**) reconstructions; 3D volumetric fat-saturated (FATSAT) T1 weighted (VIBE) with gadolinium in sagittal (**c**), axial (**d**), and coronal (**e**) reconstructions; ^{18}F-FDG PET/CT (maximal intensity projection (MIP)) (**g**) and ^{18}F-FDOPA PET/CT (MIP) (**h**). MRI shows a "lyre sign" related to a 5-cm left carotid body PGL (*red arrowheads*) arising from the carotid bifurcation, splaying the internal carotid artery (ICE) (**a–e**, *white arrows*) and external carotid artery (ECA) (**a–d**, *white arrowheads*). Note small central necrosis in the tumor (**e**, **f**, *red asterisk*) and the lack of flow voids due to high temporal resolution of 3D sequences, especially for high-field MRI. 3D reconstructions demonstrate 360° carotid invasion along the common carotid, ICA, and ECA. ^{18}F-FDG PET/CT and ^{18}F-FDOPA PET/CT show a single highly avid carotid body PGL

(i) For diagnosis, the specificity provided by functional imaging techniques using ^{18}F-FDOPA PET/CT or ^{68}Ga-DOTA-SSA is superior to anatomical imaging.

(ii) For detecting additional tumor sites (multifocality, metastases), functional imaging techniques are superior to anatomical imaging. Based on the most recent studies, both *SDHx* and non-*SDHx* HNPGLs are well detected by ^{18}F-FDOPA PET/CT and ^{68}Ga-DOTA-SSA. PHEOs are better visualized by ^{18}F-FDOPA PET/CT.

(iii) For determining the locoregional extension of HNPGLs, anatomic imaging modalities remain the first-line modalities. Temporal bone extension of TPs and JPs is better evaluated by CT, while MRI enables a better evaluation of soft tissue extension.

(iv) This algorithm should be adapted to the practical situation within each institution and should evolve with time as new techniques become available.

13.5.7 Imaging-Based Therapeutic Radiation

Nowadays, radiotherapy has gained precision with the integration of modern imaging leading to a reduced and more accurate treated volume, thereby decreasing the likelihood of complications within surrounding normal tissues. The way photons
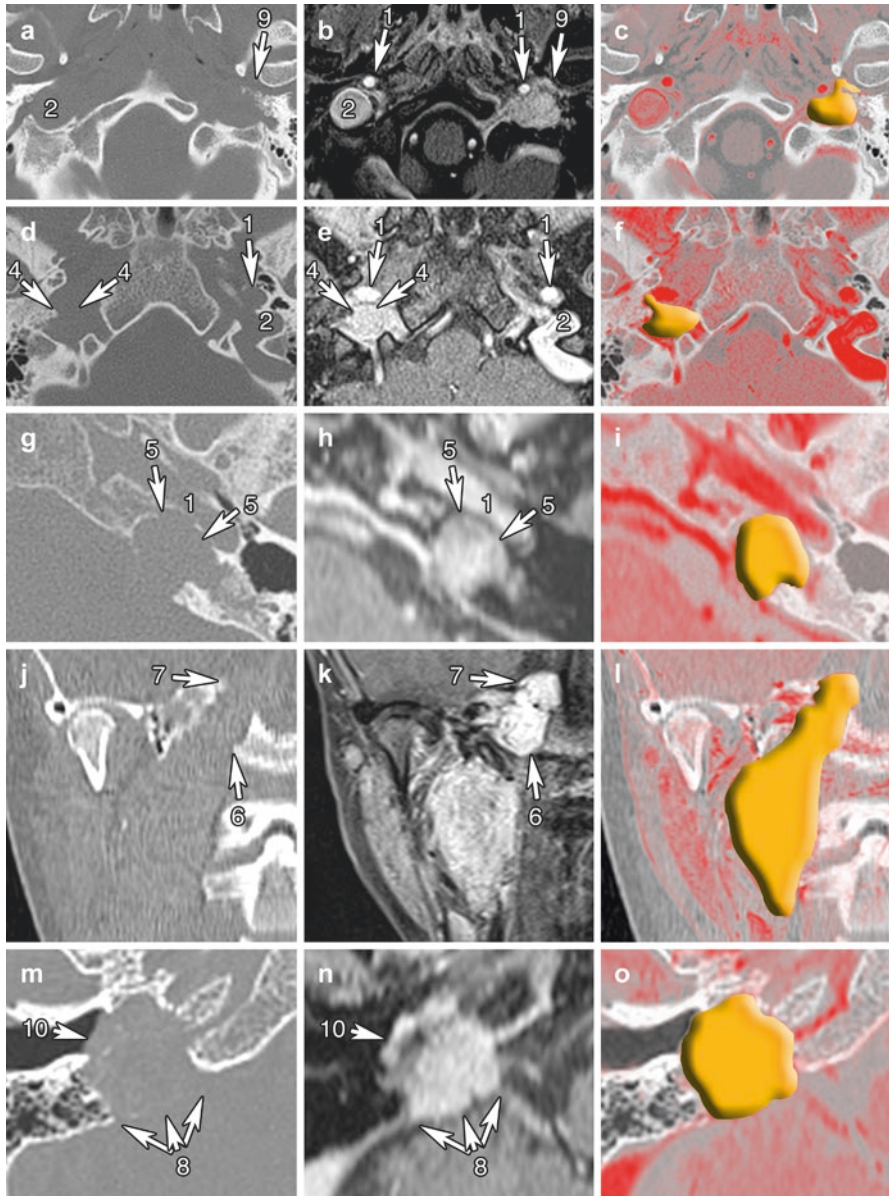
Fig. 13.12 Tumor extension of jugular PGL. Examples in several patients with jugular paragangliomas of FISCH C1 (**a–c**), C2 (**d–f**), C3 (**g–i**), C4 (**j–l**), De (**m–o**). Co-registered axial planes in CT (**a**, **d**, **g**, **j**, **m**), 3D T1 weighted with fat saturation with gadolinium (**b**, **e**, **h**, **k**, **n**), and fused modalities with drawn layer of paraganglioma in orange (**c**, **f**, **i**, **l**, **o**). *1* Internal carotid artery, *2* Jugular foramen, *3* Erosion of the carotid foramen, *4* Vertical segment of the carotid canal involved, *5* Horizontal segment of the carotid canal involved, *6* Foramen lacerum involved, *7* Cavernous sinus involved, *8* Intracranial extradural extension, *9* Temporomandibular joint involved (miscellaneous), *10* Direct extend to middle ear (miscellaneous)

are delivered within defined target volumes also radically evolved through other technological breakthroughs (intensity-modulated radiation therapy, image-guided radiation therapy, volumetric modulated arc therapy) further enhanced conformality and dramatically decreased treatment time [73, 74]. Radiosurgery (RS or SRS for stereotactic radiosurgery) is the most spatially precise form of therapeutic radiation. This attribute, when combined with the steepest possible surrounding dose gradient, enables the procedure to be most typically administered in a single outpatient session lasting less than 1 h. There are three major types of radiosurgical instruments. The oldest radiosurgical method, the Gamma Knife, utilizes a frame affixed to the skull for target localization and patient immobilization (Gamma Knife®) [75]. More recently, image-guided targeting technology has enabled a noninvasive "frameless" approach to precision targeting of radiosurgery. The pioneer in image-guided radiosurgery, the CyberKnife, utilizes real-time dual projection X-ray correlation to a pre-SRS CT [76–80]. Meanwhile modified conventional medical linear accelerators have recently demonstrated the capacity to administer highly accurate therapeutic radiation by using a pretreatment cone beam CT (such as the TrueBeam STx® series) for a patient positioning [81, 82]. By combining targeting accuracy with the steepest possible dose gradients, the above technologies have together made ablative radiosurgery readily available throughout much of the world.

Delineation of biological tumor volume of tumors may be challenging, especially after surgery. The use of PET imaging using specific tracers and optimal segmentation methods might help modify the extent of biological tumor volumes for radiotherapy planning purposes.

It is also expected that the use of specific radiopharmaceuticals in advanced PET/MRI integrated systems might also improve delineation of tumor residual masses [54].

13.6 Theranostic Approaches

The term theranostics epitomizes the inseparability of diagnosis and therapy, the pillars of medicine. In the context of nuclear medicine, it refers to the use of molecular targeting vectors (e.g., peptides) labeled either with diagnostic radionuclides (e.g., positron or gamma emitters) or with therapeutic radionuclides. For the time being, one of the most studied examples is the coupling of ^{68}Ga-DOTATATE and ^{177}Lu-DOTATATE with very promising results in the setting of neuroendocrine tumors. ^{177}Lu-DOTATATE will also be rapidly implemented into the therapeutic arsenal for HNPGLs [83], especially inoperable HNPGLs and metastatic PGLs. Recent reports have shown that cellular internalization might shorten the residual time of ^{177}Lu within tumor cells compared to radiolabeled SST antagonists. SST antagonists also have higher affinities for SST receptors than agonists and lower internalization rates resulting in a longer retention time on cell membrane. According to these observations, it is possible that SST antagonists may be considered as the next step for peptide-based internal radiotherapy with a highly elevated tumor-background uptake ratio.

References

1. Mannelli M, Castellano M, Schiavi F, Filetti S, Giacche M, Mori L, et al. Clinically guided genetic screening in a large cohort of italian patients with pheochromocytomas and/or functional or nonfunctional paragangliomas. J Clin Endocrinol Metab. 2009;94:1541–7. doi:jc.2008-2419 [pii] 10.1210/jc.2008-2419.

2. Sykes JM, Ossoff RH. Paragangliomas of the head and neck. Otolaryngol Clin North Am. 1986;19:755–67.

3. Erickson D, Kudva YC, Ebersold MJ, Thompson GB, Grant CS, van Heerden JA, et al. Benign paragangliomas: clinical presentation and treatment outcomes in 236 patients. J Clin Endocrinol Metabol. 2001;86:5210–6.

4. Lee JH, Barich F, Karnell LH, Robinson RA, Zhen WK, Gantz BJ, et al. National Cancer Data Base report on malignant paragangliomas of the head and neck. Cancer. 2002;94:730–7.

5. Jafri M, Whitworth J, Rattenberry E, Vialard L, Kilby G, Kumar AV, et al. Evaluation of SDHB, SDHD and VHL gene susceptibility testing in the assessment of individuals with non-syndromic phaeochromocytoma, paraganglioma and head and neck paraganglioma. Clin Endocrinol (Oxf). 2013;78:898–906. doi:10.1111/cen.12074.

6. Gimenez-Roqueplo AP, Dahia PL, Robledo M. An update on the genetics of paraganglioma, pheochromocytoma, and associated hereditary syndromes. Horm Metab Res. 2012;44(5):328–33.

7. Langerman A, Athavale SM, Rangarajan SV, Sinard RJ, Netterville JL. Natural history of cervical paragangliomas: outcomes of observation of 43 patients. Arch Otolaryngol Head Neck Surg. 2012;138:341–5. doi:10.1001/archoto.2012.37.

8. le Douarin N, Kalcheim C. The neural crest. 2nd ed. Cambridge: Cambridge University Press; 1999.

9. Unsicker K, Huber K, Schober A, Kalcheim C. Resolved and open issues in chromaffin cell development. Mech Dev. 2013;130:324–9. doi:10.1016/j.mod.2012.11.004.

10. Platero-Luengo A, Gonzalez-Granero S, Duran R, Diaz-Castro B, Piruat JI, Garcia-Verdugo JM, et al. An O2-sensitive glomus cell-stem cell synapse induces carotid body growth in chronic hypoxia. Cell. 2014;156:291–303. doi:10.1016/j.cell.2013.12.013.

11. Eisenhofer G, Lenders JW, Siegert G, Bornstein SR, Friberg P, Milosevic D, et al. Plasma methoxytyramine: a novel biomarker of metastatic pheochromocytoma and paraganglioma in relation to established risk factors of tumour size, location and SDHB mutation status. Eur J Cancer. 2012;48:1739–49. doi:10.1016/j.ejca.2011.07.016.

12. van Duinen N, Steenvoorden D, Kema IP, Jansen JC, Vriends AH, Bayley JP, et al. Increased urinary excretion of 3-methoxytyramine in patients with head and neck paragangliomas. J Clin Endocrinol Metab. 2010;95:209–14. doi:10.1210/jc.2009-1632.

13. van Duinen N, Corssmit EP, de Jong WH, Brookman D, Kema IP, Romijn JA. Plasma levels of free metanephrines and 3-methoxytyramine indicate a higher number of biochemically active HNPGL than 24-h urinary excretion rates of catecholamines and metabolites. Eur J Endocrinol. 2013;169:377–82. doi:10.1530/EJE-13-0529.

14. Lenders JW, Duh QY, Eisenhofer G, Gimenez-Roqueplo AP, Grebe SK, Murad MH, et al. Pheochromocytoma and paraganglioma: an endocrine society clinical practice guideline. J Clin Endocrinol Metab. 2014;99:1915–42. doi:10.1210/jc.2014-1498.

15. Johnson MH. Head and neck vascular anatomy. Neuroimaging Clin N Am. 1998;8:119–41.

16. van den Berg R, Schepers A, de Bruine FT, Liauw L, Mertens BJ, van der Mey AG, et al. The value of MR angiography techniques in the detection of head and neck paragangliomas. Eur J Radiol. 2004;52:240–5. doi:10.1016/j.ejrad.2003.12.002.

17. Neves F, Huwart L, Jourdan G, Reizine D, Herman P, Vicaut E, et al. Head and neck paragangliomas: value of contrast-enhanced 3D MR angiography. AJNR Am J Neuroradiol. 2008;29:883–9. doi:10.3174/ajnr.A0948.

18. van den Berg R. Imaging and management of head and neck paragangliomas. Eur Radiol. 2005;15:1310–8. doi:10.1007/s00330-005-2743-8.

19. Arnold SM, Strecker R, Scheffler K, Spreer J, Schipper J, Neumann HP, et al. Dynamic contrast enhancement of paragangliomas of the head and neck: evaluation with time-resolved 2D MR projection angiography. Eur Radiol. 2003;13:1608–11. doi:10.1007/s00330-002-1717-3.

20. Dong Y, Liu Q. Differentiation of malignant from benign pheochromocytomas with diffusion-weighted and dynamic contrast-enhanced magnetic resonance at 3.0 T. J Comput Assist Tomogr. 2012;36:361–6. doi:10.1097/RCT.0b013e31825975f8.

21. Bustillo A, Telischi F, Weed D, Civantos F, Angeli S, Serafini A, et al. Octreotide scintigraphy in the head and neck. Laryngoscope. 2004;114:434–40.

22. Duet M, Sauvaget E, Petelle B, Rizzo N, Guichard JP, Wassef M, et al. Clinical impact of somatostatin receptor scintigraphy in the management of paragangliomas of the head and neck. J Nucl Med. 2003;44:1767–74.

23. Koopmans KP, Jager PL, Kema IP, Kerstens MN, Albers F, Dullaart RP. 111In-octreotide is superior to 123I-metaiodobenzylguanidine for scintigraphic detection of head and neck paragangliomas. J Nucl Med. 2008;49:1232–7.

24. Muros MA, Llamas-Elvira JM, Rodriguez A, Ramirez A, Gomez M, Arraez MA, et al. 111In-pentetreotide scintigraphy is superior to 123I-MIBG scintigraphy in the diagnosis and location of chemodectoma. Nucl Med Commun. 1998;19:735–42.

25. Schmidt M, Fischer E, Dietlein M, Michel O, Weber K, Moka D, et al. Clinical value of somatostatin receptor imaging in patients with suspected head and neck paragangliomas. Eur J Nucl Med Mol Imaging. 2002;29:1571–80.

26. Telischi FF, Bustillo A, Whiteman ML, Serafini AN, Reisberg MJ, Gomez-Marin O, et al. Octreotide scintigraphy for the detection of paragangliomas. Otolaryngol Head Neck Surg. 2000;122:358–62.

27. Gimenez-Roqueplo AP, Caumont-Prim A, Houzard C, Hignette C, Hernigou A, Halimi P, et al. Imaging work-up for screening of paraganglioma and pheochromocytoma in SDHx mutation carriers: a multicenter prospective study from the PGL.EVA Investigators. J Clin Endocrinol Metab. 2013;98:E162–73. doi:10.1210/jc.2012-2975.

28. Charrier N, Deveze A, Fakhry N, Sebag F, Morange I, Gaborit B, et al. Comparison of [(1)(1)(1)In]pentetreotide-SPECT and [(1)F]FDOPA-PET in the localization of extra-adrenal paragangliomas: the case for a patient-tailored use of nuclear imaging modalities. Clin Endocrinol (Oxf). 2011;74:21–9. doi:10.1111/j.1365-2265.2010.03893.x.

29. Gabriel S, Blanchet EM, Sebag F, Chen CC, Fakhry N, Deveze A, et al. Functional characterization of nonmetastatic paraganglioma and pheochromocytoma by (18) F-FDOPA PET: focus on missed lesions. Clin Endocrinol (Oxf). 2013;79:170–7. doi:10.1111/cen.12126.

30. King KS, Chen CC, Alexopoulos DK, Whatley MA, Reynolds JC, Patronas N, et al. Functional imaging of SDHx-related head and neck paragangliomas: comparison of 18F-fluorodihydroxyphenylalanine, 18F-fluorodopamine, 18F-fluoro-2-deoxy-D-glucose PET, 123I-metaiodobenzylguanidine scintigraphy, and 111In-pentetreotide scintigraphy. J Clin Endocrinol Metab. 2011;96:2779–85. doi:10.1210/jc.2011-0333.

31. Miederer M, Fottner C, Rossmann H, Helisch A, Papaspyrou K, Bartsch O, et al. High incidence of extraadrenal paraganglioma in families with SDHx syndromes detected by functional imaging with [18F]fluorodihydroxyphenylalanine PET. Eur J Nucl Med Mol Imaging. 2013;40:889–96. doi:10.1007/s00259-013-2346-6.

32. Timmers HJ, Chen CC, Carrasquillo JA, Whatley M, Ling A, Havekes B, et al. Comparison of 18F-Fluoro-L-DOPA, 18F-Fluoro-Deoxyglucose, and 18F-Fluorodopamine PET and 123I-MIBG Scintigraphy in the Localization of Pheochromocytoma and Paraganglioma. J Clin Endocrinol Metabol. 2009;94:4757–67.

33. Naji M, Al-Nahhas A. (68)Ga-labelled peptides in the management of neuroectodermal tumours. Eur J Nucl Med Mol Imaging. 2012;39 Suppl 1:61–7. doi:10.1007/s00259-011-1990-y.

34. Naji M, Zhao C, Welsh SJ, Meades R, Win Z, Ferrarese A, et al. 68Ga-DOTA-TATE PET vs. 123I-MIBG in identifying malignant neural crest tumours. Mol Imaging Biol. 2011;13:769–75. doi:10.1007/s11307-010-0396-8.

35. Sharma P, Thakar A, Suman Kc S, Dhull VS, Singh H, Naswa N, et al. 68Ga-DOTANOC PET/CT for baseline evaluation of patients with head and neck paraganglioma. J Nucl Med. 2013;54:841–7. doi:10.2967/jnumed.112.115485.

36. Kroiss A, Shulkin BL, Uprimny C, Frech A, Gasser RW, Url C, et al. (68)Ga-DOTATOC PET/CT provides accurate tumour extent in patients with extraadrenal paraganglioma compared to (123)I-MIBG SPECT/CT. Eur J Nucl Med Mol Imaging. 2015;42:33–41. doi:10.1007/s00259-014-2892-6.

37. Sharma P, Mukherjee A, Karunanithi S, Naswa N, Kumar R, Ammini AC, et al. Accuracy of 68Ga DOTANOC PET/CT imaging in patients with multiple endocrine neoplasia syndromes. Clin Nucl Med. 2015;40:e351–6. doi:10.1097/RLU.0000000000000775.

38. Hofman MS, Lau WF, Hicks RJ. Somatostatin receptor imaging with 68Ga DOTATATE PET/CT: clinical utility, normal patterns, pearls, and pitfalls in interpretation. Radiographics. 2015;35:500–16. doi:10.1148/rg.352140164.

39. Kroiss A, Putzer D, Frech A, Decristoforo C, Uprimny C, Gasser RW, et al. A retrospective comparison between (68)Ga-DOTA-TOC PET/CT and (18)F-DOPA PET/CT in patients with extra-adrenal paraganglioma. Eur J Nucl Med Mol Imaging. 2013;40:1800–8. doi:10.1007/s00259-013-2548-y.

40. Janssen I, Blanchet EM, Adams K, Chen CC, Millo CM, Herscovitch P, et al. Superiority of [68Ga]-DOTATATE PET/CT to other functional imaging modalities in the localization of SDHB-associated metastatic pheochromocytoma and paraganglioma. Clin Cancer Res. 2015;21:3888–95. doi:10.1158/1078-0432.CCR-14-2751.

41. Janssen I, Chen CC, Millo CM, Ling A, Taïeb D, Lin FI, et al. PET/CT comparing Ga-DOTATATE and other radiopharmaceuticals and in comparison with CT/MRI for the localization of sporadic metastatic pheochromocytoma and paraganglioma. Eur J Nucl Med Mol Imaging. 2016; 43(10):1784–91.

42. Hofman MS, Hicks RJ. Moving beyond "Lumpology": PET/CT imaging of pheochromocytoma and paraganglioma. Clin Cancer Res. 2015;21:3815–7. doi:10.1158/1078-0432.CCR-15-1073.

43. Archier A, Varoquaux A, Garrigue P, Montava M, Guerin C, Gabriel S, et al. Prospective comparison of Ga-DOTATATE and F-FDOPA PET/CT in patients with various pheochromocytomas and paragangliomas with emphasis on sporadic cases. Eur J Nucl Med Mol Imaging. 2015. doi:10.1007/s00259-015-3268-2.

44. Baysal BE, Willett-Brozick JE, Lawrence EC, Drovdlic CM, Savul SA, McLeod DR, et al. Prevalence of SDHB, SDHC, and SDHD germline mutations in clinic patients with head and neck paragangliomas. J Med Genet. 2002;39:178–83.

45. Piccini V, Rapizzi E, Bacca A, Di Trapani G, Pulli R, Giache V, et al. Head and neck paragangliomas: genetic spectrum and clinical variability in 79 consecutive patients. Endocr Relat Cancer. 2012;19:149–55. doi:10.1530/ERC-11-0369.

46. Neumann HP, Erlic Z, Boedeker CC, Rybicki LA, Robledo M, Hermsen M, et al. Clinical predictors for germline mutations in head and neck paraganglioma patients: cost reduction strategy in genetic diagnostic process as fall-out. Cancer Res. 2009;69:3650–6. doi:10.1158/0008-5472.CAN-08-4057.

47. Kunst HP, Rutten MH, de Monnink JP, Hoefsloot LH, Timmers HJ, Marres HA, et al. SDHAF2 (PGL2-SDH5) and hereditary head and neck paraganglioma. Clin Cancer Res. 2011;17:247–54.

48. Baysal BE. Mitochondrial complex II and genomic imprinting in inheritance of paraganglioma tumors. Biochim Biophys Acta. 1827;2013:573–7. doi:10.1016/j.bbabio.2012.12.005.

49. Papathomas TG, Gaal J, Corssmit EP, Oudijk L, Korpershoek E, Heimdal K, et al. Non-pheochromocytoma (PCC)/paraganglioma (PGL) tumors in patients with succinate dehydrogenase-related PCC-PGL syndromes: a clinicopathological and molecular analysis. Eur J Endocrinol. 2014;170:1–12. doi:10.1530/EJE-13-0623.

50. Pasini B, McWhinney SR, Bei T, Matyakhina L, Stergiopoulos S, Muchow M, et al. Clinical and molecular genetics of patients with the Carney-Stratakis syndrome and germline mutations of the genes coding for the succinate dehydrogenase subunits SDHB, SDHC, and SDHD. Eur J Hum Genet. 2008;16:79–88. doi:10.1038/sj.ejhg.5201904.

51. Blanchet EM, Gabriel S, Martucci V, Fakhry N, Chen CC, Deveze A, et al. (18) F-FDG PET/CT as a predictor of hereditary head and neck paragangliomas. Eur J Clin Invest. 2014;44:325–32. doi:10.1111/eci.12239.

52. Timmers HJ, Kozupa A, Chen CC, Carrasquillo JA, Ling A, Eisenhofer G, et al. Superiority of fluorodeoxyglucose positron emission tomography to other functional imaging techniques in the evaluation of metastatic SDHB-associated pheochromocytoma and paraganglioma. J Clin Oncol. 2007;25:2262–9.

53. Maurice JB, Troke R, Win Z, Ramachandran R, Al-Nahhas A, Naji M, et al. A comparison of the performance of (6)(8)Ga-DOTATATE PET/CT and (1)(2)(3)I-MIBG SPECT in the diagnosis and follow-up of phaeochromocytoma and paraganglioma. Eur J Nucl Med Mol Imaging. 2012;39:1266–70. doi:10.1007/s00259-012-2119-7.

54. Strosberg JR, Wolin EM, Chasen B, Kulke MH, Bushnell DL, Caplin ME, et al. NETTER-1 phase III: Progression-free survival, radiographic response, and preliminary overall survival results in patients with midgut neuroendocrine tumors treated with 177-Lu-Dotatate. J Clin Oncol. 2016;34 (suppl 4S; abstr 194).

55. Kroiss A, Putzer D, Decristoforo C, Uprimny C, Warwitz B, Nilica B, et al. 68Ga-DOTA-TOC uptake in neuroendocrine tumour and healthy tissue: differentiation of physiological uptake and pathological processes in PET/CT. Eur J Nucl Med Mol Imaging. 2013;40:514–23. doi:10.1007/s00259-012-2309-3.

56. Cosetti M, Linstrom C, Alexiades G, Tessema B, Parisier S. Glomus tumors in patients of advanced age: a conservative approach. Laryngoscope. 2008;118:270–4. doi:10.1097/MLG.0b013e318158194b.

57. Fisch U, Mattox D. Microsurgery of the skull base. Stuttgart/New York: Georg Thieme Verlag; 1988. p. 148–281.

58. Fisch U. Infratemporal fossa approach to tumours of the temporal bone and base of the skull. J Laryngol Otol. 1978;92:949–67.

59. Netterville JL, Jackson CG, Miller FR, Wanamaker JR, Glasscock ME. Vagal paraganglioma: a review of 46 patients treated during a 20-year period. Arch Otolaryngol Head Neck Surg. 1998;124:1133–40.

60. Shamblin WR, ReMine WH, Sheps SG, Harrison Jr EG. Carotid body tumor (chemodectoma). Clinicopathologic analysis of ninety cases. Am J Surg. 1971;122:732–9.

61. Taïeb D, Hicks RJ, Pacak K. Radiopharmaceuticals in paraganglioma imaging: too many members on board? Eur J Nucl Med Mol Imaging. 2015. doi:10.1007/s00259-015-3213-4.

62. Timmers HJ, Chen CC, Carrasquillo JA, Whatley M, Ling A, Eisenhofer G, et al. Staging and functional characterization of pheochromocytoma and paraganglioma by 18F-fluorodeoxyglucose (18F-FDG) positron emission tomography. J Natl Cancer Inst. 2012;104:700–8. doi:10.1093/jnci/djs188.

63. Letouze E, Martinelli C, Loriot C, Burnichon N, Abermil N, Ottolenghi C, et al. SDH mutations establish a hypermethylator phenotype in paraganglioma. Cancer Cell. 2013;23:739–52. doi:10.1016/j.ccr.2013.04.018.

64. Lendvai N, Pawlosky R, Bullova P, Eisenhofer G, Patocs A, Veech RL, et al. Succinate-to-fumarate ratio as a new metabolic marker to detect the presence of SDHB/D-related paraganglioma: initial experimental and ex vivo findings. Endocrinology. 2014;155:27–32. doi:10.1210/en.2013-1549.

65. Imperiale A, Moussallieh FM, Roche P, Battini S, Cicek AE, Sebag F, et al. Metabolome profiling by HRMAS NMR spectroscopy of pheochromocytomas and paragangliomas detects SDH deficiency: clinical and pathophysiological implications. Neoplasia. 2015;17:55–65. doi:10.1016/j.neo.2014.10.010.

66. Imperiale A, Moussallieh FM, Sebag F, Brunaud L, Barlier A, Elbayed K, et al. A new specific succinate-glutamate metabolomic hallmark in SDHx-related paragangliomas. PLoS One. 2013;8:e80539. doi:10.1371/journal.pone.0080539.

67. Lussey-Lepoutre C, Bellucci A, Morin A, Buffet A, Amar L, Janin M, et al. In vivo detection of succinate by magnetic resonance spectroscopy as a hallmark of SDHx mutations in paraganglioma. Clin Cancer Res. 2015. doi:10.1158/1078-0432.CCR-15-1576.

68. Varoquaux A, le Fur Y, Imperiale A, Reyre A, Montava M, Fakhry N, et al. Magnetic reso-
    nance spectroscopy of paragangliomas: new insights into in vivo metabolomics. Endocr Relat
    Cancer. 2015;22:M1–8. doi:10.1530/ERC-15-0246.
69. Heesterman BL, Bayley JP, Tops CM, Hes FJ, van Brussel BT, Corssmit EP, et al. High preva-
    lence of occult paragangliomas in asymptomatic carriers of SDHD and SDHB gene mutations.
    Eur J Hum Genet. 2013;21:469–70. doi:10.1038/ejhg.2012.203.
70. Hensen EF, Jansen JC, Siemers MD, Oosterwijk JC, Vriends AH, Corssmit EP, et al. The
    Dutch founder mutation SDHD.D92Y shows a reduced penetrance for the development of
    paragangliomas in a large multigenerational family. Eur J Hum Genet. 2010;18:62–6.
    doi:10.1038/ejhg.2009.112.
71. Hes FJ, Weiss MM, Woortman SA, de Miranda NF, van Bunderen PA, Bonsing BA, et al. Low
    penetrance of a SDHB mutation in a large Dutch paraganglioma family. BMC Med Genet.
    2010;11:92. doi:10.1186/1471-2350-11-92.
72. Lepoutre-Lussey C, Caramella C, Bidault F, Deandreis D, Berdelou A, Al Ghuzlan A, et al.
    Screening in asymptomatic SDHx mutation carriers: added value of (1)(8)F-FDG PET/CT at
    initial diagnosis and 1-year follow-up. Eur J Nucl Med Mol Imaging. 2015;42:868–76.
    doi:10.1007/s00259-015-3003-z.
73. Holt A, Van Gestel D, Arends MP, Korevaar EW, Schuring D, Kunze-Busch MC, et al. Multi-
    institutional comparison of volumetric modulated arc therapy vs. intensity-modulated radia-
    tion therapy for head-and-neck cancer: a planning study. Radiat Oncol. 2013;8:26.
    doi:10.1186/1748-717X-8-26.
74. Lim CM, Clump DA, Heron DE, Ferris RL. Stereotactic Body Radiotherapy (SBRT) for pri-
    mary and recurrent head and neck tumors. Oral Oncol. 2013;49:401–6. doi:10.1016/j.
    oraloncology.2012.12.009.
75. Liscak R, Simonova G, Vymazal J, Janouskova L, Vladyka V. Gamma knife radiosurgery of
    meningiomas in the cavernous sinus region. Acta Neurochir (Wien). 1999;141:473–80.
76. Bianchi LC, Marchetti M, Brait L, Bergantin A, Milanesi I, Broggi G, et al. Paragangliomas of
    head and neck: a treatment option with CyberKnife radiosurgery. Neurol Sci. 2009;30:479–85.
    doi:10.1007/s10072-009-0138-3.
77. Gerszten PC, Ozhasoglu C, Burton SA, Vogel WJ, Atkins BA, Kalnicki S, et al. CyberKnife
    frameless single-fraction stereotactic radiosurgery for benign tumors of the spine. Neurosurg
    Focus. 2003;14:e16.
78. Golanov AV, Kapitanov DN, Pronin IN, Shelesko EV, Zolotova SV, Shchurova IN, et al. First
    experience of CyberKnife stereotactic radiotherapy for glomus jugulare tumors. Zh Vopr
    Neirokhir Im N N Burdenko. 2012;76:30–6; discussion 6.
79. Lim M, Bower R, Nangiana JS, Adler JR, Chang SD. Radiosurgery for glomus jugulare
    tumors. Technol Cancer Res Treat. 2007;6:419–23.
80. Wegner RE, Rodriguez KD, Heron DE, Hirsch BE, Ferris RL, Burton SA. Linac-based stereo-
    tactic body radiation therapy for treatment of glomus jugulare tumors. Radiother Oncol.
    2010;97:395–8. doi:10.1016/j.radonc.2010.09.004.
81. Henzel M, Hamm K, Gross MW, Surber G, Kleinert G, Failing T, et al. Fractionated stereotac-
    tic radiotherapy of glomus jugulare tumors. Local control, toxicity, symptomatology, and qual-
    ity of life. Strahlenther Onkol. 2007;183:557–62. doi:10.1007/s00066-007-1701-6.
82. Poznanovic SA, Cass SP, Kavanagh BD. Short-term tumor control and acute toxicity after
    stereotactic radiosurgery for glomus jugulare tumors. Otolaryngol Head Neck Surg.
    2006;134:437–42. doi:10.1016/j.otohns.2005.10.040.
83. Zovato S, Kumanova A, Dematte S, Sansovini M, Bodei L, Di Sarra D, et al. Peptide receptor
    radionuclide therapy (PRRT) with 177Lu-DOTATATE in individuals with neck or mediastinal
    paraganglioma (PGL). Horm Metab Res. 2012;44:411–4. doi:10.1055/s-0032-1311637.

Chapter 14
Radionuclide Imaging of Chromaffin Cell Tumors

David Taïeb and Karel Pacak

14.1 Epidemiology and Natural History

PHEOs/PGLs are rare tumors with an annual incidence of one to eight patients per million [1]. They account for about 4 % of adrenal incidentalomas with a higher prevalence in an autopsy series [2]. Pediatric PHEOs/PGLs account for about 20 % of these tumors [3]. Approximately 75–85 % are located in the adrenal gland, and the remaining tumors are found outside of the gland, most commonly in the abdomen and thorax and less frequently in the head and neck (also termed as head and neck PGLs/HNPGLs) [4]. It is estimated that in the USA, there are about 1,000–2,000 new patients per year. Approximately 10 % of these patients present with metastatic disease upon initial diagnosis [5]. Around one third of these tumors are hereditary, caused by at least a dozen, well-characterized genes, described later on in this chapter [6, 7]. It is also estimated that about 30–50 % of these tumors are unrecognized initially, resulting in serious consequences to the patient, including death [8–10].

D. Taïeb, MD, PhD (✉)
Department of Nuclear Medicine, La Timone University Hospital, CERIMED, European Center for Research in Medical Imaging, Aix-Marseille University,
264, rue Saint-Pierre, 13385 Marseille, France
e-mail: david.Taïeb@ap-hm.fr

K. Pacak, MD, PhD, DSc, FACE
Section on Medical Neuroendocrinology, Developmental Endocrine Oncology and Genetics Affinity Group, Eunice Kennedy Shriver National Institute of Child Health and Human Development, National Institutes of Health,
Building 10, CRC, Room 1E-3140 10 Center Drive MSC-1109, Bethesda, MD 20892-1109, USA

14.2   Tumor Origin

PHEOs and sympathetic-associated paragangliomas (symp-PGLs) develop from cells of the adrenal medulla or extra-adrenal chromaffin cells, respectively.

Chromaffin cells and sympathetic neurons derive from a common sympathoadrenal (SA) progenitor cell of neural crest origin. SA progenitor cells aggregate at the dorsal aorta, where they acquire a catecholaminergic neural fate. Subsequently, the cells migrate ventrally to invade the fetal adrenal cortex and form the adrenal medulla, as well as dorsolaterally to form sympathetic ganglia. Most extra-adrenal chromaffin cells regress via apoptosis. The organ of Zuckerkandl (OZ) constitutes the largest chromaffin paraganglia in the embryo and regresses after birth via autophagy [11]. Adrenal medulla and persistent extra-adrenal chromaffin cells located in the retroperitoneum and posterior mediastinum represent the chromaffin paraganglia system in adults. These cells possess the machineries to synthesize, store, release, and take up catecholamines, including the enzymes for noradrenaline synthesis. They have been named "chromaffin" by Kohn (1902) because of their characteristic staining property by chromium salts [12]. These embryological bases explain why PHEO and symp-PGL can be widely distributed along the sympathetic nervous system in the posterior mediastinum and retroperitoneum. In contrast, HNPGLs are derived from neural crest cells of the parasympathetic nervous system, with only 20 % producing and/or secreting catecholamines, usually dopamine or its metabolite 3-methoxytyramine [13–15]. Furthermore, these tumors are usually benign, except those caused by succinate dehydrogenase subunit B (SDHB) gene mutations, which are considered aggressive either locally or by the development of metastatic disease [5, 16–18].

14.3   Clinical Presentation and Diagnosis

PHEOs and symp-PGLs usually cause symptoms of catecholamine (norepinephrine or epinephrine) oversecretion (e.g., sustained or paroxysmal elevations in blood pressure, headache, episodic profuse sweating, palpitations, pallor, nervousness, or anxiety) [4]. These attacks can be caused with or without a trigger. The most common causes of catecholamine release from these tumors are direct manipulation, various drugs (mainly antidepressants, over-the-counter cold and allergy medicine, or antiemetics), stress, any type of local or general anesthesia, or excessive physical activity. If such an attack (sometimes called a "spell") occurs, catecholamine concentrations can be enormous, reaching 1,000 times the normal reference limit, resulting in serious cardiovascular consequences and, in some patients, death [19–21]. Therefore, all patients with PHEO/PGL must be put on an adrenoceptor blockade that can lessen or at least partially prevent (full prevention of catecholamine effect on any organ is impossible) the deleterious effects of catecholamines on end organs [22]. Patients with a completely biochemically silent PHEO/PGL based on repeated, normal plasma and/or urine catecholamines and metanephrines are the only exception.

14.4 Biochemical Phenotypes

PHEOs/PGLs present in three well-defined biochemical phenotypes: noradrenergic, adrenergic, and dopaminergic (Table 14.1). A noradrenergic phenotype is defined by the elevation of norepinephrine or its metabolite, normetanephrine. In these tumors, the concentration of metanephrine, a metabolite of epinephrine, is usually less than 5 % of the sum of normetanephrine and metanephrine tissue concentrations [23]. These tumors are characteristic for extra-adrenal PGLs, either sporadic or those with hereditary background, mainly including mutations in succinate dehydrogenase subunits (SDHx), von Hippel-Lindau (*VHL*), fumarate dehydrogenase (*FH*), and hypoxia-inducible factor alpha (*HIF2A*) [7] genes. Clinically, patients with these tumors mainly present with paroxysmal or sustained hypertension and, less commonly, with tachyarrhythmia. An adrenergic phenotype is defined by the elevation of metanephrine in a PHEO/PGL tissue that is at least 10 % or more of the sum of metanephrine and normetanephrine tissue concentrations [23]. Epinephrine production in these tumors reflects the presence of the enzyme Phenylethanolamine-N-methyltransferase (PNMT) which is uniquely found in the adrenal medulla. Therefore, most of these tumors, if not all of them, are located in the adrenal medulla and as previously described called PHEOs. They can be sporadic or hereditary, including mutations in RET proto-oncogene (*RET*), neurofibromatosis type 1 (*NF1*), and transmembrane protein 127 genes. Clinically, patients with these tumors mainly present with paroxysmal or sustained tachyarrhythmia and, usually, mild hypertension. Due to the significant effect of epinephrine on beta-adrenoceptors, some of these patients may even present with hypotension due to beta-adrenoceptor-mediated vasodilation [24]. A dopaminergic phenotype is characterized by significant elevation of either dopamine or its metabolite methoxytyramine, or both. Usually, dopamine or methoxytyramine elevation is associated with an increase in norepinephrine or normetanephrine, which is commonly seen in patients with *SDHx* mutations [14, 15]. If only dopamine is elevated, patients do not present with any clinical signs or symptoms, unless dopamine levels are tremendously high (very rare) and hypotension may occur.

14.5 Spectrum of Hereditary Syndromes and Phenotype-Genotype Correlations

Research in molecular genetics has resulted in the identification of more than 20 susceptibility genes for tumors of the entire paraganglia system [7, 25]. Most PHEOs occur sporadically, whereas the majority of symp-PGLs are associated with germline driver mutations. Depending on their location, the most commonly found gene mutations are (1) unilateral PHEO: succinate dehydrogenase complex subunit B or D (*SDHB* or *SDHD*) and *VHL*; (2) bilateral PHEO: *SDHB*, *RET*, *VHL*, *NF1*, MYC-associated factor X (*MAX*), and *TMEM127*; and (3) symp-PGLs with or

Table 14.1 Summary of common clinical presentations of PHEOs/PGLs with detectable mutations

	First syndromic manifestation	Context at PPGL presentation (in index cases)	PHEO at presentation	Additional extra-adrenal PGL	Predominant secretion	PPGL-associated malignancy risk
MEN2	MTC	Adult Possible phenotypic features of MEN2 Frequent family history of MTC/PHEO/PGL	Uni- or bilateral	Rare	EPI	Very low
NF1	Neurofibromas	Adult Phenotypic feature of NF1 Possible family history of NF1	Often unilateral	Rare	EPI	Very low
TMEM127	PHEO	Adult Possible family history of PHEO	Uni- or bilateral	No	EPI	Low
MAX	PHEO	Young adult Frequent family history of PHEO/PGL	Bilateral	Possible	NE	Moderate
VHL	PHEO/PGL	Young adult Frequent family history of PHEO/PGL	Uni- or bilateral	Frequent	NE	Low
SDHB	PHEO/PGL	Adult Possible family history of PHEO/PGL	Often unilateral	Frequent	NE and/or DA	High

	First syndromic manifestation	Context at PPGL presentation (in index cases)	PHEO at presentation	Additional extra-adrenal PGL	Predominant secretion	PPGL-associated malignancy risk
SDHD	PHEO/PGL	Adult Frequent family history of PHEO/PGL	Uni- or bilateral	Frequent	NE and/or DA	Moderate
SDHC	PHEO/PGL	Adult Possible family history of PPGL	Rare	Frequent	NE	Low
HIF2A	Congenital polycythemia	Adolescent-young adult Female Absence of family history of PHEO/PGL	Very rare	Almost constant	NE	Moderate

Abbreviations: *PHEO/PGL* pheochromocytoma/paraganglioma, *NE* norepinephrine, *EPI* epinephrine, *DA* dopamine, *SDHB/C/D* succinate dehydrogenase subunits B, C, and D, *MTC* medullary thyroid carcinoma, *HIF2A* hypoxia-inducible factor 2α, *VHL* von Hippel-Lindau, *TMEM127* transmembrane protein 127, *MEN2* multiple endocrine neoplasia type 2, *NF1* neurofibromatosis type 1, *MAX* MYC-associated factor X

without PHEO: *SDHB*, *SDHD*, *VHL*, and *HIF2A*. Other genes account for a small minority of cases. Recent tumor sequencing has also led to the identification of somatic events in a large number of PHEOs/PGLs (The Cancer Genome Atlas, unpublished observations) (Table 14.1). Patients presenting with metastatic disease mainly include those with *SDHB* and perhaps *SDHD* (excluding HNPGLs), *FH*, and *MAX*-related PHEOs/PGLs, although, at present, about 50 % of metastatic PHEOs/PGLs are non-hereditary [5].

14.6 Differential Diagnosis

There are several potential causes to consider for the differential diagnosis in the presence of an adrenal or extra-adrenal mass (Table 14.2). However, the masses that belong to either PHEO or PGL are usually detected by imaging-specific characteristics that include the value of Hounsfield units (HU), T2-weighted bright images, and positivity on PHEO-/PGL-specific functional imaging, as described below.

14.7 Typical PHEO/PGL Imaging Finding on CT and/ or MRI

On non-contrast computed tomography (CT), PHEO/PGL can demonstrate a variety of appearances. Two thirds of PHEO/PGLs are solid, while the remainder are complex or have undergone cystic or necrotic changes [26]. Typically, the CT attenuation of PHEO/PGL is about soft tissue attenuation and thus greater than 10 HU, with most PHEOs/PGLs 20–30 HU or higher. PHEO/PGL can present with a high attenuation due to the presence of hemorrhage or calcifications. In contrast, necrotic tissue presents with a low attenuation. Typically, a PHEO/PGL demonstrates avid enhancement (often greater than 30 HU) [27]. In addition, enhancement can be heterogeneous, or there may be no enhancement due to cystic, necrotic, or degenerated regions within the lesion [28]. On magnetic resonance imaging (MRI), the classic imaging appearance of PHEO/PGL is "light bulb" bright on T2-weighted imaging. In reality, 30 % of PHEOs/PGLs demonstrate moderate or low T2-weighted signal intensity [27, 29]. PHEOs/PGLs typically demonstrate avid contrast enhancement following the administration of intravenous gadolinium-based contrast material [30, 31].

14.8 Typical Imaging Finding on Molecular Imaging

Nowadays, positron emission tomography (PET) is a cornerstone in the evaluation of hereditary as well as non-hereditary PHEOs/PGLs. The broad diversity of PET biomarkers enables assessment of different metabolic pathways and receptors. Beyond its localization value, this imaging modality provides unique opportunities

Table 14.2 Main causes of solid extrarenal retroperitoneal masses

Localization	Cause
Adrenal masses	Adrenocortical adenoma
	Adrenocortical carcinoma (ACC)
	Pheochromocytoma
	Adrenocortical hyperplasia
	Lymphoma
	Metastasis
	Myelolipoma
	Angiomyolipoma
	Ganglioneuroma
	Hematoma (may coexist with tumors, especially PHEO)
	Oncocytoma
	Granulomatous inflammation
	Sarcoma
Extra-adrenal retroperitoneal masses	Neurogenic tumor (schwannoma, neurofibroma)
	Ganglioneuroma
	Paraganglioma
	Lymph node (malignancies, inflammatory origin, Castleman disease)
	Gastrointestinal stromal tumor (GIST)
	Sarcoma (liposarcoma, leiomyosarcoma, other)
	Solitary fibrous tumor

for better characterizing these tumors at molecular levels (e.g., the presence of cat-echolamines and their metabolites, specific cell membrane receptors and transport-ers), mirroring *ex vivo* histological classification but on a whole-body, *in vivo*, scale (Table 14.4).

Thus, successful PHEO-/PGL-specific localization depends on the presence of molecules (imaging targets) for which PET radiopharmaceuticals are currently avail-able. Based on several recent studies, it has been uncovered that PHEO-/PGL-specific imaging targets have various expressions based on whether these tumors belong to pseudohypoxic or kinase signaling clusters, present as metastatic, are located in or outside the adrenal gland, or are derived from the sympathetic or parasympathetic nervous system. Currently, ^{18}F-fluorodeoxyglucose (^{18}F-FDG) is the most accessible PET radiopharmaceutical, but lacks specificity for these tumors. ^{18}F-fluorodopamine (^{18}F-FDA) and ^{11}C-hydroxyephedrine (^{11}C-HED) are the most specific tracers for chromaffin tumors, but are available in very few centers and fail in metastatic and hereditary PHEOs/PGLs [32–34].[18]F-fluorodyhidroxyphenylalanine (^{18}F-FDOPA) is available from different pharmaceutical suppliers, but its sensitivity widely depends on the genetic background and whether the PHEO/PGL is sympathetic or parasym-pathetic [35–37]. Metastatic behavior of these tumors can also affect the expression of amino acid transporters [38]. Newly developed ^{68}Ga-labeled peptides, as in other neuroendocrine tumors, have shown very interesting results and, in our opinion, should be positioned first for many indications due to their exceptional affinity to somatostatin receptor type 2 found on these tumors [39–44].

PHEOs and PGLs usually have highly elevated uptake values with specific radio-pharmaceuticals based on their genetic background. For example, ^{18}F-FDOPA PET/CT

was replaced by ^{68}Ga-DOTATATE PET/CT as the best available imaging modality for metastatic PHEO/PGL, especially in those with *SDHB* mutations and head and neck PGLs [40–42]. The Octreoscan has been suggested not to be used anymore due to its suboptimal performance in the detection of these tumors and the growing availability of ^{68}Ga-DOTATATE PET/CT. However, the use of other ^{68}Ga-labeled DOTA analogues (^{68}Ga-DOTATOC and ^{68}Ga-DOTANOC) needs to be confirmed in a large population of patients. A variety of new radiopharmaceuticals have been developed as potential competitors of ^{68}Ga-DOTATATE (^{68}Ga-labeled somatostatin antagonists, ^{64}Cu-labeled SSA [45], or ^{18}F-SiFAlin (silicon-fluoride acceptor)-modified TATE), but they need to be evaluated [46].

14.9 Relationship Between Genotype and Imaging Phenotype

Proper evaluation of PHEO/PGL is a key point for choosing the necessary treatment plan for follow-up and outcome for these patients. The presence of *SDHx* mutations markedly influences sensitivity of ^{18}F-FDG, ^{18}F-FDOPA, and ^{68}Ga-DOTA-SSAs PET/CT. ^{18}F-DOPA PET/CT has a sensitivity approaching 100 % for sporadic PHEO and a very high specificity (95 %), but can miss tumors in SDHx-mutated patients. ^{18}F-FDOPA PET/CT still remains a very good modality for the detection of some metastatic PHEO/PGLs – it ranks as the second best for the detection of HNPGLs, and it can also be used for patients with non-hereditary metastatic PHEO/PGL [18, 35, 36, 38, 47, 48]. By contrast, SDHx tumors usually exhibit highly elevated ^{18}F-FDG uptake values. However, ^{18}F-FDG PET/CT positivity is present in about 80 % of primary PHEOs. Thus, ^{18}F-FDG PET/CT remains a good alternative for the detection of metastatic PHEO/PGL, especially those related to *SDHx* mutations [49]. Several potential diagnoses should be considered in cases of ^{18}F-FDG-avid adrenal masses (Table 14.3).

The use of ^{68}Ga-DOTA-SSAs in the context of PHEOs/PGLs has been studied less, but has shown excellent preliminary results in localizing these tumors, especially metastatic and head and neck ones, as discussed above. A head-to-head comparison between ^{68}Ga-DOTA-SSA and ^{18}F-FDOPA PET has been performed in only five studies: one retrospective study from Innsbruck Medical University (^{68}Ga-DOTATOC in 20 patients with unknown genetic background) [50], three prospective studies from the NIH (*SDHB*, HNPGL, and sporadic metastatic PHEOs/PGLs) (^{68}Ga-DOTATATE in 17 and 20 patients), and one prospective study from La Timone University Hospital (^{68}Ga-DOTATATE in 30 patients) [40–42]. In these studies, ^{68}Ga-DOTA-SSA PET/CT detected more primary head and neck PGLs as well as *SDHx*-associated PGLs than ^{18}F-FDOPA PET/CT [51]. By contrast, in the context of sporadic PHEO, ^{18}F-FDOPA PET/CT may detect more lesions than ^{68}Ga-DOTATATE, although larger studies are needed to confirm those results [51].

Table 14.3 Differential diagnosis of highly ^{18}F-FDG-avid adrenal masses (adrenal to liver SUVmax ratio >3, A/L >3)

Tumor type	Typical feature on ^{18}F-FDG PET/CT	Major criteria for diagnosis
PHEO	Well-circumscribed mass with a heterogeneous uptake Moderate to high avidity Central area of low or absent avidity BAT uptake (periadrenal)	Elevated metanephrines Family history PHEO/PGL predisposing mutation Multifocality
Adrenocortical carcinoma	Often irregular mass with a heterogeneous uptake Moderate to high avidity Often more rapid growth	Elevated steroid secretion Venous tumor extension (vena cava) Liver/lung metastases
Lymphoma	Poorly circumscribed mass with a homogeneous uptake Highly elevated A/L (often >8)	Bilateral adrenal and lymph node involvement, elevated serum lactate dehydrogenase (LDH)
Adrenal oncocytoma	Well circumscribed with a homogeneous uptake Highly elevated A/B (often >8)	Possible elevation of cortisol or androgens
Metastases	Variable features Moderate to high avidity	Personal history of cancer Often extra-adrenal metastases

Table 14.4 Comparison of different PET radiopharmaceuticals in the detection of metastases PHEO/PGL (number of sites) (40, 42Timmers, 49)

Tracer	Molecular target	Cellular retention	Specificity (%)	Sensitivity sporadic	Sensitivity SDHx
^{18}F-FDA	Norepinephrine transporter	Neurosecretory vesicles	100	78	52
^{18}F-FDOPA	Neutral amino acid transporter system L (LATs)	Decarboxylation (AADC)	>95%	75	61
^{68}Ga-SSA	Somatostatin receptors	Internalization (agonists)	90%	98	99
^{18}F-FDG	Glucose transporters (GLUTs)	Decarboxylation (hexokinase)	80%	49	86

One of the main drawbacks of ^{68}Ga-DOTA-SSA is the very high physiological uptake by healthy adrenal glands [52]. Furthermore, there are also different affinities of various DOTA-SSAs to somatostatin receptors. DOTATATE has the best affinity to somatostatin receptor type 2, mostly expressed on PHEO/PGLs, followed by DOTATOC. DOTANOC has the lowest affinity to somatostatin receptor type 2 and has some affinity to somatostatin receptor type 5, which is least abundant on PHEOs/PGLs. Therefore, the use of DOTANOC may result in suboptimal detection of PHEO/PGL, especially their metastatic lesions. Studies comparing

^{68}Ga-DOTATATE and ^{68}Ga-DOTATOC are currently unavailable. Excellent results with DOTA analogues in both sporadic as well as SDHx-related metastatic PHEOs/PGLs resulted in the use of ^{177}Lu-DOTATATE (Lutathera) in radiotherapy of these tumors [53–57]. This is followed by the preparation of clinical protocols in order to properly assess the efficacy of this treatment on a large population of well-characterized patients with metastatic or inoperable PHEO/PGL (Lin, Pacak et al. NIH protocol in preparation, 2016).

14.10   Role of Radionuclide Imaging

Successful PHEO/PGL management requires an interdisciplinary team approach. Precise identification of clinical context and the genetic status of a patient enables a personalized use of functional imaging modalities. Currently, it is recommended to adopt a tailored approach using a diagnostic algorithm based on tumor location, biochemical phenotype, and any known genetic background (Table 14.5) [48, 58].

14.10.1   Diagnosis of PHEO or Symp-PGL

14.10.1.1   Adrenal Mass

Functional imaging should be used in a minority of cases, such as those with suspicion of nonfunctioning PHEO on CT/MRI, elevation of plasma or urine normetanephrine in the presence of an adrenal mass, acute cardiovascular complication in the critical care setting together with the presence of an adrenal mass, hemorrhagic adrenal masses, and either elevated plasma metanephrine or normetanephrine in renal insufficiency. Elevation of metanephrine in the plasma or urine in the presence of an adrenal mass does not call for the use of functional imaging since metanephrine is 99 % derived from the adrenal gland. Thus, its elevation highly supports the presence of PHEO, especially when plasma or urine metanephrine is 4x above the upper reference limit. Another new promising option is the use of proton single-voxel magnetic resonance spectroscopy (^{1}H-MRS) that can detect the presence of catecholamines in PHEO and, therefore, may correctly point to the presence of this tumor [59–61].

PET imaging using ^{18}F-FDOPA, ^{18}F-FDA PET/CT, or ^{68}Ga-DOTA-SSA PET/CT is highly sensitive with ^{18}F-FDA having an excellent specificity, as described above (Fig. 14.1). The low uptake of ^{18}F-FDOPA by normal adrenals is a potential advantage over ^{68}Ga-DOTA-SSA for localizing a small PHEO (Figs. 14.2, 14.3, and 14.4).

Table 14.5 Stepwise molecular imaging approaches for PHEO/PGL

	Location	Other related tumor conditions	First line	Second line
MEN2	Adrenal	MTC, parathyroid adenoma, or hyperplasia	^{18}F-FDOPA	^{123}I-MIBG
NF1	Adrenal	Neurofibromas, MPNSTs, and gliomas	^{18}F-FDOPA	^{123}I-MIBG
TMEM127	Adrenal	RCCs	^{18}F-FDOPA	^{123}I-MIBG
MAX	Adrenal	None reported	^{18}F-FDOPA	^{123}I-MIBG
VHL	PHEO/PGL	RCC and CNS Hemangioblastomas	^{18}F-FDOPA	^{68}Ga-DOTATATE
SDHB	PHEO/PGL	GISTs and RCCs Pituitary adenoma	^{68}Ga-DOTATATE	^{18}F-FDG
SDHD	PHEO/PGL	GIST, RCC, and pituitary adenoma	^{68}Ga-DOTATATE	^{18}F-FDG
SDHC	PHEO/PGL	GIST	^{68}Ga-DOTATATE	^{18}F-FDG
HIF2A	PHEO/PGL	Somatostatinomas	^{18}F-FDOPA	^{18}F-FDA

GIST gastrointestinal stromal tumor, *MTC* medullary thyroid carcinoma, *RCC* renal cell carcinoma, *MPNST* malignant peripheral nerve sheath tumor
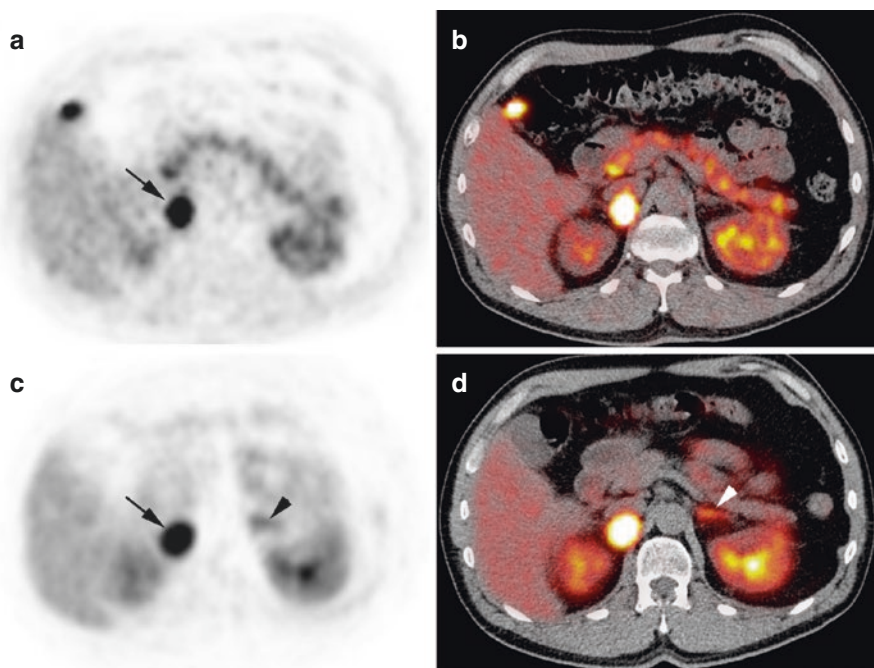
Fig. 14.1 Typical imaging features of PHEO on ^{18}F-FDOPA PET/CT and ^{68}Ga-DOTATATE. Axial ^{18}F-FDOPA PET (**a**) and PET/CT (**b**). Axial ^{68}Ga-DOTATATE PET (**c**) and PET/CT (**d**). The PHEO was positive on both imaging studies (*arrows*). Note high ^{68}Ga-DOTATATE uptake by the left normal adrenal gland (*arrowheads*)
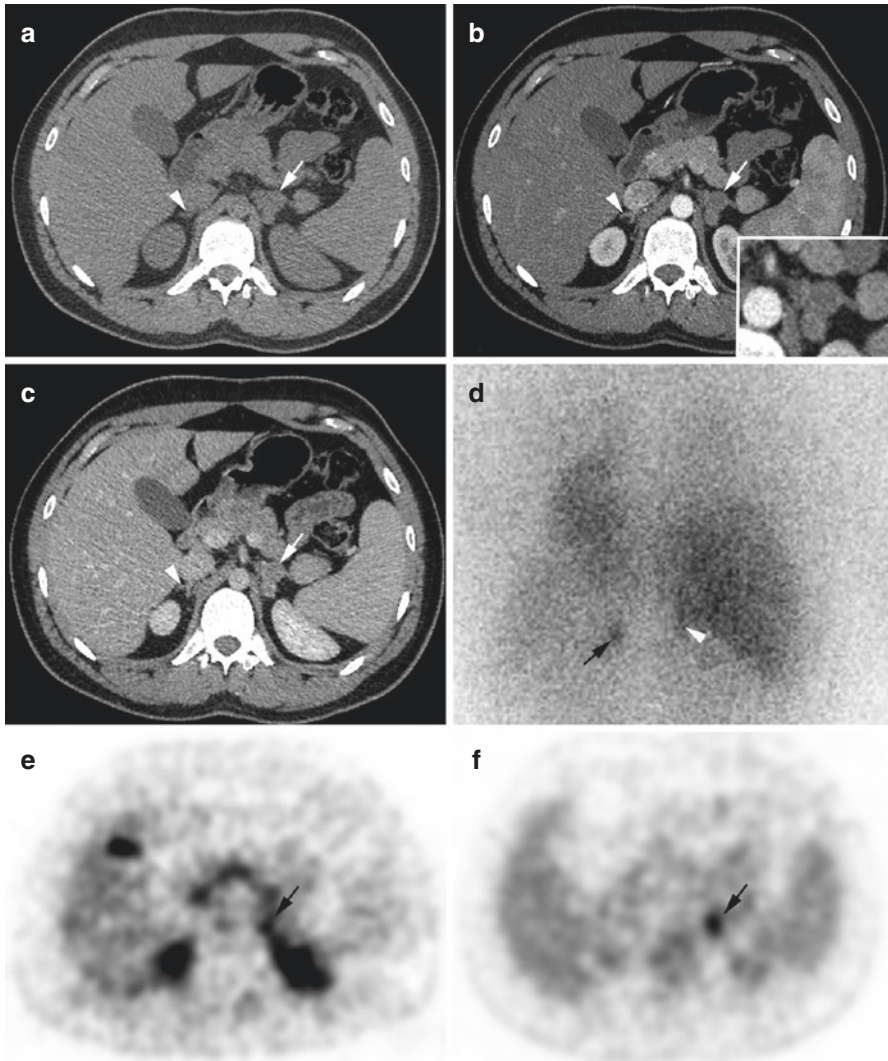
Fig. 14.2 Unilateral MEN2A-related PHEO. Multiphasic adrenal CT (**a–c**), ¹⁸F-FDOPA PET/CT, and (**e**) ¹⁸F-FDG PET/CT (**f**) showed a single left PHEO (*arrow*) with normal contralateral gland (*arrowhead*), while ¹²³I-MIBG was falsely positive for the right adrenal gland. A total left adrenalectomy was performed with subsequent normalization of metanephrine. Pathological analysis found three PHEOs (20 mm for the largest tumor)
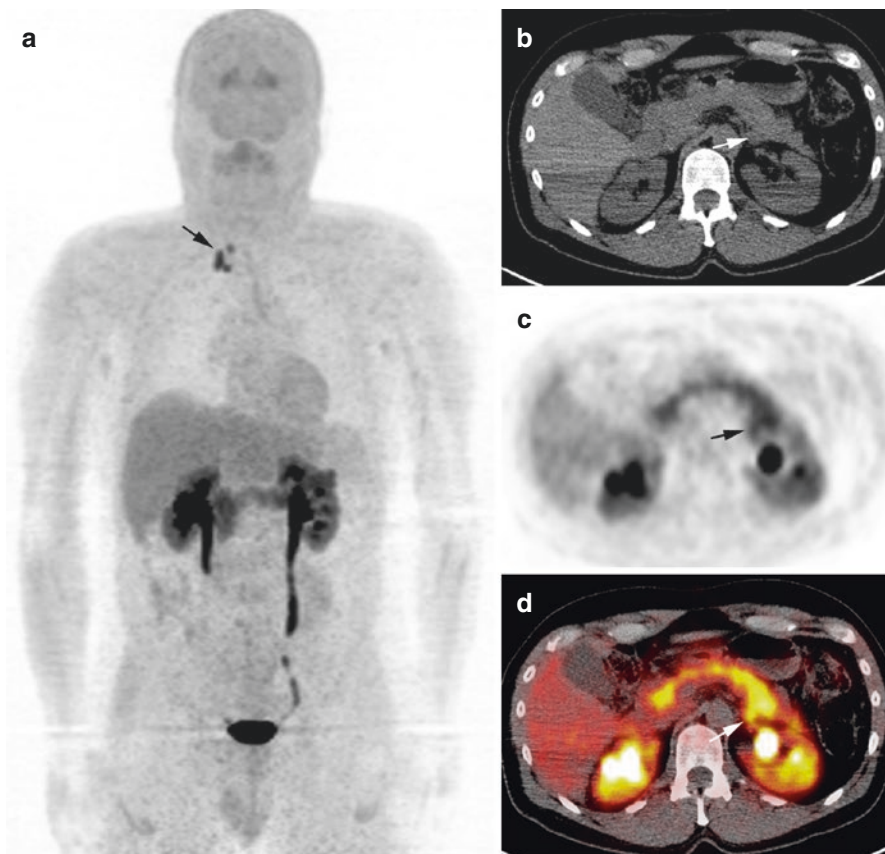
Fig. 14.3 MEN2A with PHEO and persistent MTC. (**a**) ^{18}F-FDOPA PET/CT (MIP image) showing persistent cervical metastatic lymph nodes from MTC (*arrow*), (**b**) unenhanced CT showing a left adrenal nodule, and (**c**) axial ^{18}F-FDOPA PET and PET/CT are consistent with a small left PHEO (*arrow*)

14.10.1.2 Retroperitoneal Extra-Adrenal Nonrenal Mass

In the presence of a retroperitoneal extra-adrenal, nonrenal mass, it is important to differentiate a PGL from other tumors (Table 14.2). A biopsy is not always contributory or even recommended, since it can carry a high risk of hypertensive crisis and tachyarrhythmia. Therefore, it should only be done if a PGL has been ruled out in a patient presenting with signs and symptoms of catecholamine excess. Specific functional imaging studies, which are not usually performed before biochemical results are available, are very helpful in distinguishing PGLs from other tumors (Figs. 14.5, 14.6, 14.7, and 14.8). ^{68}Ga-DOTA-SSAs are the first-line imaging since most patients are expected to have *SDHx* mutations.
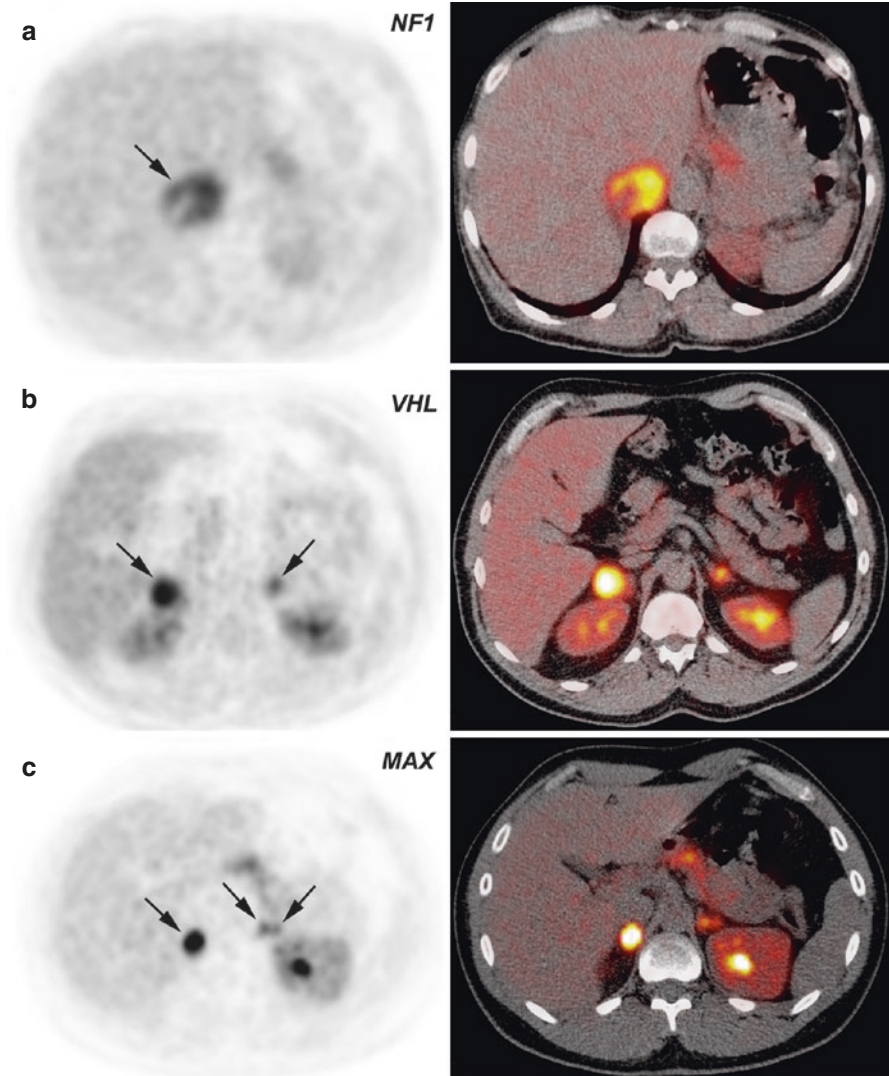
Fig. 14.4 ¹⁸F-FDOPA PET/CT findings in hereditary PHEOs. (**a**, **b**) *NF1*-related right PHEO. (**c**, **d**) Bilateral *VHL*-related PHEO. (**c**, **d**) Bilateral *MAX*-related PHEO (note the presence of two foci within the left adrenal gland)

14.10.2 Assessment of Locoregional Extension and Diagnosis of Malignancy

Presently, there are no reliable cytological, histological, immunohistochemical, molecular, or imaging criteria for determining malignancy [62]. The diagnosis of malignancy remains strictly based on the finding of metastases where chromaffin cells are not usually present, such as the lymph nodes, lung, bone, or liver.

Anatomical imaging appears sufficient in the staging of PHEO/PGL. Functional imaging is probably not necessary in the preoperative workup of PHEO patients meeting the following criteria: >40 years, no family history, small (less than 2.0 cm) PHEO-secreting predominantly metanephrine, and negative genetic testing. Functional imaging is strongly recommended for excluding metastatic disease in large adrenal tumors (>4–5.0 cm) and in *SDHB* patients, and most probably *SDHD* as well. It is widely accepted that tumors with an underlying *SDHB* mutation are associated with a higher risk of aggressive behavior, development of metastatic disease, and, ultimately, death.

To date, 18F-FDOPA PET or 68Ga-DOTA-SSA may be the imaging modality of choice in the absence of a *SDHB* mutation, or when genetic status is unknown. By contrast, 68Ga-DOTA-SSA or, if not available, 18F-FDG PET should be considered as the imaging modalities of reference for *SDHx*-related cases (for images, see Chap. 13).

14.10.3 Detection of Multifocality

Beyond malignancy risk, inherited (especially *SDHx*, *VHL,* and *MEN2*) or symp-PGL raises the problem of multifocality. Based on recent published data, 68Ga-DOTA-SSA has gained an increasing role and should get a leading position in this setting. In absence of available 68Ga-DOTA-SSA, 18F-FDG should be preferred to 18F-FDOPA in *SDHx* patients, whereas 18F-FDOPA appears to be a very good imaging tool in other genotypes and sporadic cases.

14.10.4 Imaging Follow-Up of Sporadic PHEO/PGL Patients

For sporadic PHEO/PGL patients, imaging follow-up is necessary, especially in those patients presenting with primary tumors larger than 4–5 cm and those with an extra-adrenal location [63]. Currently, there is no guideline regarding the frequency of imaging follow-up, but it is recommended to be done at least every 2 years, with either CT or MRI, preferably alternatively, to reduce the amount of radiation delivered to the patient.
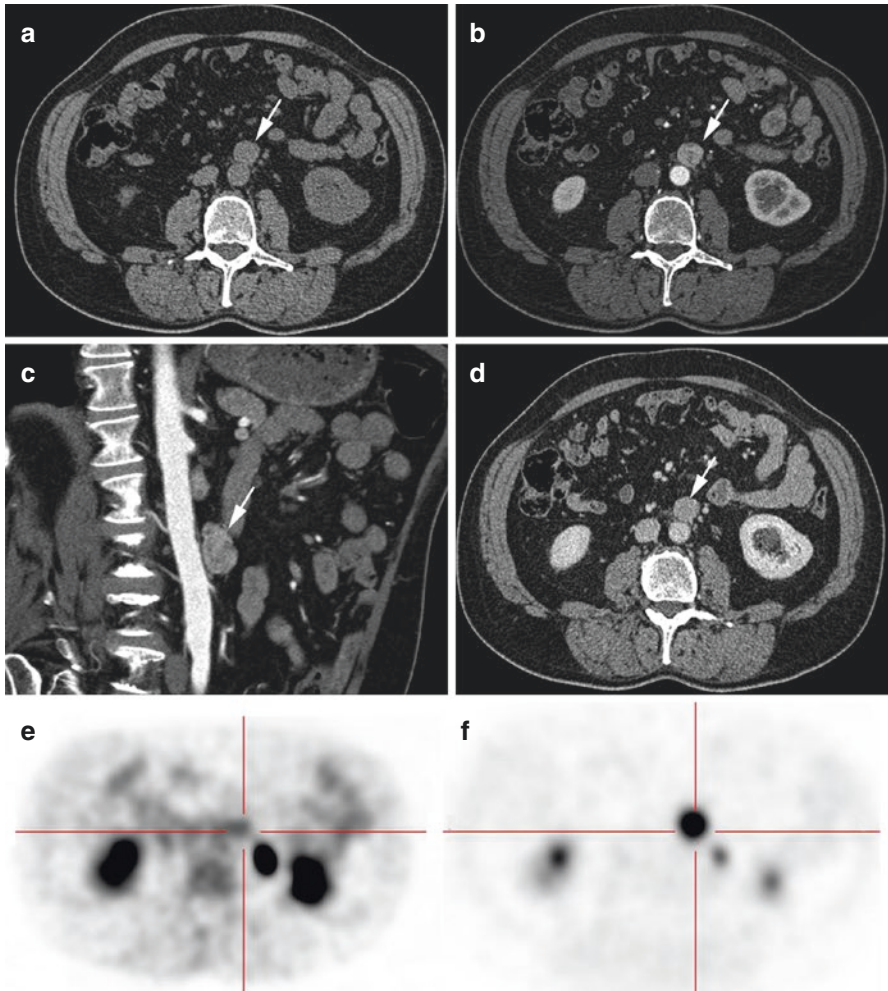
Fig. 14.5 Sporadic extra-adrenal paraganglioma. CT scan revealed a solitary preaortic mass with a rapid and marked contrast enhancement and a slow washout pattern suspected of paraganglioma. ^{18}F-FDG PET was slightly positive, but ^{18}F-FDOPA PET was pathognomonic for PGL. (**a**) Unenhanced CT, 40 HU; (**b**) arterial contrast-enhanced CT, 130 HU; (**c**) arterial contrast-enhanced CT (reconstruction); (**d**) portal-phase contrast-enhanced CT, 80 HU; (**e**) ^{18}F-FDG PET, moderate tumor uptake (SUVmax = 2.5); and (**f**) ^{18}F-FDOPA PET, high tracer uptake (SUVmax = 8.5). Pathological analysis found a typical paraganglioma
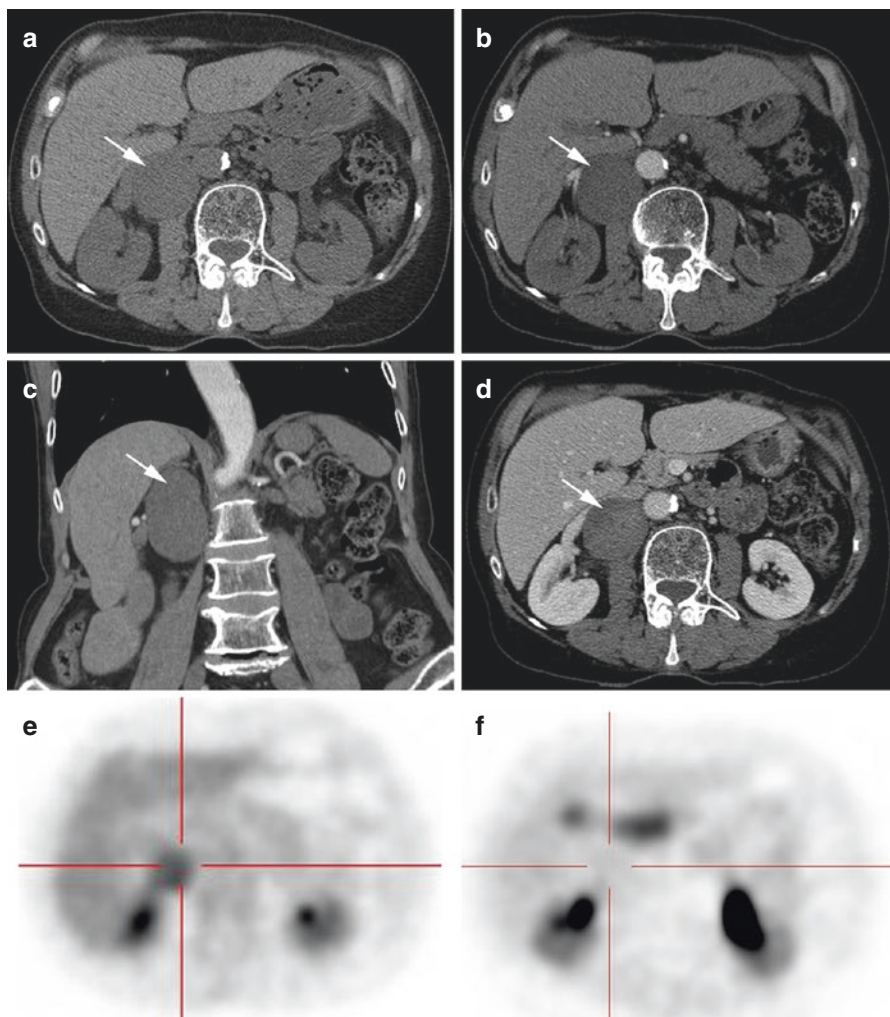
Fig. 14.6 Retroperitoneal neurofibroma. CT scan showed a retroperitoneal para-aortic solitary mass with a moderate and progressive homogeneous contrast enhancement. ^{18}F-FDG PET showed a mildly increased ^{18}F-FDG uptake, and ^{18}F-FDOPA PET was negative. (**a**) Unenhanced CT, 28 HU; (**b**) arterial contrast-enhanced CT, 36 HU; (**c**) arterial contrast-enhanced CT (reconstruction); (**d**) portal-phase contrast-enhanced CT, 70 HU; (**e**) ^{18}F-FDG, moderate tumor uptake (SUVmax = 3.6); and (**f**) ^{18}F-FDOPA PET, absence of tumor uptake. Pathological analysis found a cellular neurofibroma with atypia (Ki-67 10–15%)
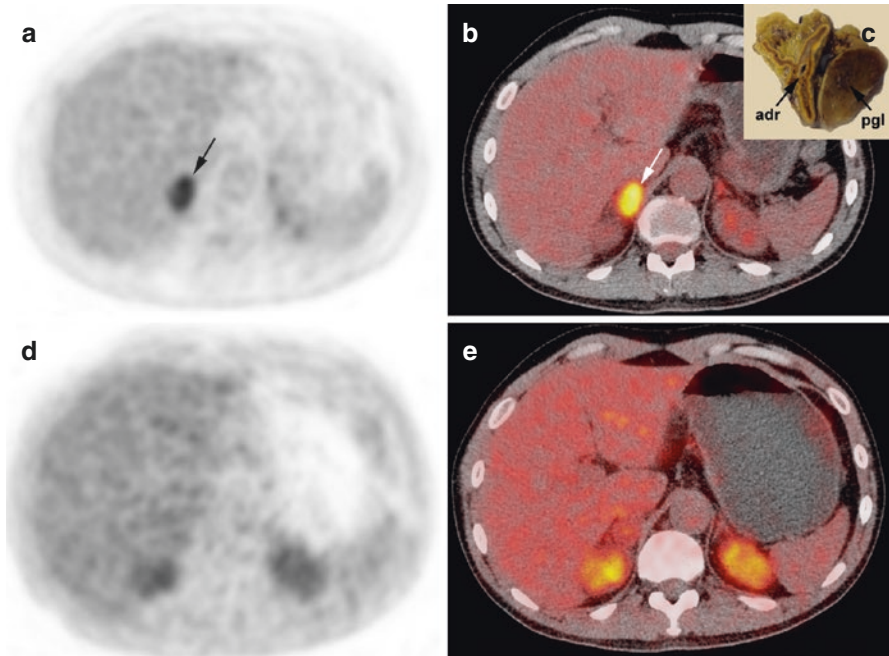
Fig. 14.7 Para-adrenal PGL in a *SDHD* patient. Axial ^{18}F-FDG PET (**a**) and PET/CT (**b**) and ^{18}F-FDOPA PET (**d**) and PET/CT (**e**). ^{18}F-FDG PET was positive, while ^{18}F-FDOPA PET was considered as falsely negative. Gross pathology showed that the tumor was developed from para-adrenal paraganglia (*adr* adrenal, *pgl* paraganglioma) (**c**)

14.10.5　Imaging Follow-Up of Mutation Carriers

An optimal follow-up algorithm has not yet been validated in mutation carriers for predisposing genes for PHEO/PGL. MRI offers several physical advantages over CT and does not expose patients to ionizing radiation, which is critical in a patient population submitted to lifelong imaging surveillance. However, MRI can be less sensitive than radionuclide imaging for detecting small lesions. Follow-up should include annual biochemical screening, and CT or MRI can be delayed on 2-year intervals. Indications for PET imaging studies should be discussed on an individual basis.

14.11　Current Proposed Imaging Algorithm in the Diagnosis and Localization of PHEO and Symp-PGL

Successful PPGL management requires an interdisciplinary team approach. Precise identification of clinical context and genetic status of patients enables a personalized use of functional imaging modalities [64–67]. Although the extra cost and availability of new PET tracers can prove problematic, the option of not employing
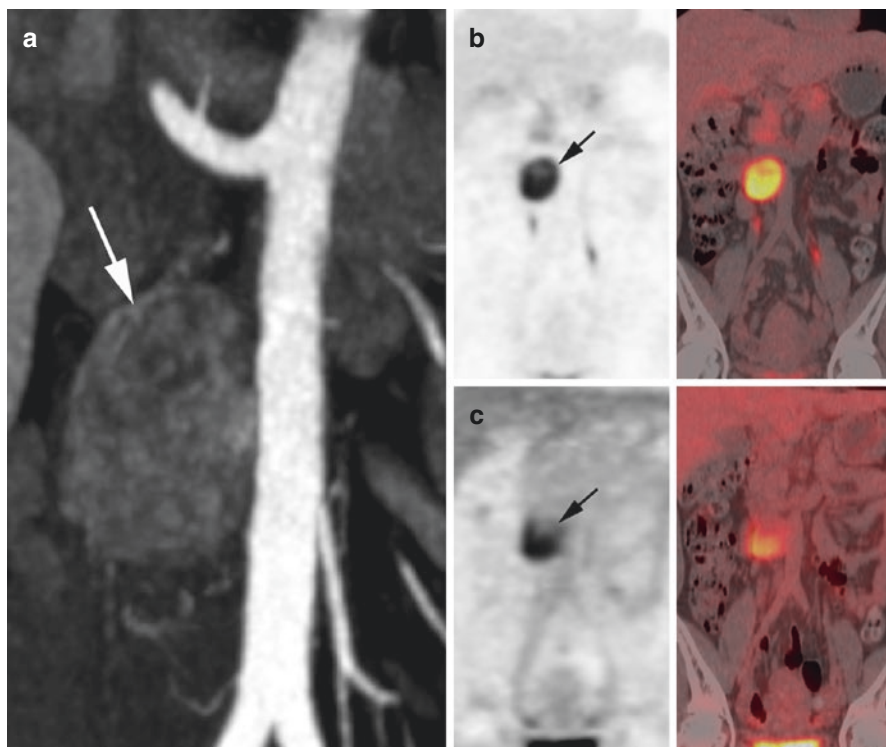
Fig. 14.8 *HIF2A*-related paraganglioma of the organ of Zuckerkandl. Contrast-enhanced CT arterial phase (**a**) showing a hypervascular and heterogeneous left para-aortic mass located at the level of the inferior mesenteric artery (*arrow*). ^{18}F-FDOPA PET/CT (**b**) and ^{18}F-FDG PET and PET/CT (**c**) showing a single tumor with heterogeneous uptake and a preferential ^{18}F-FDOPA imaging pattern, a finding which is opposite to the classical *SDHx*-associated imaging phenotype (see Fig. 14.7)

them might lead to inappropriate management with health-related consequences that should not be underestimated.

Based on the currently available imaging techniques, we propose the following approach to investigate a patient with HNPGL:

1. For diagnosis, the specificity provided by functional imaging techniques using ^{18}F-FDOPA PET/CT or ^{68}Ga-SSTa is superior to anatomical imaging.
2. For detecting additional tumor sites (multifocality, metastases), functional imaging techniques are superior to anatomical imaging. Based on the most recent studies and personal experience, PPGLs are well detected with ^{18}F-FDOPA PET/CT. ^{68}Ga-DOTA-SSA is also very sensitive for staging, regardless of the genotype. In the absence of available ^{68}Ga-DOTA-SSA, ^{18}F-FDG PET/CT should be used as the first-line radionuclide imaging tool in *SDHx* cases.
3. For determining the locoregional extension of PHEO/symp-PGL, anatomic imaging remains the first-line modality.

This algorithm should be adapted to the practical situation within each institution and should evolve with time as new techniques become available (Table 14.5). ^{18}F-FDOPA and ^{68}Ga-DOTA-SSA are currently available in many clinical and research centers around the world.

14.11.1 Image-Based Treatment of PHEOs/PGLs

14.11.1.1 Adrenal-Sparing Surgery

A subtotal (cortical-sparing) adrenalectomy is a valid option in patients with *MEN2, NF1,* or *VHL*. In cases with bilateral PHEOs, this strategy offers the advantage of potentially avoiding steroid supplementation. Therefore, it is crucial to perform regular imaging follow-ups of known PHEOs in addition to biochemical testing for determining the optimal time to schedule a cortical-sparing surgery. CT is preferable over MRI due to its excellent resolution, which provides detailed anatomical locations of tumor extension within the adrenal gland and, for *MEN2* patients, the number of tumors within the adrenal medulla. On the other hand, the advantage of using MRI over CT is the lack of exposure to ionizing radiation, which is an important factor in hereditary cases undergoing continuous follow-up. In selected cases, functional imaging may be used in addition to anatomical imaging. There is a clear advantage of ^{18}F-FDOPA PET/CT over MIBG and other specific PET tracers due to the lack of significant uptake in normal adrenal glands [68]. ^{18}F-FDOPA PET may also identify metastases from medullary thyroid carcinoma with persistent hypercalcitoninemia [69].

14.11.1.2 Theranostics

^{123}I-MIBG scintigraphy is used as a companion imaging agent to assist in radionuclide therapy selection. A special advantage of labeled SSAs is that, unlike ^{18}F-FDOPA, they can be used in the radioactive treatment of these tumors (as theranostic agents). To date, peptide receptor radionuclide therapy (PRRT) using ^{90}Y-/^{177}Lu-labeled somatostatin agonists has been evaluated in a limited number of PHEO/PGL cases [53–57, 70]. On average, response rates (mainly partial responses) have been 30–60 %. Disease stabilization is frequent but more difficult to interpret, since these tumors often exhibit a slow growing pattern. Larger studies, including various hereditary and non-hereditary PHEOs/PGLs, are needed in order to conclude which PHEOs/PGLs can best be treated using this therapy and whether PRRT should be used together or as a "replacement" to other treatment modalities.

We believe that data from PRRT in midgut NETs will provide a powerful impetus for wider application of the ^{68}Ga-/^{177}Lu-DOTATATE strategy in the management

Table 14.6 Physical characteristics of ^{111}In, ^{90}Y, ^{177}Lu, and [161]Tb [71]

	Emission	$T_{1/2}$ (d)	Total electron energy/decay (keV)	Path length (mm)	Gamma (keV)
[111]In	Auger	2.8	34.8	<0.01	171 (91%) 245 (94%)
[90]Y	Beta particles	2.7	933.1	12	–
[177]Lu	Beta particles	6.6	147.9	2	113 (6.4%) 208 (11%)
[161]Tb	Beta particles + Auger	6.9	202.5	<1	75 (10%)

of inoperable (including metastatic ones) PHEOs/PGLs. The toxicity profile (kidney, bone marrow) of ^{177}Lu-DOTATATE is acceptable due to the low penetration range of [177]Lu (Table 14.6). [90]Y has a pure beta emission with long-range particles that, besides the direct action, also lead to irradiation of non-receptor-expressing tumor cell (cross-fire effect). For these reasons, ^{90}Y-peptides could be preferable for the treatment of larger and inhomogeneous lesions. However, toxicity is more frequent than with ^{177}Lu, and clinical implementation of dosimetry is much more complex than for [177]Lu. [68]Ga can be used as a surrogate isotope for dosimetry purposes, but it provides only limited information due to its very short physical half-life (68 min) compared to ^{90}Y and [177]Lu (Table 14.6). ^{64}Cu-DOTATATE was also found to provide excellent imaging quality for NET imaging [45] and can be used for dosimetry purposes. Beyond ^{90}Y and ^{177}Lu, the terbium radioisotopes [155]Tb (SPECT), [152]Tb (PET), and [161]Tb (therapeutic isotope) can also be considered as theranostic pairs. [161]Tb has medium-energy beta particles similar to ^{177}Lu, but has the advantage over ^{177}Lu to emit a high level of internal conversion and Auger electrons that may act synergistically to beta particles. Modeling studies have shown that [161]Tb and ^{177}Lu can deliver equivalent absorbed doses in 10 mm spheres. However, [161]Tb would be more effective than ^{177}Lu at a smaller scale [71]. Therefore, the use of [161]Tb would enable destruction of macroscopic residual disease but also small cell clusters (micrometastases, isolated cells). Therapeutic nuclear medicine may also include the administration of bone-seeking radiopharmaceuticals. Beyond the use of beta particles and Auger emitters for therapeutic applications, there are significant advantages to use alpha emitters. However, until present, only a few studies have targeted NETs.

Recent reports have shown that cellular internalization might shorten the residual time of ^{177}Lu within tumor cells compared to radiolabeled SST antagonists. SST antagonists also have higher affinities for SST receptors than agonists, and lower internalization rates, resulting in a longer retention time on cell membrane. According to these observations, in the future, somatostatin antagonists might be considered as an alternative to agonists for PRRT.

References

1. Stenstrom G, Svardsudd K. Pheochromocytoma in Sweden 1958–1981. An analysis of the National Cancer Registry Data. Acta Med Scand. 1986;220(3):225–32.
2. Mantero F, Terzolo M, Arnaldi G, Osella G, Masini AM, Ali A, et al. A survey on adrenal incidentaloma in Italy. Study Group on Adrenal Tumors of the Italian Society of Endocrinology. J Clin Endocrinol Metab. 2000;85(2):637–44.
3. Barontini M, Levin G, Sanso G. Characteristics of pheochromocytoma in a 4- to 20-year-old population. Ann N Y Acad Sci. 2006;1073:30–7.
4. Lenders JW, Eisenhofer G, Mannelli M, Pacak K. Phaeochromocytoma. Lancet. 2005;366(9486):665–75.
5. Turkova H, Prodanov T, Maly M, Martucci V, Adams K, Widimsky Jr J, et al. Characteristics and outcomes of metastatic Sdhb and sporadic pheochromocytoma/paraganglioma: an National Institutes of Health Study. Endocr Pract. 2016;22(3):302–14.
6. Gimenez-Roqueplo AP, Dahia PL, Robledo M. An update on the genetics of paraganglioma, pheochromocytoma, and associated hereditary syndromes. Horm Metab Res. 2012;44(5):328–33.
7. Pacak K, Wimalawansa SJ. Pheochromocytoma and paraganglioma. Endocr Pract. 2015;21(4):406–12.
8. McNeil AR, Blok BH, Koelmeyer TD, Burke MP, Hilton JM. Phaeochromocytomas discovered during coronial autopsies in Sydney, Melbourne and Auckland. Aust N Z J Med. 2000;30(6):648–52.
9. Platts JK, Drew PJ, Harvey JN. Death from phaeochromocytoma: lessons from a post-mortem survey. J R Coll Physicians Lond. 1995;29(4):299–306.
10. Sutton MG, Sheps SG, Lie JT. Prevalence of clinically unsuspected pheochromocytoma. Review of a 50-year autopsy series. Mayo Clin Proc. 1981;56(6):354–60.
11. Schober A, Parlato R, Huber K, Kinscherf R, Hartleben B, Huber TB, et al. Cell loss and autophagy in the extra-adrenal chromaffin organ of Zuckerkandl are regulated by glucocorticoid signalling. J Neuroendocrinol. 2013;25(1):34–47.
12. Kohn A. Die Paraganglien. Arch Mikrosk Anat. 1903;52:262–365.
13. van Duinen N, Steenvoorden D, Kema IP, Jansen JC, Vriends AH, Bayley JP, et al. Increased urinary excretion of 3-methoxytyramine in patients with head and neck paragangliomas. J Clin Endocrinol Metab. 2010;95(1):209–14.
14. Eisenhofer G, Lenders JW, Siegert G, Bornstein SR, Friberg P, Milosevic D, et al. Plasma methoxytyramine: a novel biomarker of metastatic pheochromocytoma and paraganglioma in relation to established risk factors of tumour size, location and SDHB mutation status. Eur J Cancer. 2012;48(11):1739–49.
15. Eisenhofer G, Lenders JW, Timmers H, Mannelli M, Grebe SK, Hofbauer LC, et al. Measurements of plasma methoxytyramine, normetanephrine, and metanephrine as discriminators of different hereditary forms of pheochromocytoma. Clin Chem. 2011;57(3):411–20.
16. Amar L, Baudin E, Burnichon N, Peyrard S, Silvera S, Bertherat J, et al. Succinate dehydrogenase B gene mutations predict survival in patients with malignant pheochromocytomas or paragangliomas. J Clin Endocrinol Metab. 2007;92(10):3822–8.
17. Benn DE, Gimenez-Roqueplo AP, Reilly JR, Bertherat J, Burgess J, Byth K, et al. Clinical presentation and penetrance of pheochromocytoma/paraganglioma syndromes. J Clin Endocrinol Metab. 2006;91(3):827–36.
18. Taïeb D, Kaliski A, Boedeker CC, Martucci V, Fojo T, Adler Jr JR, et al. Current approaches and recent developments in the management of head and neck paragangliomas. Endocr Rev. 2014;35(5):795–819.
19. Schuttler J, Westhofen P, Kania U, Ihmsen H, Kammerecker S, Hirner A. Quantitative assessment of catecholamine secretion as a rational principle of anesthesia management in pheochromocytoma surgery. Anasthesiol Intensivmed Notfallmed Schmerzther. 1995;30(6):341–9.

20. Pacak K. Preoperative management of the pheochromocytoma patient. J Clin Endocrinol Metab. 2007;92(11):4069–79.
21. Lenders JW, Eisenhofer G. Pathophysiology and diagnosis of disorders of the adrenal medulla: focus on pheochromocytoma. Compr Physiol. 2014;4(2):691–713.
22. Luiz HV, Tanchee MJ, Pavlatou MG, Yu R, Nambuba J, Wolf K, et al. Are patients with hormonally functional phaeochromocytoma and paraganglioma initially receiving a proper adrenoceptor blockade? A retrospective cohort study. Clin Endocrinol (Oxf). 2016;85(1):62–9.
23. Eisenhofer G, Lenders JW, Goldstein DS, Mannelli M, Csako G, Walther MM, et al. Pheochromocytoma catecholamine phenotypes and prediction of tumor size and location by use of plasma free metanephrines. Clin Chem. 2005;51:735–44.
24. Kantorovich V, Pacak K. A new concept of unopposed beta-adrenergic overstimulation in a patient with pheochromocytoma. Ann Intern Med. 2005;142(12 Pt 1):1026–8.
25. Jochmanova I, Yang C, Zhuang Z, Pacak K. Hypoxia-inducible factor signaling in pheochromocytoma: turning the rudder in the right direction. J Natl Cancer Inst. 2013;105(17):1270–83.
26. Park BK, Kim CK, Kwon GY, Kim JH. Re-evaluation of pheochromocytomas on delayed contrast-enhanced CT: washout enhancement and other imaging features. Eur Radiol. 2007;17(11):2804–9.
27. Blake MA, Kalra MK, Maher MM, Sahani DV, Sweeney AT, Mueller PR, et al. Pheochromocytoma: an imaging chameleon. Radiographics. 2004;24 Suppl 1:S87–99.
28. Park BK, Kim B, Ko K, Jeong SY, Kwon GY. Adrenal masses falsely diagnosed as adenomas on unenhanced and delayed contrast-enhanced computed tomography: pathological correlation. Eur Radiol. 2006;16(3):642–7.
29. Mayo-Smith WW, Boland GW, Noto RB, Lee MJ. State-of-the-art adrenal imaging. Radiographics. 2001;21(4):995–1012.
30. Mitchell DG. Chemical shift magnetic resonance imaging: applications in the abdomen and pelvis. Top Magn Reson Imaging. 1992;4(3):46–63.
31. Varghese JC, Hahn PF, Papanicolaou N, Mayo-Smith WW, Gaa JA, Lee MJ. MR differentiation of phaeochromocytoma from other adrenal lesions based on qualitative analysis of T2 relaxation times. Clin Radiol. 1997;52(8):603–6.
32. Mamede M, Carrasquillo JA, Chen CC, Del Corral P, Whatley M, Ilias I, et al. Discordant localization of 2-[18F]-fluoro-2-deoxy-D-glucose in 6-[18F]-fluorodopamine- and [123I]-metaiodobenzylguanidine-negative metastatic pheochromocytoma sites. Nucl Med Commun. 2006;27(1):31–6.
33. Ilias I, Yu J, Carrasquillo JA, Chen CC, Eisenhofer G, Whatley M, et al. Superiority of 6-[18F]-fluorodopamine positron emission tomography versus [131I]-metaiodobenzylguanidine scintigraphy in the localization of metastatic pheochromocytoma. J Clin Endocrinol Metab. 2003;88(9):4083–7.
34. Shulkin BL, Wieland DM, Schwaiger M, Thompson NW, Francis IR, Haka MS, et al. PET scanning with hydroxyephedrine: an approach to the localization of pheochromocytoma. J Nucl Med. 1992;33:1125–31.
35. Imani F, Agopian VG, Auerbach MS, Walter MA, Imani F, Benz MR, et al. 18F-FDOPA PET and PET/CT accurately localize pheochromocytomas. J Nucl Med. 2009;50(4):513–9.
36. Fottner C, Helisch A, Anlauf M, Rossmann H, Musholt TJ, Kreft A, et al. 6-18F-fluoro-L-dihydroxyphenylalanine positron emission tomography is superior to 123I-metaiodobenzylguanidine scintigraphy in the detection of extraadrenal and hereditary pheochromocytomas and paragangliomas: correlation with vesicular monoamine transporter expression. J Clin Endocrinol Metab. 2010;95(6):2800–10.
37. King KS, Chen CC, Alexopoulos DK, Whatley MA, Reynolds JC, Patronas N, et al. Functional imaging of SDHx-related head and neck paragangliomas: comparison of 18F-fluorodihydroxyphenylalanine, 18F-fluorodopamine, 18F-fluoro-2-deoxy-D-glucose PET, 123I-metaiodobenzylguanidine scintigraphy, and 111In-pentetreotide scintigraphy. J Clin Endocrinol Metab. 2011;96(9):2779–85.

38. Taïeb D, Tessonnier L, Sebag F, Niccoli-Sire P, Morange I, Colavolpe C, et al. The role of 18F-FDOPA and 18F-FDG-PET in the management of malignant and multifocal phaeochromocytomas. Clin Endocrinol (Oxf). 2008;69(4):580–6.

39. Maurice JB, Troke R, Win Z, Ramachandran R, Al-Nahhas A, Naji M, et al. A comparison of the performance of (6)(8)Ga-DOTATATE PET/CT and (1)(2)(3)I-MIBG SPECT in the diagnosis and follow-up of phaeochromocytoma and paraganglioma. Eur J Nucl Med Mol Imaging. 2012;39(8):1266–70.

40. Janssen I, Blanchet EM, Adams K, Chen CC, Millo CM, Herscovitch P, et al. Superiority of [68Ga]-DOTATATE PET/CT to other functional imaging modalities in the localization of SDHB-associated metastatic pheochromocytoma and paraganglioma. Clin Cancer Res. 2015;21(17):3888–95.

41. Janssen I, Chen CC, Millo CM, Ling A, Taïeb D, Lin FI, et al. PET/CT comparing Ga-DOTATATE and other radiopharmaceuticals and in comparison with CT/MRI for the localization of sporadic metastatic pheochromocytoma and paraganglioma. Eur J Nucl Med Mol Imaging. 2016;43(10):1784–91.

42. Janssen I, Chen CC, Taïeb D, Patronas NJ, Millo CM, Adams KT, et al. 68Ga-DOTATATE PET/CT in the localization of head and neck paragangliomas compared with other functional imaging modalities and CT/MRI. J Nucl Med. 2016;57(2):186–91.

43. Reubi JC, Schar JC, Waser B, Wenger S, Heppeler A, Schmitt JS, et al. Affinity profiles for human somatostatin receptor subtypes SST1-SST5 of somatostatin radiotracers selected for scintigraphic and radiotherapeutic use. Eur J Nucl Med. 2000;27(3):273–82.

44. Reubi JC, Waser B, Khosla S, Kvols L, Goellner JR, Krenning E, et al. In vitro and in vivo detection of somatostatin receptors in pheochromocytomas and paragangliomas. J Clin Endocrinol Metab. 1992;74(5):1082–9.

45. Pfeifer A, Knigge U, Binderup T, Mortensen J, Oturai P, Loft A, et al. 64Cu-DOTATATE PET for neuroendocrine tumors: a prospective head-to-head comparison with 111In-DTPA-octreotide in 112 patients. J Nucl Med. 2015;56(6):847–54.

46. Niedermoser S, Chin J, Wangler C, Kostikov A, Bernard-Gauthier V, Vogler N, et al. In vivo Evaluation of (1)(8)F-SiFAlin-modified TATE: a potential challenge for (6)(8)Ga-DOTATATE, the clinical gold standard for somatostatin receptor imaging with PET. J Nucl Med. 2015;56(7):1100–5.

47. Charrier N, Deveze A, Fakhry N, Sebag F, Morange I, Gaborit B, et al. Comparison of [(1)(1)(1)In]pentetreotide-SPECT and [(1)(8)F]FDOPA-PET in the localization of extra-adrenal paragangliomas: the case for a patient-tailored use of nuclear imaging modalities. Clin Endocrinol (Oxf). 2011;74(1):21–9.

48. Taïeb D, Timmers HJ, Hindie E, Guillet BA, Neumann HP, Walz MK, et al. EANM 2012 guidelines for radionuclide imaging of phaeochromocytoma and paraganglioma. Eur J Nucl Med Mol Imaging. 2012;39(12):1977–95.

49. Timmers HJ, Chen CC, Carrasquillo JA, Whatley M, Ling A, Eisenhofer G, et al. Staging and functional characterization of pheochromocytoma and paraganglioma by 18F-fluorodeoxyglucose (18F-FDG) positron emission tomography. J Natl Cancer Inst. 2012;104(9):700–8.

50. Kroiss A, Putzer D, Frech A, Decristoforo C, Uprimny C, Gasser RW, et al. A retrospective comparison between (68)Ga-DOTA-TOC PET/CT and (18)F-DOPA PET/CT in patients with extra-adrenal paraganglioma. Eur J Nucl Med Mol Imaging. 2013;40(12):1800–8.

51. Archier A, Varoquaux A, Garrigue P, Montava M, Guerin C, Gabriel S, et al. Prospective comparison of (68)Ga-DOTATATE and (18)F-FDOPA PET/CT in patients with various pheochromocytomas and paragangliomas with emphasis on sporadic cases. Eur J Nucl Med Mol Imaging. 2016;43(7):1248–57.

52. Kroiss A, Putzer D, Decristoforo C, Uprimny C, Warwitz B, Nilica B, et al. 68Ga-DOTA-TOC uptake in neuroendocrine tumour and healthy tissue: differentiation of physiological uptake and pathological processes in PET/CT. Eur J Nucl Med Mol Imaging. 2013;40(4):514–23.

53. Delpassand ES, Samarghandi A, Zamanian S, Wolin EM, Hamiditabar M, Espenan GD, et al. Peptide receptor radionuclide therapy with 177Lu-DOTATATE for patients with somatostatin

receptor-expressing neuroendocrine tumors: the first US phase 2 experience. Pancreas. 2014;43(4):518–25.

54. Strosberg JR, Wolin EM, Chasen B, Kulke MH, Bushnell DL, Caplin ME, et al. NETTER-1 phase III: Progression-free survival, radiographic response, and preliminary overall survival results in patients with midgut neuroendocrine tumors treated with 177-Lu-Dotatate. J Clin Oncol. 2016;34 (suppl 4S; abstr 194).

55. van Essen M, Krenning EP, Kooij PP, Bakker WH, Feelders RA, de Herder WW, et al. Effects of therapy with [177Lu-DOTA0, Tyr3]octreotate in patients with paraganglioma, meningioma, small cell lung carcinoma, and melanoma. J Nucl Med. 2006;47(10):1599–606.

56. Vinik AI. Advances in diagnosis and treatment of pancreatic neuroendocrine tumors. Endocr Pract. 2014;20(11):1222–30.

57. Zovato S, Kumanova A, Dematte S, Sansovini M, Bodei L, Di Sarra D, et al. Peptide receptor radionuclide therapy (PRRT) with 177Lu-DOTATATE in individuals with neck or mediastinal paraganglioma (PGL). Horm Metab Res. 2012;44(5):411–4.

58. Lenders JW, Duh QY, Eisenhofer G, Gimenez-Roqueplo AP, Grebe SK, Murad MH, et al. Pheochromocytoma and paraganglioma: an endocrine society clinical practice guideline. J Clin Endocrinol Metab. 2014;99(6):1915–42.

59. Imperiale A, Battini S, Averous G, Mutter D, Goichot B, Bachellier P, et al. In vivo detection of catecholamines by magnetic resonance spectroscopy: A potential specific biomarker for the diagnosis of pheochromocytoma. Surgery. 2016;159(4):1231–3.

60. Imperiale A, Moussallieh FM, Roche P, Battini S, Cicek AE, Sebag F, et al. Metabolome profiling by HRMAS NMR spectroscopy of pheochromocytomas and paragangliomas detects SDH deficiency: clinical and pathophysiological implications. Neoplasia. 2015;17(1):55–65.

61. Varoquaux A, le Fur Y, Imperiale A, Reyre A, Montava M, Fakhry N, et al. Magnetic resonance spectroscopy of paragangliomas: new insights into in vivo metabolomics. Endocr Relat Cancer. 2015;22(4):M1–8.

62. Gimm O, DeMicco C, Perren A, Giammarile F, Walz MK, Brunaud L. Malignant pheochromocytomas and paragangliomas: a diagnostic challenge. Langenbecks Arch Surg. 2012;397(2):155–77.

63. Schovanek J, Martucci V, Wesley R, Fojo T, Del Rivero J, Huynh T, et al. The size of the primary tumor and age at initial diagnosis are independent predictors of the metastatic behavior and survival of patients with SDHB-related pheochromocytoma and paraganglioma: a retrospective cohort study. BMC Cancer. 2014;14:523.

64. Havekes B, King K, Lai EW, Romijn JA, Corssmit EP, Pacak K. New imaging approaches to phaeochromocytomas and paragangliomas. Clin Endocrinol (Oxf). 2010;72(2):137–45.

65. Taïeb D, Neumann H, Rubello D, Al-Nahhas A, Guillet B, Hindie E. Modern nuclear imaging for paragangliomas: beyond SPECT. J Nucl Med. 2012;53(2):264–74.

66. Timmers HJ, Taïeb D, Pacak K. Current and future anatomical and functional imaging approaches to pheochromocytoma and paraganglioma. Horm Metab Res. 2012;44(5):367–72.

67. Taïeb D, Rubello D, Al-Nahhas A, Calzada M, Marzola MC, Hindie E. Modern PET imaging for paragangliomas: relation to genetic mutations. Eur J Surg Oncol. 2011;37(8):662–8.

68. Luster M, Karges W, Zeich K, Pauls S, Verburg FA, Dralle H, et al. Clinical value of 18F-fluorodihydroxyphenylalanine positron emission tomography/computed tomography (18F-DOPA PET/CT) for detecting pheochromocytoma. Eur J Nucl Med Mol Imaging. 2010;37(3):484–93.

69. Treglia G, Rufini V, Salvatori M, Giordano A, Giovanella L. PET imaging in recurrent medullary thyroid carcinoma. Int J Mol Imaging. 2012;2012:324686.

70. Puranik AD, Kulkarni HR, Singh A, Baum RP. Peptide receptor radionuclide therapy with (90) Y/(177)Lu-labelled peptides for inoperable head and neck paragangliomas (glomus tumours). Eur J Nucl Med Mol Imaging. 2015;42(8):1223–30.

71. Hindie E, Zanotti-Fregonara P, Quinto MA, Morgat C, Champion C. Dose deposits from 90Y, 177Lu, 111In, and 161Tb in micrometastases of various sizes: implications for radiopharmaceutical therapy. J Nucl Med. 2016;57(5):759–64.

Chapter 15
Radionuclide Imaging of Gastrointestinal Neuroendocrine Tumors

Alessio Imperiale, Christophe M. Deroose, Elif Hindié, and Bernard Goichot

Neuroendocrine tumors (NETs) are rare and heterogeneous epithelial neoplasms with neuroendocrine differentiation [1]. The most common origin of primary NETs is the gastrointestinal (GI) tract (about 60 % of all cases), and within the GI tract, the small intestine represents the first site of primary tumor development [2]. Because only a small percentage of GI NETs are functional, patients are often asymptomatic, and the tumors are incidentally diagnosed by endoscopic examination or imaging studies performed for unrelated reasons. The clinical symptomatology of GI NETs is generally associated with advanced disease and the presence of systemic meta-static spread. Bowel obstruction and incidental detection of hepatic metastases are common circumstances that lead to the diagnosis. Extensive tumor bulk and

A. Imperiale, MD, PhD (✉)
Biophysics and Nuclear Medicine Department, Hautepierre Hospital, University Hospitals of Strasbourg, 1, Avenue Molière, 67098, Strasbourg Cedex 09, France

ICube, University of Strasbourg, Strasbourg, France
e-mail: alessio.imperiale@chru-strasbourg.fr

C.M. Deroose, MD, PhD
Nuclear Medicine, University Hospitals Leuven, and Department of Imaging & Pathology, KU Leuven, Herestraat 49, 3000 Leuven, Belgium
e-mail: christophe.deroose@uzleuven.be

E. Hindié, MD, PhD
Nuclear Medicine Department, Haut-Lévêque Hospital, CHU Bordeaux, University of Bordeaux, Avenue Magellan, 33604 Pessac, France

LabEx TRAIL, University of Bordeaux, Bordeaux, France
e-mail: elif.hindie@chu-bordeaux.fr

B. Goichot, MD, PhD
Internal Medicine Department, Hautepierre Hospital, University Hospitals of Strasbourg, 1, Avenue Molière, 67098, Strasbourg Cedex 09, France
e-mail: bernard.goichot@chru-strasbourg.fr

metastatic disease are the major causes of death. However, even in advanced disease, long patient survival, which is mainly related to the slowly growing pattern of many of these tumors, is not uncommon [3]. This chapter will focus on medical imaging for gastrointestinal NETs except for pancreatic NET.

15.1 Epidemiology

NETs of the GI tract derive from the embryological foregut intestine (esophagus, stomach, first portion of duodenum), midgut (duodenum, jejunum/ileum, appendix, cecum, ascending colon), and hindgut (distal large bowel, rectum). Incidence of GI NETs is classically estimated at 1/100,000 but is probably underestimated as old autopsy studies suggested that most of the cases were not diagnosed during the patient's life. Prevalence is much higher because of the relatively long survival (overall about 60 % at 5 years) [4]. Apart from ileal tumors, GI NETs are rarely associated with secretory syndrome. They are usually diagnosed on tumor symptoms or, often so, fortuitously. The revelation of GI NET by liver metastasis is frequent, presenting with general symptoms, with biological abnormalities, or as incidental findings on imaging studies.

15.2 Classification and Staging

Grading of GI NETs relies on the 2010 WHO classification [5] developed in detail in another chapter. Briefly, G1 (defined by a Ki-67 index < 3 % and a mitotic count < 2) is usually very slowly evolving tumors, G2 (defined by a Ki-67 index ranging between 3 % and 20 % or a mitotic count of 2–20) constitutes a more heterogeneous group with well-differentiated but more aggressive tumors, and G3 (Ki-67 index >20 % or a mitotic count >20) usually refers to poorly differentiated carcinomas characterized by an aggressive pattern, clear response to chemotherapy in particular platinum-based agents, and a poor overall survival. The limits of this classification is discussed elsewhere, and the two main challenges are currently to better separate G2 tumors in subgroups of different prognosis and to identify among G3 tumors a subgroup of morphologically well-differentiated tumors which might display a different sensitivity to chemotherapy. Nuclear imaging may be one of the tools that could achieve this improvement in the characterization of a "metabolic" tumor grade.

Staging of GI NET relies on TNM classification. Two different classifications are used, ENETS 2007 and UICC; they differ only for the appendix (and for the pancreas, not treated here). Stages 0 to IIIa correspond to localized tumors, IIIb to tumors with lymph node involvement, and stage IV to metastatic diseases [6].

15.3 Clinical Presentation

Tumors from the esophagus, stomach, first part of duodenum, colon, and rectum are usually diagnosed during endoscopy and may present macroscopically as polypus, ulcers, or other types of digestive tumors. They are usually non-secreting, and the main question in these cases is to ensure that there has been complete resection of the lesion. Echoendoscopy is useful to evaluate the depth of invasion and the presence of abnormal lymph nodes. This staging step is necessary to decide further therapeutic strategy. Endoscopic submucosal resection allows in most cases to avoid surgical resection.

Gastric NET is classified in three subgroups:

- Type 1 are the most frequent and are associated with atrophic gastritis (mainly Biermer's disease). They are usually < 1 cm, multiple, and benign.
- Type 2 are very rare and are associated with Zollinger–Ellison syndrome.
- Type 3 are rare, generally unique, and potentially malignant.

It is very important to distinguish type 1 and type 3 because conservative treatment is indicated in type 1, whereas more aggressive treatment, in particular surgery, is justified in type 3. Gastrin measurement and biopsy of the gastric mucosa (to show evidence of atrophic gastritis) are mandatory [7, 8].

Ileal NET often secretes various amines and in particular serotonin, whereas secretion is rare for the other GI NETs. These tumors are named "functional" if the secretion causes symptoms. The syndrome caused by serotonin secretion is named carcinoid syndrome. It associates three main symptoms: flushing, diarrhea, and more rarely bronchoconstriction as well as heart failure related to a specific cardiac complication (carcinoid heart disease) with right-side valve involvement, in particular tricuspid insufficiency. Careful cardiac evaluation is necessary in patients with serotonin-producing tumors, because carcinoid heart disease has a major impact on survival, and valve replacement may be necessary in some patients [9].

Tumors of the appendix are usually discovered during surgery for appendicitis. The majority of patients with stage I tumors do not need additional treatment or long-term follow-up. However, for depending on localization and depth of tumor invasion, some patients will require complementary surgery (right hemicolectomy).

Chromogranin A (CgA) is the most reliable plasma marker of NET. It is not specific of GI NET and is strongly correlated to tumor burden. It is usually normal in small and localized tumor. False positive is very frequent, in particular due to treatment with proton-pump inhibitors, atrophic gastritis, or renal failure. If initially elevated, CgA can be an interesting tool for the follow-up of patients, but its interpretation warrants caution in some cases as some antisecretory treatments (mainly somatostatin analogues) can decrease CgA plasma levels independently of any anti-tumor effect. Serotonin measurement is not recommended for the diagnosis and follow-up of serotonin-producing ("carcinoid") tumors due to its great variability.

Table 15.1 Summary of the main clinical features, hormonal secretion, and first-line therapeutic management in well-differentiated (G1/G2) GI NETs

	Frequent clinical features	Secretion	Management (first line)
Stomach	Mainly endoscopic discovery[a]	Rare	Depends on type (see text)
Small intestine	Often discovered on complication (obstruction, perforation, bleeding) Liver metastasis Carcinoid syndrome	30 %, mainly serotonin	Surgery Somatostatin analogues Cardiac monitoring
Appendix	Mainly incident discovery during surgery	No	Right hemicolectomy should be discussed for tumor > 1 cm
Colon	Mainly endoscopic discovery[a]	Rare	Endoscopic resection if possible Surgery
Rectum	Mainly endoscopic discovery[a]	Rare	Endoscopic resection if possible Surgery

[a]Indication for endoscopy may be abdominal pain, bleeding, cancer screening, etc.

Twenty-four-hour urinary 5-hydroxyindole-3-acetic acid (5-HIAA) is the best marker for these tumors and is partially correlated to prognosis [10].

Whatever the localization of the tumor, stage, and grade, all cases should be presented to a multidisciplinary board, and many patients will need follow-up by a multidisciplinary team with sufficient experience in neuroendocrine tumors. If cure is the goal for localized tumors, it is rarely achievable in metastatic disease. Beyond increasing survival, preservation of quality of life is essential. Control of the secretory syndrome, treatment of complications (as carcinoid heart disease), and consideration of short- and long-term therapy toxicities are crucial.

The main clinical features, hormonal secretion, and the first-line therapeutic management are briefly summarized in Table 15.1.

15.4 Role of Imaging in GI NET Diagnosis and Management

Considering surgery as the only curative treatment in patients without metastases or with limited metastatic spread [11], it is essential to define the real extent of the disease and to identify patients with inoperable disease [12, 13]. Accordingly, medical imaging plays an increasingly crucial role by (a) guiding tumor preoperative assessment (i.e., identification of the primary, assessment of locoregional extension and distant metastases), (b) expanding surgical approaches, and (c) evaluating the therapeutic outcome. In patients with a known or suspected GI NET, a multidisciplinary strategy including both radiological studies and nuclear medicine examinations is usually employed. The former provides detailed anatomical information that is indispensable for primary tumor detection, locoregional and distant metastases

identification, surgical planning optimization, and medical treatment evaluation. The latter allows a noninvasive characterization of tumoral functional status and variability at the molecular and cellular level starting from the analysis of uptake intensity and kinetics of some target-specific radiotracers. Molecular imaging techniques are also very sensitive and can detect disease at an early stage. Nuclear medicine provides further details regarding the tumoral extent improving patient staging and therapeutic strategy. In order to improve the diagnostic accuracy, anatomic and functional imaging are usually combined by using « hybrid » modalities as positron emission tomography/computed tomography (PET/CT) and single-photon emission computed tomography/computed tomography (SPECT/CT) devices. Nowadays, PET/MRI hybrid systems are also available and may be effective, although the role of PET/MR in GI NETs needs to be established and its availability in clinical routine is limited.

15.5 Diagnostic Performances of Anatomic Imaging

In the evaluation of patients with suspected or known GI NETs, a number of techniques have been proposed to identify the tumor primary site, to assess locoregional extent, and to assess the presence of distant metastases. A variable combination of endoscopy, ultrasound (US), endoscopic ultrasound (EUS), CT, and magnetic resonance imaging (MRI) is typically adopted to provide optimal patient management, taking into account the clinical context and both strengths and limitations of each diagnostic modality (Table 15.2).

15.5.1 Primary Tumor Detection

Upper and lower endoscopy enable the detection of esophageal, gastric, colorectal, and some terminal ileal NETs. Double-balloon or push enteroscopy is more efficient for small intestine lesions but remains a time-consuming technique and uncomfortable for the patient [14]. Capsule endoscopy seems an attractive technique for esophagus, stomach, and small intestine examination but does not permit lesion biopsy [15]. The main advantage of video capsule is that it is a noninvasive technique able to analyze the entire small bowel. However, it has only moderate sensitivity (46–65 %) for tumor detection [16]. The use of transabdominal ultrasonography (TAUS) in GI NET diagnosis and staging is mainly limited to the solid viscera and suffers from inter-operator variability. Overall, US has limited sensitivity (13–27 %) for the detection of gastrointestinal NETs [17]. Intraoperative US could be also performed but it prolongs operating time, and it is not free of potential risk of iatrogenic injury during the diagnostic procedure. Conversely, endoscopic US (EUS) has a remarkable role. EUS is a highly sensitive technique for the detection of gastric, duodenal, and rectal NETs permitting not only the identification of

Table 15.2 Comparison of the main anatomical imaging and endoscopic techniques currently available

TAUS	EUS	Video capsule	CT	MRI
Widely available	Highly sensitive technique for the detection of gastric, duodenal, and rectal primary NETs	Attractive technique for the detection of esophageal, gastric, duodenal, and small-bowel primary NETs	Widely available	Multiplanar contrast-enhanced images
Use limited to solid organs only	Diagnostic biopsy is possible	Analysis of the entire bowel is possible	Multiplanar contrast-enhanced images	First-choice imaging modality for detection and assessment of liver metastases (superior to CT)
High inter-operator variability	Invasive diagnostic procedure	Moderate sensitivity	First-choice imaging modality for staging and follow-up	High sensitivity for bone marrow metastases
Limited sensitivity for primary GI NET detection			Identification of tumor primary site, evaluation of local extent, and assessment of metastases	Enterography and enteroclysis are possible and can enhance sensitivity
			Enterography and enteroclysis are possible and can enhance sensitivity	Gadolinium chelate more safe than CT iodine-contrast agents as regards allergic reactions and nephrotoxicity
			Ionizing-radiation technique	No ionizing radiation

TAUS transabdominal US; *EUS* endoscopic US; *CT* computed tomography; *MRI* magnetic resonance imaging

small submucosal tumors but even to perform diagnostic procedures such as biopsy or fine-needle aspiration [18]. However, EUS remains a more invasive imaging method. In patients suspected of having small-bowel tumors, the enteroclysis and barium-contrast examinations may show fixation, separation, thickening, and angulation of the bowel loops, but they are rarely diagnostic. Small primary tumors are difficult to visualize unless there is secondary fibrosis. At present, barium-contrast studies have been largely replaced by multi-planar contrast-enhanced CT or MR imaging followed by small-bowel distention before a focused CT or MR enterography or enteroclysis to improve tumor detection. Small-bowel tumors are multifocal in about 30% of the cases [19], and they manifest as polypoid lesions or hypervascular parietal concentric or asymmetrical thickening. The sensitivity and specificity for tumor detection of CT and MR enterography or enteroclysis have been

estimated at 100 % and 86–94 %, and 96 % and 95–98 %, respectively. Overall sensitivity increases with rising tumor size [20–24]. Artifacts from bowel motion and lower spatial resolution compared with CT may be limiting factors of MR enterography or enteroclysis.

15.5.2   Tumor Staging and Metastatic Assessment

CT remains the first-choice diagnostic procedure for tumor staging allowing the assessment of local extent to the mesentery as well as metastases to lymph nodes, liver, and lungs. Typically, the appearance of mesenteric invasion by carcinoid tumor on CT is a spiculated mass with heterogeneous contours, variably associated to central calcifications and usually near the primary tumor ("cartwheel" pattern) [25]. Metastatic lymph nodes are frequently in the mesentery or retroperitoneal and paracardial gastric lymph nodes. For the assessment of metastatic hepatic disease, all available imaging modalities frequently miss lesions sized less than 5 mm [26]. Nevertheless, multiphasic imaging is recommended, with the hepatic arterial phase being the most informative for lesion detection [27]. On multiphasic contrast-enhanced CT or MR images, hepatic lesions are usually hypervascular in the arterial phase and demonstrate washout in the late phase [28, 29]. MRI is a very sensitive technique for the detection of liver metastases, and it is considered more accurate than both US and CT [26]. Multiphasic MRI with fat-suppressed contrast-enhanced T1-weighted imaging provides the best accuracy [29, 30]. Typically, NET lesions show T2 hyperintensity and T1 hypointensity. The use of diffusion-weighted imaging (DWI) and apparent diffusion coefficients (ADC) could improve the detection ability of MRI for malignant liver lesions [31]. An added advantage of using DWI is its ability to reflect lesion changes in response to treatment [32]. Finally, the advantages of MRI over CT are the lack of ionizing radiation and the use of gadolinium chelate contrast agents, which have a better safety profile in terms of allergic reactions and nephrotoxicity than iodine-contrast agents. Metastases to the bone arise more commonly from foregut primary tumors. The preferred site of metastatic spread is the axial skeleton and radiographic signs may be easily missed. On standard radiography and CT, bone metastases frequently demonstrate either an osteosclerotic or a mixed osteolytic–osteosclerotic pattern. MRI is the most sensitive technique for detection of bone marrow metastases [33–35].

15.6   Radionuclide Imaging for Molecular and Metabolic Characterization

Nuclear medicine imaging for NETs exploits some molecular characteristics that are specific for the neuroendocrine phenotype. Hence, the overexpression of specific membrane receptors as well as the ability to take up and decarboxylate amine

Table 15.3 Comparison of the main functional imaging techniques currently available

[111]In-pentetreotide SPECT/CT	^{68}Ga-somatostatin analogues PET/CT	^{18}F-FDOPA PET/CT	^{18}F-FDG PET/CT
Primary staging Restaging Evaluation of uptake before peptide receptor radiotherapy (PRRT)	Primary staging Restaging Unknown primary Evaluation of uptake before PRRT	Primary staging Unknown primary (Restaging?) Carcinoids +++	Prognostic stratification High-grade G2 and G3 NETs
Approved nuclear medicine technique for NET imaging	It will replace SRS in the near future	Sensitivity may be lower than ^{68}Ga-PET/CT for non-ileal NETs	Widely available
Low spatial resolution (>10 mm)	High spatial resolution (5 mm)	High spatial resolution (5 mm)	High spatial resolution (5 mm)
2-day procedure	1-day procedure	1-day procedure	1-day procedure
Radiation exposure	Radiation exposure	Radiation exposure	Radiation exposure

FDOPA dihydroxyphenylalanine; *FDG* fluorodeoxyglucose; *PET* positron emission tomography

precursors has been considered for diagnostic radiotracer development. Moreover, the glycolytic metabolism, which is not a specific energetic pathway of NETs, has been also proposed (Table 15.3). Accordingly, a personalized nuclear medicine exploration will be tailored for each patient taking into consideration both clinical symptomatology and the tumor characteristics.

15.6.1 Radiolabeled Somatostatin Analogue Imaging

The somatostatin receptor (SSTR) is a seven-transmembrane G-coupled receptor, of which six human subtypes have been described and which upon activation reduces endocrine secretion and cell growth and increases apoptosis [36]. Upon binding of an agonist to the receptor, the receptor/ligand complex will internalize in the cell, and the receptor will be later recycled to the cell surface. A vast majority (>85%) of intestinal NETs will have moderate to high overexpression of one of the six SSTR subtypes (1, 2A, 2B, 3, 4, and 5) [36], most frequently subtype 2A [37]. The SSTR has been used as a molecular target in nuclear medicine since more than 25 years [38]. Radioligands binding to the SSTR detected by gamma camera scintigraphy and SPECT were the first to be developed and are based on synthetic somatostatin analogues (SSAs) such as the 8 amino acid derivative octreotide or further optimized chemical variants of this vector backbone. Different chelators have been developed to allow labeling of these vector molecules with a whole range of radioisotopes. One gamma camera radiopharmaceutical is commercially available (^{111}In-pentetreotide; Octreoscan™), and technetium-99 m-labeled tracers have been

described as well, using both octreotide and octreotate backbones with a HYNIC chelator/linker. The use of somatostatin receptor scintigraphy (SRS) is recommended in the guidelines at diagnosis [1] and during follow-up [39]. It offers high sensitivity and specificity in detecting tumoral lesions in grades 1 and 2 NET, outperforming other nuclear medicine tracers such as ^{18}F-fluorodeoxyglucose (^{18}F-FDG) and ^{123}I-meta-iodobenzylguanidine (^{123}I-MIBG). In a study by Binderup and colleagues, SRS detected more lesions in all organs studied than ^{18}F-FDG or ^{123}I-MIBG with a sensitivity of 90 % vs. 57 % and 53 %, respectively [40]. Of note, in highly proliferative NET (Ki-67 > 15 %), ^{18}F-FDG had a sensitivity of 92 % vs. 69 % for SRS [40]. Besides tumor detection, SRS allows to determine functional target presence for treatment with cold SSAs. Two randomized controlled trials (RCTs) have shown a prolongation of progression-free survival (PFS) in NET patients treated with SSAs; one trial included well-differentiated metastatic midgut NETs (PROMID) [41], and the other included well-differentiated nonfunctional tumors of the pancreas, midgut, hindgut, or unknown origin (CLARINET) [42]. A positive SRS was an inclusion criterion in the CLARINET study, whereas in the PROMID trial, 73 out of 85 patients had a scintigraphy performed, with 86 % positive and 14 % negative patients [41], highlighting the importance of the scintigraphy as a selection tool for this treatment. For peptide receptor radionuclide therapy (PRRT), good uptake on pre-therapy SRS has always been considered a prerequisite. For example, in the Netter-1 RCT, a positive scintigraphy on all evaluable lesions was an inclusion criterion [43].

Uptake on whole-body planar ^{111}In-pentetreotide scintigraphy is typically scored according to the Krenning scale, with grade 1 representing tumor uptake lower than the liver, grade 2 tumor uptake equal to the liver, grade 3 uptake higher than liver, and grade 4 tumor uptake as the most intense site in the body (usually meaning higher than spleen uptake). A grade 3 uptake is typically required for PRRT candidates.

In the last decade, a novel class of radiopharmaceuticals for SSTR imaging has emerged as the current gold standard (Fig. 15.1). These tracers are based on octreotide derivatives labeled with the positron-emitting radionuclide gallium-68. Gallium-68 is a radioisotope of the metal gallium. It decays primarily through positron emission (abundance 89 %). It has a half-life ($T_{1/2}$) of 68 min and can be obtained from a germanium-68/gallium-68 generator ($T_{1/2}$: 271 days), thus allowing in-house production of labeled radiopharmaceuticals. Gallium can be chelated by a number of different chelators to label peptides or other biomolecules for detection with PET, PET/CT, or PET/MR. Labeling has to be done at the site of administration as the yield of the generator, and the half-life usually does not allow for off-site transport.

There are several gallium-68-labeled tracers for SSTR imaging that have been described and are in clinical use in Europe of which ^{68}Ga-DOTATOC, ^{68}Ga-DOTATATE, and ^{68}Ga-DOTANOC are the most commonly used. "DOTA" refers to the chelator, which is covalently bound to a slightly modified synthetic octapeptide with high affinity for the SSTR (all have high affinity for $SSTR_2$, the most overexpressed subtype). They are collectively referred to as ^{68}Ga-DOTA-peptides or ^{68}Ga-OctreoPET.
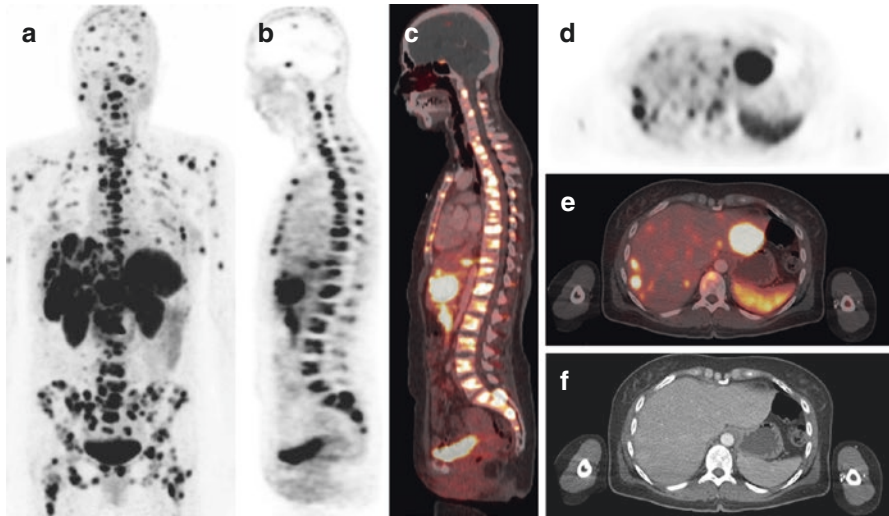
Fig. 15.1 Example of a 48-year-old NET patient with an 11-year disease history with high SSTR expression ($SUV_{max} = 36$ in the most intense lesion) and high multifocal tumor burden in the bone, pancreas, soft tissue, and liver on ^{68}Ga-DOTATATE PET/CT. The patient was sent for PRRT eligibility and was considered as candidate. (**a**) MIP image. (**b**) Sagittal PET showing diffuse bone involvement and liver metastases. (**c**) Corresponding PET/CT fusion. (**d**) Axial view showing multifocal liver metastases with several lesions exceeding the uptake level of the spleen; the lesion in the left liver lobe is the one with the highest uptake of all lesions ($SUV_{max} = 36$). Note metastases in both humeri. (**e**) Corresponding PET/CT fusion, (**f**) corresponding CT with very little findings, both in the liver (late venous contrast phase) and in the bone

These ^{68}Ga-DOTA-peptides have advantages over gamma scintigraphy-based imaging. They have a much higher affinity for $SSTR_2$ compared to ^{111}In-pentetreotide ($IC_{50} = 2.5$ nM for ^{68}Ga-DOTATOC, 0.2 nM for ^{68}Ga-DOTATATE, and 1.9 nM for ^{68}Ga-DOTANOC, vs. 22 nM for ^{111}In-pentetreotide) [44]. This better affinity profile combined with the physical advantages of current clinical PET cameras over gamma cameras, with higher spatial resolution and higher sensitivity (detected events per unit of radioactivity), allows detection of smaller lesions and detection of lesions with even low or moderate SSTR expression, resulting in a higher sensitivity (Fig. 15.2). There is strong scientific data that the ^{68}Ga-DOTA-peptides are significantly better diagnostic agents for performing SSR imaging than ^{111}In-pentetreotide. Gabriel et al. [45] compared ^{68}Ga-DOTATOC with ^{111}In-pentetreotide in 84 NET patients and found a sensitivity of 97 % for ^{68}Ga-DOTATOC vs. 52 % for ^{111}In-pentetreotide. ^{68}Ga-DOTATOC showed better performance for small lesions in lymph nodes and for bone metastases (Fig. 15.3). Buchmann et al. [46] compared ^{68}Ga-DOTATOC with ^{111}In-pentetreotide in 27 NET patients and found a sensitivity of 100 % and 66 %, respectively. They concluded that the PET ligand was superior for detection of lung and bone metastases. Van Binnebeek et al. [47] have recently shown similar results with sensitivity of
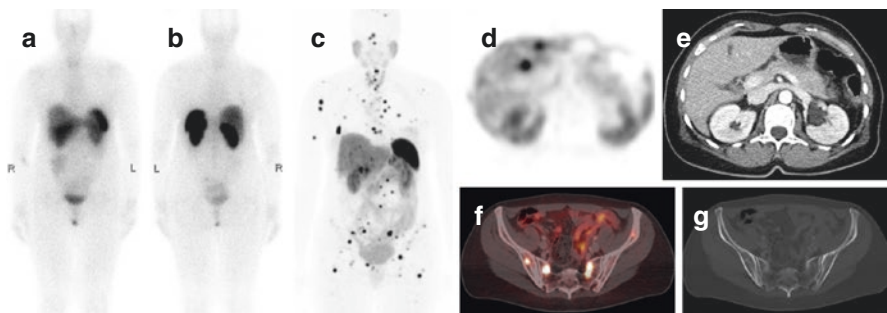
Fig. 15.2 Example of a 50-year-old female NET patient scanned with both ^{111}In-pentetreotide and ^{68}Ga-DOTATATE PET/CT. Anterior (**a**) and posterior (**b**) planar projections of ^{111}In-pentetreotide at the time of initial diagnosis. The anterior image does not show any sites of increased uptake. The posterior image shows a small focus with slightly increased uptake in the left hemisacrum. (**c**) MIP image of ^{68}Ga-DOTATATE PET/CT performed because of suspicious findings on liver MRI and rising serum chromogranin 12 months later. There are multiple small liver and bone metastases with strong to intense tracer uptake. (**d**) Transverse image showing two liver metastases with strong uptake. (**e**) Corresponding late venous phase contrast-enhanced CT with the absence of radiological correlate (the hypodense structure in the mid-liver is the falciform ligament). (**f**) Fusion image showing four pelvic bone metastases with intermediate to strong uptake; one lesion in the left hemisacrum corresponds to the location seen on the posterior ^{111}In-pentetreotide image. (**g**) CT in bone window showing only subtle changes at the site of the bone metastases seen on the fusion image

99.9 % for ^{68}Ga-DOTATOC with only 60 % for ^{111}In-pentetreotide in metastatic NET patients scheduled for PRRT. Furthermore, they showed that in up to 80 % of the patients, the PET ligand would detect at least 20 % more lesions, showing that the benefit of ^{68}Ga-DOTA-peptide PET reaches a large fraction of patients. Recent data from Northern America have shown a lesion sensitivity of 95.1 % vs. 45.3 % for anatomic imaging and 30.9 % for ^{111}In-pentetreotide SPECT/CT in 131 GEP-NETs or NETs from unknown primary [48]. In four out of 14 patients (29 %), ^{68}Ga-DOTATATE PET/CT found a previously unknown primary tumor. The therapy recommendation was changed on the basis of the ^{68}Ga-DOTATATE PET/CT in one third of the patients [48]. Again, large differences between ^{68}Ga-DOTATOC and ^{111}In-pentetreotide were reported by Morgat and colleagues in the follow-up of MEN1 patients [49].

Although there are some differences in the affinity profiles (^{68}Ga-DOTATOC: $SSTR_2 > SSTR_5$;   ^{68}Ga-DOTATATE: $SSTR_2$;   ^{68}Ga-DOTANOC $SSTR_2 > SSTR_5 > SSTR_3$), clinical comparative studies have only shown minor if there are any differences in lesion detection rate and lesion uptake when comparing head to head two of these PET SSTR ligands (Fig. 15.4). The consensus is that for the vast majority of clinical indications, these tracers are equivalent [50]. In a head-to-head comparison in the same patients ($n = 40$) between ^{68}Ga-DOTATOC and ^{68}Ga-DOTATATE, 262 and 254 (97 %) lesions were detected with an average standardized uptake value (SUV) of 20.4 and 16.0, respectively [51].
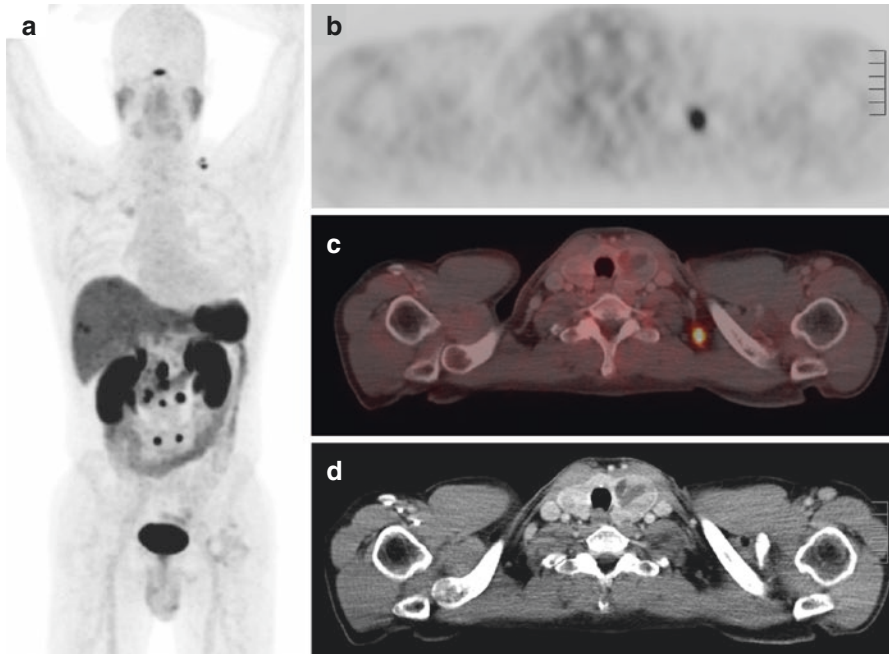
Fig. 15.3 Example of a 54-year-old male patient with a small-bowel NET with known abdominal lymph node metastases and liver metastases under cold SSA therapy. Patient was referred in a potential presurgical setting. (**a**) MIP image of a ^{68}Ga-DOTATATE PET/CT showing multiple mesenterial and retroperitoneal lymph node metastases with high uptake as well as two right-sided subcapsular liver metastases and a metastasis in the liver dome. There is also a bifocal lesion in the left supraclavicular area. (**b**) Focal strongly increased uptake in the largest of the two left-sided supraclavicular lesions, with an SUV_{max} of 8.5 (the smallest lesion – not shown – had an SUV_{max} of 4.5). (**c**) Fusion PET/CT image showing the localization of the hot spot. (**d**) CT-graphic correlate shows a non-enlarged lymph node of 7-mm diameter (the smaller lesion – not shown – has a diameter of 4 mm). In light of the extent of tumor involvement, no surgery was performed. This case illustrates the ability of ^{68}Ga-DOTA-peptide PET/CT to detect metastatic involvement in CT-graphic normal lymph nodes

The clinical impact of ^{68}Ga-DOTA-peptide PET is mainly due to:

1. Detection of smaller lesions
2. Detection of lesions with low to moderate SSR expression (Fig. 15.5)
3. Detection of more lesions that potentially will direct the patient to a different therapeutic choice
4. A much faster imaging procedure (60 min after injection [52] vs. two images at 24 and 48 h after injection [53]; reduction of 66 % of the number of hospital visits)
5. Lower radiation burden to the patient
6. Detection of an occult primary tumor, with yields as high as 30–60 % in patients negative on conventional imaging [54]
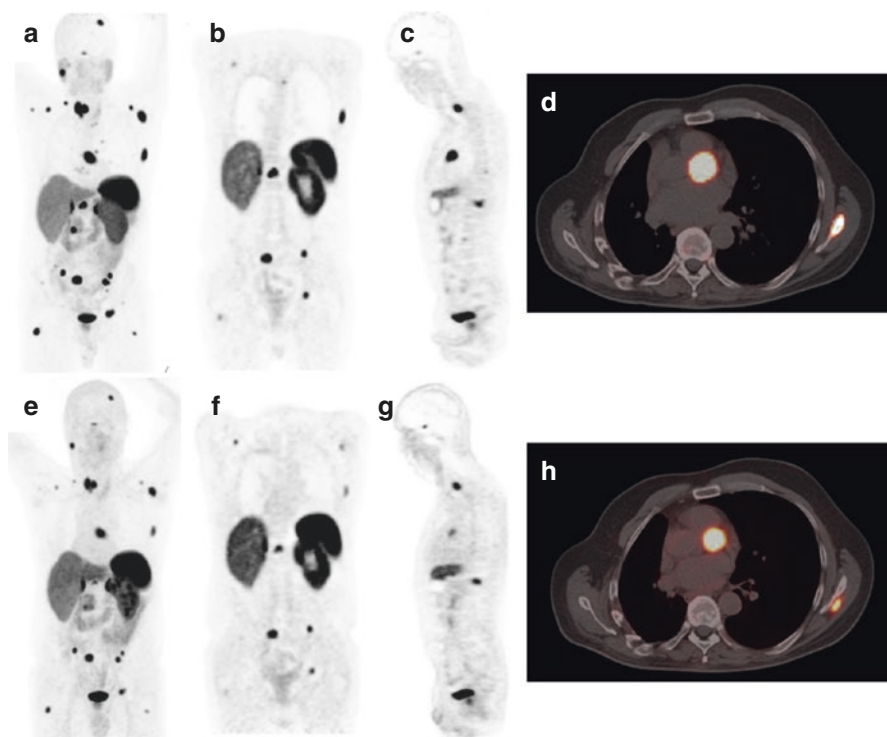
Fig. 15.4 Example of a 47-year-old male patient with a NET scanned with ^{68}Ga-DOTATATE PET/CT 14 months after a ^{68}Ga-DOTATOC PET/CT with very comparable images. (**a–d**) ^{68}Ga-DOTATATE PET/CT images. (**e–h**) ^{68}Ga-DOTATOC PET/CT images. (**a**, **e**) MIP images showing diffuse metastases with high to intense tracer uptake, with a similar pattern. (**b**, **f**) Coronal images showing three pelvic bone metastases with similar uptake and signal to background ratio; the thoracic lesions are different because of different alignment of the transection plane. (**c**, **g**) Sagittal images showing two vertebral metastases with similar uptake. (**d**, **h**) PET/CT fusion image showing similar aspect of a cardiac metastasis, which are not infrequent in NET patients and can be readily detected by ^{68}Ga-DOTA-peptide PET/CT

When comparing a ^{68}Ga-DOTA-peptide PET image with a previous scan of the same patients, one needs to be careful that visualizing more lesions does not necessarily mean that the patient is progressive.

The physiological biodistribution in normal patients is as follows: high uptake in spleen (hottest organ in normal patient), kidneys, adrenal glands, liver, pituitary gland, and the bladder (tracer excretion). There is also moderate uptake within the pancreas and more notably the uncinate process, the thyroid gland, the intestine. There is low uptake in the lungs, muscles (including myocardium), and the bone marrow.

Typical pitfalls in SSTR PET include misinterpretation of the physiological uptake in the uncinate process of the pancreas as a pancreatic NET, misinterpretation
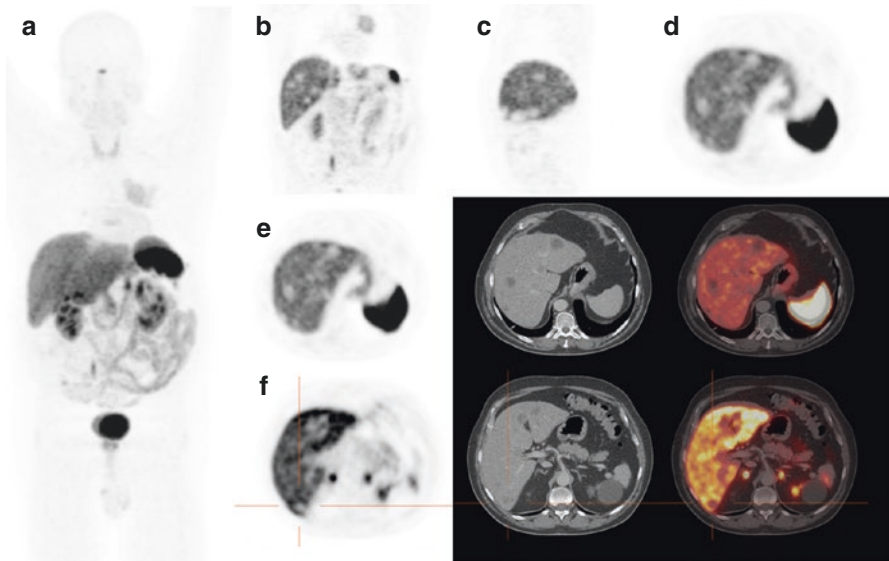
Fig. 15.5 Example of a 58-year-old patient with a NET with absent SSTR expression and diffuse liver metastases on ^{68}Ga-DOTATOC PET/CT. The patient was sent for PRRT eligibility and was not retained as a candidate, based on manifest lack of target expression. (**a**) MIP image, showing a primary lung NET with uptake lower than normal liver parenchyma and a photopenic area in the center of the liver dome, (**b**) coronal section showing the primary lung NET with rounded photopenic areas within the liver corresponding to liver metastases without SSTR expression, (**c**, **d**) sagittal and axial views through the liver showing photopenic metastases, (**e**) *axial view* of the liver with corresponding CT and fusion image, (**f**) *axial views* of the liver with corresponding CT and fusion image, with the orange crosshair centered on a photopenic liver metastasis, nicely visible on CT and on the fusion image

of a small meningioma (which can also have high SSTR expression) as a bone metastasis or brain metastasis, misinterpretation of accessory spleens, intrapancreatic spleen, or splenosis in operated or trauma patients as metastases of a NET, and classifying the mild to moderate uptake seen in inflammatory processes due to activated white blood cells as metastatic disease, in postsurgical scar tissue, or inflammatory or reactive lymph nodes, or in facet joint osteoarthritis, for example.

Several developments are currently ongoing to optimize SSTR PET imaging. A relatively recent paradigm shift is coming from radiolabeled antagonists that allow achieving higher uptake than with all previously mentioned ligands, which are agonists [55, 56]. Because some antagonist analogues are independent of the conformational status of SSTR, they can bind to a much higher fraction of the receptors present than agonists, which only bind certain specific conformations. This could lead to the emergence of second-generation ^{68}Ga-DOTA-peptides with even higher uptake ratios and potentially higher clinical detection rate. Another evolution is optimization of the labeling process. One major drawback of gallium-68-labeled peptides is the necessity to perform an on-site radiolabeling step, which requires specialized radiopharmaceutical personnel that is lacking in most nonacademic

PET centers. Some groups are developing SSTR ligands labeled with radioisotopes that would allow centralized production and distribution to peripheral sites, using, e.g., copper-64 ($T_{1/2}$: 12.7 h) [57] or aluminum-fluoride-18 ($T_{1/2}$: 110 min) complexes that can be chelated and bound to octreotide derivatives [58]. The latter isotope is produced in curie quantities in cyclotrons throughout the world to produce fluorine-18 for ^{18}F-FDG synthesis and would allow scanning 10–30 patients per production, compared to 1–4 for gallium-68-labeled peptides. For gallium-68, kits are currently being developed that would allow a more facile on-site labeling. It will be interesting to see which of these improvements will be the more adopted in clinical practice.

15.6.2 ^{18}F-Fluorodihydroxyphenylalanine PET

The cellular ability to take up, accumulate, and decarboxylate amines and amine precursors has been taken into account for the development of amino acid-based diagnostic radiotracers for nuclear medicine imaging. Accordingly, dihydroxyphenylalanine radiolabeled with fluorine-18 (^{18}F-FDOPA) has been successfully proposed for *in vivo* nuclear imaging of NETs [59]. Once internalized via the sodium independent system L, ^{18}F-FDOPA is decarboxylated to ^{18}F-dopamine by the aromatic L-amino acid decarboxylase (AADC) enzyme, transported and stored into secretory vesicles. Therefore, the high uptake of ^{18}F-FDOPA in NETs is the result of the cellular increased synthesis, storage, and secretion of biogenic amines [60, 61].

The sensitivity of ^{18}F-FDOPA PET for both primary tumor detection and metastatic spread assessment is influenced by NET embryological origin and differentiation. Specific tumoral features such as the overexpression and/or increased activity of the AADC involved in the tumoral biosynthesis of serotonin are significant elements to explain the best sensitivity of ^{18}F-FDOPA PET for carcinoids. Of interest, the metabolic tumor burden on whole-body ^{18}F-FDOPA studies is positively correlated to the amount of serotonin secretion [62]. Based on a meta-analysis by Jager et al. [63], the radiolabeled DOPA analogues show a sensitivity ranging from 65 to 96 % in a lesion-based analysis in patients with carcinoid tumor. Becherer et al. [64] reported sensitivities of 81.3 % for the liver, 100 % for the mediastinum and lymph nodes, and 90.9 % for the skeleton in the evaluation of patients with histologically proven NETs. The detection of osseous metastases is an important issue with negative prognostic implication on clinical outcomes. Concordant results are reported by Kauhanen et al. [65], who evaluated 82 patients with suspected or known gastrointestinal NETs examined for primary diagnosis and staging. Compared to histological findings and clinical follow-up, the diagnostic accuracy of ^{18}F-FDOPA PET was 89 %.

Overall, ^{18}F-FDOPA PET has excellent diagnostic performance and a relevant impact on therapeutic management of low-grade midgut NETs [66–68]. In this clinical setting, ^{18}F-FDOPA PET is indicated for tumor localization and staging,
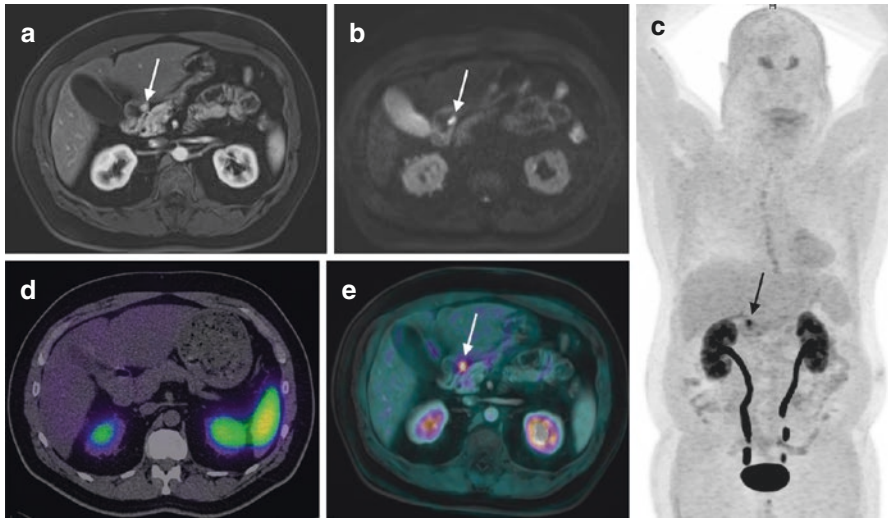
Fig. 15.6 Positive ^{18}F-FDOPA PET results in a 72-year-old man with G1 duodenal NET (pT2) appearing as a contrast-enhanced 15-mm lesion of duodenal wall (*arrow*) on MRI. Note that carbidopa premedication drastically reduced the physiological ^{18}F-FDOPA pancreatic uptake improving PET diagnostic sensitivity. SRS failed to detect the tumor. (**a**) Axial contrast-enhanced T1 MRI (arterial phase), (**b**) axial DWI MRI, (**c**) ^{18}F-FDOPA PET whole-body maximum intensity projection (MIP), (**d**) SPECT/CT SRS, (**e**) fusion of axial ^{18}F-FDOPA PET and MRI images

particularly in symptomatic patients (carcinoid syndrome) [65, 66]. At present, there are no recommendations about the utilization of ^{18}F-FDOPA PET during follow-up. Thus, indications for PET-imaging studies should be discussed on an individual basis. No specifically focused studies are available about the role of ^{18}F-FDOPA PET in hindgut or foregut NETs, including duodenal gastrinoma. In these situations, the sensitivity of ^{18}F-FDOPA PET is very low (25 %) [67]; thus, ^{68}Ga-OctreoPET and/or ^{18}F-FDG will be preferred to ^{18}F-FDOPA according to tumor grade. It is immediately evident that the tumor embryologic origin influences the nuclear medicine phenotype and plays a key role in the choice of the most appropriate diagnostic examination.

The administration of carbidopa (CD), an inhibitor of the peripheral AADC, has been shown to improve image interpretation for ^{18}F-FDOPA PET by increasing tumor-to-background uptake ratio [69]. Moreover, CD premedication drastically reduces the physiological pancreatic uptake and should facilitate the diagnosis of duodenal tumors (Fig 15.6). However, patient premedication by CD remains inconsistently performed across oncological studies using ^{18}F-FDOPA PET imaging [70, 71]. Furthermore, the CD dosage and the optimal protocol for ^{18}F-FDOPA PET/CT image acquisitions are not standardized in clinical practice (200 mg [72], 100 mg [73], 2 mg/kg [74]). At present, no recommendation exists concerning the use of carbidopa premedication, but this approach should be further evaluated.
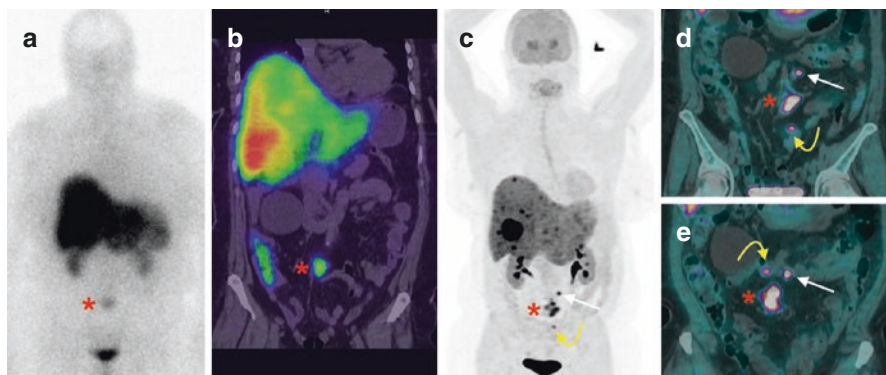
Fig. 15.7 Head-to-head comparison between SRS and ^{18}F-FDOPA PET in a patient with multiple hepatic metastases and retractile mesenteric mass from a G2 intestinal NET of unknown origin. SRS showed a pathological uptake in liver metastases and in the prevascular mesenteric lesion (*), failing to detect the primary. ^{18}F-FDOPA PET/CT confirmed both hepatic and mesenteric spread, detected a sub-centimetric focus of peritoneal carcinomatosis (*white arrow*), and allowed the identification of the primary tumor, corresponding to a G2 NET (Ki-67: 5%) of the small intestine (*yellow arrow*). Note the change of primary tumor position during time on PET images. (**a**) Whole-body planar SRS. (**b**) Abdominal and pelvic SPECT/CT SRS. (**c**) ^{18}F-FDOPA PET whole-body maximum intensity projection (MIP). (**d**) Coronal PET/CT acquisition performed 20 min after ^{18}F-FDOPA iv. injection. (**e**) Coronal PET/CT acquisition performed 60 min after ^{18}F-FDOPA iv. injection, following oral water ingestion (note the change of tumor position during time on PET images). Carbidopa premedication before PET imaging drastically reduces the physiological ^{18}F-FDOPA pancreatic uptake

Several studies have demonstrated ^{18}F-FDOPA PET superiority compared to morphological imaging (CT) and gamma camera-based SRS for the detection of lymph nodes, skeletal, and liver metastases in patients with low-grade midgut NETs (Fig 15.7). ^{18}F-FDOPA PET allows the detection of more lesions, more positive regions, and more lesions per region as compared with conventional CT and gamma camera SRS (sensitivities of ^{18}F-FDOPA PET at the patient, region, and lesion levels were 100, 95, and 96%, respectively) [70]. The increased sensitivity of PET/CT over SPECT/CT cameras for the detection of small lesions contributes to explain the better diagnostic performance of ^{18}F-FDOPA PET/CT over gamma camera SRS.

In midgut NETs, the advantages of ^{18}F-FDOPA PET in comparison with ^{68}Ga-OctreoPET are still unclear, and large prospective dedicated studies are currently lacking [75, 76]. Accuracy of ^{68}Ga-OctreoPET appears to be better than ^{18}F-FDOPA PET in metastatic NETs, both for the detection of primary tumor and metastatic spread. Moreover, ^{68}Ga-OctreoPET approach has the added advantage that it allows the assessment for PRRT, something that it is not possible by ^{18}F-FDOPA PET. In a head-to-head comparison between ^{68}Ga-DOTATATE and ^{18}F-FDOPA PET in the diagnosis of differentiated metastatic NETs, patient-based sensitivities were 96% and 56% for ^{68}Ga-DOTATATE and ^{18}F-FDOPA PET, respectively [76]. Nevertheless, the population considered for the comparison was characterized by high tumoral heterogeneity, preventing definitive conclusions. Prospective
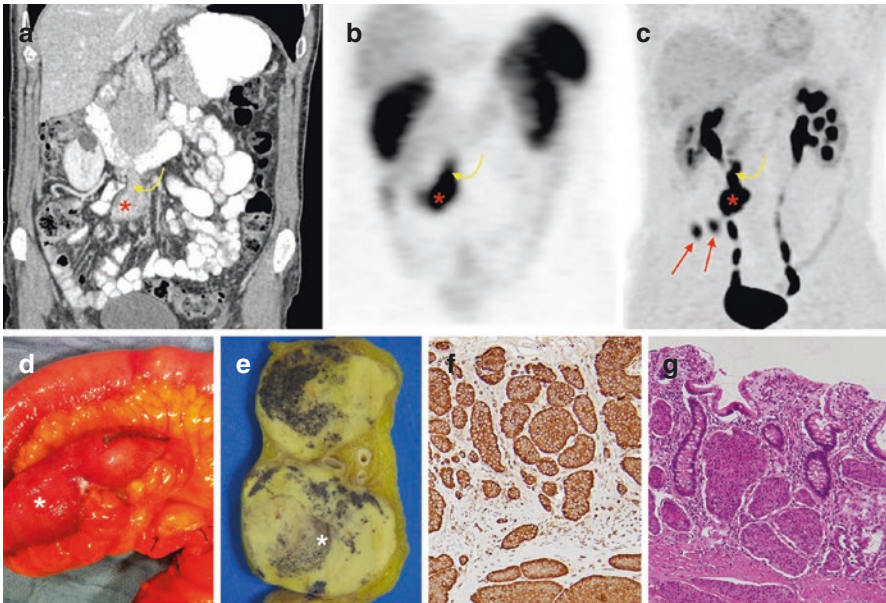
Fig. 15.8 Superiority of ^{18}F-FDOPA PET/CT to SRS in a patient with carcinoid syndrome and retractile mesenteric lesion peripheral to a small-bowel thickening. SRS showed a pathological uptake in the mesenteric lesion (*) and the adjacent intestinal tumor (*yellow arrow*). PET/CT detected two additional bowel focal uptake (*red arrows*) corresponding to two G1 NETs at pathological examination. Note that carbidopa premedication drastically reduced the physiological ^{18}F-FDOPA pancreatic uptake. (**a**) CT-enterography (plus I.V. contrast enhancement). (**b**) Abdominal and pelvic SPECT SRS. (**c**) ^{18}F-FDOPA PET maximum intensity projection (MIP). (**d**, **e**) Surgical resection specimens after tumoral excision. (**f**) Positive immunohistochemical staining for chromogranin A. (**g**) Tumoral cells arranged in a trabecular or glandular manner, invading the muscularis propria and the serosa (HE × 100)

studies in patients with midgut NETs are needed. ^{18}F-FDOPA is less frequently available throughout Europe than ^{68}Ga-OctreoPET. One indication where ^{18}F-FDOPA could be considered mandatory is in patients with biochemical proof of a tumoral process (e.g., ectopic adrenocorticotropic hormone (ACTH) production) and negative conventional, ^{68}Ga-OctreoPET and ^{18}F-FDG PET.

^{18}F-FDOPA PET also appears to be a sensitive functional imaging tool for the detection of primary NETs of midgut origin that is occult on conventional imaging or gamma camera SRS [71] (Fig 15.8). This is an important point because the localization of the primary NET remains a diagnostic challenge in clinical practice. The primary tumor is not localized in 20–50 % of GEP-NETs [77]. Gastrinomas and bowel carcinoids are particularly difficult to detect [78]. The identification of the primary tumor is crucial in treatment planning since surgical resection is associated with better symptom-free survival, overall survival, and quality of life even in patients with distant metastases [79, 80]. Furthermore, the detection of a pancreatic NET can enable the use of efficient molecular targeted therapies [81, 82].

Carcinoid tumors are multiple in approximately 30 % of cases [83]. The sensitivity of conventional presurgical diagnostic investigations is still far from being exhaustive [84]. Considering its high diagnostic power for serotonin-secreting well-differentiated NETs [85], ^{18}F-FDOPA PET/CT could potentially improve the detection of primary multifocal carcinoids. At present, published studies from adequate patient series are not available, and case reports are extremely rare [86]. Delayed two-field PET/CT acquisition centered on the abdominal and pelvic regions after water ingestion should be performed, in particular when standard images are doubtful (increased tracer uptake and visceral thickening) (Fig 15.7). The distension of intestinal loops and the negative contrast related to water ingestion could help to differentiate an intestinal lesion from the physiological radiotracer uptake, increasing sensitivity particularly for small NETs. Accordingly, focally increased ^{18}F-FDOPA uptake on one or more bowel segments, changing in position between the first study and the delayed one acquired after oral hydration, is suggestive of GI NETs and represents an additional argument to make an accurate intraoperative palpation of the entire small bowel.

15.6.3   ^{18}F-Fluorodeoxyglucose PET

[18]F-fluorodeoxyglucose (^{18}F-FDG) is a glucose analogue labeled with the positron-emitting isotope fluorine-18. It is taken up into cells by the facilitative glucose molecular transporter (GLUT). Once internalized, ^{18}F-FDG is phosphorylated by hexokinase without further metabolic processes and remained trapped within the cell.

Only limited value of ^{18}F-FDG PET is usually reported in the management of low-grade NETs, probably because of their low metabolic activity and slow growth. However, ^{18}F-FDG PET is considered the preferred technique for the identification and staging of high-grade NETs (high G2 and G3 tumors) [87]. Usually, a value of Ki-67 above or equal to 10 % is empirically considered as the cutoff to propose ^{18}F-FDG PET as the first-choice scintigraphic examination for well-differentiated endocrine tumors [88]. ^{18}F-FDG PET seems to have a potential value for prognostic stratification in patients with NETs [89]. An inverse relationship between the intensity of tumoral radiotracer uptake and patient survival has been reported [90, 91]. Accordingly, NETs with increased ^{18}F-FDG uptake have a more aggressive behavior and less favorable long-term survival supporting the evidence that an increased glycolytic rate reveals a worse prognosis [92]. FDG PET/CT was found more sensitive than both pathologic differentiation and Ki-67 in the early prediction of rapidly progressive disease in patients with low-grade GEP-NET [93, 94]. Interestingly, among patients with positive SRS, a positive ^{18}F-FDG PET permits to identify those with poorer survival [95]. Following these observations, a metabolic grading based on ^{18}F-FDG PET result has been recently proposed in patients with metastatic GEP-NETs with high predictive power regarding the overall survival. Thus, ^{18}F-FDG PET could be considered as a noninvasive and effective method for patient stratification

as a complement to conventional Ki-67-based grading with potential consequences on the modulation of treatment aggressiveness [96]. Moreover, some evidences indicate that ^{18}F-FDG PET plays a role to predict response to ^{177}Lu-PRRT monotherapy, allowing the identification of patients with grades 1 and 2 metastatic NETs that might benefit from more intensive therapy protocols including the combination of chemotherapy and PRRT [97]. Overall, ^{18}F-FDG PET appears interesting in disease prognostication, with a view on all lesions in a given patient, and being able to influence the therapeutic strategy and the aggressiveness of patient management.

15.7 Current Proposed Imaging Algorithm in the Diagnosis of GI NETs

Based on the currently available imaging techniques for the diagnosis and staging of NETs, a complex and personalized approach is usually adopted to investigate a patient with suspected or known GI NET. However, no evidence-based imaging algorithm exists at present. Morphological and functional imaging studies will be performed and variably associated according to the patient symptomatology as well as tumor origin and grade, tailoring to each clinical situation the best combination of diagnostic studies. In patients with diagnosed NET, CT is usually performed to define the local extension and the metastatic spread. MRI remains the first-choice examination for hepatic metastases, being more sensitive than both CT and US. In addition, nuclear medicine studies are usually added for staging purpose (detecting additional metastases, primary unknown, primary multifocality) and/or treatment selection according to the pathological characteristics of the primary tumor. The mismatch high uptake of radiolabeled SSA or ^{18}F-FDOPA/low ^{18}F-FDG uptake (known as flip-flop effect) is widely considered as the functional imaging pattern of low-grade GEP-NETs (Fig 15.9). Conversely, the pattern of low uptake of radiolabeled SSA or ^{18}F-FDOPA/high ^{18}F-FDG uptake is representative of high-grade tumors [98, 99] (Fig 15.10). The suggested imaging procedures for patients with GI NETs are schematically reported in Fig 15.11. Starting from these principles, the diagnostic algorithm should be adapted in each situation considering both availability of the various imaging studies and the own experience of medical team [66, 87, 100].

15.8 Functional Imaging-Based Interventional Options

Imaging-guided biopsy and locoregional treatment utilizing thermal ablation are routinely performed in patients with NETs. Despite several limitations, US, CT, and MRI are usually employed for this purpose. Nowadays, the availability of hybrid systems allows new possibilities and interesting perspectives to target tumors that are not well visualized at CT or other imaging methods. Nuclear medicine techniques and in particular PET/CT are suitable for optimal planning of image-guided
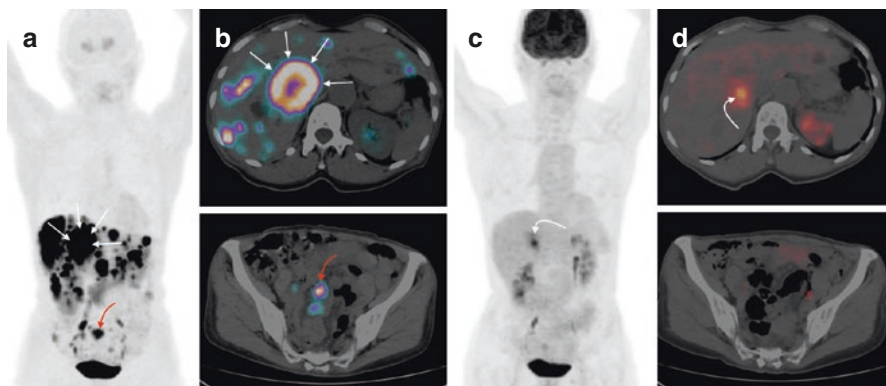
Fig. 15.9 Typical example of "flip-flop" effect in a patient with metastatic low-grade (G1) small-bowel NET. ^{18}F-FDOPA PET (**a**, **b**) showed the ileal primary tumor (*red arrow*) and multiple hepatic (*white arrows*) and lymph node metastases. On the other hand, ^{18}F-FDG (**c**, **d**) showed an exclusive pathologic uptake in the center of a hepatic metastasis of segments IV–VIII, corresponding to a photopenic area on ^{18}F-FDOPA PET
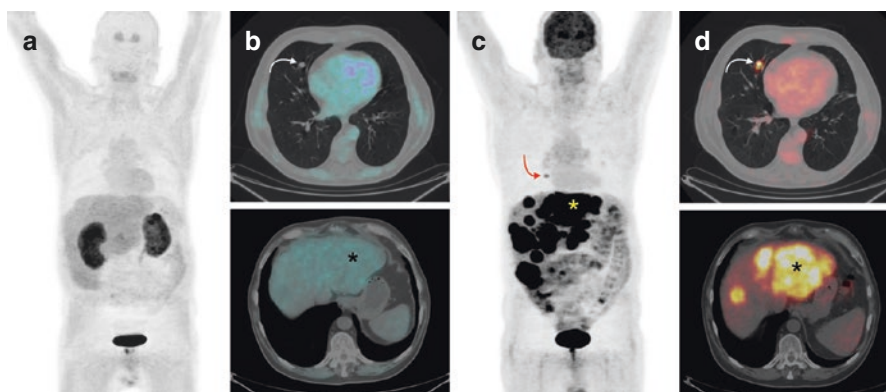
Fig. 15.10 Patient with metastatic high-grade (G3) NET of unknown origin. ^{18}F-FDOPA PET/CT showed no significant uptake abnormalities (**a**, **b**). Instead, ^{18}F-FDG PET/CT showed intense glucose metabolism in multiple hepatic metastases (*), lymph nodes, and lung metastases (*arrow*) (**c**, **d**)

invasive diagnostic procedures and treatments such as transcutaneous biopsy and radiofrequency ablation (RFA) of secondary liver or bone malignancies [101–103]. ^{18}F-FDG is the tracer that has been more widely used in this clinical setting. Functional images and their underlying anatomical correlates obtained on hybrid cameras easily provide the differentiation and the extent assessment of viable tumor tissue from the adjacent necrosis, which is usually abundant in larger NET. PET/CT-guided biopsy may be also useful to confirm the metabolic findings (potentially influencing the therapeutic strategy) when conventional imaging fails to show morphological abnormalities. The management of patients with NET largely depends on the results of pathological examination, which allows a differentiation of
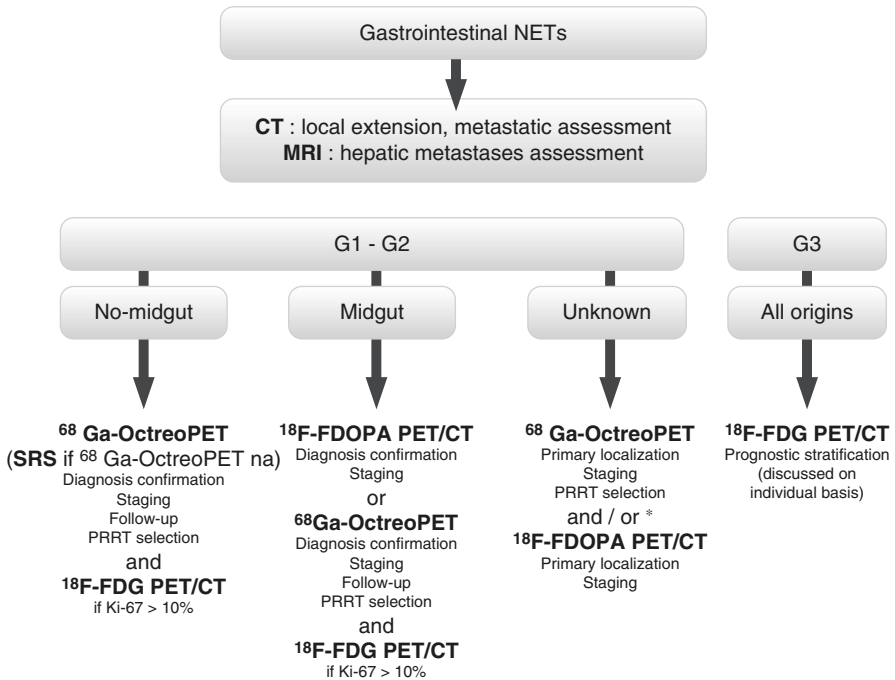
Fig. 15.11 Suggested imaging procedures for patients with GI NETs. *: based on presumption of origin and hormonal secretion if present; *na* not available

aggressive malignancies from low-grade tumors. Generally, the tumor grade is determined from a limited tissue sample obtained from biopsy or from partial surgical resection, which might be not truly representative of the whole tumor burden. On the contrary, nuclear medicine provides whole-body imaging, allowing an extensive tumor *in vivo* characterization that is potentially useful for guiding biopsy, in particular of ^{18}F-FDG avid lesions that are not clearly detectable at CT or largely necrotic. Hence, ^{18}F-FDG PET/CT could be considered as a powerful and noninvasive option to guide biopsy for optimal patient stratification according to conventional Ki-67-based grading. However, the presumed value of PET/CT for guiding biopsy-based proliferation assessments in metastatic disease should be further investigated. Beyond ^{18}F-FDG, ^{18}F-FDOPA could be also proposed in patients with NETs for planning PET/CT-guided diagnostic biopsy, ablative treatment, and immediate efficacy assessment (Fig 15.12), even in a one-step examination [104].

15.9   Toward a Personalized (Nuclear) Medicine

The knowledge of the molecular substrate of the disease as well as the advantages and limitations of each diagnostic imaging modality is essential for optimal patient management. The use of *in vivo* molecular diagnostic testing, such as nuclear
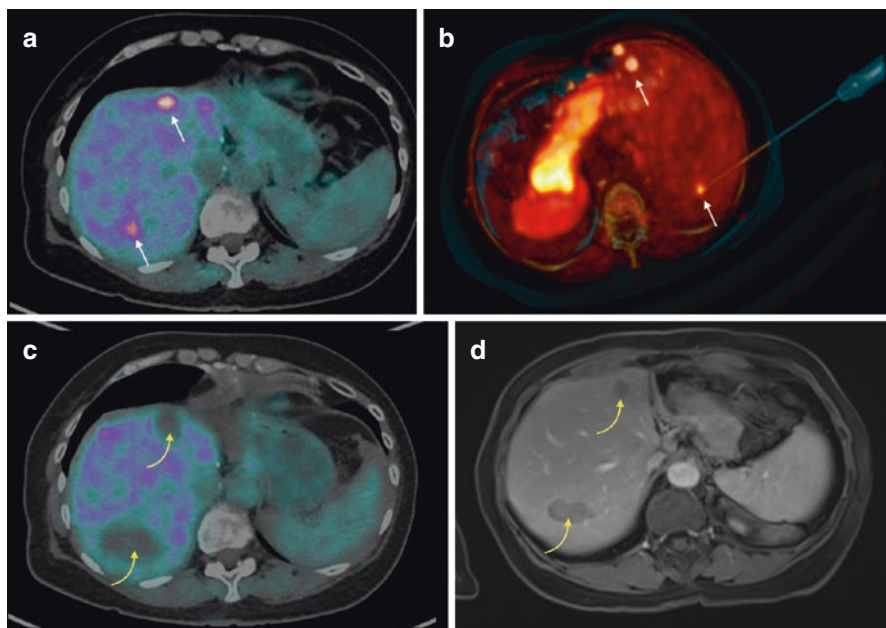
Fig. 15.12 Simultaneous ^{18}F-FDOPA PET/CT-guided biopsy and radiofrequency (RF) ablation procedures of two hepatic metastases in a patient with history of ileal G1 NET. (**a**) Baseline PET/CT showing two foci of intense ^{18}F-FDOPA uptake in hepatic segments IV and VII corresponding to metastatic spread not clearly visualized on earlier MRI examination. (**b**) Combination of CT-VRT (volume rendering technique) and PET-MIP (maximum intensity projection) images showing the RF probe positioned on segment VII metastasis. (**c**) Posttreatment PET/CT acquired 30 min after the end of radiofrequency ablation showing two photopenic areas corresponding to both treated metastases. (**d**) Posttreatment MRI performed about 3 months after RF procedure confirmed two parenchymal scars without evidence of persistent disease (PET/CT-guided diagnostic biopsy and radiofrequency ablation procedures were done in collaboration with Pr. Afshin Gangi and his team, from the Interventional Radiology Unit of the University Hospitals of Strasbourg)

medicine investigations, to explore the molecular mechanisms of an individual patient's disease, is necessary for a safe and effective therapeutic strategy, even in patients with NETs. From a clinical point of view, the integration of diagnostics and therapeutics (theranostic) by *in vivo* molecular imaging represents a major opportunity to early detect the disease and select appropriate treatment, to monitor therapy and to determine prognosis [105]. Targeted radionuclide therapy represents the most common example of patient-specific therapies based on the "image and treat approach" [106]. In the context of NETs, it means the use of molecular vectors labeled either with diagnostic or with therapeutic radionuclides, and one of the most interesting association is ^{68}Ga-DOTATATE and ^{177}Lu-DOTATATE with very promising results [44].

In conclusion, we emphasize the evolving role of nuclear medicine imaging in the management of NETs, enabling a better understanding of tumor physiopathology necessary for patient outcome improvement.

References

1. Plockinger U, Rindi G, Arnold R, Eriksson B, Krenning EP, de Herder W, et al. Guidelines for the diagnosis and treatment of neuroendocrine gastrointestinal tumours. A consensus statement on behalf of the European Neuroendocrine Tumour Society (ENETS). Neuroendocrinology. 2004;80:394–424.

2. Yao JC, Hassan M, Phan A, Dagohoy C, Leary C, Mares JE, et al. One hundred years after "carcinoid": epidemiology of and prognostic factors for neuroendocrine tumors in 35,825 cases in the United States. J Clin Oncol. 2008;26:3063–72.

3. Bilimoria KY, Talamonti MS, Tomlinson JS, Stewart AK, Winchester DP, Ko CY, Bentrem DJ, et al. Prognostic score predicting survival after resection of pancreatic neuroendocrine tumors: analysis of 3851 patients. Ann Surg. 2008;247:490–500.

4. Fraenkel M, Kim MK, Faggiano A, Valk GD. Epidemiology of gastroenteropancreatic neuroendocrine tumours. Best Pract Res Clin Gastroenterol. 2012;26:691–703.

5. Rindi G, Petrone G, Inzani F. The 2010 WHO classification of digestive neuroendocrine neoplasms: a critical appraisal four years after its introduction. Endocr Pathol. 2014;25:186–92.

6. Klöppel G, Rindi G, Perren A, Komminoth P, Klimstra DS. The ENETS and AJCC/UICC TNM classifications of the neuroendocrine tumors of the gastrointestinal tract and the pancreas: a statement. Virchows Arch. 2010;456:595–7.

7. La Rosa S, Vanoli A. Gastric neuroendocrine neoplasms and related precursor lesions. J Clin Pathol. 2014;67:938–48.

8. Kaltsas G, Grozinsky-Glasberg S, Alexandraki KI, Thomas D, Tsolakis AV, Gross D, et al. Current concepts in the diagnosis and management of type 1 gastric neuroendocrine neoplasms. Clin Endocrinol (Oxf). 2014;81:157–68.

9. Dobson R, Burgess MI, Pritchard DM, Cuthbertson DJ. The clinical presentation and management of carcinoid heart disease. Int J Cardiol. 2014;173:29–32.

10. Kanakis G, Kaltsas G. Biochemical markers for gastroenteropancreatic neuroendocrine tumours (GEP-NETs). Best Pract Res Clin Gastroenterol. 2012;26:791–802.

11. Kaltsas GA, Besser GM, Grossman AB. The diagnosis and medical management of advanced neuroendocrine tumors. Endocr Rev. 2004;25:458–511.

12. Landry CS, Scoggins CR, McMasters KM, Martin 2nd RC. Management of hepatic metastasis of gastrointestinal carcinoid tumors. J Surg Oncol. 2008;97:253–8.

13. Kocha W, Maroun J, Kennecke H, Law C, Metrakos P, Ouellet JF, et al. Consensus recommendations for the diagnosis and management of well-differentiated gastroenterohepatic neuroendocrine tumours: a revised statement from a Canadian National Expert Group. Curr Oncol. 2010;17:49–64.

14. Bellutti M, Fry LC, Schmitt J, Seemann M, Klose S, Malfetheiner P, et al. Detection of neuroendocrine tumors of the small bowel by double balloon enteroscopy. Dig Dis Sci. 2009;54:1050–8.

15. Yamagishi H, Fukui H, Shirakawa K, Oinuma T, Hirashi H, Terano A, et al. Early diagnosis and successful treatment of small-intestinal carcinoid tumor: useful combination of capsule endoscopy and double-balloon endoscopy. Endoscopy. 2007;39 Suppl 1:E243–4.

16. Liao Z, Gao R, Xu C, Li ZS. Indications and detection, completion, and retention rates of small bowel capsule endoscopy: a systematic review. Gastrointest Endosc. 2010;71:280–6.

17. Modlin IM, Gustafsson BI, Kidd M. Gastrointestinal carcinoid tumours. In: Howden CW, editor. Advances in digestive disease. Bethesda: AGA Institute Press; 2007.

18. Patel KK, Kim MK. Neuroendocrine tumors of the pancreas: endoscopic diagnosis. Curr Opin Gastroenterol. 2008;24:638–42.

19. Scherübl H, Jensen RT, Cadiot G, Stölzel U, Klöppel G. Neuroendocrine tumors of the small bowels are on the rise: early aspects and management. World J Gastrointest Endosc. 2010;2:325–34.

20. Binstock AJ, Johnson CD, Stephens DH, Lloyd RV, Fletcher JG. Carcinoid tumors of the stomach: a clinical and radiographic study. AJR Am J Roentgenol. 2001;176:947–51.

21. Woodard PK, Feldman JM, Paine SS, Baker ME. Midgut carcinoid tumors: CT findings and biochemical profiles. J Comput Assist Tomogr. 1995;19:400–5.

22. Kamaoui I, De-Luca V, Ficarelli S, Mennesson N, Lombard-Bohas C, Pilleul F. Value of CT enteroclysis in suspected small-bowel carcinoid tumors. AJR Am J Roentgenol. 2010;194:629–33.

23. Masselli G, Polettini E, Casciani E, Bertini L, Vecchioli A, Gualdi G. Small-bowel neoplasms: prospective evaluation of MR enteroclysis. Radiology. 2009;251:743–50.

24. Van Weyenberg SJ, Meijerink MR, Jacobs MA, Van der Peet DL, Van Kuijk C, Mulder CJ, et al. MR enteroclysis in the diagnosis of small-bowel neoplasms. Radiology. 2010;254:765–73.

25. Pantongrag-Brown L, Buetow PC, Carr NJ, Lichtenstein JE, Buck JL. Calcification and fibrosis in mesenteric carcinoid tumor: CT findings and pathologic correlation. AJR Am J Roentgenol. 1995;164:387–91.

26. Elias D, Lefevre JH, Duvillard P, Goéré D, Dromain C, Dumont F, et al. Hepatic metastases from neuroendocrine tumors with a "thin slice" pathological examination: they are many more than you think. Ann Surg. 2010;251:307–10.

27. Paulson EK, McDermott VG, Keogan MT, DeLong DM, Frederick MG, Nelson RC. Carcinoid metastases to the liver: role of triple-phase helical CT. Radiology. 1998;206:143–50.

28. Elsayes KM, Menias CO, Bowerson M, Osman OM, Alkharouby AM, Hillen TJ. Imaging of carcinoid tumors: spectrum of findings with pathologic and clinical correlation. J Comput Assist Tomogr. 2011;35:72–80.

29. Dromain C, de Baere T, Baudin E, Galline J, Ducreux M, Boige V, et al. MR imaging of hepatic metastases caused by neuroendocrine tumors: comparing four techniques. AJR Am J Roentgenol. 2003;180:121–8.

30. Ichikawa T, Peterson MS, Federle MP, Baron RL, Haradome H, Kawamori Y, et al. Islet cell tumor of the pancreas: biphasic CT versus MR imaging in tumor detection. Radiology. 2000;216:163–71.

31. Koh DM, Brown G, Riddell AM, Scurr E, Collins DJ, Allen SD, et al. Detection of colorectal hepatic metastases using MnDPDP MR imaging and diffusion-weighted imaging (DWI) alone and in combination. Eur Radiol. 2008;18:903–10.

32. Liapi E, Geschwind JF, Vossen JA, Buijs M, Georgiades CS, Bluemke DA, et al. Functional MRI evaluation of tumor response in patients with neuroendocrine hepatic metastasis treated with transcatheter arterial chemoembolization. AJR Am J Roentgenol. 2008;190:67–73.

33. Gibril F, Doppman JL, Reynolds JC, Chen CC, Sutliff VE, Yu F, et al. Bone metastases in patients with gastrinomas: a prospective study of bone scanning, somatostatin receptor scanning, and magnetic resonance image in their detection, frequency, location, and effect of their detection on management. J Clin Oncol. 1998;16:1040–53.

34. Scarsbrook AF, Ganeshan A, Statham J, Thakker RV, Weaver A, Talbot D, et al. Anatomic and functional imaging of metastatic carcinoid tumors. Radiographics. 2007;27:455–77.

35. Meijer WG, van der Veer E, Jager PL, van der Jagt EJ, Piers BA, Kema IP, et al. Bone metastases in carcinoid tumors: clinical features, imaging characteristics, and markers of bone metabolism. J Nucl Med. 2003;44:184–91.

36. Weckbecker G, Lewis I, Albert R, et al. Opportunities in somatostatin research: biological, chemical and therapeutic aspects. Nat Rev Drug Discov. 2003;2:999–1017.

37. Kaemmerer D, Peter L, Lupp A, et al. Molecular imaging with (6)(8)Ga-SSTR PET/CT and correlation to immunohistochemistry of somatostatin receptors in neuroendocrine tumours. Eur J Nucl Med Mol Imaging. 2011;38:1659–68.

38. Krenning EP, Bakker WH, Breeman WA, et al. Localisation of endocrine-related tumours with radioiodinated analogue of somatostatin. Lancet. 1989;1:242–4.

39. Arnold R, Chen YJ, Costa F, et al. ENETS consensus guidelines for the standards of care in neuroendocrine tumors: follow-up and documentation. Neuroendocrinology. 2009;90:227–33.

40. Binderup T, Knigge U, Loft A, et al. Functional imaging of neuroendocrine tumors: a head-to-head comparison of somatostatin receptor scintigraphy, 123I-MIBG scintigraphy, and 18F-FDG PET. J Nucl Med. 2010;51:704–12.

41. Rinke A, Muller HH, Schade-Brittinger C, et al. Placebo-controlled, double-blind, prospective, randomized study on the effect of octreotide LAR in the control of tumor growth in patients with metastatic neuroendocrine midgut tumors: a report from the PROMID study group. J Clin Oncol. 2009;27:4656–63.

42. Caplin ME, Pavel M, Cwikla JB, et al. Lanreotide in metastatic enteropancreatic neuroendocrine tumors. N Engl J Med. 2014;371:224–33.

43. FROM ECC 2015-neuroendocrine cancer: SSA therapies-(177)Lu-DOTATATE is a better one in NETTER-1. Nat Rev Clin Oncol 2015;12:684

44. Reubi JC, Schar JC, Waser B, et al. Affinity profiles for human somatostatin receptor subtypes SST1-SST5 of somatostatin radiotracers selected for scintigraphic and radiotherapeutic use. Eur J Nucl Med. 2000;27:273–82.

45. Gabriel M, Decristoforo C, Kendler D, et al. 68Ga-DOTA-Tyr3-octreotide PET in neuroendocrine tumors: comparison with somatostatin receptor scintigraphy and CT. J Nucl Med. 2007;48:508–18.

46. Buchmann I, Henze M, Engelbrecht S, et al. Comparison of 68Ga-DOTATOC PET and 111In-DTPAOC (Octreoscan) SPECT in patients with neuroendocrine tumours. Eur J Nucl Med Mol Imaging. 2007;34:1617–26.

47. Van Binnebeek S, Vanbilloen B, Baete K, et al. Comparison of diagnostic accuracy of 111In-pentetreotide SPECT and 68Ga-DOTATOC PET/CT: a lesion-by-lesion analysis in patients with metastatic neuroendocrine tumors. Eur Radiol. 2016;26:900–9.

48. Sadowski SM, Neychev V, Millo C, et al. Prospective study of 68Ga-DOTATATE positron emission tomography/computed tomography for detecting gastro-entero-pancreatic neuroendocrine tumors and unknown primary sites. J Clin Oncol. 2016;34:588–96.

49. Morgat C, Vélayoudom-Céphise FL, Schwartz P, et al. Evaluation of 68Ga-DOTA-TOC PET/CT for the detection of duodenopancreatic neuroendocrine tumors in patients with MEN1. Eur J Nucl Med Mol Imaging. 2016;28:1258–66.

50. Johnbeck CB, Knigge U, Kjaer A. PET tracers for somatostatin receptor imaging of neuroendocrine tumors: current status and review of the literature. Future Oncol. 2014;10:2259–77.

51. Poeppel TD, Binse I, Petersenn S, et al. 68Ga-DOTATOC versus 68Ga-DOTATATE PET/CT in functional imaging of neuroendocrine tumors. J Nucl Med. 2011;52:1864–70.

52. Virgolini I, Ambrosini V, Bomanji JB, et al. Procedure guidelines for PET/CT tumour imaging with 68Ga-DOTA-conjugated peptides: 68Ga-DOTA-TOC, 68Ga-DOTA-NOC, 68Ga-DOTA-TATE. Eur J Nucl Med Mol Imaging. 2010;37:2004–10.

53. Bombardieri E, Ambrosini V, Aktolun C, et al. 111In-pentetreotide scintigraphy: procedure guidelines for tumour imaging. Eur J Nucl Med Mol Imaging. 2010;37:1441–8.

54. Naswa N, Sharma P, Kumar A, et al. (6)(8)Ga-DOTANOC PET/CT in patients with carcinoma of unknown primary of neuroendocrine origin. Clin Nucl Med. 2012;37:245–51.

55. Ginj M, Zhang H, Waser B, et al. Radiolabeled somatostatin receptor antagonists are preferable to agonists for in vivo peptide receptor targeting of tumors. Proc Natl Acad Sci U S A. 2006;103:16436–41.

56. Wild D, Fani M, Behe M, et al. First clinical evidence that imaging with somatostatin receptor antagonists is feasible. J Nucl Med. 2011;52:1412–7.

57. Pfeifer A, Knigge U, Binderup T, et al. 64Cu-DOTATATE PET for neuroendocrine tumors: a prospective head-to-head comparison with 111In-DTPA-octreotide in 112 patients. J Nucl Med. 2015;56:847–54.

58. Laverman P, McBride WJ, Sharkey RM, et al. A novel facile method of labeling octreotide with (18)F-fluorine. J Nucl Med. 2010;51:454–61.

59. Gornik G, Weber W. New tracers beyond FDG in head and neck oncology. Q J Nucl Med Mol Imaging. 2011;55:529–40.

60. Minn H, Kauhanen S, Seppänen M, Nuutila P. 18F-FDOPA: a multiple-target molecule. J Nucl Med. 2009;50:1915–8.
61. Santhanam P, Taïeb D. Role of (18)F-FDOPA PET/CT imaging in endocrinology. Clin Endocrinol (Oxf). 2014;81:789–98.
62. Fiebrich HB, de Jong JR, Kema IP, Koopmans KP, Sluiter W, Dierckx RA, et al. Total (18) F-dopa PET tumour uptake reflects metabolic endocrine tumour activity in patients with a carcinoid tumour. Eur J Nucl Med Mol Imaging. 2011;38:1854–61.
63. Jager PL, Chirakal R, Marriott CJ, Brouwers AH, Koopmans KP, Gulenchyn KY. 6-L-18F-fluorodihydroxyphenylalanine PET in neuroendocrine tumors: basic aspects and emerging clinical applications. J Nucl Med. 2008;49:573–86.
64. Becherer A, Szabó M, Karanikas G, Wunderbaldinger P, Angelberger P, Raderer M, et al. Imaging of advanced neuroendocrine tumors with (18)F-FDOPA PET. J Nucl Med. 2004;45:1161–7.
65. Kauhanen S, Seppänen M, Ovaska J, Minn H, Bergman J, Korsoff P, Salmela P, Saltevo J, Sane T, Välimäki M, Nuutila P. The clinical value of [18F]fluoro-dihydroxyphenylalanine positron emission tomography in primary diagnosis, staging, and restaging of neuroendocrine tumors. Endocr Relat Cancer. 2009;16:255–65.
66. Bodei L, Sundin A, Kidd M, Prasad V, Modlin IM. The status of neuroendocrine tumor imaging: from darkness to light? Neuroendocrinology. 2015;101:1–17.
67. Montravers F, Kerrou K, Nataf V, et al. Impact of fluorodihydroxyphenylalanine-18F positron emission tomography on management of adult patients with documented or occult digestive endocrine tumors. J Clin Endocrinol Metab. 2009;94:1295–301.
68. Montravers F, Grahek D, Kerrou K, Ruszniewski P, de Beco V, Aide N, et al. Can fluorodihydroxyphenylalanine PET replace somatostatin receptor scintigraphy in patients with digestive endocrine tumours? J Nucl Med. 2006;47:1455–62.
69. Neels OC, Koopmans KP, Jager PL, Vercauteren L, van Waarde A, Doorduin J, et al. Manipulation of [11C]-5-hydroxytryptophan and 6-[18F]fluoro-3,4-dihydroxy-L-phenylalanine accumulation in neuroendocrine tumor cells. Cancer Res. 2008;68:7183–90.
70. Koopmans KP, de Vries EG, Kema IP, Elsinga PH, Neels OC, Sluiter WJ, et al. Staging of carcinoid tumours with 18FDOPA PET: a prospective, diagnostic accuracy study. Lancet Oncol. 2006;7:728–34.
71. Imperiale A, Rust E, Gabriel S, Detour J, Goichot B, Duclos B, et al. 18F-fluorodihydroxyphenylalanine PET/CT in patients with neuroendocrine tumors of unknown origin: relation to tumor origin and differentiation. J Nucl Med. 2014;55:367–72.
72. Hoegerle S, Altehoefer C, Ghanem N, Koehler G, Waller CF, Scheruebl H, et al. Whole-body 18F dopa PET for detection of gastrointestinal carcinoid tumors. Radiology. 2001;220:373–80.
73. Beuthien-Baumann B, Strumpf A, Zessin J, Bredow J, Kotzerke J. Diagnostic impact of PET with 18F-FDG, 18F-DOPA and 3-O-methyl-6-[18F]fluoro-DOPA in recurrent or metastatic medullary thyroid carcinoma. Eur J Nucl Med Mol Imaging. 2007;34:1604–9.
74. Koopmans KP, de Groot JW, Plukker JT, de Vries EG, Kema IP, Sluiter WJ, et al. 18F-dihydroxyphenylalanine PET in patients with biochemical evidence of medullary thyroid cancer: relation to tumor differentiation. J Nucl Med. 2008;49:524–31.
75. Ambrosini V, Tomassetti P, Castellucci P, Campana D, Montini G, Rubello D, et al. Comparison between[68]Ga-DOTA-NOC and ^{18}F-DOPA PET for the detection of gastro-entero-pancreatic and lung neuro-endocrine tumours. Eur J Nucl Med Mol Imaging. 2008;35:1431–8.
76. Haug A, Auernhammer CJ, Wangler B, Tiling R, Schmidt G, Göke B, et al. Intraindividual comparison of[68]Ga-DOTA-TATE and ^{18}F-DOPA PET in patients with well-differentiated metastatic neuroendocrine tumours. Eur J Nucl Med Mol Imaging. 2009;36:765–70.

77. Modlin IM, Gustafsson BI, Kidd M. Gastrointestinal carcinoid tumors. In: Howden CW, Baillie J, Buchman AL, Metz DC, Modlin IM, editors. Advances in digestive disease. Bethesda: AGA Institute Press; 2007. p. 203–18.

78. Jaenigen B, Kayser G, Steinke B, Thomusch O. Five-year long-term follow-up of a primary lymph node gastrinoma: is a pancreaticoduodenectomy justified? Case Rep Med. 2009;2009:762–91.

79. Rothenstein J, Clearly SP, Pond GR, Dale D, Gallinger S, Moore MJ, et al. Neuroendocrine tumors of the gastrointestinal tract. A decade of experience at the Princess Margaret Hospital. Am J Clin Oncol. 2008;31:64–70.

80. Hellman P, Lundström T, Ohrvall U, Eriksson B, Skogseid B, Oberg K, Tiensuu Janson E, Akerström G. Effect of surgery on the outcome of midgut carcinoid disease with lymph node and liver metastases. World J Surg. 2002;26:991–7.

81. Yao JC, Shah MH, Ito T, Bohas CL, Wolin EM, Van Cutsem E, et al. Everolimus for advanced pancreatic neuroendocrine tumors. N Engl J Med. 2011;364:514–23.

82. Raymond E, Dahan L, Raoul JL, Bang YJ, Borbath I, Lombard-Bohas C, et al. Sunitinib malate for the treatment of pancreatic neuroendocrine tumors. N Engl J Med. 2011;364:501–13.

83. Butkr AP, Thomas RM, Elsayed AM, Sobin HL. Carcinoids of the jejunum and ileum. Cancer. 1997;79:1086–93.

84. Pasquier A, Walter T, Hervieu V, Forestier J, Scoazec JY, Lombard-Bohas C, et al. Surgical management of small bowel neuroendocrine tumors: specific requirements and their impact on staging and prognosis. Ann Surg Oncol. 2015;22 suppl 3:742–9.

85. Balogova S, Talbot JN, Nataf V, Michaud L, Huchet V, Kerrou K, et al. 18F-fluorodihydroxyphenylalanine vs other radiopharmaceuticals for imaging neuroendocrine tumours according to their type. Eur J Nucl Med Mol Imaging. 2013;40:943–66.

86. Imperiale A, Averous G, Chilinseva-Natorov N, Hubelé F, Triki E, Bellocq JP, et al. Unknown multifocal ileal carcinoid revealed by (18)F-FDOPA PET/CT. J Clin Endocrinol Metab. 2014;99:1510–1.

87. Toumpanakis C, Kim MK, Rinke A, Bergestuen DS, Thirlwell C, Khan MS, et al. Combination of cross-sectional and molecular imaging studies in the localization of gastroenteropancreatic neuroendocrine tumors. Neuroendocrinology. 2014;99:63–74.

88. Abgral R, Leboulleux S, Deandreis D, Auperin A, Lumbroso J, Dromain C, et al. Performance of 18Fluorodeoxyglucose-positron emission tomography and somatostatin receptor scintigraphy for high Ki-67 (>=10%) well-differentiated endocrine carcinoma staging. J Clin Endocrinol Metab. 2011;96:665–71.

89. Strauss LG, Conti PS. The application of PET in clinical oncology. J Nucl Med. 1991;32:623–48.

90. Adams S, Baum R, Rink T, Schumm-Drager PM, Usadel KH, Hor G. Limited value of fluorine-18 fluorodeoxyglucose positron emission tomography for the imaging of neuroendocrine tumours. Eur J Nucl Med. 1998;25:79–83.

91. Belhocine T, Foidart J, Rigo P, Najjar F, Thiry A, Quatresooz P, et al. Fluorodeoxyglucose positron emission tomography and somatostatin receptor scintigraphy for diagnosing and staging carcinoid tumours: correlations with the pathological indexes p53 and Ki-67. Nucl Med Commun. 2002;23:727–34.

92. Hicks RJ. Use of molecular targeted agents for the diagnosis, staging and therapy of neuroendocrine malignancy. Cancer Imaging. 2010;10 Spec no A:S83-91.

93. Garin E, Le Jeune F, Devillers A, Cuggia M, de Lajarte-Thirouard AS, Bouriel C, et al. Predictive value of 18F-FDG PET and somatostatin receptor scintigraphy in patients with metastatic endocrine tumors. J Nucl Med. 2009;50:858–64.

94. Binderup T, Knigge U, Loft A, Federspiel B, Kjaer A. 18F-fluorodeoxyglucose positron emission tomography predicts survival of patients with neuroendocrine tumors. Clin Cancer Res. 2010;16:978–85.

95. Bahri H, Laurence L, Edeline J, Leghzali H, Devillers A, Raoul JL, et al. High prognostic value of 18F-FDG PET for metastatic gastroenteropancreatic neuroendocrine tumors: a long-term evaluation. J Nucl Med. 2014;55:1786–90.
96. Ezziddin S, Adler L, Sabet A, Pöppel AD, Grabellus F, Yüce A, et al. Prognostic stratification of metastatic gastroenteropancreatic neuroendocrine neoplasms by 18F-FDG PET: feasibility of a metabolic grading system. J Nucl Med. 2014;55:1260–6.
97. Severi S, Nanni O, Bodei L, Sansovini M, Ianniello A, Nicoletti S, et al. Role of 18FDG PET/CT in patients treated with 177Lu-DOTATATE for advanced differentiated neuroendocrine tumours. Eur J Nucl Med Mol Imaging. 2013;40:881–8.
98. Fuccio C, Musto A, Cambioli S, Castellucci P, Pantaleo MA, Nanni C, et al. When should F-18 FDG PET/CT be used instead of 68Ga-DOTA-peptides to investigate metastatic neuro-endocrine tumors? Clin Nucl Med. 2011;36:1109–11.
99. Krenning EP, Valkema R, Kwekkeboom DJ, de Herder WW, van Eijck CH, de Jong M, et al. Molecular imaging as in vivo molecular pathology for gastroenteropancreatic neuroendo-crine tumors: implications for follow-up after therapy. J Nucl Med. 2005;46 Suppl 1:76S–82.
100. Van Essen M, Sundin A, Krenning EP, Kwekkeboom DJ. Neuroendocrine tumours: the role of imaging for diagnosis and therapy. Nat Rev Endocrinol. 2014;10:102–14.
101. Cerci JJ, Pereira Neto CC, Krauzer C, Sakamoto DG, Vitola JV, et al. The impact of coaxial core biopsy guided by FDG PET/CT in oncological patients. Eur J Nucl Med Mol Imaging. 2013;40:98–103.
102. Shyn PB. Interventional positron emission tomography/computed tomography: state-of-the-art. Tech Vasc Interv Radiol. 2013;16:182–90.
103. Bonichon F, Godbert Y, Buy X, Palussière J. PET/computed tomography and thermoablation (radiofrequency, microwave, cryotherapy, laser interstitial thermal therapy). PET Clin. 2015;10:519–40.
104. Imperiale A, Garnon J, Bachellier P, Gangi A, Namer IJ. Simultaneous (18)F-FDOPA PET/CT-guided biopsy and radiofrequency ablation of recurrent neuroendocrine hepatic metasta-sis: further step toward a theranostic approach. Clin Nucl Med. 2015;40:e334–5.
105. European Society of Radiology (ESR). Medical imaging in personalised medicine: a white paper of the research committee of the European Society of Radiology (ESR). Insights Imaging. 2015;6:141–55.
106. Bouchelouche K, Capala J. 'Image and treat': an individualized approach to urological tumors. Curr Opin Oncol. 2010;22:274–80.

Chapter 16
Radionuclide Imaging of Pancreatic Neuroendocrine Tumours

Valentina Ambrosini and Stefano Fanti

16.1 Introduction radiopharm

Nuclear medicine currently plays a central role for the detection of NEN lesions and an array of various radiopharmaceuticals can be employed to study different tumor features. In fact, neuroendocrine cells present characteristic metabolic pathways and surface receptors expression that can be targeted with different radiopharmaceuticals [1]. Although the diagnostic flowchart of well-differentiated pNEN has been revolutionised by the introduction of somatostatin receptor imaging (SRI), first by means of scintigraphy and then of PET/CT, other radiopharmaceuticals may be useful in selected cases. In particular, much attention has been recently devoted to investigate the role of ^{18}F-FDG in undifferentiated tumor forms and to select patients with more aggressive disease. Another clinical setting in which SRI is not the gold standard is the detection of benign insulinoma. Although not frequent, this clinical entity is often misdiagnosed due to the misleading clinical presentation (hypoglycaemia) that can be mistakenly attributed to other conditions.

Overall nuclear medicine imaging procedures provide whole-body, functional data that are crucial for disease detection (with a higher diagnostic accuracy as compared to conventional imaging techniques), treatment planning and patients prognostic stratification.

V. Ambrosini, MD, PhD (✉) • S. Fanti, MD
Nuclear Medicine, DIMES, Alma Mater Studiorum University of Bologna, S. Orsola-Malpighi Hospital, Via Massarenti 9, 40138 Bologna, Italy
e-mail: valentina.ambrosini@unibo.it; valentina.ambrosini@aosp.bo.it

16.2 Morphological Imaging Procedures for the Detection of pNEN

Morphological imaging procedures (including CT, MR and endoscopic US) [2] may be employed for pNEN detection, although their use is generally hampered by the small dimensions that can characterise NEN lesions and by the inability to distinguish reactive nodes from secondary nodal lesions on the basis of morphological criteria alone. When compared to SRI nuclear medicine procedures, conventional imaging also fails to provide data on somatostatin receptor expression (SSTR) that is relevant for therapeutic management.

Due to its wide availability, CT is often performed for the evaluation of patients with pNEN and shows a good sensitivity for the detection of the primary pancreatic tumor (ranging between 57 and 94 %) [3]. Pre-contrast CT scan can detect the primary lesion appearing as a hypodense area with calcifications. NET generally presents as hypervascular lesions that enhance during early arterial phases, although the vascular blush is often transient, while the delayed portal venous phase usually shows washout of the contrast medium [2].

MR [2] generally shows NEN lesions as hypointense on T1 images. Primary lesions have hyperintense signal in T2 images. DWI sequences may be used to assess lesions differentiation grade: poorly differentiated NET generally shows lower ADC (apparent diffusion coefficient) values probably due to increased tumor cellularity. Post-contrast images show the same features as CT. MR has been reported to provide a diagnostic accuracy higher than CT for the detection of the primary tumor and for a more accurate characterisation of suspicious liver secondary lesions. However, it is well known that major disadvantages of MR are represented by long scanning time and by the limits imposed by the presence of metallic devices.

Among conventional imaging procedures, US has a relevant role for the assessment of pNEN. Non-functioning large pNEN can be detected by US performed as first-line imaging procedure. On the contrary, for smaller tumors, endoscopic ultrasound (EUS) and endoscopic ultrasound-guided biopsy of the lesion through fine needle aspiration (EUS-FNA) may be successfully employed. The US appearance of pNEN is generally as a well-defined, round, homogeneous hypoechoic lesion. Less commonly pNEN may present as isoechoic or, rarely, hyperechoic with irregular margins. pNEN generally presents hypervascular enhancement during the arterial phase at CEUS. EUS has become a cornerstone morphological imaging modality in the diagnosis of pNEN tumors, presenting a high sensitivity for lesions detection (ranging from 83 to 94 %) [4, 5]. Various reports described the excellent diagnostic ability of EUS-FNA for pNEN, with sensitivity of 83.3–93 % [4, 5]. EUS-FNA is imperative for preoperative diagnosis of pNEN. However, around 10–15 % of cases remain undiagnosed despite EUS-FNA. In particular, tumors located in the pancreatic head and those characterised by rich stromal fibrosis were associated with reduced sampling adequacy of EUS-FNA [6].

16.3   Nuclear Medicine Procedures for the Detection of pNEN

Nuclear medicine plays a central role for the diagnostic work-up of patients with NEN. Beta-emitting radiopharmaceuticals currently employed for the detection of pNEN include both receptor-mediated (^{68}Ga-DOTA-peptides, ^{68}Ga-exedin4) and metabolic tracers (^{18}F-FDG, ^{18}F-DOPA).

In particular, the development of tracers that bind to SSTR that are overexpressed on NEN cells totally changed the clinicians' approach to NEN lesion detection [7].

Although the first SRI procedure to be employed was scintigraphy (SRS), the introduction of PET/CT has shadowed SRS role, and PET/CT with beta-emitting somatostatin analogues is becoming the gold standard nuclear medicine procedure to study NEN. In fact, several factors are in favour of PET/CT imaging including the higher spatial resolution of PET/CT for the detection of small lesions (due to suboptimal spatial resolution of the isotopes used for SRS imaging, although improvements have been made with the introduction of novel SPECT/CT) [8–10], the relative overall lower costs [11], shorter imaging protocols (approximately 2 h for PET/CT as compared to the delayed acquisitions at 4–24 h of SRS), the possibility to semi-quantify the tracer uptake in the region of interest (by means of the SUVmax) and the relative lower liver accumulation of beta-emitting somatostatin receptor radiopharmaceuticals.

16.3.1   68Ga-DOTA-Peptide Imaging of pNEN

^{68}Ga-DOTA-peptides are a group of beta-emitting radiopharmaceuticals (^{68}Ga-DOTA-TOC, ^{68}Ga-DOTA-NOC, ^{68}Ga-DOTA-TATE) specifically binding to SSTR overexpressed on NEN cells [12, 13]. All clinically employed ^{68}Ga-DOTA-peptides present a common structure: a beta-emitting isotope (^{68}Ga), a chelant (DOTA) and the ligand to SSTR (NOC, TOC, TATE). The different clinically employed compounds (^{68}Ga-DOTA-TOC, ^{68}Ga-DOTA-NOC, ^{68}Ga-DOTA-TATE) merely differ for the binding affinity for SSTR subtypes, with ^{68}Ga-DOTA-TATE presenting the higher affinity for SSTR-2 (the most common receptor on NEN) and DOTA-NOC presenting the wider subtype affinity (binding to SSTR-2,3,5). From a clinical point of view, these compounds are considered to provide substantially equal information. Only a few papers directly compared the performance of one tracer over the other, reporting comparable diagnostic accuracy [14]. From a practical point of view, however, it should be reminded that no direct comparison of the absolute SUVmax value measured using different compounds should be performed.

At present, ^{68}Ga-DOTA-peptides represent the most promising tracers to study well-differentiated NEN. Several papers demonstrated the superiority of ^{68}Ga-DOTA-peptides imaging over SRS and conventional imaging [15, 16] for the

detection of NEN lesions at both the primary and metastatic sites. In a recent prospective trial of comparison between ^{68}Ga-DOTA-TATE PET/CT, octreotide SPECT/CT and whole-body MR, PET/CT detected more lesions in the pancreas (p=0.0455 and p=0.0455, respectively) [16]. PET/CT higher diagnostic accuracy was also reported for bone lesions as compared to both MR and SPECT/CT. Finally, as regards liver lesions, PET/CT and MR results were comparable, and both were superior to SPECT/CT.

In a recent large prospective trial, including 1258 ^{68}Ga-DOTA-TATE PET/CT scans obtained in 728 NEN patients (142/728 of whom with pancreatic primary), ^{68}Ga-DOTA-TATE sensitivity and specificity for the detection of pNEN were reported to be extremely high (94.5% and 97%, respectively) [17] (Figs. 16.1, 16.2 and 16.3).

Indications to ^{68}Ga-DOTA-peptides PET/CT [14] include staging, restaging after therapy, detection of the unknown primary tumor (in cases presenting with metastatic NEN lesions) and to assess the presence of SSTR on NET cells, in order to select patients eligible for treatment with somatostatin analogues. In fact, ^{68}Ga-DOTA-peptide PET/CT has become an unavoidable procedure before starting target therapy with either cold or hot (PRRT, peptide receptor radionuclide therapy) somatostatin analogues. The employment of ^{68}Ga-DOTA-peptide PET/CT as first-step examination in patients with only a clinical suspicion of NEN and the assessment of the response to therapy are on the contrary two clinical settings in which there is still debate on whether DOTA-peptides should be routinely employed.

The information derived from ^{68}Ga-DOTA-peptide PET/CT was reported to have an impact on clinical management, especially regarding the choice of treatment (medical, PRRT, surgical) [17–19].

Finally, ^{68}Ga-DOTA-peptide PET/CT has been reported to provide prognostic information (patients presenting lower SUVmax values were more likely to present disease progression) [20]. In fact, since ^{68}Ga-DOTA-peptide PET/CT uptake correlates with SSTR expression on NET cells [21–23], it also provides an indirect measure of cell differentiation: lesions with a high ^{68}Ga-DOTA-peptide uptake have a higher differentiation grade and are therefore associated with a better prognosis [23]. The SUVmax of pNEN has been reported to be significantly higher than the one of the patients with other NEN primary sites [20]. In a recent paper, specifically addressing SUVmax prognostic value in a population of 43 patients with pNEN with a long follow-up, the patients with a higher SUVmax were more likely to present stable disease at 24-month follow-up [23]. Finally, a recent report highlighted how patients with higher SUVmax were more likely to respond to treatment with either hot or cold somatostatin analogues [24].

Although SRI by means of PET/CT with ^{68}Ga-DOTA-peptides is at present the most accurate imaging procedure to study patients with well-differentiated pNEN, it must be remembered that other tracers are more suitable for cases presenting undifferentiated forms or in cases with variable to low expression of SSTR (e.g. benign insulinoma).
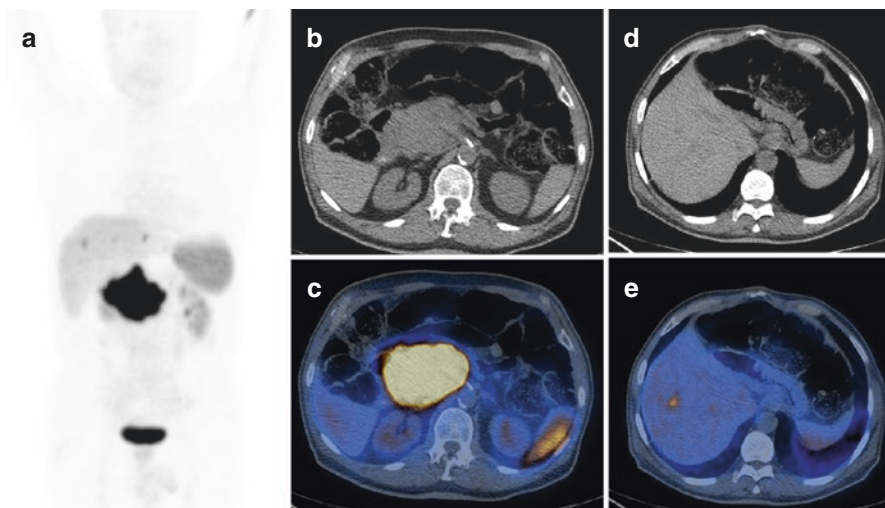
Fig. 16.1 ⁶⁸Ga-DOTA-NOC PET/CT images of a patient with a large pNEN of the pancreatic head (a,b,c; SUVmax 40) presenting three additional focal lesions at liver level (a,d,e; SUVmax=7.4). Teaching point: the very high uptake of the lesions reflects a high expression of SSTR and a high degree of tumour differentiation that is correlated with a better prognosis
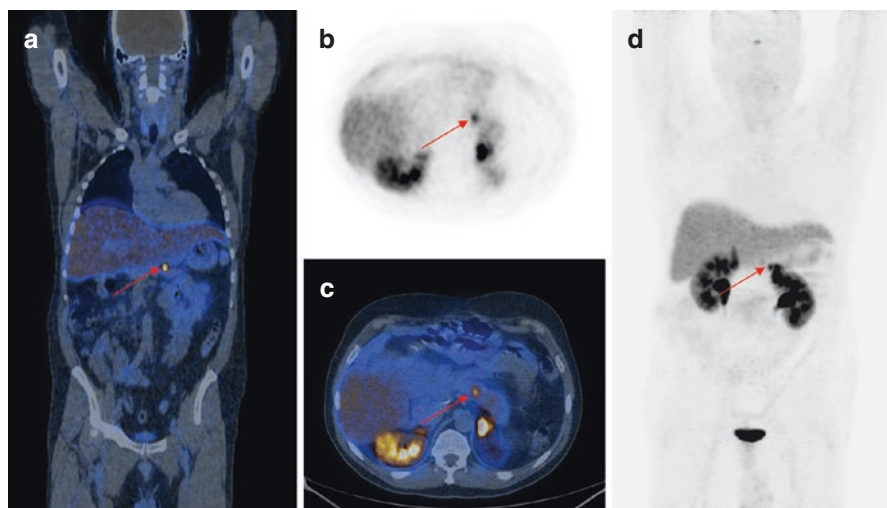
Fig. 16.2 ⁶⁸Ga-DOTA-NOC PET/CT coronal (**a**), transaxial (**b**, **c**) and MIP (**d**) images showing a focal area of pathologic tracer uptake at the pancreatic body (*arrows*) consistent with active disease localisation in a patient with MEN1 previously surgically treated for other NEN localisations (parathyroid, head of the pancreas, right liver). Teaching point: SRI PET/CT shows a high sensitivity for the detection of very small lesions
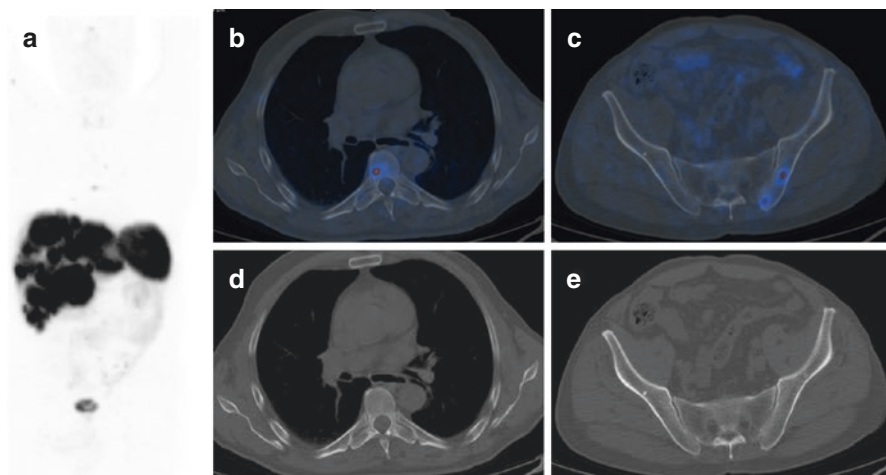
Fig. 16.3 ^{68}Ga-DOTA-NOC PET/CT image of a patient with metastatic NEN of the pancreatic tail presenting multiple liver (a; SUVmax=22) and bone (b,c,d,e; SUVmax=7) lesions. Teaching point: SRI PET/CT may document pathological lesions at bone level that do not present changes on co-registered CT

16.3.1.1 Synthesis of ^{68}Ga-DOTA-Peptides and PET/CT Imaging Protocol

The synthesis and labelling process of ^{68}Ga-DOTA-peptides [14] is quite easy and economic: gallium can be easily eluted from a commercially available Ge-68/Ga-68 generator, and therefore there is no need of an on-site cyclotron. 68Gallium (t1/2=68 min) presents an 89 % positron emission and negligible gamma emission (1077 keV) of 3.2 %. The long half-life of the mother radionuclide ^{68}Ge (270.8 days) makes it possible to use the generator for approximately 9–12 months depending upon the requirement, rendering the whole procedure relatively economic. In 2011, the EANM published guidelines for the standardisation of ^{68}Ga-DOTA-peptide PET/CT acquisition; in particular no specific patient preparation is required, and the use of contrast media is not routinely recommended [14]. In adults, images are generally acquired 60 min after the intravenous injection of approximately 100–200 MBq of the chosen ^{68}Ga-DOTA-peptide (TOC, NOc, TATE). Images should be reconstructed using the iterative reconstruction algorithm implemented in the system and with the system settings. Reconstruction may be performed with or without time of flight information, depending on the system capabilities.

16.3.1.2 ^{68}Ga-DOTA-Peptides and PET/CT Image Interpretation: Normal Biodistribution and Pitfalls

A ^{68}Ga-DOTA-peptide PET/CT scan is generally reported positive when increased tracer activity is detected at sites other than the physiological biodistribution (pituitary gland, spleen, liver, adrenal glands, head of the pancreas, the thyroid, kidneys and urinary bladder).

In order to correctly interpret ^{68}Ga-DOTA-peptide PET/CT scans, a thoughtful knowledge of the biodistribution and of common causes of false-positive and false-negative findings is mandatory.

False-positive reporting may derive from the presence of accessory spleens (rarely intra-pancreatic), splenosis, inflammation (due to the presence of SSR on activated lymphocytes and macrophages, e.g. pancreatitis) and lymphoma (e.g. primary pancreatic lymphoma). Increased tracer uptake at the head of the pancreas is a relatively frequent finding (30–60 %), not necessarily associated with the presence of disease. From a clinical point of view, the detection of a focal area of increased uptake at the head of the pancreas should be regarded more suspiciously as compared to a diffuse homogeneous uptake pattern (more likely to be benign), and further investigations should be recommended.

False-negative findings include small lesion dimension (<5 mm) and tumors with low or variable expression of SSR (e.g. benign insulinoma).

16.3.2 ^{18}F-FDG Imaging of pNEN

^{18}F-FDG, an analogue of glucose labelled with 18F and the most commonly employed radiopharmaceutical in PET/CT studies, is not the gold standard tracer to study well-differentiated NEN due to their generally slow growing rate and a low glucose metabolism. However, undifferentiated tumors may present increased glucose consumption and therefore ^{18}F-FDG uptake. In particular, FDG-positive sites may or may not correspond to ^{68}Ga-DOTA-peptide uptake sites. Therefore, much attention has been recently focused on the possibility to perform double PET tracer investigation [25–27], in order to acquire both data on SSTR expression (by means of ^{68}Ga-DOTA-peptides) and data on glucose metabolism (by means of ^{18}F-FDG), that is well known to correlate with a more aggressive tumor behaviour [28]. In particular, with the increase in pNEN detection, as a consequence of both an improvement in lesions detection techniques and therapeutic management, there is also an increase in the number of pNEN cases presenting a more aggressive behaviour, either at first presentation or during the course of the disease. Several papers recently addressed these issues, portraying the message that ^{18}F-FDG PET/CT may be useful to select patients with a more aggressive disease [27]. Although very interesting, the limited patient sample studied in each of the published reports (not to mention that only few specifically addressed patients with pancreatic primary), together with the lack of suggestions on how often to perform double tracer imaging during the course of the disease (that is in many cases quite long), fails to provide a definitive message to the clinicians, who still are therefore encouraged to discuss each individual case in multidisciplinary board meetings in order to decide when it is more appropriate to perform double tracer PET/CT.

Further studies are needed to better ascertain the role of double tracer imaging in clinical practise, and in particular it is mandatory to identify factors that may help to identify when a patient should be address to double tracer PET/CT imaging during the course of the disease.

16.3.3 *⁶⁸Ga-Exedin4 PET/CT Imaging of Pancreatic Insulinomas*

Insulinomas are the most common functioning endocrine pancreatic tumors (1–2 % of all pancreatic neoplasms) [29, 30]. Their clinical presentation is characterised by hypoglycaemia secondary to insulin secretion. Delays in the diagnosis are common because the symptoms usually precede tumor detection and may be misattributed. Since aggressive surgical resection is the primary treatment option, accurate tumor localisation is important for appropriate management [29].

Insulinomas are generally solitary, confined to the pancreas and benign. However, malignant forms, although extremely rare, were reported and are characterised by an aggressive clinical behaviour, with invasion of the surrounding soft tissues/lymph nodes or distant spread (mostly to the liver) [29, 31].

To accurately image benign insulinomas, glucagon-like peptide-1 receptor (GLP-1) imaging is generally superior to SRI, due to low expression of SSTR [32, 33]. In particular the ⁶⁸Ga-labelled exedin was reported to be superior to the 111-In-labelled compound [34]. However, negative GLP-1 receptor findings have been suggested to indicate the presence of a malignant insulinoma [32] that can be studied with ⁶⁸Ga-DOTA-peptides [35].

16.3.4 *¹⁸F-DOPA Imaging of pNEN*

¹⁸F-DOPA is a metabolic tracer that can be employed to study NEN. However, due to its normal biodistribution to the pancreas [36], it is not the tracer of choice to study pancreatic tumors at primary site. ¹⁸F-DOPA may be helpful for the characterisation of well-differentiated secondary neuroendocrine lesions. However, its accuracy in well-differentiated neuroendocrine lesions detection has been reported to be inferior to ⁶⁸Ga-DOTA-peptides [37, 38]. Recent reports also indicate a limited accuracy for the detection of insulinomas, although carbidopa premedication seems to improve it [39]. In this clinical setting, both ⁶⁸Ga-exedin and ⁶⁸Ga-DOTA-peptides seem to be more promising.

16.4 Conclusions

The diagnostic approach to well-differentiated pNEN mainly relies on somatostatin receptor imaging by PET/CT. The clinically available beta-emitting somatostatin receptor radiopharmaceuticals (⁶⁸Ga-DOTA-TOC, ⁶⁸Ga-DOTA-NOC, ⁶⁸Ga-DOTA-TATE) show a high sensitivity and specificity for the detection of well-differentiated pNEN, often superior to morphological imaging procures. Moreover, SRI PET/CT

provides data on SSTR expression on tumor cells that is crucial to accurately plan treatment (with either cold somatostatin analogues or PRRT).

Considering the heterogeneous clinical behaviour of pNEN and the increasing number of cases presenting undifferentiated lesions (either at presentation or during the disease natural history), the role of ^{18}F-FDG should also be empathised. In fact, the presence of ^{18}F-FDG-positive lesions is correlated with a worse prognosis. A complete biological characterisation of the disease would take into account the assessment of both SSTR expression and glucose metabolism and may have an impact on clinical decision making. However, the paucity of literature data on the factors that can be employed to select "when" a patient should undergo both imaging modalities during the course of the disease does not currently provide a definitive message to the clinician. At present, ^{18}F-FDG is certainly mandatory in undifferentiated cases, in pNEN with high ki-67 levels or when SSTR-negative lesions are detected at ^{68}Ga-DOTA-peptides PET/CT. Further studies in larger patients population will better answer to these issues.

Although a rare entity, benign insulinoma can be clinically challenging. A novel receptor-mediated radiopharmaceutical (^{68}Ga-exedin4), which binds to GLP-1-receptor, can be employed for accurate benign insulinoma imaging. In cases of malignant insulinoma (known to be GLP-1-receptor-negative), ^{68}Ga-DOTA-peptides may be employed.

Among metabolic tracers used for NEN imaging, ^{18}F-DOPA may be also useful; however imaging the pancreatic primary is limited by its physiological biodistribution. Well-differentiated secondary lesions can be detected by ^{18}F-DOPA; however its accuracy has been reported to be inferior to ^{68}Ga-DOTA-peptides.

References

1. Koopmans KP, Neels ON, Kema IP, Elsinga PH, Links TP, de Vries EGE, et al. Molecular imaging in neuroendocrine tumors: molecular uptake mechanisms and clinical results. Crit Rev Oncol Hematol. 2009;71(3):199–213.
2. Leung D, Schwartz L. Imaging of neuroendocrine tumors. Semin Oncol. 2013;40(1):109–19.
3. Ramage JK, Ahmed A, Ardill J, Bax N, Breen DJ, Caplin ME, et al. Guidelines for the management of gastroenteropancreatic neuroendocrine (including carcinoid) tumours (NETs). Gut. 2012;61(1):6–32.
4. Anderson MA, Carpenter S, Thompson NW, Nostrant TT, Elta GH, Scheiman JM. Endoscopic ultrasound is highly accurate and directs management in patients with neuroendocrine tumors of the pancreas. Am J Gastroenterol. 2000;95(9):2271–7.
5. Pais SA, Al-Haddad M, Mohamadnejad M, Leblanc JK, Sherman S, McHenry L, et al. EUS for pancreatic neuroendocrine tumors: a single-center, 11-year experience. Gastrointest Endosc. 2010;71(7):1185–93.
6. Hijioka S, Hara K, Mizuno N, Imaoka H, Bhatia V, Mekky MA, et al. Diagnostic performance and factors influencing the accuracy of EUS-FNA of pancreatic neuroendocrine neoplasms. J Gastroenterol. 2016;14:923–30.

7. Krenning EP, Kwekkeboom DJ, Bakker WH, Breeman WA, Kooij PP, Oei HY, et al. Somatostatin receptor scintigraphy with [111In-DTPA-D-Phe1]- and [123I-Tyr3]-octreotide: the Rotterdam experience with more than 1000 patients. Eur J Nucl Med. 1993;20(8):716–31.

8. Kowalski J, Henze M, Schuhmacher J, Mäcke HR, Hofmann M, Haberkorn U. Evaluation of positron emission tomography imaging using [68Ga]-DOTA-D Phe(1)-Tyr(3)-octreotide in comparison to [111In]-DTPAOC SPECT. First results in patients with neuroendocrine tumors. Mol Imaging Biol MIB Off Publ Acad Mol Imaging. 2003;5(1):42–8.

9. Buchmann I, Henze M, Engelbrecht S, Eisenhut M, Runz A, Schäfer M, et al. Comparison of 68Ga-DOTATOC PET and 111In-DTPAOC (Octreoscan) SPECT in patients with neuroendocrine tumours. Eur J Nucl Med Mol Imaging. 2007;34(10):1617–26.

10. Srirajaskanthan R, Kayani I, Quigley AM, Soh J, Caplin ME, Bomanji J. The role of 68Ga-DOTATATE PET in patients with neuroendocrine tumors and negative or equivocal findings on 111In-DTPA-octreotide scintigraphy. J Nucl Med Off Publ Soc Nucl Med. 2010;51(6):875–82.

11. Schreiter NF, Brenner W, Nogami M, Buchert R, Huppertz A, Pape U-F, et al. Cost comparison of 111In-DTPA-octreotide scintigraphy and 68Ga-DOTATOC PET/CT for staging enteropancreatic neuroendocrine tumours. Eur J Nucl Med Mol Imaging. 2012;39(1):72–82.

12. Gabriel M, Oberauer A, Dobrozemsky G, Decristoforo C, Putzer D, Kendler D, et al. 68Ga-DOTA-Tyr3-octreotide PET for assessing response to somatostatin-receptor-mediated radionuclide therapy. J Nucl Med Off Publ Soc Nucl Med. 2009;50(9):1427–34.

13. Ambrosini V, Campana D, Tomassetti P, Fanti S. 68Ga-labelled peptides for diagnosis of gastroenteropancreatic NET. Eur J Nucl Med Mol Imaging. 2012;39 Suppl 1:S52–60.

14. Virgolini I, Ambrosini V, Bomanji JB, Baum RP, Fanti S, Gabriel M, et al. Procedure guidelines for PET/CT tumour imaging with 68Ga-DOTA-conjugated peptides: 68Ga-DOTA-TOC, 68Ga-DOTA-NOC, 68Ga-DOTA-TATE. Eur J Nucl Med Mol Imaging. 2010;37(10):2004–10.

15. Chiti A, Fanti S, Savelli G, Romeo A, Bellanova B, Rodari M, et al. Comparison of somatostatin receptor imaging, computed tomography and ultrasound in the clinical management of neuroendocrine gastro-entero-pancreatic tumours. Eur J Nucl Med. 1998;25(10):1396–403.

16. Etchebehere EC, de Oliveira Santos A, Gumz B, Vicente A, Hoff PG, Corradi G, et al. 68Ga-DOTATATE PET/CT, 99mTc-HYNIC-octreotide SPECT/CT, and whole-body MR imaging in detection of neuroendocrine tumors: a prospective trial. J Nucl Med Off Publ Soc Nucl Med. 2014;55(10):1598–604.

17. Skoura E, Michopoulou S, Mohmaduvesh M, Panagiotidis E, Al Harbi M, Toumpanakis C, et al. The Impact of 68Ga-DOTATATE PET/CT Imaging on Management of Patients with Neuroendocrine Tumors: Experience from a National Referral Center in the United Kingdom. J Nucl Med Off Publ Soc Nucl Med. 2016;57(1):34–40.

18. Ambrosini V, Campana D, Bodei L, Nanni C, Castellucci P, Allegri V, et al. 68Ga-DOTANOC PET/CT clinical impact in patients with neuroendocrine tumors. J Nucl Med. 2010;51(5):669–73.

19. Ilhan H, Fendler WP, Cyran CC, Spitzweg C, Auernhammer CJ, Gildehaus F-J, et al. Impact of (68)Ga-DOTATATE PET/CT on the surgical management of primary neuroendocrine tumors of the pancreas or ileum. Ann Surg Oncol. 2015;22(1):164–71.

20. Campana D, Ambrosini V, Pezzilli R, Fanti S, Labate AMM, Santini D, et al. Standardized uptake values of (68)Ga-DOTANOC PET: a promising prognostic tool in neuroendocrine tumors. J Nucl Med Off Publ Soc Nucl Med. 2010;51(3):353–9.

21. Kaemmerer D, Wirtz RM, Fischer EK, Hommann M, Sänger J, Prasad V, et al. Analysis of somatostatin receptor 2A immunohistochemistry, RT-qPCR, and in vivo PET/CT data in patients with pancreatic neuroendocrine neoplasm. Pancreas. 2015;44(4):648–54.

22. Boy C, Heusner TA, Poeppel TD, Redmann-Bischofs A, Unger N, Jentzen W, et al. 68Ga-DOTATOC PET/CT and somatostatin receptor (sst1-sst5) expression in normal human

tissue: correlation of sst2 mRNA and SUVmax. Eur J Nucl Med Mol Imaging. 2011;38(7):1224–36.

23. Ambrosini V, Campana D, Polverari G, Peterle C, Diodato S, Ricci C, et al. Prognostic value of 68Ga-DOTANOC PET/CT SUVmax in patients with neuroendocrine tumors of the pancreas. J Nucl Med Off Publ Soc Nucl Med. 2015;56(12):1843–8.

24. Kratochwil C, Stefanova M, Mavriopoulou E, Holland-Letz T, Dimitrakopoulou-Strauss A, Afshar-Oromieh A, et al. SUV of [68Ga]DOTATOC-PET/CT Predicts Response Probability of PRRT in Neuroendocrine Tumors. Mol Imaging Biol MIB Off Publ Acad Mol Imaging. 2015;17(3):313–8.

25. Has Simsek D, Kuyumcu S, Turkmen C, Sanlı Y, Aykan F, Unal S, et al. Can complementary 68Ga-DOTATATE and 18F-FDG PET/CT establish the missing link between histopathology and therapeutic approach in gastroenteropancreatic neuroendocrine tumors? J Nucl Med Off Publ Soc Nucl Med. 2014;55(11):1811–7.

26. Bahri H, Laurence L, Edeline J, Leghzali H, Devillers A, Raoul J-L, et al. High prognostic value of 18F-FDG PET for metastatic gastroenteropancreatic neuroendocrine tumors: a long-term evaluation. J Nucl Med Off Publ Soc Nucl Med. 2014;55(11):1786–90.

27. Partelli S, Rinzivillo M, Maurizi A, Panzuto F, Salgarello M, Polenta V, et al. The role of combined Ga-DOTANOC and (18)FDG PET/CT in the management of patients with pancreatic neuroendocrine tumors. Neuroendocrinology. 2014;100(4):293–9.

28. Garin E, Le Jeune F, Devillers A, Cuggia M, de Lajarte-Thirouard A-S, Bouriel C, et al. Predictive value of 18F-FDG PET and somatostatin receptor scintigraphy in patients with metastatic endocrine tumors. J Nucl Med Off Publ Soc Nucl Med. 2009;50(6):858–64.

29. Okabayashi T, Shima Y, Sumiyoshi T, Kozuki A, Ito S, Ogawa Y, et al. Diagnosis and management of insulinoma. World J Gastroenterol. 2013;19(6):829–37.

30. Scherübl H, Streller B, Stabenow R, Herbst H, Höpfner M, Schwertner C, et al. Clinically detected gastroenteropancreatic neuroendocrine tumors are on the rise: epidemiological changes in Germany. World J Gastroenterol. 2013;19(47):9012–9.

31. Hirshberg B, Cochran C, Skarulis MC, Libutti SK, Alexander HR, Wood BJ, et al. Malignant insulinoma: spectrum of unusual clinical features. Cancer. 2005;104(2):264–72.

32. Wild D, Christ E, Caplin ME, Kurzawinski TR, Forrer F, Brändle M, et al. Glucagon-like peptide-1 versus somatostatin receptor targeting reveals 2 distinct forms of malignant insulinomas. J Nucl Med Off Publ Soc Nucl Med. 2011;52(7):1073–8.

33. Eriksson O, Velikyan I, Selvaraju RK, Kandeel F, Johansson L, Antoni G, et al. Detection of metastatic insulinoma by positron emission tomography with [(68)ga]exendin-4-a case report. J Clin Endocrinol Metab. 2014;99(5):1519–24.

34. Antwi K, Fani M, Nicolas G, Rottenburger C, Heye T, Reubi JC, et al. Localization of hidden insulinomas with 68Ga-DOTA-exendin-4 PET/CT: A Pilot Study. J Nucl Med Off Publ Soc Nucl Med. 2015;56(7):1075–8.

35. Ambrosini V, Campana D, Nanni C, Marzola MC, Rubello D, Fanti S. 68Ga DOTANOC PET/CT detects primary malignant insulinoma. Clin Nucl Med. 2015;40(2):e132–3.

36. Chondrogiannis S, Grassetto G, Marzola MC, Rampin L, Massaro A, Bellan E, et al. 18F-DOPA PET/CT biodistribution consideration in 107 consecutive patients with neuroendocrine tumours. Nucl Med Commun. 2012;33(2):179–84.

37. Ambrosini V, Tomassetti P, Castellucci P, Campana D, Montini G, Rubello D, et al. Comparison between 68Ga-DOTA-NOC and 18F-DOPA PET for the detection of gastro-entero-pancreatic and lung neuro-endocrine tumours. Eur J Nucl Med Mol Imaging. 2008;35(8):1431–8.

38. Haug A, Auernhammer CJ, Wängler B, Tiling R, Schmidt G, Göke B, et al. Intraindividual comparison of 68Ga-DOTA-TATE and 18F-DOPA PET in patients with well-differentiated metastatic neuroendocrine tumours. Eur J Nucl Med Mol Imaging. 2009;36(5):765–70.

39. Imperiale A, Sebag F, Vix M, Castinetti F, Kessler L, Moreau F, et al. 18F-FDOPA PET/CT imaging of insulinoma revisited. Eur J Nucl Med Mol Imaging. 2015;42(3):409–18.

Chapter 17
Radionuclide Imaging of Pulmonary and Thymic Neuroendocrine Tumors

Sellam Karunanithi, Ganesh Kumar, and Rakesh Kumar

17.1 Epidemiology

Neuroendocrine tumors (NETs) comprise a rare group of malignant tumors that have a diverse array of presentations in terms of clinicopathological and biochemical features as well as outcomes. Pulmonary carcinoid tumors comprise of 1–2 % of all lung malignancies and roughly 20–30% of all NETs [1, 2] and currently have an increasing tendency of incidence [3]. Thymic NETs comprise of 2–5 % of thymic epithelial tumors [4–6]. No specific sex predilection has been known for bronchopulmonary NETs [7]. Among thymic NETs, MEN-1-associated atypical carcinoids are known to occur more commonly in males [8, 9]. In contrast to bronchopulmonary NETs which have higher incidence of typical carcinoids, thymic NETs usually have higher occurrence of atypical carcinoids over the other pathologic subtypes [10]. No causal association have been attributed to the development of these tumors; few studies have found higher association of cigarette smoking with pulmonary atypical carcinoids as compared to typical carcinoids [11, 12].

S. Karunanithi, MD, FANMB
Department of Nuclear Medicine, Aster MIMS Hospital, Malabar Institute of Medical Sciences Ltd, Mini By-pass Road, Govindapuram P.O., Calicut 673016, Kerala, India
e-mail: drsellam84@yahoo.co.in

G. Kumar, MD
Division of Diagnostic Nuclear Medicine, Department of Nuclear Medicine, All India Institute of Medical Sciences, AIIMS Campus, New Delhi 110029, India
e-mail: m_ganeshkumar@yahoo.com

R. Kumar, MD, PhD (✉)
Division of Diagnostic Nuclear Medicine, Department of Nuclear Medicine, All India Institute of Medical Sciences, New Delhi 110029, India
e-mail: rkphulia@hotmail.com

Epidemiologically, bronchopulmonary NETs have been understood more extensively. Patients with atypical lung carcinoids (AC) tend to be older than those with typical carcinoids (TC) [13, 14]. Higher prevalence of TC has been observed in comparison to AC at a ratio of about 4:1 [15]. Most of the carcinoid tumors are centrally located [1, 16] and have a predilection to affect the right lung [1, 13].

17.2 Prognosis

Carcinoid tumors of the lung generally carry a better prognosis than other forms of pulmonary malignancy. The prognosis of the bronchopulmonary NETs generally is determined by the grade of the tumor, in that it deteriorates as the grade increases. Typical carcinoid tumors have been found to have a much better prognosis than do the atypical variety. Patients with atypical carcinoids carry a 5-year survival rate of about 61–88 % compared to 92–100 % in those with typical carcinoids [2]. Also, involvement of local lymph nodes reduces the survival rates in atypical carcinoids, whereas it does not seem to have much impact over the prognosis of the typical carcinoids [17, 18].

Thymic NETs are generally known to carry a poor prognosis as they behave aggressively and are commonly associated with invasion of adjacent mediastinal structures and show higher occurrences of local disease recurrences and metastases [10].

17.3 Etiopathogenesis

Although pulmonary NETs were initially thought to originate from the neural crest cells, more recent as well as current research suggests that these tumors originate from the Kulchitzky cells present normally in the bronchial mucosa. A premalignant neuroendocrine cell hyperplasia has been postulated as the heralding event in pathogenesis though evidence is still evolving [19].

Pathogenesis of thymic NETs is less well understood; the cell of origin is yet to be identified. However, it has been recognized from immunohistochemistry-based studies that neuroendocrine differentiation is a common feature of thymic epithelial tumors [20, 21]. It has also been postulated that a common progenitor cell of epithelial origin may be the culprit in pathogenesis of both epithelial carcinomas of the thymus and neuroendocrine tumors of the thymus [22].

17.4 Nomenclature and Histologic Classification

The spectrum of bronchopulmonary neuroendocrine tumors ranges from the low-grade typical carcinoids (TCs) at one end, through the intermediate-grade atypical carcinoids (ACs), to the high-grade tumors – large cell neuroendocrine carcinomas

Table 17.1 Histologic classification of bronchopulmonary neuroendocrine tumors

Variable	Typical carcinoid	Atypical carcinoid	Large cell NEC	Small cell NEC
Mitoses per 2 mm² (10HPF)	<2	2–10	≥10	≥10
Necrosis	Absent	Often punctate	Often, large zones	Frequent, large zones
Histologic grade	Low	Intermediate	High	High
Nuclear-cytoplasmic ratio	Moderate	Moderate	Low	High
Nucleoli	Occasional	Common	Very common	Absent/inconspicuous
Nuclear Chromatin	Finely granular	Finely granular	Usually vesicular, may be finely granular	Finely granular

HPF high power fields

(LCNECs) or small cell neuroendocrine carcinomas (SCNEC) at the other extreme of the spectrum (Table 17.1) [23].

Conversely, thymic NETs are considered to occur as a result of neuroendocrine differentiation of a preexistent epithelial tumor rather than as a de novo process. Also, these tumors bear a significant risk for recurrence, metastasis, and tumor-associated deaths despite presence of benign-looking features. Hence it has been suggested that these tumors be referred to as well-differentiated or poorly differentiated neuroendocrine carcinomas which are further subclassified based on specific histologic features [24] (Table 17.2).

17.5 Clinical Presentation

Bronchopulmonary carcinoids can present both as intrabronchial masses and intra-parenchymal pulmonary nodules. Owing to their high vascularity and tendency toward causing bronchial obstruction, the affected patients commonly present with cough, hemoptysis, and obstructive pneumonia [15]. However, tumors that are more peripherally situated are diagnosed as incidental radiologic findings. Nearly half of all the bronchopulmonary NETs have been diagnosed incidentally in asymptomatic conditions [2]. On the other hand, thymic NETs, typically the poorly differentiated NETs and about half of the well-differentiated NETs, present with local symptoms such as chest pain, cough, dyspnea, and superior vena cava syndrome [4, 5, 25].

The features of carcinoid syndrome appear quite rare in both bronchopulmonary [15] and thymic NETs [25] as many of these tumors do not secrete

Table 17.2 Histologic classification of thymic NETs

	Neuroendocrine carcinoma			
	Well differentiated		Poorly differentiated	
	Typical carcinoid	Atypical carcinoid	Large cell	Small cell
Mitotic index (10HPF)	<2	2–10	>10	
Necrosis	Absent	Present	–	–
Cytomorphology			Non-small cell	Small cell

[a]*HPF* high power fields

vasoactive substances. However, thymic NETs not uncommonly can present with an ectopic Cushing's syndrome owing to ACTH secretion [26, 27]. Rare reports of ectopic Cushing's syndrome have also been noted with atypical pulmonary carcinoids [28].

Thymic NETs are also known to be associated with MEN-1 (multiple endocrine neoplasia, type 1) syndrome [8, 29], in which case, the tumors are insidious and can manifest by local symptoms, metastases, disturbances of calcium/phosphate metabolism [10], or, rarely, with acromegaly [30]; however, manifestation in the form of an ectopic Cushing's syndrome is yet to be reported in such cases.

17.6   Conventional Diagnostic Approaches

Histopathologic examination is the gold standard for the diagnosis of NETs. Invasive diagnostic modalities such as flexible bronchoscopy and thoracotomy not only help in characterizing the tumor but are also routinely used for extracting tissue samples for diagnosis by means of washings, needle aspiration, and biopsy. However, the high vascularity of these tumors comes with a caveat that these procedures can sometimes result in severe or even life-threatening hemorrhage.

Contrast-enhanced CT is the conventional imaging modality routinely used for the diagnosis of bronchopulmonary and thymic NETs. Owing to their highly vascular nature, these tumors enhance exquisitely on administration of intravenous CT contrast. However, literature suggests that thymic NETs associated with ectopic Cushing's syndrome are comparatively small in size and may be easily missed on contrast-enhanced CT studies. Other structural imaging investigations such as chest radiography and MRI can also be used. For example, MR imaging may be used in suspect peripheral pulmonary nodules to differentiate between small carcinoids and adjacent vascular structures [31]. However, each of these modalities suffers from its own drawbacks. Also, the findings are rather nonspecific enough in establishing a diagnosis [31]. More importantly, they cannot assess the functional status of the tumor and cannot differentiate between typical and atypical carcinoids [32].

17.7   Treatment

Surgical resection is the treatment of choice for bronchopulmonary carcinoids, with lobectomy being the surgical procedure of choice for most tumors; however, limited resection maybe attempted in more peripherally situated lesion [33]. Also, as most of the poorly differentiated NETs present with locally advanced disease and tend to metastasize early, chemotherapy and radiotherapy in an adjuvant or neo-adjuvant setting are rendered necessary in these cases. However, no robust evidence is available that definitively demonstrate a benefit in the outcome [34, 35]. The prospect of theranosis has evolved into an attractive treatment option in advanced unresectable and metastatic tumors, specifically the more differentiated varieties that express somatostatin receptors [discussed later].

Thymic NETs are often aggressive in their clinical behavior. Hence, a complete resection often accompanied by mediastinal lymphadenectomy by median sternotomy approach is considered to provide the best opportunity of a curative disease removal and longer disease-free survival. Currently there are no data to suggest that an adjuvant therapy (radiation, chemotherapy, or chemoradiation) will prolong the disease-free interval or median survival [36–38].

17.8   Radionuclide Imaging of NETs

Wide arrays of SPECT and PET radiopharmaceuticals have been used in the evaluation and management of neuroendocrine tumors. In general, functional imaging with PET radiopharmaceuticals carries a higher detection rates for lesions in these patients owing to inherently better spatial resolution and a broader spectrum of radiopharmaceuticals available for targeting the various molecular mechanisms for identifying these lesions.

17.8.1   Radionuclide Imaging in Bronchopulmonary NETs

Bronchopulmonary NETs, as is the case with carcinoid tumors elsewhere in the body, express somatostatin receptors which can be used to functionally assess the various aspects in the management of these tumors. Functional imaging techniques such as somatostatin receptor and dopamine receptor imaging offer a higher sensitivity in disease detection in comparison with anatomical imaging techniques such as CT and MRI which offer sensitivities of only about 50–80 % [39].

Somatostatin receptor is an important cellular marker available in characterizing cells of neuroendocrine origin. This group of receptor consists of 7-transmembrane G-protein-coupled receptors; although five subtypes have been identified,

neuroendocrine tumors are known to express predominantly the receptor subtypes 2 and 5 [40].

17.8.1.1 Somatostatin Receptor Scintigraphy

Neuroendocrine tumors are known to express somatostatin receptors (SSRs) on their cell surface. Somatostatin (SS) by itself has a very short half-life of 1–2 min and hence has no clinical application. Octreotide analogues have a high affinity for the SSR-2 and SSR-5 subtypes and a much lower binding to the SSR-1, SSR-3, and SSR-4 subtypes [41].

[111]In-Pentetreotide Scintigraphy

The cyclic octapeptide octreotide was the first SS analogue to be used in clinical practice. This compound was initially conjugated with diethylene-triamine-pentaacetic acid (DTPA) and then coupled with various radioisotopes especially [111]In. The sensitivity of this scintigraphy technique has been reported to be about 80–90 %. Positivity on ^{111}In-DTPA-octreotide scintigraphy (octreoscan) not only helps to localize the tumor but also helps to predict the response to octreotide therapy. Octreotide can also be conjugated with the macrocyclic chelator DOTA (1,4,7,10-tetraazacyclod odecane-N,N=,N,N-tetraacetic acid), resulting in [111]In 1,4,7,10-tetraazacyclododecan e-1,4,7,10-tetraacetic acid-lanreotide (^{111}In-DOTA-lanreotide) and ^{111}In-DOTA-Tyr3-octreotide and enabling its use in the diagnosis, staging, and follow-up of patients with NETs [41]. This technique provides whole-body screening and is associated with radiation exposure comparable to that of other imaging modalities.

Sensitivity of SRS in different tumor types is related to various factors such as type and density of SS receptors expressed by the tumor, target-to-background ratio, and tumor site and the histology. In clinical practice, SRS is mainly used for localizing the primary lesion and for evaluating disease extension, monitoring the effects of treatment, as well as a prognostic parameter in predicting the response to therapy.

In a retrospective analysis of pulmonary carcinoids with ^{111}In-octreotide scintigraphy, Yellin et al. [42] reported sensitivity of 90 % for SRS. The specificity was 83 % and the positive and negative predictive values were 83 % and 91 %, respectively. Hervás Benito et al. [43] evaluated the role of octreoscan in three cases of pediatric bronchial carcinoids (one preoperative, two postoperative with residual tumor); uptake was noted in all the three cases, which were later confirmed histologically. In one case the scan was able to differentiate between the tumor and associated atelectasis.

Irrespective of the promising results provided above, octreoscan carries a few but troublesome limitations such as limited spatial resolution, low tumor-to-background ratio which might hamper visualization of smaller lesions, and a high false-positive rates due to uptake in many other tumors, granulomas, and some autoimmune disease, thus reducing its specificity.

123I/131I-MIBG (MIBG Scan)

MIBG (meta-iodobenzylguanidine) is an analogue of biogenic amine precursor resembling adrenergic neurotransmitter norepinephrine. It is taken up by active sodium and energy-dependent uptake mechanism in the cell membrane of sympathomedullary tissue and is stored in the intracellular granules [44]. This molecule can be labelled with either 123I or 131I, with 123I-labelled molecule having better characteristics such as superior spatial resolution and absence of high-energy beta emissions that are emitted from 131I. On the other hand, 131I-MIBG can be a useful cost-effective option as it is much less expensive compared to 123I-MIBG.

The use of 131I-MIBG for the detection and imaging of neuroendocrine tumors was reported as early as the 1980s, followed by papers about its therapeutic applications. The sensitivity of the MIBG scan for carcinoid tumors is reported to be a little lower than that of the ^{111}In-pentetreotide scintigraphy scan; however, a combination of these scans increases the sensitivity to 95 % [45]. MIBG scintigraphy may provide advantages over octreoscan in preoperative localization of tumors, as well as radioguided surgery of neuroendocrine metastatic lesions, if the involved site is located in proximity to highly octreotide-avid organs such as the kidneys or spleen [46].

99mTc-EDDA/HYNIC-TOC

Being a technetium-99 m-labelled radiopharmaceutical, this molecule has definitive logistical and imaging advantages over octreoscan and MIBG considering the easy availability of the radionuclide, favorable imaging properties, early imaging time, and lesser exposure to radiation to the patients. The radionuclide 99mTc and the somatostatin analogue Tyr3-octreotide are held together by a bifunctional chelator EDDA/HYNIC, a hydrazinonicotinic acid derivative with ethylenediamine N,N' diacetic acid (EDDA) acting as a coligand; this renders the molecule highly stable *in vivo* and *in vitro* [47]. This radiopharmaceutical has been sporadically used to evaluate solitary pulmonary nodules [48] and large cell neuroendocrine carcinoma [49] with rather disappointing results. It carries a low specificity due to high possibility of uptake in benign findings such as foreign body and suppurative inflammations, hamartomas, and tuberculomas [48].

17.8.1.2 Positron Emission Tomography (PET) Radiopharmaceuticals

^{18}F-FDG

The utility of ^{18}F-FDG PET scan depends principally on increased glucose metabolism and so-called metabolic trapping – greater trapping of the agent in the more metabolically active tumor cells than in surrounding tissues [50]. ^{18}F-FDG PET/CT is one of the most commonly utilized investigations in the field of oncology today. Notwithstanding, the utility of this radiopharmaceutical is somewhat limited in the evaluation of NETs. The FDG uptake in carcinoid

tumors is low, due to their low proliferative and metabolic activity and high degree of differentiation [51]. The use of ^{18}F-FDG PET/CT may be reserved for poorly differentiated neuroendocrine cancers with little or no hormone production and a high proliferative activity (Table 17.3). Also, ^{18}F-FDG PET/CT appears to show a higher SUVmax values for atypical carcinoids than typical carcinoids [57, 58]. This in turn leads to higher sensitivity for detection of atypical carcinoids compared to typical carcinoids. A disadvantage in using ^{18}F-FDG is that it may be falsely positive in the inflammatory and infective lesions of lung and lymph nodes [52]. Also, other non-carcinoid tumors which can mimic bronchopulmonary carcinoid (mucoepidermoid carcinoma, adenoid cystic carcinoma, schwannoma, and inflammatory myoblastic tumors) show ^{18}F-FDG avidity that lowers the specificity of ^{18}F-FDG PET/CT in the detection of bronchopulmonary NETs [52, 55, 59, 60]. ^{18}F-FDG has been rarely used in the evaluation of thymic carcinoids; a possible role of the modality may lie while searching for a cause of ectopic Cushing's syndrome where thymic carcinoids may be identified [61–63].

^{68}Ga-DOTA-Somatostatin Analogues (SSA)

High levels of SSTR expression are generally detected in lung carcinoids, predominantly subtypes 2, 3, and 5, which has been verified by a multitude of *in vitro* and *in vivo* studies [64]. This implies that radiopharmaceuticals which target these receptors can help in the detection of these lesions. This has best been achieved with the help of ^{68}Ga-DOTA-conjugated SSA. Three such molecules (DOTANOC, DOTATOC, DOTATATE, all labelled with ^{68}Ga) have been developed and extensively studied in assessing their role in the detection of pulmonary carcinoids apart from neuroendocrine tumors at other sites [65, 66]. They offer distinct advantages compared to their SPECT counterparts such as octreoscan in terms of superior spatial resolution and earlier imaging times. The superior spatial resolution invariably leads to higher detection rates compared to octreoscan. They have opened up horizons in terms of understanding the biological behavior of these malignancies. The binding molecular affinities and specificities to the different somatostatin receptor subtypes vary between the three molecules [65]. Hence, although they show similar biological distribution and diagnostic accuracies, one ^{68}Ga-DOTA-SSA molecule may show superior tumor-to-background ratios and SUVmax values compared to the other [67].

However, one feature common to the three molecules is their often documented inverse relationship compared with ^{18}F-FDG in uptake values between typical and atypical carcinoids. Two studies at our department also prove this point satisfactorily. The study by Venkitaraman et al. [55] and Jindal et al. [59] evaluated patients with suspected bronchial carcinoids using ^{68}Ga-DOTATOC and ^{18}F-FDG PET/CT studies. They found that the ratio of SUVmax values of ^{68}Ga-DOTATOC to ^{18}F-FDG PET scans was higher in case of typical carcinoids, while atypical carcinoids showed higher SUVmax for ^{18}F-FDG (Table 17.4).

Table 17.3 Studies depicting the utility of ^{18}F-FDG PET in pulmonary carcinoids

Serial no.	Authors	Year	Methodology	Results
1	Erasmus et al. [51]	1998	Evaluated 7 cases of pulmonary carcinoids with ^{18}F-FDG PET	Carcinoid tumors do not show high uptake on ^{18}F-FDG PET
2	Bryant et al. [52]	2006	Evaluated 585 patients of solitary pulmonary nodule with ^{18}F-FDG PET CT (14 cases were carcinoid tumors)	10/14 carcinoid showed uptake on FDG PET while 4 showed no uptake. ^{18}F-FDG PET showed increased uptake in infective lesions; lesions with SUVmax > 2.5 were more likely to be malignant
3	Kruger et al. [53]	2006	Studied 13 patients with pulmonary carcinoids (12 typical and 1 atypical). Integrated FDG PET/CT scan and surgical resection were performed in all patients	SUVmean in atypical carcinoids significantly higher than in typical carcinoids
4	Daniels et al. [54]	2007	Performed a retrospective review ^{18}F-FDG PET of 16 patients with pathologic diagnosis of bronchial carcinoid (TC-11;AC-5)	Overall sensitivity of 75 %; higher for atypical carcinoids (80 %) than typical carcinoids (72.7 %)
5	Venkitaraman et al. [55]	2014	Prospective study on ^{18}F-FDG PET/CT in 32 patients with clinical suspicion of BCs	The sensitivity of ^{18}F-FDG PET was superior in patients with atypical BCs compared to those with typical BCs (100 versus 61.9 %)
6	Gasparri et al. [56]	2015	Retrospectively evaluated 97 patients with pulmonary carcinoids (65 typical, 32 atypical) who had undergone preoperative ^{18}F-FDG PET	Overall sensitivity of 67 %; higher for atypical carcinoids (81 %) than typical carcinoids (60 %)

The performance of ^{68}Ga-DOTA-SSA in case of thymic carcinoids however has not been very promising. Apart from sporadic case reports of the radiopharmaceutical identifying metastatic thymic carcinoids (Fig. 17.1), it has not been able to distinctly detect either the presence of or the grade of the thymic carcinoids [74].

^{18}F-DOPA

^{18}F-DOPA has been used for PET imaging in humans for more than two decades and has gradually found its way into the application of oncology practice in NETs. The pathophysiological basis for PET imaging of NET with ^{18}F-DOPA is that

Table 17.4 Studies depicting the utility of ^{68}Ga-DOTA-SSA PET in pulmonary carcinoids

Serial no.	Authors	Year	Methodology	Results
1	Hofmann et al. [68]	2001	Evaluated 8 patients with histologically proven metastatic carcinoid tumors (2 bronchial, 6 abdominal) by ^{111}In-octreotide scan and ^{68}Ga-DOTATOC PET	^{68}Ga-DOTATOC PET could identify all the reference lesions, whereas ^{111}In-octreotide imaging identified 85 % of lesions. ^{68}Ga-DOTATOC PET identified 30 % more lesions
2	Kowalski et al. [69]	2003	Compared ^{68}Ga-DOTATOC PET and ^{111}In-DTPA-octreotide in 4 patients with metastatic NET	^{68}Ga-DOTATOC was better in demonstrating smaller lesions with low tracer uptake especially tumors bearing a low density of somatostatin receptors
3	Kayani et al. [70]	2008	38 cases of NET were evaluated(4 bronchial carcinoids), with ^{18}F-FDG PET and ^{68}Ga-DOTATOC PET and correlated with proliferative and mitotic index	Sensitivity of ^{68}Ga-DOTATOC PET (82 %) and ^{18}F-FDG PET (66 %); ^{68}Ga-DOTATOC PET had higher uptake in well-differentiated tumors
4	Jindal et al. [71, 72]	2011	Compared utility of ^{68}Ga-DOTATOC PET CT and ^{18}F-FDG PET CT in 20 biopsy-proven bronchial carcinoids to differentiate typical and atypical cases (13 TC,7 AC)	^{68}Ga-DOTATOC PET positive in all typical and 6/7 of atypical. ^{18}F-FDG PET negative in 6 TC, positive in all AC. SUV for TC was higher than for AC
5	Venkitaraman et al. [55]	2014	First prospective comparative study of ^{68}Ga-DOTATOC and ^{18}F-FDG PET/CT in 32 patients with clinical suspicion of BCs	Sensitivity of ^{68}Ga-DOTATOC PET was superior in patients with typical BCs compared to those with atypical BCs (100 versus 80 %, respectively), whereas the sensitivity of ^{18}F-FDG PET was superior in patients with atypical BCs compared to those with typical BCs (100 versus 61.9 %)
6	Lococo et al. [73]	2015	Multicenter study; evaluated 33 patients with confirmed pulmonary carcinoid (23 TC, 10 AC) using ^{18}F-FDG and ^{68}Ga-DOTA-SSA PET CT	^{68}Ga-DOTA-peptide PET was superior in detecting TC (detection rate 91 %), whereas ^{18}F-FDG PET was superior in detecting atypical carcinoid (detection rate 100 %)

AC atypical carcinoid, *SUV* standardized uptake value, *TC* typical carcinoid
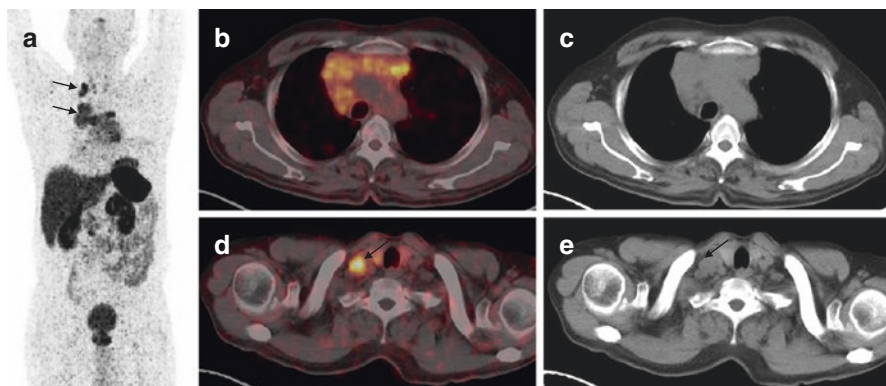
Fig. 17.1 A 46-year-old male with thymic NET underwent ^{68}Ga-DOTANOC PET/CT scan for initial staging. Maximum intensity projection PET image (**a**) and trans-axial PET/CT images revealed DOTANOC avid thymic mediastinal mass (**b**, **c**) with right supraclavicular lymph node metastasis (**d**, **e**; *arrows*)

amino acids, such as DOPA, and their biogenic amines are taken up, stored, and decarboxylated by several types of NETs [75, 76]. ^{18}F-DOPA PET has not found much utility in the management of bronchial carcinoids and thymic NETs alike – this is primarily owing to the lack of ease of production of the radiopharmaceutical and hence a low cost-to-benefit ratio which renders it less feasible option for detection of disease. Its utility has been only sporadically studied in case of bronchial carcinoids: with pooled studies showing a patient-based detection rate of 50 % as against 88 % for somatostatin receptor PET with the latter showing more foci than ^{18}F-DOPA in half of these cases [77].

17.9 Choice of Radiopharmaceutical for Imaging

In general, few points need to be kept in mind while advising the appropriate investigation for the detection and management of bronchopulmonary NETs:

1. PET radiopharmaceuticals should be given preference over SPECT radiopharmaceuticals owing to their inherently superior imaging advantages.
2. Typical bronchial carcinoids (well-differentiated NETs) show higher and more selective uptake on somatostatin receptor PET/CT than on FDG PET/CT, while the reverse is usually observed for atypical bronchial carcinoids and higher grades of lung NET.
3. If bronchopulmonary NET staging is found clinically useful, somatostatin receptor PET could be recommended, except in cases of atypical carcinoids where FDG could be recommended as first line.

4. Somatostatin receptor PET helps to predict the histology in suspected broncho-pulmonary NET as a negative study potentially rules out typical carcinoids.
5. The combination of PET/CT using ^{68}Ga-DOTA-SSA and ^{18}F-FDG seems to be very useful in predicting the histology in patients with clinical suspicion of bronchopulmonary NET.
6. In case a patient presents with advanced well-differentiated disease that cannot be rendered a definitive cure by surgery, somatostatin receptor PET should hold precedence over other radiopharmaceuticals as this would provide an opportunity in assessing the patient's disease extent and also qualify him for a theranostic trial should it be one of the options available with the treating team.

17.10 Theranosis in Bronchopulmonary NETs

The principle of theranosis in the context of NETs is based on the use of somatostatin receptor imaging using ^{68}Ga-DOTA-SSA for the diagnosis and feasibility, followed by delivery of radiation to cancerous cells at the molecular level using peptide receptor radionuclide therapy (PRRNT) by means of [177]Lu (Fig. 17.2) or ^{90}Y-labelled somatostatin analogues [78]. There is immense interest in this prospect as it provides for a safe and feasible option in the treatment of inoperable or metastatic NETs. Promising results continue to emphasize the role of PRRNT in differentiated forms of NETs that express somatostatin receptors.

Systematic studies have been able to prove a definitive benefit in prolonging survival and delaying disease progression as well as provide a favorable outcome when used in earlier stages of the disease [79].

17.11 PET/MRI in Bronchopulmonary and Thymic NETs

Though at a nascent stage in the context of this topic, the possible role of PET/MRI cannot be denied in the management of these tumors. The added advantage of superior soft-tissue contrast and better spatial resolution of MRI makes it an attractive option. Also, the availability of a variety of imaging sequences to visualize different aspects of the tumor may help in providing additional information regarding the tumor function [80]. Also, as already discussed, a widespread availability of molecular probes for PET to study the tumor behavior may have an additive effect in terms of patient evaluation and management. As of now, a single case report is available where integrated PET/MRI with ^{18}F-FDG has been helpful in decision-making in a patient with atypical pulmonary carcinoid [81]
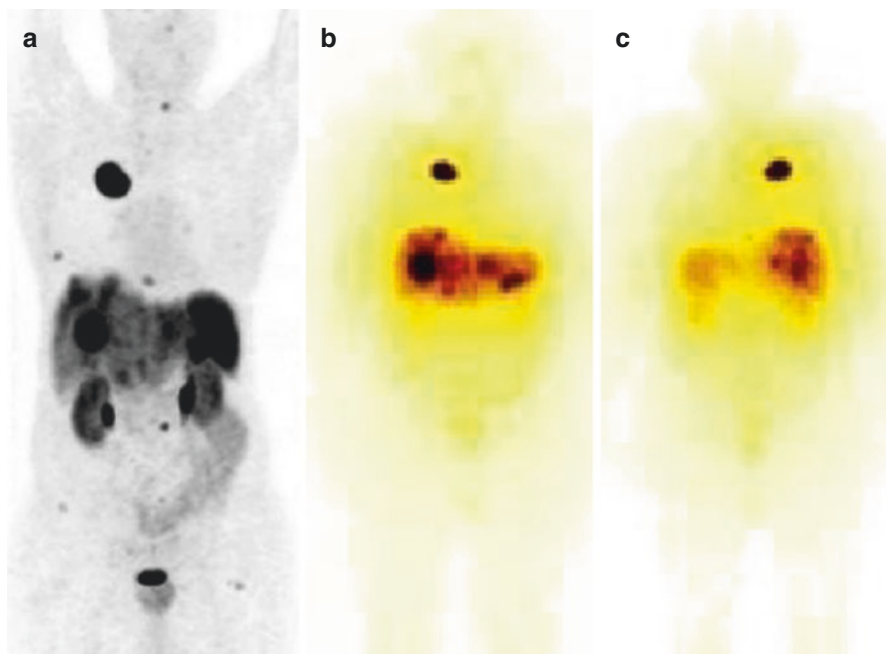
Fig. 17.2 ^{68}Ga-DOTANOC PET/CT scan in a 42-year-old male with metastatic bronchial carcinoid with hepatic and skeletal metastasis (**a**). The same patient benefited from peptide receptor radionuclide therapy (PRRNT) with 177Lu-DOTATATE (**b**, anterior, and **c**, posterior view) which demonstrated positive uptake on both the primary and metastatic lesions

References

1. Fink G, Krelbaum T, Yellin A, Bendayan D, Saute M, Glazer M, et al. Pulmonary carcinoid: presentation, diagnosis, and outcome in 142 cases in Israel and review of 640 cases from the literature. Chest. 2001;119(6):1647–51.
2. Travis WD. Advances in neuroendocrine lung tumors. Ann Oncol. 2010;21(Supplement 7):vii65–71.
3. Tsai H-J, Wu C-C, Tsai C-R, Lin S-F, Chen L-T, Chang JS. The epidemiology of neuroendocrine tumors in Taiwan: A Nation-Wide Cancer Registry-Based Study. Gorlova OY, editor. PLoS ONE. 2013;8(4):e62487.
4. Goto K, Kodama T, Matsuno Y, Yokose T, Asamura H, Kamiya N, et al. Clinicopathologic and DNA cytometric analysis of carcinoid tumors of the thymus. Mod Pathol Off J U S Can Acad Pathol Inc. 2001;14(10):985–94.
5. Moran CA, Suster S. Neuroendocrine carcinomas (carcinoid tumor) of the thymus. A clinicopathologic analysis of 80 cases. Am J Clin Pathol. 2000;114(1):100–10.
6. Valli M, Fabris GA, Dewar A, Chikte S, Fisher C, Corrin B, et al. Atypical carcinoid tumour of the thymus: a study of eight cases. Histopathology. 1994;24(4):371–5.
7. Cooper WA, Thourani VH, Gal AA, Lee RB, Mansour KA, Miller JI. The surgical spectrum of pulmonary neuroendocrine neoplasms. Chest. 2001;119(1):14–8.
8. Teh BT. Thymic carcinoids in multiple endocrine neoplasia type 1. J Intern Med. 1998;243(6):501–4.

9. Teh BT, Zedenius J, Kytölä S, Skogseid B, Trotter J, Choplin H, et al. Thymic carcinoids in multiple endocrine neoplasia type 1. Ann Surg. 1998;228(1):99–105.

10. Travis WD, World Health Organization, International Agency for Research on Cancer, International Association for the Study of Lung Cancer, International Academy of Pathology, editors. Pathology and genetics of tumours of the lung, pleura, thymus and heart. Lyon/Oxford: IARC Press/Oxford University Press (distributor); 2004. p. 344.

11. Modlin IM, Lye KD, Kidd M. A 5-decade analysis of 13,715 carcinoid tumors. Cancer. 2003;97(4):934–59.

12. Harpole DH, Feldman JM, Buchanan S, Young WG, Wolfe WG. Bronchial carcinoid tumors: a retrospective analysis of 126 patients. Ann Thorac Surg. 1992;54(1):50–4; discussion 54–5.

13. Filosso PL, Rena O, Donati G, Casadio C, Ruffini E, Papalia E, et al. Bronchial carcinoid tumors: surgical management and long-term outcome. J Thorac Cardiovasc Surg. 2002;123(2):303–9.

14. El Jamal M, Nicholson AG, Goldstraw P. The feasibility of conservative resection for carcinoid tumours: is pneumonectomy ever necessary for uncomplicated cases? Eur J Cardiothorac Surg Off J Eur Assoc Cardiothorac Surg. 2000;18(3):301–6.

15. McCaughan BC, Martini N, Bains MS. Bronchial carcinoids. Review of 124 cases. J Thorac Cardiovasc Surg. 1985;89(1):8–17.

16. Rosado de Christenson ML, Abbott GF, Kirejczyk WM, Galvin JR, Travis WD. Thoracic carcinoids: radiologic-pathologic correlation. Radiogr Rev Publ Radiol Soc N Am Inc. 1999;19(3):707–36.

17. Ducrocq X, Thomas P, Massard G, Barsotti P, Giudicelli R, Fuentes P, et al. Operative risk and prognostic factors of typical bronchial carcinoid tumors. Ann Thorac Surg. 1998;65(5):1410–4.

18. Thomas CF, Tazelaar HD, Jett JR. Typical and atypical pulmonary carcinoids : outcome in patients presenting with regional lymph node involvement. Chest. 2001;119(4):1143–50.

19. Marchevsky AM, Walts AE. Diffuse idiopathic pulmonary neuroendocrine cell hyperplasia (DIPNECH). Semin Diagn Pathol. 2015;32(6):438–44.

20. Lauriola L, Erlandson RA, Rosai J. Neuroendocrine differentiation is a common feature of thymic carcinoma. Am J Surg Pathol. 1998;22(9):1059–66.

21. Cho KJ, Ha CW, Koh JS, Zo JI, Jang JJ. Thymic carcinoid tumor combined with thymoma – neuroendocrine differentiation in thymoma? J Korean Med Sci. 1993;8(6):458–63.

22. Wick MR, Ritter JH. Neuroendocrine neoplasms: evolving concepts and terminology. Curr Diagn Pathol. 2002;8(2):102–12.

23. Travis WD, Linnoila RI, Tsokos MG, Hitchcock CL, Cutler GB, Nieman L, et al. Neuroendocrine tumors of the lung with proposed criteria for large-cell neuroendocrine carcinoma. An ultrastructural, immunohistochemical, and flow cytometric study of 35 cases. Am J Surg Pathol. 1991;15(6):529–53.

24. Rosai J, Sobin LH. Histological typing of tumours of the thymus. New York: Berlin/Springer; 1999. 65 p.

25. Soga J, Yakuwa Y, Osaka M. Evaluation of 342 cases of mediastinal/thymic carcinoids collected from literature: a comparative study between typical carcinoids and atypical varieties. Ann Thorac Cardiovasc Surg Off J Assoc Thorac Cardiovasc Surg Asia. 1999;5(5):285–92.

26. de Perrot M, Spiliopoulos A, Fischer S, Totsch M, Keshavjee S. Neuroendocrine carcinoma (carcinoid) of the thymus associated with Cushing's syndrome. Ann Thorac Surg. 2002;73(2):675–81.

27. Suster S, Moran CA. Neuroendocrine neoplasms of the mediastinum. Am J Clin Pathol. 2001;115(Suppl):S17–27.

28. Role of ^{68}Ga-DOTATOC PET/CT in carcinoids. Pathol Int. 2010;60(2):143–4.

29. Teh BT, McArdle J, Chan SP, Menon J, Hartley L, Pullan P, et al. Clinicopathologic studies of thymic carcinoids in multiple endocrine neoplasia type 1. Medicine (Baltimore). 1997;76(1):21–9.

30. Jansson JO, Svensson J, Bengtsson BA, Frohman LA, Ahlman H, Wängberg B, et al. Acromegaly and Cushing's syndrome due to ectopic production of GHRH and ACTH by a thymic carcinoid tumour: in vitro responses to GHRH and GHRP-6. Clin Endocrinol (Oxf). 1998;48(2):243–50.

31. Jeung M-Y, Gasser B, Gangi A, Charneau D, Ducroq X, Kessler R, et al. Bronchial carcinoid tumors of the thorax: spectrum of radiologic findings. Radiogr Rev Publ Radiol Soc N Am Inc. 2002;22(2):351–65.

32. Lococo F, Treglia G, Cesario A, Paci M, Filice A, Versari A, et al. Functional imaging evaluation in the detection, diagnosis, and histologic differentiation of pulmonary neuroendocrine tumors. Thorac Surg Clin. 2014;24(3):285–92.

33. Daddi N, Ferolla P, Urbani M, Semeraro A, Avenia N, Ribacchi R, et al. Surgical treatment of neuroendocrine tumors of the lung. Eur J Cardiothorac Surg Off J Eur Assoc Cardiothorac Surg. 2004;26(4):813–7.

34. Benson REC, Rosado-de-Christenson ML, Martínez-Jiménez S, Kunin JR, Pettavel PP. Spectrum of pulmonary neuroendocrine proliferations and neoplasms. Radiogr Rev Publ Radiol Soc N Am Inc. 2013;33(6):1631–49.

35. Okoye CC, Jablons DM, Jahan TM, Kukreja J, Cardozo S, Yom SS. Divergent Management Strategies for Typical Versus Atypical Carcinoid Tumors of the Thoracic Cavity. Am J Clin Oncol. 2014;37(4):350–5.

36. Fukai I, Masaoka A, Fujii Y, Yamakawa Y, Yokoyama T, Murase T, et al. Thymic neuroendocrine tumor (thymic carcinoid): a clinicopathologic study in 15 patients. Ann Thorac Surg. 1999;67(1):208–11.

37. de Montpréville VT, Macchiarini P, Dulmet E. Thymic neuroendocrine carcinoma (carcinoid): a clinicopathologic study of fourteen cases. J Thorac Cardiovasc Surg. 1996;111(1):134–41.

38. Phan AT, Oberg K, Choi J, Harrison LH, Hassan MM, Strosberg JR, et al. NANETS consensus guideline for the diagnosis and management of neuroendocrine tumors: well-differentiated neuroendocrine tumors of the thorax (includes lung and thymus). Pancreas. 2010;39(6):784–98.

39. Wong KK, Waterfield RT, Marzola MC, Scarsbrook AF, Chowdhury FU, Gross MD, et al. Contemporary nuclear medicine imaging of neuroendocrine tumours. Clin Radiol. 2012;67(11):1035–50.

40. Xu C, Zhang H. Somatostatin receptor based imaging and radionuclide therapy. BioMed Res Int. 2015;2015:1–14.

41. Rufini V, Calcagni ML, Baum RP. Imaging of neuroendocrine tumors. Semin Nucl Med. 2006;36(3):228–47.

42. Yellin A, Zwas ST, Rozenman J, Simansky DA, Goshen E. Experience with somatostatin receptor scintigraphy in the management of pulmonary carcinoid tumors. Isr Med Assoc J IMAJ. 2005;7(11):712–6.

43. Hervás Benito I, Bello Arques P, Loaiza JL, Vercher JL, Velasco RP, Rivas Sánchez A, et al. Somatostatin receptor scintigraphy in pediatric bronchial carcinoid tumor. Rev Esp Med Nucl. 2010;29(1):25–8.

44. Shulkin BL, Ilias I, Sisson JC, Pacak K. Current trends in functional imaging of pheochromocytomas and paragangliomas. Ann N Y Acad Sci. 2006;1073:374–82.

45. Taal BG, Hoefnagel CA, Valdés Olmos RA, Boot H. Combined diagnostic imaging with 131I-metaiodobenzylguanidine and 111In-pentetreotide in carcinoid tumours. Eur J Cancer Oxf Engl 1990. 1996;32A(11):1924–32.

46. Yüksel M, Eziddin S, Ladwein E, Haas S, Biersack H-J. 111In-pentetreotide and 123I-MIBG for detection and resection of lymph node metastases of a carcinoid not visualized by CT, MRI or FDG-PET. Ann Nucl Med. 2005;19(7):611–5.

47. von Guggenberg E, Sarg B, Lindner H, Melendez Alafort L, Mather SJ, Moncayo R, et al. Preparation via coligand exchange and characterization of [99mTc-EDDA-HYNIC-D-Phe1, Tyr3]Octreotide (99mTc-EDDA/HYNIC-TOC). J Label Compd Radiopharm. 2003;46(4):307–18.

48. Płachcińska A, Mikołajczak R, Kozak J, Rzeszutek K, Kuśmierek J. A visual and semi-quantitative assessment of (99m)Tc-EDDA/HYNIC-TOC scintigraphy in differentiation of solitary pulmonary nodules. Nucl Med Rev Cent East Eur. 2004;7(2):143–50.
49. Nocuń A, Chrapko B, Gołębiewska R, Stefaniak B, Czekajska-Chehab E. Evaluation of somatostatin receptors in large cell pulmonary neuroendocrine carcinoma with 99mTc-EDDA/HYNIC-TOC scintigraphy. Nucl Med Commun. 2011;32(6):522–9.
50. Pacak K, Eisenhofer G, Goldstein DS. Functional imaging of endocrine tumors: role of positron emission tomography. Endocr Rev. 2004;25(4):568–80.
51. Erasmus JJ, McAdams HP, Patz EF, Coleman RE, Ahuja V, Goodman PC. Evaluation of primary pulmonary carcinoid tumors using FDG PET. AJR Am J Roentgenol. 1998;170(5):1369–73.
52. Bryant AS, Cerfolio RJ. The maximum standardized uptake values on integrated FDG-PET/CT is useful in differentiating benign from malignant pulmonary nodules. Ann Thorac Surg. 2006;82(3):1016–20.
53. Krüger S, Buck AK, Blumstein NM, Pauls S, Schelzig H, Kropf C, et al. Use of integrated FDG PET/CT imaging in pulmonary carcinoid tumours. J Intern Med. 2006;260(6):545–50.
54. Daniels CE, Lowe VJ, Aubry M-C, Allen MS, Jett JR. The utility of fluorodeoxyglucose positron emission tomography in the evaluation of carcinoid tumors presenting as pulmonary nodules. Chest. 2007;131(1):255–60.
55. Venkitaraman B, Karunanithi S, Kumar A, Khilnani GC, Kumar R. Role of 68Ga-DOTATOC PET/CT in initial evaluation of patients with suspected bronchopulmonary carcinoid. Eur J Nucl Med Mol Imaging. 2014;41(5):856–64.
56. Gasparri R, Rezende GC, Fazio N, Maisonneuve P, Brambilla D, Travaini LL, et al. Fluorodeoxyglucose positron emission tomography in pulmonary carcinoid tumors. Q J Nucl Med Mol Imaging Off Publ Ital Assoc Nucl Med AIMN Int Assoc Radiopharmacol IAR Sect Soc Radiopharm Chem Biol. 2015;59(4):446–54.
57. Wartski M, Alberini J-L, Leroy-Ladurie F, De Montpreville V, Nguyen C, Corone C, et al. Typical and atypical bronchopulmonary carcinoid tumors on FDG PET/CT imaging. Clin Nucl Med. 2004;29(11):752–3.
58. Zeman RK, Schiebler M, Clark LR, Jaffe MH, Paushter DM, Grant EG, et al. The clinical and imaging spectrum of pancreaticoduodenal lymph node enlargement. AJR Am J Roentgenol. 1985;144(6):1223–7.
59. Jindal T, Kumar A, Kumar R, Dutta R, Meena M. Role of positron emission tomography-computed tomography in bronchial mucoepidermoid carcinomas: a case series and review of the literature. J Med Case Reports. 2010;4:277.
60. Jindal T, Kumar A, Kumar R. Inflammatory myofibroblastic tumour. Eur Respir J. 2010;35(6):1422–3.
61. Treglia G, Giovanella L, Lococo F, Bertagna F. An unusual case of thymic carcinoid causing Cushing's syndrome due to ectopic ACTH secretion detected by (18)F-FDG PET/CT. Rev Esp Med Nucl E Imagen Mol. 2014;33(4):253–4.
62. Doi M, Sugiyama T, Izumiyama H, Yoshimoto T, Hirata Y. Clinical features and management of ectopic ACTH syndrome at a single institute in Japan. Endocr J. 2010;57(12):1061–9.
63. Xu H, Zhang M, Zhai G, Zhang M, Ning G, Li B. The role of integrated (18)F-FDG PET/CT in identification of ectopic ACTH secretion tumors. Endocrine. 2009;36(3):385–91.
64. Gatto F, Hofland LJ. The role of somatostatin and dopamine D2 receptors in endocrine tumors. Endocr Relat Cancer. 2011;18(6):R233–51.
65. Maecke HR, Hofmann M, Haberkorn U. (68)Ga-labeled peptides in tumor imaging. J Nucl Med Off Publ Soc Nucl Med. 2005;46 Suppl 1:172S–8.
66. Breeman WAP, de Blois E, Sze Chan H, Konijnenberg M, Kwekkeboom DJ, Krenning EP. (68)Ga-labeled DOTA-peptides and (68)Ga-labeled radiopharmaceuticals for positron emission tomography: current status of research, clinical applications, and future perspectives. Semin Nucl Med. 2011;41(4):314–21.

67. Poeppel TD, Binse I, Petersenn S, Lahner H, Schott M, Antoch G, et al. 68Ga-DOTATOC versus 68Ga-DOTATATE PET/CT in functional imaging of neuroendocrine tumors. J Nucl Med. 2011;52(12):1864–70.
68. Hofmann M, Maecke H, Börner A, Weckesser E, Schöffski P, Oei M, et al. Biokinetics and imaging with the somatostatin receptor PET radioligand 68Ga-DOTATOC: preliminary data. Eur J Nucl Med. 2001;28(12):1751–7.
69. Kowalski J, Henze M, Schuhmacher J, Mäcke HR, Hofmann M, Haberkorn U. Evaluation of positron emission tomography imaging using [68Ga]-DOTA-D Phe(1)-Tyr(3)-Octreotide in comparison to [111In]-DTPAOC SPECT. First results in patients with neuroendocrine tumors. Mol Imaging Biol MIB Off Publ Acad Mol Imaging. 2003;5(1):42–8.
70. Kayani I, Bomanji JB, Groves A, Conway G, Gacinovic S, Win T, et al. Functional imaging of neuroendocrine tumors with combined PET/CT using 68Ga-DOTATATE (DOTA-DPhe1, Tyr3-octreotate) and 18F-FDG. Cancer. 2008;112(11):2447–55.
71. Jindal T, Kumar A, Venkitaraman B, Dutta R, Kumar R. Role of (68)Ga-DOTATOC PET/CT in the evaluation of primary pulmonary carcinoids. Korean J Intern Med. 2010;25(4):386–91.
72. Jindal T, Kumar A, Venkitaraman B, Meena M, Kumar R, Malhotra A, et al. Evaluation of the role of [18F]FDG-PET/CT and [68Ga]DOTATOC-PET/CT in differentiating typical and atypical pulmonary carcinoids. Cancer Imaging Off Publ Int Cancer Imaging Soc. 2011;11:70–5.
73. Lococo F, Perotti G, Cardillo G, De Waure C, Filice A, Graziano P, et al. Multicenter comparison of 18F-FDG and 68Ga-DOTA-peptide PET/CT for pulmonary carcinoid. Clin Nucl Med. 2015;40(3):e183–9.
74. Dutta R, Kumar A, Julka PK, Mathur SR, Kaushal S, Kumar R, et al. Thymic neuroendocrine tumour (carcinoid): clinicopathological features of four patients with different presentation. Interact Cardiovasc Thorac Surg. 2010;11(6):732–6.
75. Baker JR. Fixation in cytochemistry and electron-microscopy. J Histochem Cytochem Off J Histochem Soc. 1958;6(5):303–8.
76. Bergström M, Eriksson B, Oberg K, Sundin A, Ahlström H, Lindner KJ, et al. In vivo demonstration of enzyme activity in endocrine pancreatic tumors: decarboxylation of carbon-11-DOPA to carbon-11-dopamine. J Nucl Med Off Publ Soc Nucl Med. 1996;37(1):32–7.
77. Balogova S, Talbot J-N, Nataf V, Michaud L, Huchet V, Kerrou K, et al. 18F-Fluorodihydroxyphenylalanine vs other radiopharmaceuticals for imaging neuroendocrine tumours according to their type. Eur J Nucl Med Mol Imaging. 2013;40(6):943–66.
78. Baum RP, Kulkarni HR, Carreras C. Peptides and receptors in image-guided therapy: theranostics for neuroendocrine neoplasms. Semin Nucl Med. 2012;42(3):190–207.
79. Mariniello A, Bodei L, Tinelli C, Baio SM, Gilardi L, Colandrea M, et al. Long-term results of PRRT in advanced bronchopulmonary carcinoid. Eur J Nucl Med Mol Imaging. 2016;43(3):441–52.
80. Antoch G, Bockisch A. Combined PET/MRI: a new dimension in whole-body oncology imaging? Eur J Nucl Med Mol Imaging. 2009;36(S1):113–20.
81. Ordidge KL, Brown JM, Succony L, Navani N, Hardavella G, Lawrence DR, et al. Massive pulmonary carcinoid tumor deemed inoperable until 68Ga DOTATATE positron emission tomography/magnetic resonance imaging. Am J Respir Crit Care Med. 2014;190(5):e16–7.

Chapter 18
Radionuclide Imaging of Medullary Thyroid Carcinoma

Giorgio Treglia, Arnoldo Piccardo, and Luca Giovanella

18.1 Introduction

18.1.1 Epidemiology and Tumour Origin

Medullary thyroid carcinoma (MTC) is a neuroendocrine tumor (NET) originating from the neural crest-derived parafollicular C cells of the thyroid gland [1]. As the ultimobranchial bodies migrate from the neural crest during embryogenesis, they become entrapped within the middle and upper poles of each thyroid lobe, giving rise to C cells, which are much more numerous in males compared to females [2]. Unlike other thyroid tumors, which arise from follicular cells, MTC is a NET, being classified as a thyroid tumor because of its anatomical location [1].

MTC accounts for approximately 1–2 % of thyroid cancers in the United States, occurring either sporadically or in a hereditary form as a component of the type 2 multiple endocrine neoplasia (MEN2) syndromes [1].

G. Treglia, MD, MSc (HTA) (✉) • L. Giovanella, MD, PhD
Department of Nuclear Medicine, PET/CT and Thyroid Centre, Oncology Institute of Southern Switzerland, Via Ospedale 12, 6500 Bellinzona, Switzerland
e-mail: giorgio.treglia@eoc.ch; giorgiomednuc@libero.it; luca.giovanella@eoc.ch

A. Piccardo, MD
Department of Nuclear Medicine, Galliera Hospital,
Via Mura delle Cappuccine 14, 16128 Genoa, Italy
e-mail: arnoldo.piccardo@galliera.it

18.1.2   Genetics

The RET proto-oncogene, located on chromosome 10q11.2, encodes a transmembrane receptor of the tyrosine kinase family. Virtually all patients with MEN2 syndromes have RET germline mutations, and approximately 50 % of sporadic MTCs have somatic RET mutations [1, 3–5]. Sporadic MTCs lacking somatic RET mutations may have somatic RAS mutations in a significant proportion of cases [6, 7]. Different RET mutations are associated with different patterns of aggressiveness, expressed as development of MTC at an early age, frequently in association with metastatic disease [1].

18.1.3   Clinical Characteristics

MTC is frequently an aggressive tumor. Sporadic MTC usually occurs between the fourth and the sixth decade of life [8]. The risk designation for sporadic MTC is based on the American Joint Committee on Cancer (AJCC) classification of tumor (T), node (N) and metastases (M). Central and lateral compartment lymph nodal metastases are present, respectively, in 14 % and 11 % of patients with T1 tumors and in 86 % and 93 % of patients with T4 tumors [9]. Unfortunately, 70 % of patients with MTC who present with a palpable thyroid nodule have cervical metastases and 10 % have distant metastases. The most frequent sites of distant metastases are bone, lung and liver [10].

On univariate analysis, prognosis is directly related to patient age at diagnosis, male sex, the presence of local tumor invasion, lymph node metastases and distant metastases. On multivariate analysis, however, only age and stage of disease at the time of diagnosis are significant independent prognostic factors [11–14]. 10-year survival rates for patients with MTC stages I, II, III and IV (according to AJCC classification) are 100 %, 93 %, 71 % and 21 %, respectively [12].

About inherited syndromes two MEN2 syndromes are recognised: MEN2A and MEN2B.

Within MEN2A (incidence 1/1,973,500), which accounts for 95 % of MEN2 cases, four variants are described: classical MEN2A (the most frequent variant), represented by the uniform presence of MTC and the less frequent occurrence of pheochromocytoma (PHEO) or hyperparathyroidism (HPTH) or both depending on the specific RET mutation, MEN2A with cutaneous lichen amyloidosis, MEN2A with Hirschsprung's disease, and familial MTC (families or individuals with RET germline mutations who have MTC but neither PHEOs nor HPTH) [1].

The MEN2B syndrome (incidence 1/38,750,000) accounts for 5 % of hereditary MTCs. Patients with MEN2B develop MTC and PHEOs and exhibit a recognisable phenotype. In patients with MEN2B syndrome, the MTC often presents in infancy and is highly aggressive metastasizing early to regional lymph nodes and beyond [1].

18.2   Diagnostic Methods Beyond Imaging

Several diagnostic tests beyond imaging methods should be performed in patients with MTC including genetic testing, serum tumor markers assays and pathology analyses.

18.2.1   Genetic Testing

Patients with MEN2 syndromes should be tested for specific RET mutations. Genetic counselling and genetic testing for RET germline mutations should be even offered to first degree relatives of patients with proven hereditary MTC.

Importantly, patients with presumed sporadic MTC should have genetic counselling and genetic testing to detect a RET germline mutation, because up to 7% of these patients may have hereditary MTC [1].

18.2.2   Serum Tumour Markers

Among the secretory products of parafollicular C cells, calcitonin and carcinoembryonic antigen (CEA) are valuable tumor markers in patients with MTC, and their serum concentrations are directly related to the parafollicular C-cell mass [1, 15].

Calcitonin is the most sensitive and specific serum marker for MTC. Whereas the role of serum calcitonin as screening method for MTC in patients with thyroid nodules is widely debated, this serum marker is crucial for the assessment of disease extent and progression and post-treatment evaluation in patients with MTC [1, 15]. Basal serum calcitonin levels >100 pg/mL are suspicious for MTC when determined with an immunoradiometric or immunochemiluminometric assay. Serum calcitonin elevations below this value are of difficult interpretation [15]. Falsely high or low serum calcitonin levels might occur with a variety of clinical diseases other than MTC, and clinicians should consider this possibility when serum calcitonin levels are disproportionate to the expected clinical findings [1, 15]. Administrating potent secretagogues, such as intravenous calcium or pentagastrin, may increase the accuracy of calcitonin testing [1, 15]. Procalcitonin, a precursor of calcitonin, appears to be a very promising and reliable serum marker for the diagnosis of MTC, and it is not inferior to calcitonin. The addition of basal serum procalcitonin measurement in patients with thyroid nodules and increased serum calcitonin may significantly improve accuracy of calcitonin measurement without needing a stimulation test [16].

CEA is not a specific biomarker for MTC, but it is a useful tool for evaluating disease progression in patients with clinically evident MTC and for monitoring MTC patients following thyroidectomy [1].

In patients with MTC simultaneous elevations of serum CEA and calcitonin levels indicate disease progression. Serum calcitonin and CEA doubling times are efficient tools for assessing MTC progression and are useful prognostic factors [1]. Some patients with progressive disease have increasing serum CEA levels associated with stable or declining serum calcitonin levels. This is considered an indication of poorly differentiated MTC [1]. Rarely, patients with advanced MTC have normal or low serum levels of calcitonin and CEA; this unusual state represents either a misdiagnosis or advanced dedifferentiation of the MTC, in which case it conveys a poor prognosis [1, 17].

18.2.3 Cytology and Histology

Thyroid nodules that are 1 cm or greater in size, suspicious at ultrasound (US) and cold at thyroid scintigraphy with Technetium-99 m pertechnetate should be evaluated by fine-needle aspiration cytology (FNAC) [1]. MTC cytology is characterized by high cellularity with single cells or small clusters, absent colloid and a variable amount of amyloid substance. Cytomorphology consists predominantly of round to oval, spindle-shaped and polygonal cells. Specimens usually present a mixture of cell types and are characterized by a dispersed pattern with loosely cohesive groups [15]. FNAC is able to detect approximately one-half of MTC lesions [18]. FNAC findings that are inconclusive or suggestive of MTC should have calcitonin measured in the FNAC washout fluid [19] and immunocytochemical staining of the FNAC sample to detect the presence of markers, such as calcitonin, chromogranin and CEA, and the absence of thyroglobulin [1, 15].

Macroscopically, MTC is firm and either white, tan or red in colour. Sporadic MTC usually occurs as a solitary unilateral tumor, whereas hereditary MTC is usually multicentric and bilateral. On histological examination the MTC cells are typically round, polyhedral or spindle shaped and form sheets or nests with peripheral palisading in a vascular stroma [1, 20]. The amyloid material present in over half of MTCs is actually composed of full-length calcitonin [21].

The assessment of a thyroid tumor with any feature suggestive of MTC should include immunohistochemical (IHC) analysis to determine the presence of markers, such as calcitonin, chromogranin and CEA, and the absence of thyroglobulin [1, 20]. IHC staining of calcitonin may vary in intensity and extent, but in its absence, a diagnosis of MTC should be questioned [1]. The IHC reactivity of calcitonin is often reduced in undifferentiated tumors, whereas staining for CEA is almost always strongly positive in these neoplasms [22].

In hereditary MTC the entity C-cell hyperplasia (CCH) precedes the development of MTC and is best demonstrated by IHC staining with calcitonin antibodies [23].

18.3   Role of Imaging Methods

Different morphological and functional imaging methods may be used in patients with MTC both in the preoperative staging than in detecting persistent/recurrent disease. The pivotal role of imaging is to address therapy. The main treatment for MTC is surgical resection that is the only strategy for potential cure. In patients with metastatic disease, therapeutic options are limited as this tumor does not concentrate radioiodine and shows poor response to chemotherapy and radiation therapy. Targeted therapy with tyrosine kinase inhibitors seems to show promising results in the treatment of advanced MTC [1].

18.3.1   Preoperative Imaging

Neck US is the most important preoperative imaging study in patients with MTC. Neck US is the pivotal tool for the stratification of the risk of malignancy in thyroid nodules. Even if the US patterns are not pathognomonic for MTC, however, the finding of a solid and deeply hypoechoic nodule or the presence of intralesional (especially if coarse) calcifications should suggest the possibility of an MTC and prompt the determination of serum calcitonin [15]. As approximately 50 % of patients have clinically detectable cervical lymph node involvement or extracapsular diffusion at diagnosis, a careful US evaluation of the neck is always needed in suspicious MTC patients. US staging may guide the extent of surgery and help to define the preoperative patient prognosis [15, 24].

   If metastatic MTC is expected, and in all MTC patients with a serum calcitonin level greater than 500 pg/mL, preoperatively additional imaging procedures are indicated including computed tomography (CT), magnetic resonance imaging (MRI) and bone scintigraphy [1]. Unfortunately, no single procedure provides optimal whole body imaging [1]. Beyond bone scintigraphy, the role of other radionuclide imaging techniques in preoperative staging of MTC seems limited [1].

18.3.2   Imaging for Detection of Persistent/Recurrent MTC

Patients with increased postoperative serum calcitonin levels less than 150 pg/mL should have a physical examination and US of the neck, because persistent/recurrent MTC is almost always confined to lymph nodes in the neck. If these studies are negative, the patients should be followed with physical examinations, measurement of serum calcitonin and CEA and neck US every 6 months [1]. If the postoperative serum calcitonin levels exceed 150 pg/mL, patients should be evaluated by

systemic imaging procedures including US, CT, MRI and bone scintigraphy [1]. In this setting radionuclide imaging, and in particular positron emission tomography/CT (PET/CT) using different radiopharmaceuticals, could be used to detect MTC recurrence [1].

18.4 Focus on Radionuclide Imaging

Conventional morphological imaging modalities may be often negative or inconclusive in the presence of postoperative rising levels of serum MTC markers. Therefore, functional radionuclide imaging using different radiopharmaceuticals was explored as a way to detect persistent/recurrent MTC, whereas its role in the initial staging of MTC seems limited [25].

18.4.1 Conventional Nuclear Medicine Techniques

Whole body scintigraphy with single photon emission tracers such as Technetium-99 m pentavalent dimercaptosuccinic acid (^{99m}Tc-(V) DMSA), somatostatin analogues labelled with Indium-111 or Technetium-99 m, radioiodinated metaiodobenzylguanidine (MIBG) or radiolabelled anti-CEA antibodies are not sensitive enough to detect MTC relapse [1, 25, 26]. This is particularly true when these imaging techniques are compared with conventional radiological imaging (US, CT, MRI) and PET/CT imaging [25–29].

In the 1990s ^{99m}Tc-(V) DMSA scintigraphy seemed to be an efficient method to detect MTC lesions [25–27]. Although the ^{99m}Tc-(V) DMSA uptake mechanism was unknown [30], the sensitivity reported in localising MTC ranged from 50 to 80% [25, 26, 31]. More recent studies comparing ^{99m}Tc-(V) DMSA with PET tracers reported a very low sensitivity for ^{99m}Tc-(V) DMSA (33%) and did not recommend the use of this tracer in detecting recurrent MTC [32]. To date, the use of ^{99m}Tc-(V) DMSA is going to be neglected, and it is not commercially available in most countries [26].

Since somatostatin receptors may be expressed by MTC, somatostatin analogues labelled with Indium-111 or Technetium-99 m had been tested in the MTC diagnosis. Indeed, a great variability in term of sensitivity of somatostatin receptor scintigraphy in detecting MTC recurrence has been reported ranging between 20 and 70% [25–29]. More in general, these single photon emission tracers seemed to be more sensitive than ^{99m}Tc-(V) DMSA and radioiodinated MIBG but unable to add diagnostic information when compared with conventional radiological imaging modalities [25, 26, 33–35].

Radioiodinated MIBG is a specific tracer for tumor deriving from the neural crest, including MTC. It is a norepinephrine analogue and is actively transported into noradrenaline granules of sympathetic nerve terminals by

norepinephrine transporter [25, 36] Despite its specificity due to its uptake mechanism, the sensitivity of this tracer in detecting MTC recurrence is low, reaching only 30 % [25, 26]. However radioiodinated MIBG scintigraphy may establish the indication for targeted radionuclide therapy with iodine-131 MIBG that may be able, in same selective cases, to achieve disease partial remission or stability [37, 38].

Bone scintigraphy with Technetium-99 m diphosphonates evaluating the bone metabolism is still recognised as a useful imaging technique in MTC staging and restaging [1]. Bone scintigraphy was reported to be as sensitive as MRI and superior compared to fluorine-18-fluorodeoxyglucose (FDG) PET/CT in detecting bone metastases of MTC [39].

Results from scintigraphy with radiolabelled anti-CEA monoclonal antibodies largely vary in terms of sensitivity; the diagnostic performance of this technique seems to be related to the MTC aggressiveness [26].

Finally, promising results were obtained with cholecystokinin-B/gastrin receptor scintigraphy in recurrent MTC, but more studies in this setting are warranted [26].

18.4.2 PET/CT

Several radiopharmaceuticals evaluating different metabolic pathways or receptor status can be used as PET tracers in detecting MTC lesions, including FDG, fluorine-18-dihydroxyphenylalanine (FDOPA) and somatostatin analogues labelled with Gallium-68 [40–43].

18.4.2.1 FDG-PET/CT

FDG, a glucose analogue and the most used PET radiopharmaceutical worldwide, accumulates in neoplastic cells allowing scintigraphic visualisation of tumors that use glucose as an energy source. FDG uptake in neoplastic cells correlates with poor differentiation and high-proliferative activity. NETs usually show an indolent course and consequently low-FDG uptake [43, 44]. NETs, however, when undergoing dedifferentiation become more aggressive and may show increased FDG uptake, and this is also the case in MTC [40–44].

Overall, the studies using FDG-PET/CT have reported conflicting results about the diagnostic performance of this imaging method in patients with recurrent MTC. In particular, sensitivity ranged from 17 to 95 % whereas specificity, when reported, ranged from 68 to 100 % [43]. A possible explanation for these heterogeneous findings could be related to diversity between the studies in technical aspects and inclusion criteria (patients with known lesions versus patients with occult disease at conventional morphological imaging methods, patients with slowly progressive disease versus patients with more aggressive disease) [43, 45]. False-negative results of FDG-PET/CT could be related to small MTC lesions or to the slow growth

of NETs, both factors influencing the diagnostic accuracy of FDG-PET/CT. False-positive results are typically due to inflammatory lesions [43, 45].

A meta-analysis showed that the detection rate of FDG-PET or PET/CT in suspected recurrent MTC on a per patient-based analysis is 59 % (95 % confidence interval, 54–63 %) [45]. Therefore, a significant number of recurrent MTC, based on rising levels of tumor markers, remain unidentified by using FDG-PET/CT. On the other hand, it should be considered that FDG-PET/CT is often performed in patients with suspected recurrent MTC after negative conventional morphological imaging studies, affecting the surgical management of patients with recurrent MTC when hypermetabolic lesions are detected [43, 45].

Based on literature findings, the diagnostic performance of FDG-PET/CT in patients with recurrent MTC improves in patients with higher serum calcitonin and CEA levels [43, 45]. Also, sensitivity of FDG-PET/CT improves in patients with shorter serum calcitonin and CEA doubling times, confirming the usefulness of this imaging method in patients with more aggressive disease (with high-glucose consumption and high-FDG uptake) compared to those with slow-progressive disease (with low-glucose consumption and low-FDG uptake) [45]. In particular FDG-PET has a relevant prognostic value being able to identify MTC patients with poor survival [46, 47].

18.4.2.2   FDOPA-PET/CT

FDOPA is taken up through ubiquitous transmembrane amino acid transporter systems that are significantly upregulated in NETs, including MTC. This upregulation is presumably secondary to the increased activity of aromatic amino acid decarboxylase (converting DOPA to dopamine) in NET cells [43, 44].

Overall, the studies using FDOPA-PET/CT in detecting recurrent MTC showed wide range of sensitivity, ranging from 47 to 83 % [43]. Differences in technical aspects and inclusion criteria could explain the heterogeneity between studies about the sensitivity values reported. False-positive results of FDOPA-PET/CT in recurrent MTC are uncommon. On the other hand, possible causes of false-negative results of FDOPA-PET/CT should be kept in mind; they could be probably related to small MTC lesions or to dedifferentiation, both factors affecting the diagnostic accuracy of this imaging method [43, 48].

A meta-analysis showed that the detection rate of FDOPA-PET or PET/CT in suspected recurrent MTC on a per patient-based analysis is 66 % (95 % confidence interval, 58–74 %) [48]. This value increases to 72 % considering hybrid PET/CT (excluding studies performing PET only) [48]. However, FDOPA-PET/CT may modify the surgical management of a significant number of patients with recurrent MTC when positive [49, 50], because this functional imaging method is often performed in patients with recurrent MTC based on rising tumor markers after negative conventional morphological imaging studies [43, 48].

Based on literature findings, the diagnostic performance of FDOPA-PET/CT in recurrent MTC improves in patients with higher serum calcitonin levels and shorter

serum calcitonin doubling time, reaching a detection rate of 86 % in recurrent MTC and calcitonin doubling time lower than 24 months [48].

To improve the bioavailability of FDOPA, some teams propose premedication with carbidopa, a selective extracerebral decarboxylase inhibitor. However, a recent meta-analysis did not demonstrate a higher detection rate of FDOPA-PET/CT by using premedication with carbidopa in MTC diagnosis [48].

Interestingly, some researchers demonstrated the improvement in the detection rate of FDOPA-PET/CT in MTC brought by early images acquisition (around 15 min after radiopharmaceutical injection) compared to standard acquisition (performed 60 min after radiopharmaceutical injection) suggesting to perform dual-phase FDOPA-PET/CT in MTC [51, 52].

18.4.2.3 Somatostatin Receptor PET/CT

NETs usually overexpress somatostatin receptors on their cell surface, and this represents the rationale for using somatostatin analogues labelled with positron emitter Gallium-68 for diagnosis of these tumors by using PET/CT. In fact, somatostatin receptor PET/CT is a valuable diagnostic tool for patients with NETs [53–55]. Nevertheless, the experience with somatostatin analogues labelled with Gallium-68 in recurrent MTC is limited compared to FDG and FDOPA [32, 50, 56–61].

Overall, the diagnostic performance of somatostatin receptor PET/CT in recurrent MTC seems to be inferior compared to other NETs (such as lung and gastroenteropancreatic NETs) due to the variable somatostatin receptor expression in MTC [43, 50, 54, 62]. In particular, based on the available literature, sensitivity of somatostatin receptor PET/CT in patients with recurrent MTC largely varies from 25 to 83 %, whereas the specificity is very high [32, 50, 56–61]. As for FDG- and FDOPA-PET/CT, the detection rate of somatostatin receptor PET/CT in recurrent MTC increases in patients with higher serum calcitonin levels [32].

Compared to FDG- and FDOPA-PET/CT, somatostatin receptor PET/CT may have a theranostic value as this method could be useful in selecting metastatic MTC patients for therapy with cold or radiolabelled somatostatin analogues to treat metastatic lesions showing high expression of somatostatin receptors [54].

18.4.2.4 Comparative Analyses Between Different PET Radiopharmaceuticals

Several studies compared different PET tracers in detecting recurrent MTC [32, 40, 46, 50, 56–58, 61, 63–65] (Table 18.1 and Figs. 18.1, 18.2, 18.3, 18.4, and 18.5).

Comparative analyses between FDOPA and FDG have shown better results with FDOPA in terms of sensitivity and specificity and a complementary role of the two radiopharmaceuticals in the assessment of recurrent MTC [46, 50, 63–65]. The different behaviour of FDOPA and FDG in recurrent MTC can be explained by their

Table 18.1 Comparative analyses of different PET tracers used in detecting recurrent medullary thyroid carcinoma

PET tracer	Pooled detection rate for PET/CT	Correlation between detection rate and serum calcitonin values	Prognostic value	Tolerance	Radiation dose	Radionuclide production	Comparative costs	Comparative availability	Theranostic value
FDG	59 %	Yes	Yes	No serious undesirable effects	0.019 mSv/MBq	by cyclotron	+	+++	No
FDOPA	72 %	Yes	Uncertain	No serious undesirable effects	0.025 mSv/MBq	by cyclotron	+++	+	No
Gallium-68-somatostatin analogues	60 %	Yes	Uncertain	No serious undesirable effects	0.0167-0.023 mSv/MBq	by generator	++	+	Yes

PET/CT positron emission tomography/computed tomography, *FDG* fluorine-18 fluorodeoxyglucose, *FDOPA* fluorine-18 dihydroxyphenylalanine
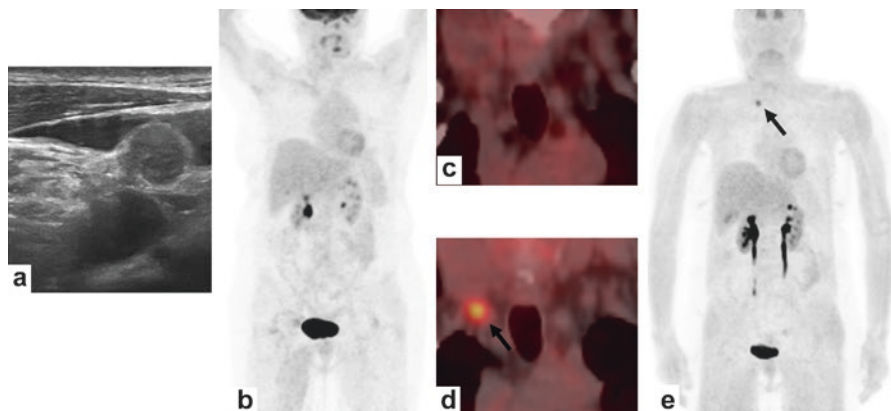
Fig. 18.1 A 54-year-old female affected by MTC with evidence of increasing serum calcitonin levels (44 pg/mL) after thyroidectomy and cervical lymphadenectomy. Serum CEA was normal. Neck ultrasonography showed a small right laterocervical (IV level) lymph node suspicious for recurrence (**a**). Maximum intensity projection FDG-PET image (**b**) and coronal FDG-PET/CT image (**c**) did not show any abnormal tracer uptake. On the other hand, maximum intensity projection FDOPA-PET image (**e**) and coronal FDOPA-PET/CT image (**d**) correctly detected the recurrence of disease (*black arrow*)
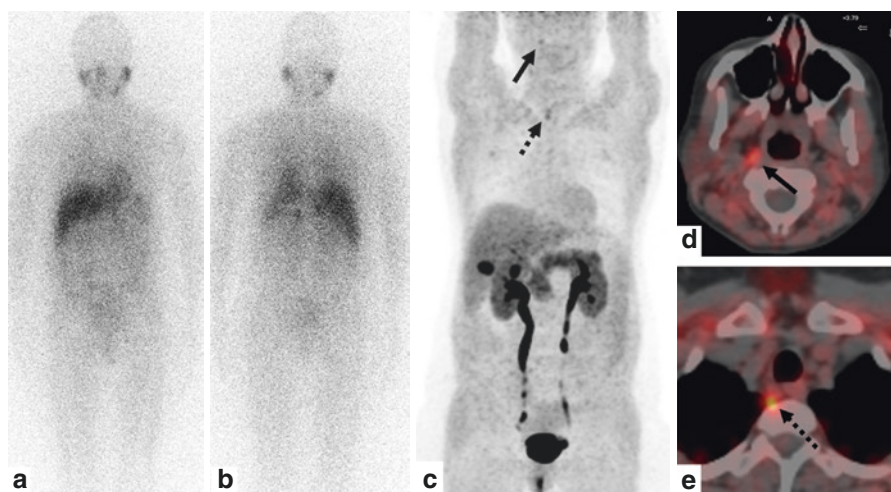
Fig. 18.2 A 44-year-old female affected by MTC with evidence of increasing serum calcitonin levels (80 pg/mL) after thyroidectomy and cervical lymphadenectomy. Serum CEA was normal. Neck ultrasonography (not shown) did not detect suspicious lymph nodal recurrence. Radioiodinated MIBG scintigraphy in anterior (**a**) and posterior (**b**) view did not demonstrate any abnormal tracer uptake. On the other hand, maximum intensity projection FDOPA-PET image (**c**) and axial FDOPA-PET/CT images (**d, e**) correctly detected disease recurrence showing tracer uptake corresponding to small retropharyngeal (*black arrow*) and paraesophageal (*dotted arrow*) lymph nodes
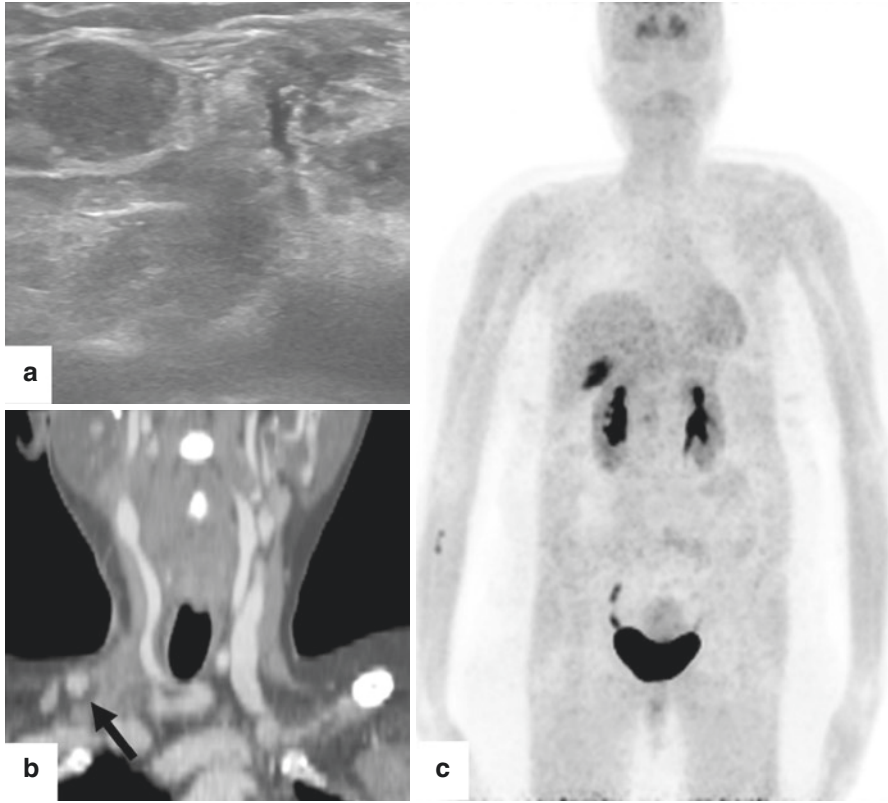
Fig. 18.3 A 48-year-old female affected by MTC with persisting high serum calcitonin levels (39 pg/mL) after thyroidectomy and right laterocervical lymphadenectomy for lymph nodal metastases. Serum CEA was normal. Neck ultrasonography (**a**) showed a right laterocervical (IV level) lymph node suspicious for metastasis adjacent to a scar tissue. Coronal contrast-enhanced CT (**b**) detected a 12 mm right laterocervical lymph node with contrast enhancement (*black arrow*). Neither FDOPA-PET/CT (**c, d**) nor FDG-PET/CT (**e, f**) demonstrate any abnormal tracer uptake corresponding to the right laterocervical lymph node (*black arrows*). Histopathology on this lymph node showed a MTC metastasis

Fig. 18.3   (continued)

different uptake mechanisms that, in turn, reflect the different metabolic pathways of NET cells, including MTC cells. FDOPA is a marker of amino acid decarboxylation that is a feature of the neuroendocrine origin of MTC. So, it can be assumed that a higher FDOPA uptake is related to a higher degree of cell differentiation, whereas a higher FDG uptake is related to a high-proliferative activity and a poor differentiation [46, 50, 63–65]. Although FDOPA-PET/CT has less prognostic value compared to FDG, it can more accurately assess the extent of the disease in patients with residual/recurrent MTC [46, 50, 63].

Comparative analyses between somatostatin analogues labelled with Gallium-68 and FDG have shown the complementary role of these PET tracers in recurrent MTC without statistically significant difference in terms of detection rate of MTC lesions [32, 50, 56, 58, 61].

To date, only one multicentric study compared FDOPA, FDG and somatostatin analogues labelled with Gallium-68 demonstrating that FDOPA-PET/CT is the
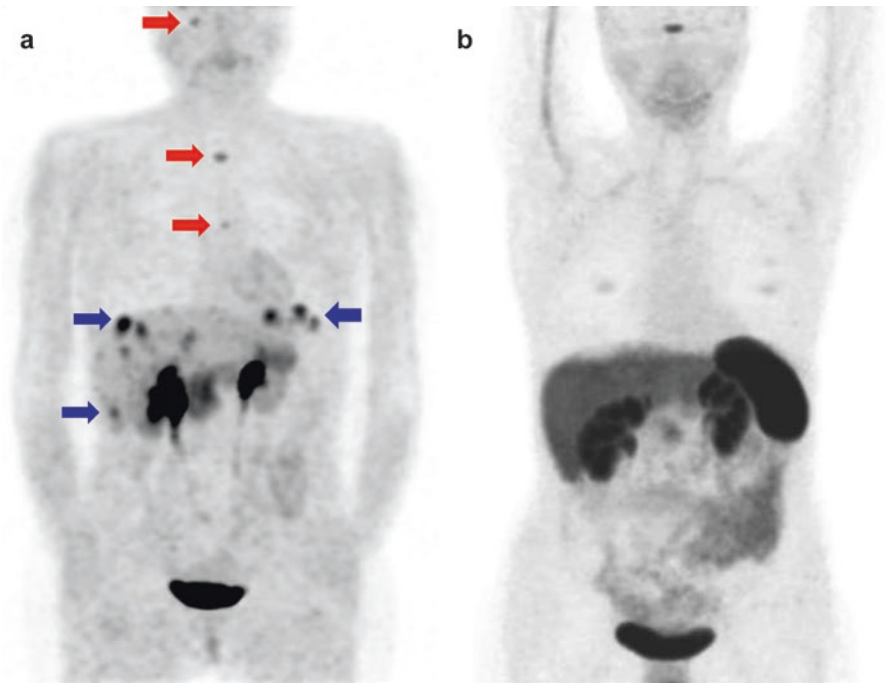
Fig. 18.4 A 47-year-old female affected by MTC with evidence of increasing serum calcitonin levels (280 pg/mL) after thyroidectomy and cervical lymphadenectomy. FDOPA-PET (**a**) showed multiple areas of abnormal tracer uptake corresponding to bone (*red arrows*) and liver metastases (*blue arrows*). On the other hand, somatostatin receptor PET was negative (**b**)
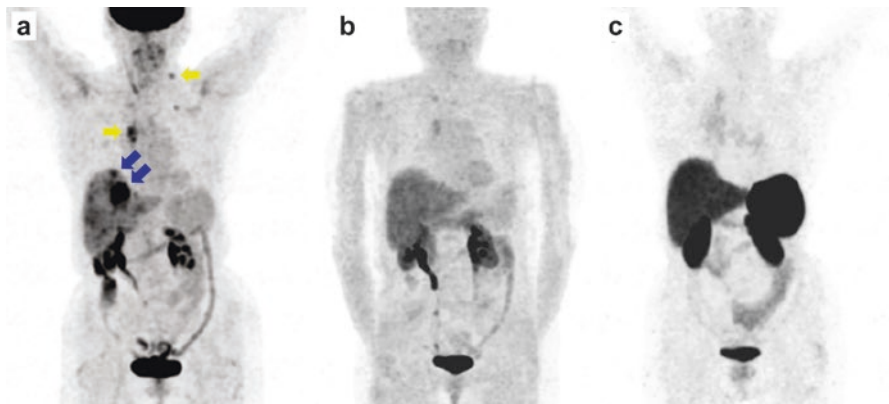
Fig. 18.5 A 80-year-old female affected by MTC with evidence of increasing serum calcitonin (480 pg/mL) and CEA (322 ng/mL) levels after thyroidectomy and cervical lymphadenectomy. FDG-PET (**a**) showed multiple areas of abnormal tracer uptake corresponding to lymph nodal (*yellow arrows*) and liver metastases (*blue arrows*). FDOPA-PET (**b**) and somatostatin receptor PET (**c**) demonstrated only minimal abnormalities

most useful functional imaging method for detecting recurrent MTC lesions in patients with increased serum calcitonin levels, performing better than FDG and somatostatin analogues labelled with Gallium-68 and leading a change in the patient management in a significant percentage of cases [50].

According to the injected activity of radiopharmaceutical and the volume of the body explored by low dose CT, the total effective dose from FDG, FDOPA or somatostatin receptor PET/CT varies between 13 and 15 mSv, and the radiation dose is very similar for all these radiopharmaceuticals [66]. The actual effective dose is currently decreasing with a trend to reduce the injected activity of radiopharmaceuticals by using time of flight PET/CT [66].

While FDG and FDOPA may be prepared industrially (for PET centres without an on-site cyclotron) and delivered ready to use, for labelling somatostatin analogues with Gallium-68, both Germanium-68/Gallium-68 generator and lyophilised peptides are needed [66]. The easy synthesis process or radiolabelled somatostatin analogues is an advantage supporting their clinical use as PET tracers [54, 55].

FDOPA is the most expensive PET tracer for evaluating recurrent MTC, mainly for its difficult synthesis, but it is questionable whether its first-line indication in recurrent or metastatic MTC will increase the total costs of diagnostic workup. In fact, FDOPA-PET/CT allowing the most precise diagnostic information among other functional imaging techniques and sometimes providing additional informational compared to conventional morphological imaging in recurrent or metastatic MTC may permit avoiding further examinations, savings which may compensate for its price [66]. Unfortunately no cost-effectiveness studies are currently available for the diagnostic workup of recurrent or metastatic MTC by using radionuclide imaging.

The limited availability of FDOPA and somatostatin analogues labelled with Gallium-68 compared to FDG is probably not a major drawback in case of a rare cancer such as MTC, a limited number of specialised centres being able to match the demand [66].

18.4.3   Proposed Algorithm About the Use of Radionuclide Imaging Methods in MTC

The role of radionuclide imaging in staging MTC before treatment seems to be limited compared to conventional morphological imaging [1].

In suspected recurrent MTC based on rising tumor markers levels after thyroidectomy, radionuclide imaging methods may provide additional information compared to conventional imaging if serum calcitonin is >150 pg/mL. In particular, PET/CT with different tracers may change the patient management in a significant percentage of cases [43, 67].

FDOPA-PET/CT should be used as first radionuclide imaging method in recurrent MTC showing significant diagnostic performance in patients with higher serum

calcitonin levels and shorter serum calcitonin doubling time. In negative cases, FDG-PET/CT should be the next radionuclide imaging method, in particular if calcitonin and CEA levels are rapidly rising or a more aggressive disease is suspected. PET/CT with somatostatin analogues labelled with Gallium-68 could be performed when neither FDOPA- nor FDG-PET/CT are conclusive or in selecting patients suitable for therapy with cold or radiolabelled somatostatin analogues. Bone scintigraphy could complement FDG-PET/CT if FDOPA is not available [66].

Conflict of Interest The authors declare that they have no conflicts of interest.

References

1. Wells Jr SA, Asa SL, Dralle H, Elisei R, Evans DB, Gagel RF, et al. Revised American Thyroid Association guidelines for the management of medullary thyroid carcinoma. Thyroid. 2015;25:567–610.
2. Guyetant S, Rousselet MC, Durigon M, Chappard D, Franc B, Guerin O, et al. Sex-related C-cell hyperplasia in the normal human thyroid: a quantitative autopsy study. J Clin Endocrinol Metab. 1997;82:42–7.
3. Mulligan LM, Kwok JB, Healey CS, Elsdon MJ, Eng C, Gardner E, et al. Germ-line mutations of the RET proto-oncogene in multiple endocrine neoplasia type 2A. Nature. 1993;363:458–60.
4. Hofstra RM, Landsvater RM, Ceccherini I, Stulp RP, Stelwagen T, Luo Y, et al. A mutation in the RET proto-oncogene associated with multiple endocrine neoplasia type 2B and sporadic medullary thyroid carcinoma. Nature. 1994;367:375–6.
5. Marsh DJ, Learoyd DL, Andrew SD, Krishnan L, Pojer R, Richardson AL, et al. Somatic mutations in the RET proto-oncogene in sporadic medullary thyroid carcinoma. Clin Endocrinol. 1996;44:249–57.
6. Boichard A, Croux L, Al Ghuzlan A, Broutin S, Dupuy C, Leboulleux S, et al. Somatic RAS mutations occur in a large proportion of sporadic RET-negative medullary thyroid carcinomas and extend to a previously unidentified exon. J Clin Endocrinol Metab. 2012;97:E2031–5.
7. Agrawal N, Jiao Y, Sausen M, Leary R, Bettegowda C, Roberts NJ, et al. Exomic sequencing of medullary thyroid cancer reveals dominant and mutually exclusive oncogenic mutations in RET and RAS. J Clin Endocrinol Metab. 2013;98:E364–9.
8. Leboulleux S, Baudin E, Travagli JP, Schlumberger M. Medullary thyroid carcinoma. Clin Endocrinol. 2004;61:299–310.
9. Machens A, Hinze R, Thomusch O, Dralle H. Pattern of nodal metastasis for primary and reoperative thyroid cancer. World J Surg. 2002;26:22–8.
10. Moley JF. Medullary thyroid carcinoma: management of lymph node metastases. J Natl Compr Canc Netw. 2010;8:549–56.
11. Kebebew E, Ituarte PH, Siperstein AE, Duh QY, Clark OH. Medullary thyroid carcinoma: clinical characteristics, treatment, prognostic factors, and a comparison of staging systems. Cancer. 2000;88:1139–48.
12. Modigliani E, Cohen R, Campos JM, Conte-Devolx B, Maes B, Boneu A, et al. Prognostic factors for survival and for biochemical cure in medullary thyroid carcinoma: results in 899 patients. The GETC Study Group. Groupe d'etude des tumeurs a calcitonine. Clin Endocrinol. 1998;48:265–73.
13. Kebebew E, Greenspan FS, Clark OH, Woeber KA, Grunwell J. Extent of disease and practice patterns for medullary thyroid cancer. J Am Coll Surg. 2005;200:890–6.

14. Roman S, Lin R, Sosa JA. Prognosis of medullary thyroid carcinoma: demographic, clinical, and pathologic predictors of survival in 1252 cases. Cancer. 2006;107:2134–42.
15. Trimboli P, Giovanella L, Crescenzi A, Romanelli F, Valabrega S, Spriano G, et al. Medullary thyroid cancer diagnosis: an appraisal. Head Neck. 2014;36:1216–23.
16. Trimboli P, Seregni E, Treglia G, Alevizaki M, Giovanella L. Procalcitonin for detecting medullary thyroid carcinoma: a systematic review. Endocr Relat Cancer. 2015;22:R157–64.
17. Trimboli P, Giovanella L. Serum calcitonin negative medullary thyroid carcinoma: a systematic review of the literature. Clin Chem Lab Med. 2015;53:1507–14.
18. Trimboli P, Treglia G, Guidobaldi L, Romanelli F, Nigri G, Valabrega S, et al. Detection rate of FNA cytology in medullary thyroid carcinoma: a meta-analysis. Clin Endocrinol. 2015;82:280–5.
19. Trimboli P, Guidobaldi L, Bongiovanni M, Crescenzi A, Alevizaki M, Giovanella L. Use of fine-needle aspirate calcitonin to detect medullary thyroid carcinoma: a systematic review. Diagn Cytopathol. 2016;44:45–51.
20. Chernock RD, Hagemann IS. Molecular pathology of hereditary and sporadic medullary thyroid carcinomas. Am J Clin Pathol. 2015;143:768–77.
21. Khurana R, Agarwal A, Bajpai VK, Verma N, Sharma AK, Gupta RP, et al. Unraveling the amyloid associated with human medullary thyroid carcinoma. Endocrinology. 2004;145:5465–70.
22. Mendelsohn G, Wells Jr SA, Baylin SB. Relationship of tissue carcinoembryonic antigen and calcitonin to tumor virulence in medullary thyroid carcinoma. An immunohistochemical study in early, localized, and virulent disseminated stages of disease. Cancer. 1984;54:657–62.
23. Mete O, Asa SL. Precursor lesions of endocrine system neoplasms. Pathology. 2013;45:316–30.
24. Trimboli P, Giovanella L, Valabrega S, Andrioli M, Baldelli R, Cremonini N, et al. Ultrasound features of medullary thyroid carcinoma correlate with cancer aggressiveness: a retrospective multicenter study. J Exp Clin Cancer Res. 2014;33:87.
25. Rufini V, Castaldi P, Treglia G, Perotti G, Gross MD, Al-Nahhas A, et al. Nuclear medicine procedures in the diagnosis and therapy of medullary thyroid carcinoma. Biomed Pharmacother. 2008;62:139–46.
26. Skoura E. Depicting medullary thyroid cancer recurrence: the past and the future of nuclear medicine imaging. Int J Endocrinol Metab. 2013;11:e 8156.
27. Clarke SE, Lazarus CR, Wraight P, Sampson C, Maisey MN. Pentavalent [99mTc] DMSA, [131I] MIBG, and [99mTc] MDP – an evaluation of three imaging techniques in patients with medullary carcinoma of the thyroid. J Nucl Med. 1988;29:33–8.
28. Frank-Raue K, Bihl H, Dorr U, Buhr H, Ziegler R, Raue F. Somatostatin receptor imaging in persistent medullary thyroid carcinoma. Clin Endocrinol. 1995;42:31–7.
29. Kwekkeboom DJ, Reubi JC, Lamberts SW, Bruining HA, Mulder AH, Oei HY, et al. In vivo somatostatin receptor imaging in medullary thyroid carcinoma. J Clin Endocrinol Metab. 1993;76:1413–7.
30. Hirano T, Tomiyoshi K, Zhang YJ, Ishida T, Inoue T, Endo K. Preparation and clinical evaluation of technetium-99m dimercaptosuccinic acid for tumour scintigraphy. Eur J Nucl Med. 1994;21:82–5.
31. Verga U, Muratori F, Di Sacco G, Banfi F, Libroia A. The role of radiopharmaceuticals MIBG and (V) DMSA in the diagnosis of medullary thyroid carcinoma. Henry Ford Hosp Med J. 1989;37:175–7.
32. Ozkan ZG, Kuyumcu S, Uzum AK, Gecer MF, Ozel S, Aral F, et al. Comparison of 68Ga-DOTATATE PET-CT, 18F-FDG PET-CT and 99mTc-(V)DMSA scintigraphy in the detection of recurrent or metastatic medullary thyroid carcinoma. Nucl Med Commun. 2015;36:242–50.
33. Arslan N, Ilgan S, Yuksel D, Serdengecti M, Bulakbasi N, Ugur O, et al. Comparison of In-111 octreotide and Tc-99m (V) DMSA scintigraphy in the detection of medullary thyroid tumor foci in patients with elevated levels of tumor markers after surgery. Clin Nucl Med. 2001;26:683–8.

34. Baudin E, Lumbroso J, Schlumberger M, Leclere J, Giammarile F, Gardet P, et al. Comparison of octreotide scintigraphy and conventional imaging in medullary thyroid carcinoma. J Nucl Med. 1996;37:912–6.

35. Kaltsas G, Korbonits M, Heintz E, Mukherjee JJ, Jenkins PJ, Chew SL, et al. Comparison of somatostatin analog and meta-iodobenzylguanidine radionuclides in the diagnosis and localization of advanced neuroendocrine tumors. J Clin Endocrinol Metab. 2001;86:895–902.

36. Bombardieri E, Coliva A, Maccauro M, Seregni E, Orunesu E, Chiti A, et al. Imaging of neu-roendocrine tumours with gamma-emitting radiopharmaceuticals. Q J Nucl Med Mol Imaging. 2010;54:3–15.

37. Maiza JC, Grunenwald S, Otal P, Vezzosi D, Bennet A, Caron P. Use of 131 IMIBG therapy in MIBG-positive metastatic medullary thyroid carcinoma. Thyroid. 2012;22:654–5.

38. Pasieka JL, McEwan AJ, Rorstad O. The palliative role of 131I-MIBG and 111In- octreotide therapy in patients with metastatic progressive neuroendocrine neoplasms. Surgery. 2004;136:1218–26.

39. Giraudet AL, Vanel D, Leboulleux S, Auperin A, Dromain C, Chami L, et al. Imaging medul-lary thyroid carcinoma with persistent elevated calcitonin levels. J Clin Endocrinol Metab. 2007;92:4185–90.

40. Treglia G, Castaldi P, Villani MF, Perotti G, Filice A, Ambrosini V, et al. Comparison of differ-ent positron emission tomography tracers in patients with recurrent medullary thyroid carci-noma: our experience and a review of the literature. Recent Results Cancer Res. 2013;194:385–93.

41. Treglia G, Muoio B, Giovanella L, Salvatori M. The role of positron emission tomography and positron emission tomography/computed tomography in thyroid tumours: an overview. Eur Arch Otorhinolaryngol. 2013;270:1783–7.

42. Treglia G, Giovanella L, Rufini V. PET and PET/CT imaging in thyroid and adrenal diseases: an update. Hormones. 2013;12:327–33.

43. Treglia G, Rufini V, Salvatori M, Giordano A, Giovanella L. PET imaging in recurrent medul-lary thyroid carcinoma. Int J Mol Imaging. 2012;2012:324686.

44. Rufini V, Treglia G, Perotti G, Leccisotti L, Calcagni ML, Rubello D. Role of PET in medul-lary thyroid carcinoma. Minerva Endocrinol. 2008;33:67–73.

45. Treglia G, Villani MF, Giordano A, Rufini V. Detection rate of recurrent medullary thyroid carcinoma using fluorine-18 fluorodeoxyglucose positron emission tomography: a meta-analysis. Endocrine. 2012;42:535–45.

46. Verbeek HH, Plukker JT, Koopmans KP, de Groot JW, Hofstra RM, Muller Kobold AC, et al. Clinical relevance of 18F-FDG PET and 18F-DOPA PET in recurrent medullary thyroid car-cinoma. J Nucl Med. 2012;53:1863–71.

47. Bogsrud TV, Karantanis D, Nathan MA, Mullan BP, Wiseman GA, Kasperbauer JL, et al. The prognostic value of 2-deoxy-2-[18F] fluoro-D-glucose positron emission tomography in patients with suspected residual or recurrent medullary thyroid carcinoma. Mol Imaging Biol. 2010;12:547–53.

48. Treglia G, Cocciolillo F, Di Nardo F, Poscia A, de Waure C, Giordano A, et al. Detection rate of recurrent medullary thyroid carcinoma using fluorine-18 dihydroxyphenylalanine positron emission tomography: a meta-analysis. Acad Radiol. 2012;19:1290–9.

49. Archier A, Heimburger C, Guerin C, Morange I, Palazzo FF, Henry JF, et al. (18)F-DOPA PET/CT in the diagnosis and localization of persistent medullary thyroid carcinoma. Eur J Nucl Med Mol Imaging. 2015. doi:10.1007/s00259-015-3227-y.

50. Treglia G, Castaldi P, Villani MF, Perotti G, de Waure C, Filice A, et al. Comparison of 18F-DOPA, 18F-FDG and 68Ga-somatostatin analogue PET/CT in patients with recurrent medullary thyroid carcinoma. Eur J Nucl Med Mol Imaging. 2012;39:569–80.

51. Soussan M, Nataf V, Kerrou K, Grahek D, Pascal O, Talbot JN, et al. Added value of early 18F-FDOPA PET/CT acquisition time in medullary thyroid cancer. Nucl Med Commun. 2012;33:775–9.

52. Treglia G, Stefanelli A, Castaldi P, Rufini V. A standardized dual-phase 18F-DOPA PET/CT protocol in the detection of medullary thyroid cancer. Nucl Med Commun. 2013;34:185–6.
53. Treglia G, Castaldi P, Rindi G, Giordano A, Rufini V. Diagnostic performance of Gallium-68 somatostatin receptor PET and PET/CT in patients with thoracic and gastroenteropancreatic neuroendocrine tumours: a meta-analysis. Endocrine. 2012;42:80–7.
54. Ambrosini V, Morigi JJ, Nanni C, Castellucci P, Fanti S. Current status of PET imaging of neuroendocrine tumours ([18F] FDOPA, [68Ga] tracers, [11C]/[18F]-HTP). Q J Nucl Med Mol Imaging. 2015;59:58–69.
55. Ambrosini V, Fanti S. 68Ga-DOTA-peptides in the diagnosis of NET. PET Clin. 2014;9:37–42.
56. Traub-Weidinger T, Putzer D, von Guggenberg E, Dobrozemsky G, Nilica B, Kendler D, et al. Multiparametric PET imaging in thyroid malignancy characterizing tumour heterogeneity: somatostatin receptors and glucose metabolism. Eur J Nucl Med Mol Imaging. 2015;42:1995–2001.
57. Tran K, Khan S, Taghizadehasl M, Palazzo F, Frilling A, Todd JF, et al. Gallium-68 Dotatate PET/CT is superior to other imaging modalities in the detection of medullary carcinoma of the thyroid in the presence of high serum calcitonin. Hell J Nucl Med. 2015;18:19–24.
58. Naswa N, Sharma P, Suman Kc S, Lata S, Kumar R, Malhotra A, et al. Prospective evaluation of 68Ga-DOTA-NOC PET-CT in patients with recurrent medullary thyroid carcinoma: comparison with 18F-FDG PET-CT. Nucl Med Commun. 2012;33:766–74.
59. Łapińska G, Bryszewska M, Fijołek-Warszewska A, Kozłowicz-Gudzińska I, Ochman P, Sackiewicz-Słaby A. The diagnostic role of 68Ga-DOTATATE PET/CT in the detection of neuroendocrine tumours. Nucl Med Rev Cent East Eur. 2011;14:16–20.
60. Pałyga I, Kowalska A, Gąsior-Perczak D, Tarnawska-Pierścińska M, Słuszniak J, Sygut J, Góźdź S. The role of PET-CT scan with somatostatin analogue labelled with gallium-68 (68Ga-DOTA-TATE PET-CT) in diagnosing patients with disseminated medullary thyroid carcinoma (MTC). Endokrynol Pol. 2010;61:507–11.
61. Conry BG, Papathanasiou ND, Prakash V, Kayani I, Caplin M, Mahmood S, Bomanji JB. Comparison of (68) Ga-DOTATATE and (18) F-fluorodeoxyglucose PET/CT in the detection of recurrent medullary thyroid carcinoma. Eur J Nucl Med Mol Imaging. 2010;37:49–57.
62. Papotti M, Kumar U, Volante M, Pecchioni C, Patel YC. Immunohistochemical detection of somatostatin receptor types 1–5 in medullary carcinoma of the thyroid. Clin Endocrinol. 2001;54:641–9.
63. Kauhanen S, Schalin-Jäntti C, Seppänen M, Kajander S, Virtanen S, Schildt J, et al. Complementary roles of 18F-DOPA PET/CT and 18F-FDG PET/CT in medullary thyroid cancer. J Nucl Med. 2011;52:1855–63.
64. Marzola MC, Pelizzo MR, Ferdeghini M, Toniato A, Massaro A, Ambrosini V, et al. Dual PET/CT with (18)F-DOPA and (18)F-FDG in metastatic medullary thyroid carcinoma and rapidly increasing calcitonin levels: Comparison with conventional imaging. Eur J Surg Oncol. 2010;36:414–21.
65. Beheshti M, Pöcher S, Vali R, Waldenberger P, Broinger G, Nader M, et al. The value of 18F-DOPA PET-CT in patients with medullary thyroid carcinoma: comparison with 18F-FDG PET-CT. Eur Radiol. 2009;19:1425–34.
66. Slavikova K, Montravers F, Treglia G, Kunikowska J, Kaliska L, Vereb M, et al. What is currently the best radiopharmaceutical for the hybrid PET/CT detection of recurrent medullary thyroid carcinoma? Curr Radiopharm. 2013;6:96–105.
67. Wong KK, Laird AM, Moubayed A, Chondrogiannis S, Marzola MC, Evangelista L, et al. How has the management of medullary thyroid carcinoma changed with the advent of 18F-FDG and non-18F-FDG PET radiopharmaceuticals. Nucl Med Commun. 2012;33:679–88.

Chapter 19
^{131}I-Meta-Iodobenzylguanidine Therapy for Pheochromocytoma/Paraganglioma and Neuroblastoma

Ioannis Ilias and Georgios Meristoudis

19.1   Introduction

Although, ideally, the aim of ^{131}I-meta-iodobenzylguanidine (^{131}I-mIBG) therapeutic administration is disease cure, for the majority of adult patients with pheochromocytoma/paraganglioma (PHEO/PG) or neuroblastoma (NB), a more realistic goal is to stabilize disease, to provide symptomatic relief, and to elicit biochemical response. For younger patients with refractory or relapsing NB, already burdened by prior therapies, therapeutic ^{131}I-mIBG is considered when other treatment options are ineffective.

19.1.1 ^{131}I-mIBG

Meta-iodobenzylguanidine is an analogue of guanethidine and shows similar molecular structure to noradrenaline (Fig. 19.1). Labeled with ^{131}I, this radiopharmaceutical, via metabolic pathways (including the pathway of norepinephrine), is selectively accumulated *in vivo* by noradrenergic tissues and neuroendocrine tumors such as PHEO/PG, NB, carcinoids, or medullary carcinoma of the thyroid [1, 2]. The intense uptake and the prolonged retention of ^{131}I-mIBG in these neuroendocrine tumors provide the basis for imaging and its potential therapeutic use. Although ^{131}I-mIBG is FDA-approved for diagnosis, it is not approved for therapy, and when used for such purposes it is done as an experimental procedure.

I. Ilias (✉)
Endocrine Unit, Elena Venizelou Hospital, 2, El Venizelou Sq, Athens GR-11521, Greece
e-mail: iiliasmd@yahoo.com

G. Meristoudis
Department of Nuclear Medicine, Hippokration Hospital, Thessaloniki GR-54642, Greece
e-mail: meristoudis@yahoo.gr
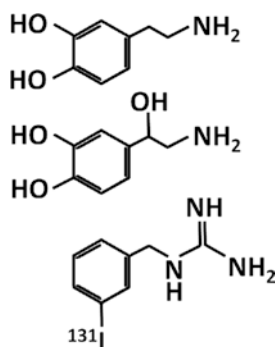
Fig. 19.1 Structural similarities of adrenaline (*upper molecule*), noradrenaline (*middle molecule*), and ^{131}I-mIBG (*lower molecule*)

19.1.2 mIBG: Uptake Mechanism

Meta-iodobenzylguanidine moves into cells by the mechanism of noradrenaline reuptake of the adrenergic presynaptic neuron, by binding to the noradrenaline transporter, a protein that is expressed in neuroendocrine tumors. It is concentrated in intracellular storage granules through vesicular monoamine transporters, as noradrenaline does, or remains in the cytoplasm (the latter is generally suggested to occur in NB). Unlike noradrenaline it shows no uptake by postsynaptic neurons and is not further metabolized. The main pathway of ^{131}I-mIBG entry into the cells is via a Na^+/ATP-dependent mechanism (uptake 1). Additionally, nonspecific low concentrations are achieved by passive diffusion (uptake 2) in the majority of cells. The half-life of ^{131}I is at 8.04 days; beta maximum energy emission is at 0.61 MeV (average energy 0.192 MeV). Its mean range of penetration in soft tissues is approximately 0.5 mm. Therapy with ^{131}I-mIBG is possible due to DNA damage and cancer cells' death following their exposure to the radionuclide's beta (β) irradiation [3]. The phenomenon of radiation-induced bystander effect might also contribute to cell death; however, its role in cytotoxicity is not well defined [4, 5].

19.1.3 Contraindications to ^{131}I-mIBG Therapy

Absolute contraindications to ^{131}I-mIBG therapeutic administration include pregnancy, lactation, less than 3 months' life expectancy (except in cases of significant bone pain), and compromised renal function requiring dialysis at short intervals [6]. Relative contraindications to ^{131}I-mIBG therapy include significant urinary incontinence, high medical risks from isolation, rapidly deteriorating renal impairment (GFR <30 ml/min), and bone marrow suppression (white blood cell count less than 3 x 10^9/L, platelet count less than 100 x 10^9/L).

In the aforementioned conditions or in case of bone marrow invasion, the administered activity should be reduced.

19.1.4   Preparation of ^{131}I-mIBG Therapeutic Administration

A prerequisite for therapy with ^{131}I-mIBG is positive imaging with ^{123}I-mIBG or ^{131}I-mIBG in adults; the former is considered the radiopharmaceutical of choice for diagnosis. Thyroid blockade is necessary from 48 to 24 h before therapy until 10–15 days after therapy (usually with 130 mg potassium iodide in combination with 400 mg potassium perchlorate/24 h). Several drug classes (cardiovascular, sympathomimetics, antipsychotics, neuroleptics, tricyclic antidepressants, and CNS stimulants) that may affect the biokinetics of ^{131}I-mIBG should be discontinued before treatment, if possible. In patients with metabolically active tumors secreting catecholamines taking alpha-adrenergic receptor antagonists to control blood pressure combined with beta-adrenergic receptor blockers for tachycardia control, withdrawal is not recommended due to the risk of complications, although the effectiveness of treatment might be diminished. Antiemetics (such as ondansetron) should be administered before treatment and for 3 days following treatment. Care must be given for complete and proper information to patients, and instructions (written and oral) should be delivered on the procedure before receiving treatment. Parents with proper guidance according to radiation safety protection can participate in the care of children receiving treatment [5]. Since more than 50 % of administered dose is excreted by the urine, a urinary catheter may be placed especially in children with NB to reduce bladder radiation dose and to avoid contamination.

19.1.5 ^{131}I-mIBG Administration Procedure

^{131}I-mIBG is administrated in a therapy unit with lead shielding rooms via a slow iv infusion over 45 min up to 4 hours (usually over an hour to 2 hours); the procedure is undertaken by appropriately trained staff. Monitoring of vital signs is necessary, including blood pressure. The latter may be elevated, especially in patients with PHEO/PG [7]; this rise may be attributed to the release of noradrenaline from storage granules, possibly due to the infusion of substantial quantities of non-radiolabeled (or "cold") mIBG (only one in 2000 molecules is labeled). In that case, short-acting alpha (followed by beta-)-adrenergic receptor blockers may be given, although usually infusion rate reduction or temporary interruption of the infusion is sufficient [5, 8]. Discharge of a patient from the special shielded room depends on national and local legislation, considering that the dose equivalent to persons with contact with the patient is insignificant (exposure rate <3 mrem/h at 1 m or in general 3–5 days).

19.1.6 Undesirable Effects of ^{131}I-mIBG Therapy

Immediate effects include nausea, vomiting (usually limited to 2 days), and transient myelosuppression (4–6 weeks after ^{131}I-mIBG administration); the latter is noted in children with NB after chemotherapy, and it is less common in adults receiving therapeutic ^{131}I-mIBG. Rarely renal function can worsen, hypertensive crisis can ensue, or the parotid glands may get swollen (but no xerostomia is observed). Long-term undesirable effects of ^{131}I-mIBG therapy include hypothyroidism (up to 25 % of patients, with lower incidence in adults), persistent bone marrow suppression, or the appearance of secondary neoplasias such as leukemia or myelodysplastic syndrome (<4 %) [9].

19.1.7 Myelosuppression

Myelosuppression is the most important undesirable effect of ^{131}I-mIBG therapy [10]; the effect is more pronounced in thrombocytopenia vis-à-vis neutropenia, because platelets show selective ^{131}I-mIBG uptake. In children with NB, bone marrow suppression peaks after 28 days after ^{131}I-mIBG therapy, but may occur earlier if combined with chemotherapy. Myelosuppression from ^{131}I-mIBG is dose dependent; it is mild at administered doses ≈ 7.4 GBq (200 mCi) in adults, while doses >444 MBq/kg (12 mCi/Kg) may cause severe myelosuppression in both adults and children. Grade III or IV thrombocytopenia and/or neutropenia requires platelet transfusion and administration of hematopoietic growth factors [6].

19.1.8 ^{131}I-mIBG Dosing

Dosages of therapeutic ^{131}I-mIBG are to their greater extent empirical. They vary depending on the patients, on toxicity (expected pretreatment and perceived posttreatment), on response to treatment, on disease progression rate, and on the accumulated experience of each center. In general, the therapeutic dose is usually 3.7–11.2 GBq (100–300 mCi). Dosing of ^{131}I-mIBG can be fixed in amounts of limited toxicity (3.7–7.4 GBq; 200 mCi) or based on patient weight (96–666 MBq/kg) (2.6–18 mCi/kg) or body surface area (3.7–14.8 GBq/m^2). Fixed doses are usually divided in multiple non-myelosuppressive segments over 3–6 months, based on response and toxicity. A high initial dose might be preferred for more responsive microscopic disease with rapid progression, whereas low repeated doses may be given to target macroscopic disease with slow progression. The doses can also be prescribed based on a dosimetric assessment of less than 2–4 Gy to total-body absorbed dose. If total-body radiation dose is higher than 2 Gy, provision for stem cells to be harvested before therapy (for autologous stem cell transplantation) should be made [6, 11–13].

19.1.9 ^{131}I-mIBG Dosimetry

The administered therapeutic ^{131}I-mIBG dose is personalized, depending on disease burden, lesion distribution, and bone marrow reserves. Dosimetry with a pretreatment ^{123}I-mIBG scan alone may underestimate the dose in 65 % of patients, but is more reproducible than that based on body weight. Posttreatment imaging is done to determine tumor targeting and its extent and retrospective dosimetry; due to high doses additional lesions may be detected in two-thirds of scans. Methods to estimate the total-body absorbed dose are either based on pretreatment dosimetry or prescribed as activity/kg, and posttreatment imaging is used to prescribe the second administration to achieve the goal of total-body dose. On the contrary to external beam radiation therapy, dosimetry of targeted radionuclide therapy may not be so precise, because of tumor volume variations and heterogeneous uptake by the targeted lesions. Nonetheless, total-body dosimetry is useful in predicting hematologic toxicity and assessing the radiation dose to tumor (usually cumulative doses of 60–150-Gy suffice), thus enabling individualized treatment [14–18].

19.2 ^{131}I-mIBG Therapy for PHEO/PG

Low (80–200 mCi; 2.96–7.4 GBq), intermediate (up to 500 mCi; 18.5 GBq), and high (>12 mCi/kg; >444 MBq/kg) doses have been used in PHEO/PG with cumulative dose up to 2,322 mCi (85,914 MBq). Patients that received a mean dose of 388 mCi (14.356 GBq) of ^{131}I-mIBG and responded to treatment had a median survival of 4.7 years versus 1.7 for those without response to treatment. Furthermore, those who received over 500 mCi (18.5 GBq) as initial doses had a median survival of 3.8 years versus 2.6 years for those who received low doses [19]. In another study, patients who received intermediate doses of 269 mCi (9.953 GBq) compared to those with low doses of 149 mCi (5.513 GBq) had a quick response, similar survival rate, and mild side effects [20]. There is evidence that ^{131}I-mIBG, given therapeutically at high activity and myelosuppressive doses (median dose 818 mCi or 12 mCi/kg, range 6–19 mCi/kg; 30.266 GBq, 444 MBq/kg, range 222–703 MBq/kg) after peripheral stem cell collection, may be associated with a higher response rate; the overall 5-year survival was 64 % compared to 44 % in patients without such therapy (based on a historical control group) [21]. At present the use of intermediate or high activities with autologous stem cell rescue is more advantageous due to the survival benefit.

Only approximately 0.05 % of ^{131}I-mIBG molecules are radiolabeled, the rest being unlabeled mIBG ("cold carrier"). The latter is considered to competitively inhibit radiolabeled mIBG uptake by its target tissues, affecting treatment efficacy and may also provide adverse effects [22, 23]. In a phase I clinical study, 11 patients with refractory PHEO/PG were treated with high-purity and specific activity of no-carrier-added ^{131}I-mIBG (radiolabeled ^{131}I-mIBG more than 94 %;

mean administered dose of 5.160 mCi (190.9 MBq). The study showed similar blood clearance and excretion characteristics to the carrier-added ^{131}I-mIBG, and no side effects were related to the study drug [22].

There are no randomized trials or any consensus for the optimal strategy or of dosing schedules of ^{131}I-mIBG therapeutic administration. Nor are there any comparative studies in patients given multiple non-myelosuppressive ^{131}I-mIBG doses vis-à-vis high doses. Few prospective type studies of ^{131}I-mIBG have been presented. Consequently, the observed differences in response to[131]I-mIBG treatment and survival could be attributed to patient selection. Several patients benefit from ^{131}I-mIBG treatment: symptomatic response is high, ranging between 75 and 90 %, biochemical response rate is 45–74 %, and morphologic response is 27–47 % [24]. Nevertheless, complete response is low, ranging from 0 to 18 %, whereas 5-year survival ranges between 45 and 85 % [6, 12, 13]. The relative ease of the process, the partial response to treatment, the noted symptomatic and biochemical improvement, and limited side effects compared to chemotherapy make – regardless of its shortcomings – ^{131}I-mIBG an attractive therapeutic option for patients with metastatic PHEO/PG.

19.3   ^{131}I-mIBG Therapy for NB

Seventy percent of patients with NB initially respond to surgery and chemotherapy, but approximately 50 % of those with high risk of relapse do so, with no reliable salvage therapy. Nonsurgical treatment for high-risk NB consists of three phases: induction, stabilization, and preservation, which can be administered with chemotherapy, radiotherapy, bone marrow transplantation, ^{131}I-mIBG, or immunotherapy [25]. Chemotherapy at myelosuppressive doses and autologous bone marrow transplantation improve survival as consolidation therapy in randomized clinical trials. ^{131}I-mIBG has been used mainly in patients with relapsed and refractory disease (alone and/or combined with chemotherapy) rather than as first-line therapy. ^{131}I-mIBG has been administered at fixed doses of 100–200 mCi (3.7–7.4 GBq) with cumulative activity of 600–1.000 mCi (22.2–37 GBq). Doses based on body weight (2.6–18.0 mCi/kg; 96.2–666 MBq/kg) or with a total-body radiation dose delivered of 1–4 Gy in dosimetry have been given in NB (for doses > 12 mCi/kg or a total-body radiation dose > 2 Gy, collection of hematopoietic cells is advocated) [6]. Nonetheless, therapeutic treatment based on dosimetric assessment is mandatory in NB due to prior therapy and the increased possibility of hematologic toxicity [18].

In a systematic review of 979 patients included in 30 studies (studies of induction treatment $n=2$, consolidation $n=1$, relapsed and refractory disease $n=27$), partial response to ^{131}I-mIBG therapy in patients with relapsed and refractory disease ranged from 0 % to 75 %, with an average value of approximately 32 % (and complete response in less than 10 %) [26]. Recently, a retrospective analysis of 218 patients with refractory or relapsed NB showed that, after ^{131}I-mIBG treatment, the

refractory cohort had higher rates of stable disease compared to those patients with prior relapse (59 % versus 39 %), lower rates of progressive disease (9 % versus 24 %), and superior 2-year overall survival (65.3 % versus 38.7 %) [27]. The use of no-carrier-added ^{131}I-mIBG (specific activity 165 MBq/μg) was recently evaluated in a clinical trial using doses ranging from 444 to 666 MBq/kg (12–18 mCi/kg) with autologous peripheral stem cell transplantation [28]. In this group of 15 patients, no other significant (non-hematologic) toxicity was observed. An important increase of total-body dose was noted by increasing the dose/kg of no-carrier-added ^{131}I-mIBG, with total-body doses analogous to those with carrier-added mIBG. Furthermore, the median tumor-absorbed dose was higher than that of carrier-added mIBG (49 Gy versus 33 Gy).

Treatment with ^{131}I-mIBG is effective; however, more data along with clinical evidence are needed to understand how best it should be incorporated in multimodal therapy of NB. Further (prospective randomized studies) are needed to asses effective compared to chemotherapy, whether there is a benefit of combination therapy with ^{131}I-mIBG and chemotherapy compared to ^{131}I-mIBG alone. Furthermore, the optimal ^{131}I-mIBG dose is yet to be defined.

19.4   Future Developments

The armamentarium for PHEO/PG/NB in the future may be enriched with ^{131}I-mIBG combined with chemotherapy given as consolidation therapy, combination ^{131}I-mIBG/topoisomerase inhibitor treatment with topotecan [29] or irinotecan [30], or ^{131}I-mIBG administered with hyperbaric oxygen [31]. High-purity, carrier-free ^{131}I-mIBG may be further used and assessed. Enhancing norepinephrine transporter expression and ^{131}I-mIBG efficacy is also sought with differentiating agents (retinoic acid, interferon alpha and gamma) [4]. Finally it remains to be seen whether newer alpha-radiation-emitting meta-astato(^{211}At)-benzylguanidine (MABG) can be a radionuclide with potential therapeutic use [32].

References

1. Aktolun C, Castellani MR, Bombardieri E. Diagnostic and therapeutic use of MIBG in pheochromocytoma and paraganglioma. Q J Nucl Med Mol Imaging. 2013;57:109–11.
2. Aktolun C, Castellani MR. Theranostic role of MIBG in neuroblastoma. Q J Nucl Med Mol Imaging. 2013;57:3–5.
3. Sisson J, Shapiro B, Beierwaltes WH, Nakajo M, Glowniak J, Mangner T, et al. Treatment of malignant pheochromocytoma with a new radiopharmaceutical. Trans Assoc Am Physicians. 1983;96:209–17.
4. Streby KA, Shah N, Ranalli MA, Kunkler A, Cripe TP. Nothing but NET: a review of norepinephrine transporter expression and efficacy of 131I-mIBG therapy. Pediatr Blood Cancer. 2015;62:5–11.

5. Giammarile F, Chiti A, Lassmann M, Brans B, Flux G. EANM procedure guidelines for 131I-meta-iodobenzylguanidine (131I-mIBG) therapy. Eur J Nucl Med Mol Imaging. 2008;35:1039–47.

6. Carrasquillo JA, Pandit-Taskar N, Chen CC. Radionuclide therapy of adrenal tumors. J Surg Oncol. 2012;106:632–42.

7. Wong T, Matthay KK, Boscardin WJ, Hawkins RA, Brakeman PR, DuBois SG. Acute changes in blood pressure in patients with neuroblastoma treated with 131I-metaiodobenzylguanidine (MIBG). Pediatr Blood Cancer. 2013;60:1424–30.

8. Kayano D, Kinuya S. Iodine-131 metaiodobenzylguanidine therapy for neuroblastoma: reports so far and future perspective. ScientificWorldJournal. 2015;2015:189135. doi:10.1155/2015/189135.

9. Mallia A, Maccauro M, Seregni E, Bampo C, Chiesa C, Bombardieri E. Radionuclide therapy of neuroendocrine tumors. In: Aktolun C, Goldsmith SJ, editors. Nuclear medicine therapy - principles and clinical applications. New York: Springer; 2013. p. 57–84.

10. DuBois SG, Messina J, Maris JM, Huberty J, Glidden DV, Veatch J, et al. Hematologic toxicity of high-dose iodine-131-metaiodobenzylguanidine therapy for advanced neuroblastoma. J Clin Oncol. 2004;22:2452–60.

11. Navalkissoor S, Alhashimi DM, Quigley AM, Caplin ME, Buscombe JR. Efficacy of using a standard activity of (131)I-MIBG therapy in patients with disseminated neuroendocrine tumours. Eur J Nucl Med Mol Imaging. 2010;37:904–12.

12. Lewington V. I-131 meta iodobenzylguanidine therapy. In: Baum R, editor. Therapeutic nuclear medicine. New York: Springer; 2014. p. 571–82.

13. Grünwald F, Ezziddin S. 131I-metaiodobenzylguanidine therapy of neuroblastoma and other neuroendocrine tumors. Semin Nucl Med. 2010;40:153–63.

14. Flux GD, Chittenden SJ, Saran F, Gaze MN. Clinical applications of dosimetry for mIBG therapy. Q J Nucl Med Mol Imaging. 2011;55:116–25.

15. Gaze MN, Chang YC, Flux GD, Mairs RJ, Saran FH, Meller ST. Feasibility of dosimetry-based high-dose 131I-meta-iodobenzylguanidine with topotecan as a radiosensitizer in children with metastatic neuroblastoma. Cancer Biother Radiopharm. 2005;20:195–9.

16. Buckley SE, Saran FH, Gaze MN, Chittenden S, Partridge M, Lancaster D, et al. Dosimetry for fractionated (131)I-mIBG therapies in patients with primary resistant high-risk neuroblastoma: preliminary results. Cancer Biother Radiopharm. 2007;22:105–12.

17. Matthay KK, Panina C, Huberty J, Price D, Glidden DV, Tang HR, et al. Correlation of tumor and whole-body dosimetry with tumor response and toxicity in refractory neuroblastoma treated with (131)I-MIBG. J Nucl Med. 2001;42:1713–21.

18. Buckley SE, Chittenden SJ, Saran FH, Meller ST, Flux GD. Whole-body dosimetry for individualized treatment planning of 131I-MIBG radionuclide therapy for neuroblastoma. J Nucl Med. 2009;50:1518–24.

19. Safford SD, Coleman RE, Gockerman JP, Moore J, Feldman JM, Leight GSJ, et al. Iodine −131 metaiodobenzylguanidine is an effective treatment for malignant pheochromocytoma and paraganglioma. Surgery. 2003;134:956–62.

20. Castellani MR, Seghezzi S, Chiesa C, Aliberti GL, Maccauro M, Seregni E. (131)I-MIBG treatment of pheochromocytoma: low versus intermediate activity regimens of therapy. Q J Nucl Med Mol Imaging. 2010;54:100–13.

21. Gonias S, Goldsby R, Matthay KK, Hawkins R, Price D, Huberty J, et al. Phase II study of high-dose [131I]metaiodobenzylguanidine therapy for patients with metastatic pheochromocytoma and paraganglioma. J Clin Oncol. 2009;27:4162–8.

22. Coleman RE, Stubbs JB, Barrett JA, de la Guardia M, Lafrance N, Babich JW. Radiation dosimetry, pharmacokinetics, and safety of ultratrace Iobenguane I-131 in patients with malignant pheochromocytoma/paraganglioma or metastatic carcinoid. Cancer Biother Radiopharm. 2009;24:469–75.

23. Ilias I, Divgi C, Pacak K. Current role of metaiodobenzylguanidine in the diagnosis of pheochromocytoma and medullary thyroid cancer. Semin Nucl Med. 2011;41:364–8.

24. van Hulsteijn LT, Niemeijer ND, Dekkers OM, Corssmit EP. (131)I-MIBG therapy for malig-nant paraganglioma and phaeochromocytoma: systematic review and meta-analysis. Clin Endocrinol (Oxf). 2014;80:487–501.
25. Mazloom A, Louis CU, Nuchtern J, Kim E, Russell H, Allen-Rhoades W, et al. Radiation therapy to the primary and postinduction chemotherapy MIBG-avid sites in high-risk neuro-blastoma. Int J Radiat Oncol Biol Phys. 2014;90:858–62.
26. Wilson JS, Gains JE, Moroz V, Wheatley K, Gaze MN. A systematic review of 131I-meta iodobenzylguanidine molecular radiotherapy for neuroblastoma. Eur J Cancer. 2014;50:801–15.
27. Zhou MJ, Doral MY, DuBois SG, Villablanca JG, Yanik GA, Matthay KK. Different outcomes for relapsed versus refractory neuroblastoma after therapy with (131)I-metaiodobenzylguanidine ((131)I-MIBG). Eur J Cancer. 2015;51:2465–72.
28. Matthay KK, Weiss B, Villablanca JG, Maris JM, Yanik GA, Dubois SG, et al. Dose escalation study of no-carrier-added 131I-metaiodobenzylguanidine for relapsed or refractory neuroblas-toma: new approaches to neuroblastoma therapy consortium trial. J Nucl Med. 2012;53:1155–63.
29. McCluskey AG, Boyd M, Gaze MN, Mairs RJ. [131I]MIBG and topotecan: a rationale for combination therapy for neuroblastoma. Cancer Lett. 2005;228:221–7.
30. DuBois SG, Allen S, Bent M, Hilton JF, Hollinger F, Hawkins R, et al. Phase I/II study of (131) I-MIBG with vincristine and 5 days of irinotecan for advanced neuroblastoma. Br J Cancer. 2015;112:644–9.
31. Melbourne GJ, Lehm JP. Quantifying the radiation exposure of nursing staff delivering hyper-baric oxygen therapy to grade IV neuroblastoma patients post 131I-MIBG therapy. Eur J Nucl Med. 2000;27:1732–3.
32. Bomanji JB, Papathanasiou ND. (1)(1)(1)In-DTPA(0)-octreotide (Octreoscan), (1)(3)(1) I-MIBG and other agents for radionuclide therapy of NETs. Eur J Nucl Med Mol Imaging. 2012; 39(Suppl 1):S113–25.

Chapter 20
Peptide Receptor Radionuclide Therapy for Neuroendocrine Tumors

Janet Pollard, M. Sue O'Dorisio, Thomas O'Dorisio, and Yusuf Menda

20.1 Somatostatin Receptors as Primary Target for Neuroendocrine Tumors

Neuroendocrine tumors (NETs) arise from the diffuse neuroendocrine system with approximately 55 % arising in the small bowel, 25 % in lung bronchioles, and 20 % in the pancreas. Less frequent sites include the appendix, cervix, ovaries, prostate, thyroid, breast, and rectum (Fig. 20.1). Pheochromocytoma and paraganglioma will not be considered in this review as excellent evaluations of genetics and imaging in these rare tumors have been published recently [1, 2]. Neuroendocrine tumors are graded according to the mitotic index and/or Ki-67 expression. Grade I tumors demonstrate neuroendocrine differentiation with mitotic index and Ki-67 < 2 %; grade II tumors are also well differentiated with a mitotic index of 3–10 % and Ki-67 index of 2–20 %. Grade III NETs may be either well differentiated or poorly differentiated with mitotic index greater than 10 % and Ki-67 greater than 20 %. Poorly differentiated, grade III tumors are classified as neuroendocrine carcinoma (NEC) and can be either small-cell or large-cell malignancies. However, it is important to recognize

J. Pollard, MD • Y. Menda, MD (✉)
Department of Radiology, University of Iowa Carver College of Medicine,
Iowa City, IA, USA
e-mail: janet-pollard@uiowa.edu; yusuf-menda@uiowa.edu

M.S. O'Dorisio, MD, PhD
Department of Pediatrics, University of Iowa Carver College of Medicine,
Iowa City, IA, USA
e-mail: thomas-odorisio@uiowa.edu

T. O'Dorisio, MD
Department of Internal Medicine, University of Iowa Carver College of Medicine,
Iowa City, IA, USA
e-mail: thomas-odorisio@uiowa.edu

Anatomical distribution of neuroendocrine tumors
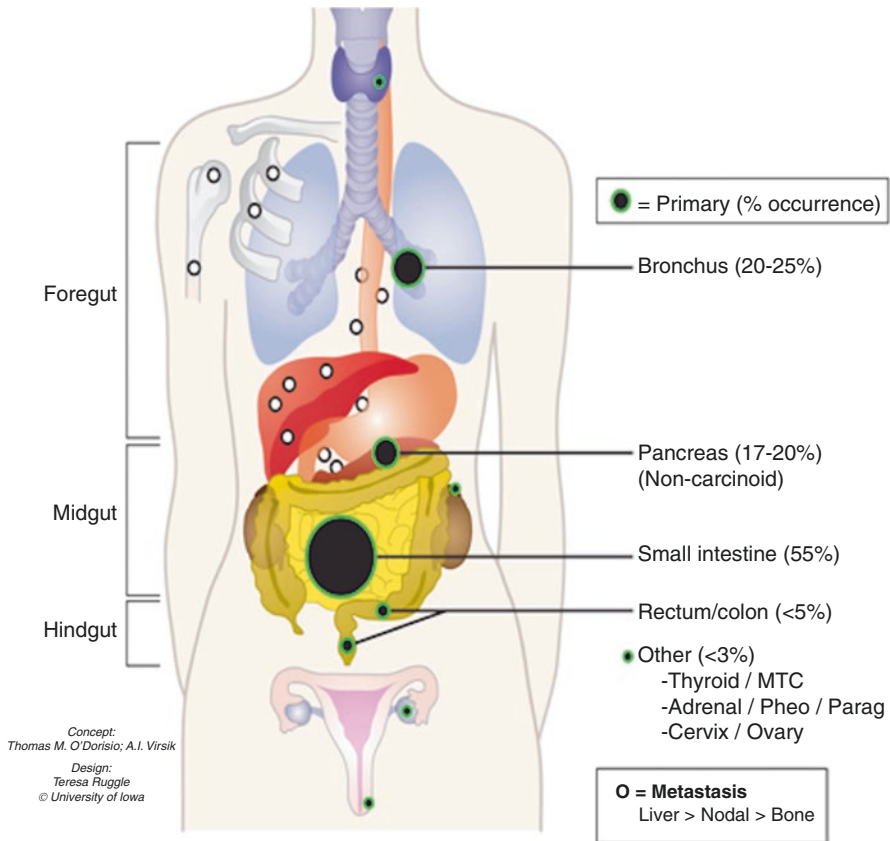
Fig. 20.1 Distribution of neuroendocrine tumors

that neuroendocrine tumors of any grade can metastasize, most often to the liver, lymph nodes, or bone. The incidence and prevalence of NETs in the USA have been tracked in the Surveillance, Epidemiology, and End Results (SEER) database of the National Institutes of Health since 1973. The most recent comprehensive analysis of SEER data with regard to neuroendocrine tumors was published in 2008 [3]; the estimated rate of new diagnoses was 5.2/100,000 person-years, with a prevalence of approximately 103,000. NETs are primarily a disease of older adults, but may also be diagnosed in childhood. According to the SEER database, the incidence of NETs in the 0–29-year age group is much lower at 0.3/100,000 with a prevalence in the USA of 7724 children and young adults referenced to 1 January 2004 [4]. A rapid increase in the worldwide incidence of NETs has been observed over the past decade as first pointed out for tumors of the lung, small bowel, and pancreas [5]. This increase was confirmed for all NETs in Norway, where the incidence increased from 13.3 to 21.3 per 100,000 person-years from 1993 to 2010 [6] and for

gastroenteropancreatic (GEP) NETs in Italy [7]. Much of this increase in incidence is likely due to both the increased sensitivity of newer diagnostic techniques and to the recognition that even NETs formerly classified as "benign" can metastasize.

Except for the undisputed role of surgery in the management of neuroendocrine tumors, the development and registration of the somatostatin analogs (congeners) octreotide and lanreotide have been critical in the management of NETs, both in symptom control and in delaying disease progression. Equally relevant, these analogs have helped unmask the unique, highly sensitive, and specific properties of most NETs, namely, somatostatin-octreotide/lanreotide cell membrane receptor (somatostatin receptor subtype 2, sstr2) kinetic [8]. As well, we now know that both octreotide and lanreotide have antiproliferative (therapeutic) action [9, 10]. Octreotide has a "mild antiproliferative" action shown with a placebo-controlled, double-blind randomized noncrossover trial [9]. The CLARINET Trial was a randomized placebo versus lanreotide-controlled double-blind study (cross=over design) that demonstrated clear antiproliferative action of lanreotide [10]. Lanreotide has been recently registered in the USA with specific indication as an antiproliferative drug for NETs.

In order to better understand the rationale for somatostatin analogs' use in both NETs diagnosis and therapy, it is necessary to briefly review the properties of the somatostatin analogs. The development of a synthetic analog for somatostatin (originally termed "somatotropin release-inhibiting factor, SRIF") began shortly after its isolation in 1973 [11]. The first analog such compound to become clinically available was octreotide (SMS 201–995) followed by lanreotide. The striking similarities between the two synthetic analogs can be appreciated in Fig. 20.2. As can be noted, both synthetic somatostatin analogs have achieved reproducing the biologically active portion of native somatostatin in the ringed amino acid residues (eight amino acids) without needing to synthetize the whole 1–14 residue native compound. Equally important is the maintenance of the lysine residue within the synthetic ring. Lysine is the purported binding unit to the somatostatin membrane receptor, sstr2 [12]. Another observation can be made from an exam of Fig. 20.2 is that the synthetic somatostatin analog tested and available for both diagnosis and therapy is a slightly modified octreotide. [Tyr(3)]-octreotide (TOC) represents the replacement of phenylalanine residue in position 3 with the tyrosine moiety. When the chelator, DOTA, is attached to TOC (DOTATOC), it can be labeled with the radiometal gallium-68 (^{68}Ga) for diagnosis and detection of sstr2 receptor avid NETs and Yttrium-90 (^{90}Y) or lutitium-177 (^{177}Lu) for therapy. As well, octreotate (TATE) is tyrosine(3)-octreotide but with an amidated form of threonine rather than threoninol. It is linked to the chelator, DOTA, and is labeled with ^{68}Ga for diagnosis and ^{90}Y or ^{177}Lu for therapy. Lanreotide has also been linked to a chelator and used for therapy with ^{177}Lu/^{90}Y, but the modified octreotide forms are now fully developed, and ^{68}Ga-DOTATE has been approved by the United States Food and Drug Administration for PET imaging of somatostatin receptor-positive tumors.

Two important works from JC Reubi helped to establish the predominate somatostatin subtype receptor 2 to be present on at least 80 % of all neuroendocrine tumors [13]. He also demonstrated the high affinity and specificity of the labeled synthetic analogs for the somatostatin receptor subtype 2. Table 20.1 has been

Fig. 20.2 Peptide structure of somatostatin and its congeners

Somatostatin and its congeners

Somatostatin
(P. Brazeau, et al.,
Science 1973)

Ala-Gly-Cys-Lys-Asn-Phe-Phe
Trp
Lys
Cys-Ser-Thr-Phe-Thr

Octreotide
(J. Pless, et al.)

Lanreotide
(D.H. Coy, et al.)

Dawn A. Wray &
M. Pedersen
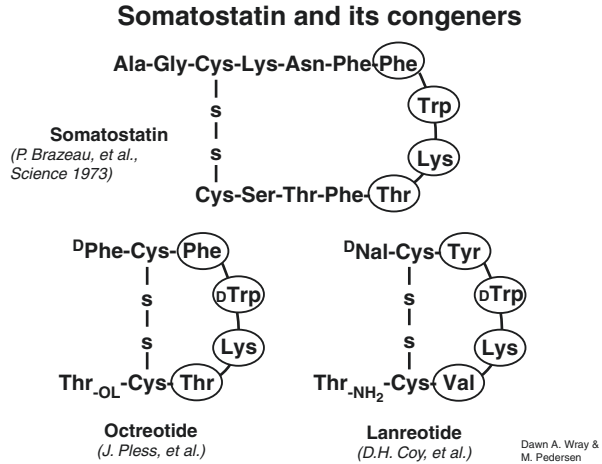
Table 20.1 Affinity profiles (IC50) of a series of somatostatin analogs to the subtypes of human somatostatin receptors (sstr2–5) modified from JC Reubi et al. [14]

Peptide	sstr2	sstr3	sstr4	sstr5
SS-28	2.7	7.7	5.6	4.0
Octreotide	2.0	187	>1000	22
DTPA-Octreotide	12	376	>1000	299
DOTATOC	14	27	>1000	103
^{68}Ga-DOTATOC	2.5	613	>1000	73
^{90}Y-DOTATOC	11	389	>10,000	114
DOTATATE	1.5	>1000	453	547
^{68}Ga-DOTATATE	0.2	>1000	300	377
^{90}Y-DOTATATE	1.6	>1000	523	187

modified from Reubi's work which compares the affinity profiles (IC50) of a series of synthetic somatostatin analogs to the subtypes of human somatostatin receptors, sstr2-5 [14]. The sstr1 responses have been deleted for clarity since all forms had IC50s greater than 10,000. Further, only the mean value for each analog for the respective receptor is shown, and the SDs were deleted for clarity. Cell lines were transfected with each somatostatin receptors. As can be noted, when compared to the IC50 of octreotide, the affinities of the synthetic analogs DOTATOC and DOTATATE were variously improved when radiolabeled with ^{68}Ga or [90]Y.

20.2 Peptide Receptor Radionuclide Therapy (PRRT): Rationale and Patient Selection

PRRT for NETs uses radiolabeled octreotide analogs to deliver targeted radiation to somatostatin receptor (primarily sstr2)-positive tumor tissue. Success of PRRT is based upon delivering high radiation dose to tumors while minimizing harmful

radiation effects to nontarget tissues. Achievement of a high therapeutic index requires selection of patients with disease with high expression of somatostatin receptor subtype 2 (sstr2) which binds the octreotide analog component of the radiolabeled PRRT compound [15]. Imaging with ^{111}In-DTPA-octreotide (Octreoscan®) or the ^{68}Ga-labeled octreotide analogs can gauge the degree of sstr2 expression in tumors and identify patients appropriate for PRRT [15]. Quantification of sstr2 expression by histology alone is limited to the site of the sample and may misgauge the sstr2 receptor expression at the remainder of disease sites [15].

PRRT agents are composed of a radionuclide bound to a somatostatin receptor analog by a chelator. Diethylenetriamine pentaacetic acid (DTPA) has been used as the chelator to label octreotide with ^{111}In; however, the current PRRT agents labeled with ^{90}Y and ^{177}Lu utilize 1,4,7,10-tetra-azacyclododecane-N,N',N'',N'''-tetra-acetic acid (DOTA) because of its improved stability of the radionuclide-peptide complex [16]. The stability of labeling is critical as free ^{177}Lu and ^{90}Y accumulate in the skeleton increasing radiation dose to the bone marrow [17]. Initial attempts in PRRT were performed with ^{111}In-DTPA-octreotide, which emits—in addition to gamma rays used for imaging—Auger and conversion electrons that have cytotoxic effects. These particles have tissue penetration of 0.02–10 μm and 200–500 μm, respectively [18]. Objective responses were rare with [111]In- DTPA-octreotide [19], which led to efforts in developing beta-emitter PRRT agents. Beta particles have higher energy and longer range tissue penetration, which increases cytotoxicity. [90]Y has tissue penetration of 11 mm, while ^{177}Lu has a shorter maximal tissue penetration of 2 mm. Although different somatostatin analogs have been developed for ^{90}Y and ^{177}Lu DOTA-chelated peptides, ^{90}Y-DOTATOC and ^{177}Lu-DOTATATE have emerged as the primary radiopharmaceuticals for PRRT for NETs.

Consensus guidelines for indications, preparation, administration, and follow-up for PRRT in NETs have been published [20]. PRRT is indicated for treatment of metastatic or inoperable NETs with positive expression of sstr2 [20]. After histologic confirmation of NET, candidacy for PRRT requires demonstration of the presence of sstr2 receptors on target tumors with somatostatin receptor imaging. As primary toxicities associated with PRRT are renal and bone marrow toxicity, poor renal function and inadequate bone marrow reserve are relative contraindications to PRRT. Given the more severe renal toxicity associated with ^{90}Y-DOTATOC, normal renal function is generally required for ^{90}Y-DOTATOC, whereas patients with mild/moderate renal impairment may be safely treated with [177]Lu [20]. The following hematological parameters are suggested prior to PRRT: white blood cell count >3000/μl, absolute neutrophil count >1000/μl, RBC >3,000,000/μl, platelets >75,000/μl for (^{177}Lu), and >90,000/μl for (^{90}Y) [20]. Patient with diffuse bone/bone marrow metastases should not be treated with ^{90}Y-DOTATOC but may be treated with ^{177}Lu-DOTATATE [21].

An amino acid co-infusion for renal radioprotection is now a standard practice for PRRT. The mechanism of action of amino acid infusion will be discussed later in the chapter. The recommended amino acids are lysine and/or arginine diluted in large volumes of saline, typically 25 g of amino acid in 1 L of normal saline with the large saline volume used for protection against electrolyte disturbances. A minimum of 50 g of arginine and/or lysine (typically given as 25 g of lysine and 25 g of

arginine) should be administered, and the amino acid infusion needs to be started 30–60 min prior to the administration of the radiopharmaceutical. Currently there is no commercially available preparation of an amino acid solution in the USA that contains only arginine and lysine; the commercially available amino acid solutions contain a multitude of amino acids with a significantly higher osmolarity, which is associated with a higher incidence of nausea and vomiting. The amino acid infusion takes approximately 4–6 h depending on the infusion rate. As the amino acid infusion is frequently accompanied by nausea and vomiting, antiemetic therapy (such as a 5-HT3 antagonist) should be given [20].

20.3 Efficacy of Peptide Receptor Radionuclide Therapy (PRRT)

20.3.1 ^{90}Y-DOTATOC

[^{90}Y-DOTA0,Tyr3]-octreotide (^{90}Y-DOTATOC) was the first beta-emitter PRRT agent. ^{90}Y is a pure β-emitter, with a maximum energy of 2.3 MeV and maximum range of 11 mm and a half-life of 64 h. The relatively long range of the β-particle of ^{90}Y allows for a bystander effect in heterogeneous tumors in which some cells may not express somatostatin receptors. ^{90}Y-DOTATOC is generally administered in fixed doses of 2.78–4.44 GBq every 6–12 weeks over 2–4 cycles [20]. ^{90}Y-DOTATOC has been investigated in several phase 1 and 2 studies; there are currently no randomized trials comparing ^{90}Y-DOTATOC with accepted standard therapy agents for NETs.

The largest study with ^{90}Y-DOTATOC in NETs was reported by Imhof et al. in 1109 patients with tumor progression in the preceding last 12 months prior to PRRT [22]. There were 821 patients with gastroenteropancreatic NETs, 185 patients had unknown primaries, and 103 with other less common NETs. Patients were treated with 3.7 GBq/m^2 per cycle, with additional treatment cycles administered if they showed stable or improving disease at follow-up; additional treatment was withheld if they showed progression or permanent toxicity. Morphologic response (any change in tumor size) was observed in 34 % of patients, although complete response was only seen in 0.6 %. Drop in tumor markers was noted in 15 %, and clinical response (improvement in symptoms and/or weight gain) was observed in 60 % of patients. Overall median survival after ^{90}Y-DOTATOC PRRT was 94.6 months, which was 2.9 times longer than historic data for metastatic NETs treated with other modalities [22]. The efficacy of ^{90}Y-DOTATOC in advanced NETs was also reported in two multicenter studies [23, 24]. The first study was a phase 1 study that included 58 patients, 47 of them with progressive disease, who were treated with a wide range of cumulative doses between 1.7 and 32.8 GBq of ^{90}Y-DOTATOC. There were no complete responses in this group; partial or minimal response was seen in 21 %, and stable disease was reported in 45 % of the patients who initially presented with progression. Symptomatic response was observed in 57 % of patients [24]. In another multicenter phase 2

study, Bushnell et al. reported the results of 90 patients with symptomatic carcinoid tumor treated with 4.4 GBq of ^{90}Y-DOTATOC, every 6 weeks over 3 cycles. Although only 4 % showed a partial response (no complete response) and 70 % had stable disease after therapy, 51–60 % of patients reported durable improvement in carcinoid symptoms including diarrhea, flushing, and abdominal pain, with an average length of symptomatic response between 8 and 12 weeks [23]. These studies along with other single-center studies show that ^{90}Y-DOTATOC therapy may provide objective disease control by stabilizing patients with progressive disease, however, rarely leads to complete or partial responses. ^{90}Y-DOTATOC therapy provides durable symptomatic relief in majority of patients and may also improve overall survival. The response to PRRT is generally worse in patients with higher tumor burden in the liver, more advanced disease, and higher grade NETs [25]. In children and young adults, a phase 1 study in 17 patients with a variety of somatostatin receptor-positive tumors including neuroblastoma, NETs, and brain tumors, PRRT with ^{90}Y-DOTATOC was safe without dose-limiting toxicities and an overall response rate of 41 % [26].

20.3.2 *[177]Lu-DOTATATE*

[177]Lu-[DOTA[0],Tyr[3]] octreotate (^{177}Lu-DOTATATE) is both a β-emitter and γ-emitter. The [177]Lu β particles have maximum energy of 0.5 MeV and maximum range of 2 mm and a half-life of 6.7 days. The lower β particle energy as compared with ^{90}Y improves irradiation of smaller-size tumors [16]. [177]Lu also emits γ-rays of energy 208 and 113 keV with relative abundance of 10 % and 6 %, respectively, which allows for imaging and dosimetry in addition to therapy [16]. Similar to ^{90}Y-DOTATOC, standard protocols for ^{177}Lu-DOTATATE therapy follow a fractionated fixed dosing regimen consisting of 3–5 cycles with a per cycle dose of 5.55–7.4 GBq [20]. Per cycle activity is reduced if dosimetry indicates radiation dose to the kidneys exceeding 23 Gy [27]. In addition to several phase 1 and 2 non-randomized/non-controlled trials, early data is now available for ^{177}Lu-DOTATATE from the first prospective randomized/controlled phase 3 trial (NETTER-1), the first of its kind for a PRRT agent. The experience of several of the largest studies and the preliminary data from the NETTER-1 clinical trial are summarized.

The largest prospective study to date reported phase 2 efficacy results for ^{177}Lu-DOTATATE in 310 patients with various types of GEP-NETs (carcinoid $n = 188$, nonfunctional pancreatic $n = 72$, unknown origin $n = 31$, gastrinoma $n = 12$, insulinoma $n = 5$, VIPoma $n = 2$), 43 % of them with disease progression prior to therapy. Overall objective tumor response rate was 46 %, including complete response (CR) in 2 %, partial response (PR) in 28 %, and minor response (MR) in 16 %. Median overall survival (OS) from the start of treatment was 46 months [27]. The pancreatic NET subgroup was the focus of two recent studies. In a prospective phase 2 trial of 52 patients with pancreatic NETs, where 26 patients received 27.8 GBq and 26 received 18.5 GBq, the high-dose cohort showed a complete

response of 12 %, partial response of 27 %, and stable disease of 46 %, compared to 4 %, 15 %, and 58 %, respectively, for the low-dose group [28]. Another retrospective analysis of 68 patients with pancreatic NETs showed comparable results with overall disease control rate of 85 % in patients with baseline progression [29]. ^{177}Lu-DOTATE was also effective in small-bowel NETs with an overall objective disease control rate of 91.8 % (PR and SD) [30]. Another study in 265 patients also demonstrated the symptomatic improvement after PRRT, with improvement in pain, nausea/vomiting, and diarrhea, observed in 53–70 % of patients regardless of the objective disease outcome [31]. In two pilot studies of pediatric patients, treatment with ^{177}Lu-DOTATE has shown objective responses in children with refractory neuroblastoma [32, 33].

The NETTER-1 study is the first phase 3 multicenter stratified randomized controlled trial of PRRT with parallel group design comparing ^{177}Lu-DOTATATE with octreotide LAR (Sandostatin® LAR Depot). The study evaluated 230 patients with inoperable progressive metastatic somatostatin receptor-positive grade 1–2 midgut NETs. Patients were randomized to either PRRT plus supportive octreotide (^{177}Lu-DOTATATE 7.4 GBq every 8 weeks for four total administrations with 30 mg Sandostatin® LAR every 4 weeks) versus octreotide alone (Sandostatin® LAR 60 mg every 4 weeks). At the time of this writing, results (abstract only) showed statistically significant favorable results for the intent-to-treat (ITT) arm including longer progression-free survival (median not reached for ITT versus 8.4 months for control) and larger objective radiographic complete and partial response rate (18 % versus 3 %). Overall survival data could not be definitively evaluated at the time of this writing, but early analysis suggests a possible improvement in survival for ITT group. The safety profile for ^{177}Lu-DOTATATE was favorable with dose-modifying toxicity occurring in only 5 % and grade 3 or 4 hematologic toxicity occurring in 9 % versus none of the controls [34, 35].

In summary, similar to ^{90}Y-DOTATOC, ^{177}Lu-DOTATATE is highly effective in achieving disease control, albeit with few partial/complete responses, and provides symptomatic relief. It improves progression-free survival compared to the standard therapy with octreotide. There are no randomized trials comparing ^{90}Y-DOTATOC with ^{177}Lu-DOTATATE in patients with neuroendocrine tumors. The reader is directed to a tabular summary of study results with both radiopharmaceuticals in the excellent review paper by Bodei et al. 2016 [25].

20.4   Toxicity from PRRT

PRRT labeled with ^{90}Y and ^{177}Lu has been proven to be generally safe and well tolerated. The most common adverse effect during administration of PRRT is acute mild-moderate nausea (25–80 %) and less often vomiting (10 %) relating to coadministration of amino acids [27, 36]. Hormonal crisis occurs in about 1 % of patients receiving PRRT [37]. Although the mechanism of hormonal crisis is not well understood, manipulation of the tumor as with PRRT, chemotherapy, induction of

anesthesia, surgery, or endoscopy can result in a sudden large release of metabolically active compounds [37]. Symptoms of hormonal excess include severe flushing, hypotension, blood pressure fluctuation, bronchoconstriction, and arrhythmia [37, 38]. These patients may benefit from subcutaneous or IV octreotide administration.

Long-term moderate and severe adverse effects are uncommon. Renal and hematologic toxicity represent the two major long-term potential adverse effects associated with PRRT. For many radiotherapies, marrow is the dose-limiting organ; however, for [90]Y- and ^{177}Lu-labeled PRRT agents, the kidneys are the critical dose-limiting organs as these agents are primarily cleared through the kidneys [39–41]. These radiolabeled small peptides are first filtered through the glomeruli, and because of their relatively small size (<70 kDa) are reabsorbed through the proximal tubules, a process mediated by the membrane protein megalin [40, 42]. Renal parenchymal retention of radiolabeled peptides increases radiation dose to the kidneys and can transiently and permanently degrade renal function and even lead to end-stage renal disease [43, 44]. Renal biopsies in patients with chronic renal failure after ^{90}Y PRRT therapy showed thrombotic microangiopathy as a cause of renal dysfunction [45].

Rates of renal failure after PRRT are low, especially when kidney dosimetry and amino acid administration are followed. In a retrospective series of 807 patients receiving various combinations of ^{90}Y-octreotide or ^{177}Lu-octreotate, nephrotoxicity of any grade and duration occurred in 34.6 %, although severe nephropathy (grade 3 or 4) was only noted in 1.5 % of patients, occurring only in the patients receiving ^{90}Y-DOTATOC [46]. In a prospective series of 1109 patients receiving ^{90}Y-DOTATOC, the nephrotoxicity was higher with 9.2 % of developed grade 4 or 5 permanent renal toxicity; the relatively higher administered activity of ^{90}Y-DOTATOC in this study per cycle, at $3.7 GBq/m^2$ per cycle, may have contributed to the relatively higher incidence of toxicity in this group [22]. In a series of 504 patients receiving ^{177}Lu-DOTATATE, no renal toxicity attributable to the therapy was observed [27]. Overall, ^{177}Lu-labeled PRRT shows lower rates of nephrotoxicity than ^{90}Y-labeled PRRT, which is likely due to the lower energy β particle emission of ^{177}Lu, which results in lower tissue penetration [16].

The maximum permissible cumulative absorbed dose to the kidney appears to be ~23–27 Gy [47, 48]. Coadministration of highly concentrated amino acids with PRRT has long been recognized as a method of reducing renal radiation dose and toxicity by competitively blocking the renal tubular reabsorption and retention of the radiolabeled peptides, resulting in a renal absorbed dose reduction of 9–53 % [39, 47, 49, 50]. The positively charged amino acids D-lysine and L-arginine have been particularly effective [47, 49, 51]. Amino acid administration is responsible for the most frequently encountered acute side effects of PRRT. Rates of gastrointestinal toxicity following amino acid infusion have ranged from 25 to 69 % depending on the infusion protocol, with higher infusion rates associated with more nausea/vomiting [27, 47]. These symptoms have been attributed to the level of osmolarity and, in particular, to the arginine component of the solution [47]. The nausea and vomiting can be successfully controlled with antiemetics [25, 27]. Another potential

Table 20.2 Grade 3–4 renal toxicity after PRRT

Grade 3–4 renal toxicity				
		PRRT	Patients	
Imhof et al. (2011) [22]	Prospective	^{90}Y-DOTATOC	$n = 1{,}109$	9.2 %
Bodei et al. (2015) [46]	Retrospective	^{177}Lu-DOTATE; ^{177}Lu-DOTATATE +^{90}Y-DOTATOC; ^{90}Y-DOTATOC	$n = 807$	1.5 %
Kwekkeboom et al. (2008) [27]	Prospective	^{177}Lu-DOTATATE	$n = 504$	None
Bodei et al. (2011) [54]	Prospective	^{177}Lu-DOTATATE	$n = 51$	None
Sabet et al. (2015) [30]	Retrospective	^{177}Lu-DOTATATE	$n = 61$	None
Ezzedin et al. (2014) [29]	Retrospective	^{177}Lu-DOTATATE	$n = 68$	None
Delpassand et al. (2014) [36]	Prospective	^{177}Lu-DOTATATE	$n = 32$	None

Note the absence of severe kidney toxicity after ^{177}Lu-DOTATATE only therapy

renoprotective agent is Gelofusine, which is a plasma tissue expander that has been shown to disrupt protein reabsorption in the kidneys, reducing renal radiation dose by 45 %, comparable to amino acid infusion [52]. A summary of studies reporting on severe renal toxicity is presented in Table 20.2.

Although serious long-term bone marrow toxicity is rare with PRRT, subacute and reversible Grade 3–4 bone marrow toxicity occurs in 10–13 % of patients [22, 46]. Evidence suggests marrow exposure is not related to sstr2 receptor uptake, but rather transchelation of the radiometal component of the radiopeptide to transferrin [53]. Imhof et al. (2011) in a prospective phase 2 study of 1109 patients receiving multiple cycles of ^{90}Y-DOTOTOC noted transient grade 3–4 hematologic toxicity in 12.8 % patients; follow-up was not sufficient to assess for long-term toxicity [22]. Bodei et al. in a retrospective study of 807 patients undergoing PRRT regimens with ^{177}Lu or ^{90}Y or combination of radiopharmaceuticals noted myelodysplastic syndrome and acute leukemia in 2.4 % and 1.1 % of patients, respectively [46].

Risk factors for the development of toxicity from PRRT have been sought as a measure for predicting outcomes from PRRT. Imhof et al. (2011) showed severe nephrotoxicity was associated with older age, low baseline glomerular filtration rate, and high kidney uptake score [22]. Bodei et al. (2015) identified several risk factors for the development of long-term renal and bone marrow toxicity. Long-term nephrotoxicity was associated more with ^{90}Y and ^{90}Y + ^{177}Lu than with ^{177}Lu alone (33.6 %, 25.5 %, and 13.4 %, respectively); hypertension and hemoglobin toxicity; other nephrotoxic drug exposure; and shorter duration of PRRT from first to last cycle. Long-term hematologic toxicity was associated with platelet toxicity grade and longer duration of PRRT. Despite known variables relating to adverse effects on kidneys and marrow, in the analysis of Bodei et al. (2015),

these factors predicted only a minority of such cases of toxicity (<30 %), which points to some as yet unidentified factors, possibly genetic, underlying adverse effects from PRRT [46].

In summary, long-term serious side effects of nephrotoxicity and hematotoxicity from PRRT are overall rare. ^{177}Lu-labeled agents generally show lower rates of nephrotoxicity than ^{90}Y, likely due to lower energy and penetration of its β particle. Radioprotection of the kidneys by amino acid infusion is standard practice. Acute side effects relating to nausea and vomiting secondary to the amino acid administration are common and can be managed with antiemetics.

20.5 Approaches to Improve the Efficacy of PRRT

20.5.1 Combination of Radiopharmaceuticals

The combination therapy with [90]Y- and ^{177}Lu-labeled DOTA-octreotide analogs uses the different penetration range of the beta particles of both isotopes (max range of 11 mm for ^{90}Y versus 2 mm for ^{177}Lu) to allow targeting of tumors of variable sizes. [177]Lu with its shorter range will be more effective than ^{90}Y for smaller lesions (as a significant portion of the energy of ^{90}Y radiation will be deposited outside the tumors), whereas ^{90}Y will deposit a higher radiation dose to larger tumors (which may be outside the range of ^{177}Lu beta particles). [177]Lu and ^{90}Y therapies have been given simultaneously or in sequence. In a prospective study by Kunikowska et al., 50 patients were randomized to receive either ^{90}Y-DOTATATE or a *combined dose* of ^{90}Y/^{177}Lu-DOTATATE (1:1 ratio) with an administered activity of 3.7 GBq/m^2 per cycle over 3–5 cycles [55]. This study found a significantly better survival in patients treated with the combination therapy, with a probability of a 24-month survival of 62 % in the group treated with ^{90}Y-DOTATATE versus 89 % in those treated with ^{90}Y/^{177}Lu-DOTATATE. In another cohort study, Villard et al. treated 237 patients with ^{90}Y-DOTATOC and 249 patients with *alternating* cycles of ^{90}Y-DOTATOC and ^{177}Lu-DOTATATE and found a significantly better survival in the combination group versus the monotherapy group (median survival of 66.1 months versus 47.5 months) [56]. There was no significant difference in renal or bone marrow toxicity between the monotherapy and combination therapy group.

20.5.2 PRRT Combined with Chemotherapy

Chemotherapeutic radiosensitizers may increase the efficacy of PRRT. Claringbold and colleagues from Australia have reported the results of several phase 1–2 studies that combine ^{177}Lu-DOTATATE with capecitabine or with a combination of capecitabine and temozolomide in patients with advanced neuroendocrine tumors

[57–60]. In their initial study of 33 patients who received PRRT along with capecitabine, the objective response rate was 24 % with a tumor control rate of 94 % achieved in patients with progressive disease [57]. As the combination of capecitabine and temozolomide (CAPTEM) is used increasingly as first-line che- motherapy regimen for metastatic NETs [61, 62], more recent studies have explored the combination of CAPTEM with PRRT. In 30 patients with progressive pancreatic neuroendocrine tumors treated with ^{177}Lu-octreotate combined with 14 days of capecitabine (at 1,500 mg/m^2) and 5 days of temozolomide (at 200 mg/m^2), the overall response rate was 80 %, with complete remission reported in 13 % and par- tial response in 70 % of the cases. These higher response rates compared to the historical results with monotherapy PRRT did also not come at the expense of higher rate of adverse events [59]. The long-term safety of the CAPTEM and ^{177}Lu-DOTATATE was also demonstrated by Kesavan et al. in 65 patients, who did not demonstrate any significant increase in hematological toxicity over a 5-year period with the combination therapy compared to what would be expected from monotherapy with ^{177}Lu-DOTATATE [60].

20.5.3   Intra-arterial PRRT of Liver Metastases

The delivery of the radiopeptide into the liver metastases may be improved through direct intra-arterial administration. This concept was demonstrated by Kratochwil et al. by the comparison of Ga-68 DOTATOC uptake in liver metastases after intra- venous and intra-arterial administration, which demonstrated an average of 3.75- fold increase in uptake after intra-arterial injection [63]. Although the translatability of this observation to therapeutic radiopeptides has been questioned by other inves- tigators due to differences in binding affinity of the radiopharmaceuticals [64], two pilot treatment studies reported promising results with intra-arterial administration of ^{90}Y-DOTA-lanreotide and ^{90}Y-DOTATOC for hepatic metastases, with partial response rates of 16 % and 53 %, respectively [65, 66].

20.5.4   Dosimetry-Based Therapy

PRRT with ^{90}Y-DOTATOC and ^{177}Lu-DOTATATE is typically administered in fixed doses. These doses are established to provide a high likelihood of tumor effect and low likelihood for renal and bone marrow toxicity, the dose-limiting organs for PRRT. The renal and bone marrow doses are, however, highly variable among the patients. With individual dosimetry, personalized treatment doses can be established to ensure that total renal doses do not exceed 23–27 Gy, and the bone marrow dose does not exceed 2 Gy, the generally accepted thresholds for organ toxicity [67, 68]. This concept is supported by the findings of dose-dependent radiation

nephrotoxicity with ⁹⁰Y-DOTATOC therapy [67] and the positive correlation demonstrated between tumor shrinkage and radiation dose to the tumor with PRRT [69]. The dosimetry protocol for PRRT depends on the radiopeptide used for therapy. ¹⁷⁷Lu-DOTATATE due to its gamma emissions can be used for pre-therapy dosimetry of the same therapeutic agent. For treatment with ⁹⁰Y-DOTATOC, ⁸⁶Y-DOTATOC PET-CT imaging is ideal for pre-therapy dosimetry; however, the cost and limited availability of ⁸⁶Y limit its routine use. The widely available ¹¹¹In-octreotide is used as a surrogate for dosimetry of ⁹⁰Y-DOTATOC; however, the significantly different binding affinity of ¹¹¹In-octreotide leads to overestimation of kidney dose and underestimation of normal liver dose [41]. Another important consideration for pretherapeutic dosimetry is the need to administer the amino acid solution to avoid overestimation of the kidney dose; however, this can cause significant nausea and vomiting as previously discussed. The widespread adaptation of dosimetry has been also hampered by the need of multiple patient visits and limited availability of expertise. Studies demonstrating the improved outcome in terms of toxicity and tumor response with the dosimetric approach would justify this complex but personalized approach to PRRT.

20.5.5 *Use of Somatostatin Receptor Antagonists*

Somatostatin receptor antagonists, unlike the agonists, are not internalized after binding to somatostatin receptors. However, antagonists appear to have significantly higher binding affinity for somatostatin receptors allowing a higher radiation dose delivery in pilot studies [70–72]. In *in vitro* samples of NET tissues, Cescato et al. found approximately four times higher binding affinity for the sstr2 by the antagonist, ¹⁷⁷Lu DOTA-BASS, compared to ¹⁷⁷Lu-DOTATATE [70]. More recently, a newer generation antagonist with higher receptor affinity, ¹⁷⁷Lu-DOTA-JR1, was investigated in a pilot treatment study of four patients with advanced NETs [72]. In all four patients, ¹⁷⁷Lu-DOTA-JR11 demonstrated a higher tumoral uptake and longer tumor residence time compared to ¹⁷⁷Lu-DOTATATE resulting in a 1.1–7.2 times higher tumor-to-kidney and tumor-to-bone marrow dose [72].

20.5.6 *Alpha Emitters*

Alpha emitters have a higher linear energy transfer and shorter path length than beta emitters. This leads to a significantly higher radiation dose delivery to the tumor cells expressing somatostatin receptors and lower dose to adjacent normal tissue. Nayak et al. demonstrated in human adenocarcinoma cell lines 3.4 times higher relative biologic effectiveness for an alpha emitter, ²¹³Bi-DOTATOC, as compared to ¹⁷⁷Lu-DOTATOC [73]. In a pilot study of seven patients who previously failed

treatment with beta-emitter PRRT, *intra-arterial* therapy with [213]Bi-DOTATOC for liver metastases ($n=6$) and intravenous therapy for bone marrow metastases ($n=1$) produced durable responses with acceptable toxicity [74].

References

1. Bjorklund P, Pacak K, Crona J. Precision medicine in pheochromocytoma and paraganglioma: current and future concepts. J Intern Med. 2016.
2. Janssen I, Chen CC, Taïeb D, et al. 68Ga-DOTATATE PET/CT in the localization of head and neck paragangliomas compared with other functional imaging modalities and CT/MRI. J Nucl Med Off Pub, Soc Nucl Med. 2016;57:186–91.
3. Yao JC, Hassan M, Phan A, et al. One hundred years after "carcinoid": epidemiology of and prognostic factors for neuroendocrine tumors in 35,825 cases in the United States. J Clin Oncol. 2008;26:3063–72.
4. Navalkele P, O'Dorisio MS, O'Dorisio TM, Zamba GK, Lynch CF. Incidence, survival, and prevalence of neuroendocrine tumors versus neuroblastoma in children and young adults: nine standard SEER registries, 1975–2006. Pediatr Blood Cancer. 2011;56:50–7.
5. Modlin IM, Oberg K, Chung DC, et al. Gastroenteropancreatic neuroendocrine tumours. Lancet Oncol. 2008;9:61–72.
6. Boyar Cetinkaya R, Aagnes B, Thiis-Evensen E, Tretli S, Bergestuen DS, Hansen S. Trends in Incidence of Neuroendocrine Neoplasms in Norway: A Report of 16,075 Cases from 1993 through 2010. Neuroendocrinology. 2015 Nov 13. [Epub ahead of print]
7. Merola E, Rinzivillo M, Cicchese N, Capurso G, Panzuto F, Delle Fave G. Digestive neuroendocrine neoplasms: a 2016 overview. Dig Liver Dis Off J Ital Soc Gastroenterol Ital Assoc Stud Liver. 2016.
8. O'Dorisio TM, Anthony LB. A 25-year experience of gastroenteropancreatic neuroendocrine tumors and somatostatin (congeners) analogs: from symptom control to antineoplastic therapy. Front Horm Res. 2015;44:177–92.
9. Rinke A, Muller HH, Schade-Brittinger C, et al. Placebo-controlled, double-blind, prospective, randomized study on the effect of octreotide LAR in the control of tumor growth in patients with metastatic neuroendocrine midgut tumors: a report from the PROMID Study Group. J Clin Oncol. 2009;27:4656–63.
10. Caplin ME, Pavel M, Cwikla JB, et al. Lanreotide in metastatic enteropancreatic neuroendocrine tumors. N Engl J Med. 2014;371:224–33.
11. Brazeau P, Vale W, Burgus R, et al. Hypothalamic polypeptide that inhibits the secretion of immunoreactive pituitary growth hormone. Science. 1973;179:77–9.
12. Patel YC, Srikant CB. Subtype selectivity of peptide analogs for all five cloned human somatostatin receptors (hsstr 1–5). Endocrinology. 1994;135:2814–7.
13. Reubi JC, Maurer R, von Werder K, Torhorst J, Klijn JG, Lamberts SW. Somatostatin receptors in human endocrine tumors. Cancer Res. 1987;47:551–8.
14. Reubi JC, Schar JC, Waser B, et al. Affinity profiles for human somatostatin receptor subtypes SST1-SST5 of somatostatin radiotracers selected for scintigraphic and radiotherapeutic use. Eur J Nucl Med. 2000;27:273–82.
15. Bodei LF D, Grana CM, Cremonesi M, et al. Peptide receptor therapies in neuroendocrine tumors. J Endocrinol Invest. 2009;32:360–9.
16. Kam BL, Teunissen JJ, Krenning EP, et al. Lutetium-labelled peptides for therapy of neuroendocrine tumours. Eur J Nucl Med Mol Imaging. 2012;39 Suppl 1:S103–12.
17. Breeman W, De jong M, de blois E, Bernard B, de Jong M, Krenning E. Reduction of skeletal accumulation of radioactivity by co-injection of DTPA in [90Y-DOTA0, Tyr3]octreotide solutions containing free 90Y3+. Nucl Med Biol. 2004;31:821–4.

18. Krenning EP, Kooij PP, Bakker WH, Breeman WAP et al. Radiotherapy with a radiolabeled somatostatin analogue, [111In-DTPA-D-Phe1]-octreotide. A case history. Ann N Y Acad Sci 1994;733:496–506.

19. Valkema R, De Jong M, Bakker WH, et al. Phase I study of peptide receptor radionuclide therapy with [in-DTPA]octreotide: the Rotterdam experience. Semin Nucl Med. 2002;32:110–22.

20. Zaknun JJ, Bodei L, Mueller-Brand J, et al. The joint IAEA, EANM, and SNMMI practical guidance on peptide receptor radionuclide therapy (PRRNT) in neuroendocrine tumours. Eur J Nucl Med Mol Imaging. 2013;40:800–16.

21. Basu S, Ranade R, Thapa P. Metastatic neuroendocrine tumor with extensive bone marrow involvement at diagnosis: evaluation of response and hematological toxicity profile of PRRT with (177)Lu-DOTATATE. World J Nucl Med. 2016;15:38–43.

22. Imhof A, Brunner P, Marincek N, et al. Response, survival, and long-term toxicity after therapy with the radiolabeled somatostatin analogue [90Y-DOTA]-TOC in metastasized neuroendocrine cancers. J Clin Oncol Off J Am Soc Clin Oncol. 2011;29:2416–23.

23. Bushnell Jr DL, O'Dorisio TM, O'Dorisio MS, et al. 90Y-edotreotide for metastatic carcinoid refractory to octreotide. J Clin Oncol Off J Am Soc Clin Oncol. 2010;28:1652–9.

24. Valkema R, Pauwels S, Kvols LK, et al. Survival and response after peptide receptor radionuclide therapy with [90Y-DOTA0, Tyr3]octreotide in patients with advanced gastroenteropancreatic neuroendocrine tumors. Semin Nucl Med. 2006;36:147–56.

25. Bodei L, Kwekkeboom DJ, Kidd M, Modlin IM, Krenning EP. Radiolabeled somatostatin analogue therapy of gastroenteropancreatic cancer. Semin Nucl Med. 2016;46:225–38.

26. Menda Y, O'Dorisio MS, Kao S, et al. Phase I trial of 90Y-DOTATOC therapy in children and young adults with refractory solid tumors that express somatostatin receptors. J Nucl Med Off Pub, Soc Nucl Med. 2010;51:1524–31.

27. Kwekkeboom DJ, de Herder WW, Kam BL, et al. Treatment with the radiolabeled somatostatin analog [177 Lu-DOTA 0,Tyr3]octreotate: toxicity, efficacy, and survival. J Clin Oncol Off J Am Soc Clin Oncol. 2008;26:2124–30.

28. Sansovini M, Severi S, Ambrosetti A, et al. Treatment with the radiolabelled somatostatin analog Lu-DOTATATE for advanced pancreatic neuroendocrine tumors. Neuroendocrinology. 2013;97:347–54.

29. Ezziddin S, Khalaf F, Vanezi M, et al. Outcome of peptide receptor radionuclide therapy with 177Lu-octreotate in advanced grade 1/2 pancreatic neuroendocrine tumours. Eur J Nucl Med Mol Imaging. 2014;41:925–33.

30. Sabet A, Dautzenberg K, Haslerud T, et al. Specific efficacy of peptide receptor radionuclide therapy with (177)Lu-octreotate in advanced neuroendocrine tumours of the small intestine. Eur J Nucl Med Mol Imaging. 2015;42:1238–46.

31. Khan S, Krenning E, Van Essen M, Kam BL, Teunissen JJ, Kwekkeboom DJ. Quality of life in 265 patients with gastroenteropancreatic or bronchial neuroendocrine tumors treated with [177Lu-DOTA0, Tyr3]octreotate. J Nucl Med. 2011;52:1361–8.

32. Kong G, Hofman MS, Murray WK, et al. Initial experience with gallium-68 DOTA-octreotate PET/CT and peptide receptor radionuclide therapy for pediatric patients with refractory metastatic neuroblastoma. J Pediatr Hematol Oncol. 2016;38:87–96.

33. Gains JE, Bomanji JB, Fersht NL, et al. 177Lu-DOTATATE molecular radiotherapy for childhood neuroblastoma. J Nucl Med Off Pub, Soc Nucl Med. 2011;52:1041–7.

34. Strosberg J, Wolin E, Chasen B, et al. NETTER-1 phase III: Efficacy and safety results in patients with midgut neuroendocrine tumors treated with 177-Lu-DOTATATE. J Clin Oncol. (Meeting Abstracts). 2016;34:suppl 4005.

35. Strosberg J, Wolin E, Chasen B, et al. NETTER-1 phase III: Progression-free survival, radiographic response, and preliminary overall survival results in patients with midgut neuroendocrine tumors treated with 177-Lu-DOTATE. J Clin Oncol. (Meeting Abstracts). 2016;34:suppl 194.

36. Delpassand E, Samarghandi A, Zamanian S, et al. Peptide receptor radionuclide therapy with 177-Lu-DOTATATE for patients with somatostatin receptor-expressing neuroendocrine tumors: The first US phase 2 experience. Pancreas. 2014;43:518–25.

37. de Keizer B, van Aken MO, Feelders RA, et al. Hormonal crises following receptor radionuclide therapy with the radiolabeled somatostatin analogue [177Lu-DOTA0, Tyr3]octreotate. Eur J Nucl Med Mol Imaging. 2008;35:749–55.

38. Lips C, Lentjes E, Hoppener J. The spectrum of carcinoid tumours and carcinoid syndromes. Ann Clin Biochem. 2003;40.

39. de Jong M, Krenning E. New advances in peptide receptor radionuclide therapy. J Nucl Med Off Pub, Soc Nucl Med. 2002;43:617–20.

40. Vegt E, de Jong M, Wetzels JF, et al. Renal toxicity of radiolabeled peptides and antibody fragments: mechanisms, impact on radionuclide therapy, and strategies for prevention. J Nucl Med Off Pub, Soc Nucl Med. 2010;51:1049–58.

41. Helisch A, Forster GJ, Reber H, et al. Pre-therapeutic dosimetry and biodistribution of 86Y-DOTA-Phe1-Tyr3-octreotide versus 111In-pentetreotide in patients with advanced neuroendocrine tumours. Eur J Nucl Med Mol Imaging. 2004;31:1386–92.

42. Vegt E, Melis M, Eek A, et al. Renal uptake of different radiolabelled peptides is mediated by megalin: SPECT and biodistribution studies in megalin-deficient mice. Eur J Nucl Med Mol Imaging. 2011;38:623–32.

43. Otte A, Herrmann R, Heppeler A, et al. Yttrium-90 DOTATOC: first clinical results. Eur J Nucl Med. 1999;26:1439–47.

44. Cybulla M, Weiner SM, Otte A. End-stage renal disease after treatment with 90Y-DOTATOC. Eur J Nucl Med. 2001;28:1552–4.

45. Moll S, Nickeleit V, Mueller-Brand J, Brunner FP, Maecke HR, Mihatsch MJ. A new cause of renal thrombotic microangiopathy: Yttrium 90-DOTATOC internal radiotherapy. Am J Kidney Dis. 2001;37:847–51.

46. Bodei L, Kidd M, Paganelli G, et al. Long-term tolerability of PRRT in 807 patients with neuroendocrine tumours: the value and limitations of clinical factors. Eur J Nucl Med Mol Imaging. 2015;42:5–19.

47. Bodei L, Cremonesi M, Zoboli S, et al. Receptor-mediated radionuclide therapy with 90Y-DOTATOC in association with amino acid infusion: a phase I study. Eur J Nucl Med Mol Imaging. 2003;30:207–16.

48. Cassady J. Clinical radiation nephropathy. Int J Radiat Oncol Biol Phys. 1995;31:1249–56.

49. Bernard B, Krenning E, Breeman W, Rolleman E, Bakker W. D-lysine reduction of indium-111 octreotide and yttrium-90 octreotide renal uptake. J Nucl Med Off Pub, Soc Nucl Med. 1997;38:1929–33.

50. Kwekkeboom DJ, Bakker WH, Kooij PP, et al. [177Lu-DOTA0, Tyr3]octreotate: comparison with [111In-DTPA0]octreotide in patients. Eur J Nucl Med. 2001;28:1319–25.

51. Hammond P, Wade A, Gwilliam M, et al. Amino acid infusion blocks renal tubular uptake of an indium-labelled somatostatin analogue. Br J Cancer. 1993;67:1437–9.

52. Vegt E, Wetzels J, Russel F, et al. Renal uptake of radiolabeled octreotide in human subjects is efficiently inhibited by succinylated gelatin. J Nucl Med Off Pub, Soc Nucl Med. 2006;47:432–6.

53. Walrand S, Barone R, Pauwels S, Jamar F. Experimental facts supporting a red marrow uptake due to radiometal transchelation in 90Y-DOTATOC therapy and relationship to the decrease of platelet counts. Eur J Nucl Med Mol Imaging. 2011;38:1270–80.

54. Bodei L, Cremonesi M, Grana CM, et al. Peptide receptor radionuclide therapy with (1)(7)(7)Lu-DOTATATE: the IEO phase I-II study. Eur J Nucl Med Mol Imaging. 2011;38:2125–35.

55. Kunikowska J, Krolicki L, Hubalewska-Dydejczyk A, Mikolajczak R, Sowa-Staszczak A, Pawlak D. Clinical results of radionuclide therapy of neuroendocrine tumours with 90Y-DOTATATE and tandem 90Y/177Lu-DOTATATE: which is a better therapy option? Eur J Nucl Med Mol Imaging. 2011;38:1788–97.

56. Villard L, Romer A, Marincek N, et al. Cohort study of somatostatin-based radiopeptide therapy with [(90)Y-DOTA]-TOC versus [(90)Y-DOTA]-TOC plus [(177)Lu-DOTA]-TOC in neuroendocrine cancers. J Clin Oncol Off J Am Soc Clin Oncol. 2012;30:1100–6.

57. Claringbold PG, Brayshaw PA, Price RA, Turner JH. Phase II study of radiopeptide 177Lu-octreotate and capecitabine therapy of progressive disseminated neuroendocrine tumours. Eur J Nucl Med Mol Imaging. 2011;38:302–11.

58. Claringbold PG, Price RA, Turner JH. Phase I-II study of radiopeptide 177Lu-octreotate in combination with capecitabine and temozolomide in advanced low-grade neuroendocrine tumors. Cancer Biother Radiopharm. 2012;27:561–9.

59. Claringbold PG, Turner JH. Pancreatic neuroendocrine tumor control: durable objective response to combination Lu-octreotate-capecitabine-temozolomide radiopeptide chemotherapy. Neuroendocrinology. 2015.

60. Kesavan M, Claringbold PG, Turner JH. Hematological toxicity of combined 177Lu-octreotate radiopeptide chemotherapy of gastroenteropancreatic neuroendocrine tumors in long-term follow-up. Neuroendocrinology. 2014;99:108–17.

61. Fine RL, Gulati AP, Krantz BA, et al. Capecitabine and temozolomide (CAPTEM) for metastatic, well-differentiated neuroendocrine cancers: The Pancreas Center at Columbia University experience. Cancer Chemother Pharmacol. 2013;71:663–70.

62. Strosberg JR, Fine RL, Choi J, et al. First-line chemotherapy with capecitabine and temozolomide in patients with metastatic pancreatic endocrine carcinomas. Cancer. 2011;117:268–75.

63. Kratochwil C, Giesel FL, Lopez-Benitez R, et al. Intraindividual comparison of selective arterial versus venous 68Ga-DOTATOC PET/CT in patients with gastroenteropancreatic neuroendocrine tumors. Clin Cancer Res. 2010;16:2899–905.

64. Brogsitter C, Faulhaber D, Kotzerke J. Intraarterial treatment of GEP NET: (68)Ga-DOTATOC SUV cannot predict (90)Y-DOTATOC uptake. Clin Cancer Res. 2011;17:2065.

65. Kratochwil C, Lopez-Benitez R, Mier W, et al. Hepatic arterial infusion enhances DOTATOC radiopeptide therapy in patients with neuroendocrine liver metastases. Endocr Relat Cancer. 2011;18:595–602.

66. McStay MK, Maudgil D, Williams M, et al. Large-volume liver metastases from neuroendocrine tumors: hepatic intraarterial 90Y-DOTA-lanreotide as effective palliative therapy. Radiology. 2005;237:718–26.

67. Barone R, Borson-Chazot F, Valkema R, et al. Patient-specific dosimetry in predicting renal toxicity with (90)Y-DOTATOC: relevance of kidney volume and dose rate in finding a dose-effect relationship. J Nucl Med: official publication, Society of Nuclear Medicine 2005;46 Suppl 1:99s–106s.

68. Chalkia MT, Stefanoyiannis AP, Chatziioannou SN, Round WH, Efstathopoulos EP, Nikiforidis GC. Patient-specific dosimetry in peptide receptor radionuclide therapy: a clinical review. Australas Phys Eng Sci Med. 2015;38:7–22.

69. Pauwels S, Barone R, Walrand S, et al. Practical dosimetry of peptide receptor radionuclide therapy with (90)Y-labeled somatostatin analogs. J Nucl Med Off Pub, Soc Nucl Med. 2005;46 Suppl 1:92S–8.

70. Cescato R, Waser B, Fani M, Reubi JC. Evaluation of 177Lu-DOTA-sst2 antagonist versus 177Lu-DOTA-sst2 agonist binding in human cancers in vitro. J Nucl Med Off Pub, Soc Nucl Med. 2011;52:1886–90.

71. Ginj M, Zhang H, Waser B, et al. Radiolabeled somatostatin receptor antagonists are preferable to agonists for in vivo peptide receptor targeting of tumors. Proc Natl Acad Sci U S A. 2006;103:16436–41.

72. Wild D, Fani M, Fischer R, et al. Comparison of somatostatin receptor agonist and antagonist for peptide receptor radionuclide therapy: a pilot study. J Nucl Med Off Pub, Soc Nucl Med. 2014;55:1248–52.

73. Nayak TK, Norenberg JP, Anderson TL, Prossnitz ER, Stabin MG, Atcher RW. Somatostatin-receptor-targeted alpha-emitting 213Bi is therapeutically more effective than beta(−)-emitting 177Lu in human pancreatic adenocarcinoma cells. Nucl Med Biol. 2007;34:185–93.

74. Kratochwil C, Giesel FL, Bruchertseifer F, et al. (2)(1)(3)Bi-DOTATOC receptor-targeted alpha-radionuclide therapy induces remission in neuroendocrine tumours refractory to beta radiation: a first-in-human experience. Eur J Nucl Med Mol Imaging. 2014;41:2106–19.

Chapter 21
Alpha Radionuclide Therapy: Principles and Applications to NETs

Jorge A. Carrasquillo

21.1 Introduction

Several radiopharmaceuticals have been used for the treatment of neuroendocrine tumors (NETs). One of the most established has been I-131 MIBG, which is used for treating carcinoids, pheochromocytoma/paraganglioma (PHEO/PARA), neuroblastoma, and other NETs. More recently, the use of radiolabeled somatostatin analogs has been established, including In-111 DTPA pentetreotide and Y-90 or Lu-177 DOTATOC, DOTATATE, DOTANOC, and other somatostatin analogs [1, 2]. In addition to these receptor-targeted agents, other radiopharmaceuticals based on affinity for bone matrix have been used occasionally. These include Sr-89 chloride, a bone-seeking radiopharmaceutical [3–7] and possibly Sm-153 EDTMP. An additional approach for the treatment of metastatic disease to the liver has been the use of radiolabeled Y-90 resin or glass microspheres that depend on local delivery via blood flow [8–10]. For all of the above reagents, the radionuclides' therapeutic emissions are beta particles, with the exception of In-111, an auger emitter.

In contrast to beta particles for therapeutic applications, there are significant advantages to using alpha emitters. The path length of alpha emitters is in the range of 50–100 microns compared to that of beta emitters, which is generally in the range of millimeters. Compared to the low linear energy transfer (LET) of beta emitters, alpha emitters have high LET. As a result, alpha emitters deposit much more energy along their path than beta emitters, resulting in greater biological effectiveness of the deposited radiation than seen with beta radiation. With alpha emitters, the generation of double-strand DNA breaks gives rise to cytotoxicity that is independent of dose rate, cell cycle growth phase, and oxygen concentration [11]. It has been

J.A. Carrasquillo, MD
Molecular Imaging and Therapy Service, Department of Radiology, Memorial Sloan Kettering Cancer Center, 1275 York Avenue, New York, NY 10065, USA
e-mail: carrasj1@mskcc.org

Table 21.1 Physical key properties of promising alpha-emitting radiopharmaceuticals

Radionuclide	T1/2 (h)	Emission	Energy deposited (MeV maximum)[a]	Source
Ra-223	273.6	4 Alpha 2 Beta 4 Gamma 2 X-ray	Alpha 5.6, 6.8, 7.4, (6.6 or 7.50) Beta 0.48, 0.50 Gamma, 0.154, and 0.270, 0.351 X-ray 0.81, 0.84	Th-227 decay chain
At-211	7.21	1 Alpha 0 Beta 0Gamma 2 X-ray	Alpha 5.86 or 7.45 Beta none Gamma none X-ray 0.077–0.079	Cyclotron Bi-209 (alpha, 2n)
Bi-212	1.01	1 Alpha 1or 3 Beta 3 Gamma	Alpha 6.05 or 8.8 Beta 0.83 or (0.44, 0.53, 0.65) Gamma (0.51, 0.58, 2.60, 0.86)	Th-228 decay chain. Ra-224 generator
Bi-213	0.76	1 Alpha 3 Beta 1 Gamma	Alpha 8.4 or 5.9 Beta 0.49, 0.32, 0.2 Gamma 0.440	Ac-225 decay chain
Ac-225	238	4 Alpha 3 Beta 2 Gamma	Alpha 5.8, 6.3, 7.1, (8.4 or 5.9) Beta 0.49, 0.32, 0.2 Gamma, 0.218, 0. 440	Th-229 decay chain or Ra-226 (p,2n) reaction
Pb-212	10.6	1 Alpha 2or 4 Beta 3 Gamma	Alpha 6.05 or 8.8 Beta 0.177 and 0.83 or (0.44,0.53, 0.65) Gamma (0.51, 0.58, 2.60, 0.86)	Th-228 decay chain

[a]Beta energy average MeV, only those gamma or beta greater than 10% included

shown that transversal of alpha particles through the nucleus and not the cell membrane or cytoplasm is related to induction of cell death [12]. According to estimates, as few as 1–20 alpha tracks crossing the nucleus will result in cell death [11], which is brought about through a number of mechanisms such as apoptosis, autophagy, necrosis, and mitotic catastrophe. A list of the most promising alpha emitters to date and their characteristic emissions is shown in Table 21.1.

Several clinical examples of therapeutic applications of alpha emitters exist, predominantly using antibodies as the targeting vehicle [13–16]. Radiolabeling methods to attach the various alpha emitters to radiopharmaceuticals have been described [17]. Ra-223 dichloride (formerly known as Alpharadin and more recently known as Xofigo™) is the only approved alpha emitter radiopharmaceutical to date [18]. While Ra-223 is only approved in the setting of metastatic prostate cancer, promising results have been reported in breast cancer [19, 20], and a single case report for a patient with metastatic paraganglioma has been published [21].

Although the clinical applications of alpha emitters in NETs are limited thus far, their feasibility and safety have been evaluated in diverse clinical studies. In this

chapter, we review the rationale for alpha emitters (see above); touch on some of the clinical trials in the non-NET literature, as they provide some preliminary feasibility and safety data for alpha-based radiopharmaceuticals that may be applicable to NETs; and discuss preclinical and, where available, clinical work with alpha emitters in NETs.

21.2   Application of Alpha Emitters in Cancer (Preclinical and Clinical)

21.2.1   Ac-225 and Bi-213

Ac-225 for clinical use is typically produced from Th-229 [22], although accelerator-based methods for Ac-225 production have been described. Ra-226 (p,2n) and Ac-225 are yet to be used clinically [23]. Bi-213 is normally obtained from an Ac-225/Bi-213 generator [24]. Scheinberg et al. from Memorial Sloan Kettering have been pioneers in the field of alpha therapy, performing the first radioimmunotherapy studies in humans using Bi-213 huM195 directed against CD33 in patients with acute myelocytic leukemia (AML) [25]. Bi-213 has predominantly been attached to antibodies via a chelator such as 1,4,7,10-tetraazacyclododecane-1,4,7,10-tetraacetic acid (DOTA), the same chelate used for attaching metals to somatostatin analogs. In clinical studies, activities ranging from 0.6 to 1.6 GBq were administered intravenously [15]. A clinical trial combining Bi-213 huM195 with cytarabine in patients with AML delivering activity ranging from 18.5 to 46.25 MBq/kg showed a maximum tolerated dose (MTD) of 37 MBq/kg due to myelosuppression. That study concluded that the combination of alpha-emitting radionuclide therapy with cytarabine was tolerable and could induce remission in patients with AML [25].

Bi-213 9.2.27 anti-melanoma monoclonal antibody has been used in patients with metastatic melanoma. Following intravenous administration of 46–925 MBq of the Bi-213 9.2.27 antibody, 38 patients were followed for response and toxicity. The MTD was not achieved and no adverse events occurred. An objective partial response rate of 10 % was observed, with 40 % stable disease at 8 weeks and a median survival of 8.9 months [26].

The utilization of intralesional delivery of Bi-213 with anti-melanoma 9.2.27 monoclonal antibody was well tolerated and induced tumor kill [27]. Furthermore, intra-tumoral injection of Bi-213 substance P in patients with brain gliomas (1.1–7.36 GBq) demonstrated proof of principle, with pathological evidence of tumor necrosis on resection and no relevant toxicity [28].

One disadvantage of Bi-213 is its short physical half-life of 0.76 h, making it logistically difficult to elute and label enough activity in a timely manner, thus requiring production on-site with an Ac-225/Bi-213 generator. To solve this problem, McDevitt and Scheinberg's group at MSKCC developed the concept of an

in vivo generator using Ac-225, a longer-lived alpha emitter that could be conjugated to antibody and results in the generation of multiple alpha particles in situ [29]. This longer-lived Ac-225 with a T1/2 of 240 h allows for the production of a radiopharmaceutical that can be shipped from a local manufacturing site to end users. Its use has been validated in preliminary phase I multicenter trials [13, 30] with Ac-225 lintuzumab (huM195) provided by a commercial manufacturer, Actinium Pharmaceuticals, Inc (www.actiniumpharma.com).

The use of Bi-213 DOTATOC in metastatic NETs to the liver has been reported [31]. The rationale for intra-arterial (IA) delivery is the superiority of IA hepatic administration of Ga-68 DOTATOC that resulted in a 3.7-fold higher intrahepatic tumor accumulation compared with IV infusion [32], consistent with significant first-pass extraction. Given the short T1/2 of Ga-68 DOTATOC, it was not clear how translatable this would be when a longer-lived radionuclide such as In-111, Lu-177, or Y-90 was utilized. Thus, in a subsequent study of a longer-lived In-111 DOTATOC, this group also showed tumor uptake immediately after IA that was four times greater than systemic administration, decreasing to 1.3 times greater at 72 h [33]. In 15 patients treated with IA somatostatin analogs of Lu-177 or Y-90 DOTATOC, a 7 % complete response (CR), 53 % partial response (PR), and 40 % stable liver metastasis were noted [33]. However, the pharmacokinetics of longer-lived isotopes showing a decrease in tumor uptake at 72 h compared to immediately post-infusion [33] suggest that short-lived radionuclides such as Bi-213-labeled somatostatin analogs are preferential compared to longer-lived isotopes when locally delivered to tumor, given that they would deliver their payload before significant release from tumor.

Animal studies with Bi-213 or Ac-225 somatostatin analogs have shown promising results in preclinical tumor models [34, 35]. Given the favorable preclinical data with Bi-213 DOTATOC, seven patients with NETs refractory to cold octreotide and Y-90/Lu-177 DOTATOC received compassionate use of Bi-213 DOTATOC IA [31]. An Ac-225/Bi-213 generator was used to obtain the Bi-213 [36]. The Bi-213 DOTATOC had radiochemical purity of 99.7 ± 0.3 %, and the specific activity was typically 80 MBq/nmol peptide at the time of injection. Injections were performed 15 ± 2 min after generator elution. Tumor concentration was demonstrated by planar and SPECT imaging of the 414 keV gamma ray of Bi-213. These patients received 1–5 treatment cycles (median 4.5) with single doses ranging from 3.3 to 10.5 GBq (median 7.1 GBq) and cumulative activities of 3.3 to 20.8 GBq (median 17.65 GBq). Enduring responses in liver metastasis were seen in all patients, and no evidence of tumor progression in the liver was noted by RECIST criteria during a follow-up period of 24–34 months, resulting in 1 CR, 2PR, and 3 SD. Response of extrahepatic disease was also noted in several patients. Hematopoietic toxicity was less than that observed in patients who had received Lu-177 or Y-90 DOTATOC. Grade 2 thrombocytopenia was seen in one patient, and no greater than Grade 1 thrombocytopenia was noted in other patients. Other hematologic toxicities were mild. One patient was diagnosed with MDS and AML at 2-year follow-up. The mean GFRs determined with Cr-51 EDTA were 115 ml/min, 101 ml/min, and 83 ml/min at baseline, 1 year post-therapy, and 2 years post-therapy, respectively. Only one of seven

patients had a serum creatinine of 1.5 times higher than the upper limit of normal (ULN). Notably, these patients had received prior peptide receptor radionuclide therapy, which on its own can contribute to a decrease in GFR. These preliminary results, which demonstrated tumor response at therapeutically effective doses with limited toxicity, are encouraging [31].

A preliminary dose escalation trial of Ac-225 DOTATOC has been reported in abstract form on the treatment of patients with progressive NETs. Thirty-six patients were administered 48 treatments of Ac-225 DOTATOC intravenously, with 17 patients receiving 2-year follow-up. The single MTD was 40 MBq. Alternative multiple fractions with 25 MBq every 4 months or 18.5 MBq every 2 months were delivered. A cumulative activity of 75 MBq was found tolerable with respect to delayed toxicity. Detailed response data was not provided, although radiologic treatment responses were observed in some patients [37].

21.2.2 Lead-212 (Pb-212)

Pb-212 is another alpha-emitting radionuclide that has undergone extensive preclinical work by Brechbiel et al. at the NIH [38] and some clinical evaluation. It can be obtained from a Ra-224 generator [39]. The clinical development of Pb-212 has been promoted by AREVA Med (http://www.arevamed.areva.com). Chelators utilized for binding Pb-212 include DOTA or 2-(4-isothiocyanotobenzyl)-1,4,7,10-tetraaza-1,4,7,10-tetra-(2-carbamoyl methyl)-cyclododecane (TCMC) chelates, with some advantage in the stability of the complex of Pb with TCMC [40]. Pb-212 has been conjugated to trastuzumab and used for intraperitoneal administration in patients with metastatic HER2-positive malignancy [41]. For clinical trials, the TCMC-chelated trastuzumab was radiolabeled on-site because of the short 10.6 h T1/2 of Pb-212. Patients were administered escalating doses of Pb-212 TCMC trastuzumab intraperitoneally at 7.4, 9.6, 12.6, 16.3, and 21.1 MBq/m2 after predosing with intravenous administration of trastuzumab at 4 mg/kg. This proof of principal study showed little toxicity, as expected, based on dosimetric estimates. Assessment of tumor response was difficult to evaluate in these patients with intraperitoneal disease [42].

21.2.3 Bi-212

Bismuth-212 is obtained from the decay chain of Th-228 using a generator system [39]. It has a half-life of 60.6 min and emits one of two alpha particles (Table 21.1). Part of its decay scheme also involves emission of a 2.6 MeV gamma ray that is difficult to shield and may pose radiation safety issues. Although some preclinical work has been performed with Bi-212-radiolabeled antibodies [43, 44], no preclinical studies in NET models or clinical studies have been performed. Preclinical work

with Bi-212 DOTPM, a bone-seeking radiopharmaceutical, has also been performed [45]. It appears that rather than Bi-212 development, the approach with the Bismuth radionuclide has gravitated to Bi-213 as previously discussed.

21.2.4 At-211

At-211 is a cyclotron-produced alpha emitter with a 7.2 h T1/2 [46]. Various pre-clinical trials have been performed with At-211-radiolabeled (1) antibodies [47–52], (2) MIBG analogs [53–55], and (3) octreotate analogs [56]. Zalutsky and his group have been pioneers in the use of At-211-labeled pharmaceuticals and methods for radiolabeling proteins [46, 50, 57].

At-211-labeled ch81C6 anti-tenascin antibody has been used clinically via intra-cavitary delivery in patients with primary recurrent supratentorial tumors that were candidates for resection. After gross resection of the tumor, a Rickham reservoir and catheter were placed within the surgical resection cavity (SCRC). The SCRC was then directly injected with 71–347 MBq of the At-211 ch81C6. Some Grade 2 neu-rologic toxicity was noted. The 2-year survival probability was 61 % and the median overall survival was 54.1 weeks [14]. Because At-211 is a halogen and accumulates in the thyroid, thyroid blocking is required due to the possible release of free At-211. Minimal toxicity was observed in these patients [14].

Another study with At-211-labeled MX35 F (ab) 2 in patients with ovarian can-cer used activity of 83–355 MBq delivered intraperitoneally. This study concluded that therapeutically effective amounts of i.p. therapy could be administered without causing any acute or deterministic radiation toxicities [52]. In this and other studies with At-211, gamma camera imaging has been performed to assess biodistribution and targeting [58].

Preclinical work has been done with octreotate derivatives that have been modi-fied with two prosthetic groups: one containing a carbohydrate unit and the other, a tin group-containing aryl moiety, both amenable to At-211 labeling [56]. Unfortunately, these derivatives have less than ideal tumor targeting and internaliza-tion, and clinical trials have not been performed.

Preclinical studies have also been performed with At-211-labeled analogs of MIBG. Norepinephrine transporters are overexpressed in neuroblastoma, PHEO/PARA, carcinoids, and other NETs. Iodine-labeled MIBG uptake is based on bind-ing to the norepinephrine transporter and has been used extensively for the imaging and therapy of these NETs [59–61]. Based on MIBG, Zalutsky et al. have developed various At-211-labeled analogs of MIBG with high affinity. The first reagent labeled was meta-[At-211] astatobenzylguanidine [49]. Following a technique used for the preparation of no-carrier-added MIBG, At-211 MABG has been prepared in good yields [49], and it behaves *in vitro* like MIBG with respect to its *in vitro* binding to SK-N-SH human neuroblastoma cells. Its tissue distribution in normal mice has been determined [62]. In clonogenic assays with the SK-N-SH human neuroblas-toma cell line, the inherent radiosensitivity, or Do value, of [At-211] MABG was

0.2 kBq/ml compared with 384 kBq/ml for no-carrier-added I-131 MIBG, indicating a more than 1,000-fold greater cytotoxicity for the alpha particle-emitting analog compared to I-131 MIBG under single-cell conditions [63]. A kit method for the synthesis of relatively high amounts of At-211 MABG in good radiochemical yields has been developed; this method is adaptable to a kit formulation, and the quality control characteristics of the final dose are consistent with those appropriate for clinical studies [54]. To date, however, no clinical trials have been performed with At-211-labeled MABG analogs.

21.3 Bone Metastasis: NETs and PHEO/PARA

Many cancers present or develop bone metastases, which can lead to adverse clinical sequelae including pain, fractures, spinal cord compression, bone marrow dysfunction, and hypercalcemia, known as skeletal-related events (SRE). These lead to significant morbidity, which impact performance status and patient quality of life.

Various NETs also frequently metastasize to the bone. In a report of 86 consecutive patients with carcinoid tumors that had metastasized to the liver, the frequency of bone metastasis was 10 % (9/86 patients) [64]. The median interval between diagnosis of metastatic carcinoid and bone metastasis was 37 months. In that report, they evaluated the use of bone scan, In-111 pentetreotide, and I-131 MIBG for detection. In all patients with metastatic bone disease, the disease was noted on the bone scan, whereas I-131 MIBG detected only two of nine patients with bone metastasis and In-111 pentetreotide detected only four of eight patients. Other reports have shown sensitivity for bone metastasis of 70 % for In-111 pentetreotide scintigraphy and 90 % for bone scintigraphy [65]. In contrast to In-111 pentetreotide, the sensitivity of newer Ga-68 somatostatin analogs has been much higher. In one study, Ga-68 DOTANOC PET/CT was able to identify more lesions than CT (246 vs. 194), resulting in higher sensitivity (100 % vs 80 %) and specificity (100 % vs. 98 %) [66]. Similarly, using Ga-68 DOTATOC PET/CT, the sensitivity for detection of skeletal metastases was 100 % compared to 58 % for CT [67]. This provides an opportunity for the use of somatostatin analogs such as DOTANOC, DOTATOC, and DOTATATE radiolabeled with an alpha emitter for targeting bone and soft tissue disease in NETs.

In an autopsy series of NETs, the incidence of bone metastases was much higher than recognized clinically, with an incidence of 42 % [68]. NETs and PHEO/PARA involving bone had a high incidence of SRE [69]. The most common SRE in PHEO/PARA was severe pain (33 %), followed by pathological fractures (27 %) and spinal cord compression (25 %). Median time from diagnosis to first bone metastasis to first SRE was 4.3 months. These SREs usually happened after the bone metastases were diagnosed, and SRE were often the first manifestation of malignant disease as well (31 %) [70]. FDG PET imaging was able to identify 95 % of skeletal metastases, allowing the use of this reagent for assessment of tumor response. In contrast, MIBG identified only 70 %; it is important to identify this group, which can then be

directed toward MIBG therapy. The exact incidence of bone-only metastatic disease has not been well determined. In a series of 15 patients with metastatic PHEO treated with I-131 MIBG, four patients had soft tissue disease only, and 4 had bone disease only [71].

Overall, most NET bone metastases are found to be osteoblastic [72, 73], which has implications for bone-seeking radionuclides, as they are more likely to localize in blastic bone lesions than in exclusively lytic lesions and in bone scan-positive rather than bone scan-negative disease. Given the incidence of metastatic bone disease that accumulates bone-seeking radiopharmaceutical in NETs, this should allow the use Ra-223 dichloride, which requires having a positive bone scan. In addition, PHEO/PARA have a high incidence of metastatic disease to the bone with up to 71 % incidence reported in a series of 137 malignant PHEO [70]. Most of the PHEO/PARA patients with metastatic disease have widespread bone metastases, which tend to be lytic. Nonetheless, PHEO/PARA bone metastases accumulate bone-seeking agents and thus are likely amenable to Ra-223 dichloride therapy [74].

21.3.1 Ra-223 Dichloride (Xofigo or Alpharadin)

Radium-223 dichloride (Ra-223) is a novel, bone-seeking calcium mimetic alpha emitter that accumulates in areas of increased bone turnover. It has been approved for the treatment of metastatic prostate cancer to the bone. Among its advantages are its availability from a long-lived actinium-227/thorium-227 generator [75] and a physical half-life of 11.4 days, which allows for easy shipping to end users with a long time between manufacturing and expiration. Similar to other alkaline earth elements such as calcium, Ra-223 is absorbed into bone matrix at sites of active mineralization [76]. The path length of the alpha particles emitted (<100 μm) is much shorter than the beta particles of Sm-153 and Sr-89, resulting in less hematologic toxicity [77].

Following the promising results in the Alpharadin in Symptomatic Prostate Cancer (ALSYMPCA) Phase III Ra-223 multinational, placebo-controlled trial in 921 subjects with prostate cancer, the FDA granted full approval in May 2013 [18, 78], with subsequent approval in the European Union. The trade name of Ra-223 dichloride is Xofigo, previously known as Alpharadin.

21.4 Pharmacokinetics and Biodistribution

Two studies have evaluated the blood pharmacokinetics of Ra-223 [79, 80]. Ra-223 clears rapidly from blood and less than 1 % of initial activity is present at 24 h. Gamma camera imaging is suboptimal but feasible, based on the gamma rays emitted in conjunction with the alpha emissions [79–81]. Elimination is mainly intestinal. Specifically, early excretion is seen into the small bowel, presumably

transluminal, with a median of 52 % in bowel at 24 h and up to 2–82 % removed from the body at approximately 1 week [80]. Very little urinary excretion is noted (typically <5 %).

21.5 Clinical Studies with Ra-223

Ra-223 dosing is on an activity/kg basis. The initial Phase I study used single escalating doses ranging from 46 to 250 kBq/kg [79]. Several Phase II trials used single injections of ≤ 200 kBq/kg or cumulative activity of up to 240 kBq/kg, with demonstrated benefit and limited toxicity. The clinically approved dose is 50 kBq/kg with repeat injections × 6, based on the ALSYMPCA Phase III trial [78]. It should be noted that recently and subsequent to these studies National Institutes of Standards (NIST) have identified that the previous calibration for Ra-223 was 10 % low indicating that the 50kBq really represents 55kBq, thus the new treatment dose corresponds to 55kBq/kg.

Clinical trials with Ra-223 have consistently shown a decrease in alkaline phosphatase [79, 80, 82]. Markers of bone turnover such as uNTX-1, CTX-1, and procollagen I N-terminal propeptide also have shown significant decreases in patients treated with Ra-223 vs. control [19, 82]. Variable changes in PSA have been observed; in patients treated with four doses of Ra-223 at 50 kBq/kg every 4 weeks, a 23.8 % PSA drop was noted, compared to a 44.9 % increase in the placebo control group. Furthermore, the median time to PSA progression was 26 weeks vs. 8 weeks in the control group [82]. A dose response was seen in patients receiving three injections of 25, 50, or 80 kBq/kg, with ≥ 30 % drop in PSA found in 5 %, 17 %, and 26 % of the patients treated, respectively [83]. Note that a consistent drop in PSA was not observed in the ALSYMPCA trial.

A more important outcome is a decrease in SREs, including pain, a significant problem in patients with prostate cancer. In a group of 64 patients, with XRT plus 50 kBq/kg × 4 doses of Ra-223 compared to XRT plus placebo, the median time for the first SRE was 14 weeks in the Ra-223 group compared to 11 weeks in the placebo group [82]. In the ALSYMPCA trial, the time to first SRE was significantly delayed, with a median time to SRE of 15.6 months vs. 9.4 months for the control group and hazard ration of 0.66 [78]. With respect to pain, several of the Ra-223 clinical trials demonstrated improvement following Ra-223 [83].

Furthermore, in contrast to other bone-seeking radiopharmaceuticals, Ra-223 therapy has demonstrated significant improvements in survival. The median overall survival (OS) at 18 months was 14.9 months compared to 11.3 months for the control group [78]. A second look at the data at 24 months confirmed this effect, with overall survival of 16.3 months compared to 11.6 for the placebo group in favor of the Ra-223 arm [84]. Furthermore, at 2 years, 30 % of the Ra-223 group was alive, compared to only 13 % of the placebo group. Interestingly, patients receiving the four intended injections had longer OS than those receiving placebo (93 weeks vs. 49 weeks, respectively) [84].

21.6 Toxicity

Dosimetry estimates using standard approaches have been compared to cell-level dosimetry using a model that accounts for the expected localization of Ra-223 relative to marrow cavity architecture by Hobbs et al. [77]. These investigators estimated the percentage of cells that received a potentially toxic-absorbed dose (2 or 4 Gy). Based on their model, it was estimated that the majority of the radiation dose will be deposited near the trabecular bone, in which case increasing the activity of Ra-223 may not substantially increase the risk of marrow toxicity [77]. Organ-based dosimetry based on patient studies and utilizing the MIRD method and OLINDA software are provided in the product monograph (http://www.bayer.ca/omr/online/xofigo-pm-en-10mar2015-161312.pdf).

Compared to beta emitters, Ra-223 has the theoretical advantage of sparing much of the marrow from irradiation, given its short-range emissions [77, 85, 86]. None of the studies performed to date have determined the maximum tolerated single or fractionated Ra-223-administered activity. The activity administered has ranged from single injections of 5 to 250 kBq/kg and maximum fractionated activity of up to 300 kBq/kg [83]. The question remains whether higher doses, achieved by administering higher single doses or increasing the number of cycles of multiple lower doses, will have additional benefits.

Ra-223 myelotoxicity is very infrequent, typically with no Grade 4 toxicity (utilizing NCI common toxicity criteria) [79, 82] and rare occurrence of Grade 3 toxicity. Of 33 patients receiving 50 kBq/kg × 4, none developed Grade 4 myelotoxicity and only one developed Grade 3 leukopenia, neutropenia, and anemia [79]. Mild hematopoietic toxicity is seen and appears to be dose related when single doses are administered [87]. With activities between 25 and 80 kBq/kg given × 3 every 6 weeks, significant hematologic toxicity was infrequent with no Grade 3 or 4 neutropenia and only one Grade 4 thrombocytopenia at the 50 kBq/kg dose level. Two patients developed Grade 4 anemia. In all cases, recovery occurred by 24 weeks, with the exception of those with anemia in whom recovery took longer [83].

In most cases, non-hematologic adverse events are mild to moderate in intensity. Most studies reported diarrhea, fatigue, nausea, vomiting, and bone pain [79, 82, 83], some of which were believed to be dose related. In one trial, various constitutional symptoms such as these were no more common in the Ra-223 group than in the control group, with the exception of a higher incidence of constipation in the control group [82].

In the package insert, based on 600 patients treated with Ra-223 and 301 subjects in the placebo group, the most commonly reported side effects occurring in >10 % of treated patients were nausea, diarrhea, vomiting, and peripheral edema. While these were slightly more common in the Ra-223 group, they were also among the most frequent side effects in the control group. Hematopoietic Grade 3/4 leukopenia and thrombocytopenia occurred in <3 % of the Ra-223 group and <1 % of the placebo group.

21.7   Late Toxicity

Long-term follow-up in patients receiving Ra-223 is limited, given that the initial clinical studies were performed in 2005 and considering the relative short survival of patients with advanced prostate or breast cancer. Late effects from another alpha emitter, Ra-224, have been reported but primarily in individuals treated as children or young adults and involving high-dose regimens with a lag time of 8 years for bone tumors, whereas no increased risk was observed in adults treated with the same regimen [88]. In a separate cohort of patients treated with lower doses (1 MBq × 10 doses of Ra-224), a slightly increased incidence of acute myeloid leukemia was noted [89]. Data from the radium dial painters have also demonstrated an increased risk of bone cancer secondary to Ra-226 and Ra-228 ingestion, with higher risk in younger subjects. The incidence of carcinomas of the head was also higher in these subjects [90]. These studies also showed a lag period of at least 3–7 years and often decades before presentation. A 24-month follow-up of castration-resistant prostate cancer patients with metastases to the bone receiving Ra-223 at 25, 50, or 80 kBq/kg × 3 at 6-week intervals showed that 57 % of patients died, with similar proportions per group, generally attributable to progression of disease. No cases of MDS, AML, or aplastic anemia occurred [83]. In ten patients alive 2 years after four injections of 50 kBq/kg, none developed AML, MDS, or aplastic anemia. One case of bladder cancer and one case of pancreatic cancer occurred, but these were deemed to be unrelated to Ra-223 [84].

More recently, 23 patients with metastatic breast cancer to the bone were treated with 50 kBq/kg of Ra-223 × 4 doses every 4 weeks. Evidence of biologic activity was noted in terms of bone alkaline phosphatase and urinary bone resorption markers. Each lesion was classified as having a metabolic response based on FDG PET/CT (>25 % decrease of SUVmax from baseline), stable disease (SD, <25 % decrease and 25 % increase of SUVmax from baseline), or progressive disease (PD, >25 % increase of SUVmax from baseline) [19]. By these criteria, evidence of bone response was noted in 41.5 % of patients at week 17 [19]. Treatments were well tolerated with infrequent treatment-related adverse events.

Experience in NETs with Ra-223 is very limited. A case report has described favorable pain palliation from extensive metastatic bone disease in a subject with SDHB mutation paraganglioma [21].

21.8   Radiation Safety Precautions with Alpha Emitters

In general, instructions for patients receiving alpha emitters are limited and similar to those that should be given to patients and caregivers when administering other therapeutic radiopharmaceuticals. Due to the limited gamma emissions of Ra-223 and other alpha emitters and the relatively low doses of administered activity, the patient as a source is not usually a risk to the general public and caregivers. Thus, an

isolation period is typically not required. However, some high-energy gamma rays can be problematic with large amounts manipulated during the labeling process (i.e., 2.6 MeV gamma ray for Bi-212). Soiled clothing and bodily fluids should be handled using gloves, and universal precautions are sufficient to protect from radiation contamination, which is the main radiation safety issue.

21.9 Summary

Alpha emitters are much more potent than beta emitters and have significant potential advantages as therapeutic agents. A limited but slowly increasing number of studies have been performed in NETs due to problems with availability of some of the radionuclides, as well as radiochemistry challenges. Preliminary studies with various alpha-emitting radiopharmaceuticals have already shown proof of principle with safety and initial efficacy data in NETs. Although there is some preliminary experience, larger systematic clinical trials are needed before determining the role of alpha emitters in NETs.

References

1. Bodei L, Cremonesi M, Grana CM, Chinol M, Baio SM, Severi S, et al. Yttrium-labelled peptides for therapy of NET. Eur J Nucl Med Mol Imaging. 2012;39:93–102.
2. Baum RP, Kulkarni HR, Carreras C. Peptides and receptors in image-guided therapy: theranostics for neuroendocrine neoplasms. Semin Nucl Med. 2012;42(3):190–207.
3. Vishne TH, Ron IG. Strontium-89 (Sr-89) analgesia for rare thymic carcinoid tumor with bony metastases. Am J Clin Oncol Cancer Clin Trials. 1998;21(6):602–4.
4. Takeshima T, Namura K, Sekiguchi Z, Takizawa A, Tsuchiya F, Iwasaki A, et al. [A case of multiple bony pain due to metastatic malignant pheochromocytoma successfully treated with strontium-89]. Hinyokika kiyo Acta urologica Japonica. [Case Reports]. 2014;60(3):109–13.
5. Oshiro C, Kamigaki S, Arai T, Nakamura Y, Fukunaga M, Ichida W, et al. A case of thyroid medullary carcinoma with multiple painful bone metastases successfully treated with strontium-89 chloride. Gan to kagaku ryoho Cancer chemother. 2012;39(6):951–3.
6. Naganuma A, Mayahara H, Morizane C, Ito Y, Hagihara A, Kondo S, et al. Successful control of intractable hypoglycemia using radiopharmaceutical therapy with strontium-89 in a case with malignant insulinoma and bone metastases. Jpn J Clin Oncol. 2012;42(7):640–5.
7. Montesano T, Giacomobono S, Acqualagna G, Colandrea M, Di Nicola A, Travascio L, et al. Our experience on pain palliation of bone metastasis with Sr-89 or Sm-153 in cancer patients resistant to a conventional analgesic therapy. A retrospective study. Clin Ter. 2009;160(3):193–9.
8. Devcic Z, Rosenberg J, Braat AJA, Techasith T, Banerjee A, Sze DY, et al. The efficacy of hepatic Y-90 resin radioembolization for metastatic neuroendocrine tumors: a meta-analysis. J Nucl Med. 2014;55(9):1404–10.
9. Kennedy A, Coldwell D, Sangro B, Wasan H, Salem R. Integrating radioembolization into the treatment paradigm for metastatic neuroendocrine tumors in the liver. Am J Clin Oncol Cancer Clin Trials. 2012;35(4):393–8.

10. Shaheen M, Hassanain M, Aljiffry M, Cabrera T, Chaudhury P, Simoneau E, et al. Predictors of response to radio-embolization (TheraSphere (R)) treatment of neuroendocrine liver metastasis. HPB. 2012;14(1):60–6.

11. Sgouros G, Roeske JC, McDevitt MR, Palm S, Allen BJ, Fisher DR, et al. MIRD pamphlet no. 22 (Abridged): radiobiology and dosimetry of alpha-particle emitters for targeted radionuclide therapy. J Nucl Med. [Review]. 2010;51(2):311–28.

12. Soyland C, Hassfjell SP. Survival of human lung epithelial cells following in vitro alpha-particle irradiation with absolute determination of the number of alpha-particle traversals of individual cells. Int J Radiat Biol. 2000;76(10):1315–22.

13. Jurcic JG, Ravandi F, Pagel JM, Park JH, Smith BD, Douer D, et al. Phase I trial of alpha-particle therapy with actinium-225 (Ac-225)-lintuzumab (anti-CD33) and low-dose cytarabine (LDAC) in older patients with untreated acute myeloid leukemia (AML). J Clin Oncol. 2015;33(15).

14. Zalutsky MR, Reardon DA, Akabani G, Coleman E, Friedman AH, Friedman HS, et al. Clinical experience with alpha-particle-emitting at-211: treatment of recurrent brain tumor patients with at-211-labeled chimeric antitenascin monoclonal antibody 81C6. J Nucl Med. 2008;49(1):30–8.

15. Sgouros G, Ballangrud AM, Jurcic JG, McDevitt MR, Humm JL, Erdi YE, et al. Pharmacokinetics and dosimetry of an alpha-particle emitter labeled antibody: Bi-213-HuM195 (anti-CD33) in patients with leukemia. J Nucl Med. 1999;40(11):1935–46.

16. Allen BJ, Rizvi SMA, Tian Z. Preclinical targeted alpha therapy for subcutaneous melanoma. Melanoma Res. 2001;11(2):175–82.

17. Kim YS, Brechbiel MW. An overview of targeted alpha therapy. Tumor Biol. 2012;33(3):573–90.

18. Kluetz PG, Pierce W, Maher VE, Zhang H, Tang SH, Song PF, et al. Radium Ra 223 dichloride injection: US food and drug administration drug approval summary. Clin Cancer Res. 2014;20(1):9–14.

19. Coleman R, Aksnes AK, Naume B, Garcia C, Jerusalem G, Piccart M, et al. A phase IIa, non-randomized study of radium-223 dichloride in advanced breast cancer patients with bone-dominant disease. Breast Cancer Res Treat. 2014;145(2):411–8.

20. Takalkar A, Paryani B, Adams S, Subbiah V. Radium-223 dichloride therapy in breast cancer with osseous metastases. BMJ Case Rep. 2015;2015:211152.

21. Makis W, McCann K, McEwan AJ, Sawyer MB. Palliation of extensive metastatic bone disease with 223Ra-dichloride alpha-particle therapy in a patient with malignant hereditary paraganglioma-pheochromocytoma syndrome with SDHB mutation. Clin Nucl Med. 2016;41(2):144–7.

22. Boll RA, Malkemus D, Mirzadeh S. Production of actinium-225 for alpha particle mediated radioimmunotherapy. Appl Radiat Isot. 2005;62(5):667–79.

23. Melville G, Liu SF, Allen BJ. A theoretical model for the production of Ac-225 for cancer therapy by photon-induced transmutation of Ra-226. Appl Radiat Isot. [Article]. 2006;64(9):979–88.

24. McDevitt MR, Finn RD, Sgouros G, Ma DS, Scheinberg DA. An Ac-225/Bi-213 generator system for therapeutic clinical applications: construction and operation. Appl Radiat Isot. 1999;50(5):895–904.

25. Rosenblat TL, McDevitt MR, Mulford DA, Pandit-Taskar N, Divgi CR, Panageas KS, et al. Sequential cytarabine and alpha-particle immunotherapy with bismuth-213-lintuzumab (HuM195) for acute myeloid leukemia. Clin Cancer Res. 2010;16(21):5303–11.

26. Allen BJ, Singla AA, Rizvi SMA, Graham P, Bruchertseifer F, Apostolidis C, et al. Analysis of patient survival in a phase I trial of systemic targeted alpha-therapy for metastatic melanoma. Immunotherapy. 2011;3(9):1041–50.

27. Allen BJ, Raja C, Rizvi S, Li Y, Tsui W, Graham P, et al. Intralesional targeted alpha therapy for metastatic melanoma. Cancer Biol Ther. [Article]. 2005;4(12):1318–24.

28. Cordier D, Forrer F, Bruchertseifer F, Morgenstern A, Apostolidis C, Good S, et al. Targeted alpha-radionuclide therapy of functionally critically located gliomas with

Bi-213-DOTA- Thi(8), Met(O-2)(11) -substance P: a pilot trial. Eur J Nucl Med Mol Imaging. 2010;37(7):1335–44.

29. McDevitt MR, Finn RD, Ma D, Larson SM, Scheinberg DA. Preparation of alpha-emitting Bi-213-labeled antibody constructs for clinical use. J Nucl Med. 1999;40(10):1722–7.

30. McDevitt MR, Ma DS, Lai LT, Simon J, Borchardt P, Frank RK, et al. Tumor therapy with targeted atomic nanogenerators. Science. 2001;294(5546):1537–40.

31. Kratochwil C, Giesel FL, Bruchertseifer F, Mier W, Apostolidis C, Boll R, et al. Bi-213-DOTATOC receptor-targeted alpha-radionuclide therapy induces remission in neuroendo-crine tumours refractory to beta radiation: a first-in-human experience. Eur J Nucl Med Mol Imaging. 2014;41(11):2106–19.

32. Kratochwil C, Giesel FL, Lopez-Benitez R, Schimpfky N, Kunze K, Eisenhut M, et al. Intraindividual comparison of selective arterial versus venous Ga-68-DOTATOC PET/CT in patients with gastroenteropancreatic neuroendocrine tumors. Clin Cancer Res. 2010;16(10):2899–905.

33. Kratochwil C, Lopez-Benitez R, Mier W, Haufe S, Isermann B, Kauczor HU, et al. Hepatic arterial infusion enhances DOTATOC radiopeptide therapy in patients with neuroendocrine liver metastases. Endocr Relat Cancer. 2011;18(5):595–602.

34. Norenberg JP, Krenning BJ, Konings I, Kusewitt DF, Nayak TK, Anderson TL, et al. Bi-213-DOTA(0), Tyr(3) octreotide peptide receptor radionuclide therapy of pancreatic tumors in a preclinical animal model. Clin Cancer Res. 2006;12(3):897–903.

35. Miederer M, Henriksen G, Alke A, Mossbrugger I, Quintanilla-Martinez L, Senekowitsch-Schmidtke R, et al. Preclinical evaluation of the alpha-particle generator nuclide Ac-225 for somatostatin receptor radiotherapy of neuroendocrine tumors. Clin Cancer Res. 2008;14(11):3555–61.

36. Morgenstern A, Bruchertseifer F, Apostolidis C. Bismuth-213 and actinium-225–generator performance and evolving therapeutic applications of two generator-derived alpha-emitting radioisotopes. Curr Radiopharm. 2012;5(3):221–7.

37. Kratochwil C, Bruchertseifer F, Giesel F, Apostolidis C, Haberkorn U, Morgenstern A. Ac-225-DOTATOC – an empiric dose finding for alpha particle emitter based radionuclide therapy of neuroendocrine tumors. J Nucl Med. 2015;56(3):1232.

38. Baidoo KE, Milenic DE, Brechbiel MW. Methodology for labeling proteins and peptides with lead-212 (Pb-212). Nucl Med Biol. 2013;40(5):592–9.

39. Atcher RW, Friedman AM, Hines JJ. An improved generator for the production of PB-212 and BI-212 from RA-224. Appl Radiat Isot. [Article]. 1988;39(4):283–6.

40. Chappell LL, Dadachova E, Milenic DE, Garmestani K, Wu CC, Brechbiel MW. Synthesis, characterization, and evaluation of a novel bifunctional chelating agent for the lead isotopes Pb-203 and Pb-212. Nucl Med Biol. 2000;27(1):93–100.

41. Meredith RF, Torgue J, Azure MT, Shen S, Saddekni S, Banaga E, et al. Pharmacokinetics and imaging of Pb-212-TCMC-trastuzumab after intraperitoneal administration in ovarian cancer patients. Cancer Biother Radiopharm. 2014;29(1):12–7.

42. Meredith R, Torgue J, Shen S, Fisher DR, Banaga E, Bunch P, et al. Dose escalation and dosimetry of first-in-human alpha radioimmunotherapy with Pb-212-TCMC-trastuzumab. J Nucl Med. 2014;55(10):1636–42.

43. Andersonberg WT, Strand M, Brechbiel M, Atcher RW, Gansow OA. BI-212 labeled monoclonal-antibodies for use in radioimmunotherapy. J Nucl Med. 1986;27(6):1040.

44. Kozak RW, Atcher RW, Gansow OA, Friedman AM, Hines JJ, Waldmann TA. Bismuth-212-labeled anti-tac monoclonal-antibody – alpha-particle-emitting radionuclides as modalities for radioimmunotherapy. Proc Natl Acad Sci U S A. [Article]. 1986;83(2):474–8.

45. Hassfjell SP, Bruland OS, Hoff P. Bi-212-DOTMP: an alpha particle emitting bone-seeking agent for targeted radiotherapy. Nucl Med Biol. 1997;24(3):231–7.

46. Zalutsky MR, Zhao XG, Alston KL, Bigner D. High-level production of alpha-particle-emitting At-211 and preparation of At-211-Labeled antibodies for clinical use. J Nucl Med. 2001;42(10):1508–15.

47. Zalutsky MR, Garg PK, Friedman HS, Bigner DD. Labeling monoclonal-antibodies and F(AB')2 fragments with the alpha-particle-emitting nuclide astatine-211 – preservation of immunoreactivity and in vivo localizing capacity. Proc Natl Acad Sci U S A. 1989;86(18):7149–53.

48. Hadley SW, Wilbur DS, Gray MA, Atcher RW. Astatine-211 labeling of an antimelanoma antibody and its FAB fragment using n-succinimidyl para-astatobenzoate – comparisons in vivo with the para- 125I iodobenzoyl conjugate. Bioconjug Chem. 1991;2(3):171–9.

49. Vaidyanathan G, Zalutsky MR. 1-(m-[211At]astatobenzyl)guanidine: synthesis via astato demetalation and preliminary in vitro and in vivo evaluation. Bioconjug Chem. [Comparative Study Research Support, U.S. Gov't, P.H.S.]. 1992;3(6):499–503.

50. Vaidyanathan G, Affleck DJ, Bigner DD, Zalutsky MR. N-succinimidyl 3- At-211 astato-4-guanidinomethylbenzoate: an acylation agent for labeling internalizing antibodies with alpha-particle emitting At-21. Nucl Med Biol. 2003;30(4):351–9.

51. Zhang M, Yao Z, Zhang Z, Garmestani K, Talanov VS, Plascjak PS, et al. The anti-CD25 monoclonal antibody 7G7/B6, armed with the alpha-emitter At-211, provides effective radioimmunotherapy for a murine model of leukemia. Cancer Res. 2006;66(16):8227–32.

52. Cederkrantz E, Andersson H, Bernhardt P, Back T, Hultborn R, Jacobsson L, et al. Absorbed doses and risk estimates of at-211-MX35 F(ab ')(2) in intraperitoneal therapy of ovarian cancer patients. Int J Radiat Oncol Biol Phys. 2015;93(3):569–76.

53. Vaidyanathan G, Affleck DJ, Alston KL, Zalutsky MR. A tin precursor for the synthesis of no-carrier-added *I MIBG and At-211 MABG. J Label Compd Radiopharm. 2007;50(3–4):177–82.

54. Vaidyanathan G, Affleck DJ, Alston KL, Zhao XG, Hens M, Hunter DH, et al. A kit method for the high level synthesis of [211At]MABG. Bioorg Med Chem. [Research Support, N.I.H., Extramural Research Support, Non-U.S. Gov't Research Support, U.S. Gov't, Non-P.H.S.]. 2007;15(10):3430–6.

55. Makvandi M, LeGeyt B, Mikitsh JL, Hou C, Pryma DA. Targeted-alpha-therapy with astatine-211-meta-astatobenzylguanidine (at-211-MABG) in the treatment of pheochromocytoma. Pancreas. 2015;44(2):348–9.

56. Vaidyanathan G, Affleck DJ, Schottelius M, Wester H, Friedman HS, Zalutsky MR. Synthesis and evaluation of glycosylated octreotate analogues labeled with radioiodine and At-211 via a tin precursor. Bioconjug Chem. 2006;17(1):195–203.

57. Garg PK, Harrison CL, Zalutsky MR. Comparative tissue distribution in mice of the alpha-emitter at-211 and I-131 as labels of a monoclonal-antibody and F(AB')2 fragment. Cancer Res. 1990;50(12):3514–20.

58. Turkington TG, Zalutsky MR, Jaszczak RJ, Garg PK, Vaidyanathan G, Coleman RE. Measuring astatine-211 distributions with SPECT. Phy Med Biol. [Research Support, Non-U.S. Gov't Research Support, U.S. Gov't, P.H.S.]. 1993;38(8):1121–30.

59. Carrasquillo JA, Pandit-Taskar N, Chen CC. Radionuclide therapy of adrenal tumors. J Surg Oncol. [Review]. 2012;106(5):632–42.

60. Chen CC, Carrasquillo JA. Molecular imaging of adrenal neoplasms. J Surg Oncol. [Review]. 2012;106(5):532–42.

61. Carrasquillo JA, Chen CC. I-131 MIBG therapy. In: Strauss HW, Mariani G, Volterrani D, Larson SM, editors. Nuclear oncology: pathophysiology and clinical applications. New York/Heidelberg/Dordrecht/London: Springer; 2013. p. 691–714.

62. Vaidyanathan G, Strickland DK, Zalutsky MR. Meta-[211At]astatobenzylguanidine: further evaluation of a potential therapeutic agent. Int J Cancer J International du cancer. [Research Support, U.S. Gov't, P.H.S.]. 1994;57(6):908–13.

63. Strickland DK, Vaidyanathan G, Zalutsky MR. Cytotoxicity of alpha-particle-emitting m-[211At]astatobenzylguanidine on human neuroblastoma cells. Cancer Res. 1994;54(20):5414–9.

64. Zuetenhorst JM, Hoefnageli CA, Boot H, Olmos RAV, Taal BG. Evaluation of In-111-pentetreotide, I-131-MIBG and bone scintigraphy in the detection and clinical management of bone metastases in carcinoid disease. Nucl Med Commun. 2002;23(8):735–41.

65. Meijer WG, van der Veer E, Jager PL, van der Jagt EJ, Piers BA, Kema IP, et al. Bone metastases in carcinoid tumors: clinical features, imaging characteristics, and markers of bone metabolism. J Nucl Med. 2003;44(2):184–91.

66. Ambrosini V, Nanni C, Zompatori M, Campana D, Tomassetti P, Castellucci P, et al. Ga-68-DOTA-NOC PET/CT in comparison with CT for the detection of bone metastasis in patients with neuroendocrine tumours. Eur J Nucl Med Mol Imaging. 2010;37(4):722–7.

67. Putzer D, Gabriel M, Henninger B, Kendler D, Uprimny C, Dobrozemsky G, et al. Bone metastases in patients with neuroendocrine tumor: Ga-68-DOTA-Tyr(3)-octreotide PET in comparison to CT and bone scintigraphy. J Nucl Med. 2009;50(8):1214–21.

68. Ross EM, Roberts WC. The carcinoid syndrome: comparison of 21 necropsy subjects with carcinoid heart disease to 15 necropsy subjects without carcinoid heart disease. Am J Med. [Comparative Study]. 1985;79(3):339–54.

69. Van Loon K, Zhang L, Keiser J, Carrasco C, Glass K, Ramirez MT, et al. Bone metastases and skeletal-related events from neuroendocrine tumors. Endocr Connect. 2015;4(1):9–17.

70. Ayala-Ramirez M, Palmer JL, Hofmann MC, de la Cruz M, Moon BS, Waguespack SG, et al. Bone metastases and skeletal-related events in patients with malignant pheochromocytoma and sympathetic paraganglioma. J Clin Endocrinol Metab. 2013;98(4):1492–7.

71. Krempf M, Lumbroso J, Mornex R, Brendel AJ, Wemeau JL, Delisle MJ, et al. Use of M- I-131 iodobenzylguanidine in the treatment of malignant pheochromocytoma. J Clin Endocrinol Metab. 1991;72(2):455–61.

72. Kavecansky J, Wei L, Caronia L, Ramirez MT, Bloomston M, Shah MH. Bone metastases in well-to-moderately differentiated neuroendocrine tumors a single institutional review from the Ohio state university medical center. Pancreas. 2015;44(2):198–203.

73. Sabet A, Ezziddin S, Heinemann F, Guhlke S, Muckle M, Willinek W, et al. Osseous metastases of gastro-enteropancreatic neuroendocrine tumours diagnostic value of intra-therapeutic Lu-177-octreotate imaging in comparison with bone scintigraphy. Nuklearmedizin Nucl Med. 2012;51(3):95–100.

74. Zelinka T, Timmers H, Kozupa A, Chen CC, Carrasquillo JA, Reynolds JC, et al. Role of positron emission tomography and bone scintigraphy in the evaluation of bone involvement in metastatic pheochromocytoma and paraganglioma: specific implications for succinate dehydrogenase enzyme subunit B gene mutations. Endocr Relat Cancer. 2008;15(1):311–23.

75. Henriksen G, Hoff P, Alstad J, Larsen RH. Ra-223 for endoradiotherapeutic applications prepared from an immobilized Ac-227/Th-227 source. Radiochim Acta. 2001;89(10):661–6.

76. Neuman WF, Hursh JB, Boyd J, Hodge HC. On the mechanism of skeletal fixation of radium. Ann N Y Acad Sci. 1955;62(6):125–36.

77. Hobbs RF, Song H, Watchman CJ, Bolch WE, Aksnes AK, Ramdahl T, et al. A bone marrow toxicity model for Ra-223 alpha-emitter radiopharmaceutical therapy. Phys Med Biol. 2012;57(10):3207–22.

78. Parker C, Nilsson S, Heinrich D, Helle SI, O'Sullivan JM, Fossa SD, et al. Alpha emitter radium-223 and survival in metastatic prostate cancer. N Engl J Med. 2013;369(3):213–23.

79. Nilsson S, Larsen RH, Fossa SD, Balteskard L, Borch KW, Westlin JE, et al. First clinical experience with alpha-emitting radium-223 in the treatment of skeletal metastases. Clin Cancer Res. 2005;11(12):4451–9.

80. Carrasquillo JA, O'Donoghue JA, Pandit-Taskar N, Humm JL, Rathkopf DE, Slovin SF, et al. Phase I pharmacokinetic and biodistribution study with escalating doses of (223)Ra-dichloride in men with castration-resistant metastatic prostate cancer. Eur J Nucl Med Mol Imaging. [Clinical Trial, Phase I Research Support, Non-U.S. Gov't]. 2013;40(9):1384–93.

81. Hindorf C, Chittenden S, Aksnes AK, Parker C, Flux GD. Quantitative imaging of Ra-223-chloride (Alpharadin) for targeted alpha-emitting radionuclide therapy of bone metastases. Nucl Med Commun. 2012;33(7):726–32.

82. Nilsson S, Franzen L, Parker C, Tyrrell C, Blom R, Tennvall J, et al. Bone-targeted radium-223 in symptomatic, hormone-refractory prostate cancer: a randomised, multicentre, placebo-controlled phase II study. Lancet Oncol. 2007;8(7):587–94.

83. Parker CC, Pascoe S, Chodacki A, O'Sullivan JM, Germa JR, O'Bryan-Tear CG, et al. A randomized, double-blind, dose-finding, multicenter, phase 2 study of radium chloride (Ra 223) in patients with bone metastases and castration-resistant prostate cancer. Eur Urol. 2013;63(2):189–97.
84. Nilsson S, Franzen L, Parker C, Tyrrell C, Blom R, Tennvall J, et al. Two-year survival follow-Up of the randomized, double-blind, placebo-controlled phase II study of radium-223 chloride in patients with castration-resistant prostate cancer and bone metastases. Clin Genitourin Cancer. 2013;11(1):20–6.
85. Larsen RH, Saxtorph H, Skydsgaard M, Borrebaek J, Jonasdottir TJ, Bruland OS, et al. Radiotoxicity of the alpha-emitting bone-seeker Ra-223 injected intravenously into mice: Histology, clinical chemistry and hematology. In Vivo. 2006;20(3):325–31.
86. Lassmann M, Nosske D. Dosimetry of Ra-223-chloride: dose to normal organs and tissues. Eur J Nucl Med Mol Imaging. 2013;40(2):207–12.
87. Nilsson S, Strang P, Aksnes AK, Franzen L, Olivier P, Pecking A, et al. A randomized, dose–response, multicenter phase II study of radium-223 chloride for the palliation of painful bone metastases in patients with castration-resistant prostate cancer. Eur J Cancer. 2012;48(5):678–86.
88. Nekolla EA, Kellerer AM, Kuse-Isingschulte M, Eder E, Spiess H. Malignancies in patients treated with high doses of radium-224. Radiat Res. 1999;152(6):S3–7.
89. Wick RR, Nekolla EA, Gossner W, Kellerer AM. Late effects in ankylosing spondylitis patients treated with Ra-224. Radiat Res. 1999;152(6):S8–11.
90. Fry SA. Studies of US radium dial workers: an epidemiological classic. Radiat Res. 1998;150(5):S21–9.

Chapter 22
Nanoparticles for Radionuclide Imaging and Therapy: Principles

Sybille Kennel, Ananda Appavoo, Jürgen Schulz, and Philippe Barthélémy

22.1 Introduction

Nanoparticles and nanoscale technologies have gained great interest in biomedical fields, and their use for the treatment, diagnosis, monitoring, and control of biological systems has been referred to as "nanomedicine" by the National Institutes of Health [1]. Nanoparticles mainly employed in nanotechnology usually refer to materials with dimensions less than several hundred nanometers. With the size comparable to biological molecules such as antibodies, enzymes, and receptors, and about 100–10000 times smaller than human cells, these small structures can extravasate through the endothelial cell layers and can be designed to interact with biomolecules both on the surface of or inside the cells. Nowadays nanoparticles can be designed to improve delivery efficacy and *in vivo* stability of drugs by varying the size, charge, or surface modification. For example, nanoparticles are typically coated with polyethylene glycol to reduce their uptake by the reticuloendothelial system and to increase their plasma half-life. Another noteworthy property of nanoparticles is their very high surface-to-area volume ratio, which enables surface chemistry for targeting but also high loading capacity for diagnostic or therapeutic payload. Hence, several nanoparticles for radionuclide imaging [2–8] and therapy [9–11] featuring different functionalities have been investigated (Fig. 22.1).

S. Kennel, PhD • J. Schulz (✉)
Université de Bordeaux, Bordeaux F-33076, France

CNRS, INCIA, UMR 5287, F-33400 Talence, France
e-mail: jurgen.schulz@u-bordeaux.fr

A. Appavoo • P. Barthélémy, PhD (✉)
Université de Bordeaux, Bordeaux F-33076, France

INSERM U1212, UMR CNRS 5320, Bordeaux F-33076, France
e-mail: philippe.barthelemy@inserm.fr
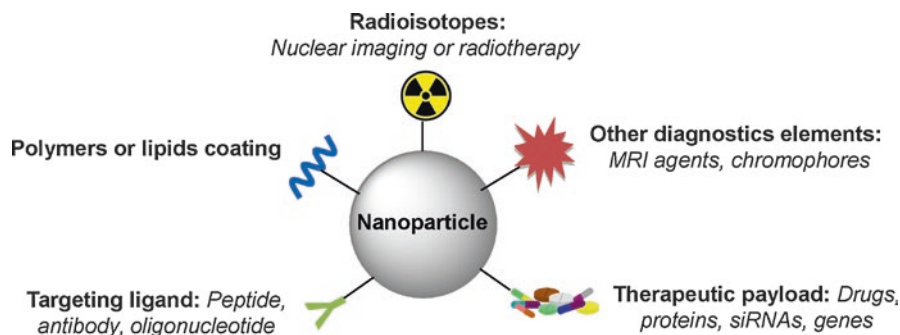
Fig. 22.1 Schematic drawing of nanoparticles used for multimodal radionuclide imaging and therapy

These nanoparticles can be classified according to their chemical composition (Fig. 22.2). The following families can be distinguished: (1) metal-based nanoparticles including quantum dots, iron oxide, and gold nanoparticles, (2) carbon-based nanoparticles such as nanotubes or fullerenes, (3) polymer nanoparticles such as nanocapsules or dendrimers, (4) lipid-based nanoparticles including liposomes and solid lipid nanoparticles, and (5) a new class based on nucleolipid nanoparticles (Fig. 22.2). Two main radiolabeling strategies for nanoparticles have been investigated. One is to radiolabel the nanostructure itself, either on the surface or in the core. The other approach is to radiolabel the payload encapsulated inside the nanoparticles.

One main concern in the design of nanoparticles for nanomedicine is the efficacy of the targeting to minimize size effect during therapy or false positive in diagnosis. Two approaches are generally used: a passive or an active targeting. In passive targeting, nanoparticles can take advantage of the increased vascular permeability and pass through the leaky vasculature of tumor bed but not transport through tight inter-endothelial junctions in normal tissues. Such spontaneous accumulation is known as the enhanced permeability and retention effect (EPR effect). In active targeting, molecules such as antibodies or specific ligands can be attached to the surface of the nanoparticles to interact with receptors that are overexpressed on tumor or other cells resulting in enhanced accumulation and preferential cellular uptake through receptor-mediated process.

Consequently one major application of nanomedicine is in the field of cancer. Many systems were primarily designed for therapeutic purposes especially for a more efficient delivery of chemotherapeutic drugs to pathologic sites while reducing their accumulation in healthy tissues. Thus, several therapeutic nanoparticles are routinely used in clinic including Doxil (encapsulation of doxorubicin), Ambisome (amphotericin B), or Abraxane (paclitaxel) [12, 13].

The aim of this review is to highlight some of the recent advances in the area of nanoparticles for radionuclide imaging and therapy. We wish to underline that these
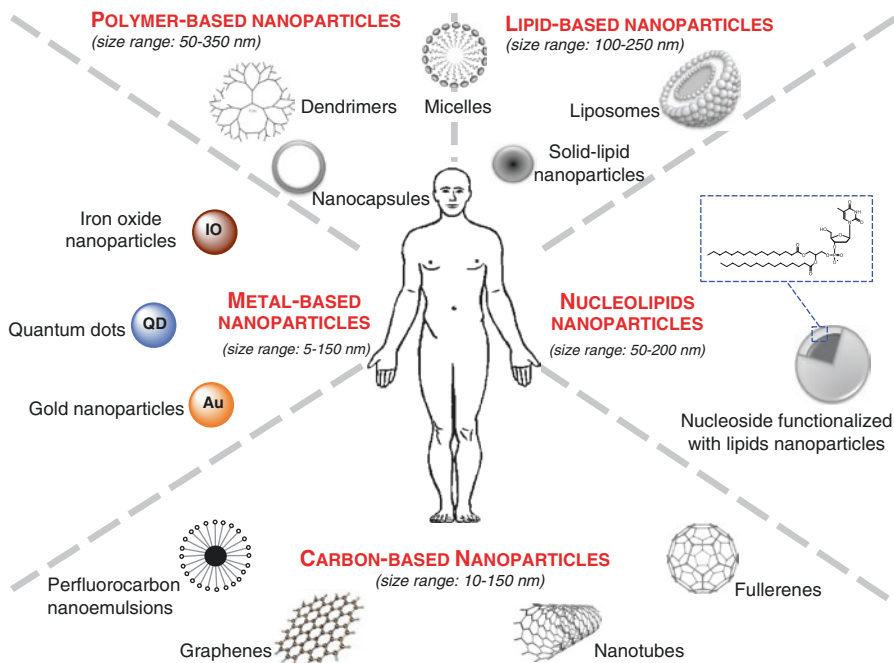
Fig. 22.2 Schematic illustration showing the nanoparticles classified according to their chemical composition

nanoparticles offer new perspectives in the fields of biomedicine. First, we will focus on the previous works realized on carbon-based nanoparticles. This section includes several examples of fullerenes, carbon nanotubes, graphene oxide, and perfluorocarbon emulsions. Second, we present several metal-based nanoparticles currently developed for nanomedicine. Third, polymer-based nanoparticles are presented with the example of dendrimers. The fourth section is dedicated to the lipid-based particles. The last section underlines recent examples of investigations on promising bioinspired nanoparticles constructed via the supramolecular assemblies of hybrid nucleoside lipids (nucleolipids).

22.2 Carbon-Based Nanoparticles

In recent years, carbon-based nanomaterials have attracted considerable attention in nanomedicine due to their unique properties. These materials such as fullerenes, carbon nanotubes, graphene oxide, and perfluorocarbon nanoemulsions provide unique advantages and opportunities for drug delivery, therapeutics, diagnostics, and imaging.

22.2.1   Fullerenes

The discovery of the buckminsterfullerene (C_{60}) by Kroto et al. in 1985 gave rise to carbon technology era [14]. Fullerene's structures are composed of closed carbon cages formed by 12 pentagons and a number of hexagons that increased with the number of carbon [15]. Their unique chemical and physical properties make them attractive candidates for diagnostic, therapeutic, and theranostic applications [16, 17]. Several studies report radiolabeling of water-soluble C_{60} [18–24]. Nikolić et al. developed a novel method for radiolabeling nanoC_{60} with radioactive iodine, ^{125}I. Biodistribution studies indicated higher accumulation for ^{125}I-nanoC_{60} compared to the radioactive tracer Na^{125}I in the liver and spleen and also lower accumulation in the thyroid, stomach, lungs, and intestines. The described radiolabeling method might offer opportunities for cancer radiotherapy applications by using ^{131}I instead of ^{125}I [25]. Shultz et al. described the encapsulation of ^{177}Lu, gamma emitter used in SPECT imaging, in a fullerene cage. This agent was conjugated with an interleukin-13 (IL13) peptide to target an overexpressed receptor in globastoma multiform tumors. By complexation of other radioisotopes such as ^{166}Ho and ^{90}Y, other diagnostic and therapeutic applications might be elaborated using that kind of nanoplatform [26]. More recently, the same team developed a metallofullerene radiolabeled with lutetium 177, ^{177}Lu-DOTA-f-Gd$_3$N@C$_{80}$. This theranostic agent is able to deliver effective brachytherapy (with ^{177}Lu) and imaging functionality (MRI exam with Gd). The efficacy of this agent was demonstrated on orthotopic xenograft brain tumor models of glioblastoma multiform (GBM) [27,28]. Alternatively, Diener et al. opted to use ^{212}Bi, an $\boldsymbol{\alpha}$-emitter, for radio-immunotherapeutic purpose. In order to overcome its short half-life ($t_{1/2} = 60.6$ min), they prepared a C_{60} fullerene radiolabeled with its parent isotope, ^{212}Pb ($t_{1/2} = 10.6$ h). This nanoplatform was synthetized by recoil following α-decay of its short-lived radioisotope parent ^{216}Po generated *in situ* by the decay of ^{224}Ra. A preliminary biodistribution study demonstrated that encapsulation of ^{212}Pb in C_{60} prevented bone accumulation of ^{212}Pb but showed a rather slow clearance. Another limitation highlighted is that 36 % of the ^{212}Bi formed was released from the fullerene during the β-decay of ^{212}Pb [29].

22.2.2   Carbon Nanotubes

Carbon nanotubes have been first described by Ijima in 1991 [30]. They are homogenous tubes of rolled graphene sheets between 50 nm and 1 cm diameter. Nanotubes are classified in two different categories according to the number of graphene layers: (i) the single-walled carbon nanotube (SWCNT) from 1 to 2 nm diameter and (ii) the multi-walled carbon nanotube (MWCNT) from 10 to 100 nm diameter [31]. Different carbon nanotubes are used in imaging or therapy [32]. Mc Devitt et al.

functionalized an SWCNT with a DOTA derivative for the introduction of ^{86}Y and ^{111}In, radioisotopes used in PET and SPECT, respectively. Whole-body PET images showed an accumulation of radiotracer essentially in the liver, intestine, spleen, and at a lower level in bones [33]. Thereafter, a similar SWCNT was synthetized by the same team with a DOTA macrocycle grafted for ^{111}In chelation and also an antibody targeting CD20 epitopes overexpressed in Burkitt's lymphoma human cells. This resulting tracer succeeded in selectively targeting *in vitro* tumoral cells and *in vivo* tumors [34]. Villa et al. synthesized two new SWCNTs with two moieties (i) a single-stranded oligonucleotide, which undergoes self-assembly in the presence of the complementary-stranded, and (ii) a radiotracer component, made up of a ^{111}In-DOTA and a targeting component, consisting of an RGD peptide [35]. Liu et al. developed an SWCNT functionalized with PEG phospholipids. In this study, they attached DOTA macrocycles for ^{64}Cu introduction and c(RGDyK) peptides in order to target positive $\alpha_V\beta_3$ integrin tumors (U87MG) in mice. The high tumor uptake of the ^{64}Cu-SWCNT-PEG-RGD visualized by PET imaging was attributed to the multivalent effect (several RGD grafted by nanotubes). Raman spectroscopy revealed the presence of SWCNT-PEG-RGD in the liver and tumor and at a lower level in the kidney, but no SWCNT Raman signal was observed in the muscle [36]. Ruggiero et al. developed neo-vessels and irregular tumor vessels targeting nano-objects. For this purpose, this team synthetized two new functionalized SWCNTs with endothelial angiogenic cell-specific antibody, E_4G_{10}. The first derivative was composed of a DFO chelate allowing ^{89}Zr chelation to follow its accumulation by PET imaging. The second derivative was a DOTA chelate for ^{225}Ac introduction, α emitters used in radiotherapy. This study showed that those two nano-objects were specific to the targeted vessels. SWCNT-DFO^{89}Zr-E_4G_{10} gave PET imaging with a good contrast, and SWCNT-DOTA^{225}Ac-E_4G_{10} presented a significant therapeutic effect [37].

22.2.3   Graphene Oxide

Graphene oxide (GO) is made of monoatomistic carbon atom layers in a honeycomb structure. Graphene oxide has excellent electrical, thermal, mechanical, and optical properties [38]. In addition to their hydrophilic properties, their surface can be easily functionalized with, for example, hydrophilic polymers. GO has carefully been studied for biomedical applications in numerous studies [38–41] more particularly for imaging and therapeutic purposes [42–45]. Shi et al. synthetized a reduced graphene oxide (RGO) conjugated to two moieties: (i) an antibody TRC105 anti-CD105 and (ii) a ^{64}Cu-labeled NOTA macrocycle, allowing tumor vasculature targeting and PET imaging on mice model of breast cancer. ^{64}Cu-NOTA-RGO-TRC105 showed excellent *in vitro* and *in vivo* stability and vascularized tumor specificities [46]. More recently, this team used a new ^{64}Cu-labeled GO derivative, functionalized with a VEGF ligand to enhance tumor

vasculature targeting. *In vivo* studies were done on mice with U87MG tumors. ^{64}Cu-GO-VEGF nanoconjugate showed effective targeting for VEGFR on U84MG tumor models and showed great stability [47]. Chen et al. described the design and synthesis of a PEG-coated reduced nano-graphene oxide (RGO) labeled with [131]I. This RGO derivative had the advantage of giving access to radiotherapy and photothermal therapy simultaneously. After a 10 mg/kg ^{131}I-RGO-PEG (200 uCi) dose-injection on mouse tumor models, an effective elimination of the tumor after irradiation at 800 nm for 20 min had been shown. Toxicological data revealed no toxicity of the ^{131}I-RGO-PEG derivative at administrated dose on treated mice [48]. Another interesting idea developed by Fazaeli et al. was to radiolabel GO-aminopropylsilyl derivative with [198/199]Au nanoparticles to target and visualize by SPECT imaging fibrosarcoma tumors. This nanoconstruct allowed a fast and effective tumor visualization. However, the low lipophilicity of this structure induced also a fast body excretion (24 h) through kidneys [49].

22.2.4   *Perfluorocarbon Nanoemulsion*

Perfluorocarbon nanoemulsions are composed of perfluorocarbon liquid encapsulated in a phospholipidic monolayer and dispersed in water. Those particles are widely used for medical applications, more precisely for drug delivery [50,51], atherosclerosis [52], tumors, and plaque angiogenesis [53] diagnostic and treatment. For imaging, perfluorocarbon derivatives are widely studied as ^{19}F MRI contrast agents [54–56] as well as bimodal ^{19}F MRI-optical imaging agents [57–60]. Few studies also reported an application for PET imaging. In this context, Hu et al. developed ^{111}In-labeled perfluorocarbon nanoparticles for $\alpha_V\beta_3$ integrin targeting and cancer-induced angiogenesis detection. The *in vivo* studies were done on Vx-2 rabbit tumors. Nanoparticles provided a high tumor signal and accumulation in nascent tumors as a function of both specific and passive entrapment within the neovasculature [61]. More recently, Fabiilli et al. encapsulated ^{18}F-fluorodeoxyglucose (FDG) in a double perfluorocarbon emulsion and performed emulsion or solution injections in rats bearing gliosarcoma. When FDG solution was compared to FDG emulsions, FDG uptake decreased by 36 % in the brain and 44 % in tumors (calculated from the AUC_{SUV}). Moreover, dynamic micro-PET imaging indicated no accumulation of FDG emulsions in the lungs, which is critical in minimizing PFC-related bioeffects [62].

As we briefly resumed in this section, carbon-based nanomaterials possess intrinsic physicochemical properties that are wisely exploited. However, potential toxicity of those nanomaterials has been pointed out in the last decade and is well highlighted and described in extensive toxicological review and studies [63–68]. Size, shapes, surface properties and chemistry, concentration, agglomeration, dose, and preparation of carbon-based nanomaterials are all determinants for their biological activities that may also lead to toxicity.

22.3   Metal-Based Nanoparticles

22.3.1   Gold Nanoparticles

In biomedical field, gold nanoparticles have received increasing attention due to their biocompatibility and optical properties, conferred by their localized surface plasmon resonance (SPR) in particular in imaging (x-ray [69] and photoacoustic [70] imaging) and cancer therapy [71–73]. Gold nanoparticles (AuNPs) consist of a Au core with surface coating. They are colloidal or clustered particles with diameters in the range of a few to several hundred nanometers. In order to control optical properties, size and shape can be easily tuned to obtain 1 nm to 150 nm AuNPs with diverse morphologies. Recent studies have reported AuNPs radiolabeling for therapy [74, 75] and nuclear imaging [76–86].

Karmani et al. studied conjugation influence of the distribution of an antibody, the cetuximab on gold nanoparticle labeled with [89]Zr in mice bearing A431 xenografts. Immuno-PET studies showed that conjugation of cetuximab to AuNP did not affect EGFR-dependent tumor uptake. However, compared to [89]Zr-cetuximab, the higher reticuloendothelial system uptake for AuNP-[89]Zr-cetuximab could be a limitation of radioactive nanoparticle use for systemic metabolic radiotherapy [79].

Felber et al. described a new coating ligand for Qds and AuNPs allowing direct labeling with $[^{99m}Tc(OH_2)_3(CO)_3]^+$ in the last step. The ligand comprises (i) a thiol group as anchor for the NPs surface, (ii) a PEG linker, (iii) and 2,3-diaminopropionic acid to act as chelator for $[^{99m}Tc (CO)_3]^+$ and for the introduction of a small prostate-specific membrane antigen (PSMA) inhibitor *via* an amide link. Biodistribution of various sized (7 and 14 nm) AuNPs performed by micro-SPECT showed rapid clearance from the blood pool through hepatobiliary pathway, in mice bearing LNCaP xenografts. 7 nm AuNPs revealed higher stability and significantly higher bone uptake than 14 nm AuNPs [82].

Zhang et al. reported functionalized gold nanoparticles preparation through nucleic acid-directed assembly. Oligodeoxynucleotide-derivative gold nanoparticles were assembled with a library of pre-functionalized complementary PNAs (peptide nucleic acid). PNAs were functionalized with either (i) ^{64}Cu-DOTA for PET imaging, (ii) PEG for stealth properties, or (iii) with Cy5 for fluorescent imaging. The resulting AuNPs showed a good *in vitro* and *in vivo* stability [84]. Another interesting strategy developed by Black et al. consisted in the preparation of multispectral SPECT agent to quantify MMP9 expression in tumors. AuNPs were radiolabeled by two distinct nuclides, ^{125}I and ^{111}In, separated by an MMP9-cleavable peptide [85].

[177]Lu-labeled AuNPs conjugated to different peptides were proposed as a new class of theranostic agents and have been recently reviewed [74]. In this context, Luna-Gutiérrez et al. evaluated the potential of ^{177}Lu-labeled gold nanoparticle (20 nm) conjugated to cyclo-[RGDfK(C)] peptide *via* the cysteine thiol group, as a plasmonic photothermal therapy and targeted radiotherapy system in MCF7 breast cancer cells. After laser irradiation, [RGDfK(C)]-AuNPs' presence in cells caused a

significant decrease in MCF7 viability, down to 9 %, and after treatment, with [177]Lu-[RGDfK(C)]-AuNP, the MCF7 proliferation was significantly inhibited [87]. They also evaluated [177]Lu-[RGDfK(C)]-AuNP therapeutic response in athymic mice bearing $\alpha_V\beta_3$-integrin-positive C6 gliomas. The nanoconstruct significantly decreased glioma tumor progression. No uptake in nontarget organs or renal toxicity induction was observed [88].

22.3.2   Iron Oxide Nanoparticles

Iron oxide nanoparticles are superparamagnetic particles especially used as MRI contrast agents. Several studies reported their radiolabeling for use in MRI/PET or MRI/SPECT bimodal imaging and have been recently reviewed [89].

22.3.3   Other Metal-Based Nanoparticles

A particularly interesting idea, developed by Pérez-Campaña et al., consists in ^{18}F radiolabeling of ^{18}O-enriched aluminum oxide NPs by direct irradiation with 16 MeV protons. Size and crystalline phase of those NPs were not altered during the irradiation step. Biodistribution studies were conducted in male rats after intravenous injection. PET imaging has shown NP rapid accumulation in the liver. Radioactivity was also detected in the lungs, kidney, heart, and stomach. This labeling strategy is promising for activation of metal oxide particles or powder [90]. A more recent study, published by the same group, presented an analogous strategy for ^{13}N radiolabeling of commercially available aluminum oxide with different sizes *via* the [16]O (p,α)[13]N nuclear reaction. PET imaging performed after intravenous injection in rats allowed to determine NP accumulation in organs up to 68 min postinjection, despite the short half-life of radioactive [13]N. Results have shown that large NPs were uptaken in the lungs, while small particles were accumulated in the stomach, heart, kidney, and bladder. Moreover, a high accumulation in the liver was observed regardless of the NP size (Fig. 22.3) [91].

22.4   Polymer-Based Nanoparticles

22.4.1   Dendrimers

Dendrimers are highly branched macromolecules with a well-defined number of peripheral groups discovered by Tomalia et al. in the early 1980s [92]. They formed spherical object in the nanometer range. Size, architecture, density, and surface
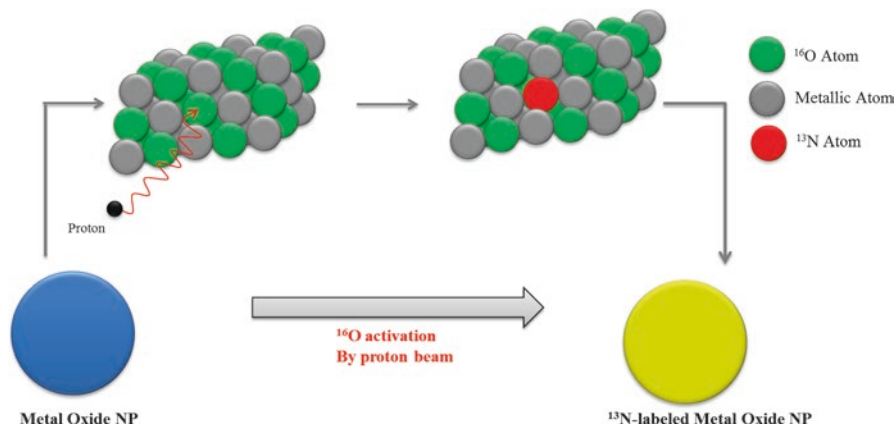
Fig. 22.3 Activation of Al_2O_3 NPs by proton irradiation via the ^{16}O $(p,\alpha)^{13}N$ nuclear reaction. Metal oxide NPs are directly irradiated with protons, converting ^{16}O atoms to ^{13}N atoms by collision. Adapted from [91]

groups are easily tunable. They are widely used in nuclear imaging and therapy fields, especially due to the possibility to incorporate several recognition units in order to improve targeting [93]. Moreover in imaging field, dendritic structures are also used to design multivalent or multimodal contrast agents [94]. However, the question of their biodegradability is highly discussed, and biocompatible dendrimer designs are reviewed by Cheng et al. [95].

A PAMAM dendrimer DOTA conjugate was designed by Ghai et al. ^{68}Ga radiolabeling was achieved with high radiochemical yield (79 % decay corrected), and the subsequent tracer presented good stability. Preliminary PET imaging studies in mice bearing EAT (Ehrlich's ascites tumors) showed a ^{68}Ga-dendrimer accumulation in tumor through passive targeting and excretion through kidney [96].

McNelles et al. reported the synthesis of a PEGylated fifth-generation aliphatic dendrimers functionalized with peripheral vinyl groups and a dipicolylamine Tc(I) chelate core. The radiolabeling was achieved with high radiochemical purity (>99 %) using $[^{99m}Tc (CO)_3(H_2O)_3]^+$. SPECT imaging of healthy rats indicated that the radiolabeled dendrimer circulated in the blood up to 24 h postinjection mainly due to PEG chains. SPECT imaging experiments were then performed on xenografted murine tumor model. Results demonstrated a dendrimer accumulation within the tumor through the EPR effect 6 h postinjection [97].

Laznickova et al. described the synthesis of ^{177}Lu-radiolabeled G1 and G4 PAMAM dendrimer functionalized with DOTA-monopyridine-N-oxide. Biodistribution studies on rats revealed that ^{177}Lu-G1-PAMAM dendrimer injection induced a lower residence time of radioactivity in the blood and organs, in comparison with ^{177}Lu-G4-PAMAM dendrimer. However, the latter allowed the conjugation of higher number of metal chelator and thus radiometal per molecule [98]. A recent study achieved by Kovacs et al. described also the synthesis of ^{177}Lu-G4-PAMAM dendrimers functionalized with DOTA to determine the elementary changes in

tumors caused by ionizing radiations. C57BL/6 mice tumor tissues treated with ^{177}Lu-DOTA-dendrimer showed decreases in Br, Ca, Cl, K, and Na concentrations and increases in Fe, Mg, Rb, S, and Zn concentrations, when compared to untreated tumors tissues [99].

Zhao et al. developed a ^{131}I radiolabeled theranostic platform for SPECT imaging and radiotherapy of an MMP-2 overexpressing xenografted glioma model *in vivo*. Generation five amine terminated poly(amidoamine) was used to conjugate (i) PEG, (ii) targeting agent chlorotoxin (CTX), and (iii) 3-(4'-hydroxyphenyl)propionic acid-OSu (HPAO). The HPAO phenol groups allowed ^{131}I radiolabeling with good stability and high radiochemical purity. The ^{131}I-dendrimer biodistribution was studied by SPECT imaging. Dendrimers were highly uptaken in the liver, and a low accumulation was observed in the tumor, lungs, stomach, heart, kidney, spleen, intestines, and soft tissues. It should be noted that tumor uptake was higher for the ^{131}I-CTX-dendrimer in comparison with the ^{131}I-dendrimer without CTX. Those data confirmed the targeting role mediated by the CTX moiety. It was also demonstrated that after treatment with the ^{131}I-CTX-dendrimer, the tumor grows slower than those of the mice treated by either saline, Na[131]I, or ^{131}I-dendrimer without CTX [100].

22.4.2   Nanocapsules

Nanocapsules are vesicular colloidal system constituted with a liquid core and polymeric shell. Such structures can be obtained from a large variety of monomers or polymers through direct chemical reaction or through precipitation of preformed template at the interface of the droplet. Size, morphology, and functionalization can be controlled [101]. Few examples of radiolabeled nanocapsules with ^{99m}Tc have been reported [102–104]. In this context, Pereira et al. radiolabeled nanocapsule with ^{99m}Tc-HMPAO (*D,L*-hexamethylpropyleneamine oxime) in order to identify inflammatory process in rats. Nanocapsules were prepared with biodegradable polymers poly(*D,L*-lactic acid) (PLA) and were PEGylated or not. The authors demonstrated that both types of nanocapsules were able to encapsule ^{99m}Tc-HMPAO. However, as shown by AFM, physical and structural properties of PEGylated nanocapsules were more homogeneous. Biodistribution studies have shown similar uptake in inflamed and control paws for ^{99m}Tc-HMPAO-NC and free ^{99m}Tc-HMPAO, while PEGylated ^{99m}Tc-HMPAO-NC have shown a greater uptake. The authors have concluded that the latter could be useful as radiotracer for inflammatory process imaging [105, 106]. Polyglucosamine-/squalene-based nanocapsules (PG-NC) were radiolabeled with ^{111}In by Vicente et al. to monitor the biodistribution of PG-NC and their affinity for the draining lymph nodes. After injection in New Zealand white rabbits, γ-scintigraphy imaging revealed slower clearance than for the control [111]InCl$_3$ and progressive accumulation in popliteal lymph node [107].

22.5   Lipid-Based Nanoparticles

22.5.1   Liposomes

Liposomes are defined as phospholipid vesicles consisting of one or more concentric lipid bilayers with an aqueous internal cavity. With a wide range of physicochemical and biophysical properties (particles size, charge, number of lamellae, lipid composition, surface modification), liposomal formulations can be modified to control their biological behaviors. Liposomal systems have received widespread attention as nanocarriers for a wide range of biomedical applications by overcoming obstacles to cellular and tissue uptake, stabilizing therapeutic compounds, and improving biodistribution of lipophilic and hydrophilic compounds to target sites [108]. Numerous studies described the radiolabeling of liposomes for diagnostic or therapeutic applications [9, 109–111].

Recently De Barros et al. prepared long circulating and pH-sensitive liposomes (SpHL) containing bombesin radiolabeled with ^{99m}Tc (^{99m}Tc-BBN$_{(7-14)}$) to target breast cancer tissues. Liposomes presented a diameter in the range of 160 nm and a ^{99m}Tc-BBN$_{(7-14)}$ encapsulation percentage around 30 % in the presence of glucose (SpHLG). Moreover the authors demonstrated that the liposomes remained stable up to 120 days of storage. When injected in breast tumor-bearing nude mice, SpHLG-^{99m}Tc-BBN$_{(7-14)}$ exhibited a high tumor/muscle and tumor/blood ratio. Furthermore, scintigraphic studies revealed a strong signal in tumor area suggesting the tumor specificity of the radiotracer [112]. Ogawa et al. reported the synthesis of ^{111}In-radiolabeled liposome modified with phosphatidylserine for atherosclerotic plaque imaging. It was demonstrated that the tracer allowed macrophages and artherosclerotic region targeting in Apo E −/− mice. However, too rapid blood clearance was also observed [113]. In order to solve this problem, the authors developed new liposomes-PS modified with PEG. As expected, slower blood clearance was observed with PEGylated liposomes. Nevertheless, PEGylation did not improve the uptake in artherosclerotic plaques *in vivo* [114]. Bandekar et al. evaluated the potential of PEGylated liposomes radiolabeled with ^{225}Ac to selectively kill PSMA-expressing human (LNCaP and HUVEC induced to express PSMA) and rat (Mat-Lu) cell lines *in vitro*. Two targeting ligands were compared: (i) the mouse antihuman PSMA J591 antibody and (ii) the A10 PSMA aptamer. J591-liposomes showed higher level of specific binding to all cell lines than A10-liposomes did. It has also been shown that radiolabeled J591-labeled liposomes are more cytotoxic than radiolabeled A10-liposomes. Moreover relatively low LD$_{50}$ values of J591-labeled liposomes both on LNCaP and on PSMA-expressing HUVEC suggested the potential of these liposomes for selective antivascular α-radiotherapy [115]. Petersen et al. described theranostic liposomes and evaluated their potential in human xenografted mouse model. For this purpose PEGylated liposomes were radiolabeled either with ^{64}Cu for PET imaging or with ^{177}Lu for internal tumor radiotherapy. They investigated also the optimal level of PEGylation in liposomes. The authors demon-

strated that 10 % mol PEGylated liposomes showed higher tumor uptake than 5 % mol PEGylated liposomes. PET imaging with ^{64}Cu-liposomes allowed clear tumor visualization. High-absorbed doses to the tumor were estimated by dosimetric analysis for ^{177}Lu-liposomes. This result suggested that ^{177}Lu-liposomes could achieve adequate delivery of therapeutic internal radiation to solid tumors. However, the therapeutic potential of ^{177}Lu-liposomes must be further evaluated in a tumor-bearing mice model [116].

22.5.2   Solid Lipid Nanoparticles

Solid lipid nanoparticles (SLNs) consist in spherical solid lipid particles dispersed in water or in aqueous surfactant solution. They are usually constituted with a hydrophobic solid core coated with a phospholipid monolayer. They are highly used as drug carrier [117–119]. Radiolabeled SLNs have been designed as potential nuclear imaging agent particularly as SPECT imaging agents by ^{99m}Tc radiolabeling [120–124]. In a recent study, Banerjee et al. described the synthesis of SLNs encapsulating paclitaxel radiolabeled with ^{99m}Tc by a novel method. Taxol was radiolabeled also, in order to compare their biodistribution in normal rats. It was found that brain uptake of ^{99m}Tc-SLNs was 5 times higher than ^{99m}Tc-Taxol. This result suggests that ^{99m}Tc-SLNs are able to deliver more paclitaxel in the brain than Taxol formulation [125]. Andreozzi et al. developed a method for SLNs radiolabeling by ^{64}Cu for PET imaging. A BAT chelator (6-[p-(bromoacetamido) benzyl]-1,4,8,11-tetraazacyclotetradecane-N,N',N'',N'''-tetraacetic acid) was conjugated with a synthetic lipid and incorporated into the SLN monolayer. ^{64}Cu-SLNs were obtained with 67 % radiolabeling yield after incubation with [64]CuCl$_2$. PET imaging and gamma counting suggested that ^{64}Cu-SLNs are circulating in the bloodstream after 3 h but are almost entirely cleared after 48 h. The authors planned to coat SLNs with hydrophilic polymers such as PEG to reduce SLNs clearance from the RES and increase the blood half-life [126].

22.5.3   Micelles

Micelles are colloidal dispersions belonging to a group of association or amphiphilic colloids, which form spontaneously under certain concentration and temperature phase. Polymeric and non-polymeric micellar systems are subject of many publications addressing various biomedical applications due to favorable biodistribution and lower toxicity of encapsulated therapeutic agents [127]. Radiolabeled micelles have been extensively studied during the last few years [128–140]. A recent study described the use of lipid-coated magnetite micelles to act simultaneously as vehicle for vaccine and as radiotracer for SPECT/PET imaging. Similarity between Ga^{3+} and Fe^{3+} in charge and size allowed achieving gallium radiolabeling by exchange in

biomolecule metalation. Antigen (OVA) and TLR9 agonists (CpGS) were accommodated in the hybrid micelles for efficient delivery in the lymph nodes. SPECT imaging demonstrated migration from the injection site to regional and non-regional lymph nodes. In addition, *in vitro* and *in vivo* studies showed that cellular and hormonal immune responses were greatly enhanced and provided protection against tumor [141]. You et al. used a combination of core cross-linked polymeric micelles radiolabeled with [177]Lu (CCPM-^{177}Lu) and cyclopamine solubilized in lipid-liquid nanoparticle system (CPA-LLP). Cyclopamine is a potent inhibitor of Hedgehog pathway studied for anticancer effect. It has also been investigated for enhancing tumor response to radiation therapy. As expected clonogenic assays demonstrated that CPA-LLP significantly enhances cell response to CCPM-^{177}Lu radiotherapy. Moreover, combination of CPA-LLP and CCPM-^{177}Lu delayed tumor growth more than monotherapy alone, in 4T1 Miapaca-2 mouse xenografted models [142]. Multifunctional theranostic unimolecular micelles have been generated by Guo et al. They conjugated brush-shaped amphiphilic block copolymers to a monoclonal antibody anti-CD105 (TRC105) and to NOTA macrocycle for ^{64}Cu introduction. In addition doxorubicin was loaded into the unimolecular micelle. It has been demonstrated that these multifunctional unimolecular micelles offer pH-responsive drug release and noninvasive PET imaging capability, together with both passive and active tumor-targeting [143].

22.6 Nucleolipid-Based Nanoparticles

The self-assembly properties of biomolecules play a fundamental role in biology, and these principles have been widely exploited for the implementation of supramolecular structures and nanodevices [144]. The multiple cooperative non-covalent interactions (e.g., H-bonding, $\pi-\pi$ stacking, hydrophobic effects, etc.) between biomolecules allow the synthesis of complex biological systems and structures. Scientists are taking advantage of these biological principles for the design of hybrid amphiphiles based on the combination of biological units such as amino acids [145]. Peptides [146–149], sugar [150–152], nucleic acids [153, 154], and lipids are currently emerging as new class of biocompatible molecules for biomedical applications. The combination of lipid with nucleoside/nucleotide moieties has been reported to improve the cellular internalization of nucleoside drugs [155] in the treatment of certain diseases including cancers. Nucleolipids [156–158] have been the object of intense investigations due to their unique self-organization properties and their potential applications in the biomedical field. For example, nucleolipids featuring reduced cytotoxicity have been used for the transfection of DNA [159] and siRNA [160, 161].

Ten years ago our group has reported the formation of microspheres simply by hydrating phosphocholine-based nucleolipids with aqueous solutions containing either actinide or lanthanide salt [162, 163]. These actinide and/or lanthanide microspheres were prepared as independent objects suspended in

aqueous media. Such a result was the first step in the exploration of nucleolipid behaviors in the presence of radionuclides. The formation of these microspheres demonstrated the versatility and utility of nucleolipids in this field and the importance of combining nucleolipids and inorganic metals to create new structures for the synthesis of nano- and microscale materials using the principles of supramolecular assembly.

[99m]Tc has long track records for use in drug development as SPECT imaging agents [164]. Considering the above and the potential of ^{99m}Tc for labeling nanoparticles, recently, we investigated advanced formulations featuring nucleolipids. Interestingly, it was demonstrated that nucleolipid-based nanoparticles can be labeled with ^{99m}Tc in the absence of chelating agent such as DOTA (1,4,7,10-tetraazacyclododecane-1,4,7,10-tetraacetic acid). These nanoparticles were implemented using a bottom-up strategy involving positive, negative nucleoside lipids (NLs) and PEGylated nucleoside lipids (Fig. 22.4). The direct labeling of these nanoparticles was realized with ^{99m}Tc using stannous chloride as a reducing agent to reduce pertechnetate oxidation state from +7 to +5. We hypothesized that in these conditions ^{99m}Tc forms a complex with uridine moieties (Fig. 22.5). The labeling efficiency was found to be quantitative (yield higher than 97 %). Importantly, it was shown that such functionalized and labeled nanoparticles loaded with cisplatin (active principle ingredient, API) can address pharmacokinetic and biodistribution issues. Indeed, it was found that these nanoparticles increase the half-life of the API *in vivo* and accumulate in tumor tissue, indicating that nucleolipid-based formulations could provide novel radiotracer labeled nanoparticles with potential applications in the field image-guided therapies.
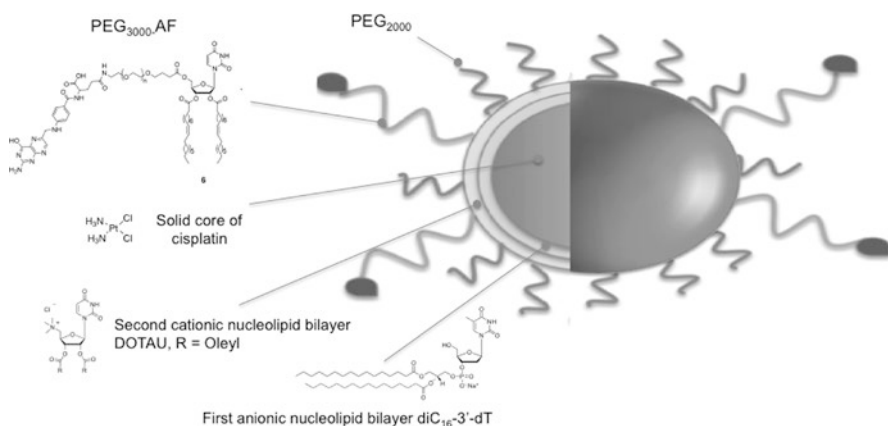
Fig. 22.4 Drawing of the nucleolipid-based nanoparticles. These PEGylated (PEG2000 and PEG3000 folic acid) nanoparticles feature a solid core of cisplatin (high drug loading) stabilized by two layers of nucleolipids (anionic nucleotide-lipid, diC16-3'-dT, and cationic-nucleoside-lipid DOTAU)

Fig. 22.5 Proposed
^{99m}Tc-pyrimidine complex
allowing the labeling of the
NPs in the absence of
DOTA
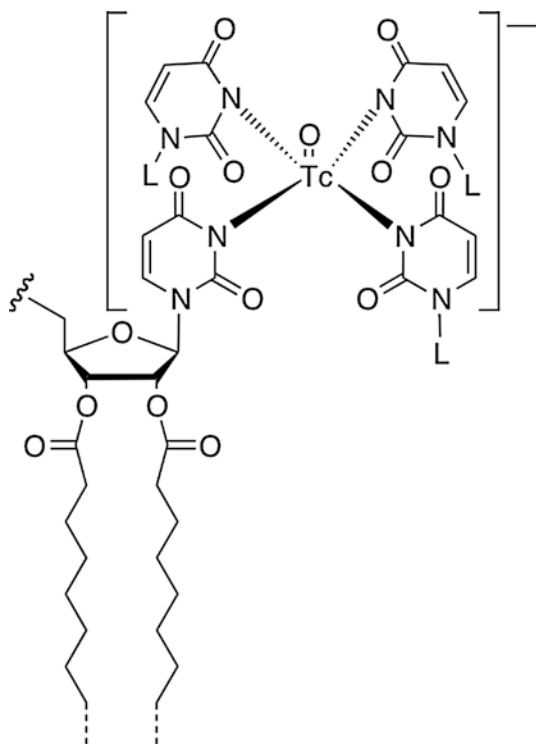
22.7   Conclusion

Multiple radiolabeled nanoplatforms have been investigated and developed in the last two decades, and these approaches have demonstrated their potential use in diagnostic, imaging, and therapy. Targeted radionuclide therapies of cancer provide a viable alternative to chemo- and external beam radiation therapies of tumor cells, including neuroendocrine tumors (NETs).

NETs arise from the neuroendocrine system and are a heterogeneous group of disease, including pluripotent endocrine cells in different sites, presenting with different signs and symptoms, various malignant potential, and different prognosis. Due to this biological diversity, the early recognition of a tumor's potential for progression is very important. Somatostatin receptors (SR) are overexpressed in a majority of neuroendocrine tumors and are targeted using ^{111}In-pentetreotide (SRS; Octreoscan®). A.I. Petersen et al., investigated a somatostatin peptide analog (TATE) as a targeting moiety on 100 nm PEGylated liposomes to evaluate somatostatin targeting and cancer diagnostic potential, using PET imaging [165]. The positron emitter ^{64}Cu is used as imaging agent and was encapsulated in liposomes. To evaluate the diagnostic imaging agent, the tumor-to-muscle (T/M) ratio of ^{64}Cu-TATE-liposomes and free peptide uptake were compared in neuroendocrine carcinoma H727-bearing mice. The experiments seem to show a significantly higher

T/M ratio for targeted liposomes, making liposomes a promising biomedical agent for visualizing NETs. Recently, researchers have developed radiopeptide conjugated to gold nanoparticles and functionalized PAMAM dendrimers as multimeric and multivalent systems for NETs imaging [166]. Those two nanosized multimeric systems, ^{99m}Tc-PAMEM-Tyr[3]-octreotide and ^{99m}Tc-AuNP-Tyr[3]-octreotide, showed high and specific somatostatin-positive tumor uptake in mice bearing AR42J tumors and therefore potential radiolabeled nanoplatforms for NET imaging. Abou et al. reported the synthesis of PEGylated liposomes radiolabeled with Gd and with [89]Zr for bimodal MRI/PET imaging of neuroendocrine tumors. Liposomes were conjugated with octreotide to target human receptor somatostatin subtype-2 (SSTr2) [167]. Arora et al. developed a PEG-coated ^{177}Lu-DOTATATE-PLGA nanoparticles for neuroendocrine tumor therapy. PLGA (polylactic-co-glycolic acid) was chosen because of its biocompatibility and biodegradability properties. *In vivo* studies have shown reduced renal uptake suggesting the potential of PEG-coated ^{177}Lu-DOTATATE-PLGA 50:50 nanospheres towards reducing nephrotoxicity and unnecessary radiation dose to normal tissues [168].

One of the greatest advantages of the nanoparticles technology is the ability to generate functionalized particles from materials of diverse chemical nature (polymers, carbon, metals, lipids, nucleolipids), with different morphology and with a wide variety of targeting ligands. Radiolabeled nanoparticles will undoubtedly lead a revolution for drug delivery, therapeutics, diagnostics, and multimodality imaging. More and more scientific research teams will join this field in order to prepare nanoparticle-based platforms, which can allow for efficient, specific *in vivo* delivery of diagnostic agents without toxicity.

References

1. Moghimi SM. Nanomedicine: current status and future prospects. FASEB J. 2005; 19:311–30.
2. Minchin RF, Martin DJ. Minireview: nanoparticles for molecular imaging—an overview. Endocrinology. 2010;151:474–81.
3. de Barros A, Tsourkas A, Saboury B, Cardoso V, Alavi A. Emerging role of radiolabeled nanoparticles as an effective diagnostic technique. EJNMMI Res. 2012;2:39.
4. Liu Y, Welch MJ. Nanoparticles labeled with positron emitting nuclides: advantages, methods, and applications. Bioconjug Chem. 2012;23:671–82.
5. Xing Y, Zhao J, Conti PS, Chen K. Radiolabeled nanoparticles for multimodality tumor imaging. Theranostics. 2014;4:290–306.
6. Kiessling F, Mertens ME, Grimm J, Lammers T. Nanoparticles for imaging: top or flop? Radiology. 2014;273:10–28.
7. Stockhofe K, Postema J, Schieferstein H, Ross T. Radiolabeling of nanoparticles and polymers for PET imaging. Pharmaceuticals. 2014;7:392–418.
8. Xing Y, Zhao J, Shi X, Conti PS, Chen K. Recent development of radiolabeled nanoparticles for PET imaging. Austin J Nanomedicine Nanotechnol. 2014;2:1016.
9. Hong H, Zhang Y, Sun J, Cai W. Molecular imaging and therapy of cancer with radiolabeled nanoparticles. Nano Today. 2009;4:399–413.

10. Phillips WT, Goins BA, Bao A. Radioactive liposomes. Wiley Interdiscip Rev Nanomed Nanobiotechnol. 2009;1:69–83.
11. Xie J, Lee S, Chen X. Nanoparticle-based theranostic agents. Adv Drug Deliv Rev. 2010;62:1064–79.
12. Bae KH, Chung HJ, Park TG. Nanomaterials for cancer therapy and imaging. Mol Cells. 2011;31:295–302.
13. Nyström AM, Wooley KL. The importance of chemistry in creating well-defined nanoscopic Embedded therapeutics: devices capable of the dual functions of imaging and therapy. Acc Chem Res. 2011;44:969–78.
14. Kroto HW, Heath JR, O'Brien SC, Curl RF, Smalley RE. C60: buckminsterfullerene. Nature. 1985;318:162–3.
15. Astefanei A, Núñez O, Galceran MT. Characterisation and determination of fullerenes: a critical review. Anal Chim Acta. 2015;882:1–21.
16. Dellinger A, Zhou Z, Connor J, Madhankumar A, Pamujula S, Sayes CM, Kepley CL. Application of fullerenes in nanomedicine: an update. Nanomed. 2013;8:1191–208.
17. Partha R, Conyers JL. Biomedical applications of functionalized fullerene-based nanomaterials. Int J Nanomedicine. 2009;4:261–75.
18. Yuguo L, Xiaodong Z, Qingnuan L, Wenxin L. Radioiodination of C60 Derivative C60(OH) xOy. J Radioanal Nucl Chem. 2001;250:363–4.
19. Yu-guo L, Xuan H, Riu-li L, Qing-nuan L, Xiao-dong Z, Wen-xin L. Synthesis of [14C] quincetone. J Radioanal Nucl Chem. 2005;265:127–31.
20. Qingnuan L, Yan X, Xiaodong Z, Ruili L, Qieqie D, Xiaoguang S, Shaoliang C, Wenxin L. Preparation of 99mTc-C60(OH)x and its biodistribution studies. Nucl Med Biol. 2002;29:707–10.
21. Ji ZQ, Sun H, Wang H, Xie Q, Liu Y, Wang Z. Biodistribution and tumor uptake of C60(OH) x in mice. J Nanoparticle Res. 2005;8:53–63.
22. Xu J-Y, Li Q-N, Li J-G, Ran T-C, Wu S-W, Song W-M, Chen S-L, Li W-X. Biodistribution of 99mTc-C60(OH)x in sprague–dawley rats after intratracheal instillation. Carbon. 2007;45:1865–70.
23. Yamago S, Tokuyama H, Nakamura E, Kikuchi K, Kananishi S, Sueki K, Nakahara H, Enomoto S, Ambe F. *In vivo* biological behavior of a water-miscible fullerene: 14C labeling, absorption, distribution, excretion and acute toxicity. Chem Biol. 1995;2:385–9.
24. Cagle DW, Kennel SJ, Mirzadeh S, Alford JM, Wilson LJ. *In vivo* studies of fullerene-based materials using endohedral metallofullerene radiotracers. Proc Natl Acad Sci. 1999;96:5182–7.
25. Nikolić N, Vranješ-Đurić S, Janković D, Đokić D, Mirković M, Bibić N, Trajković V. Preparation and biodistribution of radiolabeled fullerene C 60 nanocrystals. Nanotechnology. 2009;20:385102.
26. Shultz MD, Duchamp JC, Wilson JD, et al. Encapsulation of a radiolabeled cluster Inside a fullerene cage, 177LuxLu(3−x)N@C80: an interleukin-13-conjugated radiolabeled metallofullerene platform. J Am Chem Soc. 2010;132:4980–1.
27. Shultz MD, Wilson JD, Fuller CE, Zhang J, Dorn HC, Fatouros PP. Metallofullerene-based nanoplatform for brain tumor brachytherapy and longitudinal imaging in a murine orthotopic xenograft model. Radiology. 2011;261:136–43.
28. Wilson JD, Broaddus WC, Dorn HC, Fatouros PP, Chalfant CE, Shultz MD. Metallofullerene-nanoplatform-delivered interstitial brachytherapy improved survival in a murine model of glioblastoma multiforme. Bioconjug Chem. 2012;23:1873–80.
29. Diener MD, Alford JM, Kennel SJ, Mirzadeh S. (212)Pb@C(60) and its water-soluble derivatives: synthesis, stability, and suitability for radioimmunotherapy. J Am Chem Soc. 2007;129:5131–8.
30. Iijima S. Helical microtubules of graphitic carbon. Nature. 1991;354:56–8.
31. Liu Z, Tabakman S, Welsher K, Dai H. Carbon nanotubes in biology and medicine: *in vitro* and *in vivo* detection, imaging and drug delivery. Nano Res. 2010;2:85–120.

32. Martincic M, Tobias G. Filled carbon nanotubes in biomedical imaging and drug delivery. Expert Opin Drug Deliv. 2015;12:563–81.

33. McDevitt MR, Chattopadhyay D, Jaggi JS, et al. PET imaging of soluble yttrium-86-labeled carbon nanotubes in mice. PLoS One. 2007;2:e907.

34. McDevitt MR, Chattopadhyay D, Kappel BJ, Jaggi JS, Schiffman SR, Antczak C, Njardarson JT, Brentjens R, Scheinberg DA. Tumor targeting with antibody-functionalized, radiolabeled carbon nanotubes. J Nucl Med. 2007;48:1180–9.

35. Villa CH, McDevitt MR, Escorcia FE, Rey DA, Bergkvist M, Batt CA, Scheinberg DA. Synthesis and biodistribution of oligonucleotide-functionalized, tumor-targetable carbon nanotubes. Nano Lett. 2008;8:4221–8.

36. Liu Z, Cai W, He L, Nakayama N, Chen K, Sun X, Chen X, Dai H. *In vivo* biodistribution and highly efficient tumour targeting of carbon nanotubes in mice. Nat Nanotechnol. 2007;2:47–52.

37. Ruggiero A, Villa CH, Holland JP, Sprinkle SR, May C, Lewis JS, Scheinberg DA, McDevitt MR. Imaging and treating tumor vasculature with targeted radiolabeled carbon nanotubes. Int J Nanomedicine. 2010;5:783–802.

38. Wu S-Y, An SSA, Hulme J. Current applications of graphene oxide in nanomedicine. Int J Nanomedicine. 2015;10(Spec Iss):9–24.

39. Zhou X, Liang F. Application of graphene/graphene oxide in biomedicine and biotechnology. Curr Med Chem. 2014;21:855–69.

40. Byun J. Emerging frontiers of graphene in biomedicine. J Microbiol Biotechnol. 2015;25:145–51.

41. Liu J, Cui L, Losic D. Graphene and graphene oxide as new nanocarriers for drug delivery applications. Acta Biomater. 2013;9:9243–57.

42. Li J-L, Tang B, Yuan B, Sun L, Wang X-G. A review of optical imaging and therapy using nanosized graphene and graphene oxide. Biomaterials. 2013;34:9519–34.

43. Yang K, Feng L, Shi X, Liu Z. Nano-graphene in biomedicine: theranostic applications. Chem Soc Rev. 2013;42:530–47.

44. Feng L, Wu L, Qu X. New horizons for diagnostics and therapeutic applications of graphene and graphene oxide. Adv Mater Deerfield Beach Fla. 2013;25:168–86.

45. Orecchioni M, Cabizza R, Bianco A, Delogu LG. Graphene as cancer theranostic tool: progress and future challenges. Theranostics. 2015;5:710–23.

46. Shi S, Yang K, Hong H, Valdovinos HF, Nayak TR, Zhang Y, Theuer CP, Barnhart TE, Liu Z, Cai W. Tumor vasculature targeting and imaging in living mice with reduced graphene oxide. Biomaterials. 2013;34:3002–9.

47. Shi S, Yang K, Hong H, Chen F, Valdovinos HF, Goel S, Barnhart TE, Liu Z, Cai W. VEGFR targeting leads to significantly enhanced tumor uptake of nanographene oxide *in vivo*. Biomaterials. 2015;39:39–46.

48. Chen L, Zhong X, Yi X, Huang M, Ning P, Liu T, Ge C, Chai Z, Liu Z, Yang K. Radionuclide 131I labeled reduced graphene oxide for nuclear imaging guided combined radio- and photothermal therapy of cancer. Biomaterials. 2015;66:21–8.

49. Fazaeli Y, Akhavan O, Rahighi R, Aboudzadeh MR, Karimi E, Afarideh H. *In vivo* SPECT imaging of tumors by 198,199Au-labeled graphene oxide nanostructures. Mater Sci Eng C. 2014;45:196–204.

50. Gupta R, Shea J, Scaife C, Shurlygina A, Rapoport N. Polymeric micelles and nanoemulsions as drug carriers: therapeutic efficacy, toxicity, and Drug Resistance. J Control Release. 2015;212:70–7.

51. Rapoport N, Gupta R, Kim Y-S, O'Neill BE. Polymeric micelles and nanoemulsions as tumor-targeted drug carriers: insight through intravital imaging. J Control Release. 2015;206:153–60.

52. Caruthers SD, Cyrus T, Winter PM, Wickline SA, Lanza GM. Anti-angiogenic perfluorocarbon nanoparticles for diagnosis and treatment of atherosclerosis. Wiley Interdiscip Rev Nanomed Nanobiotechnol. 2009;1:311–23.

53. Lanza GM, Winter PM, Caruthers SD, Hughes MS, Hu G, Schmieder AH, Wickline SA. Theragnostics for tumor and plaque angiogenesis with perfluorocarbon nanoemulsions. Angiogenesis. 2010;13:189–202.

54. Patel SK, Williams J, Janjic JM. Cell labeling for 19F MRI: new and improved approach to perfluorocarbon nanoemulsion design. Biosensors. 2013;3:341–59.

55. Temme S, Grapentin C, Quast C, et al. Noninvasive imaging of early venous thrombosis by 19F magnetic resonance Imaging with targeted perfluorocarbon nanoemulsions. Circulation. 2015;131:1405–14.

56. Lemaire L, Bastiat G, Franconi F, Lautram N, Duong Thi Dan T, Garcion E, Saulnier P, Benoit JP. Perfluorocarbon-loaded lipid nanocapsules as oxygen sensors for tumor tissue pO2 assessment. Eur J Pharm Biopharm. 2013;84:479–86.

57. Patel SK, Zhang Y, Pollock JA, Janjic JM. Cyclooxygenase-2 inhibiting perfluoropoly (ethylene glycol) Ether theranostic nanoemulsions—*in vitro* study. PLoS One. 2013. doi:10.1371/journal.pone.0055802.

58. Vasudeva K, Andersen K, Zeyzus-Johns B, Hitchens TK, Patel SK, Balducci A, Janjic JM, Pollock JA. Imaging neuroinflammation *in vivo* in a neuropathic pain rat model with near-infrared fluorescence and 19F magnetic resonance. PLoS One. 2014. doi:10.1371/journal.pone.0090589.

59. Wang Y-G, Kim H, Mun S, Kim D, Choi Y. Indocyanine green-loaded perfluorocarbon nanoemulsions for bimodal 19F-magnetic resonance/nearinfrared fluorescence imaging and subsequent phototherapy. Quant Imaging Med Surg. 2013;3:132–40.

60. Bae PK, Jung J, Lim SJ, Kim D, Kim S-K, Chung BH. Bimodal perfluorocarbon nanoemulsions for nasopharyngeal carcinoma targeting. Mol Imaging Biol MIB Off Publ Acad Mol Imaging. 2013;15:401–10.

61. Hu G, Lijowski M, Zhang H, et al. Imaging of Vx-2 rabbit tumors with αvβ3-integrin-targeted 111In nanoparticles. Int J Cancer. 2007;120:1951–7.

62. Fabiilli ML, Piert MR, Koeppe RA, Sherman PS, Quesada CA, Kripfgans OD. Assessment of the biodistribution of an [18F]FDG-loaded perfluorocarbon double emulsion using dynamic micro-PET in rats. Contrast Media Mol Imaging. 2013;8:366–74.

63. Sanchez VC, Jachak A, Hurt RH, Kane AB. Biological interactions of graphene-family nanomaterials: an interdisciplinary review. Chem Res Toxicol. 2012;25:15–34.

64. Bussy C, Ali-Boucetta H, Kostarelos K. Safety considerations for graphene: lessons learnt from carbon nanotubes. Acc Chem Res. 2013;46:692–701.

65. Zhang Y, Petibone D, Xu Y, Mahmood M, Karmakar A, Casciano D, Ali S, Biris AS. Toxicity and efficacy of carbon nanotubes and graphene: the utility of carbon-based nanoparticles in nanomedicine. Drug Metab Rev. 2014;46:232–46.

66. Godwin H, Nameth C, Avery D, et al. Nanomaterial categorization for assessing risk potential to facilitate regulatory decision-making. ACS Nano. 2015;9:3409–17.

67. Bhattacharya K, Mukherjee SP, Gallud A, Burkert SC, Bistarelli S, Bellucci S, Bottini M, Star A, Fadeel B. Biological interactions of carbon-based nanomaterials: from coronation to degradation. Nanomedicine Nanotechnol Biol Med. 2015. doi:10.1016/j.nano.2015.11.011.

68. Ema M, Gamo M, Honda K. A review of toxicity studies of single-walled carbon nanotubes in laboratory animals. Regul Toxicol Pharmacol. 2016;74:42–63.

69. Cole LE, Ross RD, Tilley JM, Vargo-Gogola T, Roeder RK. Gold nanoparticles as contrast agents in x-ray imaging and computed tomography. Nanomed. 2015;10:321–41.

70. Li W, Chen X. Gold nanoparticles for photoacoustic imaging. Nanomed. 2015;10:299–320.

71. Her S, Jaffray DA, Allen C Gold nanoparticles for applications in cancer radiotherapy: mechanisms and recent advancements. Adv Drug Deliv Rev. doi:10.1016/j.addr.2015.12.012.

72. Singh M, Harris-Birtill DCC, Markar SR, Hanna GB, Elson DS. Application of gold nanoparticles for gastrointestinal cancer theranostics: a systematic review. Nanomedicine Nanotechnol Biol Med. 2015;11:2083–98.

73. Zhao J, Lee P, Wallace M, Melancon M. Gold nanoparticles in cancer therapy: efficacy, biodistribution, and toxicity. Curr Pharm Des. 2015;21:4240–51.

74. Ferro-Flores G, Ocampo-García B, Santos-Cuevas C, María Ramírez F, Azorín-Vega E, Meléndez-Alafort L. Theranostic radiopharmaceuticals based on gold nanoparticles labeled with ^{177}Lu and conjugated to peptides. Curr Radiopharm. 2015;8:150–9.

75. Ferro-Flores G, Ocampo-García B, Santos-Cuevas C, Morales-Avila E, Azorín-Vega E. Multifunctional radiolabeled nanoparticles for targeted therapy. Curr Med Chem. 2013;21:124–38.

76. Xie H, Wang ZJ, Bao A, Goins B, Phillips WT. *In vivo* PET imaging and biodistribution of radiolabeled gold nanoshells in rats with tumor xenografts. Int J Pharm. 2010;395:324–30.

77. Shao X, Zhang H, Rajian JR, Chamberland DL, Sherman PS, Quesada CA, Koch AE, Kotov NA, Wang X. 125I-labeled gold nanorods for targeted imaging of inflammation. ACS Nano. 2011;5:8967–73.

78. Yang M, Cheng K, Qi S, Liu H, Jiang Y, Jiang H, Li J, Chen K, Zhang H, Cheng Z. Affibody modified and radiolabeled gold–iron oxide hetero-nanostructures for tumor PET, optical and MR imaging. Biomaterials. 2013;34:2796–806.

79. Karmani L, Labar D, Valembois V, et al. Antibody-functionalized nanoparticles for imaging cancer: influence of conjugation to gold nanoparticles on the biodistribution of 89Zr-labeled cetuximab in mice. Contrast Media Mol Imaging. 2013;8:402–8.

80. Zhao Y, Sultan D, Detering L, Cho S, Sun G, Pierce R, Wooley KL, Liu Y. Copper-64-alloyed gold nanoparticles for cancer imaging: improved radiolabel stability and diagnostic accuracy. Angew Chem Int Ed. 2014;53:156–9.

81. Frigell J, García I, Gómez-Vallejo V, Llop J, Penadés S. 68Ga-labeled gold glyconanoparticles for exploring Blood–brain barrier permeability: preparation, biodistribution studies, and improved brain uptake via neuropeptide conjugation. J Am Chem Soc. 2014;136:449–57.

82. Felber M, Bauwens M, Mateos JM, Imstepf S, Mottaghy FM, Alberto R. 99mTc radiolabeling and biological evaluation of nanoparticles functionalized with a versatile coating ligand. Chem – Eur J . 2015;21:6090–9.

83. Felber M, Alberto R. 99mTc radiolabelling of Fe3O4–Au core–shell and Au–Fe3O4 dumbbell-like nanoparticles. Nanoscale. 2015;7:6653–60.

84. Zhang Z, Liu Y, Jarreau C, Welch MJ, Taylor J-SA. Nucleic acid-directed self-assembly of multifunctional gold nanoparticle imaging agents. Biomater Sci. 2013;1:1055–64.

85. Black KCL, Akers WJ, Sudlow G, Xu B, Laforest R, Achilefu S. Dual-radiolabeled nanoparticle SPECT probes for bioimaging. Nanoscale. 2014;7:440–4.

86. Rambanapasi C, Barnard N, Grobler A, Buntting H, Sonopo M, Jansen D, Jordaan A, Steyn H, Zeevaart JR. Dual radiolabeling as a technique to track nanocarriers: the case of gold nanoparticles. Molecules. 2015;20:12863–79.

87. Luna-Gutiérrez M, Ferro-Flores G, Ocampo-García BE, Santos-Cuevas CL, Jiménez-Mancilla N, De León-Rodríguez LM, Azorín-Vega E, Isaac-Olivé K. A therapeutic system of 177Lu-labeled gold nanoparticles-RGD internalized in breast cancer cells. J Mex Chem Soc. 2013;57:212–9.

88. Vilchis-Juárez A, Ferro-Flores G, Santos-Cuevas C, Morales-Avila E, Ocampo-García B, Díaz-Nieto L, Luna-Gutiérrez M, Jiménez-Mancilla N, Pedraza-López M, Gómez-Oliván L. Molecular targeting radiotherapy with cyclo-RGDfK(C) peptides conjugated to 177Lu-labeled gold nanoparticles in tumor-bearing mice. J Biomed Nanotechnol. 2014;10:393–404.

89. Bouziotis P, Psimadas D, Tsotakos T, Stamopoulos D, Tsoukalas C. Radiolabeled iron oxide nanoparticles as dual-modality SPECT/MRI and PET/MRI agents. Curr Top Med Chem. 2013;12:2694–702.

90. Pérez-Campaña C, Gómez-Vallejo V, Martin A, Sebastián ES, Moya SE, Reese T, Ziolo RF, Llop J. Tracing nanoparticles *in vivo*: a new general synthesis of positron emitting metal oxide nanoparticles by proton beam activation. Analyst. 2012;137:4902–6.

91. Pérez-Campaña C, Gómez-Vallejo V, Puigivila M, Martín A, Calvo-Fernández T, Moya SE, Ziolo RF, Reese T, Llop J. Biodistribution of different sized nanoparticles assessed by

positron emission tomography: a general strategy for direct activation of metal oxide particles. ACS Nano. 2013;7:3498–505.

92. Tomalia DA, Baker H, Dewald J, Hall M, Kallos G, Martin S, Roeck J, Ryder J, Smith P. A new class of polymers: starburst-dendritic macromolecules. Polym J. 1985;17:117–32.

93. Ghobril C, Lamanna G, Kueny-Stotz M, Garofalo A, Billotey C, Felder-Flesch D. Dendrimers in nuclear medical imaging. New J Chem. 2012;36:310–23.

94. Röglin L, Lempens EHM, Meijer EW. A synthetic "tour de force": well-defined multivalent and multimodal dendritic structures for biomedical applications. Angew Chem Int Ed Engl. 2011;50:102–12.

95. Cheng Y, Zhao L, Li Y, Xu T. Design of biocompatible dendrimers for cancer diagnosis and therapy: current status and future perspectives. Chem Soc Rev. 2011;40:2673–703.

96. Ghai A, Singh B, Panwar Hazari P, Schultz MK, Parmar A, Kumar P, Sharma S, Dhawan D, Kumar Mishra A. Radiolabeling optimization and characterization of 68Ga labeled DOTA–polyamido-amine dendrimer conjugate – animal biodistribution and PET imaging results. Appl Radiat Isot. 2015;105:40–6.

97. McNelles SA, Knight SD, Janzen N, Valliant JF, Adronov A. Synthesis, radiolabeling, and *in vivo* imaging of PEGylated high-generation polyester dendrimers. Biomacromolecules. 2015;16:3033–41.

98. Laznickova A, Biricova V, Laznicek M, Hermann P. Mono(pyridine-N-oxide) DOTA analog and its G1/G4-PAMAM dendrimer conjugates labeled with 177Lu: radiolabeling and biodistribution studies. Appl Radiat Isot. 2014;84:70–7.

99. Kovacs L, Tassano M, Cabrera M, Zamboni CB, Fernández M, Anjos RM, Cabral P. Development of 177Lu-DOTA-dendrimer and determination of its effect on metal and Ion levels in tumor tissue. Cancer Biother Radiopharm. 2015. doi:10.1089/cbr.2014.1675.

100. Zhao L, Zhu J, Cheng Y, Xiong Z, Tang Y, Guo L, Shi X, Zhao J. Chlorotoxin-conjugated multifunctional dendrimers labeled with radionuclide 131I for single photon Emission computed tomography imaging and radiotherapy of gliomas. ACS Appl Mater Interfaces. 2015;7:19798–808.

101. Musyanovych A, Landfester K. Polymer micro- and nanocapsules as biological carriers with multifunctional properties. Macromol Biosci. 2014;14:458–77.

102. Cahouet A, Denizot B, Hindré F, Passirani C, Heurtault B, Moreau M, Le Jeune J, Benoît J. Biodistribution of dual radiolabeled lipidic nanocapsules in the rat using scintigraphy and gamma counting. Int J Pharm. 2002;242:367–71.

103. Jestin E, Mougin-Degraef M, Faivre-Chauvet A, Remaud-Le Saëc P, Hindre F, Benoit JP, Chatal JF, Barbet J, Gestin JF. Radiolabeling and targeting of lipidic nanocapsules for applications in radioimmunotherapy. Q J Nucl Med Mol Imaging Off Publ Ital Assoc Nucl Med AIMN Int Assoc Radiopharmacol IAR Sect Soc Radiopharm Chem Biol. 2007;51:51–60.

104. de Assis DN, Mosqueira VCF, Vilela JMC, Andrade MS, Cardoso VN. Release profiles and morphological characterization by atomic force microscopy and photon correlation spectroscopy of 99mTechnetium-fluconazole nanocapsules. Int J Pharm. 2008;349:152–60.

105. Pereira MA, Mosqueira VCF, Vilela JMC, Andrade MS, Ramaldes GA, Cardoso VN. PLA-PEG nanocapsules radiolabeled with 99mTechnetium-HMPAO: release properties and physicochemical characterization by atomic force microscopy and photon correlation spectroscopy. Eur J Pharm Sci Off J Eur Fed Pharm Sci. 2008;33:42–51.

106. Pereira MA, Mosqueira VCF, Carmo VAS, Ferrari CS, Reis ECO, Ramaldes GA, Cardoso VN. Biodistribution study and identification of inflammatory sites using nanocapsules labeled with (99m)Tc-HMPAO. Nucl Med Commun. 2009;30:749–55.

107. Vicente S, Goins BA, Sanchez A, Alonso MJ, Phillips WT. Biodistribution and lymph node retention of polysaccharide-based immunostimulating nanocapsules. Vaccine. 2014;32:1685–92.

108. Sercombe L, Veerati T, Moheimani F, Wu SY, Sood AK, Hua S. Advances and challenges of liposome assisted drug delivery. Front Pharmacol. 2015. doi:10.3389/fphar.2015.00286.

109. Boerman OC, Laverman P, Oyen WJ, Corstens FH, Storm G. Radiolabeled liposomes for scintigraphic imaging. Prog Lipid Res. 2000;39:461–75.
110. Goins BA. Radiolabeled lipid nanoparticles for diagnostic imaging. Expert Opin Med Diagn. 2008;2:853–73.
111. Phillips WT, Bao A, Sou K, Li S, Goins B. Radiolabeled liposomes as drug delivery nano-theranostics. In: Li C, Tian M, editors. Drug Delivery Applications of Noninvasive Imaging: Validation from Biodistribution to Sites of Action. Hoboken, NJ. 2013. p 252–67.
112. De Barros ALB, Mota LDG, Coelho MMA, Corrêa NCR, De Góes AM, Oliveira MC, Cardoso VN. Bombesin encapsulated in long-circulating pH-sensitive liposomes as a radio-tracer for breast tumor identification. J Biomed Nanotechnol. 2015;11:342–50.
113. Ogawa M, Umeda IO, Kosugi M, Kawai A, Hamaya Y, Takashima M, Yin H, Kudoh T, Seno M, Magata Y. Development of 111In-labeled liposomes for vulnerable atherosclerotic plaque imaging. J Nucl Med. 2014;55:115–20.
114. Ogawa M, Uchino R, Kawai A, Kosugi M, Magata Y. PEG modification on 111In-labeled phosphatidyl serine liposomes for imaging of atherosclerotic plaques. Nucl Med Biol. 2015;42:299–304.
115. Bandekar A, Zhu C, Jindal R, Bruchertseifer F, Morgenstern A, Sofou S. Anti–prostate-specific membrane antigen liposomes loaded with 225Ac for potential targeted antivascular α-particle therapy of cancer. J Nucl Med. 2014;55:107–14.
116. Petersen AL, Henriksen JR, Binderup T, Elema DR, Rasmussen PH, Hag AM, Kjær A, Andresen TL. *In vivo* evaluation of PEGylated 64Cu-liposomes with theranostic and radio-therapeutic potential using micro PET/CT. Eur J Nucl Med Mol Imaging. 2015;43:941.
117. Thukral DK, Dumoga S, Mishra AK. Solid lipid nanoparticles: promising therapeutic nano-carriers for drug delivery. Curr Drug Deliv. 2014;11:771–91.
118. Naseri N, Valizadeh H, Zakeri-Milani P. Solid lipid nanoparticles and nanostructured lipid carriers: structure, preparation and application. Adv Pharm Bull. 2015;5:305–13.
119. Ezzati Nazhad Dolatabadi J, Valizadeh H, Hamishehkar H. Solid lipid nanoparticles as effi-cient drug and gene delivery systems: recent breakthroughs. Adv Pharm Bull. 2015;5:151–9.
120. Videira MA, Botelho MF, Santos AC, Gouveia LF, de Lima JJP, Almeida AJ. Lymphatic uptake of pulmonary delivered radiolabelled solid lipid nanoparticles. J Drug Target. 2002;10:607–13.
121. Reddy LH, Sharma RK, Chuttani K, Mishra AK, Murthy RR. Etoposide-incorporated tripal-mitin nanoparticles with different surface charge: Formulation, characterization, radiolabel-ing, and biodistribution studies. AAPS J. 2004;6:55–64.
122. Harivardhan Reddy L, Sharma RK, Chuttani K, Mishra AK, Murthy RSR. Influence of administration route on tumor uptake and biodistribution of etoposide loaded solid lipid nanoparticles in Dalton's lymphoma tumor bearing mice. J Control Release. 2005;105:185–98.
123. Tiwari R, Pathak K. Nanostructured lipid carrier versus solid lipid nanoparticles of simvas-tatin: comparative analysis of characteristics, pharmacokinetics and tissue uptake. Int J Pharm. 2011;415:232–43.
124. Varshosaz J, Ghaffari S, Mirshojaei SF, et al. Biodistribution of amikacin solid lipid nanopar-ticles after pulmonary delivery. BioMed Res Int. 2013;2013:e136859.
125. Banerjee I, De K, Chattopadhyay S, Bandyopadhyay AK, Misra M. An easy and effective method for radiolabelling of solid lipid nanoparticles. J Radioanal Nucl Chem. 2014;302:837–43.
126. Andreozzi E, Seo JW, Ferrara K, Louie A. A novel method to label solid lipid nanoparticles (SLNs) with 64Cu for positron emission tomography (PET) imaging. Bioconjug Chem. 2011;22:808–18.
127. Torchilin VP. Micellar nanocarriers: pharmaceutical perspectives. Pharm Res. 2006;24:1–16.

128. Benezra M, Hambardzumyan D, Penate-Medina O, et al. Fluorine-labeled dasatinib nanoformulations as targeted molecular imaging probes in a PDGFB-driven murine glioblastoma model. Neoplasia. 2012;14:1132–43.

129. Nakao R, Schou M, Halldin C. Rapid metabolite analysis of positron emission tomography radioligands by direct plasma injection combining micellar cleanup with high submicellar liquid chromatography with radiometric detection. J Chromatogr A. 2012;1266:76–83.

130. Xiao W, Luo J, Jain T, Riggs JW, Tseng HP, Henderson PT, Cherry SR, Rowland D, Lam KS. Biodistribution and pharmacokinetics of a telodendrimer micellar paclitaxel nanoformulation in a mouse xenograft model of ovarian cancer. Int J Nanomedicine. 2012;7:1587–97.

131. Xiao Y, Hong H, Javadi A, Engle JW, Xu W, Yang Y, Zhang Y, Barnhart TE, Cai W, Gong S. Multifunctional unimolecular micelles for cancer-targeted drug delivery and positron emission tomography imaging. Biomaterials. 2012;33:3071–82.

132. Cho H, Lai TC, Kwon GS. Poly(ethylene glycol)-block-poly(ε-caprolactone) micelles for combination drug delivery: evaluation of paclitaxel, cyclopamine and gossypol in intraperitoneal xenograft models of ovarian cancer. J Control Release Off J Control Release Soc. 2013;166:1–9.

133. Guo J, Hong H, Chen G, Shi S, Zheng Q, Zhang Y, Theuer CP, Barnhart TE, Cai W, Gong S. Image-guided and tumor-targeted drug delivery with radiolabeled unimolecular micelles. Biomaterials. 2013;34:8323–32.

134. Kao H-W, Chan C-J, Chang Y-C, Hsu Y-H, Lu M, Shian-Jy Wang J, Lin Y-Y, Wang S-J, Wang H-E. A pharmacokinetics study of radiolabeled micelles of a poly(ethylene glycol)-block-caprolactone copolymer in a colon carcinoma-bearing mouse model. Appl Radiat Isot. 2013;80:88–94.

135. Hong Y, Zhu H, Hu J, Lin X, Wang F, Li C, Yang Z. Synthesis and radiolabeling of (111) In-core-cross linked polymeric micelle-octreotide for near-infrared fluoroscopy and single photon emission computed tomography imaging. Bioorg Med Chem Lett. 2014;24:2781–5.

136. Jensen AI, Binderup T, Kumar EKP, Kjær A, Rasmussen PH, Andresen TL. Positron emission tomography based analysis of long-circulating cross-linked triblock polymeric micelles in a U87MG mouse xenograft model and comparison of DOTA and CB-TE2A as chelators of copper-64. Biomacromolecules. 2014;15:1625–33.

137. Lesniak WG, Sikorska E, Shallal H, Azad BB, Lisok A, Pullambhatla M, Pomper MG, Nimmagadda S. Structural characterization and *in vivo* evaluation of β-hairpin peptidomimetics as specific CXCR4 imaging agents. Mol Pharm. 2015;12:941–53.

138. Seo JW, Ang J, Mahakian LM, et al. Self-assembled 20-nm 64Cu-micelles enhance accumulation in rat glioblastoma. J Control Release. 2015;220(Part A):51–60.

139. Starmans LWE, Hummelink MAPM, Rossin R, Kneepkens ECM, Lamerichs R, Donato K, Nicolay K, Grüll H. 89Zr- and Fe-labeled polymeric micelles for dual modality PET and T1-weighted MR imaging. Adv Healthc Mater. 2015;4:2137–45.

140. Shih Y-H, Peng C-L, Chiang P-F, Lin W-J, Luo T-Y, Shieh M-J. Therapeutic and scintigraphic applications of polymeric micelles: combination of chemotherapy and radiotherapy in hepatocellular carcinoma. Int J Nanomedicine. 2015;10:7443–54.

141. Ruiz-de-Angulo A, Zabaleta A, Gómez-Vallejo V, Llop J, Mareque-Rivas JC. Microdosed lipid-coated (67)Ga-magnetite enhances antigen-specific immunity by image tracked delivery of antigen and CpG to lymph nodes. ACS Nano. 2016. doi:10.1021/acsnano.5b07253.

142. You J, Zhao J, Wen X, Wu C, Huang Q, Guan F, Wu R, Liang D, Li C. Chemoradiation therapy using cyclopamine-loaded liquid–lipid nanoparticles and lutetium-177-labeled core-crosslinked polymeric micelles. J Control Release. 2015;202:40–8.

143. Guo J, Hong H, Chen G, Shi S, Nayak TR, Theuer CP, Barnhart TE, Cai W, Gong S. Theranostic unimolecular micelles based on brush-shaped amphiphilic block copolymers for tumor-targeted drug delivery and positron Emission tomography imaging. ACS Appl Mater Interfaces. 2014;6:21769–79.

144. Petitjean A, Khoury RG, Kyritsakas N, Lehn J-M. Dynamic devices shape switching and substrate binding in ion-controlled nanomechanical molecular tweezers. J Am Chem Soc. 2004;126:6637–47.
145. Tang C, Ulijn RV, Saiani A. Effect of glycine substitution on fmoc–diphenylalanine self-assembly and gelation properties. Langmuir. 2011;27:14438–49.
146. He C, Han Y, Fan Y, Deng M, Wang Y. Self-assembly of Aβ-based peptide amphiphiles with double hydrophobic chains. Langmuir. 2012;28:3391–6.
147. Ziserman L, Lee H-Y, Raghavan SR, Mor A, Danino D. Unraveling the mechanism of nano-tube formation by chiral self-assembly of amphiphiles. J Am Chem Soc. 2011;133:2511–7.
148. Ku T-H, Chien M-P, Thompson MP, Sinkovits RS, Olson NH, Baker TS, Gianneschi NC. Controlling and switching the morphology of micellar nanoparticles with enzymes. J Am Chem Soc. 2011;133:8392–5.
149. Dong H, Dube N, Shu JY, Seo JW, Mahakian LM, Ferrara KW, Xu T. Long-circulating 15 nm micelles based on amphiphilic 3-helix peptide–PEG conjugates. ACS Nano. 2012;6:5320–9.
150. Chae PS, Gotfryd K, Pacyna J, et al. Tandem facial amphiphiles for membrane protein stabilization. J Am Chem Soc. 2010;132:16750–2.
151. Szilluweit R, Hoheisel TN, Fritzsche M, et al. Low-temperature preparation of tailored carbon nanostructures in water. Nano Lett. 2012;12:2573–8.
152. Méndez-Ardoy A, Guilloteau N, Di Giorgio C, Vierling P, Santoyo-González F, Ortiz Mellet C, García Fernández JM. β-cyclodextrin-based polycationic amphiphilic "click" clusters: effect of structural modifications in their DNA complexing and delivery properties. J Org Chem. 2011;76:5882–94.
153. McLaughlin CK, Hamblin GD, Sleiman HF. Supramolecular DNA assembly. Chem Soc Rev. 2011;40:5647.
154. Patwa A, Gissot A, Bestel I, Barthélémy P. Hybrid lipid oligonucleotide conjugates: synthesis, self-assemblies and biomedical applications. Chem Soc Rev. 2011;40:5844–54.
155. Rosemeyer H. Nucleolipids: natural occurrence, synthesis, molecular recognition, and supramolecular assemblies as potential precursors of life and bioorganic materials. Chem Biodivers. 2005;2:977–1063.
156. Barthélemy P. Nucleoside-based lipids at work: from supramolecular assemblies to biological applications. Comptes Rendus Chim. 2009;12:171–9.
157. Allain V, Bourgaux C, Couvreur P. Self-assembled nucleolipids: from supramolecular structure to soft nucleic acid and drug delivery devices. Nucleic Acids Res. 2012;40:1891–903.
158. Gissot A, Camplo M, Grinstaff MW, Barthélémy P. Nucleoside, nucleotide and oligonucleotide based amphiphiles: a successful marriage of nucleic acids with lipids. Org Biomol Chem. 2008;6:1324–33.
159. Chabaud P, Camplo M, Payet D, Serin G, Moreau L, Barthélémy P, Grinstaff MW. Cationic nucleoside lipids for gene delivery. Bioconjug Chem. 2006;17:466–72.
160. Ceballos C, Prata CAH, Giorgio S, Garzino F, Payet D, Barthélémy P, Grinstaff MW, Camplo M. Cationic nucleoside lipids based on a 3-nitropyrrole universal base for siRNA delivery. Bioconjug Chem. 2009;20:193–6.
161. Ceballos C, Khiati S, Prata CAH, Zhang X-X, Giorgio S, Marsal P, Grinstaff MW, Barthélémy P, Camplo M. Cationic nucleoside lipids derived from universal bases: a rational approach for siRNA transfection. Bioconjug Chem. 2010;21:1062–9.
162. Moreau L, Ziarelli F, Grinstaff MW, Barthélémy P. Self-assembled microspheres from f-block elements and nucleoamphiphiles. Chem Commun. 2006;21:661–1663.
163. Moreau L, Campins N, Grinstaff MW, Barthélémy P. A fluorocarbon nucleoamphiphile for the construction of actinide loaded microspheres. Tetrahedron Lett. 2006;47:7117–20.
164. Phillips WT, Rudolph AS, Goins B, Timmons JH, Klipper R, Blumhardt R. A simple method for producing a technetium-99m-labeled liposome which is stable *In Vivo*. Int J Rad Appl Instrum B. 1992;19:539–47.

165. Petersen AL, Binderup T, Jølck RI, Rasmussen P, Henriksen JR, Pfeifer AK, Kjær A, Andresen TL. Positron emission tomography evaluation of somatostatin receptor targeted 64Cu-TATE-liposomes in a human neuroendocrine carcinoma mouse model. J Control Release. 2012;160:254–63.
166. Orocio-Rodríguez E, Ferro-Flores G, Santos-Cuevas CL, Ramírez Fde M, Ocampo-García BE, Azorín-Vega E, Sánchez-García FM. Two novel nanosized radiolabeled analogues of somatostatin for neuroendocrine tumor imaging. J Nanosci Nanotechnol. 2015;15:4159–69.
167. Abou DS, Thorek DLJ, Ramos NN, Pinkse MWH, Wolterbeek HT, Carlin SD, Beattie BJ, Lewis JS. 89Zr-labeled paramagnetic octreotide-liposomes for PET-MR imaging of cancer. Pharm Res. 2013;30:878–88.
168. Arora G, Shukla J, Ghosh S, Maulik SK, Malhotra A, Bandopadhyaya G. PLGA nanoparticles for peptide receptor radionuclide therapy of neuroendocrine tumors: a novel approach towards reduction of renal radiation dose. PLoS One. 2012;7, e34019.

Index